DOE/NASA/2749-79/2 Vol 2
NASA CR-159671
C00-2749-43

Upgraded Automotive Gas Turbine Engine Design and Development Program Final Report

Edited By
C.E. Wagner and R.C. Pampreen
Chrysler Corporation
Detroit, Michigan 48288

June 1979

Prepared for
National Aeronautics and Space Administration
Lewis Research Center
Under Contract EY-76-C-02-2749.A011

for
U.S. Department of Energy
Office of Conservation and Solar Applications
Division of Transportation Energy Conservation

DOE/NASA/2749-79/2 Vol 2
NASA CR-159671
C00-2749-43

Upgraded Automotive Gas Turbine Engine Design and Development Program Final Report

Vol. 2

Edited By
C. E. Wagner and R.C. Pampreen
Chrysler Corporation
Detroit, Michigan 48288

June 1979

Prepared for
National Aeronautics and Space Administration
Lewis Research Center
Cleveland, Ohio 44135
Under Contract EY-76-C-02-2749.A011

for
U.S. Department of Energy
Office of Conservation and Solar Applications
Division of Transportation Energy Conservation
Washington, D.C. 20545
Under Interagency Agreement EC 77-A-31-1040

Acknowledgement

This report covers all work performed under DOE Contract No. EY-76-C-02-2749.A011 from November, 1972, to June, 1979. The contract was initiated by the U.S. Environmental Protection Agency, was subsequently transferred to the Heat Engine Systems Branch, Division of Transportation Energy Conservation of the U.S. Department of Energy. Mr. Charles E. Wagner was the Chrysler Corporation Program Manager. Mr. Paul T. Kerwin, NASA-Lewis Research Center has been the Project Officer since 1977. Previous Project Officers were David G. Evans, NASA-Lewis Research Center, and Thomas M. Sebestyen, EPA. Mr. Robert A. Mercure, DOE -Division of Transportation Energy Conservation, has been the Project Coordinator since the technical management was turned over to NASA-Lewis Research Center through an interagency agreement.

Contributors to this report were: A. Billington, T Golec, J.V. Gross, H.P. LeFevre, E.M. Kohl, H.E. Koontz, J.J. Lewakowski, C.H. Mader, T.D. Nogle, E.Z. Trieskey (Laboratory Personnel), K Buyukataman, A.A. Ladhani, F. Dosenberger, D.S. Musgrave, R.C. Pampreen, L.J. Pritchard, N.W. Sparks, R. Swiatek (Design and Analysis), C. Belleau, J.M. Corwin, F.A. Hagen, J.R. Kirberg, A. Roy, R.J. Warren and P.J. Willson (Materials), and R.W. Bloor, R.A. Jaynes, R F. Pauley and L. Sevek (Drafting).

A number of companies participated in this program, and their contributions are acknowledged. Ceramic material support was provided by Carborundum, Inc., and the ceramic regenerator cores were made by Corning Glass Works. The Garrett Corporation provided use of a rubber-mold manufacturing process for casting turbine rotors. Pratt and Whitney Aircraft Group, Government Products Division, provided use of the Gatorizing process for casting turbine rotors. Engine control work was performed by the Garrett Corporation and Ultra, Inc. The testing and analysis of the gas generator and power turbine shafting and the design of the air bearing were carried out by Mechanical Technology Incorporated. Aerodynamic model testing of the power turbine exhaust diffuser and of the flow distribution of the regenerator core were conducted at Creare, Incorporated. Three aerodynamic consultants were used on the program. Dr. O.E. Balje (Consultant 1 in the report) and Pratt and Whitney Aircraft of Canada (Consultant 2) provided consulting services for the compressor-turbine, and Noel Penny Turbines Ltd. (Consultant 3) provided consultation on the power turbine and carried out an alternate design Many of the compressor and turbine parts were provided by the Atlas Tool Company and the Howmet Turbine Components Corporation.

Acknowledgement is also given to the engineering staff members of NASA-Lewis Research Center for their ongoing technical support of the program They include M.R. Galvas, T Katsanis, M.G Kofsfey, K.L. McLallin, R C. Nussle, R.J. Roelke J Winter, and R.Y. Wong.

Finally, the authors wish to express thier appreciation to J.N Kolman and others of Chrysler's Graphic Arts Department, and to S J. Piekarski, Supervisor, for the outstanding artwork and copy preparation evident in all four volumes of this report.

TABLE OF CONTENTS

TABLE OF CONTENTS (continued)

TABLE OF CONTENTS (continued)

Abstract

This is the second of four volumes of the contract final report, which summarizes all of the work performed in a government-sponsored Automotive Gas Turbine Development Program (D.O.E. Contract No. EY-76-C-02-2749.A011). In this second volume of the contract final report, results are presented for the design and development of an Upgraded Engine. The design incorporated technology advancements which resulted from development testing on the Baseline Engine.

The final engine performance with all retro-fitted components from the development program showed a value of 91 HP at design speed in contrast to the design value of 104 HP. The design-speed SFC was 0.53 versus the goal value of 0.44. The miss in power was primarily due to missing the efficiency targets of small-size turbomachinery. Most of the SFC deficit was attributed to missed goals in the heat recovery system relative to regenerator effectiveness and expected values of heat loss.

Vehicular fuel consumption, as measured on a chassis dynamometer, for a vehicle inertia weight of 3500 lbs., was 15 MPG for combined urban and highway driving cycles. The Baseline Engine achieved 8 MPG with a 4500 lb. vehicle. Even though the goal of 18.3 MPG was not achieved with the Upgraded Engine, there was an improvement in fuel economy of 46% over the Baseline Engine, for comparable vehicle inertia weight.

1.0 SUMMARY

Specific goals of this part of the program were to demonstrate an experimental gas-turbine-powered automobile which would meet the 1978 Federal Emissions Standards, have significantly improved fuel economy over the Baseline Engine, and be competitive in performance, reliability and potential manufacturing cost with the conventional piston-engine-powered, standard-size American automobile (3500-lb inertia weight). These goals were to be achieved by the design and development of an Upgraded Engine, which was to incorporate concepts evaluated on the Baseline Engine in an extensive component development program.

Initial testing of the Upgraded Engine took place on 13 July 1976. This engine, though mechanically sound, started out about 43% deficient in power. The principal problems were the low efficiencies of the aerodynamic components. The efficiency deficits were consequences of the compromises made to satisfy packaging/interface and other design constraints. Changes to the compressor and to the compressor-turbine, along with some reductions in leakage and pressure drop, reduced the power deficiency to about 25%. To fully eliminate these deficiencies, major redesigns were carried out for the compressor-turbine and power turbine. These redesigns were made possible by reconsideration and relaxation of stress and overspeed constraints.

The final engine performance with all retro-fitted components showed a value of 91 HP at design speed in contrast to the design value of 104 HP. The design-speed SFC was 0.53 versus the goal of 0.44. During the program, the original goals were revised as a result of a re-assessment of the component efficiencies to values that were thought to be more likely in turbomachinery of this size. This resulted in revised design-point goals of 95.6 HP at an SFC of 0.49. Detailed examination of final engine data indicated that even the revised turbine efficiency goals could not be met in this size. Full evaluation would take place on component rig tests at NASA-Lewis.

Cycle analysis showed that, at low speeds, most of the SFC deficit came from heat loss. At 60% speed at constant power, for example, 73% of the SFC deficit was due to heat loss. Of this figure, 58% was attributed to lack of heat recovery due to bulkhead-cooling heat loss; the rest could be attributed to a miss in regenerator effectiveness of 2 points.

Vehicular fuel consumption tests for both cold '75, hot '74, and FEC were conducted on chassis rolls for an inertia weight of 3500 pounds. Fuel consumed (gasoline) was weighed directly. The best combined cycle fuel economy was 15 MPG.

2.0 INTRODUCTION

This part of the contract consisted of the design, build and development of an Upgraded Engine which incorporates the component improvements evaluated on the Baseline Engine. This was identified as Task 7.0. The design part of this work was identified as Task 7.1. The engine build and development work was identified as Task 7.5. Installation of the engine into three Upgraded Vehicles and vehicle testing were identified as Task 8.0. Vehicle testing consisted of control work and documentation of vehicle performance.

3.0 ENGINE DESIGN FEATURES

The prominent design features which distinguish the Upgraded Engine from the Baseline Engine are:

1. Higher cycle temperature
2. Power augmentation
3. Power-turbine-driven accessories (Free rotor)
4. Single regenerator
5. Air bearing

The maximum cycle temperature for the Upgraded Engine is 1925°F versus the value of 1850°F for the Baseline Engine. The design power is 104 HP without power augmentation and 123 HP with augmentation. The Baseline Engine was rated at 150 HP without augmentation. The engine accessories for the Baseline Engine were driven off of the gas generator shaft. For the Upgraded Engine, these accessories are driven off of the power turbine. This is referred to as the "Free-Rotor" concept. The Upgraded Engine has a single regenerator, whereas the Baseline Engine had two regenerators. A general description of the Upgraded Engine is given on Table 1.

3.1 Cycle Characterization

The characterization of the engine cycle in the unaugmented mode is given on Tables 2a and 2b for the metric and English units, respectively. The engine station numbers are identified on Table 3.

At idle, the variable inlet guides (VIGV) are activated to a +60-degree setting (swirl in direction of engine rotation). Vehicle fuel economy is improved through lowered values of mass flow and pressure ratio and maintenance of high turbine inlet temperature. At maximum power, the VIGV are set to —30 degrees (swirl opposite engine rotation). This was intended to increase power from 104 HP to 112 HP. For operation above 60°F, water injection further augments power to 123 HP on a standard 85°F-day with zero relative humidity. The cycle characterizations for VIGV-augmented power are given on Table 4.

3.2 Water Injection

Water injection is simple to implement, requiring no more than a water fogging nozzle at the air intake bowl and a water tank pressurized from the compressor discharge. However, a water flow rate slightly larger than the fuel flow rate is needed in order to get 10% boost in maximum engine power Therefore, to keep the water tank a reasonable size, the injection system is only activated at maximum power, which is normally a small fraction of total operating time. Use of water injection only at ambients greater than 15°C (60°F) serves to conserve water and obviates the need for freezing protection. Commercial grade distilled water is used to minimize compressor performance deterioration from scale deposits. In addition, the forward, or inducer, section of the compressor is made from steel to minimize the effect of water-droplet erosion.

3.3 VIGV

Augmentation with VIGV is accomplished by imparting swirl to the air at the compressor inlet opposite to the direction of rotation. In this way, the change in angular momentum is increased for the fluid passing through the compressor. This results in increased pressure ratio and flow as though the compressor were running faster. Swirl in the plus or co-rotational direction is used at low vehicle speeds to regulate engine power while still maintaining engine temperature and efficiency. Positive swirl reduces pressure rise and flow as though the compressor were running slower. The guide vane is an articulated configuration with a stationary forward section and a movable flap.

3.4 Free Rotor

A "free rotor" configuration is a design in which all power take-offs have been removed from the gas generator rotor. Thus all engine auxiliaries such as the oil pump, atomizing air pump and regenerator are driven from the power turbine instead of the gas generator. Such a free-rotor design has a number of advantages.

a) It is conducive to the use of a gas bearing. By removing a fraction of the bearing load due to power take-off, the bearing requirements are eased.

b) It is quieter. Previous power take-off drives have been the source of identifiable gear noise.

c) It is potentially less costly. The high-speed gear system of a geared rotor is a significant cost item.

d) Vehicle driveability is improved. Although tests and calculations show small improvement in rotor response, experience with a prototype system suggests improved vehicle "feel". In particular, the combination of a free rotor and gas bearing will have superior cold-starting performance.

At the same time there are a number of disadvantages and consequences for the Upgraded Engine as a result of the free-rotor choice.

a) The accessory drive is complex. Some means had to be provided to supply lubricating oil to the gas generator and atomizing air to the burner during the start sequence prior to the power turbine assuming the drive. It was presumed that technology advances will eventually eliminate the need for these services during the initial start period and that this disadvantage will not exist for future free-rotor engines.

b) The fuel control philosophy is changed. Previous fuel controls have been based on a mechanical governor driven from the gas generator. Removal of the accessory drive requires an electronic speed sensor as input to the fuel control. This is a consequence of the free-rotor choice, but is not a disadvantage for the Upgraded Engine since other considerations resulted in the choice of an electronic fuel control. Under other circumstances, the lack of a convenient mechanical drive could be a disadvantage as a control limitation.

c) The thermal loading distribution is altered. An air bearing being cooled by compressor discharge air at 232°C (450°F) maximum as compared to the oil bearing running at a maximum oil temperature of 121°C (250°F) will cause higher temperatures in the shaft, bearing and support structure during both running and soakback conditions.

During the initial stages of the design layout, these factors were recognized and weighed as to relative importance. On balance, it was decided that the advantages outweighed the disadvantages for the Upgraded Engine. Since the consequences of this choice are important, each of the above topics is discussed below.

3.4.1 Gas-Generator Bearings

The development of the bearing system for the gas generator is described in Ref. 1. The air bearings are physically larger than their oil counterparts because of their load-carrying characteristics. In fact, the front bearing is carried over as an oil bearing primarily because an air thrust bearing would be so large as to pose an inertia problem. Moreover the rear bearing in its design configuration contributes a small but measurable amount to the rotor inertia. If the bearing had to carry the additional radial load associated with a power take-off, a further rotor inertial penalty would be incurred. The additional size would also pose an awkward design problem since space in the vicinity of the compressor turbine nozzle and vortex is very limited. It is also worth mentioning that interest in gas bearing technology is in part in anticipation of its potential use in high temperature non-metallic applications.

3.4.2 Noise

Generally speaking, high speed gearing tends to create noise that is an annoyance in a vehicle. One high-speed pinion on the power turbine shaft is necessary, but the use of the free-rotor concept eliminates a second high-speed gear drive. The effect of this arrangement on noise is most noticeable at idle where the power turbine may be idling as low as 20% speed. On a geared-rotor engine, the gas generator never gets below 50% speed at idle, and its contribution to engine noise is appreciable.

3.4.3 Cost

Engine designs that minimize the noise problems of high-speed gearing require, among other features, high-quality precision gears and bearings that tend to be expensive. To the extent that the free-rotor design eliminates one such gear set, it represents a cost saving. Of course, as noted above, the accessory drive of the Upgraded Engine has become complex, and this implies a cost penalty. This complication would be unnecessary if the burner and the engine bearings could function without the atomizing air and oil pumps during the portion of the starting sequence prior to the time when the power turbine is driving the engine accessories. For oil supply, a simple oil storage system is one of several possible solutions that appears practical. Therefore the major obstacle to this simplification was the development of a low-emission burner that did not require supplementary air. Taking the long term view, then, it appeared that the free-rotor concept was consistent with an eventual simple, low-cost design.

3.4.4 Gas Generator Response Time

The time to accelerate the gas generator shaft from 50% to 100% speed (response time) was not to exceed the 1.25-second response time of the gas generator shaft of the Baseline Engine. Certain design differences between the two engines influenced this requirement. The impeller of the Upgraded Engine is backswept, the work coefficient of the compressor-turbine is 2.1, and the shaft has an air-film journal bearing. The impeller of the Baseline Engine is radial-bladed, the work coefficient of the compressor-turbine is 2.4, and the shaft has an oil-film journal bearing. On a dimensionless basis the gas generator of the Upgraded Engine would have proportionately larger polar moment of inertia. On the other hand, the lower parasitic loss of the air bearing would make more power available for acceleration.

The actual estimate of response time for the Upgraded Engine could not be accurately evaluated until the design was finished. Only after completion of the design could accurate values of the polar moments of inertia of the shaft and the turbomachinery be calculated and the integral of the angular equation of motion be evaluated. Response time is calculated from:

$$t = Ip \int (\Delta T)^{-1} \, d\omega$$

where t = Time, seconds

Ip = Polar moment of inertia, ft-lb-sec^2

ΔT = Acceleration torque, ft-lbs

ω = Angular velocity, rad/sec

However, in order to establish a design inertia goal, preliminary estimates of response time were calculated from values of inertia based on estimates of the anticipated sizes of the shaft and the turbomachinery. The integral of the equation of motion was estimated from acceleration data from the Baseline Engine. On the basis of these calculations, a design goal of 0.0117 in-lb-sec^2 was set for the total gas generator shaft assembly polar moment of inertia.

3.5 Housing Geometry

In the selection of the housing concept for the Upgraded Engine there were numerous factors to consider, many of them confining. For example, a prime requirement for the engine was good fuel economy, particularly at ordinary road load conditions. This required a large regenerator, and tended to conflict with a parallel approach to fuel economy - the compact car. The regenerator (or equally for a recuperator as well) is a bulky component and large heat exchangers become increasingly difficult to package in a conventional-vehicle engine-compartment. There was, however, a future potential for minimizing this situation through the use of high-pressure, high-temperature cycles. For the Upgraded Engine this option was not open.

3.5.1 Regenerator Configuration

In selecting the housing geometry, a choice had to be made whether to provide for a single or a multiregenerator configuration. The choice was not easy since, in addition to the obvious differences in unit sizes required, there were other differences such as leakage paths and overall costs to consider. Gas leakage paths, in spite of sophisticated regenerator seals, are a continual concern to the turbine engine designer. Two main considerations in determining the magnitude of these leaks are the length of sealing surface and the distortions of the housing as it is exposed to the various conditions of its operating range. The single regenerator has less sealing length but requires an asymmetrical housing. In addition, the single regenerator requires fewer parts, seals, drive gears, exhaust ducts, etc. This general subject has been discussed in Reference 2.

Reference to Figures 1a through 1d show that the single regenerator concept won out for the Upgraded engine. Probably the most significant factor in this selection was the installation of the regenerator in a non-vertical plane. Tilting the regenerator 20° from the vertical permitted the large, single regenerator to fit between the side rails and suspension of the vehicle. Locating the regenerator on the right-hand side of the compartment permitted the exhaust duct to be free of the steering components. The general overall geometry of the engine appeared to fit reasonably well into the available space as shown in Figure 1e.

3.5.2 Compressor Collector

Although the single regenerator solved the width problem, it created a length problem. The regenerator and compressor were now in conflict with one another. A radial compressor and an efficient radial diffuser take up considerable space in a radial direction. For dual regenerators it is conventional to put the compressor forward of the regenerator and provide simple ducting to get the air from the compressor discharge to the face of the regenerator. The space limitations for the engine did not permit this conventional approach, so the compressor was "tucked" in under the front of the regenerator with the result that the compressor diffuser must include a radial-to-axial bend prior to dumping into the collector duct. A somewhat unusual flow path for collecting the compressor discharge air was selected. The discharge air was moved radially inward in front of the diffuser cover and then periodically moved radially outboard into ducts. Two of these ducts - or passages - lead directly to the regenerator face through openings in the forward portion of the regenerator platform. The third duct provides a passage to the high-pressure bulkhead area for cooling both the bulkhead and the variable-power-turbine-nozzle mechanism.

With regard to bulkhead cooling, a choice can be made to use either the high-pressure compressor-discharge air or the low-pressure regenerator-discharge air for the cooling medium. These two media differ in temperature by the regenerator "ineffectiveness" of the order of 50°C. The choice was a debatable one involving many factors such as the direction and magnitude of the pressure difference across the variable power turbine nozzle stems and the resulting leakage. Probably the one factor most significant in selecting compressor-discharge air as the cooling source relates to the development potential of the engine. An obviously desirable direction of development is toward higher cycle temperatures. Such increases generally cause the cooling requirements of various parts to become more critical and it was deemed that even the relatively small 50°C-difference in favor of the compressor-discharge air could be significant in the development potential.

3.5.3 Front-Bearing Lubrication

One final comment on the gas generator assembly as it fits into and affects the housing geometry concerns the provision for supplying and draining the lubricating oil for the front bearing of the gas generator rotor. It was decided that external oil lines are preferable to internal ones. Internal lines require appropriate seals between the gas generator assembly and the housing, and this was considered to be an undesirable approach. In order to provide a lubricating oil path from the bearing to a fitting on the outside surface of the engine, a system of flanges and pilots was worked out. The solution for the oil drain is shown in Figure 2.

3.5.4 Thermal Insulation

A critical feature of the housing that represents a change from the Baseline configuration is the housing thermal insulation. It is essential to keep the structure temperature in bounds, excessive heat loss and the resultant waste of fuel has disastrous effects on fuel economy and engine-compartment temperatures. The Baseline Engine has metal insulation liners to contain the insulating material. Not only were these liners relatively expensive and difficult to install, but the insulation could easily become loose and migrate into the engine, interfering with seals and causing trouble. Considerable effort was expended in developing a "linerless" insulation that is, a molded insulation that can be cemented to the housing and can in itself form the flow passages within the housing and not erode from scrubbing action of the gas flow. Significant success was achieved through the Baseline Engine testing. The results are discussed in Volume 1 of the contract final report.

3.6 Power-Level Selection

The Upgraded Engine was initially conceived for an unaugmented design output of 120 horsepower (HP) and an augmented output of 150 HP. The aerodynamic features of the engine consisted of variable inlet guide vanes (VIGV), a radial-bladed compressor impeller and a compressor-turbine with a work coefficient of 2.4. The mechanical features consisted of a free-rotor gas generator, oil-lubricated bearings and two regenerator cores. The VIGV and the free rotor were features which differed from the Baseline Engine.

During the period of the turbomachinery design, the vehicle size and engine performance specifications were reviewed at the request of the EPA. Comparisons were made of power versus performance and fuel economy for vehicles of 3500-lb and 4200-lb test weights. The result of these studies was a decision to revise the power goals to 100 HP, unaugmented, and to 122 HP, augmented. The aerodynamic features of the final design selection consisted of VIGV, a backswept impeller and a compressor-turbine with a work coefficient of 2.1. The mechanical features consisted of a free rotor, an air-fed journal bearing for the gas generator, and a single regenerator core. In contrast, the Baseline Engine has no VIGV, a radial-bladed impeller, a compressor-turbine with a work coefficient of 2.4, accessories driven off the gas generator shaft, all oil-lubricated bearings, and two regenerator cores. These features are shown in a cutaway of the engine design in Fig. 3.

3.7 Outline of Report

This concludes the discussion of the prominent features which distinguish the Upgraded Engine from the Baseline Engine. The following sections discuss the aerodynamic design of the turbomachinery and the mechanical design of all the engine hardware. Sections 4-6 discuss the turbomachinery designs. Fig. 3B shows the modules into which the mechanical design discussions are divided (Sections 7-10). The regenerator design is discussed in Section 11, and the combustor is discussed in Section 12. The engine and vehicle performance estimate are presented in Section 13. The test and development work is discussed in Sections 14-20.

4.0 COMPRESSOR DESIGN

4.1 Aerodynamic Design

A preliminary design was carried out at Chrysler to identify flowpath specifications consistent with the regenerator core and VIGV interfaces. The results are summarized in Refe.ence 3. The aerodynamic design of the rotor blading and of the diffuser vane shapes was carried out at NASA. This section summarizes the final design results. Detailed discussion is presented in Reference 4.

The final compressor flowpath is shown in Figure 4. The velocity diagrams are shown in Figure 5. The blade loading plots are shown in Figure 6 for 18 blades. The channel diffuser configuration is shown in Figure 7. The deswirl vane shape and estimated loading are shown in Figure 8. The flow at the exit of the flared annular diffuser discharges into a collector with three differently-sized lobes. See Figure 9. The two largest lobes pass flow to the regenerator core; the smallest lobe passes flow through the bulkhead for cooling.

4.2 VIGV Design

The VIGV design was configured with the same vane shape as that of the vanes used in testing on the Baseline Engine. The trailing edge of the movable flap was located 2.2 chord lengths from the impeller leading edge. It was hoped that this large spacing would reduce inlet noise and the VIGV-rotor interaction losses that occurred with the Baseline Engine installation. Experimental evidence to support this is shown in References 5 and 6.

4.3 Intake-Housing Design

The engine intake was analyzed by an incompressible flow streamline calculation. The boundary conditions consisted of the filter box position, the exterior housing configuration, and the definition of the intake itself, as shown in Figure 10. Because of flow symmetry, only half of the intake system was needed for analysis. Figure 10a shows a meridional view of the compressor inlet. Figure 10b shows the streamline pattern entering the VIGV inlet. Sixty percent of the flow was calculated to be above the hor'-ontal centerline and 40% below. Figure 10c shows a configuration which would split the flow equally. Space did not permit the use of this configuration.

The VIGV inlet configuration is shown in Figure 11. The two major design goals were:

1. low diffusion along the shroud contour, and

2. nearly uniform velocity along the span of the guide vane leading edge.

About a half-dozen designs were investigated, using various hub and shroud contours. While both the diffusion of 5.5 m/s (18 ft/sec) and the spanwise velocity variation of 7.3 m/s (24 ft/sec) are larger than alternative designs, they were considered acceptable. An additional consideration was the spacing from the tip radius to the bowl which surrounds it. This additional space was expected to exploit the three-dimensionality of the intake arrangement. This was desirable, since the two-dimensional analysis showed flow distortion into the opening of the flowpath.

4.4 Flowpath and Performance Estimate

The complete compressor system is shown in Figure 12 The estimated compressor performance is shown on Figs 13 and 14. Included on the maps are the operating lines with and without augmentation

4.5 Impeller Mechanical Design

During the development period, the impeller blade number was changed from 18 to 24 The stress analysis discussed here is for the 24-blade impeller. The impeller is a two-piece assembly. It consists of a 17-4PH, stainless-steel inducer and a 2618-T61 aluminum-alloy impeller The inducer is shrunk onto the impeller and is aligned with the impeller by means of a pin as shown in Figure 15. Steel-inducer blading provides better vibratory fatigue life and is resistant to water injection erosion. The mechanical design for both components is based on the finite element approach and includes calculations of blade-disc centrifugal and thermal stresses and deflections, disc shrink-fit stress, and inducer blade vibration.

The 24-blade impeller is designed to operate at the design speed of 58,500 rpm. The maximum equivalent stress in the bore of the inducer is 389 MPa (56 ksi). The blade maximum principal stress is 363 MPa (52.7 ksi). The impeller maximum equivalent bore stress and blade maximum equivalent stress are 223 MPa (32.4-ksi) and 125.5 MPa (18.2-ksi) respectively. These stresses are within the minimum yield strength of each material for its estimated operating temperature as shown in Figure 15. The combined centrifugal and thermal deflection of the impeller tip is 0.25 mm (.010 in) outward and 0.33 mm (.013 in) forward. The inducer trailing edge and impeller leading edge deflections are reasonably compatible.

The inducer blade vibration analysis results are presented in the interference diagram, Figure 16, in which the natural frequencies are plotted versus rotational speed. Also shown is the excitation line for the 13 guide vanes. The diagram shows no first-mode resonance condition within the operating speed range. However, there is a possible resonance of the 2nd inducer blade mode with 13 pressure pulses produced by the 13 guide vanes. This condition occurs in the engine operating range at an undesirable speed of 39,800 rpm (68% design speed) as shown on the interference diagram.

If the disturbances caused by the guide vanes are severe, the blade could be excited until fatigue failure occurs. The basic method of evaluating the mechanical integrity of turbo-machinery blading is to plot the stresses on a Goodman diagram, Figure 17. This is a curve of fatigue strength (usually 10^7 cycles) versus applied steady stress, starting at the pure fatigue strength at zero mean stress and ending at the ultimate strength at zero vibratory stress. The steady centrifugal stress at 39,800 rpm is 20.5 ksi. The gas bending stress is 2.3 ksi. The total steady state stress on the blade is then 22.8 ksi.

Calculations of vibratory stresses are very difficult, and considerable analytical research is underway to find adequate methods to calculate such stresses in blades. However, for practical design purposes, the method of Trumpler and Owens (Ref. 7) has been much in use in the design of turbomachinery. Essentially it assumes that the aerodynamic excitation is related directly to the gas-bending forces and provides a curve of multiplier factor on the gas bending stress versus the blade resonance order.

For the case of the inducer blade, the natural frequency of the blade is at about the 8.7th harmonic of the running speed and the amplification factor is 4.5 from Ref. 7. A reasonable estimate of stress concentration at the blade root is 1.5. Then the vibratory stress in the blade is about

$$1.5 \times 4.5 \times 2300 = 15{,}400 \text{ psi}$$

The steady stress and vibratory stress are plotted as coordinates on the Goodman diagram. It can be seen that the point falls well within the boundary curve, and therefore it should be a safe design.

The inducer blade-vibration mode-shapes are shown on Fig. 18. A structural summary for the inducer and impeller is shown in Figures 19 through 23.

5.0 COMPRESSOR-TURBINE DESIGN

5.1 Aerodynamic Design

The design details of the compressor-turbine are presented in Reference 8. The design report describes a 56-blade design which is at variance with the final design configuration. As reported in the "Tenth Quarterly Progress Report", NASA originally designed a 63-blade rotor. However, ribs could not be designed with enough thickness to adequately feed metal to the blade with enough remaining space for a sufficient crack-stopper pocket-radius. The problem is illustrated in Figure 24.

To alleviate this problem, NASA revised the design to 56 thinner blades, as shown in Figure 25. This design, however, was abandoned because of high untwist blade stresses and the probability of blade resonance in the engine operating range. The final blade selection was the original design with an even number of blades, 62 instead of 63, and with pairs of blades sharing a common rib. The philosophy of design and the blade loadings are, however, representative of those described in Reference 8.

The flowpath is shown in Figure 26. The velocity diagrams are shown in Figure 27. The nozzle geometry and vane loadings are shown in Figures 28 and 29, respectively. The aerodynamic loading plots for the final rotor blade design are shown in Figure 30. Comparisons with the Baseline Engine design are shown in Figs. 31a-31e.

5.2 Vortex Chamber Design

The complete compressor-turbine flowpath is shown on Fig. 32. The vortex-chamber volute was designed for a vorticity of 104 ft²/sec. A side view showing sections near the extremities of the volute is shown in Figure 32. The nozzle inlet flowpath (also shown on the figure) was designed by use of a computer program coded for compressible flow with streamline curvatures. The inlet was designed to provide smooth geometric and aerodynamic transitions from the volute to the nozzle leading edge. The design philosophy was to obtain smooth distributions of velocity and curvature versus distance and to avoid excessive overvelocities on the shrouds. The resulting distribution of flow parameters at the nozzle leading edge is shown on Table 5.

5.3 Performance Estimate

The estimated performance is shown on Figs. 33 and 34.

5.4 Compressor-Turbine Mechanical Design

The major constraints on the structural design of the turbine rotor were:

1) design of a rotor with 1000 hours of design point stress rupture life

2) nozzle inlet temperature of 1052 C (1925 F)

3) minimal polar moment of inertia.

Since the life of the rotor is limited by thermal fatigue associated with the rotor disc rather than the blading, careful attention was given toward the design of the disc to control rim cracking due to severe transient thermal gradients associated with engine cold starts. Thus, the design of this component incorporates "pockets", which make the disc rim area discontinuous to a region where temperature and stress are within the capability of the material. The scheme being used is to cast very shallow axial grooves at the rim platform between the blades as "crack starters" with slots in the rotor at the base of the pockets as "crack stoppers". The principle is to let the rim crack since it will do so in any case, but to control the cracks so that they will not propagate beyond the rim area. This design also inherently lowers the inertia of the rotor.

The rotor was initially integrally cast in IN 792/Hf by the AiRefrac reusable pattern process. Although the Baseline rotor was successfully cast in this relatively new alloy by this process (Vol. 1, Sec. 8.2), no sound Upgraded rotor castings were produced. The material was subsequently changed to Mar-M 246, and satisfactory castings were obtained (Vol. 1, Sec. 14.1). Mar-M 246 is a higher strength alloy with less resistance to hot corrosion attack.

At the turbine inlet temperature of 1052 C (1925 F) and the design speed of 6126 rad/sec (58,500 rpm), the average blade root stress is 140 MPa (20,300 psi), which is below the expected 1000-hour stress rupture for the calculated maximum metal temperature of 940 C (1725 F) at the blade root. The turbine disc operates at an average tangential stress of 232 MPa (33,600 psi) at the design speed. Based on an estimated minimum value of 830 MPa (120,000 psi) or 80% of the typical ultimate strength for an average disc temperature of 700°C (1300°F), the calculated burst speed is 9985 rad/sec (95350 rpm). This provides ample margin of safety in the event of engine overspeed.

The disc tangential, radial and equivalent steady-state stresses and temperature distribution for the rotor are presented in Figure 35. The disc temperature gradient for these calculations was obtained by adjusting previously measured Baseline Engine turbine rotor gradients for the turbine inlet temperature increase. Since the measured gradients were for an oil-lubricated bearing, the gradient for the Upgraded Engine rotor with a gas bearing is expected to be lower. This was later verified by the results of the gas generator rotor thermal study conducted by Mechanical Technology Inc. The maximum combined centrifugal and thermal stress at the disc center is 319,000 kPa (46,300 psi), which is well within the expected minimum (80% typical) 0.2% yield strength for IN-792+Hf or 690,000 kPa (100,000 psi) at the operating temperature.

Figure 36 depicts the blade Campbell diagram on which the natural blade frequencies are plotted versus rotational speed. Also shown is the excitation line for the 15 nozzle vanes. The diagram shows no fundamental mode resonance condition within the engine operating speed.

The Modified Goodman diagram for the blade is shown in Figure 37. This is a curve of fatigue strength (usually 10^7 cycles) versus applied steady stress, starting at pure fatigue strength at zero mean stress and ending at the ultimate strength at zero vibratory stress. The steady centrifugal stress at 6126 rad/sec (58,500 rpm) is 141.2 MPa (20,500 psi). The total stress on the blade is then 158.4 MPa (23,000 psi). Calculations of vibratory stress are very difficult. However, for practical design purposes, the method of Trumpler and Owens (Ref 7) has been much in use in the design of turbomachinery. Based on that method of analysis, the estimated blade vibratory stress is 62 MPa (9,000 psi). The steady-state stress and vibratory stress are plotted on the Goodman diagram.

It is shown that the point for the blade root falls within the design limit curve.

6.0 POWER TURBINE DESIGN

6.1 Aerodynamic Design

The design details of the power turbine are presented in Reference 9. The aerodynamic design-point conditions are presented on Table 6. The flowpath is shown in Figure 38. The velocity diagrams are shown in Figure 39. The nozzle and rotor geometries are shown in Figure 40, along with a comparison with the Baseline Engine design. The aerodynamic loadings for the nozzle vanes and rotor blades are shown in Figures 41 and 42, respectively.

The hub and shroud velocity distributions for the interstage duct are shown in Figures 43 and 44 for design-point and the 50%-speed match point, respectively. The design-point velocity distributions for the exhaust diffuser are shown in Figure 45. The estimated performance characteristics are shown in Figs. 46 and 47 for power and efficiency, respectively. Lines are included on Fig. 46 for 2nd-gear and 3rd-gear road-load requirements for a 3500-lb vehicle.

6.2 Power Turbine Mechanical Design

The power turbine rotor is integrally cast with rim pockets for control of thermal fatigue cracking. The material to be used for this rotor must provide sufficient strength for a low-inertia disc with a 20% minimum burst-speed safety-factor.

At the stress design speed of 7330 rad/sec (70,000 rpm), the blade root stress due to centrifugal and gas bending loads is 380,000 kPa (55,000 psi). The turbine inlet temperature is 880°C (1617°F), and the blade temperature is 804°C (1480°F).

In view of the relatively high stresses predicted for the blade and rib areas of the rotor, only the strongest nickel-base super-alloys were considered for this application. The alloy, MM 00_, was selected since, on the basis of available data, it has the highest strength of the commercially available alloys in the 1300°F to 1500°F range. The data on Table 7 was used in checking material properties with design requirements.

Unlike the bladed components on the gas generator, the power turbine must operate over a wide range of conditions which involve a speed range of 8:1, along with variable nozzle vanes. Because of the wide speed range, it is practically impossible to find a combination of nozzle vane and rotor-blade frequency which avoids interference somewhere in the operating range as shown in Campbell diagram, Figure 48. The aerodynamic excitation can be severe because of the heavy wakes in the flow when the nozzles are in the braking position. Unfortunately, a larger number of nozzle vanes (to keep the lower vibration modes at lower power turbine speeds) was not possible because of space limitations. A turbine blade shroud (to damp blade vibration) would increase inertia and create manufacturing and cost problems. Therefore, the choice reduces to doing whatever possible with the nozzle, which is the major source of excitation. Experience with the Baseline Engine showed that staggering the nozzle vanes controls the vibratory stress and results in adequate blade life. This same procedure was followed for the Upgraded Engine.

The Goodman Diagram of Figure 49a indicates some margin for vibratory stress at the blade root using the typical 1000-hr. rupture stress and assuming the alternating stress to be 200% of the gas bending stress. In addition, the following factors should be considered, which tend to support the selection of the best available material:

- The unknown vibratory stress is expected to be higher at resonance
- The blade root stress of 55,000 psi without any vibratory stress exceeds the minimum 1000 hr. rupture stress of 52,700, assuming it to be 85% of typical.

The power turbine disc operates at an average tangential stress of 44,000 kPa (63,700 psi) at the design speed. This provides a 32% burst-speed margin based on a minimum ultimate material strength of 1,000,000 kPa (145,000 psi). The tangential, radial, and equivalent steady-state stress and an estimated temperature distribution for the disc are presented in Figure 49b. The maximum combined centrifugal and thermal stress at the disc center is 512,000 kPa (74,300 psi), which is well below the yield strengths of the materials.

The turbine was released coated, but it was run initially without a coating to obtain maximum properties. The maximum speed of the rotor was reduced from 70,000 rpm to the range of 60,000-to-65,000 rpm (approximate vehicle speed of 140 km/hr (88 mph)) in direct drive until some actual operating experience was obtained.

7.0 ENGINE HOUSING

The shape of the housing was determined essentially by the envelope of the vehicle engine-compartment plus the space and location requirements of the engine components, the sump, vehicle and engine accessories, and intake and exhaust systems. These contraints resulted in a housing with the regenerator slanted and its centerline offset. Despite this asymmetry, the housing must not deflect or distort with operating pressures and temperature gradients that will cause excessive misalignment between the internal aerodynamic and mechanical components.

Additional factors considered in the housing configuration were as follows:

1. Promising development of insulation without sheet metal liners permitted the design of a single-piece, integral engine housing with resulting savings in weight (flange elimination) and reduced machining.

2. The design should be such that the tooling will be reasonably simple, and a satisfactory casting can be made in high-silicon, cast nodular iron.

3. Compressor-outlet air-cooling for the bulkhead area required a suitable duct (from compressor outlet to the bulkhead cavity) be provided so that sufficient cooling flow would be assured.

In line with the above criteria, preliminary sketches and a model of the housing were completed and an evaluation conducted with the following results:

- Housing Bulkhead Stress and Deflection - The bulkhead section of the housing was analyzed with predicted pressure loadings and an estimated temperature distribution, based on Baseline Engine bulkhead temperatures adjusted for a 1051°C (1925°F) turbine inlet temperature. The results showed excessive asymmetric deflections of 0.76 to 1.12 mm (.030 - .044 in).

- Exhaust Diffuser Outlet Flow Restriction - Sections taken to examine the exhaust-diffuser-exit flow-condition indicated a restriction with the preliminary configuration.

- Integral Sump Studies - The housing walls forming the proposed sump were examined, and the thermal insulation of the regenerator-drive pinion bearing-supports from adjacent hot sections of the housing was found to be borderline.

- Thin-Wall, Integral-Casting Capability - To assure that the overall housing design is consistent with technological requirements for a thin-wall, nodular-iron, integral casting, efforts were closely coordinated with pattern and foundry vendors. The pattern vendor expressed some concern regarding a possible problem in casting the sump wall at the regenerator-drive pinion.

- Gas Generator Flange and Housing Front Section - Problems in providing sufficient space for initial compressor diffuser and collector designs became apparent.

The engine housing was subsequently modified as follows to eliminate or reduce the above deficiencies:

- The ribs connecting the bulkhead with the burner cavity wall were relocated and extended to increase stiffness and reduce axial deflections without restricting the flow of cooling air in the bulkhead cavity; see Figure 50. A finite-element model of the housing bulkhead area, Figure 51, was used to calculate deflections from estimated temperatures and the pressure loads of 460 kPa (66 psi), including an 8000N (1800 lb) thrust load across the interstage. The deflection and stress results are shown in Figure 52. The axial deflection ranged from 0.53 to .787 mm (.021 to .031 in) with a maximum equivalent stress of 112 kPa (16 ksi). The deflections are satisfactory, and the stress is considerably below the yield point of 407 kPa (59 ksi) for this material at 466°C (870°F).

- The shape of the rear portion of the housing was changed to provide sufficient circumferential flow area for the exit gas from the exhaust diffuser to pass into the regenerator.

- **The integral sump walls were removed from the engine housing and cast integral with the reduction-gear case.**

- **The gas generator compressor diffuser was changed to include an axial deswirl section. A "collector" was provided in the compressor cover inboard of the deswirl section to duct air circumferentially to three passages leading to the ducts in the engine housing. This diffuser and collector configuration resulted in a shorter engine by allowing the compressor section to be moved rearward behind the front edge of the regenerator housing.**

Two of the above-mentioned passages connect with ducts at the top and bottom of the housing to carry the air to the regenerator inlet. The other gas generator passage connects with a housing duct which supplies the bulkhead cavity with cooling air. This air exits the bulkhead cavity through holes in the burner (forward bulkhead) wall at each end of the crossarm and continues onward to the regenerator inlet.

With the housing configuration established as described above, detail design efforts on the casting were initiated. Drawings were made and models constructed. One model of foam was utilized in checking installation in an engine compartment (Fig. 53), and another model of plywood and foam-board (Figs. 54, 55, and 56) was used to show construction details of all walls including the inner ones. As detail drawings were completed, work on the patterns progressed. Close liaison with the pattern and casting vendors expedited the design of a casting which would meet both the engine design and manufacturing requirements of the housing. The patterns are shown in Figures 57 through 59.

The un-insulated regenerator cross-arm section of the housing which supports the regenerator seal is a heat-loss path which reduces engine fuel economy. For this reason, an insulated cross-arm as shown in Figure 60 was investigated. This cross-arm used cast bosses to support the regenerator-seal base-plate. Estimated stresses on the base-plate were excessive if it were assumed that the insulation did not contribute to base-plate support. Two options to provide an insulated cross-arm were considered.

1. Reduce the unsupported spans on the existing seal base-plate;

2. Redesign the seal base-plate in the cross-arm area.

The first option required so many additional supports that the insulation became impractical, while the second option required a major redesign and development of the cross-arm system. Because of these difficulties, the heat loss through the regenerator cross-arm-seal platform was estimated. Baseline Engine temperature measurements were used to determine the degree of benefit obtainable from an insulated cross-arm. This estimate showed that the heat loss was less than 0.9 Kw (3000 Btu/hr) and is invariant with gas generator speed. Since this heat loss is small (less than 3% of the exhaust-pipe losses at idle), the effort required to insulate the cross-arm was not considered justified. Therefore, the housing was released with an uninsulated cross-arm.

7.1 Linerless Insulation

The single-piece engine housing requires that insulation be used that does not require sheet-metal liners. Tests on linerless insulation in the Baseline Engine showed promise of satisfactory performance with suitable development. Therefore, this insulation concept was carried forward for the Upgraded Engine.

Studies of the insulation requirements were made both by Chrysler and Foseco, Inc., using the engine models and preliminary sketches. Foseco, Inc. submitted cost and time estimates for (1) insulation components, (2) ancillaries, and (3) tooling for the various areas of the engine. It was determined that Chrysler would make the insulation for the engine-housing high- and low-pressure sides, the burner cap, and the compressor-turbine nozzle. This material, proprietary to Chrysler, has a density of 17 lbs/ft^3 and an insulating "K" factor of 1.11. A mold was made from the engine-housing pattern for use in tooling for the housing insulation. Foseco, Inc. provided insulation for the Gas Generator Support, Power Turbine Housing (Inner Diffuser), Interstage Access Panel, Interstage-Access-Panel Bolts, Power Turbine Nozzle Support, and Outer Exhaust Diffuser. When Foseco ceased production of this material, Chrysler prepared the latter parts as well.

8.0 GAS GENERATOR SECTION

The gas generator assembly is shown in Fig. 61; specifications for some of the major components given on Table 8. The assembly includes: the high speed shaft assembly with the compressor and turbine rotors, the compressor-turbine nozzle, the gas generator support structure, the compressor diffuser, the rear bearing carrier, the variable inlet guide vane assembly, and the vortex chamber which directs gas from the burner to the turbine nozzle.

The significant factors considered in the design of the various components and subsystems of the gas generator are discussed below. The selection of a "free rotor" engine concept results in a simple shaft and rotor assembly since the space and support requirements and the loads associated with gears do not have to be considered. The absence of one high-speed gear mesh also provides a significant benefit in reduced noise. The shaft assembly is supported on two bearings with overhung impeller and turbine rotors. This results in a compact rotor bearing system. Mechanical Technology, Incorporated (MTI) was selected to do detailed shaft-dynamics analyses and develop the shaft-bearing system under a subcontract.

8.1 Shaft, Bearings, and Seals

The design and development of a shaft/rotor-bearing system for stable dynamic performance throughout the operating speed range is imperative to assure adequate bearing life and to minimize noise, which is especially important in an automotive engine. In selecting bearings which could be used in this application, factors such as life, cost, and power loss were considered in addition to the potential of the bearing to control shaft dynamics and operate at the expected temperature levels of this and future engines. Oil film bearings satisfied the requirements of previous engines and could have been used at both locations in the Upgraded Engine. However, the higher speeds and cycle temperatures of advanced engines would be expected to result in increasing power losses and excessive bearing soakback temperatures at the turbine end of the shaft. An air bearing, which has low power loss and higher temperature limits, was therefore proposed for the rear location.

An air journal bearing could have been used at the front location; however, an air thrust bearing would require a large thrust plate for sufficient thrust capacity. T would incur a marked increase in shaft assembly inertia with a corresponding penalty in engine response. Since an oil thrust bearing is impractical adjacent to an air journal, an oil journal bearing was released for the front location.

Mechanical Technology, Inc. (MTI) conducted an initial study under a separate EPA/MTI support contract to determine the feasibility of using their Hydresil foil air bearing at the turbine rotor in the Upgraded Engine application. This study, based on bearing size requirements for the anticipated loads plus critical speed and rotor response analyses, indicated that a practical design could be achieved. A subcontract was subsequently let to MTI for the design and development of the bearing and shaft system for the Upgraded Engine. The Hydresil bearing concept (Fig. 62) allows for adjustments in bearing spring rate thru design changes in the bump foil configuration. This can be advantageous in controlling critical speeds. Initial analyses (using specifications shown in Appendix A) were completed on this configuration including critical speed and response studies for the shaft assembly. Film thickness and shaft motion determinations were also made for air bearing loads; see Fig. 63.

A simulator was designed and built by MTI using shafting and dummy rotors representative of that used in the gas generator. The shaft assembly was driven with a cold-air turbine machined into the dummy compressor rotor. Fixture components, oil, and bearing cooling air were heated to the operating temperature levels calculated for the engine as described in Section 8.2. Controlled gap seals similar to those used in previous engines were specified for the simulator. These seals, utilizing a carbon ring with a steel band shrunk over it to maintain clearance control with the shaft, gave good performance in previous turbine engines. The simulator was completely instrumented with capacitance type displacement probes at each end of the rotor to determine dynamic motions and was equipped for measuring speed, flows, and pressures as required.

Initial simulator runs were successfully made through the speed range with cool lube oil, and several hundred start-stop cycles were run. However, problems were experienced with instabilities at oil temperatures above 160°F. Excessive synchronous and subsynchronous deflections were observed, and air bearing failures occurred. It was subsequently decided to revert to the use of an o-ring mounted rigid front bearing similar to that used in previous engines. The journal bearing section on this unit was integral with the thrust section.

A complete unbalance response and critical speed analysis (Figs. 64-66) was made. However, as a result of the integral journal and thrust sections, the bearing cartridge radial motion was found to be inhibited by rotor thrust loads. This caused excessive subsychronous vibrations. Some evidence of the controlled gap seals having a detrimental effect on shaft deflections was also noted. The oil bearing was redesigned to separate the thrust section from the journal and to incorporate an oil damper in the journal bearing. Test runs were successfully completed through the speed range, up to predicted operating temperature and with a maximum of 0.006 oz.-in. unbalance. Shock loads were run up to 4gs at idle and 16gs at 90% speed to simulate gyroscopic loading. Simulator tests were terminated due to lack of funds when an air bearing failure occurred during development tests for optimizing oil damper and air bearing tests. Inspection showed some welds holding bearing components to the cartridge had separated; however, it was not clear if this was a cause or result of the failure.

Engine tests were run meanwhile using the rigid oil bearing having integral journal and thrust sections. No air bearing seizures had been encountered to date, with one bearing accumulating a total of 140 hours before being removed from service because of excessive coating wear. Three other bearings were removed from engines because the spacer foil (placed between the bump foil and the cartridge to control bearing clearance) became dislodged and moved axially out of position. This problem was noted during routine inspections and did not progress to the point of failure. Since funds for simulator operation were exhausted and engine tests were relative successful, development testing was discontinued.

Air bearing performance during subsequent engine testing is discussed in Section 18.2.

8.2 Thermal Analysis

A thermal analysis of the gas generator was conducted to determine operating and soakback temperatures at several critical points such as the air bearing, its journal, and the housing and shaft near the mid-shaft seal. The temperature levels and thermal gradients calculated for the turbine rotor were also used in the design of this component.

The thermal model of the gas generator consisted of a lumped-parameter network which was solved by a finite difference program (CINDA). The analysis was conducted at a maximum power steady-state condition. This condition was also the initial point for soakback analysis. The steady-state temperatures calculated are shown in Fig. 67. The following boundary conditions were used in the model.

Fixed Temperature Boundaries

1) Front end of shaft; 115 F

2) Average impeller temperature; 250 F

3) Nozzle platform; 1925 F

4) Wheel rim; 1705 F (Relative total gas temperature)

5) Oil in front bearing and discharge cavity; 225 F

6) Air bearing cooling air at inlet: 475 F

The following convection coefficients were estimated for the analysis.

1) Oil in discharge cavity estimated from Baseline Engine heat rejection data; 150 BTU/hr-ft^2-F

2) Bearing cooling air in "bump foil" estimated from bump geometry; 39 BTU/hr-ft^2-F

3) Turbine wheel rims and disc given as shown in Ref. 10; 0 to 120 BTU/hr-ft^2-F

4) Compressor air to diffuser plate from MTI; 115 to 180 BTU/hr-ft^2-F

The bearing cooling air flow of 0.5% of engine air flow was used as recommended by MTI.

The air bearing cartridge is relieved at the outside diameter to help isolate the bearing from the rear support. The temperatures of the support near the bearing range from about 490 F up to 700 F. The highest bearing temperature, at the rear of the cartridge, is below the upper limit of bearing temperatures set at 650 F by MTI.

The steady-state temperature distribution at maximum power as shown in Figure 67 was used as the initial condition of the soakback calculation. This implies a virtually instantaneous shutdown from a peak power condition which would be a severe and infrequent occurrence during the life of the engine. The actual hardware would normally experience some cooling during the intervening idle and/or coast down period prior to soakback. the steady-state heat sources were removed for this calculation so that only the thermal energy stored within the various components would be considered. The only means provided for the removal of heat from the gas generator was by natural convection from the shaft, impeller and the diffuser plate.

The transient behavior at some of the significant locations is shown in Figure 68 These curves are coded to locations designated in Figure 67.

The following peak soakback temperatures were obtained:

	°C	°F
Rear Seal	524	975
Mid Seal	257	495
Air Bearing - Journal	273	523
Air Bearing - Cartridge	341	645
Oil Bearing	207	404
Housing, Oil Cavity	214	417
Shaft Sleeve, Oil Cavity	230	446

All of the peak temperatures are acceptable except on the shaft sleeve near the mid seal. The shaft sleeve is exposed to residual oil in the cavity which has a soakback temperature goal of 230 C (450 F) to avoid coking. This analysis indicates that oil temperatures in this area are marginal. However, this may not be a serious problem due to the conservative basis for the analysis. In addition, successful engines in the past have approached 450 F oil soakback temperatures under extreme ambient conditions. Development testing was expected to determine the extent of the thermal problem if any in this area.

8.3 Compressor-Turbine Nozzle

The structural design of the Upgraded Engine compressor-turbine nozzle is very similar to the proven Baseline Engine design. However, due to the increased turbine inlet temperature, material changes were necessary. In view of the severe requirements of this critical component, it was not possible at the time to select a single material with any certainty of success The nozzle must be capable of operating with metal temperatures up to 1925 F in a highly oxidizing and corrosive environment. In addition, relatively high cyclic thermal stresses were expected in the inner shroud cone area. Furthermore, the inherent complexity and the high degree of restraint present in this part demanded that special consideration be given to castability, particularly susceptibility to hot tearing. Based on previous experience with similar nozzles operating at lower temperatures and with other materials, there was reason for concern about selecting a single alloy that would satisfactorily meet all of the Upgraded Engine requirements.

Therefore, to ensure a supply of parts for engine running, three different nozzle materials were released. All of the alloys required a coating for this application. The important characteristics of the alloys selected are summarized below:

Alloy	Castability	Strength	Oxidation Resistance	Sulfidation Resistance
MM 002	Very Good	Very Good	Good	Poor
IN 792/Hf	Poor	Good	Good	Good
Mar-M 509	Good	Low	Fair	Very Good

In summary, MM 002 is the strongest available commercial alloy, but, even with a coating, hot corrosion resistance may not be adequate. IN 792/Hf has better sulfidation resistance, but is somewhat weaker and is known to be susceptible to hot tearing during solidification. The strength of cobalt-base Mar-M 509 may prove to be inadequate. However, it has excellent hot corrosion resistance and has been used extensively for integral nozzles in other automotive and aircraft turbine engines.

8.4 Compressor Cover

Since structural stiffness is essential to limit impeller/shroud running clearances to maintain compressor efficiency, the primary objective of the compressor-cover design was to provide for a lightweight, rigid component. The material that was selected was aluminum alloy C-355 because it offers excellent castability and good strength at moderate temperatures.

A three-dimensional stress analysis was conducted to determine stress and deflections under combined steady-state thermal and pressure-loading conditions. The structure was subjected to a pressure of 456 kPa (67.6 psi) corresponding to a 4.6:1 pressure ratio. The applied temperature distribution was estimated from measured Baseline Engine cover temperature values. The finite element model for the cover is shown in Figure 69.

The maximum calculated equivalent stress is 37.2 mPa (5.4 ksi) for an anticipated metal temperature of 204 C (400 F). The maximum axial deflection is 0.15 mm (0.006 in) as shown in Figure 70. Both stress and deformations are within acceptable levels. A summary of stresses, deflections and estimated temperature is shown in the table on Figure 70.

It should be noted that the compressor cover and its mating part, the gas generator support were designed to eliminate axial cover deflection at the impeller shroud and diffuser vanes. This was done by setting the appropriate dimensions to give an interference greater than the calculated deflection, effecting a preload in the cover.

8.5 VIGV and Air Intake Mechanical Design

The variable inlet guide vane assembly (VIGV) includes thirteen vanes located two chord lengths upstream of the compressor rotor blade leading edge and the actuating system. Each vane has a stationary front portion fixed at a minus ten degree axial flow angle setting (opposite engine rotation) and a movable rear portion with an angular rotation range from minus thirty degrees to plus sixty degrees relative to the gas generator axis. The fixed vanes are an integral part of a cast aluminum shroud which defines the outer surface of the air inlet bell mouth and provides support for the inner flow surface at the compressor rotor inlet. The movable vanes are cast of stainless steel with an integral bent stem and ball end. The ball is engaged in slots of a ring that is trapped between the cast shroud and a machined aluminum support which is attached to the compressor cover. This steel ring is rotated about the engine exis by a tangential force applied by a hydraulic piston actuator. These components are shown on the gas generator cross-section, Fig. 61, and the air inlet cross-section, Fig. 71, with the VIGV at an axial setting. The ring is rotated clockwise (viewed from the front of the engine) for the positive VIGV angle settings utilized at engine idle speed. The schedule of VIGV position as a function of actuator piston position was determined using IMP, a computerized linkage and mechanism motion analysis program. The relationships are shown on Table 9. The actuator force required with the vanes at the minus 30-degree position at maximum engine speed is 8.2 newtons (1.8 pounds force).

The position control of flow surface at the compressor rotor inlet hub is achieved by piloting the mating shroud to the compressor cover. The holes locating the vane stems at the mating joint of the shroud pieces and the final shroud pilot surface machining are performed as a machining assembly, with dowels used for precise reassembly.

The use of water injection into the inlet air for engine power output augmentation imposes material corrosion protection requirements: the aluminum shrouds are anodized, the steel actuating ring is chrome plated and the stainless steel variable vanes are protected from direct water impingement by the fixed vanes integrally cast with the shrouds.

The air intake housing serves as the transition element between the vehicle mounted air filter assemblies and provides air flow path control for the compressor as discussed in Section 4.3. An aluminum casting is used to minimize weight while providing adequate strength for supporting the engine starter load. This load includes the weight of the starter as well as the starter drive belt tension and inertial and reaction loads. The housing is piloted to the compressor cover, as shown on Fig. 61, to control the starter clutch alignment with the engine axis as well as to control the starter alignment with the engine auxiliary drive clutch used to transmit drive power during engine starts.

The flow path surfaces are used as-cast for the inner bell-mouth surface, and a sound deadening water repellant insulation is used to line the interior surface of the housing. The casting is anodized to provide corrosion protection for water injection operation. A rubber boot is used to provide flexibility between the housing and the air filter assembly (required for vehicle installation position tolerances and relative engine-vehicle motion during operation) and to seal the filtered air flow path.

9.0 POWER SECTION

The power section consists of the mechanical components of the power turbine shaft and the reduction-gear assembly as shown on Fig. 72. The major areas in the design of the shafting were: the configuration of the shaft, the sizing of the bearings, the compliance of the bearing supports and the design of the reduction-gear pinion. The major design areas in the reduction-gear assembly were the gears and bearings.

9.1 Power Turbine Shafting

Several shaft designs were evaluated to define an arrangement which would meet engine requirements. The following factors were considered in this evaluation.

1) Shaft stiffness, since it influences:

   a) shaft deflection, which affects bearing capacity and pinion crown requirements.

   b) critical speed and shaft dynamics.

2) Bearing type and size and related power losses.

3) Fabrication and assembly procedures which could affect rotor balance repeatability.

4) Quantity and complexity of shaft components.

The shaft design selected is shown on Figure 73. This differs from the shaft and reduction-gear pinion arrangement of the Baseline Engine This latter arrangement consisted of a power-turbine shaft which splined into another shaft on which the pinion was mounted. This design proved to be reliable, and the four bearings (two for each shaft) allowed negligible shaft deflection at the pinion. However, in the interest of fuel economy, a two-bearing arrangement was selected to reduce bearing power losses.

The design shown in Figure 73 has a number of favorable features. These include low shaft deflection, simple assembly, positive indexing and piloting, and minimum unbalance.

The deflection of the shaft assembly is low enough with the estimated applied loads to allow a moderate pinion crown of 0.012mm without edge-loading of the pinion teeth. The slope of the journals at the bearing is such that journal bearings could be specified which have relatively low losses.

The final rotor assembly consists of only two major parts - the turbine with an integral tie-bolt and the reduction-gear pinion, which is integral with the sleeve. These parts, plus the thrust-bearing runner, are designed to operate as an integral unit when clamped together in assembly.

The turbine (Material: MM002) is inertia welded to the tie-bolt (Material: AISI 8640) just forward of the front bearing. A pair of three-lobed polygons is provided on the tie-bolt to allow positive indexing and piloting of the pinion-sleeve assembly relative to the turbine shaft. These polygons also assure that there will be no relative motion between rotor parts during adverse torque applications.

The sleeve is inertia-welded to the pinion to provide a single component which can be balanced as a unit. After the pinion teeth are finish-machined and the sleeve is semi-finish-machined, they are welded and finish-machined relative to the pinion teeth. Note the small inside diameter, which allows minimum unbalance from machining eccentricities and/or oil which may inadvertently collect in the cavity Internal polygons at each end of the pinion-sleeve mate with those on the turbine shaft. This integral pinion-sleeve permits a relatively simple rotor assembly. The rotor performed satisfactorily and demonstrated good balance repeatability, despite some problems with the welding, which required special considerations in subsequent machining.

Design considerations for the two bearings included not only load capacity and power loss, but also noise generation or transmissibility. An initial rotor design that was investigated incorporated a journal bearing at the turbine end and a ball bearing behind the pinion gear. A Baseline Engine was modified to test a power turbine shaft having the above bearing arrangement. Peak-power

comparison tests showed that the prototype assembly yielded greater output power throughout the operating range and lower heat rejection when compared to the original arrangement with four journal bearings and a thrust washer. However, the noise level of the assembly was not acceptable by commercial standards. The noise level was reduced somewhat with added oil to the pinion, and this agreed with sound recordings that showed strong peaks related to the gearing frequencies. A Baseline Engine Power turbine shaft was later assembled using two journal bearings and run successfully over the speed range. The audible noise was comparable to the level normally experienced on the Baseline Engine, and the heat rejection was slightly less than that of the two-bearing shaft with one bearing.

Anti-friction bearing manufacturers were contacted, and the application requirements for the Upgraded Engine including torque, speed, lubrication, power loss, duty cycle, bearing life and noise control were discussed. Some concern was initially expressed for the light thrust loading under some engine conditions; such loading could induce ball skidding and premature failure. It was subsequently stated, however, that this phenomenon could be controlled in high-speed applications where initial internal clearances of new bearing mounting interferences and temperature considerations are in proper balance. An elastomer material applied to the outside diameter of the bearing was proposed as a means of isolation and noise control; however, this approach would require development for this application. Since the effective control of noise remained some question, it was decided to design the rotor for two journals and a thrust bearing. A study of the most critical operating condition for the thrust bearing showed a condition that occurred during maximum engine output with the power turbine shaft operating at 19,500 rpm. At this point, the gear load of 690N (155 lb.) was assumed.

Table 10 tabulates the performance of the new thrust bearing at its critical operating points. This indicates that the film thickness of the thrust bearing at the 1-2 upshift of the transmission will vary between 8 to 9 μm (315 to 358 micro-inches). However, angularity of the thrust collar from shaft deflection would require an oil film about 50% thicker. To avoid this, the bearing was placed on a spherical seat, as shown in Figure 73

The anti-thrust bearing is a duplicate of the thrust bearing, since the anti-thrust forces which depend on engine braking cannot be precisely determined analytically. It was anticipated that its design might be revised when actual loading information was available.

The most critical conditions for the journal bearings were determined to be at 52,500 rpm during the 1-2 upshift of the transmission, where inertia loads are included. At this point, the gear load is 3800N (850 lb.) with a turbine load of 6700N (1500 lb.); this was calculated from a conservatively assumed deflection of the turbine from bearing center. The smallest optimum bearing sizes were determined from parametric studies. Tapered lands or grooves were not included in the analysis of the journal bearings. These were required in the front bearing, however, to maintain stability. Considering a minimum-required film thickness of 40 micro-inches at the above speed and load with 250 F oil temperature (MS-4228 transmission fluid), calculations showed the minimum front-bearing size required [21.3 mm (.84 in.) dia. x 21.1 mm (.83 in.) long]. A final design iteration including polygon size requirements resulted in a final bearing-size selection of 22.1 mm (0.87 in.) dia. x 22.5 mm (0.886 in.) long.

A prime consideration in the design of the rear bearing was the shaft deflection during the 1-2 upshift of the transmission. Analysis indicated the bearing should be designed for a minimum film thickness of 375 micro-inches to allow for the misaligned journal. Figure 74 describes the bearing performance at this operating point for the range of bearing clearance shown; consideration was given to dimensional tolerances and the effect of expected temperature levels. Figure 75 shows the power loss, oil-film thickness, and oil-flow requirement for the road load speed-range and the maximum power point.

It should be noted that the total power-loss of the rear journal and the main thrust bearing is 1.80 KW (2.4 hp) at 70,000 rpm. This value is comparable to the estimated power losses of the ball bearing previously considered for that location - 1.7 to 2.2 KW (2.2 to 2.9 hp). Presuming satisfactory operation of these bearings, it therefore, appeared that optimized hydrodynamic bearings could have efficiencies comparable to those of ball bearings (along with the improved noise-damping characteristics) during operation at high speed.

9.2 Shaft Dynamics

The large speed range (9,000 to 70,000 rpm) for the power-turbine shaft suggested that its bearing performance and shaft dynamics be checked before high-speed engine operation. An existing test fixture capable of being driven by a dynamometer up to design speed was modified to accept a simulated Upgraded Engine power turbine shaft.

Six proximity probes were located in the perpendicular planes at three positions along the shaft to monitor shaft deflection. This fixture shaft was designed with preliminary values of turbine weight and inertia. In addition, the shaft was not a precise copy of the engine shaft, since the mechanical design of the engine shaft had not yet been completed. Therefore, some differences existed between the fixture and the engine designs, and the calculated critical speeds were not the same. Assuming rigid bearings, the critical speed of the engine shaft was calculated to be 38,970 rpm, whereas that of the fixture was 42,000 rpm.

The fixture was initially run with a rigidly-mounted oil-film bearing at the point end of the shaft and rigidly-mounted 3-ramp bearing at the turbine end of the shaft. The unbalance was low, and the 3-ramp-bearing clearance was 0.038 mm (0.0015 in.). The latter bearing failed at 45,000 rpm. Peak diametral displacement of 0.002 inch was measured at the turbine end of the shaft at a speed of about 42,000 rpm. This corresponded to the value of critical speed calculated with rigid bearing-mounts.

The 3-ramp bearing clearance was increased to 0.046 mm (0.0018 in.), and the fixture was run with an oil inlet temperature of 120 C (240 F) to increase the oil flow through the bearing. The critical speed decreased to 40,000 rpm, which implied a higher film thickness and better damping, and the peak diametral synchronous shaft-motion dropped somewhat to 0.0016 in. However, the shaft was generally very noisy, and shaft displacement was noted to increase markedly with a rapid approach to 45,000 rpm. The shaft was subsequently run up to 60,000 rpm with no bearing failure.

A flexible, spring-mounted bearing was designed at the turbine end of the shaft to reduce shaft deflections, noise, and the critical speed. The assembly consisted of a three-ramp-type bearing inserted into a light carrier which was supported in the housing by two coil springs, each of which was formed into a toroidal shape. Passages in the housing and in the carrier supplied the lubricating oil.

Tests at 240 F oil temperature and at gradually decreasing pressures from 100 to 45 psi were successfully completed. Maximum shaft speed, limited by fixture capability, was 60,000 rpm. Shaft displacements were measured using photographs of oscilloscope displays. Analysis by Lissajou's display was possible only at speeds below 13,000 rpm where the display was not to complex. At higher speeds, the picture complexity, combined with large magnification, resulted in loss of display clarity. Standard display of pick-up signal versus time base was used at all other speeds.

The test results showed two frequencies of oscillation. One was a synchronous frequency with a diametral amplitude of shaft displacement of 0.0006 inch. The other was a subsynchronous frequency of 0.1 shaft speed with a maximum amplitude of shaft displacement of 0.003 inch. This subsynchronous vibration might have been generated by the drive gear, which had a gear ratio of 10:1. The existence of a well-defined critical speed was not observed.

Operation of the shaft at 60,000 rpm did not present a mechanical problem that could be observed on the oscilloscope or could be heard. Shaft noise was much less than that with the rigid bearing mount. Consequently, these tests confirmed the mechanical design of the power turbine shaft and its bearing and bearing-mount configurations for the Upgraded Engine.

9.3 Power Turbine Reduction-Gear Assembly

The selection of the reduction gear arrangement for the Upgraded Engine was based on previous studies considering high speed rotors (> 50,000 rpm) of advanced gas turbine engines. Based on these studies (which included factors such as package size, cost, gear noise, gear manufacturing, and consideration of methods of driving vehicle accessories), a two-stage gear-set was chosen for the Upgraded Engine. A 15-to-1 gear ratio was specified from performance studies. This gear ratio gave a proper speed range for the transmission and prop-shaft with a maximum rotor speed of 70,000 rpm.

In addition to the usual performance requirements, several interacting packaging factors constrained the gear selection. These were as follows:

1. The size of the pinion thrust washer and its clearance to the second stage pinion.

2. The bearing mounting of the intermediate shaft and its relationship to the flange opening in the engine housing.

3. The center-to-center distance from the power turbine shaft to the transmission input shaft.

4. The limiting speed of the accessory chain drive.

A first-stage gear ratio of 5.6429 and a second-stage gear ratio of 2.6489 (for an overall ratio of 14.8909), allows for a design which meets the above constraints.

The analysis of the gears was performed with the aid of several modified computer programs. The modifications were made to incorporate the lastest theories in elastohydrodynamic oil film thickness and stress wave interaction in the Hertzian contact area. Tooth profiles, generated from standard tooling, were optimized for stress (surface and bending), life, noise, and cost.

Optimization studies of the two-stage reduction gears were completed and showed that both gears must have combined action (recess and approach), and they both must be generated with standard 36-pitch and 20°-pressure-angle gear-generating hobs with a 39-degree helix angle. The helix angle of the first- and second-stage gears is 39° for both stages. The helix angle of 39° was selected for the first stage to provide the maximum possible elastohydrodynamic film thickness for quiet operation at road load without excessive power loss at the power turbine thrust bearing. The helix angle of 39° for the second stage would also maintain the highest practical film thickness without excessive tooth bending stresses at the 1-2 upshift point of the transmission. Figure 76 shows the peak speed elastohydrodynamic film thickness and 1-2 upshift bending stress variation versus gear helix angle.

Figure 77 shows the bending stresses of the optimized gear sets for the Upgraded Engine and for the Baseline Engine. The high bending stresses of the optimized gears resulted from the reduced face width and higher unit loads, Figure 78. However, bending stresses were below the endurance limit and not found critical for the second-stage gears of the Upgraded Engine.

Figure 79 shows the elastohydrodynamic oil film thickness of the Upgraded and Baseline Engine reduction gears at road-load operating conditions. The peak film thickness of the first-stage gear was increased seven times, and the peak film thickness of the second-stage gear was increased 4.5 times compared to the film thickness of the Baseline Engine gears. This was expected to result in quieter operation within the road-load range. The thicker oil film in combination with the low contact time of the first-stage gears also allows a degree of isolation of high speed shaft vibrations (due to shaft unbalance, bearing irregularities and gear mesh) to the supporting structure of the power plant.

The degree of isolation varies with the speed of the power turbine shaft as described in Figure 80. Isolation would be considered complete when the contact time is less than that required for vibrations to pass through the oil film at all points on the tooth. This is the situation above 42,000 rpm. Below 22,500 rpm, this form of isolation does not exist and between 22,500 and 42,000 rpm, the partial isolation would help to alleviate the transmitted vibrations. Of course some vibrations will be transmitted through the oil film of the high-speed-shaft bearings to the engine housing, but direct transmission from gear to gear (steel to steel) would not take place at speeds above 42,000 prm. Ref. 11 was used as the basis of this analysis.

Figures 81 and 82 show the sliding velocities and the scoring factors of the Baseline and Upgraded Engine reduction gears. Lower sliding velocities along with lower scoring factor were goals of the gear design for quieter operation, long life, and torque-transmitting efficiency. As shown in Figure 83 the total torque (power) transmitting efficiency of the two-stage gears is higher than that for the gears of the Baseline Engine.

A three-dimensional stress analysis was conducted for the gears of the Upgraded Engine using 50% greater tooth crown per inch of face width than for the gears of the Baseline Engine. This crown permits greater shaft deflections and misalignment without loss of conjugate action. The analysis indicated that compression and shear stresses (Figures 84 and 85) will be lower than the corresponding stresses of the Baseline Engine gears throughout the operating range. The surface tensile stresses will also be satisfactory, although the stress levels are somewhat higher in the second-stage gears of the Upgraded Engine than those of the gears for the Baseline Engine (Figure 86).

The quality of the Upgraded Engine reduction gears (36 normal pitch) was selected to be between AGMA Grades 12 and 13 (precision grade). By comparison, the coarser Baseline Engine gears (18 pitch) with approximately the same tolerance levels as the Upgraded gears fall between Grade 12 and Grade 15 (ultra-precision grade). This is because a larger tooth of the same grade level has proportionately larger tolerances. (Note: Grade 16 in AGMA Standards represents the ultimate (master gear) tolerances).

The hardness of the Upgraded Engine gears (35 Rc) is the same as that for the gears of the Baseline Engine. Higher hardness material would not be suitable for hobbing and shaving and would thereby require grinding. Final surface treatment is Tufftriding.

9.4 Auxiliary and Accessory Components and Drive Systems

9.4.1 Drive System Requirements

Layout studies and evaluations were made of several accessory drive arrangements and oil sump configurations to aid in selecting the final design. Many factors were considered in the design of the drive system. A schematic of the accessory drive system selected for the Upgraded Engine is shown in Figure 87 and described below. Table 11 provides a list of data on the gears and sprockets used in the Upgraded Engine.

Engine auxiliaries driven by the power turbine are an oil pump, an alternator and an air pump (for the droplet diffusion combustor). Other engine auxiliaries are the electric starter motor and the electrically driven fuel pump. The vehicle accessories driven by the power turbine are the power steering pump and the air conditioning compressor. The regenerator is driven by the power turbine, but the design details are discussed in Section 7.1.

The operating speed range for the auxiliaries of a free rotor engine arrangement is determined by the power turbine idle to maximum speed ratio. The engine idle speed, 600 rpm (output of power section), is dictated by transmission pump capacity while the maximum engine speed, 4645 rpm, corresponds to the maximum allowable power turbine rotor stress speed. If a governor is not used, the accessories and auxiliaries must be able to operate over this nearly 8-to-1 speed range, but their required design life at the maximum speed is minimal since this maximum is reached only at vehicle speeds in excess of 100 mph. The maximum engine output speed "normally" experienced is limited to 4000 rpm or less by the wide-open throttle gear shift points, and the maximum steady-state speed is limited to about 2500 rpm by the maximum legal highway speed of 55 mph.

The cost and complexity of the system was minimized while maintaining the life requirements of an automotive engine. The drive gears and shafts were located to meet certain mechanical requirements. There was a need for an adequate drain angle from regenerator drive pinion bearing to the sump. The regenerator drive had to be positioned to minimize regenerator core hub loads within the space limitations imposed by the shape of the engine housing and vehicle compartment. An air pump and drive were provided to permit use of the droplet-diffusion combustor as an alternate to the lean, pre-mixed/pre-vaporized combustor concept.

The vehicle accessories and most engine auxiliaries are power turbine driven during normal engine operation. However, the start of power turbine rotation lags that of the gas generator by about one second for a warm engine start-up and from five to ten seconds for a cold engine, cold ambient start-up. To insure bearing lubrication pressure and adequate air pressure for fuel atomization during start-up, the pumps are driven through an alternate drive path from the rear of the starter through an electrically actuated clutch

Driving the air and oil pumps during starting add complexity and restricted the location of the drive system. The pump assembly bolts onto the reduction gear assembly and is driven during starting via a quill shaft as shown in Figure 88. This shaft spans the gap between the starter gear case output and the clutch input. The shaft ends are of crowned hexagonal configuration to tolerate misalignment between the members and transfer torque to the clutch. The overrunning clutch, provides the drive later in the start cycle and during the normal run mode.

9.4.2 Drive System Description

A common shaft, keyed the ends, drives both pumps (Fig. 88). The shaft is supported at the front end by a babbit bearing and at the rear by the cast iron oil pump housing. A simple integral eccentric and counterbalance drives the air pump. The front bearing is direct pressure lubricated, and an annulus in the shaft directs oil to the air pump eccentric through an internal passage. The rear bearing is lubricated by oil pump bleed back to the sump. The air pump is replaced with a spacer housing when the premixed/prevaporized combustor is used. A shaft without eccentric/counterbalance is also used with the spacer housing. The clutch is an electromagnetic clutch having a torque capacity of 7.91 N-m (70 in-lbs) to 6.21 N-m (55 in-lbs) at 12 VDC over the specified air gap tolerance. This capacity is twice that of the engine starting requirements.

As the engine accelerates through the start cycle, the regenerator drive worm (Fig. 87) increases in speed until it can drive the air and oil pumps through the overrunning clutch. The overall ratio from the power turbine rotor to the regenerator core is 2188:1 which includes the engine reduction gear of 14.89:1, the auxiliary drive ratio 1.18:1, the worm gear drive 15:1 and the regenerator core ring gear/pinion of 8.28:1. The regenerator drive worm gear is supported by two bearings on a rigid shaft along with the regenerator drive pinion. The regenerator worm, the auxiliary drive gear and the oil and air pumps are all mounted in a forward extension of the reduction gear housing (Fig. 72) to maintain alignment for these components and minimize the number of bearings required.

This relatively simple configuration is lower in cost as compared to some other systems studied. However, several parts require close tolerances to minimize regenerator drive pinion (mounted on the reduction gear sump) mislocation relative to the regenerator drive ring gear (mounted on the core supported from the engine housing crossarm). An eccentric adjustment was provided at the core center bearing to control spur gear backlash at assembly.

Alternate arrangements were studied which featured the regenerator drive mounted on the engine housing for reduced center distance variation with the regenerator gear. Designs with the sump integral with the engine housing were also evaluated. These arrangements, however, were generally more complex. Other schemes involving crossed axis gears, double enveloping worm gears, and conical involute gears were investigated but rejected.

A preliminary evaluation was made of an arrangement assuming that the air pump would not be required and that the oil pump could be located on the engine output shaft (with delayed lube pressure during starting). The most promising design used a top rear regenerator drive with the worm driven through a timing belt/sprocket arrangement off the power turbine accessory shaft. This system is simpler than the selected Upgraded Engine design, would likely effect a cost benefit, and is worthy of further investigation. However, the reliability of a belt-driven regenerator, the availability of space at the upper rear section of the engine compartment, and the performance of bearings with no oil pressure during starts would have had to be thoroughly evaluated and proof tested before proceeding.

The vehicle accessories are belt driven from a shaft (Fig. 72) which is chain driven from a sprocket on the intermediate shaft. The chain shown was selected for long life and quiet operation at the high chain speeds (7800 ft/min.) which exist at maximum output speeds.

9.4.3 Engine Auxiliaries

Starter System

The starter, (Fig. 88) rated at 2.01 kilowatts (2.7 hp) nominal, is a commercially available automotive starter modified for application to the Upgraded Engine. One end cap serves as a gear case half for the two-stage, grease-packed, spur gear 6:1 reduction gear assembly. The opposite end of the starter drives the high speed clutch/gas generator thru a 5.0:1 step-up pulley/polyflex belt system.

Air Pump

This pump is required only with the droplet-diffusion combustor. It is a single-piston, double-acting pump of 69.8 mm (2.75 in) bore and 9.3 mm (0.37 in) stroke. The aluminum piston/graphite piston ring runs in a cast iron cylinder which is piloted to the main housing. A simple bronze crank, pinned and free to swivel on the piston shaft, engages the eccentric to actuate the pump. Dual acting reed valves provide the required inlet and outlet porting. A surge chamber/orifice system, tuned to the pump, damps out pulses to the fuel nozzle. This pump is a repackaged version of the Baseline Engine pump and has exhibited trouble-free operation over thousands of nours of combined test cell and vehicle applications.

Oil Pump

This automotive-type pump, Fig. 88, has an internal capacity of 29.8 cm^3 (1.82 $inch^3$)/rev. utilizing cast iron housings and powdered metal rotors. The lube oil pump displacement was selected to provide high speed rotor lubrication at the critical point during the engine start cycle when the starter has disengaged and the pump is being driven by the power turbine which has not yet come up to full idle speed. This conservative design approach resulted in excessive pump capacity at normal operating speed. The pump could be readily downsized by reducing rotor width, but no attempt was made to determine the minimum pump size required to adequately lubricate the high speed rotor bearings during the start cycle.

Alternator

A conventional 12-volt alternator with a nominal 65-ampere rated output is used to supply the electrical requirements. In addition to the usual vehicle and engine electrical requirements, the fuel pump and control system are electrically driven as are the fans for air conditioning condensor and engine and transmission oil cooler, and the water circulating pump for the passenger compartment heater system.

Fuel Pump And Control

The electrically driven fuel pump has a nominal current rating of 6 amperes. Fuel flow rate is proportional to voltage, and the Electronic Control Unit (ECU) requires 2.5 amperes for operation.

10.0 INTERSTAGE SECTION

The interstage assembly, as shown in Fig. 89, consists primarily of the shrouds and the variable power turbine vanes. The vanes are retained in a nozzle support which also locates the shrouds via three struts. The support is mounted on the bulkhead flange of the engine housing and is cooled with compressor outlet air passing between the two walls of the bulkhead. Insulation placed between the hot outer shroud and the support minimizes heat loss and permits the use of a relatively inexpensive ferritic stainless steel support casting The shrouds are austenitic stainless steel to minimize distortion with long term operation.

The nozzle vanes are varied with a gear system, as shown in Fig. 89. This consists of powdered metal sector gears used "as sintered" and mounted on tapered squares machined on the ends of the nozzle vanes. This design allows no backlash between the sector gear and nozzle vane stem. The sector gears mate with a ring gear which rotates on the support and is connected to the actuator through a flexible link.

The nozzle support is preoxidized after machining to provide a low-friction wear surface for the nozzle vane stems. A coating is applied for the same purpose on the nozzle support at the pilot surface for the ring gear and on the retainer for the ring gear.

10.1 Struts

The three interstage struts support the inner shroud through the outer shroud. The struts are subjected to the compressor-turbine exit gas load and the axial load due to the pressure differential across the conical inner shroud. The resulting combined stress under these loads is 22,400 psi. This is well below the material (IN 713LC) yield strength at the estimated temperature of 1600 F.

10.2 Power Turbine Nozzle and Actuator

The variable power turbine nozzle is made from a Chrysler proprietary superalloy identified as CRM 18D. The nozzle vane is subjected to gas bending stresses and the maximum stress is only 2,300 psi.

The nozzle linkage actuating system is shown in Fig. 90. The linkage rod is designed to withstand the compression and bending stresses as the result of the load imposed by the actuator to rotate the nozzle vanes. Under normal actuator operation the rod will be subjected to a compressive load which will also cause bending of the rod as the nozzles are rotated.

The combined stress for this condition under maximum capacity load (88 lb) of the actuator is 26,000 psi in compression. This stress would occur from nozzle sticking. The critical buckling load which can be applied if there is no bending in the rod is 271 lbs, which is well above the maximum capacity of the actuator.

The calculated force required to drive the nozzles is 50 lb based on an assumed coefficient of friction of 0.3. This load is well within the capacity of the actuator.

10.3 Ring Seals

As shown in Fig. 89, two ring seals are installed with the interstage assembly to provide leak path seals. These seals minimize leakage past the power turbine-seal (X)--and the high pressure side of the regenerator core --seal (Y). The seals are machined to maintain ring compression in the bore throughout the range of operating temperatures. The pressure drop is relatively low across both these seals under most engine operating conditions and consequently the pressure forces are usually insufficient to slide the ring axially. Therefore, the ring groove width is set to allow free ring movement, but still provide an effective restriction to leakage.

Ring seal (Z) is mounted in a groove on the compressor-turbine shroud and seats in a bore on the front of the interstage nozzle support as shown in Fig. 89. This seal controls gas leakage past the compressor-turbine and, as such, is a major factor in engine performance. Therefore this seal, operating with the pressure difference across the turbine stage, must always seat against both face "F" and diameter "I" despite relative movements between the compressor-turbine shroud and the interstage nozzle support. The ring designed as shown in the inset has demonstrated reliable performance. The rear face is relieved, or pressure balanced, so that the net axial pressure force "P" will not restrain the ring from sliding relative to F and seating on diameter I.

The relief at the outside diameter allows an increase in radial pressure force on the ring for better sealing on the outside diameter, while still allowing the ring to slide axially. The relief on the outside diameter also inhibits debris from accumulating which can cause the ring to lift off the surface and cause a leak, thermal gradients in the ring, and possible excessive distortion. A special machining procedure is used for the outside diameter of the ring so that the ring will have a slight compression in the bore at all operating temperature levels, assuring sealing contact at the outside surface.

11.0 REGENERATOR

The principal areas for the mechanical design of the regenerator consisted of the core seals, the drive and support system, the stress analysis for the cover and the thermal analysis of the core. Except for the latter, all of these areas are discussed in this section. The thermal analysis of the matrix used in the Upgraded Engine was carried out as part of the Baseline Engine program for advanced concepts. Subsequent testing confirmed the structural integrity of the matrix. These tests were conducted on cores having the same material, wall thickness, and hydraulic diameter as the matrix used on the regenerator core for the Upgraded Engine. Temperature levels of the Upgraded Engine were imposed on the cores in these tests, and results are presented in Volume I of the Final Report.

11.1 Regenerator Seal Design

Rubbing seals and static seals are needed to effectively seal the high pressure side of the regenerator from the low pressure. Three rubbing seals are required: the inner rim seal, the inner crossarm seal, and the outer "D" seal. Static seals are required to seal both the inner and the outer assembly between the rubbing seal and the seal platform on the housing. The static seals can be either the bridge type or the "L" type.

The clamping force between the high temperature graphite inner seal rim and the ceramic regenerator core was set at 4 lbf per inch of seal in order to minimize leakage while keeping wear and the torque required to turn the core at acceptable levels. Included in this analysis is the positioning of the static seal in such a manner so as to minimize the overturning moment and the wear by evenly distributing the pressure. A similar pressure balance was done on the crossarm seal which was loaded at 10 lbf per inch of seal. In addition, the crossarm seal will warp when heated due to the difference in coefficients of linear expansion between the Inconel X-750 metal substrate and the nickel oxide/calcium fluoride plasma coating.

The seal system is completed with a bridge seal or an L-seal (see Fig. 91), which is substantially simpler than the bridge type and is a small fraction of its cost. Once positioned in the groove the L-seal is held in place by a spring and the pressure differential between the high and low pressure sides. Limited engineering tests using the L-seal showed it to have exceeded the performance of the bridge seal.

11.2 Regenerator Drive and Support System

The regenerator drive and support system consists of a worm and worm gear driving a pinion and that pinion driving a hub-supported ceramic core by its rim through an elastomer-mounted ring gear. A rim support was investigated but the hub support was found to be simpler and lighter in weight.

The regenerator core graphite sleeve center bearing load and the hub load were minimized through careful analysis of the vector sum of the weight of the core, the force of the rubbing seal friction, the gear drive force, the gear separating force and the external forces due to the acceleration of the car.

The high temperature Upgraded Engine incorporates a ceramic regenerator thus requiring a silicone rubber elastomer to accommodate the thermal expansion difference between the ceramic core and the metal ring gear. The elastomer was designed to transmit the drive torque while supporting the ring gear in the hot engine environment. When flexible mounts were successfully included to allow for elastomer shrinkage, (Fig. 92), the alternative, a mechanical ring gear support, was abandoned because of its complexity.

The ring gear and a conical pinion, with slight tooth crowning (see Fig. 93), are unlubricated spur gears designed to tolerate a 2-mm center distance variation. These gears have been optimized, resulting in satisfactory contact patterns, lower sliding velocities, and lower gear tooth stresses than the Baseline gears despite higher loads. A flexible connection between the 14-pitch pinion and the worm gear was considered, but the final design incorporated a rigid shaft.

To complete the sizeable speed reduction needed to drive the slowly rotating regenerator, a 20.5:1 worm gear set was initially specified. The engine lubricant is transmission fluid, MS 4228, and not a recommended worm gear lubricant such as Sun gear oil 7C; consequently during fixture tests excessive worm gear wear occurred. In order to provide better balance in the life of the two gear sets, the worm gear ratio was reduced from 20.5:1 to 15:1, and the pinion-ring gear ratio was increased from 6.2:1 to 8 3:1. Despite this change, the stresses in the pinion-ring gear set of the Upgraded Engine are still far below those of the Baseline Engine, as shown in Fig. 94.

11.3 Regenerator Cover Stress Analysis

The regenerator cover was analyzed using a finite-element technique. Several alternate designs were studied as a result of the highly stressed original cover design. Large deflections in the center of the cover induced excessive stresses in regions with small radii of curvature; reducing that deflection reduced the resulting stresses.

Two designs were pursued to reduce the locally excessive stresses calculated for the original cover; one incorporated ribs and the other involved a change in the radius of curvature at a highly stressed area. The ribbed cover offered the greatest improvement as is seen in the following summary of finite-element results:

	Equivalent Stress (psi)*			Maximum Deflection (In.)
Design	Node 409	Node 1008	Node 465	
Original	26,090	18,454	23,279	0.035
Large Radius of Curvature	16,314	22,251	22,812	0.033
Ribbed	11,788	7,057	7,350	0.021

12.0 COMBUSTOR

The combustor of the Upgraded Engine is a fixed-geometry, lean, premixed/prevaporized (LPP) concept. It has a pressure loss between 2% and 3% and is capable of multi-fuel operation. Another concept considered was the droplet diffusion combustor. The LPP combustor was selected however, since, on Baseline Engine testing, it had demonstrated the potential to meet the emission standards of 0.41 gr/mi HC, 3.4 gr/mi CO and 0.10 gr/mi NOx in a 3500-lb vehicle. On the other hand, the LPP combustor would require extensive development for cold starting at -10 F and for combustion stability during and at the end of transient operations. Cost was another consideration. The droplet diffusion combustor with its air pump was estimated to cost 1/3 more than the LPP with its torch.

Emissions from combusted hydrocarbon fuels can be controlled in the combustion process by limiting temperature at which the fuel is burned. NOx formation rate is temperature and time dependent. Since residence time is limited by engine design constraints the reaction zone **maximum** allowable temperature to prevent NOx formation is 3200 F. Control of CO and HC, however, require long residence time and an **average** minimum reaction zone temperature of approximately 2000 F to oxidize these emission species. The Upgraded Engine combustor was configured to meet these constraints.

The lean premixed/prevaporized combustor is comprised of three sub-assemblies, the premixer/injector, torch ignitor and reaction chamber, as shown in Fig. 95. Configuring the reaction chamber as a separate entity which is not constrained by the premixer or torch makes it suitable for fabrication from ceramic materials.

The premixer/injector introduces the fuel through four tubes at a minimum pressure drop (<10 psi) into a zone of counterswirled air equivalent to approximately 33% of the engine mass flow. Except during the initial cold start, no burning occurs in the premixer, and consequently it may be fabricated of a lesser quality material, such as AISI 304. Vaporization of the fuel discharging from the four tubes is dependent on the regenerated air. The homogeneous lean mixture is directed into the reaction chamber where the torch ignites the mixture.

The torch is comprised of a simplex fuel nozzle, flowing approximately 2 lbs/hr of fuel. Combustion air is supplied from a total pressure pickup positioned at the discharge of the compressor. This air (approximately 2% of the engine airflow) bypasses the regenerator and is a loss in fuel economy. Torch fuel/air ratio is rich to minimize NOx formation. HC and CO are consumed in the reaction zone. A conventional automotive spark plug is used for ignition; the torch remains on during all engine operation.

The design of the reaction chamber introduces the fuel mixture tangentially to promote vortex recirculation for stable operation. Fuel/air ratio as lean as 0.01 (0.15 of stoichiometric ratio) has been demonstrated on the Baseline Engine. A second consideration in the reaction chamber design was to provide a wall constriction midway in the flow path to redirect gases which may have accumulated on the walls into the main stream. The reaction chamber is sized to provide adequate residence time to complete oxidation of the fuel. Its external walls are convectively cooled by the regenerator outlet air. Dilution holes are positioned and sized to provide good mixing. A comparison of reaction zone conditions for the Upgraded and Baseline Engines is shown in Fig. 96.

13.0 POWERTRAIN AND VEHICLE SYSTEMS; PERFORMANCE PREDICTIONS

The Upgraded Engine was designed for installation into a compact vehicle --the two- and four-door 1976 Plymouth Volare and Dodge Aspen models. These are six-passenger, front-engine, rear-wheel drive vehicles with a three-speed automatic transmission and lock-up torque converter. The vehicles are equipped with power steering, power brakes and air conditioning. The Upgraded Engine is in the same relative location as the spark ignition engine which it replaces.

13.1 Powertrain Systems

The powertrain system, as defined here, consists of the basic engine with its auxiliaries, the engine-driven vehicle accessories, the transmission, and the drive line components necessary to transmit the engine power to the vehicle tires. The engine auxiliaries are those items required for basic engine operation such as the starter, engine oil pump, alternator, fuel control system, and, if required, the air pump for fuel atomization. The engine-driven accessories include the power steering pump and the air conditioning compressor.

The auxiliary and accessory functional descriptions are:

Starter - 12-volt automotive type rated at 2.7 hp.

Oil pump - 1.82 cubic inch per revolution Gerotor type.

Air pump - Double acting, single piston with a 2.75 in. bore and 0.37 in. stroke.

Alternator - 65-amp rating; 10.5-amp output used for engine ignition and fuel control system operation.

Power steering pump - 0.94 cubic inch displacement per revolution vane type unit used for vehicle steering and braking assists as well as for the engine actuators.

Air conditioning compressor - 10 cubic inch displacement per revolution with 4 cylinders arranged radially.

The auxiliary and accessory drive power requirements are shown on Fig. 97 for operation at the peak power condition for the various gas generator operating speeds. The air conditioning compressor power requirements are not shown since the air conditioning is not normally used during engine or vehicle performance and fuel economy evaluations and because the power requirements are also highly dependent on the ambient conditions. The power steering pump power requirements are also not shown since they are highly dependent on the system pressure demand, which varies significantly with the vehicle steering and braking maneuvers, as well as with engine and vehicle speeds.

Also shown on the figure are the drive power requirements of the power turbine shaft bearings and the reduction gear train losses. These drive requirements are referred to as parasitic losses since they reduce the available output power of the engine.

The estimated gross output power characteristics of the engine are shown on Fig. 46 for various gas generator operating speeds and VIGV positions. The minimum brake specific consumption characteristic for net engine output conditions is shown on Fig. 98. This represents the output power available to drive the vehicle accessories, transmission and vehicle.

The vehicle transmission is a slightly modified three-speed automatic transmission with a lock-up torque converter designed for use with a six-cylinder spark ignition engine. The modifications include transmission valve body changes for modulating gear shift time as a function of engine output power level and for engaging the torque converter lock-up clutch in both intermediate and direct gear ranges. The transmission gear ratios are 2.45:1 low, 1.45:1 intermediate and 1:1 direct. The transmission-to-engine carburetor control linkage used with the spark ignition engine is replaced by an electric position sensor connected to the engine Electronic Control Unit (ECU).

The torque converter maximum torque ratio is 1.9:1, and the input (transmission impeller) speed is 2050 rpm at stalled output with a 200 ft-lb input torque. A lengthened drive shaft is required with the somewhat altered transmission location in the vehicle.

The rear axle ratio is 3.23:1, and the tires are FR78 x 14, which travel 800 revolutions per mile at 45 miles per hour.

13.2 Vehicle Systems

The number and nature of significant vehicle system changes from the "normal" spark ignition engine vehicle installation are small. The basic structure and suspension are unchanged except for minor engine and transmission mount location changes; See Fig. 99. The larger exhaust duct used with the gas turbine engine requires vehicle underbody changes in the transmission and drive shaft tunnel area. The single duct terminates ahead of the rear axle. The power brakes are hydraulically actuated, similar to those used for diesel engine applications rather than the vacuum type normally used with spark ignition engines.

The most extensive changes are required in the passenger comfort systems--the heater and air conditioner. The components are essentially the same as for the spark ignition engine except that an electric motor driven fan is used to cool the air conditioning condenser since there is no engine driven fan, and a hot gas to water heat exchanger is used since the gas turbine engine is not water cooled. The heat exchanger, located in the engine compartment, uses power turbine exit gas to heat the water which is circulated through the normal vehicle heater by an electric motor driven water pump. The control and actuator functions are pressure rather than vacuum operated.

The engine-vehicle installation arrangement for a four-door sedan is shown on Figure 99. The calculated vehicle fuel economy for the Federal Register specification for vehicle chassis rolls testing in a 3500-pound inertia weight class, with the specified dynamometer power absorber setting of 11.2 hp, and with use of unleaded gasoline fuel is:

14.8 mpg. Federal Urban Driving Cycle

25.7 mpg, Federal Highway Fuel Economy Cycle

18.3 mpg, Combined Cycle

The calculated vehicle acceleration time for an idle start up to 60 mph is 13.5 seconds.

14.0 ENGINE ASSEMBLY

The Upgraded Engine is comprised of seven modular subassemblies that are described below. The modular configuration facilitates installation and removal of the subassemblies in the engine housing. The assembled engine is shown in Figs. 100a and 100b; an expanded engine displaying the subassemblies in their relative positions is shown in Fig. 101.

14.1 Engine Housing

The engine housing is a nodular iron single piece casting that contains the flowpath cavities for the compressor and the power turbine discharge flows and for the cooling air to the power turbine nozzle assembly. The gas generator, power turbine nozzle assembly and power-turbine/reduction -gear assemblies are piloted into the housing to maintain radial alignment. Axial clearances are controlled by shims.

14.2 Power Turbine Nozzle Assembly

This assembly is built up as a unit and installed into the interstage bulkhead of the engine housing via a hot and cold pilot arrangement. Critical to engine performance is the vane-to-shroud clearance which is closely held to a minimum of 0.08 mm (0.003 in). The nozzle assembly hydraulic actuator is mounted externally and is controlled by the Electronic Control Unit (ECU). The nozzle assembly is shown in Fig. 104.

14.3 Gas Generator Assembly

The gas generator assembly contains the aluminum bearing carrier and cover, impeller and compressor-turbine stage; see Figs. 105 and 106. This assembly is built up as a unit and piloted into the forward flange of the engine housing with a steel pilot ring held concentric to the aluminum carrier with 9 radial pins. Critical clearance control of the aerodynamic components is essential to maintain component efficiency. Typical rotor/nozzle shroud radial clearance is held to 0.15/0.23 mm (0.006/0.009 in). Axial clearance between the impeller front face and the mating shroud is 0.23/0.28mm (0.009/0.011 in). The tiebolted rotor assembly is supported by an air bearing at the turbine end and an oil sleeve/thrust bearing at the impeller. The rotor assembly is balanced to less than 0.005 oz-inches. Sealing around the rotor shaft is provided by three control gap carbon seals.

14.4 Power Section Assembly

The power section assembly is comprised of two components: the power turbine rotor assembly with an aluminum housing and a cast iron gear box with engine auxiliaries and vehicle accessories; see Figs. 107 and 108. The aluminum power turbine rotor housing assembly which supports the power turbine rotor, pinion and bearings is the heat sink for the bearings, following engine shut down. Radial blade-to-shroud clearance is 0.30/0.25mm (0.012/0.010 in). The gearbox contains the two-stage reduction gear, four auxiliary-drive gears for the regenerator and air/oil pump drive, a sump for 4 quarts of oil and the breather blow-by system. When assembled the unit is piloted into the rear flange of the engine housing. An internal chain drives the pulley for the vehicle accessories.

14.5 Air/Oil Pump Assembly

This unit is built separately and attached to the forward end of the reduction gearbox. See Fig. 109. The forward end of the assembly is aligned with the starter motor reduction gear box. During the start cycle, the starter motor drives the unit via an electric clutch to provide air/oil pressure requirements. The reduction gear drives the pumps in the running mode through an overrunning clutch.

14.6 Variable Inlet Guide Vane Assembly

This sub-assembly is piloted to the gas generator compressor cover. The assembled unit is shown in Fig. 110. A hydraulic actuator mounted below the intake actuates the 13 moveable vanes through a slotted ring.

14.7 Intake/Starter Assembly

This package is made up of two sub-assemblies:

- The intake bowl assembly houses the starter clutch and driven pulley. The bowl is also flowpath for the entry of air into the VIGV assembly.
- The starter motor assembly is suspended beneath the intake bowl and drives the starter clutch. As mentioned before the starter motor also drives the air/oil pump assembly via an electric clutch during the start cycle.

The intake/starter assembly is shown in Fig. 111.

14.8 Insulation

Linerless insulation is used throughout the engine. The insulation is provided in preformed pieces. Minor alteration is usually needed to fit it properly to the mating metal part. It is cemented to the mating metal part with high-temperature adhesive and, when necessary, the flowpath surfaces are restored with erosion resistant coatings. Figs. 102 and 103 display a typical engine housing with insulation installed.

15.0 INSTRUMENTATION

The following sections discuss details of instrumentation for four major test rigs, engine test cell installation, and vehicle dynamometer testing. The test rigs were a compressor rig, a turbine nozzle cold-flow rig, a power turbine rig and a regenerator rig. Each facility is described and is followed by details of instrumentation type and location. Emphasis is placed on measurements of temperature, pressure, air flow, flow angle and fuel flow. The test rigs are discussed first, followed by the engine and vehicle test facilities.

15.1 Rig Testing

15.1.1 1.26 Scale Compressor Rig

A compressor test rig was designed, procured, built and checked out for component testing at NASA-Lewis. The compressor was a 1.26 scale of the Upgraded Engine compressor. Rig shakedown and five preliminary tests were conducted before shipping the rig to NASA.

Facility

Power to drive the compressor rig was supplied by a 1500-HP constant-speed DC electric motor. The output speed of this electric motor was stepped up through a 5:1 gearbox, the output of which drove an eddy-current clutch used for speed control. A further speed increase was obtained through a 21:1 gearbox, which was connected to the test rig with a splined coupling.

Inlet air for the test rig was taken from the roof of the laboratory building, preheated, filtered, cooled and dehumidified and heated once again. The air flows through the second heater into a plenum, entered a straightening screen and then continued into an airflow measuring nozzle. The airflow nozzle was connected to the rig by a transition pipe approximately 3-1/2 pipe diameters long (see Fig. 112). The first test (1.26 scale) impeller is shown installed on the test rig in Fig. 113.

Instrumentation

Compressor inlet pressure and temperature conditions were measured with six chromel-alumel thermocouples and six pressure taps in the inlet plenum just upstream of the compressor. At the compressor discharge, eighteen chromel-alumel thermocouples, ten total pressure probes and six collector-static pressure taps are incorporated. The total pressure probes were constructed of 0.043-inch (1.08mm)-diameter stainless tubing. These probes were relatively insensitive to flow angle as indicated in Figure 114.

In addition, the compressor rig had an array of static pressure taps on the impeller shroud surface and on the diffuser shroud wall. The locations of these taps are illustrated in Figures 115 and 116.

Rub probes were installed to sense impeller deflection. These probes consisted of a copper core with a ceramic sheath inserted into a compression type fitting. The tip consisted of a thin flexible copper shim that was the contacting element of the probe. After setting the shim at the desired height above the shroud, the probe tip section was encased in epoxy. If the impeller struck the shim, a momentary electrical path to ground was established. An electronic network sensed this drop in resistance and lit an indicator lamp. The tip clearance was known from the preset height of the shim.

15.1.2 Turbine Nozzle Cold-Flow Facility

Facility

The nozzle cold-flow test facility consisted of a regulated air supply, ASME airflow measuring nozzle, settling tank and plenum (Fig. 117). The nozzle assembly under test was located in the plenum. The nozzle flow discharge into a duct which was routed through a silencer to the roof of the laboratory. The nozzle cold-flow rig is illustrated in Fig. 118.

Two general types of tests were conducted with this rig. The first type of test was for airflow calibration for engine data analysis. The second category of test work included detailed flow surveys at the nozzle inlet and discharge planes.

Nozzle Flow Calibration

Engine leakage flow estimates can be made if the flow characteristic of the nozzle is known. A typical nozzle flow characteristic is shown in Fig. 119. The airflow rate is determined from a calibrated 2.25-inch diameter ASME nozzle. The temperature and pressure correction factors, θ_5 and δ_5, are computed from plenum temperature and pressure measurements. The nozzle discharge shroud pressure is determined from three taps equally spaced circumferentially at the trailing edge discharge plane. Leakage estimates in engine testing can be made by computing the turbine mass flow from the corrected airflow obtained from the calibration curve at the measured nozzle pressure ratio. After many nozzles have been calibrated, it is possible to estimate the flow size of the nozzle from the mean throat measurement, Fig. 120.

Nozzle Surveys

The nozzle cold-flow rig was also used to survey flow-field conditions. A minature cobra probe was used for much of the survey work. This probe, illustrated in Fig. 121, is constructed of 0.01 inch (0.254 mm) diameter stainless tubing. The probe diameter is progressively stepped up for the rigidity and compatibility with the actuator system. Three probe circumferential positions at the nozzle inlet and exit were surveyed. These locations are illustrated in Fig. 122. Several static pressure measurements were made during the survey work. Included, also, are nozzle inlet and exit taps at the hub and shroud walls. For some nozzles, vane suction and pressure surface taps were included in the shroud wall, as shown in Fig. 123.

15.1.3 Power Turbine

Test Facility

A schematic of the facility used to evaluate the performance of the power turbine is shown in Figure 124. Air was supplied from a central powerhouse located in the Chrysler Engineering and research complex. Airflow rate is measured with a calibrated 2.250-inch (57.15 mm)-diameter ASME nozzle located in the supply pipe upstream of the test rig. Supply pressure is controlled with a pneumatic valve and controller.

Torque was measured using a Lebow 300-pound-capacity load cell mounted to sense dynamometer restraining torque. Power turbine efficiencies in this report are dynamometer based, rather than temperature based. Experience has shown that dynamometer-based efficiencies are more consistent than temperature-based efficiencies. This is probably due to the difficulty in measuring the steep temperature gradients, typically present in small axial turbines, resulting primarily from heat transfer effects.

Power Turbine Test Rig

The power turbine test rig incorporated a standard engine housing and power turbine reduction gearbox. A special front housing replaced the standard gas generator. This housing consisted of a long burner, mounted axially, with a set of swirl vanes at the discharge to provide the desired flow distribution. Figure 125 shows the power turbine rig installed in the test facility.

This test rig can be operated at cycle compressor turbine discharge temperatures if a regenerator is incorporated. In this mode of operation, a separate flow calibration test must be conducted to establish regenerator flow leakage. A second mode of operation incorporates a "dummy" regenerator core, which necessitates ambient inlet temperatures, but which has virtually no leak paths, since no sliding seals are needed. Regenerator leakage flow calibration data can be obtained when the rig is in this second mode (cold inlet and dummy regenerator) of operation.

The decision to build a regenerative power turbine rig was one of expediency and not a desire to have a power turbine rig with an additional element in the flow path. The expediency came about because the rig used several engine components which were readily available and did not require additional design and procurement time. There were two additional advantages also:

1. The engine asymmetrical exhaust diffuser discharge was duplicated.
2. If the rig were run at ambient inlet temperature, the disadvantage of having to estimate regenerator leakage was eliminated.

Instrumentation

A crossectional schematic of the power turbine rig flowpath is illustrated in Figure 126. Also shown are the locations of instrumentation used during these tests and the instrumentation-plane station identification numbers. Additional instrumentation in the exhaust plenum housing is shown in Figure 127.

Shielded, aspirating thermocouples were incorporated at Station 6.0 because of the proximity of the burner. All stationary total pressure probes were of the kiel type, since they are quite insensitive to yaw angle. Figure 128 illustrates the interstage nozzle assembly and the installation of these probes at Station 6.0. Static pressure taps were made by swaging 0.0312 inch (0.794 mm) diameter tubing into a 0.0292 inch (0.742 mm) diameter hole where wall thickness was not conducive to a counterbored hole. Where necessary, these tubes were ground flush with the flow surface, and all burrs were removed.

The swirl vane assembly was used to control inlet swirl to the power turbine interstage. The intent of incorporating these vanes was to approximate the desired discharge condition from the compressor-turbine stage. Cobra type probes were used to survey stations 6.0, 6.3 and 7.0. Figure 129 illustrates the location of these probes in the meridional plane.

15.1.4 Regenerator Flow Distribution Rig

Figure 130 illustrates the method used to measure the airflow distribution at the regenerator inlet face. This testing was performed in a partial engine assembly, in which a high-volume, low-pressure blower pumped cold air to the regenerator cover, and through the matrix, where it dumped to atmosphere. Pressure drop through the matrix was maintained at engine design levels. A sliding graphite button was manually positioned at various points on the discharge face of the matrix. A static port in the button was connected with flexible tubing to an inclined water manometer. This system permitted measuring the stagnation pressure at the inlet of the matrix passages blocked by the graphite button. The regenerator inlet pressure distribution was mapped by moving the button across the matrix. Modelling clay was used to reshape the regenerator cover contours until the desired uniformity of inlet pressure was attained.

Figure 131 shows the final flow distribution fence developed by the above method. A temperature grid installed in the engine verified the improvement in flow distribution.

15.2 Engine Testing

15.2.1 Dynamometer Facility

The engine performance characteristics were assessed under simulated vehicle conditions and vehicle systems, as much as practical. The test cell air delivery plenum system was adapted to the engine filter box with appropriate ducting. A brass box reservoir simulated the vehicle tank environment of zero gage supply pressure and fuel system return/vent functions.

Selected engine performance and vibration parameters were recorded on tapes in initial testing but discontinued as confidence and reliability were acquired. A block diagram is shown in Fig. 132 and actual installation and facilities shown in Figs. 133 and 134.

Engine Air Flow

Engine airflow was measured with a turbine type flow meter. A conditioned signal output was displayed on solid state counter/event displays.

Engine Speed

The traditional pulse generating devices with reluctance-type pickups were used for both gas generator and power turbine speeds. The steel inducer section of the compressor was used to produce gas generator speed pulses. Two independent pickups provided a readily available backup should either fail. The pickup for the Electronic Control Unit (ECU) was generally used independently, allowing the backup unit to be used for speed readout indications. Power turbine output speed was sensed at the dynamometer shaft. A 60-tooth signal generator integrated into the vehicle accessory drive pulley allowed an alternate (back-up) means of sensing speed. This speed signal is used in an ECU underspeed/overspeed routine, for vehicle application.

Fuel Flow

Steady-state fuel consumption is indicated on t. ype flowmeters calibrated for both unleaded gasoline and diesel fuel.

Engine Torque

Torque was registered on a Toledo scale via the conventional dynamometer cradle knife edge link system.

Temperature

Temperatures were indicated on a digital solid state readout and manually recorded.

Pressure

Pressures were indicated on water manometers, Wallace and Tiernan gages and/or a Scani-Valve transducer system with remote digital readout.

Engine Blow-By

The blow-by discharge was ducted to a calibrated sharp-edge orifice system. The differential pressure was registered on an inclined manometer. The inlet temperature was also monitored and required in the computation of equivalent engine air by-pass.

Engine Oil Temperature

An automatic temperature control device with readout was used throughout the program.

Engine Oil Pressure

Auxiliary pressure gages at the engine supplemented the normal gage on the control console. These gages responded faster than the console gage and were used during engine starting.

Electronic Control System Diagnostic

The cells were equipped with a breakout box and diagnostic module. This allowed any engine/control function to be monitored or changed from within the control room. The diagnostic panel provided the means of monitoring full time dedicated parameters for troubleshooting and recording purposes.

Emission Sampling System

A remotely located system is used to monitor steady-state emissions (HC, CO, NO, NOx, CO_2 and O_2). The equipment was constantly updated to conform to state-of-the-art improvements.

Calculation ranges allowed very low values (near zero) to be monitored and registered.

Power Turbine Nozzle Angle

Nozzle angle was read directly on a digital readout, with one vane coupled directly to an appropriate signal sending unit.

15.2.2 Performance Instrumentation

Fig. 135 shows the engine station , and Figs. 136-146 describe the standard instrumentation used on all test cell engines during the development phase of the program. Chromel-Alumel thermocouples were used exclusively throughout the engine. Low temperature applications (under 600 F) used glass-on-glass material while the hot zones used commercially available Inconel sheathed swaged stock. Junctions were spot welded and hand dressed to keep the junction within wire size diameter. Commercially available total pressure probes were used in the cold environments (less than 600 F) and in-house fabricated probes used for the hot zones. Tempered Inconel 600 tubing was used exclusively throughout the engine for all pressure parameters.

Measurement Of Engine Airflow

Engine airflow measurements were made with an Autotronic Series 100 airflow transducer. This is a low pressure drop turbine flowmeter suitable for installation at the engine inlet. A calibration check on its measurement accuracy was made to confirm the factory calibration.

The test facility used to calibrate the Autotronic flow meter is illustrated in Fig. 136. An ASME nozzle, located in a pipe upstream of the plenum, was used to obtain the reference flow measurement. The output signal from the Autotronic transducer for each test point was displayed on an oscilloscope and photographed. Frequency comparisons of the oscilloscope trace and electronic counter showed good agreement. At some airflows the signal was unstable, and a subsequent investigation revealed sporadic random pulses. The error caused by these pulses, however, was found to be less than 1%.

The result of the calibration is shown in Fig. 137. The agreement between the ASME nozzle and Autotronic meter is good. The remaining doubt is the effect of somewhat different inlet conditions of the meter installed in the test cell versus the calibration installation. In the engine test cell, air is drawn directly from a plenum into the cylindrical flow meter. To eliminate any possible vena-contracta errors, a bellmouth was fabricated to insure good inlet conditions.

Station 1

Figs. 138 and 139 define the compressor inlet probe positions. The circumferential locations were a compromise due to the odd number of VIGV stators. The commercially available total pressure probes were placed sufficiently upstream to be unaffected by VIGV leading edge. The thermocouples were placed at the eye of the impeller for an accurate indication of compressor inlet since some minor inlet heating was experienced.

Station 2

Three temperature and total pressure probes were centered in the 3 compressor discharge lobes as shown in Figs. 140 and 141. The average value of each probe type was used to compute compressor performance.

Station 3

One static pressure tap was located on the regenerator cover. Although station 3 is shown as the inlet to the regenerator, thermocouples were placed near this cavity within the engine housing at the bulkhead inlet and outlet cooling passages. These locations were used to assess the bulkhead heat loss to the compressor discharge air.

Station 4

This area was not normally instrumented; however NASA-Lewis had an engine fully instrumented with station 3, 4, 8 and 9 temperature grids.

Station 5

Probe positions are shown in Figs. 142 and 143. One total pressure probe was placed in the vortex chamber to determine burner pressure drop and the compressor-turbine inlet total pressure Three thermocouples, equally spaced, were used to measure turbine inlet temperature.

Three static pressure taps at station 5.5 equally spaced on the compressor-turbine nozzle shroud at the vane discharge are calibrated under cold flow conditions. The measurements from these taps were used to calculate engine leakage and turbine inlet temperature. The locations are indicated on Fig. 123 at the vane exit; actual installation shown on Fig. 144.

Station 6

A total of 9 measurements were taken at this location, i.e., 3 static pressures, 3 total pressures and 3 total temperatures. the three static pressures we e equally spaced and placed in the compressor-turbine nozzle outer shroud immediately aft of the compressor-turbine rotor blading. Placement is defined in Fig. 142, and actual installation shown in Fig. 144.

The positions of the three total pressure and temperature probes, shown in Fig. 145, were asymmetrically located relative to nozzle trailing edge position. These were also located between the support struts. The angle of the probes was set at the design absolute exit angle of the compressor-turbine rotor.

Station 7

Three static taps shown in Fig. 145 were equally spaced circumferentially. Thermocouples placed at the exhaust diffuser discharge station 7.5 were originally used to set the cycle temperature. However, a temperature correction was later applied so that the calculated turbine inlet temperature was equivalent to the design value for which the turbine was designed. As such a better assessment of engine/component performance was possible.

Station 8

Thermocouples placed adjacent to the regenerator core face generally agreed well with the station 7.5 readings. A static pressure measured at the heater flange cover represented an average value of power turbine discharge static pressure.

Station 9

Engine exhaust temperatures and distribution were sensed by 4 thermocouples placed in the cell exhaust pipe in the center of 4 equal areas. These were located in a circular cross section immediately downstream of the rectangular-to-circular transition section. A total pressure probe centered in the circular section was used to calculate core pressure drop.

Special Aerodynamic Instrumentation

Early in the program additional instrumentation was required to define deficient areas within the engine. Special instrumentation was required to evaluate various compressor and compressor-turbine rotor configurations. Here the conventional methods were employed to gather the data. In addition, flow visualization was used to aid in interpretation of the data and identify possible problem areas. Chromium oxide was injected at the compressor inlet and/or compressor discharge for various engine operation conditions. Subsequent disassembly and examination revealed: bulk flow area; flow paths; stagnation and separation areas and leak paths. A more definitive approach for the compressor was the use of India ink and/or lamp black in a liquid. Here boundary layer effects, back-flow separation and bulk flow were evident. External shop air to the air bearing was required to prevent contamination.

Compressor-Turbine Rotor

Evaluation of the compressor-turbine rotor was accomplished by traversing the rotor discharge in the engine. This task represented a major effort and required fabrication, calibration and installation of a small cobra probe. The position of the probe is shown in Fig. 146. The probe was remotely actuated and used an L.C. Smith actuating system.

Compressor

Compressor surge was evaluated by injecting additional air at the compressor discharge and holding a constant turbine inlet temperature. This technique allowed surge to be evaluated at any ambient temperature level without exceeding absolute temperature limits within the engine.

Excellent data correlation resulted between this technique and the method of increasing turbine inlet temperature. The additional amount of air was measured with a flow meter.

15.3 Vehicle Dynamometer Testing

Fuel economy and emission testing took place at the Contractor's Chassis Rolls Dynamometer Facility. The standard vehicle instrumentation (gages and warning lights) was supplemented by a control panel which had two full-time analog meters displaying gas generator speed and engine temperature. Indicator LED's (light emitting diode) on this panel display discreet control system functions. A connector which teed into the ECU harness allowed in-vehicle evaluation of the control system using a diagnostic box. The diagnostic box was equipped with two digital voltmeters to monitor the 0-10 VDC programmed diagnostics. Rotary switches allowed any two of the assigned diagnostics to be monitored. In addition, banana plugs allowed access to multiple parameters to be recorded during vehicle road evaluation. A multi-pen recorder powered by an inverter was used for preliminary control development.

15.3.1 Emission Testing

Fig. 147 depicts the emission test set up. The three-bag system normally used by spark ignition vehicles was not applicable to the turbine due to the higher exhaust mass flow. As such, emissions were determined by integrating the emission tapes and recording gas generator speed to calculate engine air flow.

The emissions were recorded simultaneously on paper and FM tapes. The paper tapes allowed a real time reference to determine emission conditions. The FM tapes were processed through a computer program for computation of emission species mass rate.

In addition a modal analysis computer routine coupled to the emission analyzer printed out and recorded, on a cassette tape, average emission levels at 2-second intervals throughout the Federal Emission Drive Cycle. The modal analysis routine was used as a first approximation of emission mass rates.

15.3.2 Fuel Economy Tests

Fuel economy tests for cold '75, hot '74 and FEC were conducted on the chassis rolls dynamometer for an inertia weight of 3500 pounds. The dynamometer power absorber setting was 11.2 hp, as specified by the Federal Register. The fuel used was unleaded gasoline, and fuel consumption was determined by directly weighing the fuel.

16.0 ENGINE PERFORMANCE DEVELOPMENT

This section summarizes the development work carried out to achieve the final engine performance. The original power and SFC goals were not achieved, but significant progress was made over the Baseline Engine SFC values. Initial testing showed that the engine power was 40% below goal at 80% speed, which was the development program reference speed. The principal problems were efficiency deficits in the aerodynamic components and larger values of leakage and heat loss than expected. Minor changes to the compressor and to the compressor-turbine, along with reduction in leakage, reduced the power deficiency to 32%. The deficiency was reduced to 13% with major redesigns to the compressor-turbine and to the power turbine. The following subsections review these development highlights as the performance levels improved.

16.1 Initial Test Results

Figure 148 shows original and revised program goals, the power-scaled performance of the Baseline Engine and the initial test results of the Upgraded Engine with as-designed turbine configurations but the rig-developed compressor configuration. The revised goals were established as a result of a re-assessment of the component efficiencies to values that were thought to be more likely in turbomachinery of this size. The power-scaled performance characteristic of the Baseline Engine is shown as the reference against which improvement in SFC can be measured, both for the goal values and for the values actually achieved. To obtain the characteristic, the Baseline Power levels at different engine speeds were reduced by the ratio of maximum unaugmented power of the Upgraded Engine to the maximum power of the Baseline Engine.

As the figure shows, the initial test results showed performance poorer than that of the power-scaled Baseline Engine. At 80% speed, the output power was 29.3 HP versus the goal value at this speed of 48.6 HP. In the test program, it was necessary to select some appropriate off-design speed for reference, and 80% speed served this purpose. This was done for two reasons. First, the engine could not be operated satisfactorily at design speed with the original compressor-turbine. Secondly, it was possible at this speed to evaluate turbine modifications with machined parts made from material with lower strength than that required at design speed.

16.2 Engine Development Summary

Figure 149 shows five test results that highlight the engine development effort. The engine build configurations are distinguished by the build identifying numbers and letters shown on the figure. The change in engine power at 80% speed is displayed on Table 12.

The test results of build 2-3Q represent the performance achieved with the final diffuser modification to the original compressor, which had a splitterless 24-blade impeller. The diffuser modifications were undertaken as a result of a 5-point drop in compressor efficiency between test-rig data and engine-installed data. The final diffuser modification restored about 4 points in efficiency, and the engine performance shown on this figure shows a small increase in performance relative to Figure 148. At 80% speed, the power increased 9% (Table 12).

The next compressor configuration had an impeller with 18 full blades and 18 splitters and a radial diffuser with 40% increased area ratio. This was combined in Build 3-9X with a compressor-turbine in which the rotor blade shape was an 0.8X scale of the Baseline Engine compressor-turbine rotor blades. The test results in Figure 149 show little change in engine performance. As shown on Table 12, the power increased 4%.

Test rig data analysis showed extremely low values of rotor hub reaction for the power turbine at engine operating conditions. To increase reaction, the blades were twisted closed 11° at the tip, diminishing to zero twist near the hub. While this could not increase reaction at the hub, it was hoped that whatever increase could be achieved over the rest of the span would increase performance. The engine build with this change is 3-9Y, and the test results on Figure 149 show improved performance. Table 12 shows a power increase of 5%; the SFC reduction on Figure 149 at 80% speed is 7.5%. In addition to the power turbine change, baffles were installed on the regenerator cover to improve the cold side flow distribution, and the exhaust diffuser exit area was increased to help hot side flow distribution. These two changes improved heat recovery, which contributed to the SFC reduction.

After extensive in-house data analysis and reviews with aerodynamic consultants, it was decided that the compressor-turbine should be completely re-designed. The revised design was identified as Mod 3. The engine build with this turbine is indicated as 10-14M on Figure 149. The compressor

rotor used in this test was the original 24-blade impeller. The diffuser was the same as in Build 3-9Y. The test results showed a significant increase in power. At 80% speed, the power increased 17% (Table 12), and the SFC reduced 17%.

Finally, with consultant concurrence, the power turbine was also redesigned. The revised design was identified as Mod 1. The engine build with this power turbine and with the Mod 3 compressor-turbine is indicated as 3-13I on Figure 149. The compressor was restored with the 18-blade splitter impeller for this build. The test results showed a small gain in performance. At 80% speed, power increased 4% with no change in SFC, which must be attributed to some heat transfer loss. At design speed, 91 HP was achieved at an SFC of 0.533.

The development program ended at this point. At 80% speed, the engine power was 13% below goal and SFC was 21% from goal. Achievement of goal power would require further development of all the turbomachinery components. Achievement of goal SFC would require completion of efforts toward improving heat recovery and reducing heat loss. To isolate these effects and accurately evaluate the development problems which remained at the close of the program, a detailed cycle analysis was conducted on Build 10-14M, and the results are presented below.

16.3 Thermal Loss Assessment

The test results obtained with a specific engine build were analyzed using the design-intent engine characterization model, as described by Tables 2a and 2b. The purpose was to identify the component contributions to the deficit in overall engine efficiency and output power.

The test data used for the analysis was from engine Build 10-14M, with engine efficiency measured as brake specific fuel consumption, BSFC. At the specific gas generator speeds identified in the characterization, the engine BSFC ranged from 19 to 38 percent high, and the output power ranged from 15 to 21 percent low. Figure 150 shows a graphical comparison of the engine test data to the characterization values of BSFC and output power.

The measured values of compressor mass flow rate, pressure ratio and efficiency and the analytically determined values of compressor-turbine and power-turbine efficiency were substituted for the characterization values. The net effect of the actual aerodynamic component parameters on the engine output characteristics is identified on Figure 150 as Curve I. The actual and goal values of component parameters are listed on Table 13. Use of the actual component performance values results in essentially duplicating the measured output power of engine build 10-14M. However, this accounts for only a portion of the BSFC discrepancy from the design intent at the lower engine speed points.

The influence of actual internal engine heat transfer was assessed using temperature measurements from another engine build 3-9Y. These measurements indicated that the actual heat transfer from the "hot zones" of the engine to the compressor discharge air is from 3 to 6 times the values intended in the engine design. Adding this increased heat leakage to the actual aerodynamic performance accounts for most of the discrepancy between the measured and design intent engine output characteristics, which is shown on Figure 150 as Curve II. The residual BSFC discrepancy could be eliminated by either attributing it to a single component, say, the regenerator, or by distributing the loss to increased parasitic power, heat and flow leaks as well as to lower regenerator effectiveness. A 2-point reduction in the design values of regenerator effectiveness would, by itself, account for the BSFC discrepancy. This particular engine had air flow baffles in the regenerator cover to promote good regenerator effectiveness by reducing air flow maldistribution. In a previous test, these baffles reduced the engine BSFC about 5 percent; thus, a further improvement in this area would appear to be feasible since the baffle configuration was not optimized.

16.4 Final Performance Assessment

In summary, Figure 150 highlights the performance assessment of the engine. The difference between Curve I and design intent represents the effect of the turbomachinery performance on the miss in engine performance goals. The difference between Curves I and II is due to the amount of heat loss that was actually measured. The difference between Curve II and the actual engine test results is due to a possible combination of a small miss in regenerator effectiveness (2 points or less) or of larger values of parasitic loss (such as windage), heat loss or flow leakage.

The miss in engine performance due to the turbomachinery is mostly due to missed efficiency targets at all speeds and partially due to missed mass flow targets. The miss in mass flow ranged from 2.5% to 5% along the operating line for Build 10-14M and from 1.1% to 2.2% on Build 3-13I (cf. Figure 149). The miss in operating line mass flows is a result of adjusting the engine operating line to achieve approximately 90 HP at design speed. The reason for this adjustment was due to the fact that the pressure ratio at design mass flow was significantly below target. This was a consequence of attempting to design the impeller close to choke at design speed in order to provide a wide range of surge-free flow at 50% speed. Significant gain in surge margin was made at 50% speed, but a slight adjustment could be made (impeller cutback) to obtain a better compromise between design-point conditions and 50%-speed surge margin. The program ended before this optimization was undertaken. This modification would allow Curve I of Figure 150 to continue to parallel the design intent up to design speed.

The next diffuser configuration should be restaggered 1° to increase design-speed surge margin. This same amount of restagger was required on the original compressor configuration for the same reason. Time did not permit implementing this change. Because of the small surge margin at design speed, there was no attempt made to augment power with the variable inlet guide vanes.

The misses in target turbomachinery efficiencies are partially due to installation effects and partially due to size effects. The compressor efficiency dropped 5 points from a 1.26X-scale rig configuration with a symmetrical exit plenum to the engine configuration with an asymmetrical collector. The loss could be due to the difference in discharge geometry, to clearance differences resulting from shroud, thermal, or structural distortion differences between rig and engine or to heat paths that exist on the engine that did not exist on the rig. The low specific speed (about 70 in English units) could also have contributed to difficulties in achieving installed performance.

The miss in turbine efficiency is due primarily to the small size and secondarily to installation effects on clearance. Substantial data exists which corroborates the difficulty in achieving good efficiency with turbines with blade heights of about 1/2 inch. Although running clearances were not measured, estimates from thermal growth calculations gave computed clearance values of about 3% for both turbines, which amounts to about 6 points in total-total efficiency. While these are large values of clearance, they are values to be expected for this size of engine due to manufacturing tolerances and to geometrical changes in parts as a result of thermal growth and structural elongation.

However, even if the component efficiencies could not be improved, but if the impeller/diffuser matching of the compressor were improved such that Curve I in Figure 150 parallels the design curve up to design speed, the engine performance would be quite close to design intent if, as well, the heat transfer losses were reduced and heat recovery improved. Although some work was performed in these areas, it was not pursued with the same level of effort as was the turbomachinery development. Heavy work in these areas had only begun at the close of the program.

Lastly, it should be mentioned that a great deal of effort was spent on control of flow leaks around the regenerator and turbine seals. In addition, the mechanical design of the power turbine structure and the effect of thermal growth make it difficult to control clearances for the power turbine. Likewise, because of the size effect on the efficiency of axial turbines, a radial turbine should be considered in a future design. The experience obtained in this development program would lead to a recommendation to consider a single-shaft engine for a future engine design. Even for a 2-shaft engine, efficiency of the compressor-turbine could be improved with use of a radial turbine provided that response time could be resolved with use of ceramic material or by control logic.

17.0 COMPONENT PERFORMANCE DEVELOPMENT

17.1 Compressor Development

The compressor development program began with test-rig evaluation of scaled hardware. The plan was to obtain a compressor map of a scale of the original design, identify any necessary correction, and test redesigned and/or modified hardware prior to engine parts release. A scale size of 1.2588 was selected in order to adapt to the NASA Baseline Engine compressor test rig and to facilitate testing with existing VIGV hardware. The test rig was designed, procured and built at Chrysler and shipped to NASA after mechanical shakedown and some initial development testing. NASA continued the rig testing with scaled versions of the final configuration released for the first engine build. Subsequent rig testing evaluated additional modifications to the rotor and diffuser.

The following sections discuss the rig and engine test results, the performance differences between rig and engine, and the development program carried out to try to bring the engine-installed performance up to the rig performance.

17.1.1 Initial Results from 1.26-Scale Test Rig

A cutaway drawing of the test rig was shown in Fig. 115. Flowrate was measured using a calibrated inlet bellmouth. Inlet conditions were measured by total pressure and temperature probes located upstream of the impeller nose fairing. Exit conditions were measured at the positions shown on the discharge collector. Static pressure taps were installed along the rotor and diffuser shroud surfaces to track the static pressure rise through the compressor system and to obtain impeller efficiency.

In addition to the as-designed hardware, a 24-blade impeller was included in the test program. The level of the aerodynamic blade loading of the 18-blade impeller was reviewed in light of current Chrysler advanced compressor development work. This work suggested that the velocity difference between suction and pressure surfaces might be too large to achieve program goals of pressure ratio and efficiency. Therefore, a 24-bladed rotor was to be tested in addition to the original design of 18 blades. The velocity difference with 24 blades is consistent with past successful designs. There was a small possibility that design flow might be missed by about two percent. This was expected to be rectified, if required, by slightly cutting back the leading edge of every blade. Fig. 151 shows a photograph of an engine-size impeller. NASA also expressed concern about the aerodynamic loading, and carried out the design for a splitter-blade version of the impeller.

The performance obtained with the as-designed hardware is shown on Fig. 152. The miss in efficiency was due to the diffuser; checks on impeller efficiency showed that the rotor met or exceeded program goals. Figs. 153 and 154 show impeller efficiency versus mass flow rate at 50 percent and 90 percent speeds, respectively. The results show higher efficiency and work coefficient with 24 blades than with 18 blades; however, intended efficiency values are met with both values of blade number.

Static pressure data showed that the diffusion from the channel diffuser exit to the compressor exit was only about half the intended amount. Dye traces revealed separation at the point of maximum camber of the deswirl vanes.

To improve the static pressure recovery, an alternate vane profile was configured with an NACA 65-(18)06 section. The two profiles are compared in Fig. 155. The performance results are shown in Fig. 156. The stage efficiency increased 2-3 points over the speed range from 50 percent to 100 percent speeds.

The first test configuration evaluated at NASA consisted of the 24-bladed impeller, the original 14-channel diffuser with the vanes restaggered +1° (to lower surge flow at design speed), and the revised deswirl vane design. The results are shown in Fig. 157. Performance is presented for two values of clearance at design speed. The lower value scales to 0.0087 inch, which is the equivalent engine-size dimension. Engine test experience subsequently showed that running clearance at design speed may be as low as 0.003 inch.

The test data on Fig. 157 for the lower clearance value was considered to be essentially indicative of performance to be expected for the engine-size compressor. The difference in clearance of 0.0057 between the scaled rig value and the engine value should amount to almost two points in efficiency. This was expected to be more than enough compensation for the effect of the 1.26 scale. This rig performance characteristic was used in all subsequent comparisons between engine and rig results, even when modifications were made to the engine rotor and diffuser hardware.

The test rig results show that the efficiency goals were met at 50 percent and 60 percent speeds; efficiency was close to goal at 70 percent speed and missed the goals by one point from 80 percent to design speed. The surge line is essentially as desired except at design speed, where the surge flow is about two percent high. Choke flow at design speed is low but acceptable.

17.1.2 Initial Results from Engine Testing

Figure 158 shows a comparison of the installed performance of the compressor versus rig data. The results show 4.5 points lower efficiency. Rig values of work coefficient were used to compute efficiency because of heat transfer effects influencing temperature-rise measurements. There is a significant impact on the surge line, but it should be noted that surge pressure ratio is more affected than surge flowrate. Engine surge data was acquired by injecting shop air into the collector. The engine surge line is only approximated at the 90 percent-speed data point since audible surge was not encountered before the air supply limit was reached.

Examination of the data showed higher compressor exit Mach number than observed for the rig data. Fig. 159 compares the exit Mach number levels computed from engine and rig data, together with the measured difference in total and static pressure measurements. Total pressure was measured by a chamfered impact probe, aligned to the axial direction at the plane of the diffuser exit. Static pressure was measured in each of the three lobes of the collector. As the figure shows, the exit Mach number for the engine installation is almost double the level obtained on the test rig. The lack of diffusion accounts for one point of the four-point difference in static-total pressure ratio between engine and rig data. (Data taken later on the compressor test rig showed closer values of Mach number between rig and engine results. The initial conclusion was drawn from limited data sampling on engine testing in contrast to vane-to-vane total pressure sampling on the rig.)

The absolute value of the Reynolds numbers of the rig and engine configurations would show no change in loss, based on published data. If, however, it is assumed that the loss were to vary as the one-fifth power of Reynolds number, the scale effect would be only one point in efficiency. Consequently, other effects were reviewed to determine the difference between rig and engine efficiencies.

There were three differences, other than size, between rig and engine compressor configurations. The rig inlet was axial; the engine inlet consisted of the vehicle intake system including filters. The rig rotor had integral blading; the engine rotor blading is split at approximately 15 percent of the meridional distance from the rotor leading edge. The engine configuration was split to provide a steel inducer section for water injection during augmentation. The rig had a circumferentially uniform exit collector (cf. Fig. 115); the engine collector has three discrete lobes of unequal area. Two of these lobes discharge flow to the regenerator; the third lobe discharges flow to the bulkhead for cooling. A fourth influence was heat transfer to the aluminum housing on the engine that differed from the steel housing on the rig.

To determine the sensitivity of compressor performance on inlet arrangement, tests were conducted with (1) an axial and (2) a modification to the standard air intake assembly. These configurations are shown in Fig. 160. For the axial inlet tests, the standard intake assembly was replaced with a bellmouth-type inlet and bullet nose, similar to the compressor test rig. For the other test, the modification to the standard air intake consisted of removal of the hub-piece of the inlet flowpath. The purpose was to see if this piece was interfering with the entry-flow instead of providing controlled guidance as intended.

The results on compressor efficiency are shown in Fig. 161. For the axial inlet, there was less than 0.5 point increase in efficiency at 60 percent and 80 percent speeds; at 70 percent speed, there was an increase of 0.8 point. The trend was similar to that found when clearance was varied in the rig.

For the modified intake, there was less than 0.5 point increase at all speeds tested, but the results were clouded by the fact that the inlet pressure measurements were unstable. The results were further obscured by data uncertainty, with the standard intake measurements varying from 0.1 to 0.6 point in efficiency.

On the average, the effect of the engine intake is about one-half point. Consequently, the test results show that the intake configuration is not a strong contributor to the efficiency difference between rig and engine hardware.

To investigate the influence of the inducer-impeller gap, a test was run on engine hardware with the gap filled. The results were compared to data obtained with the unfilled gap and are summarized on Fig. 162. Except for 50 percent speed, the gap reduces efficiency less than one percentage point.

Table 14 summarizes the breakdown of the estimated total-total efficiency loss between rig and engine configurations. The total loss is two points if viscous loss is included. Added to this is one point loss in static-total efficiency due to the exit Mach number differences between rig and engine. This accounts for three of the 4.5 points lost. The unaccounted loss was assumed to be due to the influence of the difference in exit collector configuration between rig and engine.

The development program which followed consisted of tests with modifications to the:

1. Collector - to reduce the influence of the compactness of the engine collector on compressor performance.

2. Diffuser - to reduce the exit Mach number and to reduce the flowpath size relative to the collector.

3. Rotor - to compensate for the efficiency deficit by improved rotor efficiency by adding splitters to reduce blade loading near the rotor exit.

17.1.3 Collector Modifications

It was assumed that the compactness and asymmetry of the exit collector were affecting the recovery of the diffuser system as well as possibly causing the unaccounted loss of 1.5 points in total-total efficiency. To alleviate the compactness to some degree, the collector was enlarged locally as shown in Fig. 163. The test results are shown on Table 15, within test accuracy, there was no change in efficiency. In another approach, deflectors were installed at the lobes shown in Fig. 164. The test results are shown on Table 16. The randomness of the efficiency changes at various engine speeds indicated little or no change in efficiency.

An incompressible flow analysis was conducted to get some theoretical insight into the influence of the collector on the value of Mach number achieved at the compressor exit plane. The streamline pattern of the flow leaving the diffuser and passing out the middle-sized lobe is shown in Fig. 165. This pattern yielded a static pressure recovery in the flare diffuser that is virtually identical to that expected for axial discharge to infinity. Since the regions between lobes pass flow circumferentially to the lobes, the true pattern is the result of the interference of the flare exit flow field and the passage of flow between lobes. This interference was simulated as shown in Fig. 166. Line "x" indicates a line source for circumferential flow passing radially into the lobe. Calculations were performed for values of circumferential flowrates equal to and twice the value of flow rate discharging from the flare. The results on shroud static pressure recovery are shown in Fig. 167. The increase in streamline curvature due to the circumferential flow field reduces shroud recovery. At the hub surface, extremely large recovery was computed ($\simeq 1$); it was assumed that separation would occur before these values could be achieved.

The results of the analysis showed that asymmetry can cause the exit static pressure to be lower than that of a symmetrical collector. The selected proximity of the collector wall to the compressor exit plane was not found to affect the exit static pressure. If these theoretical results correctly modeled the physical case, then simply enlarging the collector would have no influence on performance, and this was confirmed by test. Rather, it would be necessary to eliminate the asymmetry in order to achieve the performance obtained on the rig.

In order to further resolve the difference in engine versus test rig performance, a detailed investigation of the static pressure rise through the elements of the engine compressor was performed. Twenty-eight static pressure taps were installed in the compressor, many of them in locations identical to those used for the compressor test rig. The results showed recovery in the channel and deswirl vanes virtually identical to that of the rig.

Fig. 168 compares typical engine performance with the rig performance for 80 percent gas generator speed. Results are shown for the original vane shape for the 14-channel diffuser. Fig. 169 reveals that the rig performance is achieved if the ordinate is shifted to let the engine impeller data fall on the rig impeller data. Similar results were obtained for other gas generator speeds.

The low impeller static pressure corresponds to about 2.5 points in efficiency. This is one point larger than the unaccounted loss of 1.5 points. If there were truly no Reynolds number effect (cf. Table 14), then the unaccounted loss would be 2.3 points. This suggests that perhaps about 2.5 points of the rig/engine efficiency difference are due solely to a reduction in impeller efficiency, with no contribution to viscous effects.

Besides the asymmetry of the engine collector, the deflection of the engine housing due to heat transfer could be another influence. For two points to be attributed to additional shroud clearance, the clearance would have to increase 0.010 inch. There may be some difference in clearance characteristic between rig and engine configurations, but it was considered improbable that clearance alone could be the cause of the efficiency deficit. Only test with a rig-type collector would identify the impact of the difference in collector configurations and clearance values.

17.1.4 Diffuser Modifications

It was thought that the small engine collector was adversely affecting the diffuser recovery through a back-pressure effect. To counter this effect, measures were taken to minimize the effect through improved diffuser exit conditions and through modifications to the diffuser itself.

A second cascade was installed behind the deswirl vane to remove the remaining swirl and lower the exit Mach number to values obtained on the test rig. The feasibility of this approach was explored with a simple flatplate cascade. A proper cascade configuration was designed to achieve the Mach number reduction with a net gain in static-total efficiency. In addition, reductions were made in the channel diffuser vane trailing edge thickness to minimize the width of the wakes discharging into the deswirl vanes. It was hoped that thinner wakes would contribute toward minimizing the back-pressure effect. Furthermore, a 28-channel diffuser with much thinner vanes was designed by NASA and tested. Vane setting angles of +1° and +2° from nominal were tested along with the nominal setting. The alternate angles were selected on the basis of providing adequate surge margin in case the nominal setting adversely affected the surge line.

The configuration of the tandem deswirl vanes is shown in Fig. 170. Design parameters are listed on Table 17. The first row is the revised profile discussed in the section on rig testing. Fig. 171 shows the modifications made to the original 14-channel diffuser, the shape of the 28-channel diffuser and the modification made to it.

The test results are shown in Fig. 172. Tandem deswirl vane increased static-total efficiency slightly (0.5 - 1.0 point). Reduction of trailing edge thickness on the 14-channel diffuser increased efficiency in a range from 0.4 - 1.4 points, depending on speed. The 28-channel diffuser was tested with tandem deswirl vanes and without VIGV. No appropriate base without tandem deswirl vanes was available for this data. The data show increased efficiency with increased setting angle. This would be expected as the pressure-ratio characteristic shifts to higher flows with decreasing setting angle.

Figure 173 summarizes the results of this series of tests. The best diffuser configuration consisted of the 28-channel diffuser in combination with the tandem deswirl vanes. The test results with this configuration are compared to the test results with the original design configuration, the test rig results and the program goals. The static-total efficiency increased from three points at 80 percent speed to four points at 50 percent speed, due to the diffuser modifications. The installed efficiency was still approximately one point less than the test-rig efficiency.

The final attempt to minimize the collector backpressure effect consisted of a configuration with increased area ratio on the channel diffuser. The vane-shape of the 28-channel diffuser was retained (no trailing edge taper). The exit width of the flowpath was increased to be 40 percent larger than that at the throat. This increased the channel area ratio from 2.23 to 3.12. With the 4°-taper at the trailing edge, the area ratio was 2.45. The height of the first deswirl vane-row was increased to match the exit width of the channel diffuser. This increased the aspect ratio of the vane from 0.16 to 0.22. The second row of vanes were removed, and the flowpath terminated at

the first row vane trailing edge. The change in exit-plane position put the plane 7.5 exit-widths from the collector wall. The exit plane for the tandem deswirl vanes was 6.0 widths from the collector wall.

The test results are shown on Fig. 173. There is improvement in static-total efficiency over the 14-channel diffuser with a single deswirl vane-row. However, the difference between total-total and static-total efficiency values varied from 2.2 points at 50 percent speed to 1.4 points at 95 percent speed. This is in contrast to the results obtained with the original 28-channel diffuser configuration with a tandem row of deswirl vanes. For the latter, the total and static efficiency difference varied from 1.1 points at 50 percent speed to 0.4 point at 95 percent speed.

These results were obtained with the 24-blade impeller. The static-total efficiency differences between the two diffuser configurations were reversed with another rotor configuration. These results are discussed in the next section.

17.1.5 Rotor Modifications

To reduce the aerodynamic loading on the rear half of the blades, a rotor was configured with 18 full blades and 18 splitters. The test results are shown in Fig. 174. There was an efficiency increase of one point at 50 percent speed but no change from 60 percent and 80 percent speeds, with the change in blading and with the original 28-channel diffuser configuration. When the splitter-bladed rotor was combined with the 40 percent increased-area-ratio diffuser, there was 0.5 point efficiency increase from 60 to 90 percent speeds and about a two-point increase at 90 percent speed. The difference between total-total and static-total efficiencies varied from 2.9 points at 50 percent speed to 1.8 points at 90 percent speed.

This difference is 0.7 point and 0.3 point higher at 50 percent and 90 percent speeds, respectively, than the differences with the 24-blade rotor. It would appear that the replacement of the second deswirl vane-row would yield the efficiency level achieved on the test rig at 70 percent and 80 percent speeds. The efficiencies at 50 percent and 60 percent speeds exceed rig values up to one point.

The final compressor performance is compared to the rig map of the original compressor configuration in Fig. 175. Note the large differences between the surge lines of the two configurations. In contrast to the engine surge line for scaled rig configuration, the surge flows for the final configuration are about five percent higher than the rig values at 80 percent and 90 percent speeds. This shows that the 28-channel diffuser should be rotated +1°. This may tend to lower the operating line pressure ratios at these speeds since the choke flow is set by the diffuser. However, maximum power could be increased since maximum flow at design speed is determined by the rotor. Alternatively, some measure of VIGV augmentation could be achieved.

17.2 Compressor-Turbine Development

During the development program the efficiency assessment of the compressor-turbine was determined solely from data taken from engine measurements. Assessment was made primarily at 80% speed. This was high enough in speed to minimize measurement uncertainty and low enough to evaluate modifications with machined parts made from lower-strength materials than those used for engine parts.

Data showed that the turbine efficiency was between 3.5 and 7.5 points below the goal of 0.845 at 80% speed. Survey data taken at the nozzle inlet and exit showed from 3 to 7 degrees added incidence angle and from 6 to 9 degrees lack of turning at the tip and hub, respectively. Vane-shape redesigns were performed to better match the inlet conditions, but no efficiency gain could be identified outside of experimental and analytical uncertainties.

Design-review meetings between NASA and Chrysler personnel and three consultants concluded that the efficiency of the turbine could be as low as indicated by engine data analysis. It was stated that the major reasons for the miss in goal efficiency were:

1. the life requirement of 1000 hours, which contributed to the blade height selection,
2. the endwall effects caused by the inlet plenum, and
3. the diffusion limits selected for the blading (Published NASA limit is 0.25; consultant recommended 0.10 or less).

It was recommended that the turbine be redesigned with

1. lower inlet vorticity,
2. larger blade span,
3. lower diffusion limit,
4. a contoured shroud for the nozzle, and
5. a variable work distribution for the rotor.

A second turbine was redesigned, built and tested. The engine-based assessment showed no change in total-total efficiency; however, the power turbine efficiency increased 9 points. The results showed that the benefit achieved with the redesign was an improvement in inlet conditions to the power turbine.

The compressor-turbine development program ended at this point. The following sections summarize the program highlights.

17.2.1 Initial Efficiency Estimate from Engine Tests

The need for a development program was based on estimates of low efficiency from early engine test data. The estimate of compressor turbine efficiency was based on compressor work (computed from test rig data), and calculated bearing power. Inlet temperature and pressure were measured, but three methods were used to deduce the average outlet total pressure. The first method was a pitchline loss analysis which used simple radial equilibrium and rotor exit tip static pressure to compute an average total pressure. The second method employed full radial equilibrium with variable loss. The third method used the mean-radius total pressure measurement.

The first method is approximate since the flowfield may not be precisely a free vortex. The second method is better but still depends on assumptions of deviation angle and blockage. The third method depends on the quality of the data sampling to obtain an appropriate average total pressure. Initial estimates of turbine efficiency came from the first method. Later estimates by the other two methods came after more data was available.

To obtain the data needed for the analysis, instrumentation was installed on a special engine build. This consisted of inlet total temperature and pressure, nozzle exit and rotor exit tip static pressures, and rotor exit total pressure at the average radius between hub and tip. The efficiency was deduced from an off-design vector diagram analysis computer program. The magnitude of the loss model in the program was artificially increased by a multiplier until the computed rotor static pressure closely matched the experimental value at the required work

A number of data points were reviewed for pitchline analysis. The one which typified the results is shown on Table 16. The nozzle exit tip static pressure could not be matched precisely, since the computer program coding did not permit individual adjustments of loss multiplier to the nozzle and rotor. As the table shows, the estimated efficiency at the 80% speed operating point was 0.775. Since this was seven points below goal, experimental and analytical work was begun to investigate the miss in efficiency. The test program began with diagnostic probe surveying of the nozzle and rotor. This information was used to check the efficiency estimate from full radial equilibrium calculations and to check aerodynamic loading of the vanes and blades under test conditions.

17 Development Summary of Original Design

The results of the nozzle probe surveys are shown in Fig. 176 and Fig. 177. Fig. 176 shows the lack of vorticity delivered by the vortex chamber at the hub and tip. Fig. 177 shows the radial variation of nozzle incidence angle and exit flow angle. The lack of vorticity in the hub and tip regions gives rise to large values of positive incidence angle, which could contribute to the large miss in nozzle exit air angle at the hub and tip.

It was concluded that the vortex chamber vorticity should be increased to provide a more favorable variation of incidence angle. To investigate a vortex chamber with increased vorticity, clay was installed in an existing chamber; and a test was conducted on the nozzle flow rig.

Flow tests of the increased-vorticity vortex chamber showed 5 to 8 degrees change in air angle at mid-span with smaller values in the upper half of the span and larger values in the lower half. Within the data scatter, there was not much change in the inlet total-pressure loss distribution. The exit data showed little change in exit air angle, despite the large reduction in incidence angle, even near the endwalls. Consequently, the endwall blade-sections were not originally at incidence angles indicative of maximum turning or stall.

This is confirmed in Fig. 178 in plots of turning angle versus incidence angle. Plots are presented at every 10% vane height from the hub. The values of turning angle increase virtually linearly with incidence angle. This indicates nearly constant deviation angle, and, hence, no indication of stall at the higher values of incidence angle. On the other hand, there is a lack of turning angle indicated near the endwalls, which suggests larger values of deviation angle than expected.

The dashed lines on Fig. 178 indicate the turning-angle values expected at the hub and tip based on the change in camber angle relative to mid-span. The lower 30% of the span is well below the expected turning. In addition, turning-angle values in the upper half of the vane fail to achieve values higher than those at mid-span. The section at 90% height is significantly below expected turning. One interpretation of these results is that the endwalls strongly affect local turning as well as total-pressure loss.

In an alternate approach, it was decided to redesign the nozzle vane shape to match the measured inlet conditions. Two such nozzles were configured. However, no significant change in efficiency could be detected. Table 19 shows efficiency values based on radial equilibrium calculations and on mean-radius total pressure measurements (methods two and three described above). No radial equilibrium calculation was performed for the Mod 2 nozzle. The results show an average stage total-total efficiency from about 0.76 to 0.78, depending on the calculation. Comparison of Run 128 with Run 140 shows a possible uncertainty of 1.4 points.

The results of the radial equilibrium calculations were used to compute the aerodynamic loading on the blading of the original design and of an 0.8 scale version of the Baseline Engine rotor blading. The results showed larger diffusion gradients on the suction surface of the Upgraded Engine blading. Chromic oxide dye injection showed heavy deposit on the suction surface of the Upgraded Engine blading but not on the Baseline Engine blading. Since this corroborated the aerodynamic analysis, a scaled version was machined and identified as Mod 1. A mean-radius efficiency comparison between the original and Mod 1 configurations is shown in Fig. 179. The test results show about a two-point increase in efficiency with the Mod 1 blading.

A summary of mean-radius efficiency values for combination of nozzles and rotors is shown in Fig. 180. The plot shows an efficiency loss of about four points with the Mod 1 nozzle. However, it was discovered that the total pressure probes were located in different circumferential positions relative to the trailing edge of the vanes of the two nozzles. Measurement showed a relative position difference of one-half pitch. Such positioning suggests that, relative to wake pitch spacing, high efficiency data could come from between-wake sampling and low-efficiency data could come from near-wake sampling. Consequently, it was not possible with the data available to precisely determine the efficiency of the compressor-turbine from pitchline total-pressure measurements alone.

Taking the average of the data sets in Fig. 180, the efficiency could be anywhere from 0.77 to 0.81. This range is consistent with the values obtained by the other methods, as shown on Tables 18 and 19. This concluded the engine-based assessment of the original compressor-turbine design.

At this point, reviews were made by two consultants. These reviews were conducted to obtain independent estimates of the efficiency potential of the original design.

17.2.3 Consultant Review

The analysis of Consultant 1 was carried out at 90% speed and was based on overall design parameters, such as specific speed and Reynolds number. An efficiency of 0.815 was estimated for the original design, excluding the vortex chamber loss. This was based on the Reynolds number and aerodynamic loading of the blading and possible endwall effects on the low-camber nozzle in combination with the vortex chamber. If the blade loading of the rotor were reduced, the efficiency was estimated to increase to 0.825.

The analysis of Consultant 2 was carried out at 100% speed and consisted of a detailed examination of the blade loading with highly distorted flow from the vortex chamber. An efficiency of 0.77 was estimated for the blading as designed. As expected, blade loading estimates with highly distorted vortex flow were higher for both the nozzle and rotor blading. With blade redesign, it was estimated that the best the efficiency could be was 0.81. To improve the efficiency, it was further recommended that reaction should be increased, the nozzle inlet vorticity should be reduced, the nozzle shroud be contoured, and the blade span should be increased 15%.

The faults found with the vortex chamber were the relatively high inlet Mach number (=0.122) and the narrowness of the flowpath from the vortex chamber to the nozzle leading edge. The latter was criticized for being a strong boundary layer generator. This point was made by both consultants. It was recommended that the volume be increased and the nozzle inlet flowpath widened. It was also recommended that the nozzle shroud be contoured to provide good boundary layer control at the shroud.

The recommendations to increase the blade span and reduce the work factor were also made by NASA at the time of the design. However, Chrysler specification of stress limit and rotational speed dictated the resultant blade height. On the other hand, published studies show significant gain in efficiency at low values of flow coefficient, for a rotor aspect ratio of 1.0. Consequently, for a redesign, it was decided to accept the increase in stress for the sake of efficiency improvement.

The decision was made to perform a redesign based on the consultant recommendations. The sections below discuss the design results and the efficiency assessment from engine data. This redesign was identified as Mod 3.

17.2.4 Compressor-Turbine Redesign (Mod 3)

The flowpath of the Mod 3 design is shown in Fig. 181. The rotor blade shapes are compared with those of the original design in Figs. 182 and 183. Rotor geometric parameters are displayed on Fig. 184 and aerodynamic parameters on Fig. 185. The plastic flow visualization model of the enlarged vortex chamber is shown in Fig. 186. The nozzle meridional and front views are shown on Fig. 187 and the vane shapes on Fig. 188. The geometric and aerodynamic parameters are shown on Fig. 189. The vector diagrams for design speed and 50% speed are shown on Figs. 190 and 191, respectively. Nozzle-exit calculations used 8% blockage; rotor-exit calculations used zero blockage to represent mixed-out conditions.

The efficiency estimate for this design is 0.85, based on calculations performed by Consultant 2. It was estimated that 0.6 point was due to improved inlet conditions as a result of the redesigned vortex chamber. The rest is due to the features incorporated into the turbomachinery design.

An attempt was made to obtain an independent assessment of the efficiency potential by reviewing available published test results of small turbines. A summary of this review is shown in Fig. 192 in a plot of total-total efficiency versus work coefficient. Data points are shown for 13 turbines with blade heights from 0.22 to 1.14 inch and true-chord aspect ratios varying from 0.53 to 1.7. The data band indicates an expected efficiency between 0.81 and 0.835 at the design work coefficient of 2.06.

The data band shown on the plot contains most of the data points. The three low points were left out, since there were points at similar aspect ratios but higher efficiency. The highest efficiency points shown could be an indication of the potential to be obtained with an exceptionally good design. On the other hand, its high design pressure ratio suggests vector diagram conditions somewhat dissimilar from the other designs. It could also be interpreted that the Consultant 2 data indicates the plausibility of higher efficiency with improved design features, small clearances loss, and well-fabricated parts.

Despite lack of agreement on the estimated efficiency potential, the design incorporated the latest advances available in today's turbine technology. As such, it represented the best attempt for performance improvement.

17.2.5 Mod 3 Efficiency Estimate

The efficiency of the Mod 3 design was estimated by the same methods used above for the original design. On Table 20, the efficiency of the compressor-turbine was computed from measured values of inlet and exit total pressure and calculated turbine work. The exit total pressure was a mean-radius measurement at a position 0.8 axial chord length from the rotor. The work was obtained from a calculated value of compressor work, based on rig work coefficient, and the estimated value of bearing parasitic power.

The performance of the Mod 3 compressor-turbine from overall engine data can be evaluated from the test-point comparison on Table 20. This table compares the change in engine parameters with the change in compressor-turbine configuration. The reference configuration consisted of the Mod 2 nozzle and the 0.8x scale of the Baseline Engine rotor. Engine power increased 12% with a corresponding 12% reduction in BSFC. Power turbine efficiency increased 9 points, but compressor-turbine efficiency dropped 0.8 point. Since the pressure ratio of the compressor-turbine changed only 0.2%, it is likely that the calculated actual work is the result of the uncertainties of the measured turbine mass flow, rather than any real loss in efficiency. Assuming that this is true, the engine performance gain is due to reduction of interface loss between turbines rather than any gain in total-total efficiency for the compressor-turbine.

The data from the air injection tests show about the same efficiency results. Note that the net power with air injection is 97% of goal. This evaluation is a little artificial, since the power was obtained at an efficiency 10 points below goal and a mass flow 6% above goal. Power turbine pressure ratio at goal efficiency is 1.55. The data showed a pressure ratio of 1.56.

Detailed effort was expended to estimate efficiency from pitchline analysis and from radial equilibrium analysis. Included in the analysis was an evaluation of the uncertainty of the values obtained due to nozzle mass flow measurement, windage, and deviation angle assumption. The analyses yielded an efficiency range from 0.784 to 0.828. In the calculations, a windage estimate was added to the temperature-rise-measured impeller work. If this windage work is not added (as was true in the analysis of the original design), the upper limit is 0.814. This gives an average value of 0.80. The estimated efficiency range for the original design is 0.76 to 0.81, which covers all the estimating methods. The average efficiency of the original design is 0.785. The conclusion is that the total-total efficiency improved 1.5 points with the Mod 3 design. Only a comparison of test-rig results can confirm this.

17.3 Power Turbine Development

It was not possible to obtain a clear performance evaluation of the power turbine from engine data. Large discrepancies existed between results from analytical estimates based on static pressure measurements and mean-radius total-pressure measurements. To get a clearer resolution, a test rig was designed and built. This rig had uniform inlet conditions of temperature and pressure and a guide vane to simulate compressor-turbine exit swirl.

The results showed that the basic design was down 6 points from goal. Because of the uniform inlet conditions, it also showed that engine-based efficiency values were lower because of the exit conditions from the original compressor-turbine design. This condition was rectified with the Mod 3 redesign. The results also showed that efficiency might be increased, if the rotor blades were twisted closed to increase rotor reaction. This modification made a small but significant increase in engine power. This was the only modification made to the original design.

A consultant was engaged to review the design. As a result of that review, it was recommended that another stage be designed with much lower flow coefficient. This redesign was built and tested; but no performance difference from the modified original design could be detected from power or other engine data.

The following sections summarize the program highlights.

17.3.1 Initial Efficiency Estimate from Engine Tests

The power turbine system consists of interstage and exhaust ducts as well as the bladed stage. Performance assessment was made at 80% gas-generator-speed conditions. Efficiency estimates were made with pitchline vector diagram analysis and with mean-radius total-pressure probe measurements.

The initial efficiency estimate came from vector diagram analysis. The input to the analysis was provided by the calculated output conditions from the compressor turbine analysis. The results are shown on Fig. 193. No loss multiplier was applied to the program loss model. The data point shows close agreement between test and analysis. The results show peak efficiency to be about five points lower than peak efficiency for the program goal. The difference is due to the low pressure ratio available to the power turbine, brought about by the low outlet pressure from the original compressor turbine. This analysis showed that the only deficit in the power turbine efficiency was due to the deficit in compressor-turbine efficiency.

The analytical result was checked by artificially injecting air into the engine at the compressor exit. This provided a check on power at 80% speed with the goal pressure ratio applied across the turbine. The results are shown in Fig. 194. With goal pressure ratio (total-static) applied, the power goal could not be achieved. The efficiency implied by this result is 0.63; this is seven points lower than the estimate from the vector diagram analysis.

A third method of determining efficiency was to use the measured output and mean-radius total-pressure data. This was computed automatically on every data point as part of the data reduction process. The efficiency level was generally between 0.54 and 0.57. This is about a fifteen-point discrepancy with the analysis.

On a subsequent analytical check, engine power could not be matched analytically without tripling the duct losses. This suggested that the analytical discrepancy may be due in part to data uncertainty and to possibly a distorted velocity profile from the compressor turbine.

To more clearly identify the power turbine performance, a test rig was built.

17.3.2 Test Rig Results

The rig was configured to test the entire power turbine system with uniform inlet conditions of temperature and pressure. Compressor-turbine exit swirl was simulated with fixed guide vanes. The results from this rig were expected to isolate the influence of the compressor-turbine exit conditions on power turbine performance. A drawing of the rig is shown in Fig. 195.

A summary of the test results at 80%-speed gas-generator conditions is shown in Fig. 196. Tests 2 and 3 were conducted at the prescribed cycle pressure ratio for the equivalent gas generator speed of 80%. Test 3 was run at cycle turbine inlet temperature, while Test 2 was with ambient turbine inlet temperatures. In Test 5, typical pressure ratios observed in engine tests were set. Engine simulation was attempted by duplicating not only pressure ratio and temperature but corrected gas flow rate as well, by closing the nozzle setting by 2°.

There are four efficiency levels: program goal; that obtained at intended 80%-speed pressure ratio and nozzle angle; the efficiency obtained with rig simulation of the engine conditions; and, finally, the efficiency obtained with measurements taken during engine tests. The degradation in performance can be categorized into three general areas:

1. A miss in stage efficiency of approximately six points due to stage design (goal vs. tests 2 and 3 in Fig. 196).

2. An additional five point loss due to stage flow mismatch and deficient gas generator performance, both of which cause the nozzle to operate more closed (tests 2 and 3 vs. test 5 in Fig. 196).

3. A further loss of six points in engine performance, presumably because of less favorable inlet conditions (test 5 results vs. engine test results in Fig. 196).

Detailed surveys were conducted at the stations indicated in Fig. 197. Fig. 198 illustrates the power turbine nozzle inlet survey results. A severe shroud separation is occurring, as evidenced by the highly tangential flow near the shroud. Measured flow angles near the wall were greater than 90°.

At the rotor exit, examination of the vector diagrams revealed a separated flow condition. Computed relative flow angles are illustrated in Fig. 199. Also shown is the rotor blade exit angle distribution.

One would expect that, for unseparated flow, the difference between the exit blade angle and the exit relative flow angle would change very little from hub to tip. The results show that this is not the case. Apparently, the flow is separated at the hub and tip regions. The severity of the separation decreases at the hub as the nozzle is closed. The increase in efficiency as the nozzle opens, therefore, must be due primarily to increased stage reaction. The closed nozzle condition does not improve conditions at the tip, however. The tip flow condition is probably being aggravated by the separated flow at the nozzle inlet tip section. There is also a high amount of deviation at the mean section, about twice the estimate obtained by using Carter's rule.

Recovery values for the interstage and exhaust ducts are summarized on Table 21. Comparison is made to program goals at 80% speed. The interstage duct recovery is about eight points low. The exhaust diffuser recovery is about nine points low.

Hub reactions were computed (tip reactions were not available) to gain an insight into the reasons for the dramatically different performance levels. Results are illustrated in Fig. 200. As expected, reaction increased as the nozzle vanes were opened. Note the low (-12%) hub reaction obtained with the engine simulation test which is certainly a detriment to performance. One-dimensional computations indicated that a 5° twist at the power turbine blade at the meanline would increase reaction by 11%. A blade bending fixture was designed and fabricated to accomplish the required bend. Back-to-back testing with the same gas generator showed a power gain of 4.7% and an efficiency gain from 0.543 to 0.575 with the twisted blade configuration, at 80% speed. This was the only modification made to the blading.

17.3.3 Consultant Review

The design review carried out by Consultant 3 is described below in an excerpt from the review report.

> A critical appraisal of the power turbine section of the ERDA/Chrysler Upgraded Engine is made, and a comparison with NPT tested designs is given. The scope of this appraisal has been widened to cover the gasifier section because of the critical influence this component has on the power turbine section.
>
> This is consistent with NPT's normal approach to good automotive turbine design, which involves analysis of the total system, i.e., from combustor outlet to heat exchanger inlet. This approach to aerodynamic design involves optimisation of every aspect of the flow path to obtain a high overall system performance within all the constraints e.g., low cost, durability, response, life and part load performance.
>
> NPT have proved over many tested turbine systems that this design method produces a balanced good level of performance in each section, without compromising the overall performance due to over design in any one component area.
>
> Criticism of the Upgraded Engine turbine system is covered in three main sections:
>
> a. the overall design concept
>
> b. the analytical modelling
>
> c. blading design parameters

Following are the recommendations made by the consultant.

> In order to achieve significantly improved performance from the Upgraded Engine, it is important that the total system design approach should be adopted. Further, the following steps must be taken:
>
> a. The gasifier turbine inlet duct should be changed from the vortex chamber type to the semi-plenum type.
>
> b. Good incidence tolerance should be designed into the gasifier turbine nozzles to cope with recommendation a.

c. The flow coefficient and stage loading factor of the gasifier turbine should be reduced and the reaction increased.

d. The flow coefficient of the power turbine should be reduced and the design total-to-static efficiency goal raised.

e. The area ratio of the interstage duct should be increased to 2.5 to 2.8 in order to accommodate recommendations c and d. The duct length should be kept to a minimum, consistent with an acceptable level of loss.

f. The Upgraded Engine axial to radial power turbine exhaust diffuser be replaced by an axial to dump diffuser.

g. The analytical thermodynamic/aerodynamic modelling leading to the design velocity triangles should include estimates of radial distribution of losses throughout the turbine system and should also include work variation with radius for the turbine rotors.

17.3.4 Alternate Power Turbine Design

An alternate power turbine was designed based on the consultant's recommendations. it was identified as the Mod 1 design. The rotor blade shapes are compared with those of the original design in Fig. 201. The nozzle vane shapes are shown in Fig. 202. The flowpath of the Mod 1 power turbine is shown in Fig. 203, in combination with the flowpath of the Mod 3 compressor turbine. The aerodynamic parameters at design point are shown in Table 22; the geometric parameters are shown in Table 23. Design-point, mixed-out vector diagrams are shown in Fig. 204.

17.3.5 Performance Comparison—Alternate vs. Modified Original Turbines

Performance comparison of the Mod 1 design versus the original design is shown in Figs. 205 and 206. The power and SFC characteristics are compared in Fig. 205; within data scatter, there is no difference in performance. The performance achieved relative to goals is plotted in Fig. 206. Power is approximately 80% to 84% of the original goal; SFC is high by 20% to 40%, depending on the gas generator speed.

Included on both plots are curves identified as corrective development goals. It became clear after significant amount of testing in the development program that the original turbomachinery efficiency goals might not be met. Revised engine performance estimates were made, based on what was thought to be achieved with the final component hardware configurations.

One of the expectations was that the power turbine would come within two points of the original goals. However, mean-radius probe measurements show an efficiency of 0.66 for the original design with the blade twist. From the overall power comparison, it must be concluded that there must not be a significant change in efficiency with Mod 1 power turbine design. It remains for rig testing to explain why all the revisions which were made to both turbine stages made no difference in total-total performance of the compressor turbine or in the total-static performance of the power turbine, despite the application of all the latest aerodynamic concepts and design techniques.

17.4 Combustor Testing

Initial testing of the lean, premixed/prevaporized combustor indicated incorrect proportioning of air to the premixer and to the dilution zone as evidenced by high NOx levels, a flashback condition and excessive metal temperatures in the reaction zone. The primary zone of the combustor was too rich, causing fuel droplets to burn in the premixer and resulting in the high NOx levels and excessive metal temperatures in the reaction zone of the burner liner. Two iterations were required to achieve the desired air proportions for emission control and lower metal temperatures. Table 24 shows good emission control at steady-state speeds with the use of gasoline fuel. Pressure losses are close to target values of $\Delta P/P \sim 3\%$ with turbine inlet temperature gradients of approximately 125 F based on four thermocouples. Final tests of the combustor showed pressure losses reduced to values approaching 2%. Cold starting at ambients 60 F with gasoline fuel showed that pressure loss and combustor stability were within acceptable limits for a developing engine. The engine program ended with the development of the combustor system left incomplete. This was due to lack of available time caused by the amount of program time consumed to develop the engine power and fuel economy.

17.5 Regenerator Development

17.5.1 Flow Distribution - High Pressure Side

Analysis of test data from initial engine runs showed a deficit of 4% in regenerator effectiveness. To determine the effect of engine flow distribution on regenerator performance, studies were conducted for each half of the core, with an outside sub-contractor evaluating the low pressure side (as discussed below), and with Chrysler testing the high pressure side.

The test rig shown schematically on Fig. 130 for testing on the high pressure side was used. it consisted of an engine housing with a blocked opening for the variable nozzle, a gas generator without a turbine and a ceramic regenerator with seals. A regenerator cover completed the flow path. Since only the high pressure side of the regenerator was investigated, the discharge air from the core was allowed to escape to atmosphere. The air was pumped by an electric blower to duplicate engine Reynolds number and pressure drop. Typically, data surveys were taken at conditions duplicating idle, 80% speed and design speed.

The instrumentation consisted of plug probes on the downstream surface of the core which measured the stagnation pressure at the upstream core surface. An initial survey indicated deficient flow near the rim. Modifications to the cover to uniform the flow were made using modelling clay as a filler. Fig. 207 shows the final flow baffle chosen. It consists of a circular wall at the 200 mm (8 in.) radius, 20 mm (3/4 in.) wide and extending to within 16 mm (5/8 in.) of the matrix surface. Flow distribution before and after modification is shown on Fig. 208.

From the clay form, molds were made, and a duplicate baffle was cast from Sylgard 186 (the elastomer used to mount the regenerator drive gear) into a regenerator cover. An A-B-A engine test sequence was then run to evaluate performance with and without the baffle. There was a slight loss of power on the last test, but this was later traced to two broken regenerator seals. The results are shown on Fig. 209, and the data clearly show a 5% improvement in BSFC as a result of the cover change.

17.5.2 Flow Distribution - Low Pressure Side

Testing of the low pressure side of the regenerator core was performed on a scale model at Creare, Inc., Ref. 12. The turbine exhaust diffuser and the collector in front of the core entry were modeled, and the flow distribution and exhaust diffuser recovery were measured for five diffuser inlet swirl levels. A schematic of the test model is shown on Fig. 210. Tests were conducted with and without a free runner at the exhaust diffuser entry to model the presence of the turbine blading. Instrumentation details are shown in Figs. 211 and 212.

The test data showed the majority of flow in the area of the exhaust diffuser shadow on the regenerator core. Some results are shown in Fig. 213.

The top of the figure shows contours of local velocity relative to an average velocity computed from the mass flow, local density and flow area. The bottom of the figure shows the variation of mass flow distribution with radius. The mass flow percentages indicate the local percent of mass flow passing through a ring of width 2.5 mm (0.1 in.) at any given radius.

The plots indicate improvement in core flow distribution as swirl angle increases. Test results showed no change with or without a free runner at the inlet to the exhaust diffuser. However, the results did show an increase of exhaust diffuser recovery from about 0.20 to about 0.30 in the absence and presence of the runner, respectively.

17.6 Engine Braking

Engine braking tests were conducted during the development program on an engine which had the compressor and turbine modifications available at the time of the tests. The results and the component descriptions are presented in Fig. 214. The engine performed well throughout the tests with no mechanical problems. The LPP combustor was used on these tests, and there was stable combustion throughout the testing even though the power turbine exit temperature was as low as 1000 F.

18.0 ENGINE MECHANICAL DEVELOPMENT

18.1 Engine Housing-Bulkhead Temperature Control

Initial engine testing revealed an apparent thermal expansion problem in the regenerator centerbolt area. A .050 in. gap was observed to form, during warmup, between the regenerator cover and the centerbolt washer. The gap gradually closed at higher speeds, and was fully closed above 80% Ngg. This occurence was a matter of concern for two reasons:

1) A loss of .050 inch of operation clearance would impair proper functioning of the regenerator seals, and possibly result in matrix/seal damage.

2) A distortion of this magnitude elsewhere in the engine could affect performance through restriction of seal ring movement and misalignment of aerodynamic flow paths.

Investigation of the problem led to extensive documentation of cover and housing temperature gradients and showed the probable cause to be inadequate cooling of the center portion of the housing crossarm.

18.1.1 Centerbolt Relative Motion

Measurements made with dial indicators showed that the centerbolt tip moved out (relative to engine center line) a maximum of 0.052 inch at idle, and then gradually moved inward at higher speeds. The cover did not move inward but gradually deflected outward in response to increases in compressor pressure. To eliminate thermal growth of the centerbolt as a factor in the measurements, the bolt was drilled to the plane of the crossarm seal platform, and a glass-ceramic rod of extremly low expansion coefficient (4.4×10^{-7}/F) was installed. With this change, housing deflection was still 0.035 inch. This confirmed that the bulkhead deflection was the primary source of the problem.

18.1.2 Engine Housing Temperatures

To determine the influence of housing thermal gradients on bulkhead distortion, an engine housing was instrumented with 21 skin and internal metal thermocouples. The measured values were significantly lower than ex: ected, particularly in the bulkhead area. The results showed excessive heat rejection to the bulkhead and inadequate crossarm cooling.

18.1.3 Regenerator Inlet Air Heating

Another check was made with a 24-point thermocouple grid at the regenerator inlet (cf Fig. 131). The results are shown in Fig. 215a; the temperature readings at the corners (where the bulkhead cooling-flow cavities are) show values that are up to 80 degrees above the average value inlet temperature and 120 degrees above the compressor exit temperature (T_2).

To reduce the heat input to the regenerator inlet, baffles were installed at the corners. The temperature measurements with the baffles installed are shown in Fig. 215b. The results show a reduction in maximum temperature of 38 degrees in one corner and 79 degrees in the other. While the regenerator inlet thermal distribution was reduced by the presence of the baffles, the heat rejection to the bulkhead cavity still remained, and the problem was not resolved before the program terminated.

18.2 Air Bearing

Engine testing with the air bearing spanned three years in seven engines and three vehicles; some bearings accumulated 150 hours and 700 starts. The development problems that occurred were:

1. Fatigue cracking of the top foil at the spot-welded joint,
2. Partial spacer foil movement,
3. Dry film coating wear, and
4. Lack of repeatability of foil surface contour and axial flatness.

The fatigue cracking problem of the spot weld was relieved by improved spot welding techniques and by better quality control. Examination of bearings at the end of the program showed improved uniformity of welds and spacing. Alternate foil attachment methods were studied to improve the mechanical design, but no alternate design was carried out before the end of the program.

Spacer foil axial movement was corrected by relocating the spot welding zone from the ends of the foil to the center. This eliminated the thermally induced stresses at the edge points.

Loss of dry film lubricant coating occurred adjacent to the weld zone at the end of the foil and at the rear third of the foil, generally 180° away from weld seam and migrating circumferentially toward the seam. A small improvement was achieved by changing the coating from commercial resin bonded Mo S_2 to HL-800 cadmium oxide-graphite sodium silicate bonded coating. However, wear continued to be the major cause of bearing replacement and refurbishment at the end of the program.

Local variations in foil contour were caused by local contact with the journal, which accelerated foil wear. The problem was corrected by improved assembly and inspection procedures. The problem with axial flatness was the fact that many bearings were made with flatness values 3-5 times larger than print tolerance. This problem was corrected by improved fabrication procedures and by flatness checks at final assembly by the vendor.

18.3 Variable Inlet Guide Vanes (VIGV)

A troublesome anomaly in the inlet guide vane development program was the inability of the local casting vendor to produce the stator casting. The support is comprised of the 13 stator vanes, and inner and outer shrouds. It is located just forward of the moveable vanes. Consistently poor vane fill, shroud contour deviations and nonuniformity, part to part, dictated a vendor or manufacturing change--possibly away from the present sand casting method. Contact with other casting vendors revealed that sand casting would not supply satisfactory parts and investment casting was necessary.

Investigation into synthetics disclosed that glass reinforced thermoplastic polyester had the thermal and structural qualities necessary. Furthermore, parts could be made directly to final print dimensions, eliminating the need for finish machining. This method was selected, and the parts received were dimensionally excellent. At the end of the program 309 hours had been accumulated on these parts with no distress.

18.4 Power Turbine Thrust Bearings

The design of the power turbine thrust bearing was reviewed subsequent to failures during vehicle operation. Maximum bearing loads were encountered at wide open throttle during the transmission upshift. The oil film thickness at this condition was close to the minimum for the range of operating conditions encountered in a vehicle. However, this condition did not normally occur in test cell operation. Initial vehicle tests showed the originally designed bearings would fail in less than 20 miles of normal driving.

The film thickness at the maximum load condition (during transmission upshift) was calculated to be 0.0048 mm for design bearing geometry and 250 F oil temperature. This film thickness is lower than the original calculated value of 0.0081 mm, probably because of conservative assumptions made in applying idealized analytical data in the literature to the design of a working bearing. Testing the original bearing under minimum film thickness conditions verified the design to be marginal. The diameter of the bearing was increased from 38.5 mm to 47 mm to obtain a calculated film thickness increase from 0.0048 mm to 0.010 mm.

Vehicle tests while cycling between power and braking (where load cycles between thrust and anti-thrust surfaces) showed that oil pressure supply to the unloaded surface would go to zero. The oil supply system was revised to increase oil feed line size and restrict oil leakage from the anti-thrust bearing supply. The above improvements were incorporated in an engine which accumulated 2697 miles of vehicle operation without incident. Vehicle road tests showed good oil supply pressures to both thrust and anti-thrust bearings at the conditions tested. A flat support for the thrust bearing was also substituted for the spherical seal of the original bearing. The effect of this change, however, was not documented. The flat support thrust bearing is a simpler, lower cost configuration.

18.5 Parasitic Losses

In an effort to verify the design estimates of parasitic losses, an engine was modified and coupled to an electric dynamometer having absorbing and motoring capabilities. The engine modifications included removal of all the blades from the power turbine rotor and documentation of all bearing clearances and rotor disc fore and aft shroud clearances. A power turbine shaft without a disc was also tested. Oil temperature into the engine was controlled at 100, 150 and 200 F. A standard gas

generator was run at steady state while the power turbine speed was varied through the operating speed range. The results showed that:

1. Upgraded Engine parasitic losses showed reasonable agreement with design estimates,
2. Turbine disc windage losses were not excessive,
3. Heat rejected to the oil was within anticipated values, and
4. The Upgraded Engine power deficiency could not be associated with parasitic losses.

18.6 Power Turbine Metal Temperature Surveys

Metal temperature surveys were documented for the variable power turbine nozzle assembly. Start-up, steady-state, and soak-back temperatures in the power turbine nozzle assembly were recorded and are shown on Figs. 216, 217, and 218 respectively. Fig. 217 shows the thermocouple locations.

18.7 Regenerator Mechanical Development

18.7.1 Regenerator Core

The first 15 regenerators tested were of the thinwall (.003") LAS composition, identical to the matrix design endurance-tested over 500 hours in the Baseline Engine program. Because of the susceptibility of LAS to premature failure when exposed to fuels of high sulfur content, the Upgraded Engine testing was confined to unleaded gasoline. The final three program regenerators were identical in structure and fabricated from the more sulfur-resistant AS composition. These AS cores showed identical heat transfer performance to the LAS type and could be used for any future work with diesel fuel.

The elastomeric mounting system generally functioned satisfactorily, except for a few isolated incidents of partial tearing of the outer layer of matrix. One complete gear/matrix separation occurred, but this was attributed to moisture absorption during previous cold-flow rig testing with this matrix. Partway through the program the manufacture of Sylgard 187 Elastomer was discontinued, forcing a change to Sylgard 186. The 186 was said to be identical to 187 except for the absence of the graphite colorant, but differences in mixing and curing properties suggested the need for further study of its long-term strength properties.

18.7.2 Core Seal Development

The sealing system for the ceramic regenerator was unchanged from the Baseline Engine design. The inner rim and outer "D" sealing elements continued to be fabricated of high-temperature graphite, which has the advantages of low weight, low friction, and freedom from distortion. Extensive operation at regenerator inlet temperatures as high as 788 C (1450 F) was well tolerated by this material. The most critical seal element, the inner crossarm seal, consisted of an Inconel X-750 substrate with a plasma-sprayed coating of 85% nickel oxide and 15% calcium fluoride. Problems in the continued development of this coating system are discussed below.

Other sources of continued difficulty were the diaphragm-type seal baseplate assemblies that retain the rubbing seal elements, hold them in intimate contact with the matrix, and provide sealing between the rubbing elements and the engine housing. These baseplates required frequent rework to maintain cold leakage measurements below 6%. Factors contributing to this problem include:

1) As shown on Fig. 219A, the diaphragm-type seal is a complex weldment and mechanical assembly of varying thicknesses of stainless steel sheet. It requires extensive tooling and great skill to assemble properly. Due to the loss of key personnel, the vendor for the Baseline Engine seals could not do the job, and a new fabricating vendor had to be developed for the Upgraded Engine parts.

2) The larger size and higher operating temperature led to severe distortion of early seals, necessitating doubling the thickness of the main component of this assembly. This led to even greater difficulty in seal fabrication.

3) Welded assembly of this part made replacement of the diaphragm foils extremely difficult. These diaphragms are fragile and subject to buckling and denting during the frequent teardowns inherent in a development program of this type.

In an attempt to overcome these problems, an alternate seal system was designed, as shown in Fig. 219b. This highly simplified design consists of a narrow strip of René 41 sheet, 0.08 mm (0.003 in) thick, bent to a 100° angle. The "L" elements are retained in rectangular channels milled in the engine housing (or regenerator cover). A spiral back-up spring of the same stock is used to retain the "L" seals during assembly; the elements and springs are heat treated to impart proper spring properties. The rubbing seals are restrained from rotation with simple sheet metal retaining clips.

The "L" seal concept has several advantages:

1) One mechanic can easily fabricate a full engine set in an hour's time. The only tooling required is a simple, hand-operated roll-forming tool for the curved sections, a sheet metal bending brake for the straight sections, and a tack-welder for assembling them. The spiral spring is formed by winding strip stock around a stainless steel rod and heat treating as wound.

2) Because cost is reduced by a factor of at least 10, damaged elements are more economically replaced than repaired.

3) Sealing is inherently improved through a reduction of leakage paths.

4) The "L" does not have the disadvantage of being exposed to the gas stream, and is thus protected from contamination and high thermal gradients.

5) The enclosed location also protects the elements from handling damage.

6) Baseplate distortion is eliminated - a principal cause of graphite seal breakage.

Over 300 test hours were run on "L" seals in engine 3, proving them to be relatively trouble-free and equal to the diaphragm-type in leakage. Virtually no development has been done on "L" seals due to other program priorities, so their full potential has not yet been realized. Furthermore, the Upgraded Engine was not sized with sufficient casting stock for full-sized "L" seal grooves. This forced use of "L" seals only half the size of those initially tested in the Baseline Engine. The only problem noted in the test program was minor buckling of the "L" elements where they contact the spiral spring. This problem could be fixed by replacing the spiral spring with a knitted stainless steel wire sleeve, of the type used to reinforce exhaust pipe gaskets. This material has adequate resiliency, and should apply more uniform loading to the "L" element.

18.7.3 Crossarm Seal

The crossarm seal consists of an Inconel X-750 substrate coated with NiCrAlY alloy bond coat and a mixture of NiO (85%) and CaF_2 (15%) to provide a low-friction, wear-resistant top coat. Although this coating was used on the Baseline Engine, the 25% longer seal length for the Upgraded Engine seriously accentuated the following effects:

1. Seal bow due to ditferential thermal expansion of coating to substrate. (The increased length caused a 90% increase in this effect.)

2. Seal waviness due to temperature gradient along seal length.

3. Seal distortion due to oxidation of metallic nickel in the top coat during engine operation. (Up to 30% of NiO is reduced to Ni during plasma spraying.)

4. Seal distortion due to effects 1, 2 and 3, above, coupled with a top coat thickness that represented 28% of the total seal thickness.

5. Cold start sealing problems caused by the above distortions being permanently set in the seal due to hardening of the X-750 substrate during engine operation at 760 C (1400 F).

The following factors have reduced the above problems to the point that less than a 0.26 mm (0.010 inch) bow is in the seal after processing and after many hours of engine use:

1. After substrate machining, the X-750 is overaged at 871 C (1600 F) for 20 hours. This prevents substrate hardening during engine operation.

2. The substrate is prebowed 13 mm (0.50 inch), convex, prior to coating.

3. The top coat thickness has been reduced to only 9% of the total seal thickness.

4. The seal is pre-oxidized at 760 C (1400 F) for 70 hours before finish grinding.

5. After finish grinding, the seal is oxidized for 20 hours at 788 C (1450 F). This is the maximum running temperature.

6. Final straightening at 760 C (1400 F) is done as needed on a pre-loaded and pre-countoured fixture that forces the X-750 to creep into a flat and relatively stress-free state.

Although these seals meet flatness, wear, and friction requirements for long term durability, consideration must be given to the formation of corrosion products resulting from reaction of the CaF_2 with the bond coat and/or the X-750 substrate. It is felt that this corrosion is accelerated during the processing step 5, above, since the processing is performed at temperatures higher than engine operating temperatures.

19.0 CONTROL SYSTEM

The electronic control system for the Upgraded Engine has full authority over engine operation. It is a four function system. The fuel control modulates engine power by governing gas generator speed according to driver's command and accessory load, provides overspeed protection, and limits acceleration temperature and burner emissions. Variable power turbine nozzle (PTN) control optimizes part-load fuel economy by maintaining the highest allowable cycle temperature, and provides engine braking. Variable inlet guide vane (VIGV) control minimizes idle fuel consumption by reducing compressor work and output power and provides design speed power augmentation with negative preswirl.

The free rotor concept necessitated the use of a non-mechanical sensor for speed governing and overspeed protection. The unit performed fuel, power turbine nozzles, inlet guide vane, water injection, and automatic start sequencing control functions. All Upgraded Engine control functions were integrated into a single system incorporating an electronic control unit (ECU) as a central controller.

Control system hardware and engine-related components are shown schematically in Fig. 220. The ECU receives input signals from various sensors and switches to monitor operator commands, engine operating status, vehicle speed, and ambient conditions. A fuel flow sensor and a power turbine nozzle (PTN) actuator position sensor also provide feedback to the control system. The ECU then converts all input signals to a voltage proportional to the value of the measured variable. These voltages are then used to compute the current requirement of several electro-mechanical actuators. The ECU supplies or "outputs" the required current to actuators in the fuel, power turbine nozzle, and starting systems. A detailed description of the basic control unit can be found in Refs 13, 14 and 15.

Ease of operation and passenger safety were not compromised. Several failsafe or "limp home" modes of operation to limit the effect of potential engine or control system failure were provided. On-board instrumentation and dealer service diagnostics can easily be accommodated.

The following discussions describe segments of the Upgraded Engine control system: fuel control, sensors, PTN control, VIGV control and automatic start sequencing.

19.1 Fuel Control

The fuel delivery system developed for the low emission premixed/prevaporized combustor is shown in Figs. 221 and 222. The motor driven, positive displacement fuel pump is mounted on the tank and draws through a standard screened pick up. It is manufactured in volume production for fuel injection systems. Output pressure is limited by an internal relief valve set between 75 and 80 psig.

The fuel passes through a 10 micron, low pressure drop (.5 psid at 100 pph) filter to the fuel shut-off solenoid valve. A relay in parallel with the starter solenoid energizes both the normally closed shut-off valve and the fuel pump during the start sequence. Once the engine is running, three safety switches in series keep the fuel relay engaged only above minimum fuel, oil, and collector pressures. This shuts off fuel flow in the event of fuel line rupture, loss of bearing lubrication, or power turbine or gas generator underspeed.

Fuel then passes the torch igniter, allowing the torch sufficient time during start to develop a flame before fuel reaches the main injector. A pressure atomizing fuel nozzle with integral screen is used, delivering approximately 2 pph fuel under all engine operating conditions. Air for the torch (up to 2% of total) is bled from the collector. The igniter for the torch is a standard side electrode resistive spark plug with a gap set at .050". Excitation is provided by a transistorized coil at 130 Hz.

Metered fuel for the main injector is accomplished by a pressure compensated variable flow control valve. See Fig. 223. The unit is vendor supplied and adapted from aircraft and industrial applications. A fast response differential pressure regulator provides a constant 20 psid for metering and torch nozzle atomization, and discharges excess pump flow to the tank return line. The 0.125-inch diameter metering nozzle is pressed in line with the inlet fitting with 70 micron filter and outlet fitting. Adjacent to the nozzle outlet is the flapper. A sealed torque motor works against a torsion spring to modulate flapper displacement and fuel flow. The nominal performance

characteristic is linear with a range of 0 pph at 0 ma to 100 pph at 300 ma. Specified tolerances are 3 pph maximum leakage flow and ± 10% at full range. Each unit is bench checked to establish calibration constants programmed into and used by the ECU.

A turbine type electronic flowmeter at the outlet of the fuel metering valve supplies the ECU with a signal frequency proportional to fuel flow. Temperature control during rotor accelerations is achieved by precise fuel metering. The flowmeter has provided an accurate check of fuel metering valve performance and was a vital link in developing an alternate "close loop" fuel flow control routine.

Four 0.032" i.d. injector tubes distribute the metered fuel in the combustor premixer. To maintain low fuel line pressure, pressure drop through the injector is low, approximately 4 psid at 100 pph. Although no atomizing air is required in this design, a slight compressor air bleed cools the injector manifold, preventing fuel line vaporization and reducing burner flash back.

During steady speed or deceleration conditions, a portion of the metered fuel bleeds through a 0.020" port in the injector, through a bleed solenoid valve to drain. This added flow assists in cooling the injector and improves idle fuel governing. An added benefit is the overall decrease of system response, desirable for steady state operation, once the high system gains for good transient response have been established.

The normally open bleed solenoid valve is energized during rotor accels, stopping flow through the injector bleed port. This aids in NOx control, providing a step change in combustor fuel flow from lean to rich. Also, acceleration temperatures are limited by direct fuel metering and optimized fuel schedules. During decels, the bleed remains open, purging the injector of fuel, which otherwise would contribute to hydrocarbon emissions.

A line back to the tank returns fuel from the bleed valve and metering valve regulator discharge. In conjunction with the fuel shut-off valve exhaust port and a set of check valves, the return line purges the injector, the torch nozzle, and metering valve of fuel during engine shut-down.

Fig. 224 depicts the test cell electronic fuel control block diagram. A corrected speed reference is computed from a schedule. Inputs to the schedule are accelerator pedal position (α) for the driver's power requirement, power turbine (Na) underspeed proportional governor to prevent loss of regenerator, oil pump, and vehicle accessory drives, and a neutral/drive idle reference. The difference between the speed reference and gas generator speed (Ngg) corrected to ambient temperature ($1/\sqrt{\theta}$) results in a speed error signal (ϵNgg) to the isochronous range governor which establishes a steady state fuel flow command signal (Wfd). The gas generator overspeed governor limits mechanical speed to 75% in neutral/park and 100% in drive gears.

The fuel flow command signal is limited to a 0 pph below 10% Ngg, 100 pph above 10% Ngg, 25 pph above 100% Na, and to a start/accel temperature limiting schedule, a function of Ngg/$\sqrt{\theta}$. An additional 12 pph increment of fuel is allowed for cold atarts.

Fuel metering valve calibration constants are then applied to the limited fuel flow command signal to yield an overall 15 pph/volt static system sensitivity. The signal is then directed to the analog output. This output, a current driver having a linear output/input characteristic of 50 ma per volt, drives the fuel metering valve torque motor.

19.2 Sensors

The gas generator speed (Ngg) sensor is mounted in the compressor cover. Gas generators with steel inducers are fitted with a small magnetic pickup assembly generating a 2 to 6 volt peak to peak waveform with .015" clearance to the inducer tip. An auxiliary proximity sensing system requiring a separate power supply has been adopted for test cell use with aluminum impellers.

The power turbine speed (Na) sensor is identical to the Ngg sensor. It is mounted on the reduction gear cover, excited by a 60-tooth accessory drive pulley sheave.

Chromel-Alumel exposed junction thermocouples are used for sensing turbine inlet (T_5) and turbine outlet (T_9) temperature. This scheme requires signal conditioning with cold junction

compensation. Thermocouple life at station T_5 is generally less than 100 hours. Thermocouples are thus an undesirable candidate for automotive production applications but have provided the accuracy and fast response required for control system development.

Ambient temperature sensor (T_1) generates the correction factor $1/\sqrt{\theta}$ for computing corrected gas generator speed utilized in the range governor and the start-acceleration fuel schedule. It is also used for a partial correction on turbine outlet temperature. A nickel iron temperature sensitive resistance wire sensor is mounted in the air filter housing to supply the ECU with an inlet air temperature signal.

Two sensors are involved in monitoring control subsystems. A fuel flow transducer with integral photo-electronics produces a linear frequency output as a function of fuel flow (W_f). It is primarily used as a diagnostic tool but has been a control element in an optional closed loop fuel flow control for improved rotor response. The power turbine nozzle actuator design dictates ECU knowledge of trim piston position (β). A low cost conductive plastic linear resistance potentiometer has been proven in service.

A transmission governor pressure switch signals the ECU to disable the PTN actuator braking at low car speeds to prevent power turbine stall.

Driver controls consist of an accelerator pedal position (α) rotary cermet resistance potentiometer and production transmission neutral safety and ignition switches.

All of the above sensors are ECU inputs. Independent control elements activate heater/air conditioner, fuel supply, and charging systems by oil, fuel, and compressor discharge pressure switches, and field & load relays. Transmission shift pattern is mechanically controlled from the accelerator pedal. Shift quality is modulated hydro-pneumatically by compressor discharge pressure regulating transmission line pressure.

19.3 Power Turbine Nozzle Control

Inordinate fabrication and assembly difficulties, unacceptable response time, and instability experienced with the original design power turbine nozzle actuator warranted a reevaluation of this concept. An intensive effort did not result in satisfactory actuator operation. A new modular design concept was initiated and is described here.

The actuator is comprised of an inner and outer piston which can be locked hydraulically in the retracted or extended position. In the retracted position, Fig. 225, (inner piston locked against the outer piston) the actuator will modulate the power turbine nozzle vanes in the power or driving mode. When oil pressure is directed such that it causes the inner piston to separate and lock in the extended position (referred to as the braking position), the actuator can be modulated in the braking mode, Fig. 226. Modulation is accomplished by an electromechanical device (linear solenoid/null valve) which applies pressure on a trimmer piston directly coupled to the inner/outer piston assembly.

The signal for the linear solenoid is sourced in the electronic control unit which processes an engine temperature signal (thermocouple), in this instance turbine outlet temperature. A feedback potentiometer attached to the trimmer piston positions the power turbine nozzle vanes so that the desired (closed loop) engine cycle temperature is maintained.

In the event of an oil pressure failure, springs are provided to return the inner/outer piston to the start/failsafe mode position (low engine cycle temperature) as a fail-safe feature. Should a power loss occur in the electronic control system, the electromechanical system will also return the inner/outer piston assembly to the start/failsafe mode.

Two units were assembled and successfully applied to a test cell powerplant and to a vehicle (4000 miles of driving experience). Since additional power turbine nozzle actuators would be required for the program, the design of the unit was revised. The modular concept was configured as an integral unit and a feature was incorporated which hydraulically reverses the null valve logic of the trimmer piston such that increasing the linear solenoid voltage will increase engine cycle temperature in both power and braking modes. Reversing of logic within the ECU would require an external switching and fail safe system which could not be provided for without a great deal of complexity.

Two units were procured, the actuators were assembled and bench tested. Their functions were also satisfactorily demonstrated in a cold chamber. One unit is scheduled for application to the NASA transient test engine, the second unit will ultimately be programmed for vehicle use.

Note the simplified attachment to the power turbine nozzle mechanism as shown in Fig. 225. An adjustable stop on the valve controlled by transmission governor pressure can be calibrated to vary the slew rate and reduce actuator response when shifting from the power mode to braking mode. Fig. 226. This procedure will reduce the excessive engine braking feel experienced with the protytype units. Fig. 227 shows the assembled actuator ready for engine installation

Although the "integral" units have only been bench tested at the time of this writing, their success is assured by the experience accumulated with the "modular" concept.

19.4 Variable Inlet Guide Vane Control

The design and fabrication of the five vendor supplied units was contracted for and delivered in 1977. Slow response and external oil leakage problems warranted a developmental period extending through 1978. Leakage problems were readily controlled utilizing Loc-Tite 290 sealant. Actuator response, however, could not be readily corrected due to the inflexibility of the casting, i.e., porting size, traverse limits of the linear solenoid, et cetera. Therefore the function of the unit was compromised as a fixed, 2 position device, -- +60° at idle and 0° from 52% to 100% speeds.

An additional control requirement was that of engine runaway during shutdown. This condition is particularly objectionable after high speed vehicle operation. Control can be implemented by throttling airflow at the air inlet or at the variable power turbine nozzles. The fast response, two-position actuator is configured such that the VIGV move to the throttling mode (+60°) after engine shutdown, thus minimizing engine runaway. The simplicity of the control logic dictates that the VIGV be used to perform this function. Several units were so modified and are shown schematically on Fig. 228. The program was concluded utilizing the 2-position actuator.

19.5 Start Sequencing and Safeties

A flowchart depicting start sequencing and engine safeties is shown in Figs. 229 and 230. Start fuel is delivered above 10% Ngg as a function of corrected speed and initial engine temperature. The light-off detector allows fuel flow for a maximum of ten seconds if combustor temperature rise is not sensed. A twenty-five second timer limits starter engagement. Either condition shuts off the fuel metering valve, disengages the starter, and trips an abort timer. A re-start is not allowed for thirty seconds, allowing residual fuel to drain.

Normal starter cut-out occurs at 35% Ngg, after which fuel flow is modulated by the gas generator range governor. Overrides are provided to limit gas generator and power turbine idle and maximum speeds. Acceleration temperatures are limited by a corrected speed fuel schedule. A back-up safety shuts down the engine in the event of a two second over-temperature condition. A flame out allowing gas generator speed to fall below 32% shuts off the fuel solenoid valve.

The power turbine nozzle subroutine tests the two T_8 thermocouples for open circuits and selects the higher of the two signals for controlling. In the event that both T_8 sensors are open circuit, the power turbine nozzle actuator reverts to the start on failsafe position.

A bank of indicator lamps display go/no go conditions as well as sensor status. A separate safety circuit (not shown in Fig. 230) energizes the fuel pump and main shutoff valve above 35% Ngg. The circuit requires minimum fuel, oil, and compressor discharge pressure to maintain fuel delivery.

20.0 IN-VEHICLE POWERTRAIN DEVELOPMENT

Powertrain development consisted of the work required to match actual engine and transmission performance characteristics, to develop the engine control system, to perform endurance testing and to obtain the emission and fuel economy data of the developed hardware at the end of the program.

20.1 Transmission Work

A production high-stall torque converter was used in the program vehicles and was modified to lock up in the 1-2 upshift. Transmission shift quality was achieved after the usual experimental valve body work required to match the transmission to the engine. Creep torque was found to be commercially acceptable; a vehicle speed of only 16 mph in 3rd gear was achieved with the power available at idle speed.

20.2 Control Development

Control development centered around the power turbine nozzle actuator, nozzle angle scheduling and fuel flow scheduling. After normal development, the modular nozzle actuator, discussed in Section 19, performed satisfactorily. This actuator accumulated 226 hours and 4078 miles of trouble-free operation.

Two nozzle angle routines were evaluated in a vehicle with the aid of a keyboard programmer. In one routine, the nozzle position was scheduled with gas generator speed at steady state, with an additional 4° opening at each speed during acceleration. In the other routine, nozzle position was determined by a schedule of power turbine exit temperature with gas generator speed by means of closed loop logic. During acceleration, the nozzles are opened an additional 4° from steady-state values. The latter was the selected routine used at the end of the program.

A dual fuel schedule was needed to start the engine. A single schedule was too lean for cold-engine starts at engine temperatures less than 50 F and too rich for engine temperatures greater than 700 F. Cold light-off capability with the dual schedule was improved down to 30 F, with the droplet diffusion combustor. Successful ambient temperature (≈70 F) starts were achieved with both the droplet diffusion and LPP combustors.

20.3 Endurance Cycle Testing

The endurance cycle included both freeway and city traffic driving under actual road conditions. This testing was combined with transmission shift quality evaluations and nozzle actuator response tests.

The endurance cycle specifications are given below:

Number of Starts: 10

Distance: 119 km (74 miles)

Driving Time: 140 minutes

Total Time: 200 minutes

Average Speed: 51 km/hr (32 mph)

20.4 Fuel Economy and Emission Tests

Fuel consumption characteristic tests for both cold '75, hot '74, and FEC were conducted on chassis rolls for an inertia weight of 3500 pounds. Fuel consumed (gasoline) was weighed directly. The best combined economy was 15 mpg with gasoline. The test results of November 9, 1978 (without engine braking) were used for this calculation. See Table 25. Steady-state fuel economies (chassis rolls) for Vehicle U-2 yielded the following results:

Speed	Economy MPG Gasoline (3900 A)
20	19.12
30	21.80
40	23.67
50	20.73

Details are shown on Table 25. Steady-state emission tests for both the droplet-diffusion and premixed, prevaporized combustors are tabulated on Table 26.

20.5 Gas Generator Response Time

The intended gas generator response time was 1.1 seconds. Fig. 231 shows the intended response curve of the Upgraded Engine, the response curve from data taken on a Baseline Engine, and the actual response curve from data taken on an Upgraded Engine. The actual response time for the Upgraded Engine is approximately twice the value of the intended acceleration time. The measured polar moment of inertia of the gas generator shaft is 0.01331 in-lb-sec^2; a value of 0.0117 in-lb-sec^2 was the design intent. Since the actual value is only 14 percent higher than intended calculations were performed to investigate if the miss in response time was due to failure to meet goal power and possibly due to differences in acceleration power as a percentage of design speed output power.

The change in response time due to change in engine output power was obtained from Equation 7 in Appendix B by scaling the value of the acceleration power. The output power from PP 10-14M was 87.38 HP, and the average acceleration power was 12.96 HP, or 14.8% of the maximum output power. If the goal power of 104 Hp had been achieved, and if the same percentage is used for acceleration power, the value of acceleration power would be 15.42 HP. The response time would reduce from 1.82 seconds to 1.53 seconds (19% change). The calculated acceleration power for the Baseline Engine was 17.7% of its output power. If the Upgraded Engine had the same percentage, the response time would reduce from 1.53 seconds to 1.28 seconds (19% change). Thus, even if the goal value of polar moment of inertia had been achieved, the response time of the Upgraded Engine would be 19% longer because design power was missed and another 19% longer because the acceleration power is a lower percentage of output power.

The lack of power is due to the difference in turbine efficiency between values deduced from engine data and the goal values. At 80% speed, for instance, the ratio of the product of the compressor and turbine efficiencies, using deduced values from engine data and the goal values, accounts for 15 of the 19 percentage points. Time did not permit investigating the reason for the lower value of acceleration power as a percentage of output power.

20.6 Engine Status and Retrofit Schedule

The program ended with seven engines, whose disposition at the end of the program is shown on Table 27. The definition of a retrofit engine includes: replacement of the original compressor-turbine with the Mod 3 design, installation of a droplet diffusion combustor, and replacement of the power turbine with one of the following configurations:

Mod 1 - Noel Penny design power turbine, Fig. 232

Mod 2 - Original power turbine with the blade trailing edges closed 11° and modified power turbine exhaust diffuser, Fig. 233.

21.0 CONCLUSION

The final engine performance with all retro-fitted components showed a value of 91 HP at design speed in contrast to the design value of 104 HP. The design-speed SFC was 0.53 versus the goal of 0.44. During the program, the original goals were revised as a result of a re-assessment of the component efficiencies to values that were thought to be more likely in turbomachinery of this size. This resulted in revised design-point goals of 95.6 HP at an SFC of 0.49. Detailed examination of final engine data indicated that even the revised turbine efficiency goals could not be met in this size. Full evaluation would take place on component rig tests at NASA-Lewis.

Cycle analysis showed that, at low speeds, most of the SFC deficit came from heat loss. At 60% speed at constant power, for example, 73% of the SFC deficit was due to heat loss. Of this figure, 58% was attributed to lack of heat recovery due to bulkhead-cooling heat loss; the rest could be attributed to a miss in regenerator effectiveness of 2 points.

Vehicular fuel consumption tests for both cold '75, hot '74, and FEC were conducted on chassis rolls for an inertia weight of 3500 pounds. Fuel consumed (gasoline) was weighed directly. The best combined cycle fuel economy was 15 mpg. The Baseline Engine achieved 8 mpg (gasoline) with a 4500-lb vehicle. For this same weight, the Upgraded Engine fuel economy calculates to be 11.7 mpg. Even though the goal of 18.3 mpg was not achieved with the Upgraded Engine, there was an improvement in fuel economy of 46% over the Baseline Engine, for comparable vehicle inertia weight.

References

1. Gray, S., Sparks, N , and McCormick, J.: The Application of Gas and Oil Lubricated Foil Bearings for the ERDA/Chrysler Automotive Gas Turbine Engine. ASME Paper 76-GT-115, March, 1976.

2. Collman, J.S., Amann, C.A., Matthews, C.C., Stettler, R.J. and Verkamp, F.J.: The GT-225 -An Engine for Passenger-Car Gas-Turbine Research. SAE Paper 750167, February, 1975.

3. Seventh Quarterly Progress Report. Baseline Gas Turbine Development Program. Edited by F.W. Schmidt and C.E. Wagner; July 31, 1974.

4. Galvas, Michael R.: A Compressor Designed for the Energy Research and Development Agency Automotive Gas Turbine Program. NASA TM X-71719; May, 1975.

5. Crigler, John L. and Copeland, W. Latham: Noise Studies of Inlet-Guide-Vanes - Rotor Interaction of a Single-Stage Axial-Flow Compressor, NASA TN D-2962.

6. Crigler, John L; Copeland, W. Latham; and Morris, Garland J.: Turbojet-Engine Noise Studies to Evaluate Effects of Inlet-Guide Vane - Rotor spacing, NASA TN D-4690.

7. Trumpler, W.E. Jr. and Owens, H.H.: Turbine-Blade Vibration and Strength. Trans. ASME, April, 1955.

8. Roelke, Richard J. and McLallin, Kerry L.: The Aerodynamic Design of a Compressor-Drive Turbine for Use in a 75 KW Automotive Engine. NASA TM X-71717, April, 1975.

9. Kofskey, Milton G. and Katsanis, Theodore: Aerodynamic Design of a Free Power Turbine for a 75 KW Gas Turbine Automotive Engine. NASA TM X-71714, April, 1975.

10. Evans, D.M.: Calculation of Temperature Distribution in Multi-Stage Axial Gas Turbine Rotor Assemblies when Blades are Cooled. ASME Paper 73-GT-8, 1973.

11. Wasley, Richard J.: Stress Wave Propagation in Solids. Marcel Dekkler Inc., New York, 1973.

12. Patel, B.R. and Goebel, J.H.: Evaluation of the Regenerator Core Flow Distribution for the ERDA/Chrysler Automotive Gas Turbine Engine. Creare, Inc., Technical Memorandum TM-559, September, 1977.

13. Dent, J.R. and Bergman, A.D.: Developments in Programmable Analog Control Systems. ASME Paper 74-GT-117.

14. Dent, J.R. and LeFevre, H.P.: Advancements and Application on Programmable Analog Control Technology. ASME Paper 76-GT-122.

15. Court, D.J.: Application of a Programmable Engine Control to the Gas Turbine. SAE Paper 770963.

TABLE 1

Upgraded Engine Description

General

Type: Regenerative gas turbine

*Rated Output: Power - 92kW (123 hp) @ 3280 rpm output shaft speed
Torque - 480 N.m (355 lb-ft) @ zero output shaft speed

Augmentation: Variable inlet guide vanes and water injection

Weight: 180 kg (400 lbs)

Engine Configuration: Free rotor, designed for compact vehicle installation

Maximum gas generator acceleration, idle-to-full speed: 1.1 sec.

Fuels: Unleaded gasoline, diesel fuel, kerosene, JP-4, etc.

Components

Compressor: Backward Curved Centrifugal with variable inlet guide vanes

Compressor Turbine: Axial

Power Turbine: Axial, variable geometry stator

Regenerator: One rotating ceramic disc

Burner: Fixed Geometry

Design Point Characteristics

Maximum gas generator shaft speed: 58,500 rpm

Maximum Power Turbine Speed: 70,000 rpm

Maximum output speed (after reduction gears): 4,700 rpm

Maximum Regenerator Speed: 31 rpm

Compressor Pressure Ratio: 0.61 kg/s (1.34 lb/s) design
0.69 kg/s (1.52 lb/s) augmented

Compressor Turbine Inlet Temperature: 1052°C (1925°F) design

Power Turbine Outlet Temperature: 748°C (1378°F)

*Ambient Conditions: Temperature 29°C (85°F)
Pressure 1.013 bar (14.696 psia)

TABLE 2A

Upgraded Engine Characterization

29.4°C, 1.013 bar (SI Units)

Gas Generator Speed, RPM	29 250	35 100	40 950	46 800	52 650	55 575	58 500
FRACTION	0.5	0.6	0.7	0.8	0.9	0.95	1.0
Power Turbine Speed, RPM	26 000	34 000	40 600	44 500	50 000	52 000	50 000
Compressor Pressure Ratio	1.498	1.788	2.177	2.700	3.383	3.770	4.185
Component Efficiency							
Compressor, 1-2*	0.769	0.784	0.798	0.804	0.804	0.797	0.785
Compressor Turbi. ., 5-6	0.832	0.836	0.841	0.843	0.846	0.847	0.846
Power Turbine, 6-8	0.719	0.719	0.741	0.755	0.764	0.765	0.762
Burner	0.998	0.998	0.999	0.999	0.999	0.999	0.999
Regenerator	0.957	0.948	0.939	0.928	0.916	0.911	0.905
Parasitic Loss, kW							
Gas Generator	0.63	0.90	1.23	1.61	2.03	2.26	2.51
Power Turbine	1.46	2.15	3.12	3.90	5.15	5.73	5.57
Output Power, kW Net	4.87	10.69	20.71	36.24	56.70	67.48	77.81
Fuel Flow, kg/h Diesel	2.49	4.10	6.55	10.20	15.16	18.02	21.01
Specific Fuel Consumption, g/w-h	0.512	0.384	0.316	0.281	0.267	0.267	0.270
Gas Flow, kg/s							
Station 1	0.196	0.256	0.323	0.408	0.503	0.555	0.606
3	0.191	0.249	0.315	0.397	0.489	0.538	0.587
4	0.191	0.249	0.314	0.396	0.488	0.537	0.586
5	0.192	0.250	0.315	0.397	0.489	0.539	0.588
6	0.194	0.253	0.320	0.403	0.497	0.548	0.598
8	0.196	0.255	0.322	0.407	0.502	0.554	0.604
9	0.197	0.256	0.324	0.410	0.506	0.558	0.610
Pressure, kPa							
Station 1	101.17	101.05	100.89	100.64	100.28	100.05	99.80
2=3	151.55	180.68	219.64	271.71	339.23	377.19	417.69
4	150.40	179.38	218.23	270.20	337.66	375.60	416.08
5	147.95	175.90	213.67	264.35	330.56	367.86	407.76
6	120.41	132.10	147.31	165.41	186.19	195.61	203.37
8	103.30	104.13	105.20	106.76	108.84	110.10	111.48
9	101.59	101.79	102.12	102.68	103.54	104.11	104.77
Temperature, °C							
Station 1	29.4	29.4	29.4	29.4	29.4	29.4	29.4
2	77.7	99.2	123.8	152.6	185.4	203.4	222.7
3	83.8	103.0	125.7	153.3	184.9	202.4	221.3
4	700.7	700.1	698.1	695.6	692.8	692.2	691.2
5	829.4	864.7	907.3	954.7	1005.6	1029.6	1051.7
6	776.1	792.1	812.6	834.1	855.5	863.4	868.5
7.5	747.8	747.8	747.8	747.8	747.8	747.8	747.8
8	738.8	740.7	740.8	741.5	742.1	742.3	742.5
9	128.7	152.8	180.0	212.3	248.3	266.8	286.8

*Numerics refer to station notation

TABLE 2A (cont.) **29.4°C, 1.013 bar (SI Units)**

Upgraded Engine Characteristics

Flow Leaks, kg/kg Compressor Air Flow							
Station i to j							
ij = 20	.00242	.00251	.00257	.00266	.00280	.00285	.00286
25	.00431	.00360	.00308	.00270	.00242	.00230	.00218
34	.00251	.00220	.00199	.00170	.00152	.00143	.00135
36	.00910	.00942	.00971	.01011	.01068	.01093	.01104
38	.00345	.00360	.00371	.00384	.00399	.00404	.00402
39	.00478	.00546	.00616	.00696	.00785	.00826	.00852
46	.00539	.00577	.00616	.00667	.00735	.00768	.00792
48	.00133	.00186	.00245	.00312	.00386	.00422	.00450
68	.00236	.00245	.00247	.00245	.00239	.00232	.00218
Heat Leaks, J/kg Compressor Air Flow							
ij = 30	3031.	3128.	3238.	3324.	3566.	3691.	3796.
40	4994.	4045.	3359.	2824.	2454.	2305.	2203.
43	6178.	4654.	3503.	2624.	2010.	1761.	1582.
50	2468.	2058.	1737.	1463.	1263.	1175.	1096.
60	495.	402.	328.	267.	226.	207.	191.
63	788.	619.	488.	381.	305.	272.	249.
80	5734.	4350.	4315.	3787.	3415.	3270.	3142.
83	2089.	1593.	1219.	926.	721.	635.	574.

TABLE 2B

Upgraded Engine Characterization

85°F, 14.696 PSIA (English Units)

Gas Generator Speed, RPM	29,250	35,100	40,950	46,800	52,650	55,575	58,500
FRACTION	0.5	0.6	0.7	0.8	0.9	0.95	1.0
Power Turbine Speed, RPM	26,000	34,000	40,600	44,500	50,000	52,000	50,000
Compressor Pressure Ratio	1.498	1.788	2.177	2.700	3.383	3.770	4.185
Component Efficiency							
Compressor, 1-2*	.769	.784	.798	.804	.804	.797	.795
Compressor Turbine, 5-6	.832	.836	.841	.843	.846	.847	.846
Power Turbine, 6-8	.719	.719	.741	.755	.764	.765	.762
Burner	.998	.998	.999	.999	.999	.999	.999
Regenerator	.957	.948	.939	.928	.916	.911	.905
Parasitic Loss, HP							
Gas Generator	.84	1.21	1.63	2.15	2.72	3.04	3.37
Power Turbine	1.95	2.89	4.19	5.22	6.90	7.68	7.46
Output Power, HP Net	6.53	14.33	27.77	48.60	76.04	90.50	104.34
Fuel Flow, Lb/Hr Diesel	5.49	9.05	14.44	22.49	33.43	39.72	46.33
Specific Fuel Consumption, Lb/Hp-Hr	.842	.631	.520	.463	.440	.439	.444
Gas Flow, Lb/Sec							
Station 1	.433	.564	.713	.900	1.110	1.223	1.335
3	.421	.549	.694	.875	1.078	1.186	1.295
4	.421	.548	.693	.874	1.076	1.185	1.293
5	.423	.550	.695	.876	1.079	1.187	1.296
6	.428	.558	.704	.889	1.096	1.207	1.318
8	.431	.562	.711	.898	1.107	1.220	1.332
9	.433	.565	.715	.904	1.116	1.230	1.344
Pressure, PSIA							
Station 1	14.673	14.657	14.633	14.596	14.544	14.511	14.476
2=3	21.980	26.206	31.856	39.409	49.201	54.706	60.580
4	21.814	26.017	31.651	39.190	48.974	54.476	60.348
5	21.458	25.513	30.990	38.341	47.944	53.353	59.141
6	17.463	19.159	21.365	23.990	27.004	28.370	29.495
8	14.983	15.102	15.258	15.484	15.785	15.968	16.169
9	14.734	14.764	14.811	14.893	15.018	15.100	15.196
Temperature, °F							
Station 1	85.0	85.0	85.0	85.0	85.0	85.0	85.0
2	171.9	210.6	254.8	306.8	365.8	398.1	432.8
3	182.8	217.3	258.3	307.8	364.9	396.3	430.4
4	1293.3	1292.1	1288.5	1284.1	1279.0	1277.9	1276.2
5	1525.0	1588.4	1665.2	1750.4	1842.0	1885.3	1925.0
6	1429.0	1457.5	1494.6	1533.4	1571.9	1586.2	1595.2
7.5	1378.0	1378.0	1378.0	1378.0	1378.0	1378.0	1378.0
8	1361.8	1364.7	1365.4	1366.8	1367.7	1368.1	1368.6
9	263.7	307.1	355.9	414.1	479.0	512.3	548.3

*Numerics refer to station notation

TABLE 2B (cont.) **85°F, 14.696 PSIA (English Units)**

Upgraded Engine Characteristics

Flow Leaks, lb/lb Compressor Air Flow							
Station i to j							
ij = 20	.00242	.00251	.00257	.00266	.00280	.00285	.00286
25	.00431	.00360	.00308	.00270	.00242	.00230	.00218
34	.00251	.00220	.00199	.00170	.00152	.00143	.00135
36	.00910	.00942	.00971	.01011	.01068	.01093	.01104
38	.00345	.00360	.00371	.00384	.00399	.00404	.00402
39	.00478	.00546	.00616	.00696	.00765	.00826	.00852
46	.00539	.00577	.00616	.00667	.00735	.00768	.00792
48	.00133	.00186	.00245	.00312	.00386	.00422	.00450
68	.00236	.00245	.00247	.00245	.00239	.00232	.00218
Heat Leaks, BTU/LB. Compressor Air Flow							
ij = 30	1.303	1.345	1.392	1.429	1.533	1.587	1.632
40	2.147	1.739	1.444	1.214	1.055	.991	.947
43	2.656	2.001	1.506	1.128	.864	.757	.680
50	1.061	.885	.747	.629	.543	.505	.471
60	.213	.173	.141	.115	.097	.089	.082
63	.339	.266	.210	.164	.131	.117	.107
80	2.465	1.870	1.855	1.628	1.468	1.406	1.351
83	.898	.685	.524	.398	.310	.273	.247

TABLE 3

Engine Characterization Schematic Station Notation

Upgraded Engine

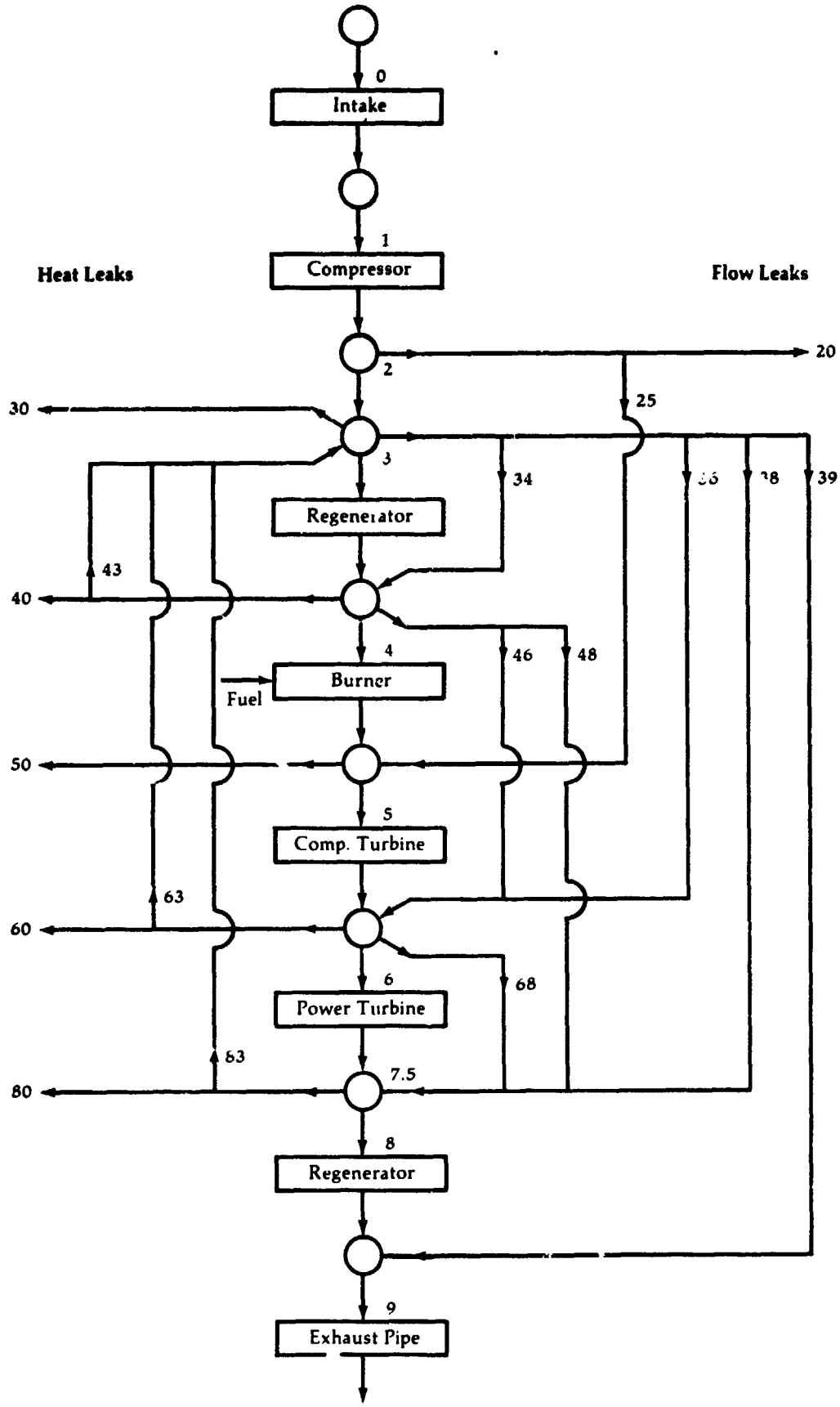

TABLE 4

Engine Characteristics at Maximum Gas Generator Speed

	VIGV Angle	Turbine Inlet Temperature, F°	Compressor Pressure Ratio	Compressor Air Flow, pps	Output Power, hp
Design Point*	0°	1925	4.18	1.335	104.
Power Augmentation					
VIGV Only	-30°	1925	4.55	1.450	113.
VIGV & Water Injection	-30°	1925	4.94	1.521	123.

*Ambient Conditions: 85F dry bulb, 51F wet bulb
14.696 psia

TABLE 5

Hub-to-Tip Variation of Nozzle Inlet Design Parameters

Abs. Air Ang., Deg	53.1	52.2	50.2	48.3	46.5	44.9	44.1
Radius. Inches	1.750	1.801	1.898	1.989	2.073	2.152	2.190
Abs. Vel., Fps	932.0	916.9	894.5	879.2	868.0	859.5	855.8
Abs. Tan. Vel., Fps	745.7	724.5	687.5	656.2	629.5	606.4	595.9
Abs. Mach	.407	.400	.390	.383	.378	.374	.373
Mer. Vel., Fps	55	561.9	572.4	585.0	597.6	609.1	614.2

TABLE 6

Power Turbine Design Operating Values

	Engine Operation	Equivalent Condition
Inlet total temperature, T', K	1154	283.2
Inlet total pressure, p', N/cm²	19.55	10.13
Mass flow, kg/sec	0.590	0.624
Specific work, Δh, J/g	137.1	35.1
Turbine rotative speed, rpm	46150	23343
Rotor blade speed (mean section). U_m, m/sec	331.4	167.6
Work factor $\Delta h \times 10^3 / U_m^2$	1.247	1.247
Total-to-total pressure ratio, p'_1/P'_2	1.678	1.712
Total efficiency	0.850	0.852
Static efficiency	0.741	0.771

Tables 4, 5 and 6

TABLE 7

Material Properties of MM 002

MFB Samples (Machined From Blades) C. Lund, March 1976

	Stress Rupture				(Typical)
	100 Hr.		1000 Hr.		
Temperature °C (°F)	kPa	(ksi)	kPa	(ksi)	
740 (1370)	745,000	108	579,000	84	
800 (1480)	586,000	85	427,000	62	
	Ultimate Tensile Strength		0.2% Yield Strength		Elongation, Percent
°C (°F)	kPa	(ksi)	kPa	(ksi)	
RT	1,034,000	150	862,000	125	8
760 (1400	1,000,000	145	862,000	125	8
980 (1800)	517,000	75	310,000	45	15

TABLE 8

Gas Generator Component Specifications

Component and Description

Support-Gas Generator
Material: Aluminum cast.
Pilot Ring of steel pinned to Support and machined concentric.
Circular pilot with engine housing.
Internal passages for oil, air and oil drain.
Mounts separate turbine wheel air bearing carrier and compressor oil bearing carrier.

Diffuser - Compressor
Material: Aluminum
Integral machined vanes
Pilots into cover

Cover - Gas Generator
Aluminum Casting
Intermittent pilot with Support
Collects compressor outlet air and routes it into three integral lobes which discharge into engine housing.
Provides mount for VIGVs and air intake housing.

Air Bearing Carrier
Material: Cast Iron
Pilot: Long "finger" to cope with thermal gradients.
Alternate: Provision for oil bearing.
Sub-Components: Bearing assembly.
Graphite seal assemblies.

TABLE 9

VIGV Control Schedule

Vane Angle,°	Ring Gear Rotation Degrees From Ref.	Actuation Piston Motion, mm From Ref.	Vane Torque Per Piston Force, mm (1 Vane)
−30	−7.3956	−12.0035	18.313
−24	−6.1335	− 9.9747	20.408
−18	−4.7478	− 7.7358	22.317
−12	−3.2525	− 5.3087	23.995
− 6	−1.6638	− 2.7198	25.400
0	0	0	26.489
6	1.7189	2.8160	27.232
12	3.4714	5.6905	27.604
18	5.2353	8.5842	27.597
24	6.9878	11.4571	27.211
30	8.7067	14.2705	26.462
36	10.3705	16.9875	25.376
42	11.9592	19.5745	23.985
48	13.4545	22.0017	22.329
54	14.8402	24.2433	20.448
60	16.1023	26.2778	18.381

TABLE 10

Power Turbine Thrust Bearing Performance

Definition	PTW RPM	Ngg %	Net Thrust Lbs	Req. (1) Oil Flow GPM	Min. Oil Film Micro In	Oil Film Ratio	Power Loss HP	Oil Temp Incr. °F	Oil Inlet Temp °F
Peak Speed (2)	70000	100% +VIGV+H_2O	83	.78 .73	1020 938	1.55 1.70	.63 .56	10 8	275 300
102 Upshift	52500	100% +VIGV+H_2O	576	.25 .22	358 315	2.60 2.85	.95 .85	41 40	275 300
Peak Power	46150	100%	190	.33 .30	590 530	2.00 2.10	.47 .42	16 15	275 300
Road Load Point	39000	68%	66	.40 .35	878 799	1.65 1.70	.25 .21	7 6	275 300
Peak Stall	27500	100%	344	.12 .11	332 293	2.75 2.95	.30 .25	24 23	275 300
Rapid Accell	19000	90%	256	.10 .08	319 280	2.80 3.05	.15 .12	17 17	275 300

Thrust Runner

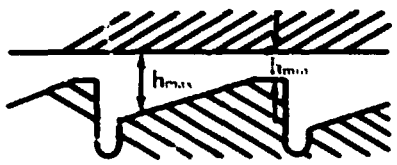

oil film ratio = $\frac{h_{max}}{h_{min}}$

OD = 1.40 In.
ID = 1.00 In.
No. of Pads = 6
Ramp Slope=.00077/.0015 In/In
Ramp Depth=.0004/.0008 In

(1) Required oil flow to form the EHD action (varies ±12% with the ramp slope)
(2) Power losses double if the oil flow decreased to .50 GPM
Note: Analysis assumes effective area 80% and parallel surfaces.

TABLE 11

Gear and Sprocket Data

No.	Description	Max. RPM	Material	Face Width In.	No. of Teeth	Pitch Dia. In.	Press. Angle Deg.	Location
A	Power Turbine Pinion	70,000	SAE 6150 Steel	1.1	28	1.0	20	P.T. Reduction
B	Intermediate Gear	12,405	SAE 6150 Steel	1.0	158	5.65	20	P.T. Reduction
C	Intermediate Pinion	12,405	SAE 6150 Steel	1.2	72	2.59	20	P.T. Reduction
D	Engine Output Gear	4,701	SAE 6150 Steel	1.1	190	6.79	20	P.T. Reduction
E	Auxiliary Drive Pinion	4,701	Nodular Iron	0.8	66	4.12	30	Auxiliary Drive
F	Auxiliary Drive Gear	3,978	SAE 1010 Steel	0.7	75	4.88	30	Auxiliary Drive
G	Worm	3,978	SAE 8620 Steel	1.75	6	.84	20	Accessory Drive
H	Worm Gear	265	Manganese Bronze	.62	90	3.99	20	Accessory Drive
I	Regenerator Pinion	265	SAE 1046 Steel	1.0	38	2.71	20	Accessory Drive
J	Regenerator Gear	32	Gray Cast Iron	.62	315	22.50	20	Regenerator
K	V.P.T.N. Sector Gear	—	Stainless Steel	.3	20	1.1	20	Interstage
L	V.P.T.N. Ring Gear	—	Gray Cast Iron	.6	150	8.2	20	Interstage
M	Driver Sprocket	12,405	SAE 1141 Steel	.5	21	2.4	—	P.T. Reduction
N	Driven Sprocket	5,210	SAE 1045 Steel	.5	50	6 0	—	Ancillary Drive
O	Starter Pinion	6,825	SAE 8640 Steel	98	16	.44	20	Accessory Drive
P	Starter Idler Gear	4,748	Sintered Bronze	.70	23	.64	20	Accessory Drive
Q	Starter Gear	1,285	SAE 8640 Steel	.83	85	2.36	20	Accessory Drive

TABLE 12

Engine Power Summary at 80% Speed

Build Identif.	Horsepower	Pct. of Goal
3-1AL	29.15	60.0
2-3Q	31.87	65.6
3-9X	33.09	68.1
3-9Y	34.65	71.3
10-14M	40.58	83.5
3-13I	42.25	86.9
Goal	48.60	100.0

TABLE 13

Engine Component Characteristics

	Design Characterization			Engine Build 10-14M		
Gas Generator Speed, Design Speed Fraction	0.5	0.8	1.0	0.5	0.8	1.0
Output Power, hp	6.53	48.60	104.34	5.18	40.58	87.38
Specific Fuel Consumption, lb/hp-hr	.842	.463	.444	1.166	.559	.537
Compressor						
Air Flow, lb/sec.	.433	.900	1.335	.42	.86	1.302
Pressure Ratio	1.498	2.700	4.185	1.527	2.699	4.048
Efficiency	.769	.804	.785	.773	.774	.741
Compressor-Turbine Efficiency	.832	.843	.846	.74"	.800	.810
Power-Turbine Efficiency	.719	.755	.762	.680	.740	.740

TABLE 14

Breakdown of Estimated 80%-Speed Total-Total Efficiency Loss Between Engine and Rig Compressor Configurations

Loss Source	Points Lost
Reynolds No.	0.8 (Based on 1/5th Power Model)
Intake	0.4
Inducer-Impeller Gap	0.8
Totals	1.2 (Without Reynolds No. Loss)
	2.0 (With Reynolds No. Loss)

TABLE 15

Comparison of Compressor Efficiency With Original and Increased Collector Volumes

Gas Generator Speed, %	Efficiency	
	Original Collector Configuration	Enlarged Collector Configuration
	PP 3-1 AF Runs 317-321	PP 3-1 AH Runs 337-340
50	0.734	0.732
60	0.749	0.749
70	0.754	0.755
80	0.755	0.757
90	0.751	

TABLE 16

Comparison of Compressor Efficiency With and Without Deflectors in Collector

Gas Generator Speed, %	Efficiency	
	Original Collector Configuration	Deflectors Installed at Lobes
	PP 2-3H Runs 62-69	PP 2-3G Runs 54-59
50	0.749	0.747
60	0.755	0.760
70	0.775	0.771
80	0.771	0.775
90	0.764	0.768
95	0.759	0.761

TABLE 17

Deswirl Vane Design Parameters

1st Row [NACA 65-(18)06]		2nd Row [NACA 65-(12)06]	
Inlet Air Angle, Degrees	60.6	Inlet Air Angle, Degrees	24.6
Exit Air Angle, Degrees	24.6	Exit Air Angle, Degrees	0
Inlet Mach Number	0.34	Inlet Mach Number	0.18
Diffusion Factor	0.65	Exit Mach Number	0.09
Solidity	1.87	Diffusion Factor	0.67
Aspect Ratio	0.16	Solidity	1.30
		Aspect Ratio	0.24

N.B.: Velocities computed with assumed blockage of 21%

TABLE 18

Upgraded Engine Compressor-Turbine Parameter Comparisons at 80% Speed

Engine PP 2-3, Run 41

	$\frac{\Delta H}{\theta_5}$ (BTU/LB)	$\frac{P_5}{P_6}$	P_{T6} δ (Mean Radius) (PSIA)	P_{S6} δ (Tip) (PSIA)	P_{S55} δ (Tip) (PSIA)	P_{T5} δ (PSIA)	η
Off-Design Estimate	13.99	1.601	23.99	21.46	25.39	38.37	0.843
Test Data	15.625	1.762 (Mean Radius)	21.41	18.66	21.80	37.75	0.791 (Mean Radius)
Computer Match on P_{S6}, $\frac{\Delta H}{\theta_5}$, Flow	15.590	1.782	21.18	18.67	22.10	37.75	0.775

5 - Nozzle Inlet
55 - Rotor Inlet
6 - Rotor Exit

S - Static
T - Total

TABLE 19

Compressor-Turbine Efficiency Estimates at 80% Speed with Original Rotor and 3 Nozzle Configurations

Type of Calculation	Nozzle Configuration: Original	Mod 1	Mod 1 (Repeat)	Mod 2
Radial Equilibrium Calculation	0.763	0.754	0.760	
Mean-Radius Total Pressure	0.772	0.765	0.779	0.782
PP 2-3, Run No.	41	128	140	443

TABLE 20

Engine Performance Comparison Mod 3 CT vs Mod 2 Noz + 0.8X Scale Rotor

Compressor:	Plastic VIGV, 18/18 IMP., 28- chan. diff. with 40% incr. exit area, single-row deswirl vanes.	
Power Turbine:	Original design with 10° tip-bend and enlarged exhaust diffuser.	
Miscellaneous:	Modified regenerator cover, air pump on power turbine accessories.	
Results at 80% Speed		
Power Plant	PP 3-9Y	PP 10-12B
Run Number	251	15
Comp. Turb. Config.	Mod 2 Nozzle, 0.8 scale rotor	Mod 3 Design, 1.012 size nozzle
Horse Power	31.70 (34.65)	36.04 (38.94)
BSFC, Lbs/HP-HR	0.705 (0.674)	0.611 (0.588)
Sta. 2-5 Leakage, %	2.06	3.41
Comp. Flow, Lbs/Sec.	0.911	0.911
Comp./CT Pr. Ratios	2.657/1.686	2.648/1.682
$\eta ct/\eta pt$	0.787/0.575	0.779/0.664
Air Injection Test Results		
Run Number	267	17
Air inj., Lbs./HR	400	300
HP	41.97 (46.17)	44.78 (47.24)
BSFC, Lbs/HP-HR	0.568 (0.541)	0.526 (0.512)
Leakage, %	-13.82	-4.57
Comp. Flow, Lbs/sec.	0.816	0.858
Comp./CT Pr. Ratios	2.766/1.585	2.745/1.617
$\eta ct/\eta pt$	0.783/0.558	0.779/0.652

TABLE 21

Comparison of Duct Recoveries with Program Goals

	Nozzle Position (Degrees)	Cp Interstage	Cp Exhaust Diffuser
	28	.53	.39
	34	.48	.47
Goal	32	.58	.47

TABLE 22

Up ,raded Engine Power Turbine

Design Mass Averaged Pitch Line Data

Gasifier speed	%	50	80	100
Mass Flow	lb/s	.409	.863	1.318
	kg/s	.1855	.392	.598
Temperature	R	1888.6	1993.1	2055.0
	K	1049.2	1107.3	1141.7
Pressure	psia	17.27	23.39	28.45
	k Pa	119.1	161.3	196.2
Meridional Velocity	ft/s	148	250.4	328.1
	m/s	45.1	76.32	100.0
Swirl Angle	o	-34.0	-39.9	-47.8
Expansion Ratio		1.15	1.494	1.71

Power Turbine Aerodynamic Coefficients at Design Point

Stage Loading	(Mean)			1.16
Flow Coefficient	(Mean)			.398
Specific Work	(Mean)		J/kgK.	125.7
Reaction Δt Rotor	Hub			.615
ΔT Stage	Mean			.630
	Tip			.800
Absolute Gas Angle	Stator Out			71.6
	Rotor Out			70.0
Blade Speed	(Mean)		m/s	346.1
Outlet Abs. Velocity Head		$\frac{(P-p)}{P}$	%	4.5
Throat Reynolds Number	(Mean)		Stator	18,240
(Hydraulic Mean Dia.)			Rotor	13,100

TABLE 23

Upgraded Engine Power Turbine Blading Details

Section	Units	Symbol	Nozzle			Rotor		
			Hub	Mean	Tip	Hub	Mean	Tip
Section Radius	m	r	.0608	.0721	.0834	.0608	.0721	.0834
No. of Vanes/Blades		n		23			47	
Blade Pitch	m	s	.0166	.0197	.0228	.00813	.009645	.0111
Blade Chord	m	c	.0193	.0229	.0265	.0113	.0121	.0146
Maximum Thickness	m	t	.00332	.00394	.00456	.00343	.00288	.00068
s/c	-		.859	.859	.859	.72	.800	.76
t/c	-		.172	.172	.172	.304	.238	.0466
Leading Edge Radius	m		.000691	.000800	.000902	.0005	.0005	.00019
Trailing Edge Radius	m		.000116	.000134	.000151	.00023	.00023	.00023
Trailing Edge Thickness	m	te	.000232	.000268	.000302	.00046	.00046	.00046
te/s	-		.0140	.0136	.0133	.0407	.0380	.0315
Throat Opening	m	Ot	.00527	.00625	.00723	.00307	.00322	.00357
Aspect Ratio (Blade Height)		h/Ot		3.76			7.00	
L.E. Included Angle	o		60	60	60	62	72	19
T.E. Included Angle	o		8	8	8	11.5	10.5	1.0
Inlet Angle	o			-12			-10	
Hub/Tip Ratio	-		.729	.865	1.00	.729	.865	1.00
Blade Back Turning	o		5.0	5.0	5.0	16.5	18.5	13.0
Blade Back Radius	m	e	.0650	.0768	.0888	.022	.0260	.060
s/e	-		.2565	.2565	.2565	.369	.415	.185
Axial Chord	m	Cax	.00832	.00987	.0114	.00973	.00920	.00797

TABLE 24

Upgraded Engine Emissions

(Raw-Not Corrected For Inlet)

%Ngg	PPM			ΔP/P, %
	HC_6	CO	NOx	
50	0.8	202	4.2	3.2
60	0.3	31	3.5	3.2
70	0.2	12	3.0	3.15
80	0.2	12	2.8	3.1
90	0.2	12	4.0	3.0
95	0.2	12	5.5	2.9
100	0.2	12	9.0	2.8
Inlet Conditions	1.30	15	0.6	

TABLE 25

Summary Fuel Economy

Vehicle U2-Test Inertia-3500 lbs. 11.2 Hp (No Air Conditioning) - Fuel: Gasoline

Date	Test Schedule	Test Cycle	Comp. Inlet T.	Fuel Lbs. (3900A)	Cycle Mpg.
10/27/78	Heater Disconnected Tires F78 x 14 Bias Belted (G.Y.)	Hot 7? (1371 Sec.)	87	3.95	11.80
10/27/78	Heater Disconnected Tires F78 x 14 Bias Belted (G.Y.)	FEC	87	3.15	20.32
10/31/78	VIGV Reprogrammed to Pedal Position (+60° Closed Throttle)	Hot 74	86	3..	.?.95
10/31/78	VIGV Reprogrammed to Pedal Position (+60° Closed Throttle)	Hot 74	89	3.75	12.43
10/31/78	Same as Above-Change Driver	Hot 74	89	3.70	12.61
11/01/78	By-Pass Blow-By to Atmosphere	Cold 75	67 Initially		
		At 505 Sec.	79	2.45	9.13
		At 1371 Sec.	89	4.70	9.92
		At 505 Sec. Hot	84	1.65	12.43
11/01/78	By-Pass Blow-By to Atmosphere	FEC	84	3.10	20.53
			85	2.90	21.97
			85	3.05	21.95
11/02/78	By-Pass Blow-By to Atmosphere	Cold 75	64		
		At 505 Sec.	78	2.4	9.32
		At 1371 Sec.	77	4.6	10.13
		At 505 Sec. Hot	79	1.6	13.56
11/02/78	Increase T_s Ref. for Part Throttle Operation	Hot 74	89 Initially		
		At 505 Sec.	84	1.55	14.43
		At 1371 Sec.	84	3.55	13.13
11/02/78	Reset T_s Ref. Back to Original Setting	Hot 74	88 Initially		
		At 505 Sec.	89	1.55	14.33
		At 1371 Sec.	88	3.60	12.95
11/08/78	Increased Braking Stroke	Hot 74			
		At 505 Sec.	78	1.7	12.80
		At 1371 Sec.	80	3.55	13.13
		At 505 Sec.	80	1.37	15.88
		At 1371 Sec.	80	3.40	13.71
11/08/78	Change Tires-FR 78/14	Hot 74			
		At 505 Sec.	80	1.59	13.68
		At 1371 Sec.	84	3.71	12.56
		FEC	83	3.07	20.73
		Hot 74			
		At 1371 Sec.	83	3.60	12.95

TABLE 25 (cont.) **Vehicle U2-Test Inertia-3500 lbs. 11.2 Hp (No Air Conditioning) - Fuel: Gasoline**

Summary Fuel Economy

Date	Test Schedule	Test Cycle	Comp. Inlet T.	Fuel Lbs. (3900A)	Cycle Mpg.
11/09/78	Re-install Original Tires F78/14	Hot 74			
		At 505 Sec.	79	1.55	14.03
		At 1371 Sec.	92	3.60	12.95
		FEC	91	3.00	21.21
	Eliminate Braking This data used to compute combined fuel economy	Hot 74			
		At 505 Sec.	92	1.45	15.00
		At 1371 Sec.	94	3.55	13.13
		FEC	83	2.95	21.57
		Hot 74			
		At 505 Sec.	83	1.50	14.50
		At 1371 Sec.	—	3.60	12.95
11/10/78	Active Braking Back In ViGV's Lock at 0°	Hot 74			
		At 505 Sec.	79	1.60	13.60
		At 1371 Sec.	83	3.65	12.77
		FEC	84	3.05	20.87
11/10/78	VIGV's Active— Reshimmed for +50° at Closed Throttle, —10° at Open Throttle	Hot 74			
		At 505 Sec.	91	1.60	13.60
		At 1371 Sec.	—	3.63	12.84
	By-Pass Filters Remove Covers	Hot 74			
		At 505 Sec.	97	1.55	14.03
		At 1371 Sec.	—	3.65	12.77
		FEC	92	3.00	21.21

NOTE: Rear Axle Ratio 2.94 Hi-stall Lock-Up Converter

TABLE 26

Steady State Chassis Rolls Emission Vehicle U-2 Fuel/Gasoline

Pre-Mix/Pre-Vaporized Combustor							Droplet-Diffusion Combustor					
T_1 °F	T_2 °F	% Speed	HC Ppm	NOx Ppm	CO Ppm	Car Speed	CO Ppm	NOx Ppm	HC Ppm	% Speed	T_2 °F	T_1 °F
76	—	45	2.5	2.0	166	Idle Park	—	—	—	—	—	—
76	—	50	4.5	1.0	170	Idle Drive	3[illegible]	13	4.5	50	1288	86
78	1350	54.8	16.0	Indi-cation	283	20	20	14	4.5	54	1361	84
77	1348	58	3.0	0.4	51	30	15	15.5	4.5	58	1366	85
77	1369	63.5	2.0	0.4	42	40	13	20	4.5	65	1378	85
76	1386	70	2.5	0.8	22	50	7	3	4.5	70	1388	86

TABLE 27

Engine Status and Retrofit Schedule

Engine No.	Retrofit I.D.	Power Turb. MOD	Status
1	R1	1	Chrysler Test Cell
2	R4	2	Vehicle U 1
3	R5	2	NASA Test Cell
4		Orig.	NASA Test Cell
5		Orig.	Vehicle U 3 (Display/Demo)
6	R2	2	Venicle U 2
7	R3	1	NASA Test Cell

Upgraded Engine Powertrain Views

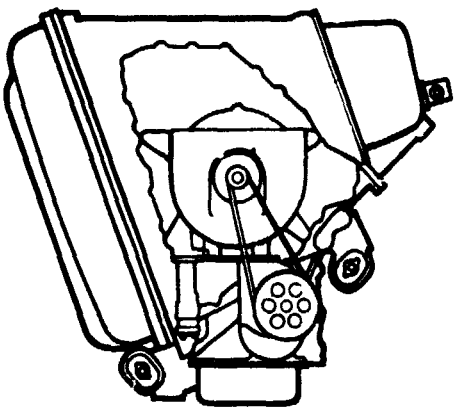

Figure 1A
Front View

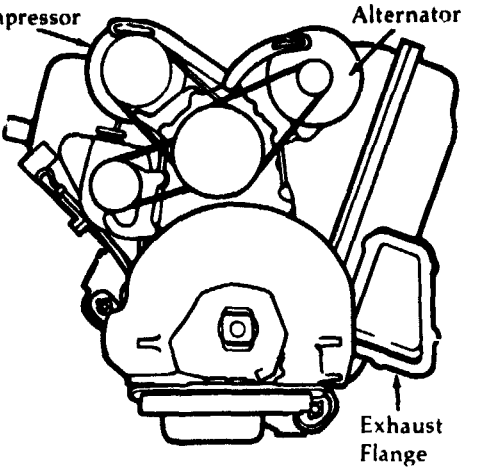

Figure 1B
Rear View

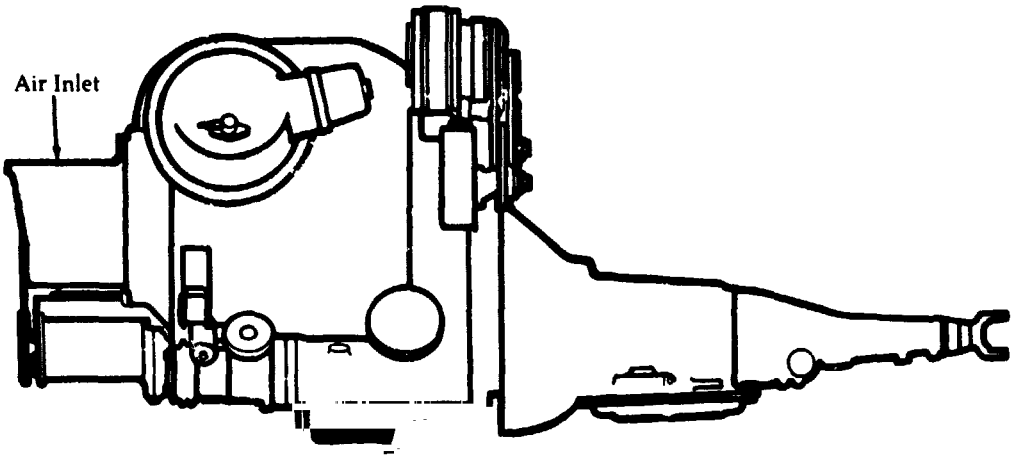

Figure 1C
Left Side View

Upgraded Engine Power train Views

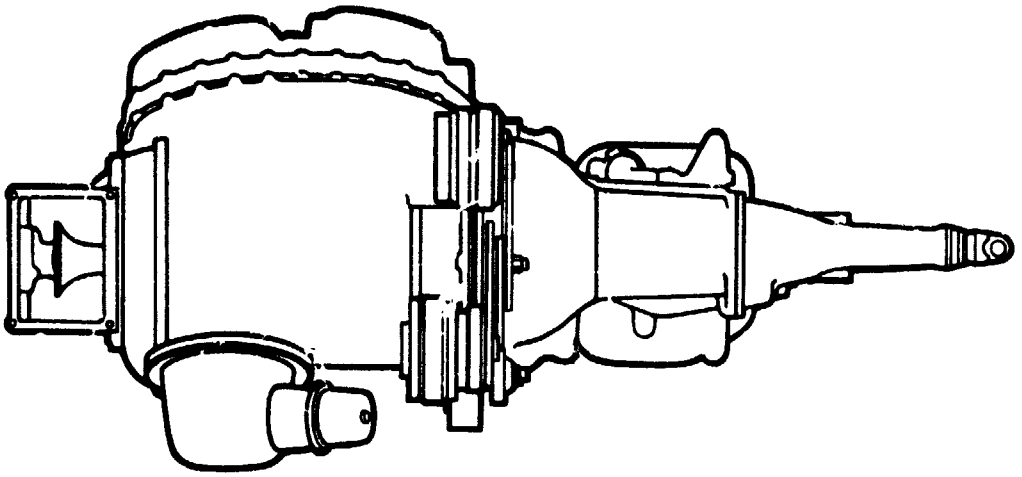

Figure 1D
Top View

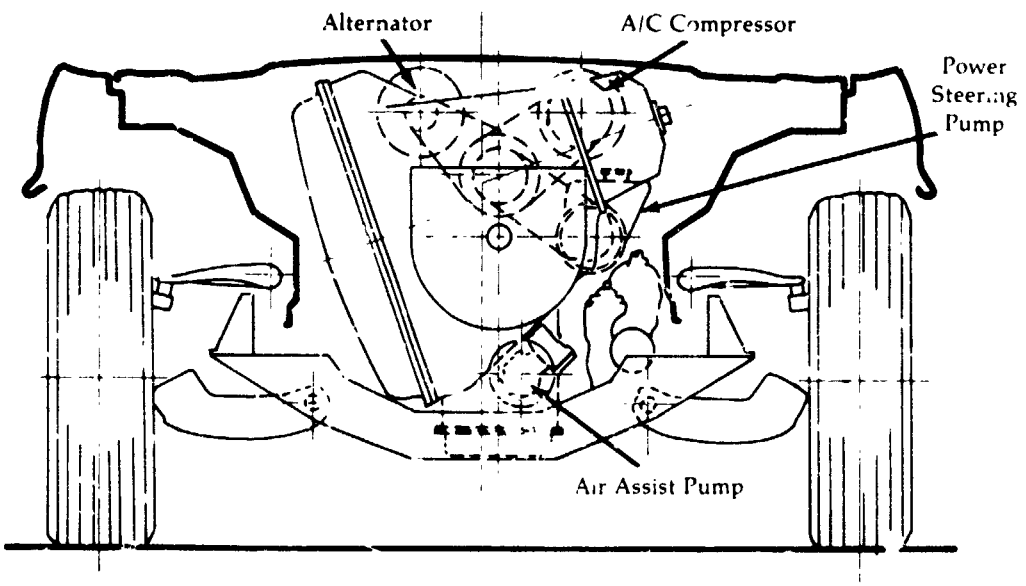

Figure 1E
Upgraded Engine Installation

Figures 1D and 1E

Gas Generator
Oil Drain

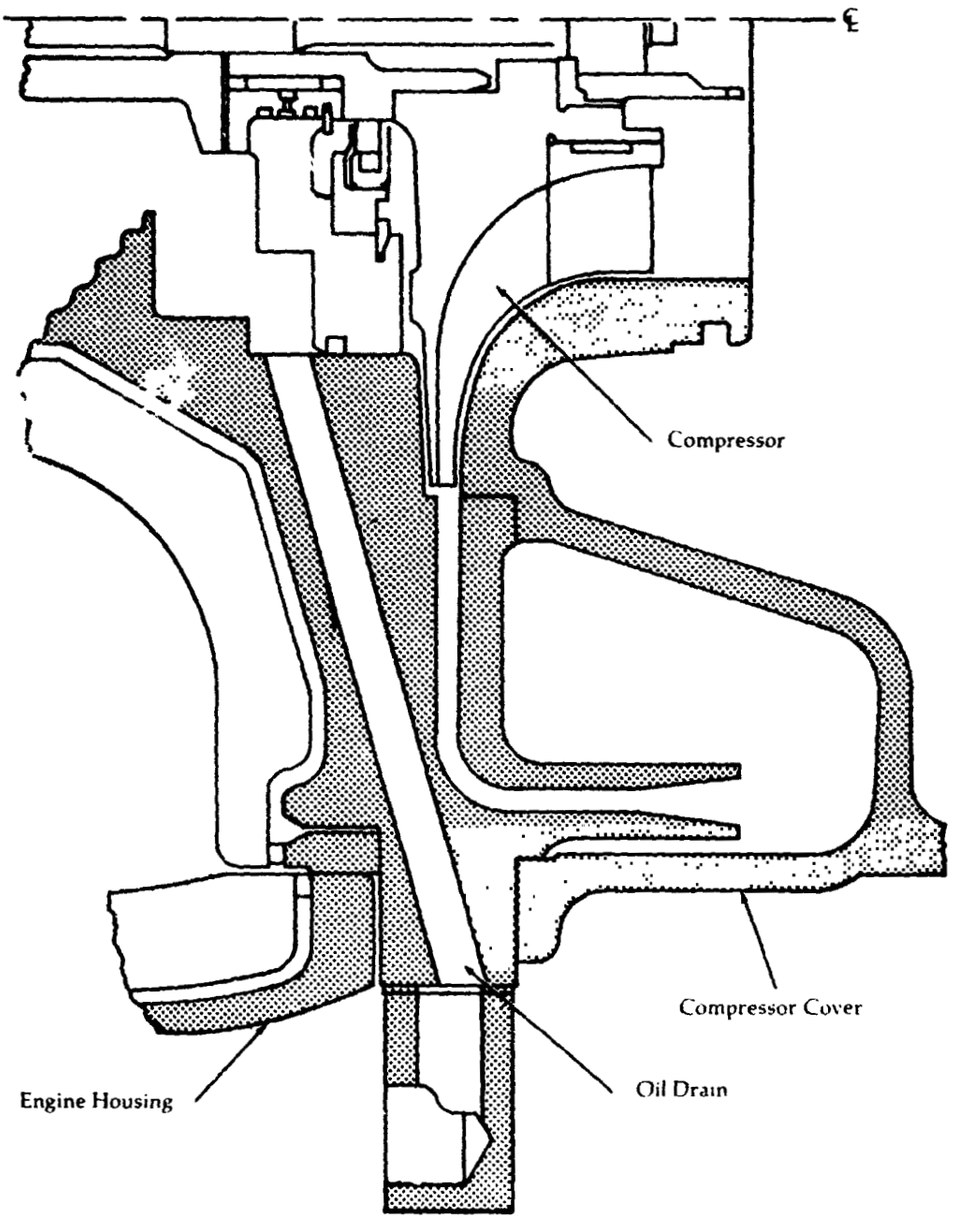

Figure 2

Cross-Section of Upgraded Engine as Originally Designed

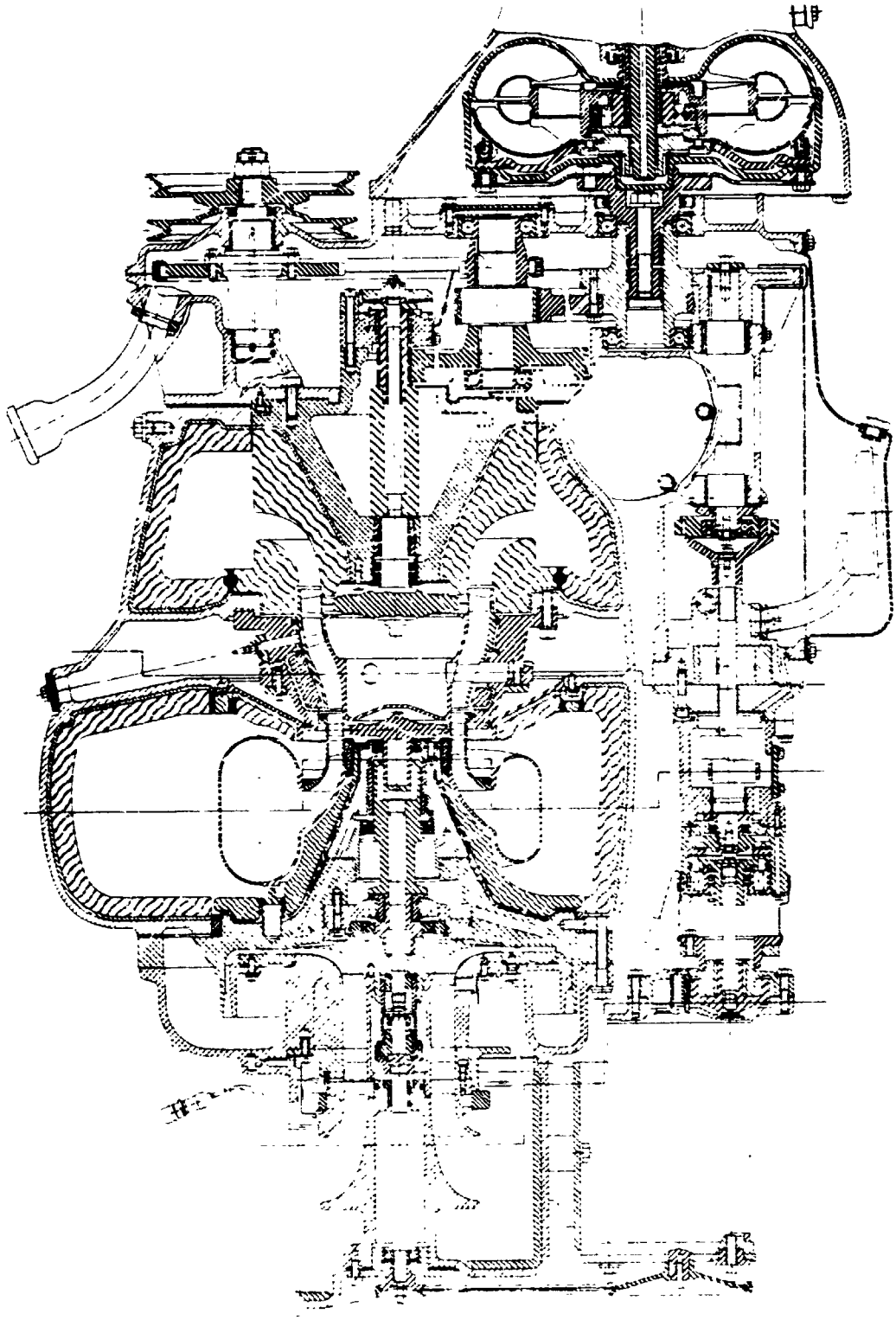

Figure 3A

Upgraded Engine Modular Division of Engine Design

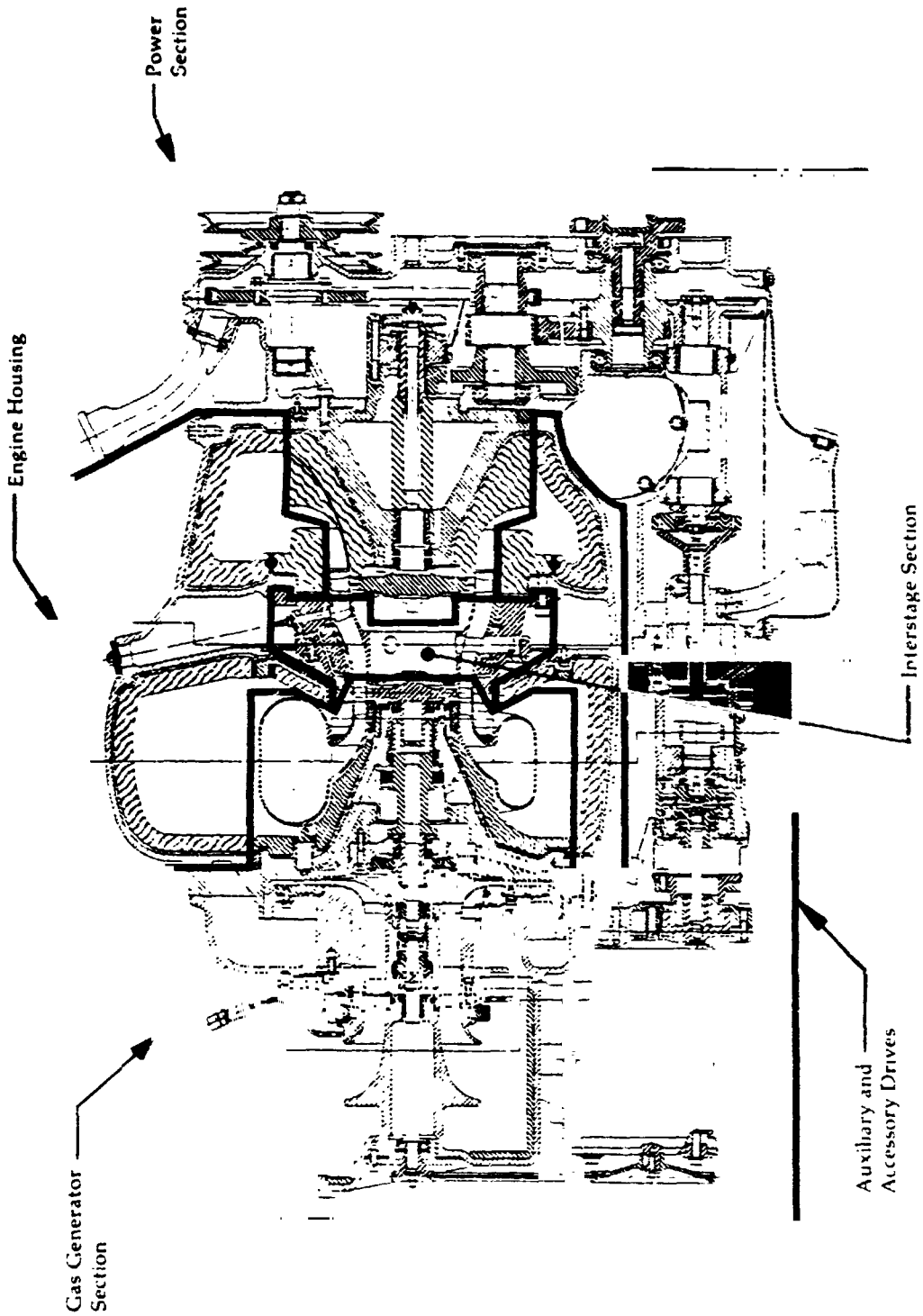

Figure 3B

Upgraded Engine

Flowpath of Original Compressor Design-taken from NASA TM X-71719

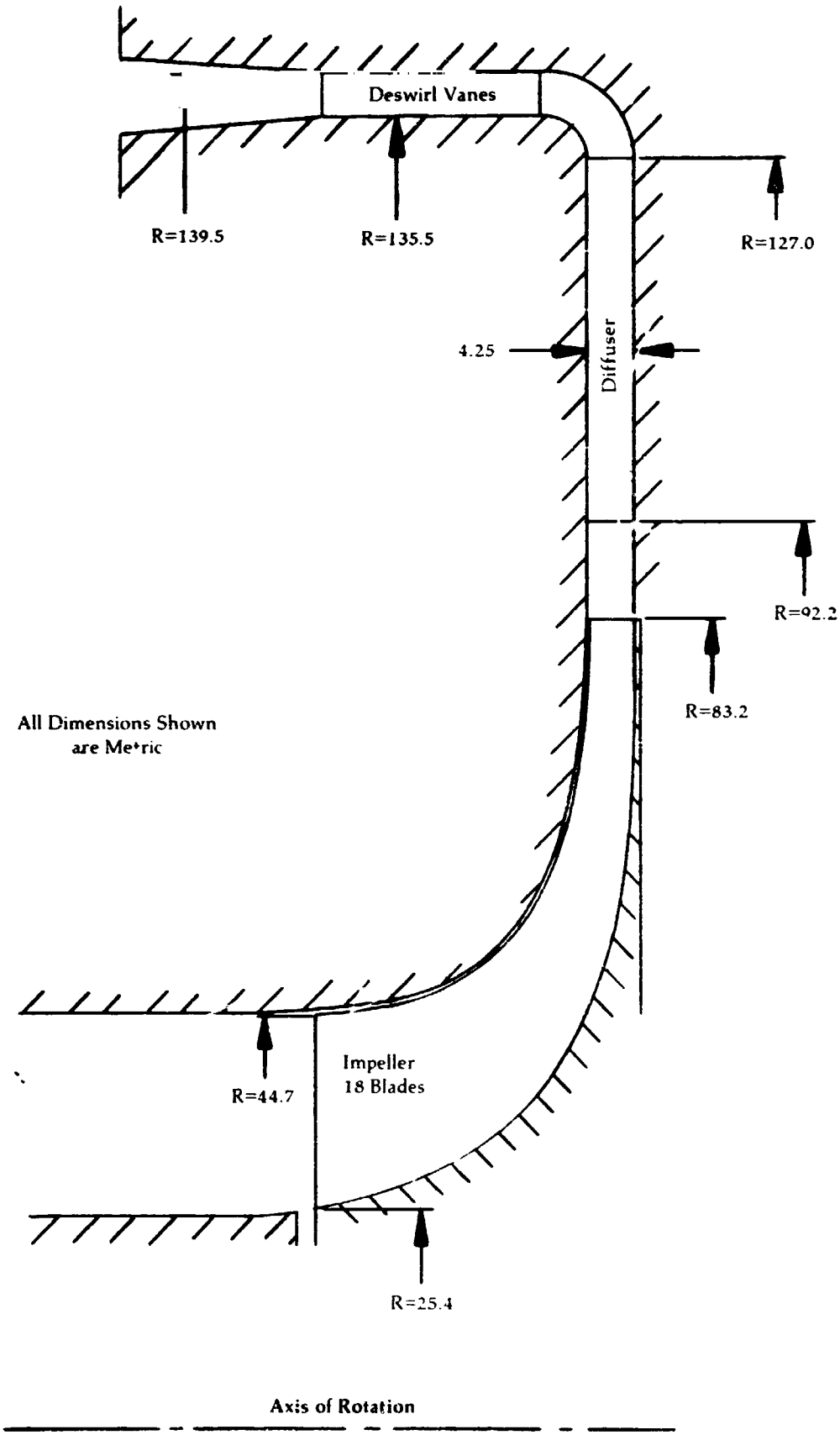

Figure 4

Upgraded Engine

Design Point Velocity Diagrams

Impeller Velocity Diagrams

Inlet

p^1=Total Pressure
T^1=Total Temperature
U, V, W=Velocities In m/s
Taken From NASA TM X-71719

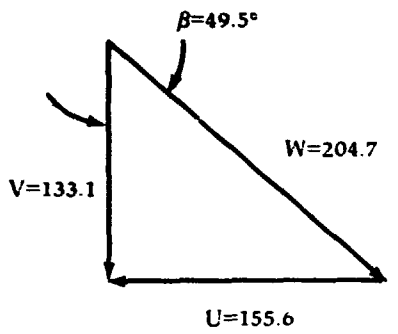

Hub

p^1=9.98 N/cm²
T^1=302.8°K

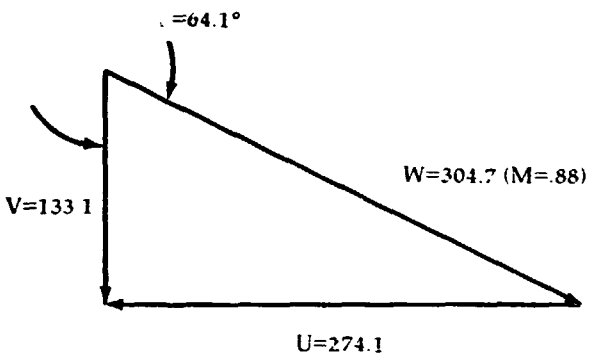

Tip

Exit Mean

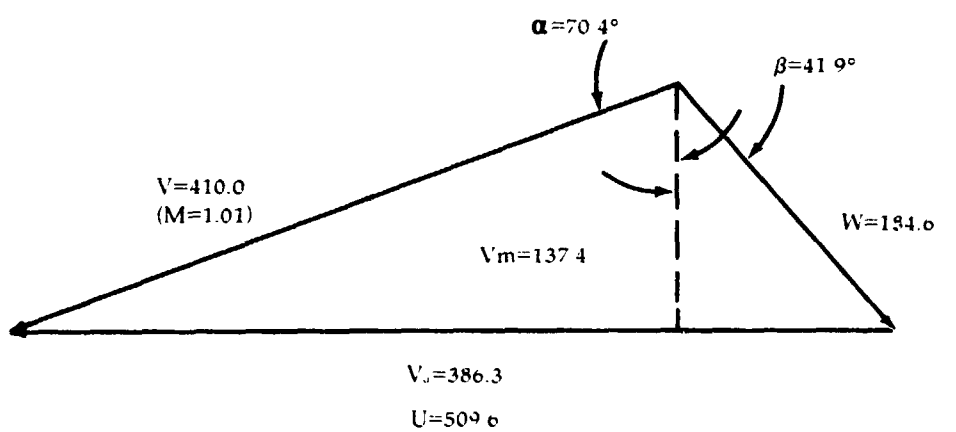

p^1=46 5 N/cm²
T^1=492°K

Figure 5A

Upgraded Engine
Design Point
Velocity Diagrams
(concl'd)

Diffuser Velocity Diagrams

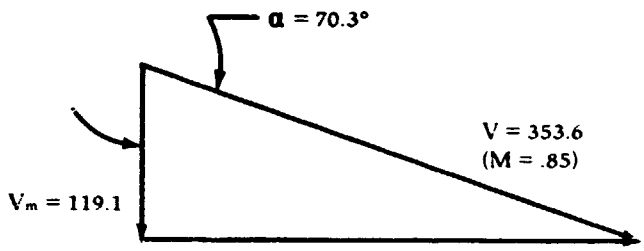

Inlet

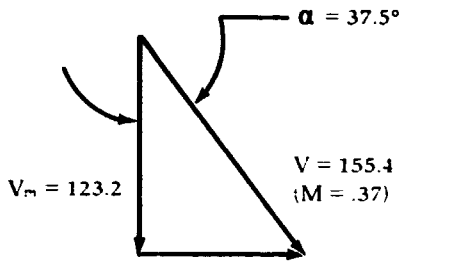

Exit (Inside Channel)

Turning Duct Velocity Diagrams Mean Streamline

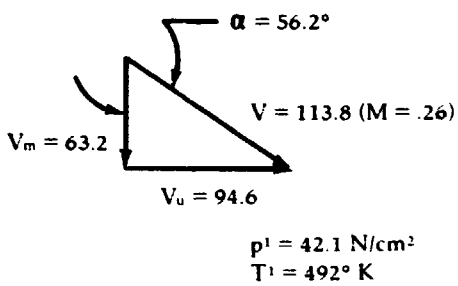

Inlet

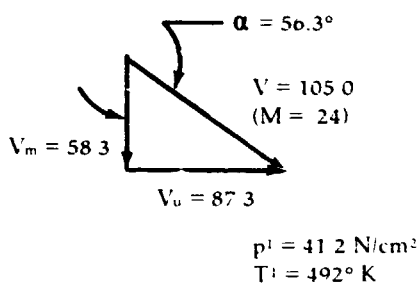

Exit

Desw irl Vane Velocity Diagrams Mean Streamline

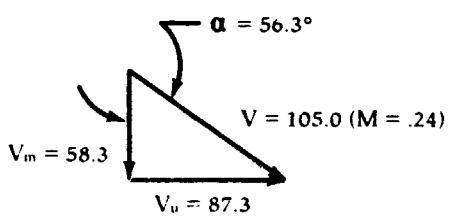

Inlet

α = 0°

V = Vm = 57 88
(M = .13)

p¹ = 41 0 N/cm²
T¹ = 492° K

Exit

Figure 5B

Upgraded Engine Compressor Rotor Blade Loadings

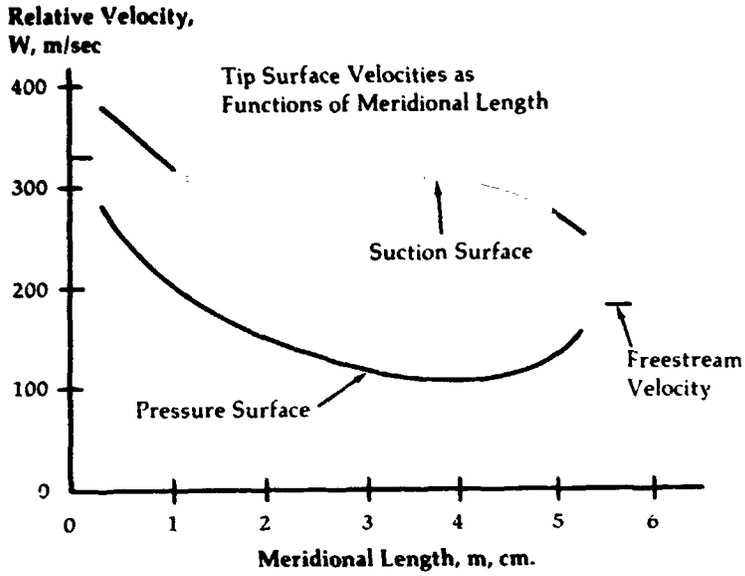

Taken from:
NASA TM X-71719

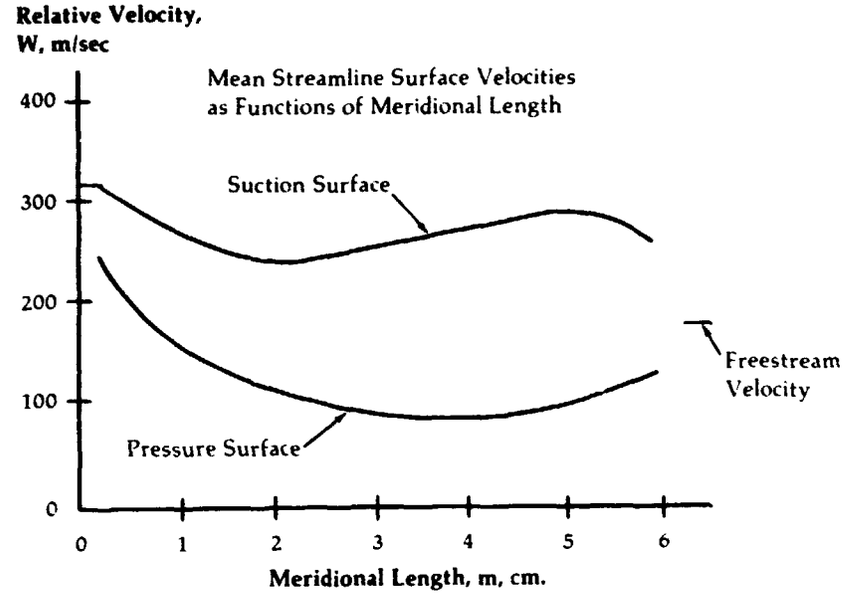

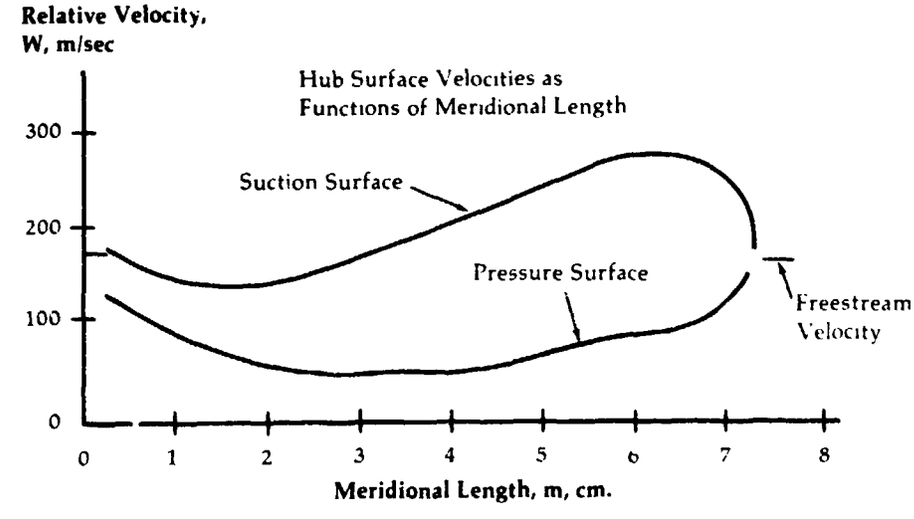

Figure 6

Upgraded Engine

Original Compressor Channel Diffuser Geometry

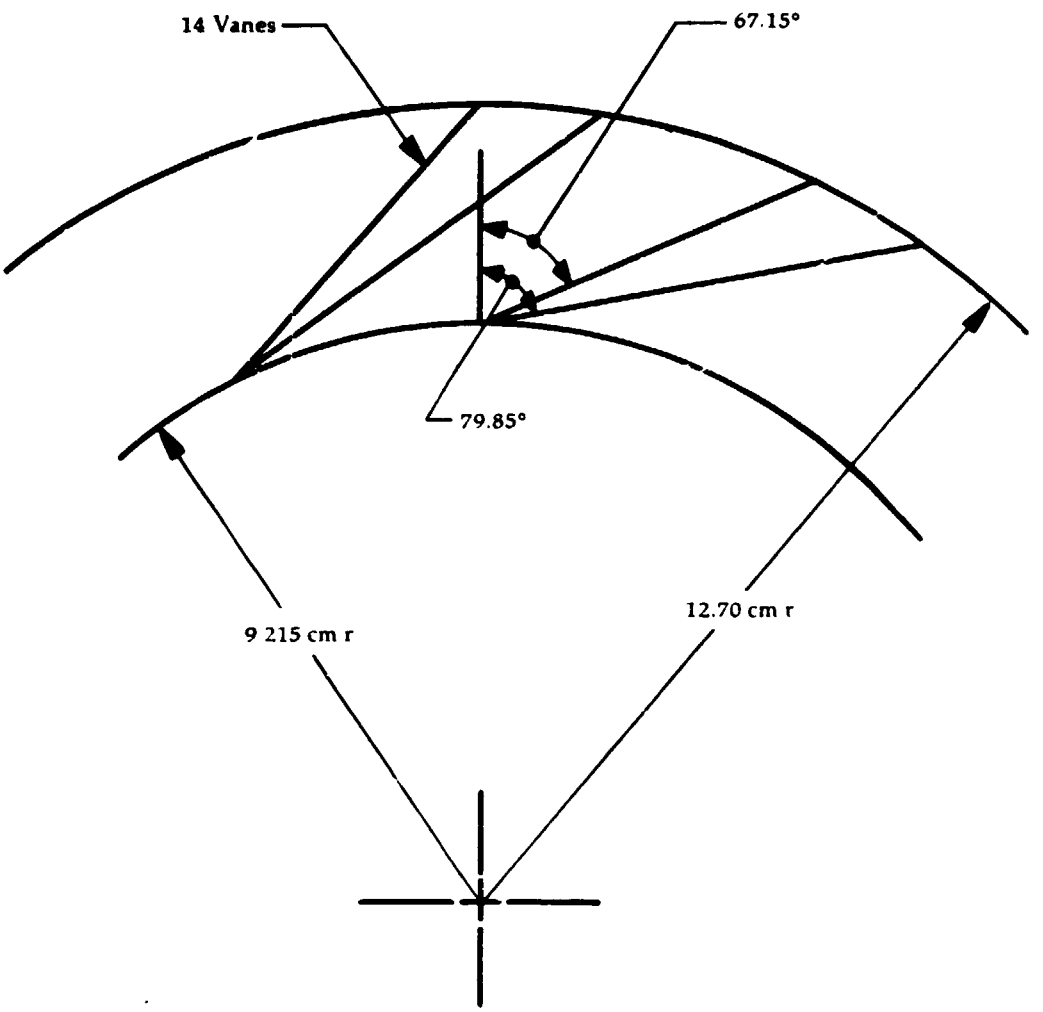

Figure 7

Upgraded Engine

Compressor Deswirl Vane Geometry and Aerodynamic Loading

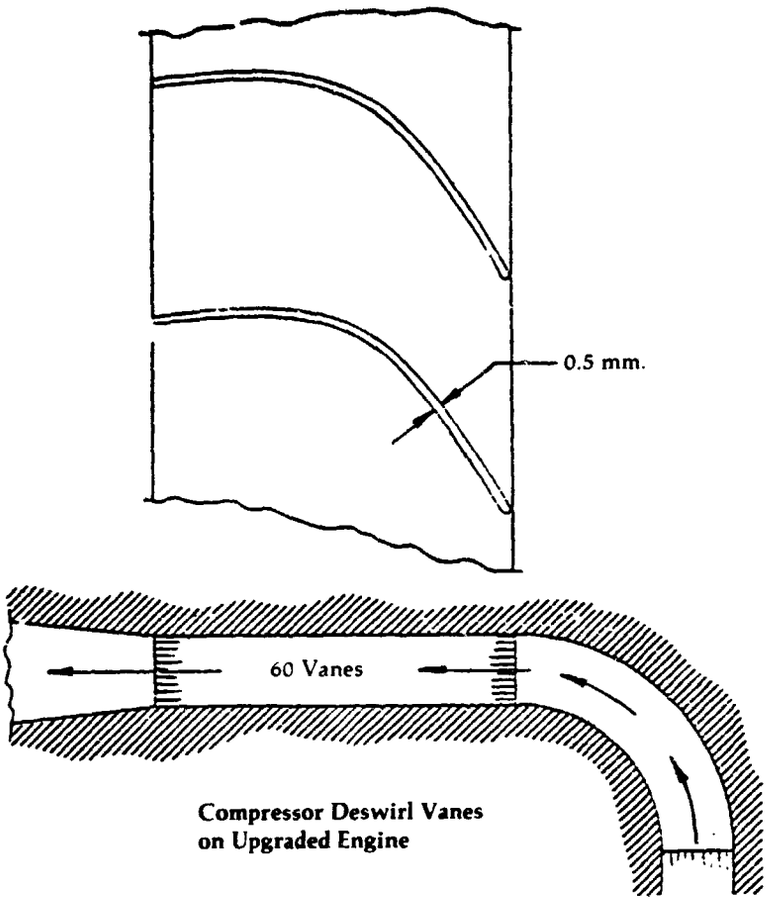

Compressor Deswirl Vanes on Upgraded Engine

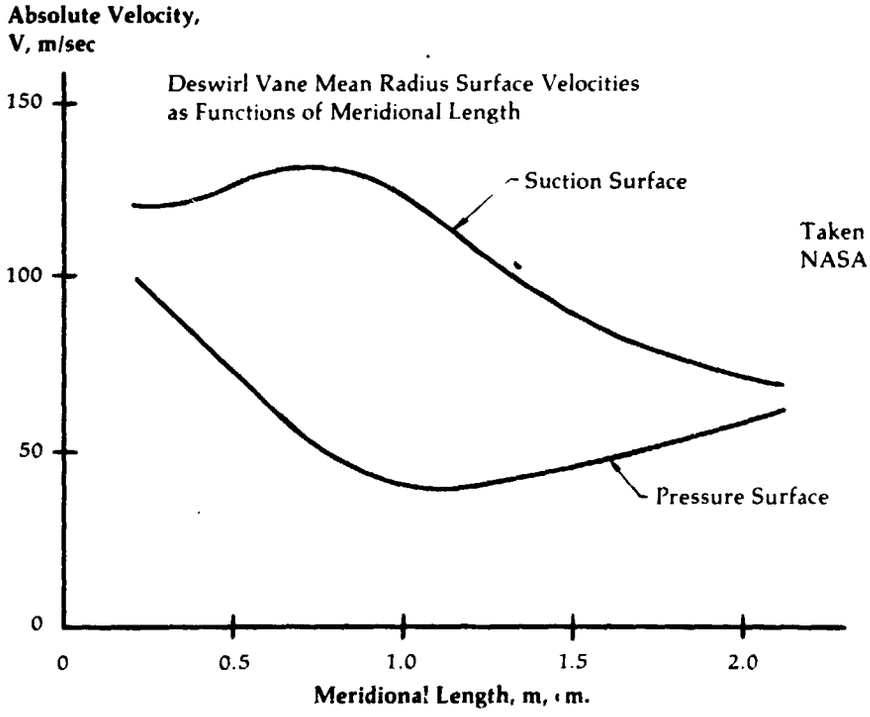

Taken from:
NASA TM X-71719

Figure 8

Upgraded Engine Compressor Collector Configuration

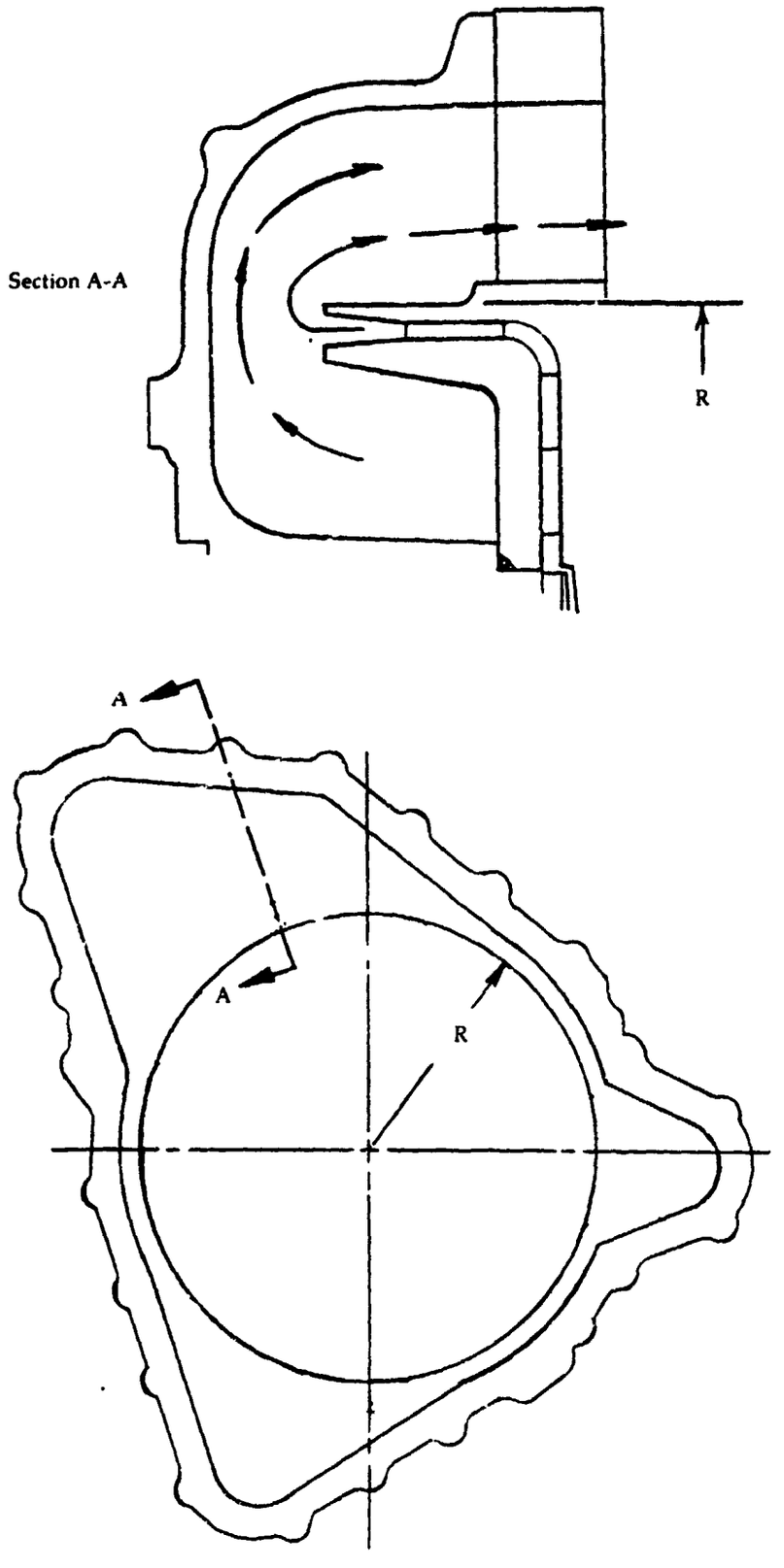

Front View with Compressor Cover Removed

Figure 9

Upgraded Engine Aerodynamic Analysis of Engine Air Intake System

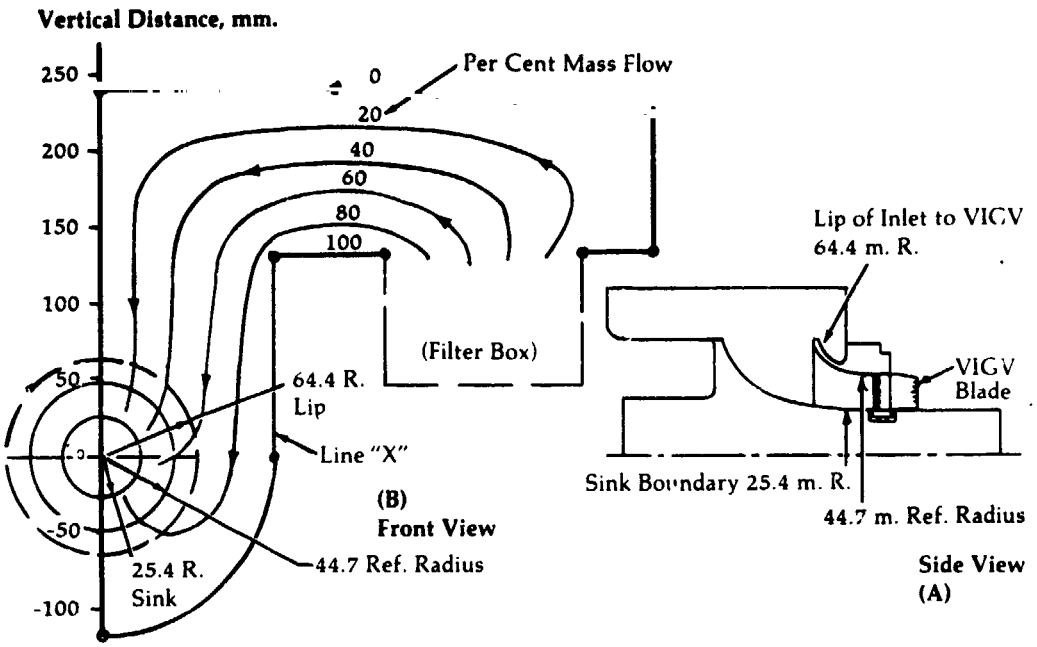

Calculated Streamline Pattern for Original Upgraded Engine Intake Design

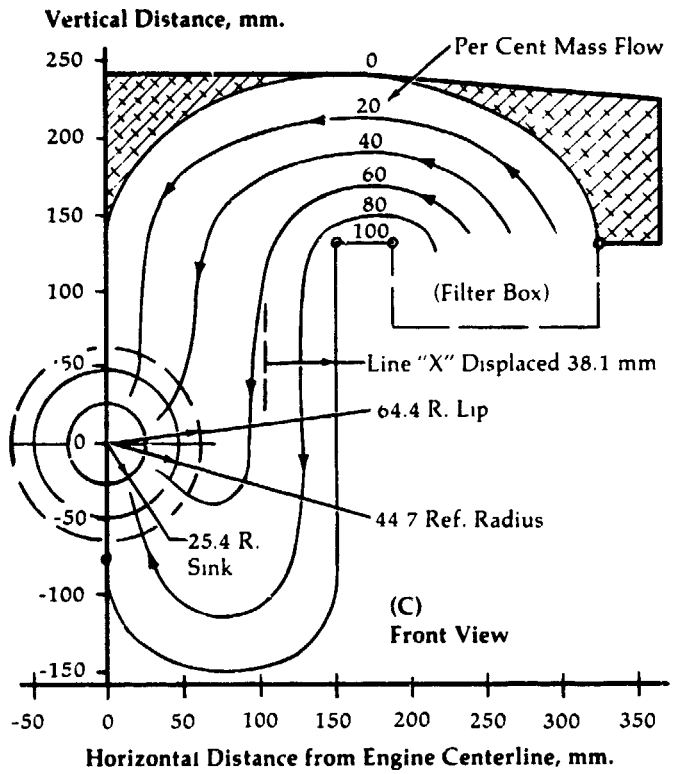

Calculated Streamline Pattern for Improved Upgraded Engine Intake Design

Figure 10

Upgraded Engine
VIGV Inlet

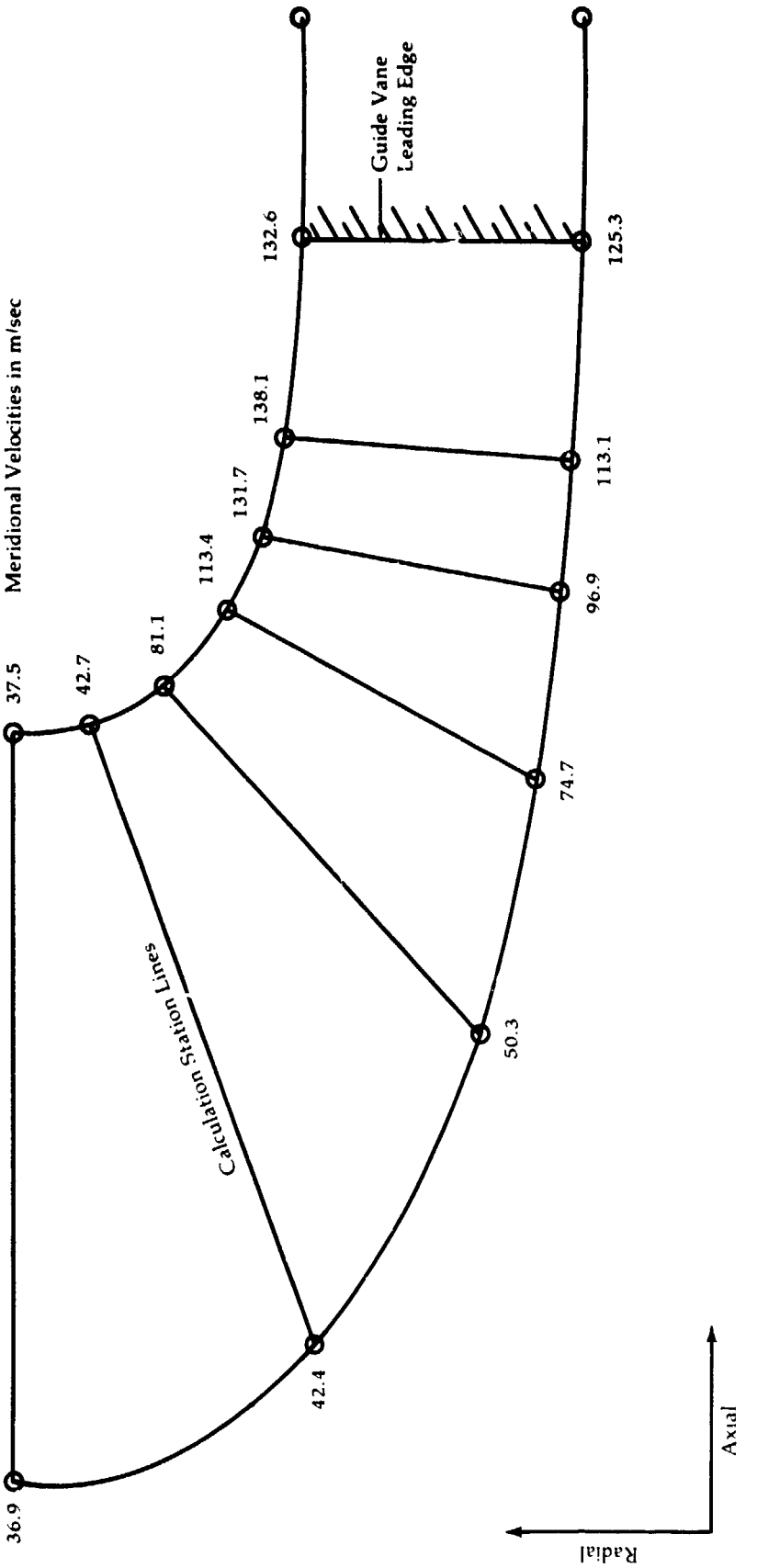

Final Design - Meridional View
(R_{tip} = 64.4 mm)

Figure 11

Upgraded Engine Air Inlet Configuration, Variable Inlet Guide Vane Assembly and Compressor Flowpath

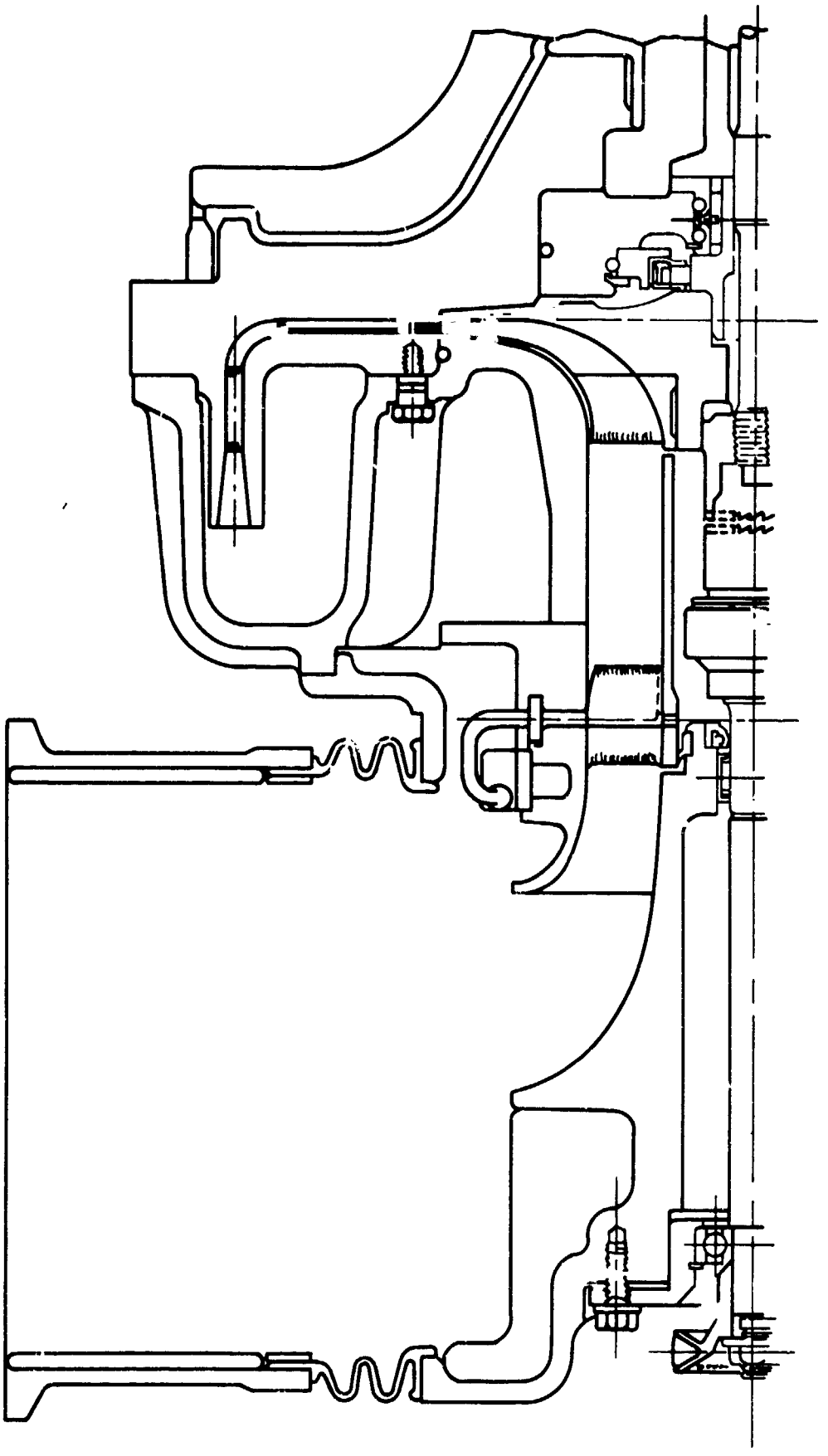

Figure 12

Upgraded Engine Compressor Performance Estimate

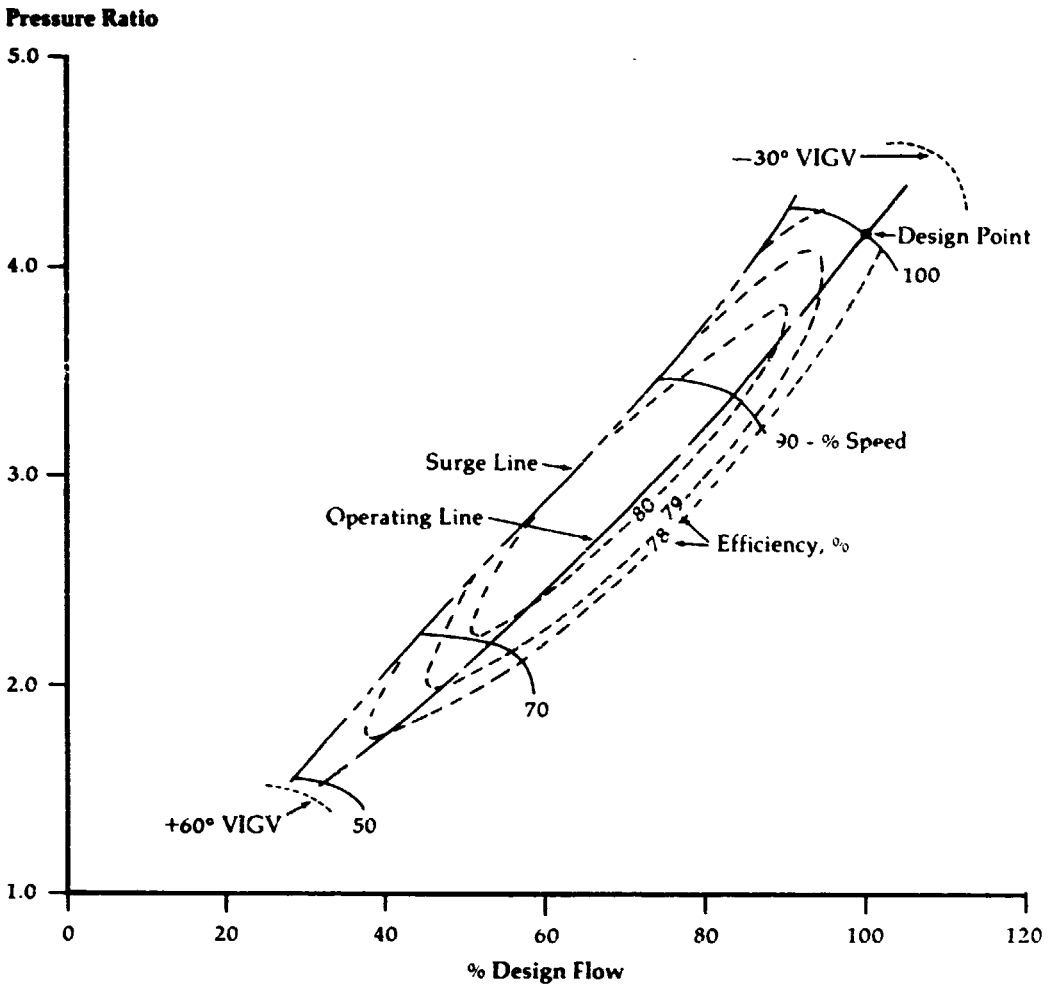

Figure 13

Upgraded Engine Water Injection and Overspeed Compressor Performance Estimate

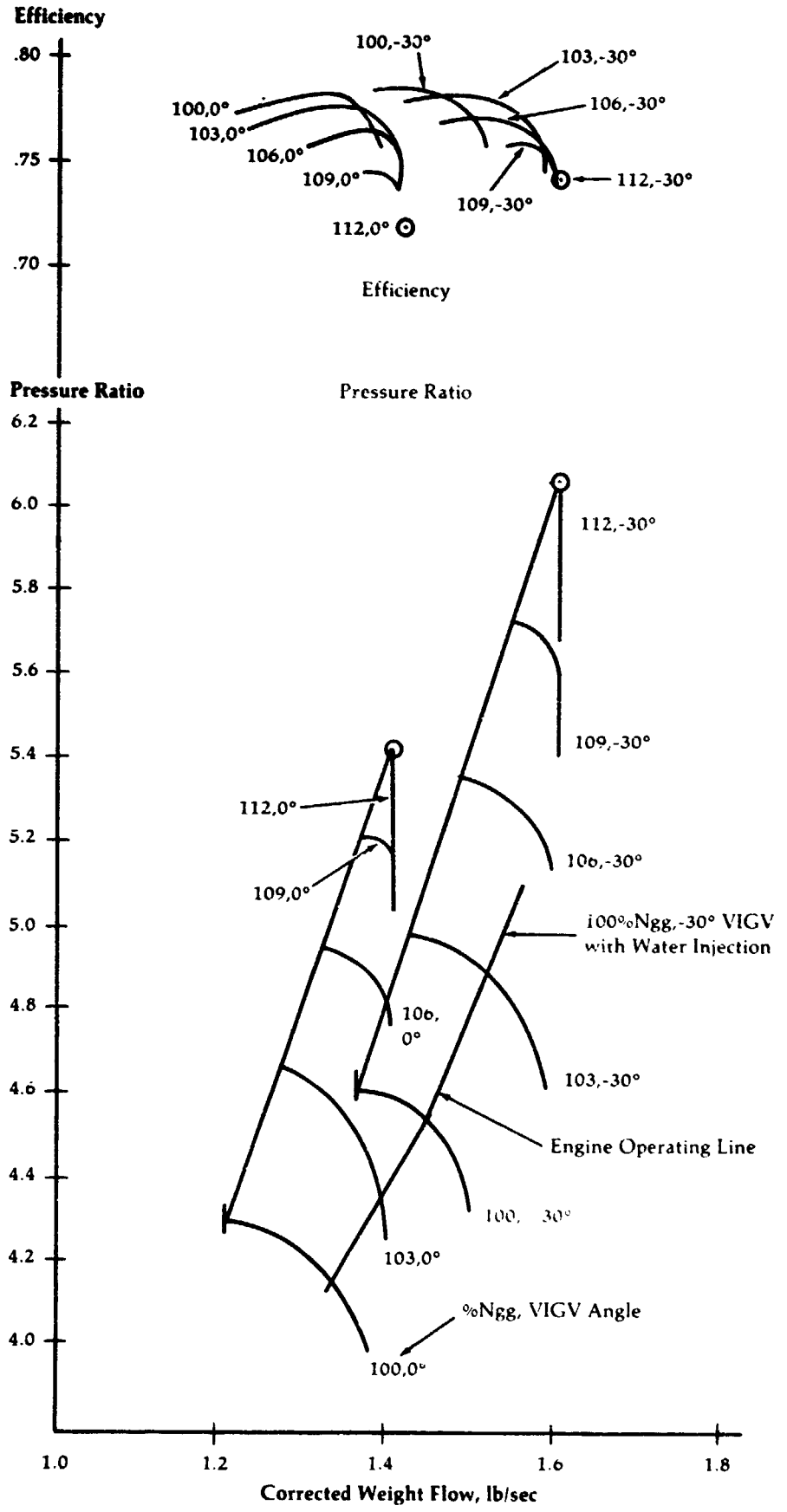

Figure 14

Upgraded Engine Impeller Structural Summary - Steady State

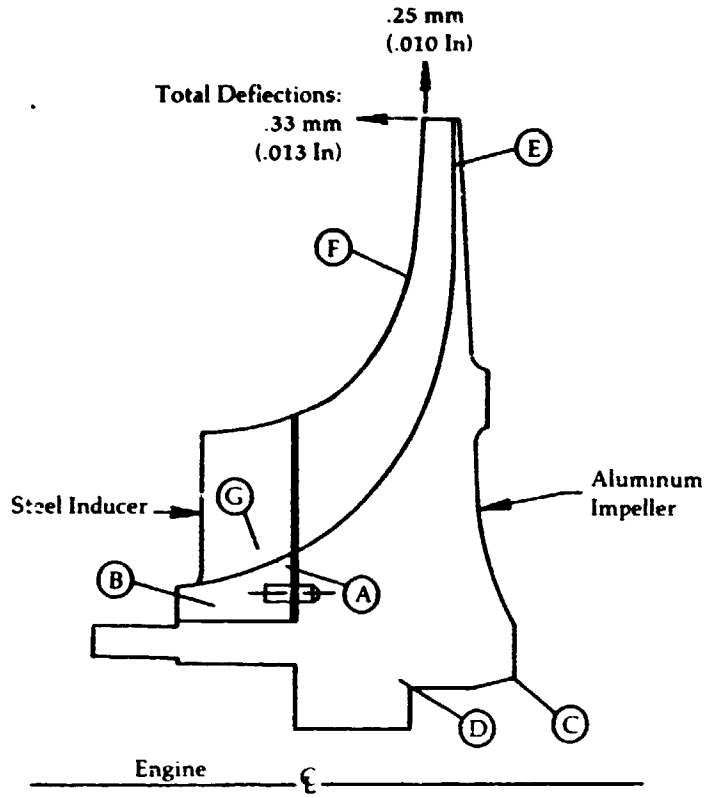

Inducer:

Material - 17-4 PH Steel
Mechanical Speed - 6126 rad/sec (58,500 RPM)
Ave. Tangential Stress - 306 MPa (44.4 KSI)
Burst Margin - 1.59
Burst Speed - 9739 rad/sec (93,000 RPM)

Impeller:

Material - 2618-T61 Aluminum
Mechanical Speed - 6126 rad/sec (58,500 RPM)
Ave. Tangential Stress - 105.5 MPa (15.3 KSI)
Burst Margin - 1.53
Burst Speed - 9372 rad/sec (89,500 RPM)

Location	Estimated Temp °C (°F)	*Minimum Materials Properties-MPa (KSI)		Maximum Applied Disc Stress - MPa (KSI)			Maximum Applied Blade Stress - MPa (KSI)		
		.2% Yield	Ultimate	Radial	Tangential	Equivalent	Min. Principal	Max. Principal	Equivalent
A	66 (150)	875.5 (127 0)	1027.2 (149.0)	24.8 (3.6)	405.4 (58.8)	389 4 (5o.5)			
B	52 (125)	881.0 (127.8)	1034.1 (150.0)	44.8 (6.5)	304.0 (44.1)	288.9 (41.9)			
C	116 (240)	281.3 (40.8)	351.6 (51.0)	28.3 (4.1)	231.6 (33.6)	223 4 (32.4)			
D	93 (200)	293.0 (42.5)	364 7 (52 9)	171.0 (24.8)	193 0 (28.0)	125 5 (18 2)			
E	182 (360)	234.4 (34.0)	281.3 (40.8)				95 8 (13.9)	205 4 (29 8)	99.3 (14.4)
F	132 (270)	252.3 (36.6)	346.1 (50.2)				30 3 (4.4)	171.7 (24 9)	125.5 (18.2)
G	66 (150)	875.5 (127.0)	1027.2 (149.0)				139.0 (20.2)	423 3 (61 4)	363.3 (52.7)

*Minimum Properties = 85% Typical Properties

Figure 15

Upgraded Engine Inducer Blade Interference Diagram

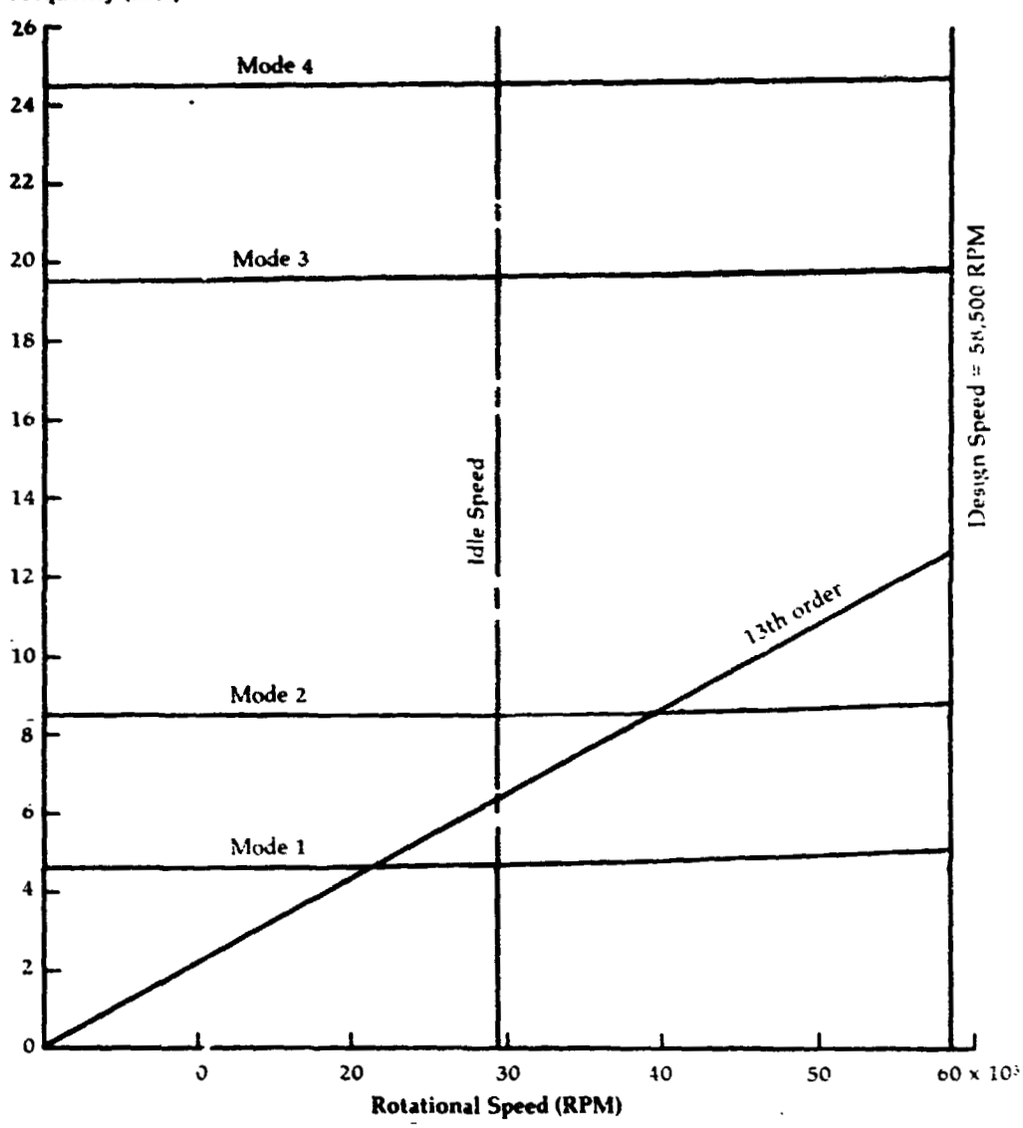

Figure 16

Upgraded Engine
Modified Goodman Diagram
Inducer Blade
Fatigue Analysis

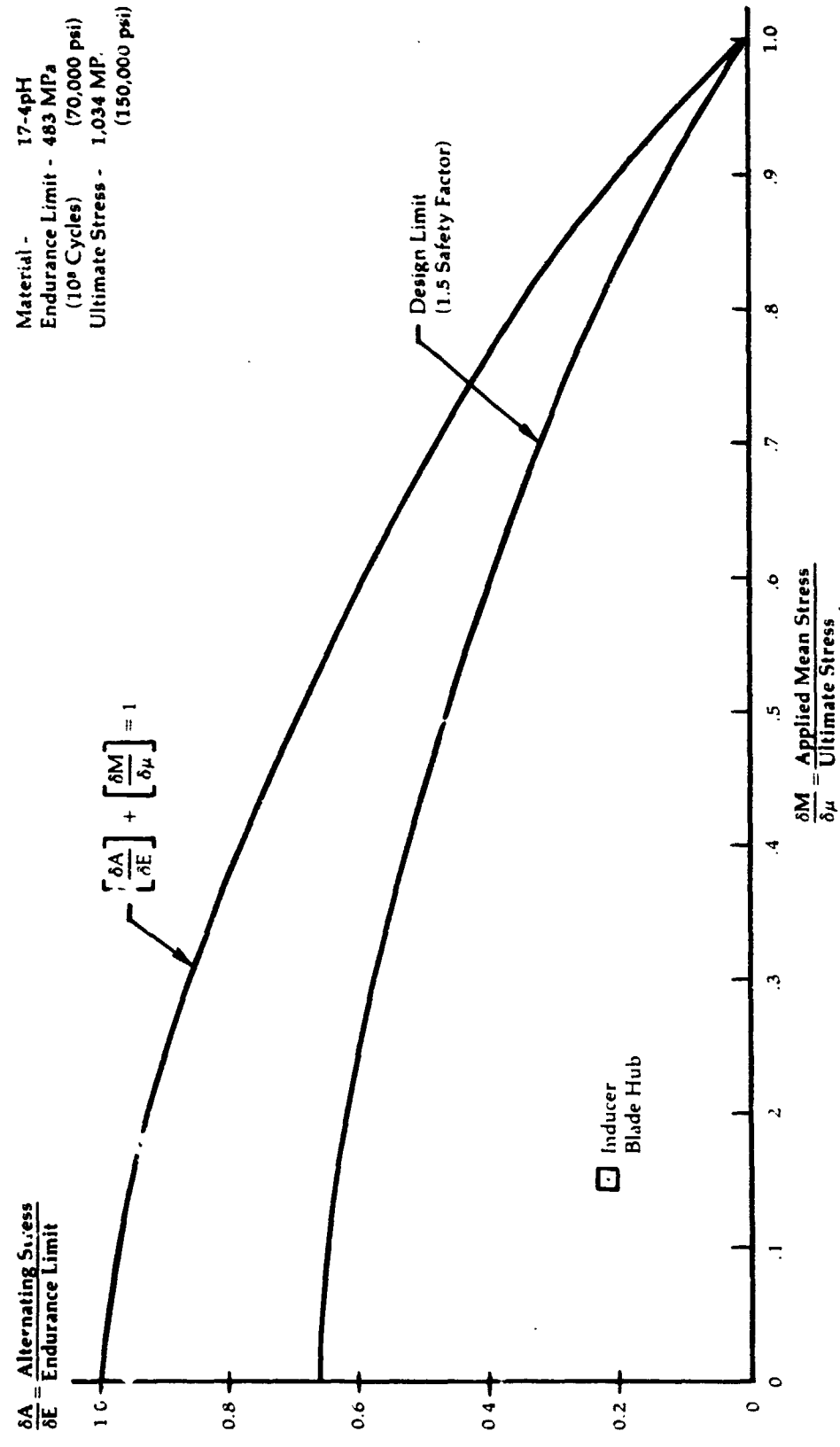

Figure 17

Upgraded Engine Inducer Blade Vibration Mode Shapes

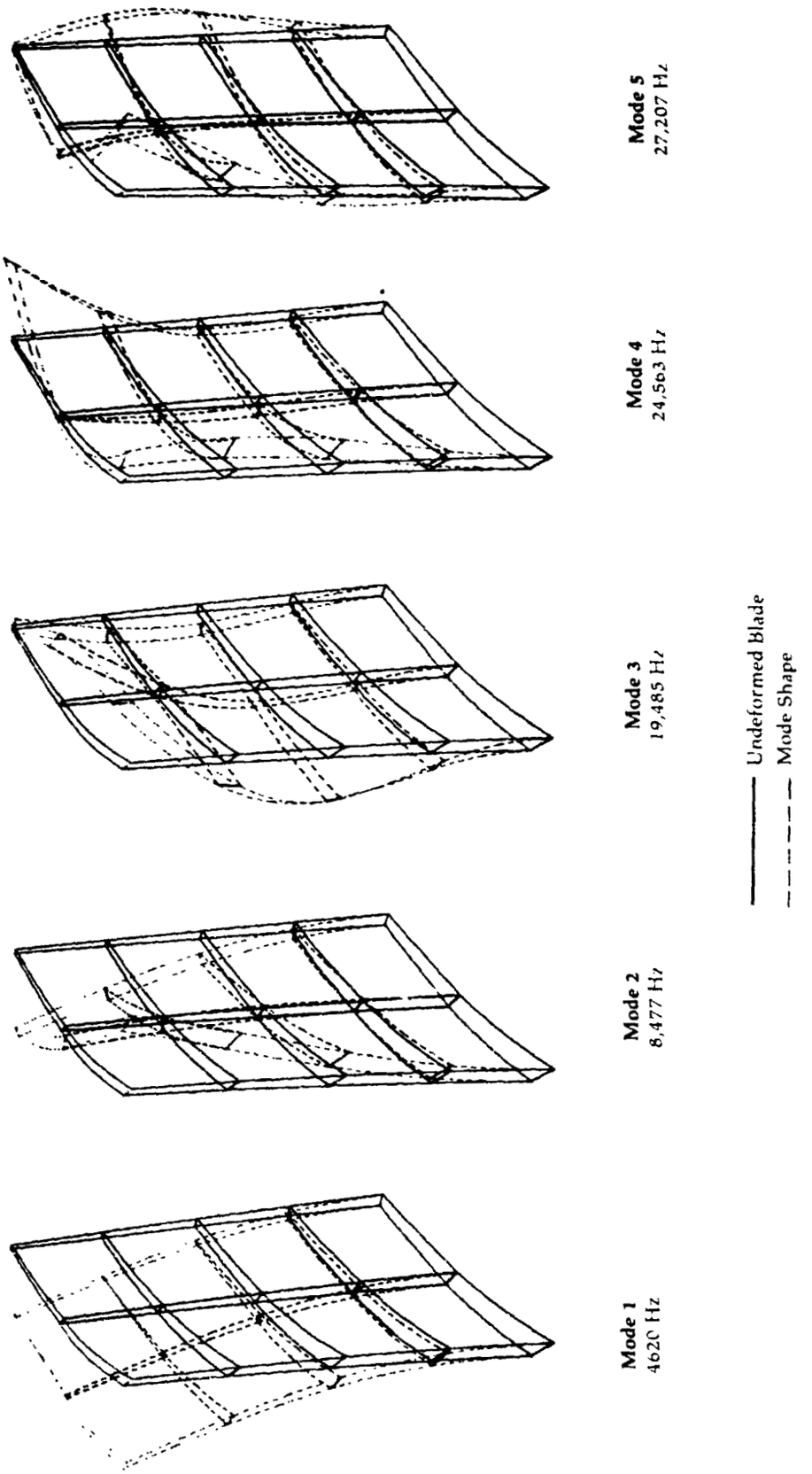

Figure 18

Upgraded Engine
Inducer Disc
Stress Contours
(PSI)
Steady State

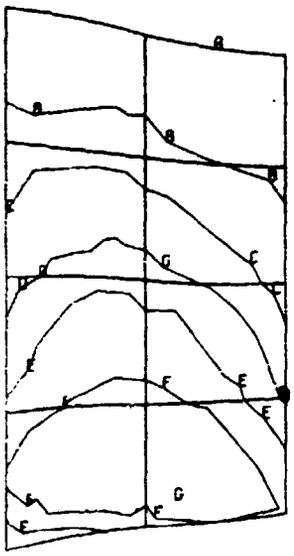

Legend
A = +3.8297048E+3
B = +1.2089052E+4
C = +2.0348399E+4
D = +2.8607746E+4
E = +3.6867092E+4
F = +4.5126439E+4
G = +5.3385786E+4
H = 0.0000000E 0

Blade Suction Side
Equivalent Stress

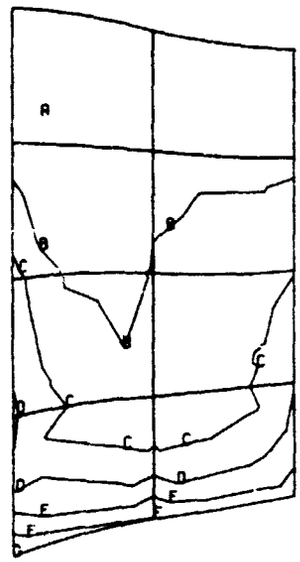

Legend
A = +2.2251872E+3
B = +1.0743292E+4
C = +1.926139oE+4
D = +2.7779501E+4
E = +3.6297605E+4
F = +4 4815709E+4
G = +5.3333814E+4
H = 0.0000000E 0

Blade Pressure Side
Equivalent Stress

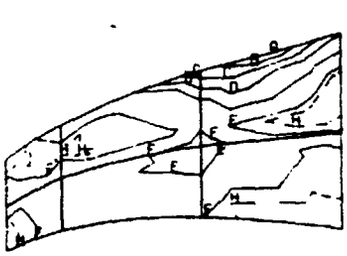

Legend
A = −1.0926036E+4
B = −8.8634650E+3
C = −6.8008939E+3
D = −4.7383227E+3
E = −2.675751oE+3
F = −o.1318040E+2
G = +1.4493908E+3
H = 0.0000000E 0

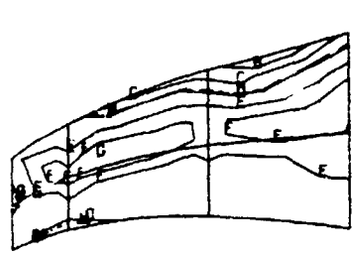

Legend
A = −4 398125oE+3
B = −2.8639977E+3
C = −1.3298697E+3
D = +2 0425820E+2
E = +1.73838o1E+3
F = +3.2725141E+3
G = +4.80oo420E+3
H = 0.0000000E 0

Disc Principal Stresses

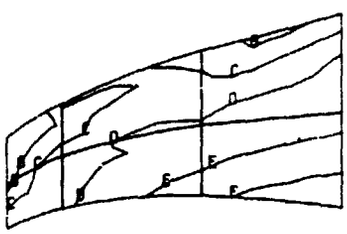

Legend
A = +4.0186333E+4
B = +4.3707295E+4
C = +4.7228258E+4
D = +5.0749220E+4
E = +5.4270182E+4
F = +5.7791144E+4
G = +o.1312107E+4
H = 0.0000000E 0

Disc Principal Stress

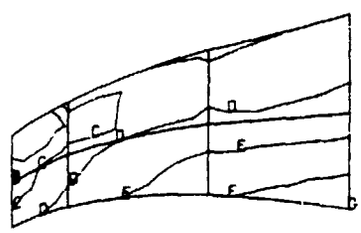

Legend
A = +3.9875820E+4
B = +4.3325218E+4
C = +4.6774o17E+4
D = +5 022401oE+4
E = +5 3o73414E+4
F = +5.7122813E+4
G = +o 0572211E+4
H = 0 0000000E 0

Disc Equivalent Stress

Figure 19

Upgraded Engine
Impeller Disc
Stress Countours
(PSI)
Steady State

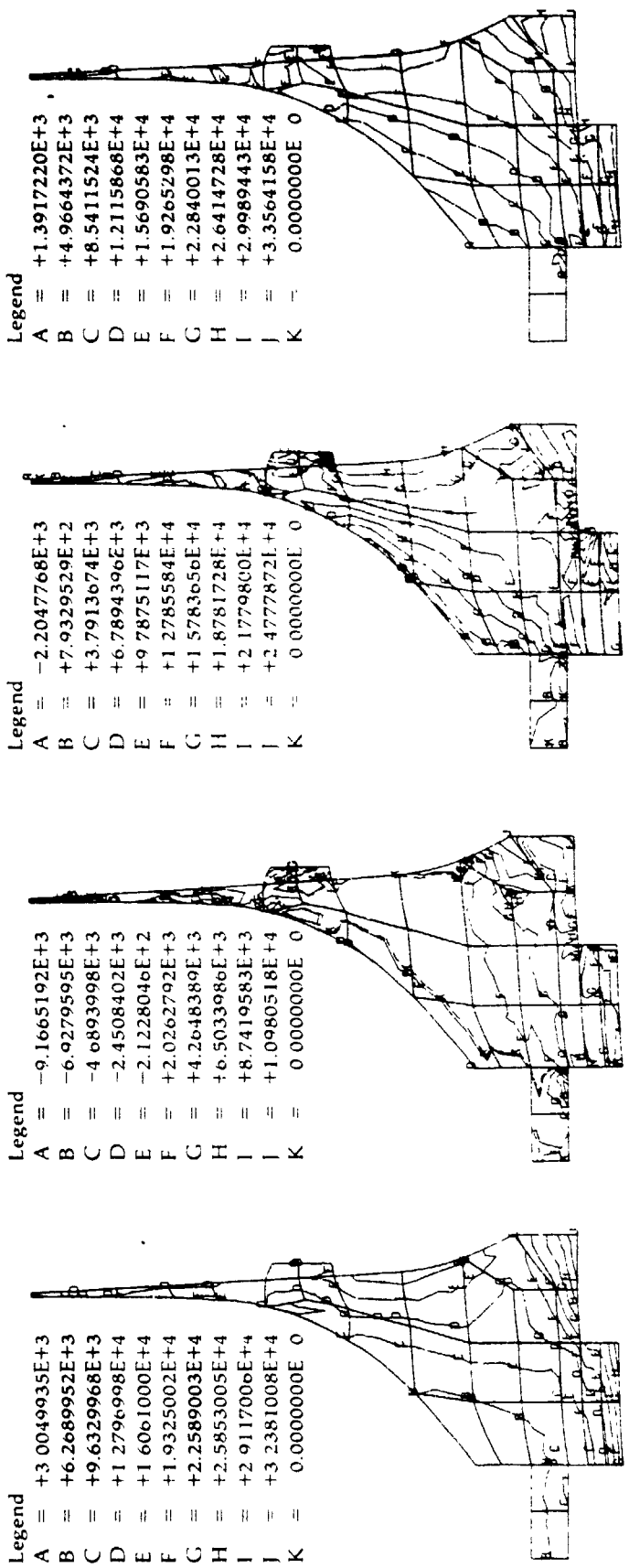

Figure 20

Upgraded Engine
Impeller Blade
Stress Contours
(PSI)
Steady State

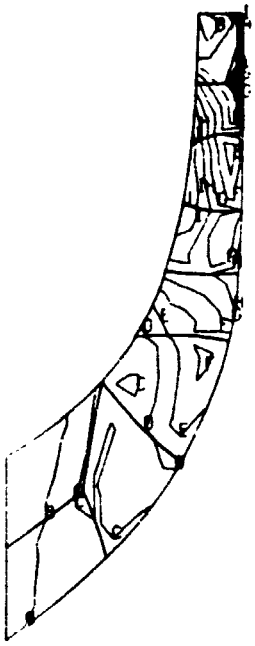

Legend
A = +2.0360282E+3
B = +3.9456724E+3
C = +5.8553165E+3
D = +7.7649607E+3
E = +9.6746049E+3
F = +1.1584249E+4
G = +1.3493893E+4
H = +1.5403537E+4
I = +1.7313182E+4
J = +1.9222826E+4
K = 0.0000000E 0

Pressure Side
Max. Principal Stress

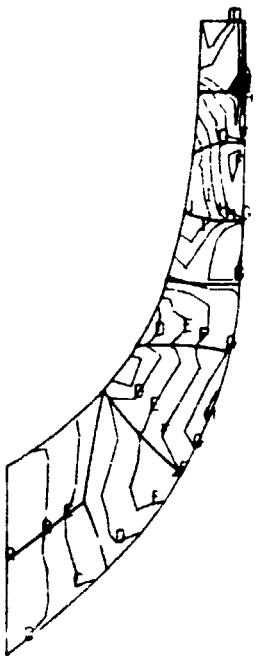

Legend
A = +9.9886305E+2
B = +2.9113708E+3
C = +4.8238785E+3
D = +6.7363863E+3
E = +8.6488940E+3
F = +1.0561402E+4
G = +1.2473909E+4
H = +1.4386417E+4
I = +1.6298925E+4
J = +1.8211433E+4
K = 0.0000000E 0

Pressure Side
Equivalent Stress

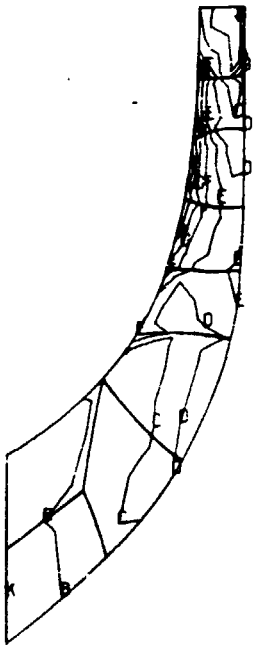

Legend
A = −5.8232723E+1
B = +3.1554411E+3
C = +6.3691149E+3
D = +9.5827887E+3
E = +1.2796462E+4
F = +1.6010136E+4
G = +1.9223810E+4
H = +2.2437484E+4
I = +2.5651158E+4
J = +2.8864831E+4
K = 0.0000000E 0

Suction Side
Max. Principal Stress

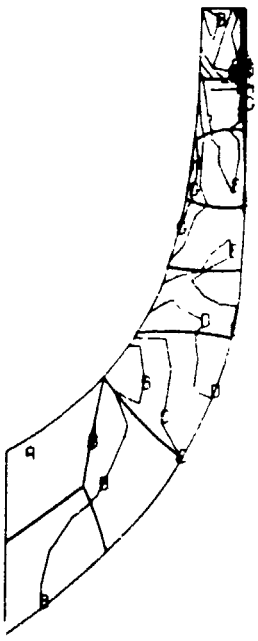

Legend
A = +7.7214710E+2
B = +3.9988116E+3
C = +7.2254761E+3
D = +1.0452141E+4
E = +1.3678805E+4
F = +1.6905470E+4
G = +2.0132134E+4
H = +2.3358799E+4
I = +2.6585463E+4
J = +2.9812128E+4
K = 0.0000000E 0

Suction Side
Equivalent Stress

Figure 21

Upgraded Engine Impeller Stress Contours (PSI) Due to Assembly Shrink Fit at Engine Soak-Back Conditions

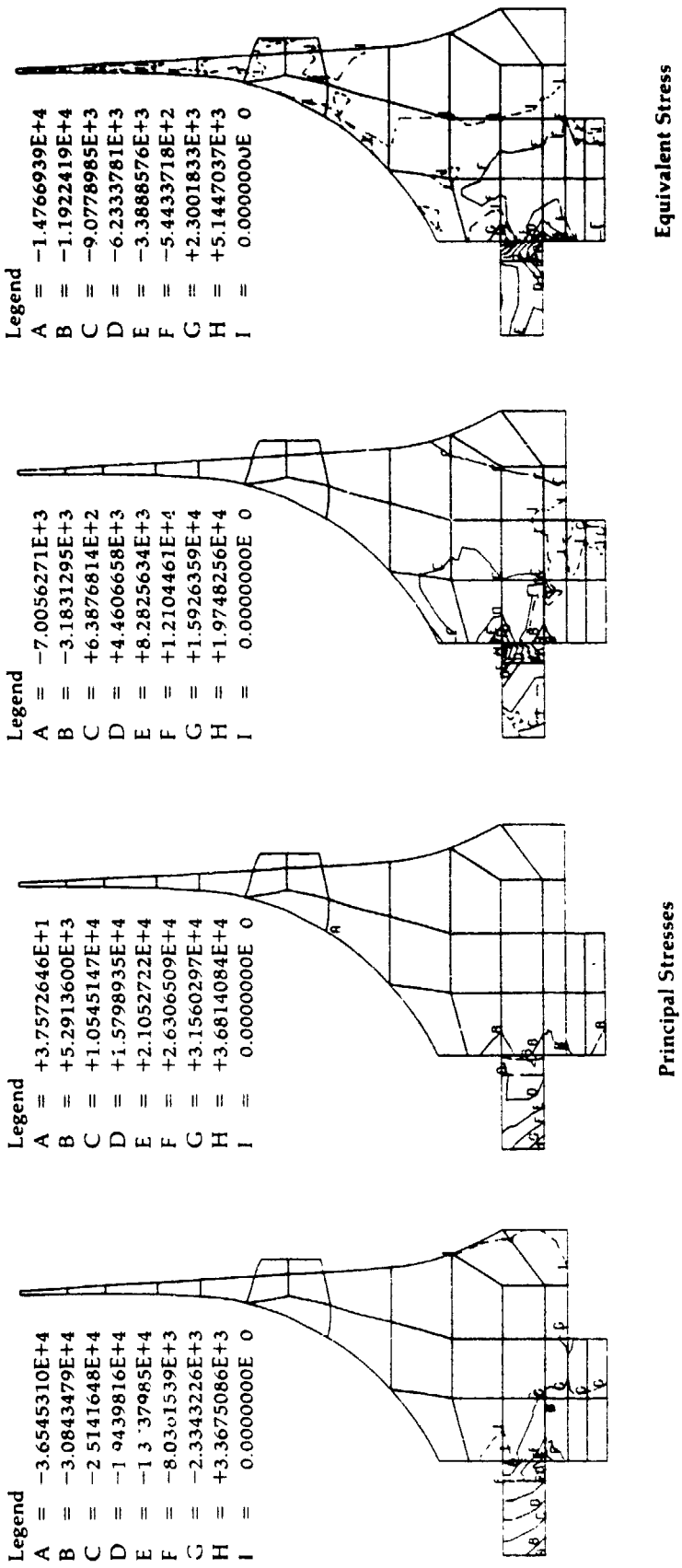

Figure 22

Upgraded Engine Impeller-Hub Stress Contours (PSI) Due to Assembly Shrink Fit

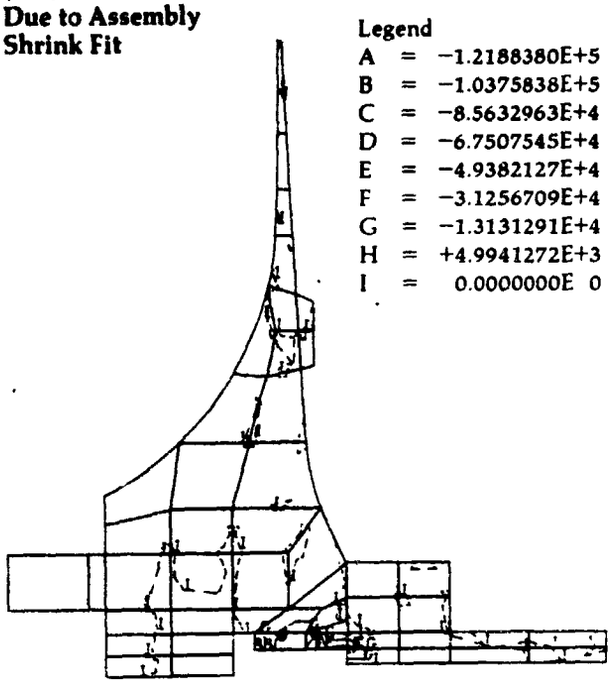

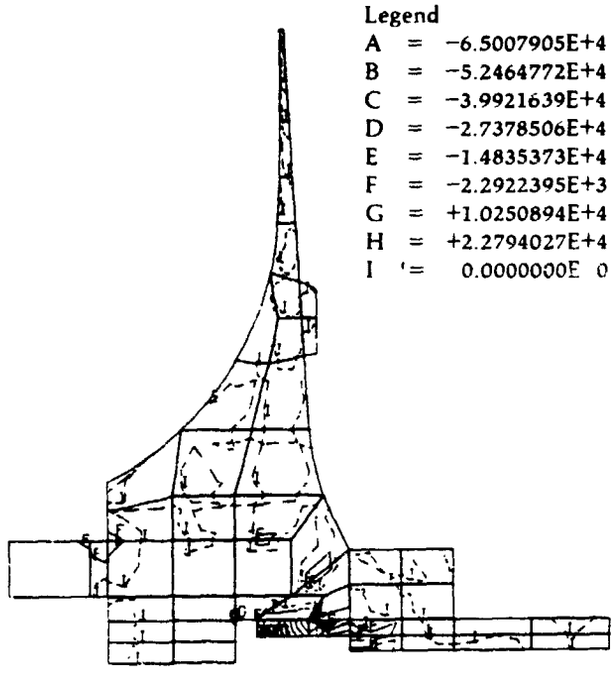

Principal Stresses

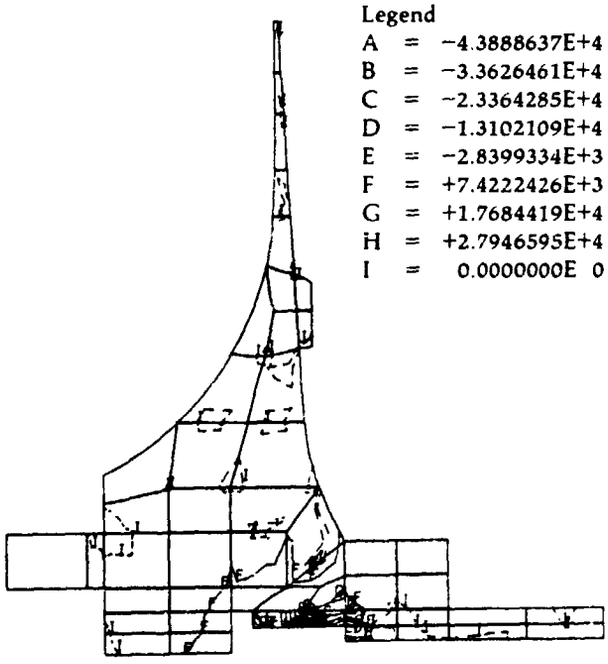

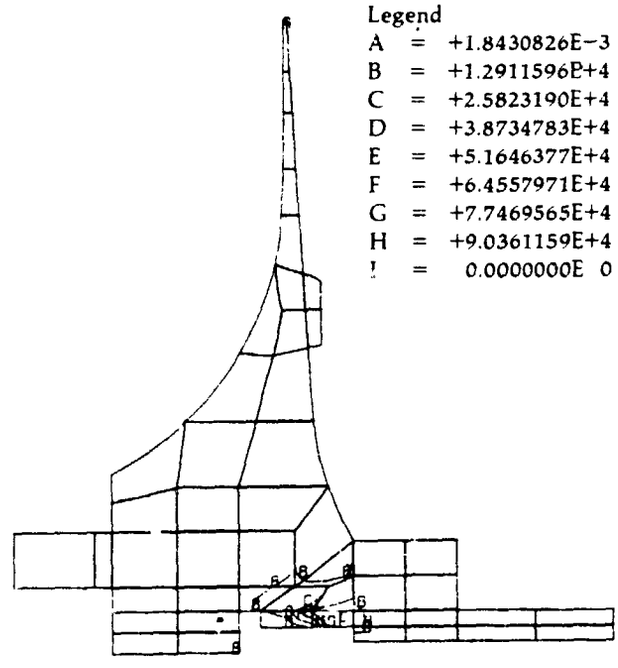

Equivalent Stress

Figure 23

Upgraded Engine

Views Showing Sectioning of Compressor Turbine for Casting Requirements

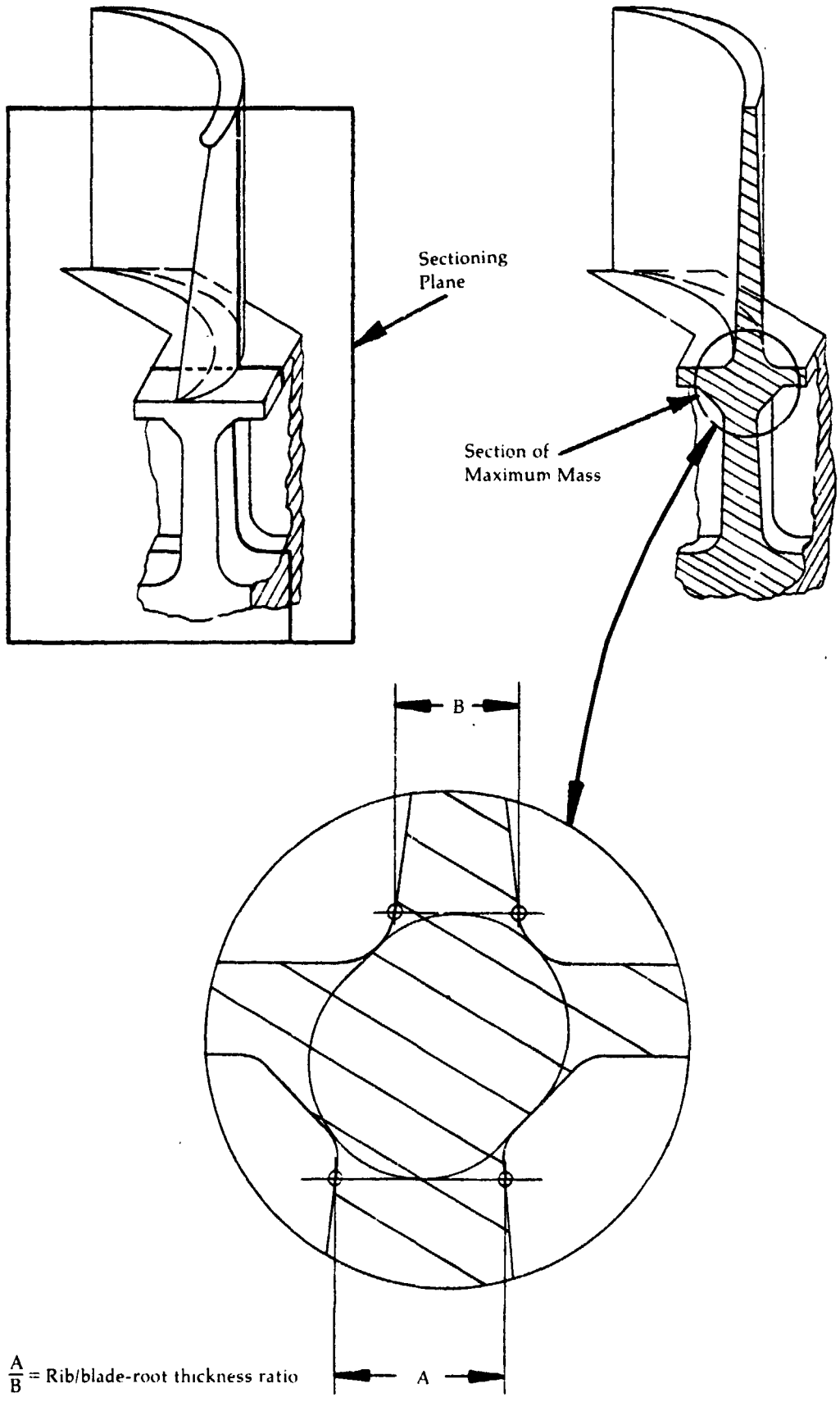

Figure 24

Upgraded Engine Compressor-Turbine Rotor Blade Profiles-

Comparison of Original Blading vs. Thin Blade Revision

Tip Section

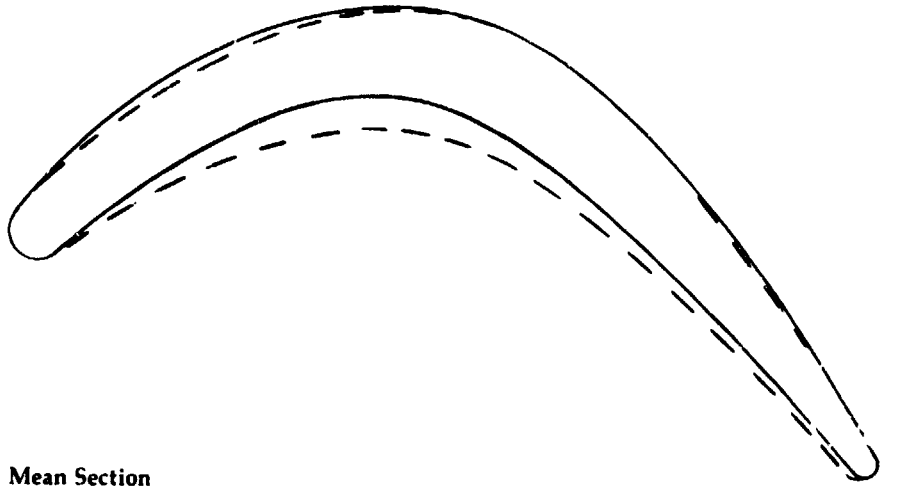

Mean Section

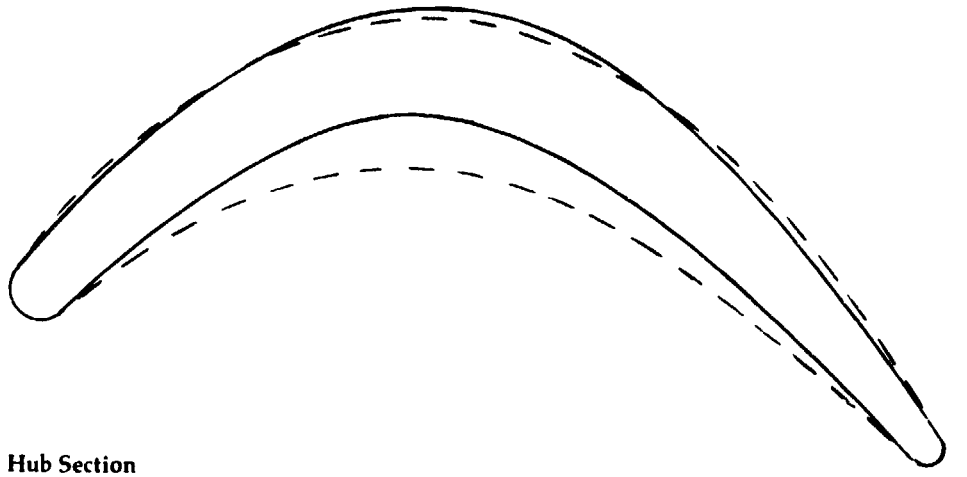

Hub Section

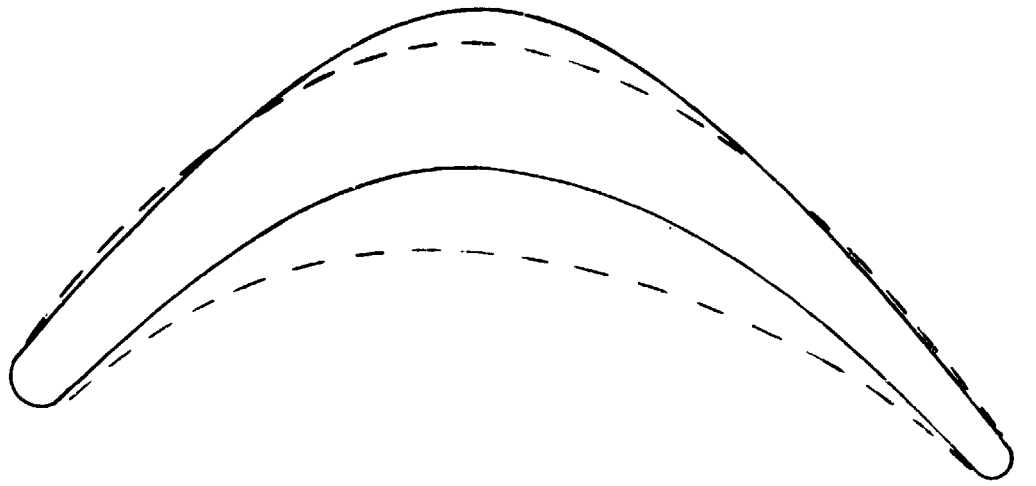

— — — — =Original Blading.
———— =Thin Blade Revision

Figure 25

Upgraded Engine Compressor Drive Turbine Flow Path

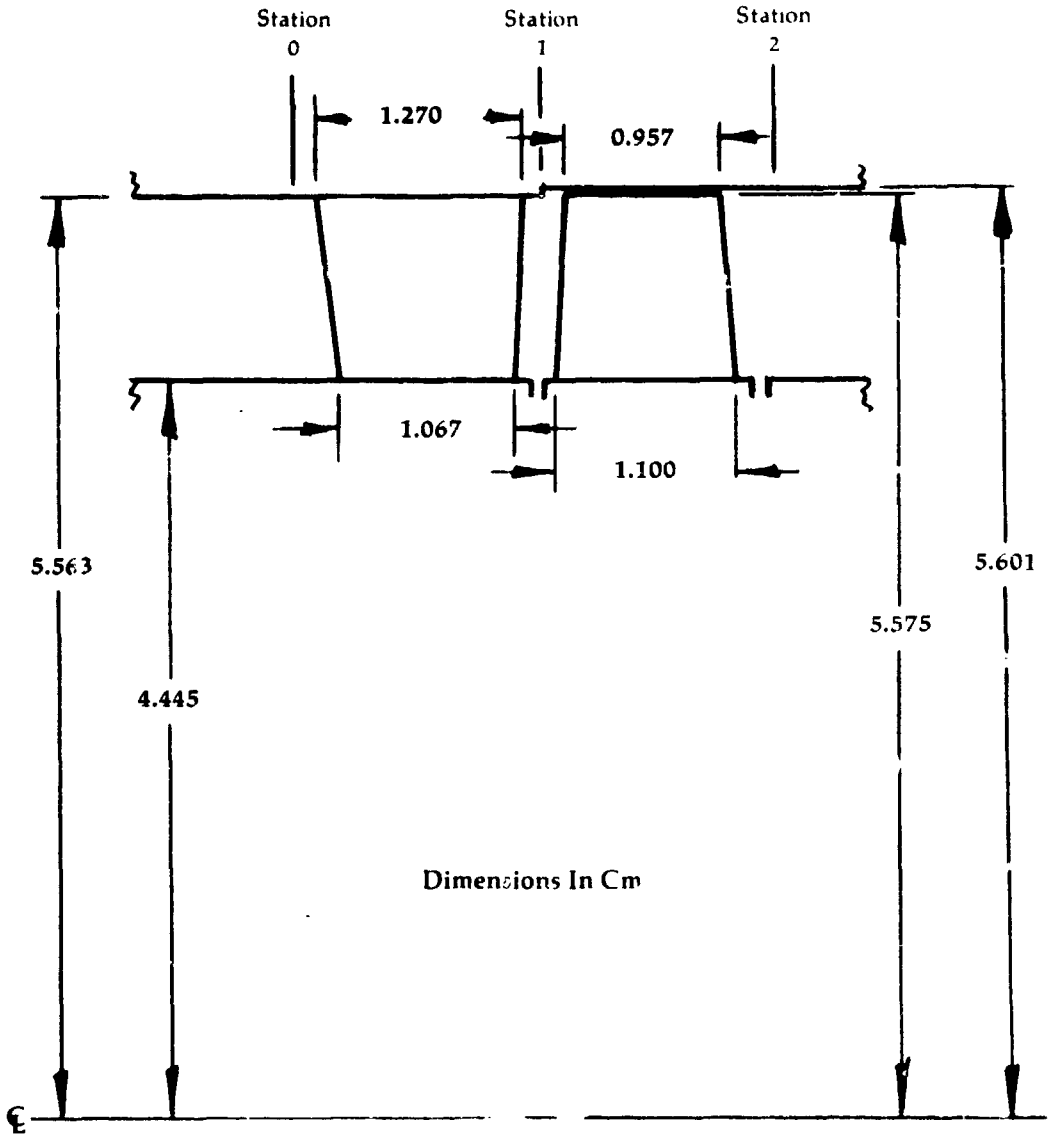

Taken from NASA TM X-71717

Figure 26

Figure 27

Upgraded Engine Compressor Turbine Design Velocity Diagrams (Velocities In m/s)

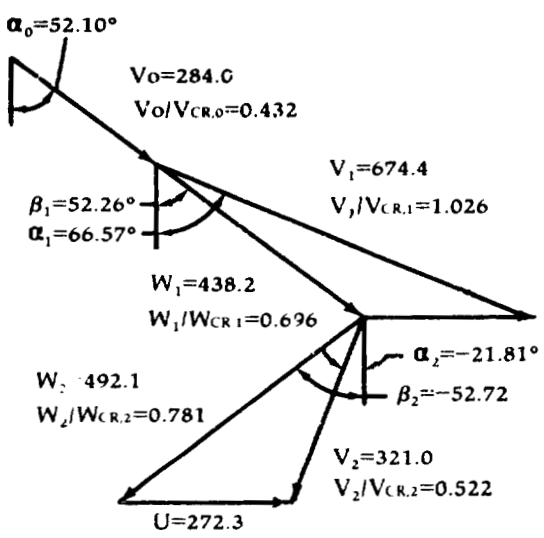

Hub
r=4.445 cm

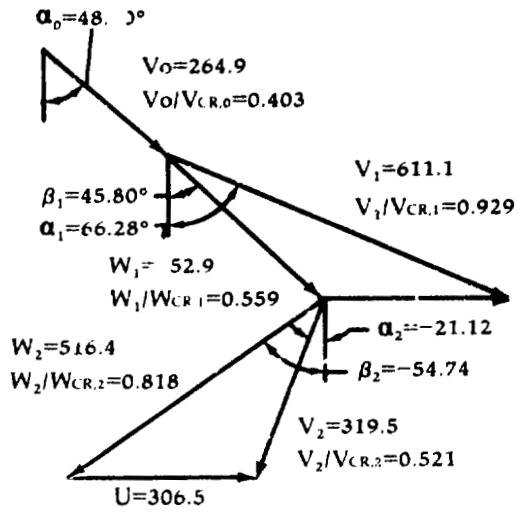

Mean
r=5.004 cm

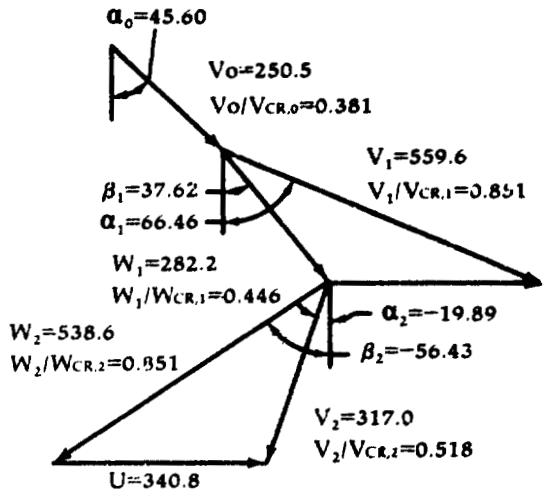

Tip
r=5.563 cm

Taken from NASA TM X-71717

Upgraded Engine
Compressor
Turbine Nozzle
Original Design

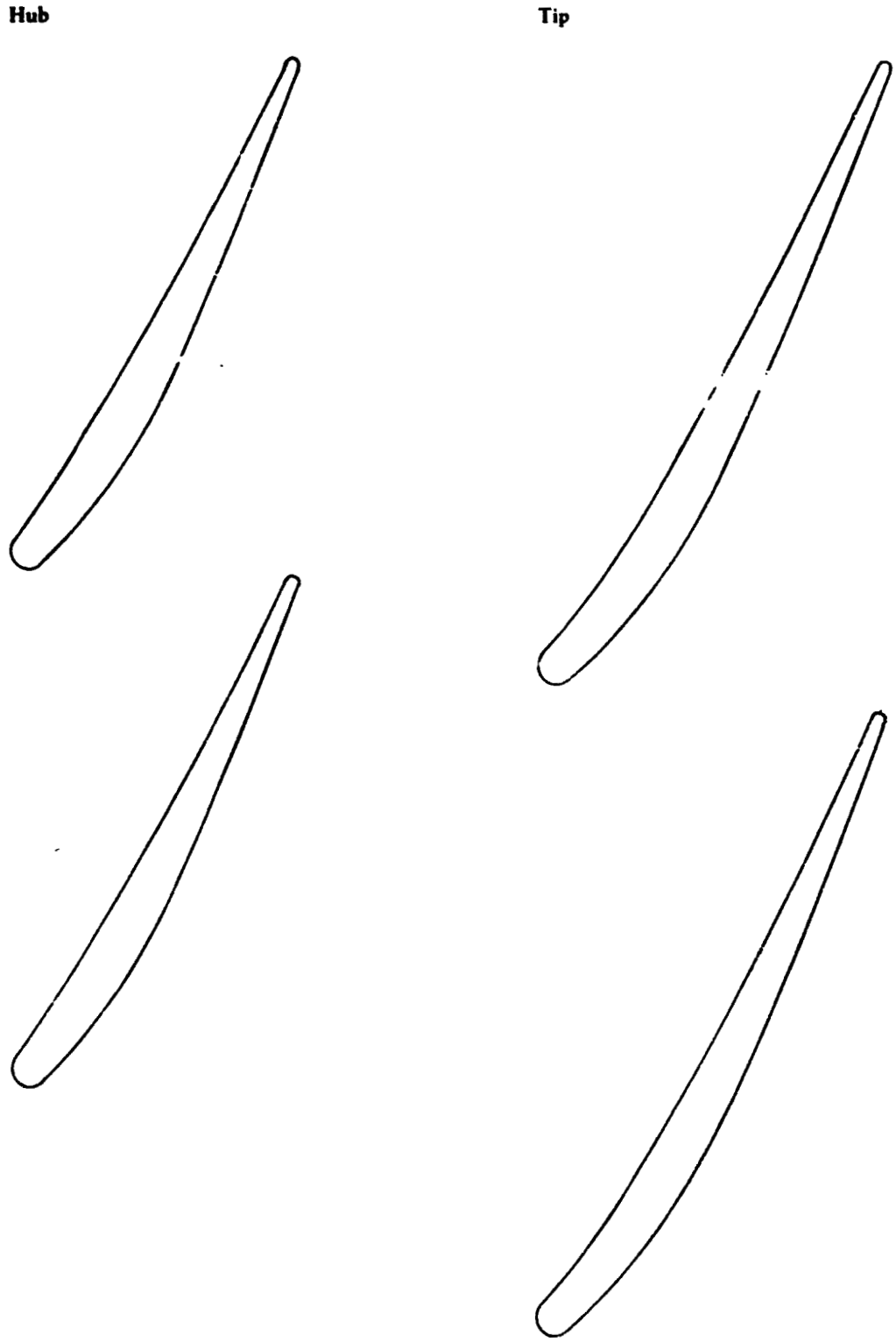

Figure 28

Figure 29

Upgraded Engine Compressor Turbine Nozzle Aerodynamic Loading

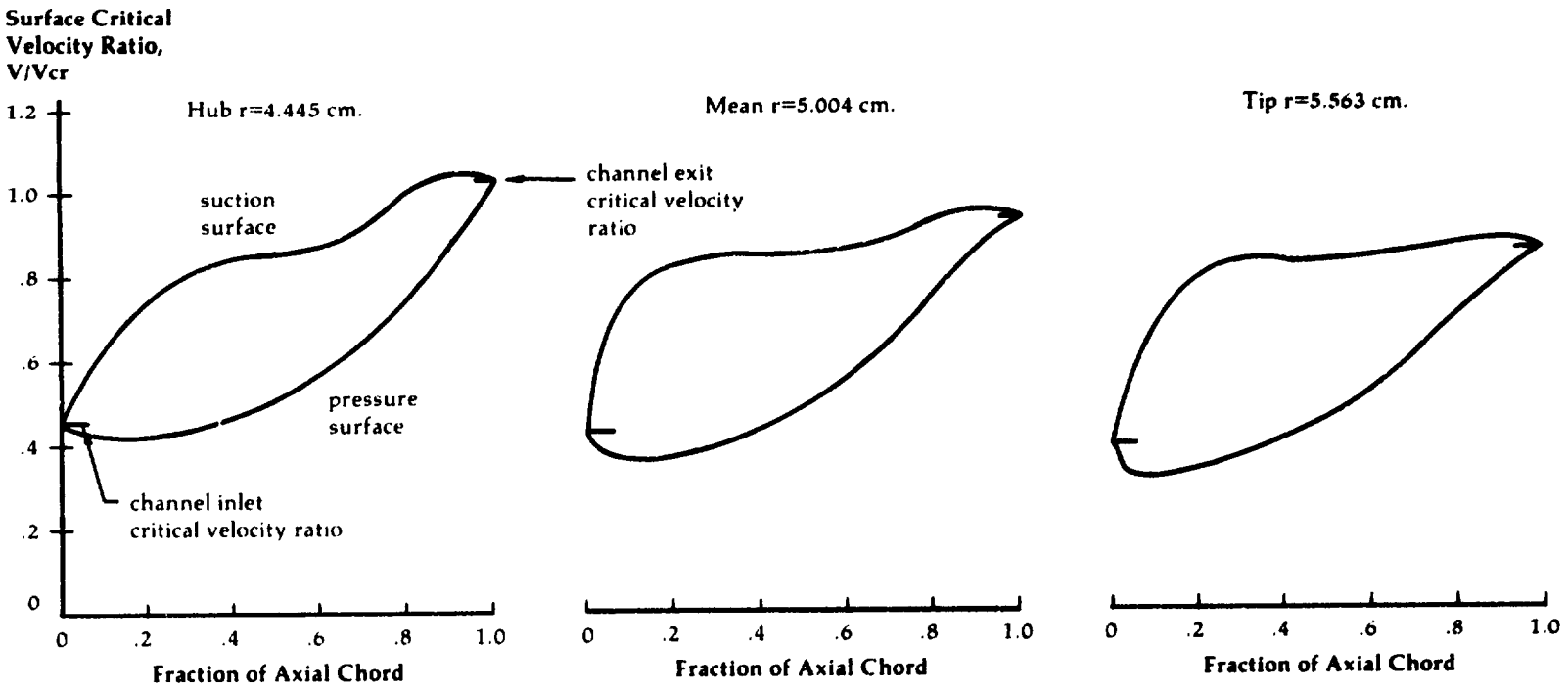

Taken from:
NASA TM X-71719

Upgraded Engine
Compressor
Turbine Rotor
Aerodynamic
Loading

design inlet total pressure = 56.4 psia

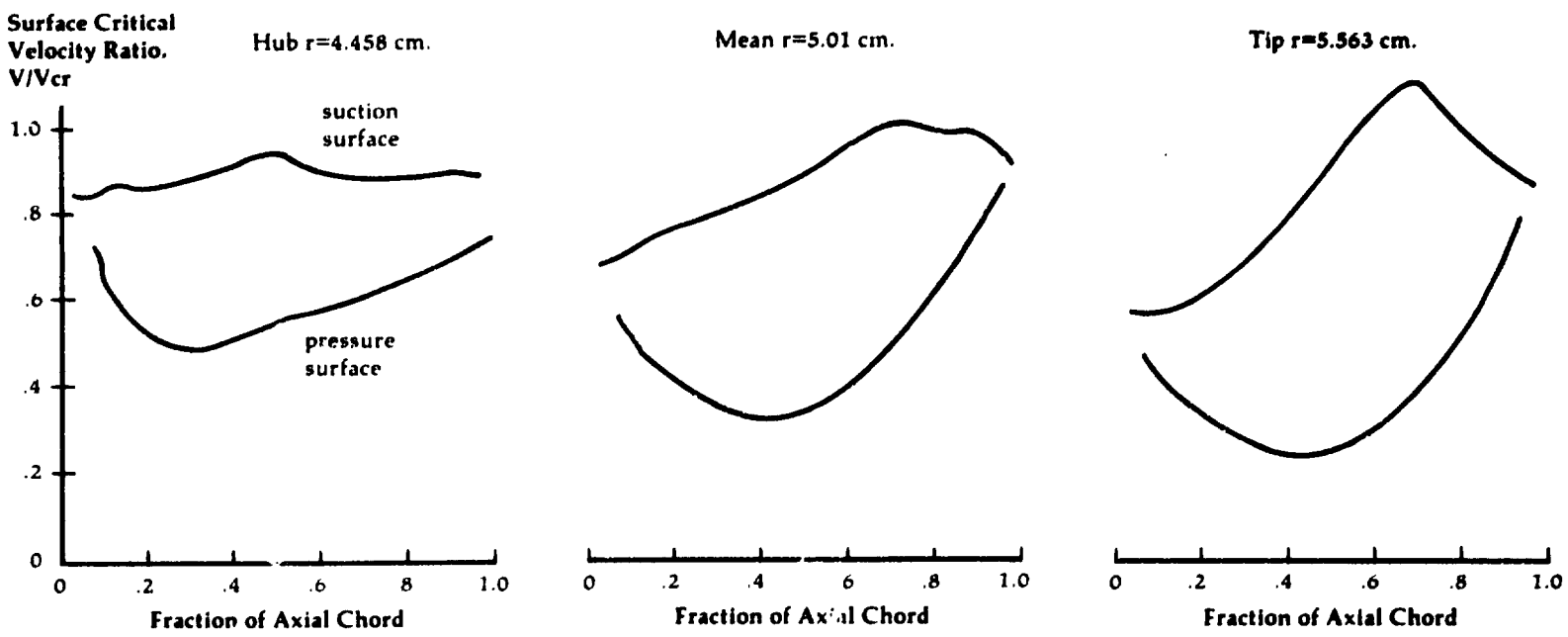

Figure 30

Comparison of Upgraded and Baseline Engines Compressor Turbine Nozzle Configurations

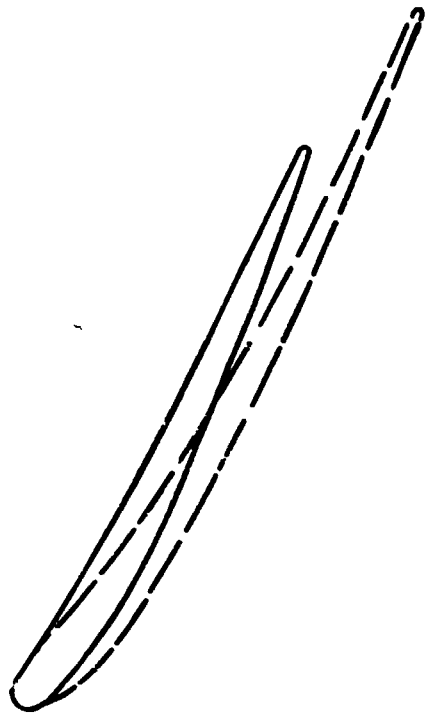

Vane Profile Comparison Near Mean Radius

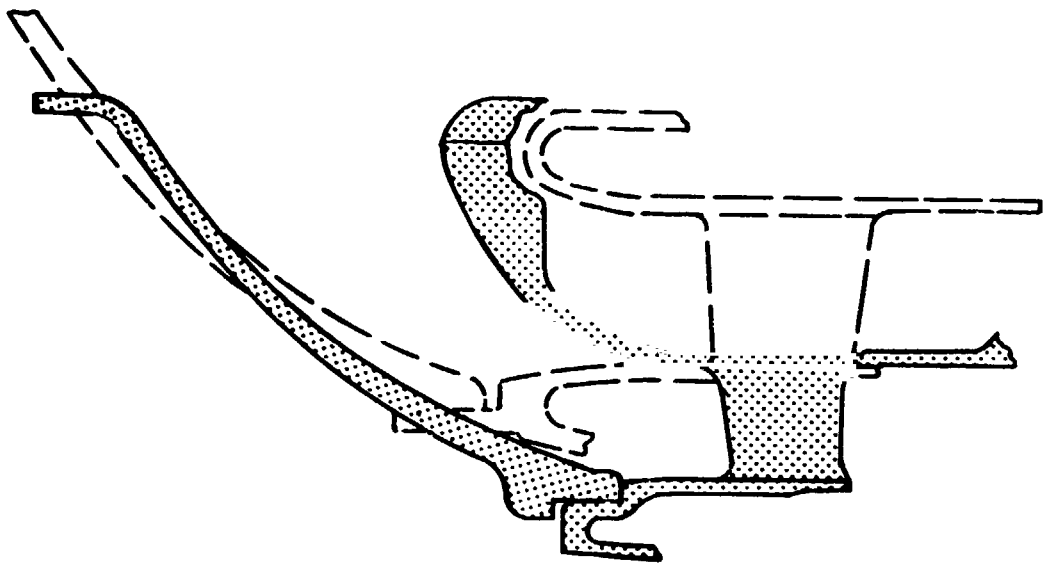

Flow Path Comparison

— — — — = Baseline Engine
———— = Upgraded Engine

Figure 31A

Comparison of Upgraded and Baseline Engines Compressor Turbine Rotor Configurations

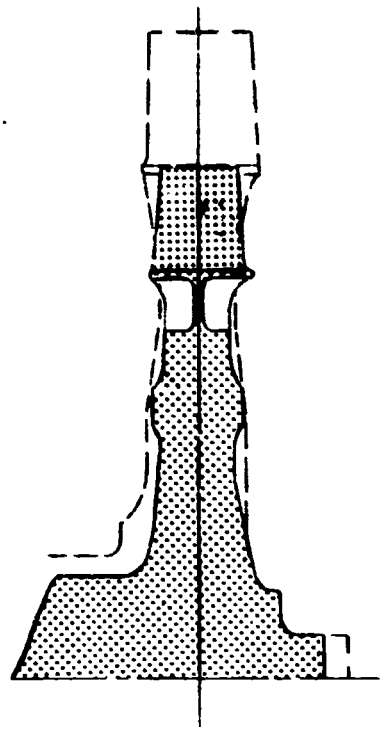

Rotor Comparison

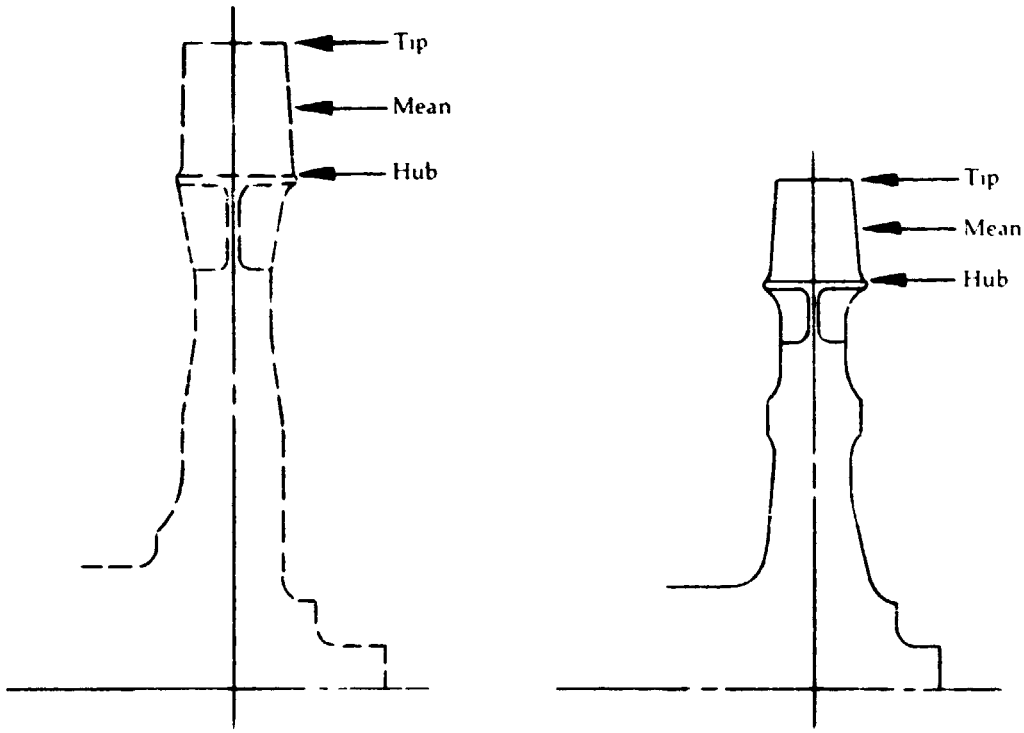

Baseline **Upgraded**

Baseline Engine
Upgraded Engine

Figure 31B

Comparison of Upgraded and Baseline Engines Pocket Section Configurations Compressor Turbine Rotor

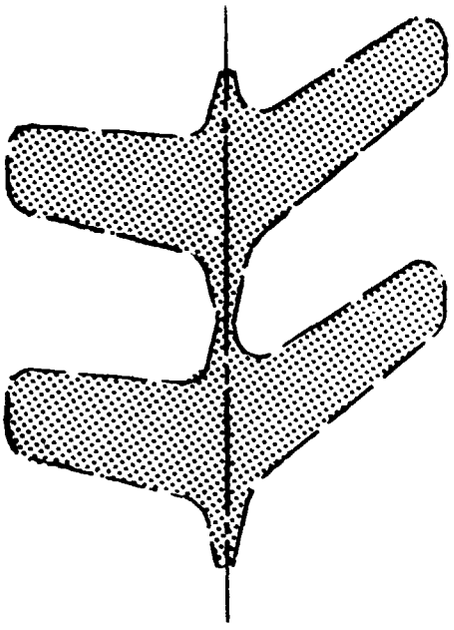

Section A-A
Enlarged View

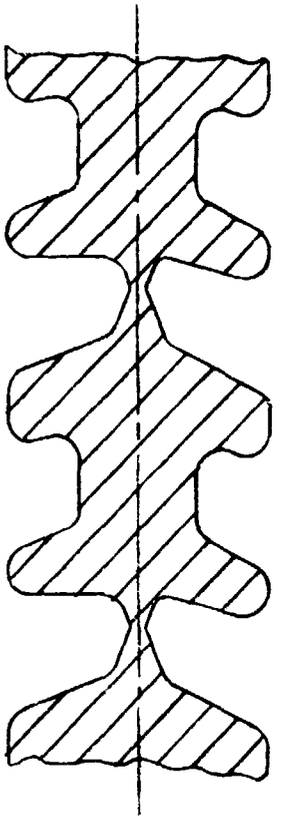

Section A-A
Enlarged View

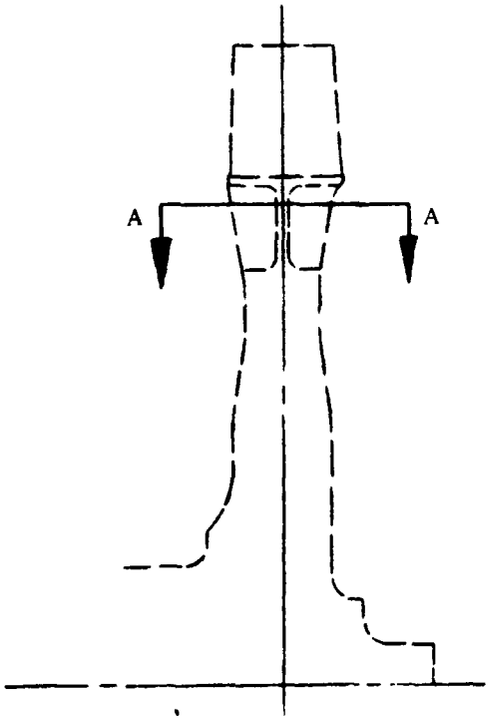

Baseline

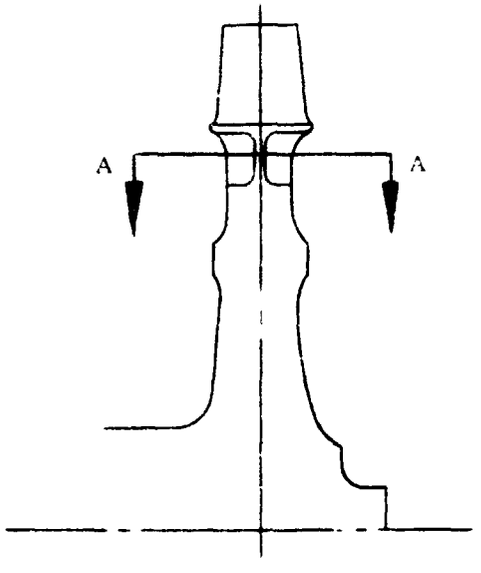

Upgraded

— — — — = Baseline Engine
——— = Upgraded Engine

Figure 31C

Comparison of Upgraded and Baseline Engines Compressor Turbine Rotor Blade Spacing

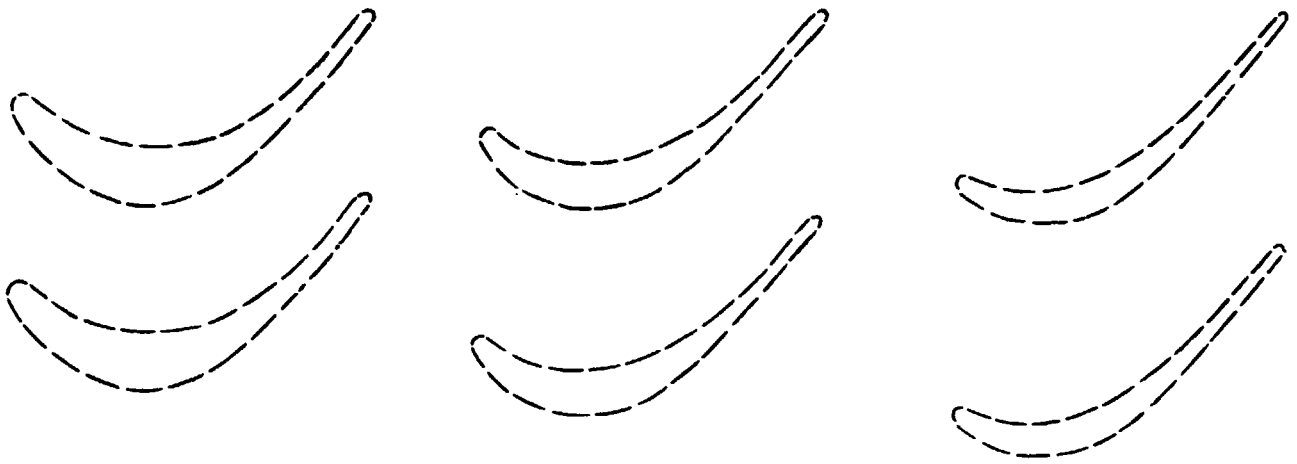

Hub Mean Tip

Baseline Engine

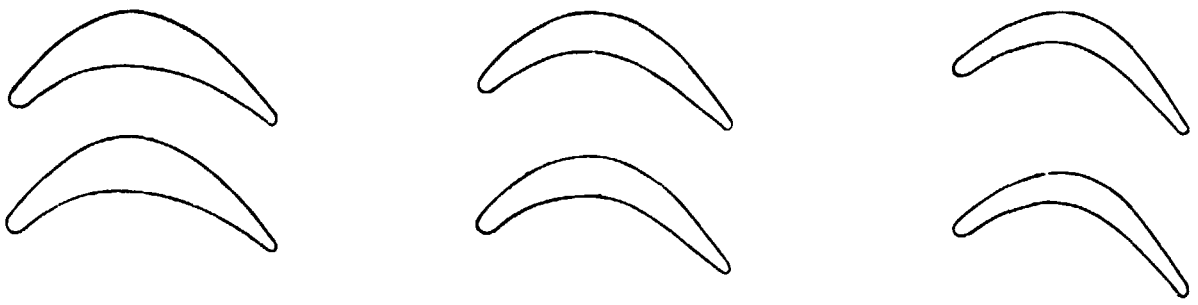

Hub Mean Tip

Upgraded Engine

— — — — = Baseline Engine
———— = Upgraded Engine

Figure 31D

Comparison of Upgraded and Baseline Engines Compressor Turbine Rotor Blade Configurations

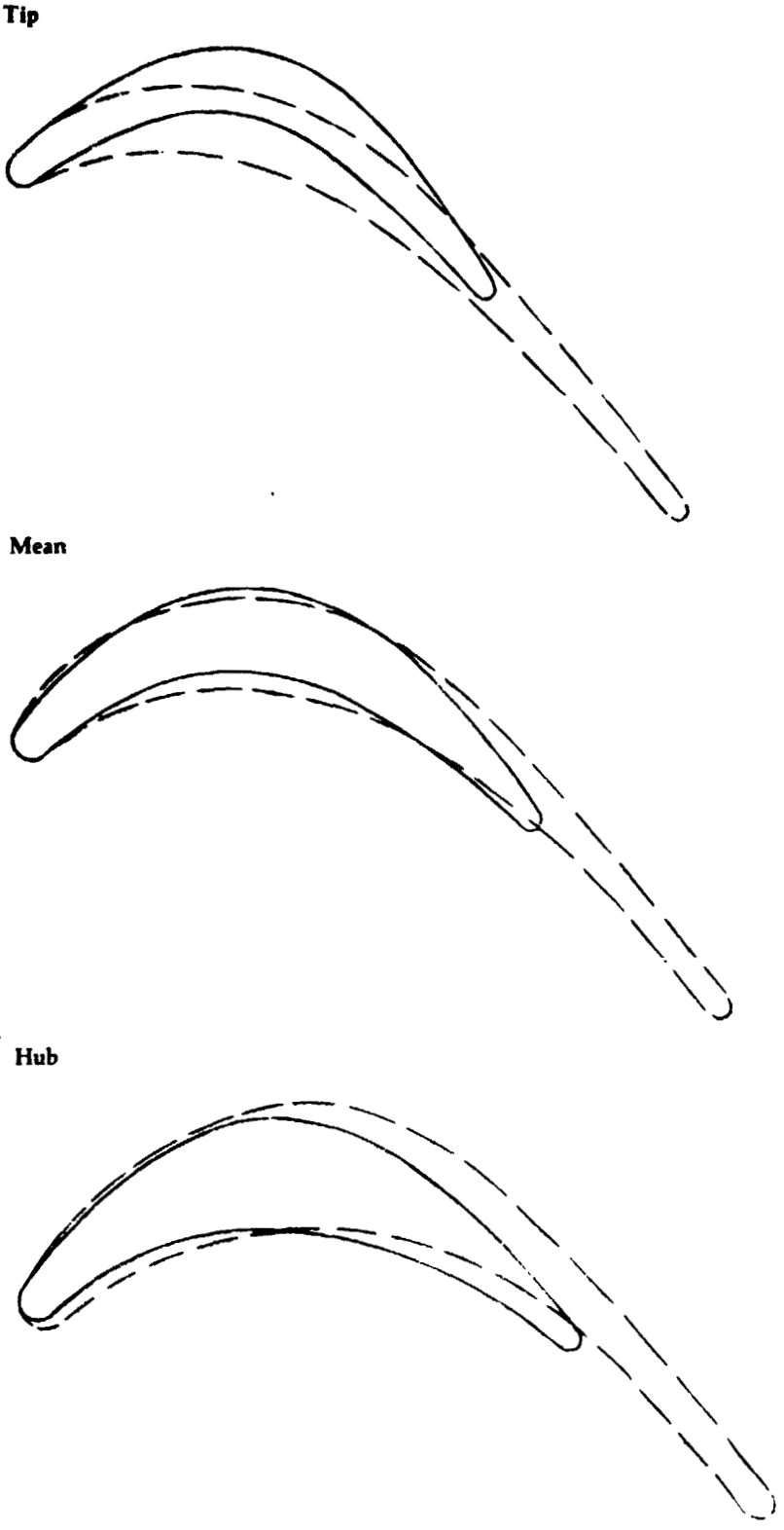

Figure 31E

Upgraded Engine Vortex Chamber and Turbine Inlet Configurations for Compressor Turbine

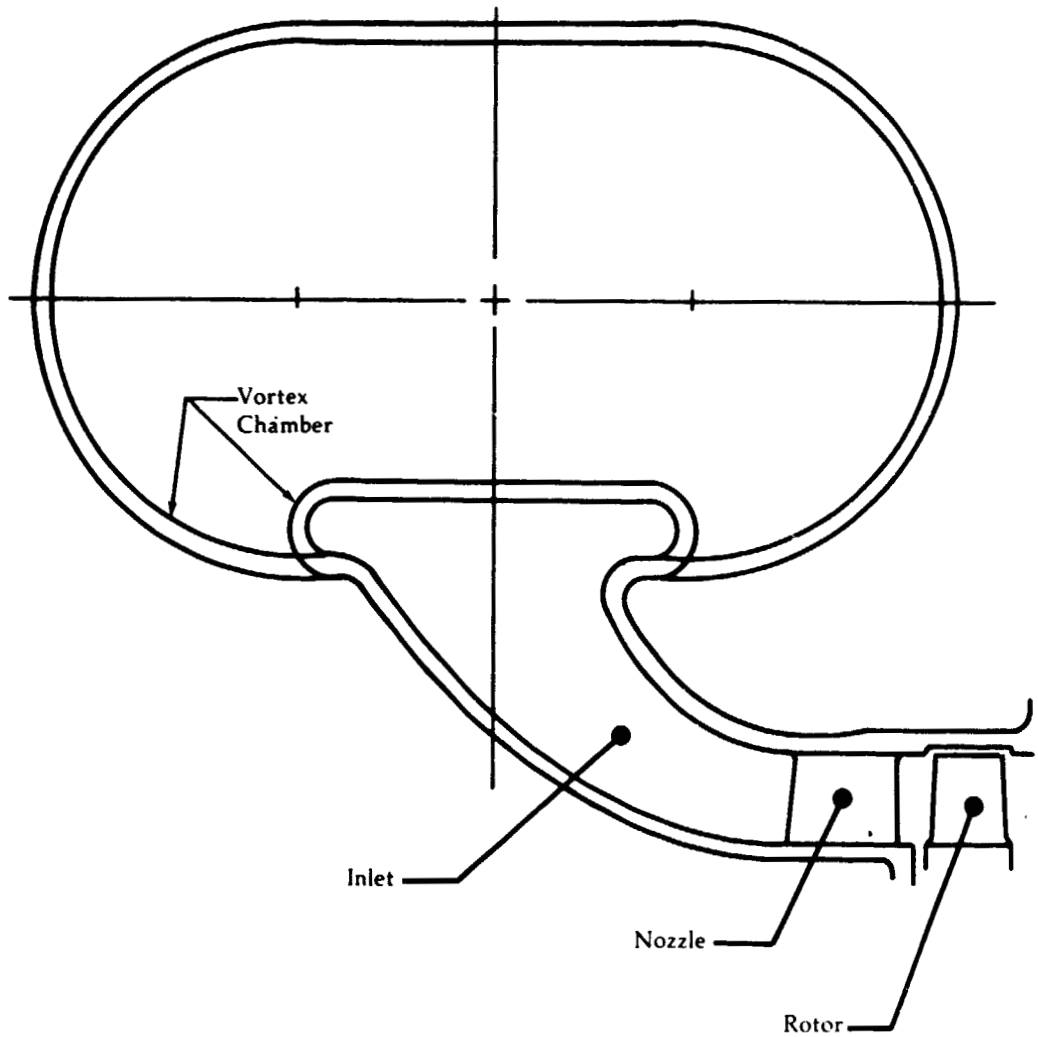

Figure 32

Upgraded Engine Compressor Turbine Performance Goal

Corrected Work vs. Flow Speed Parameter

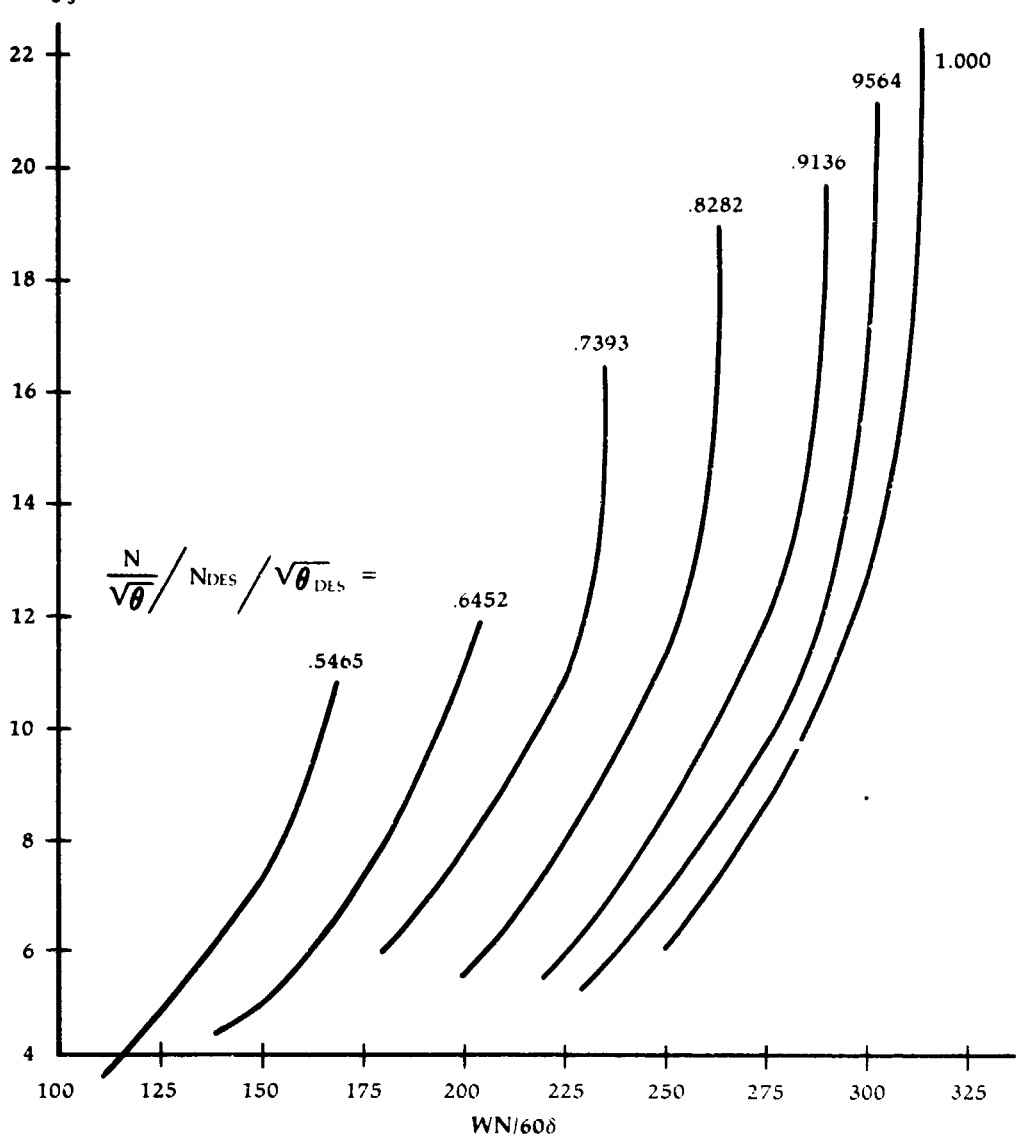

Figure 33

Upgraded Engine Compressor-Turbine Performance Estimate

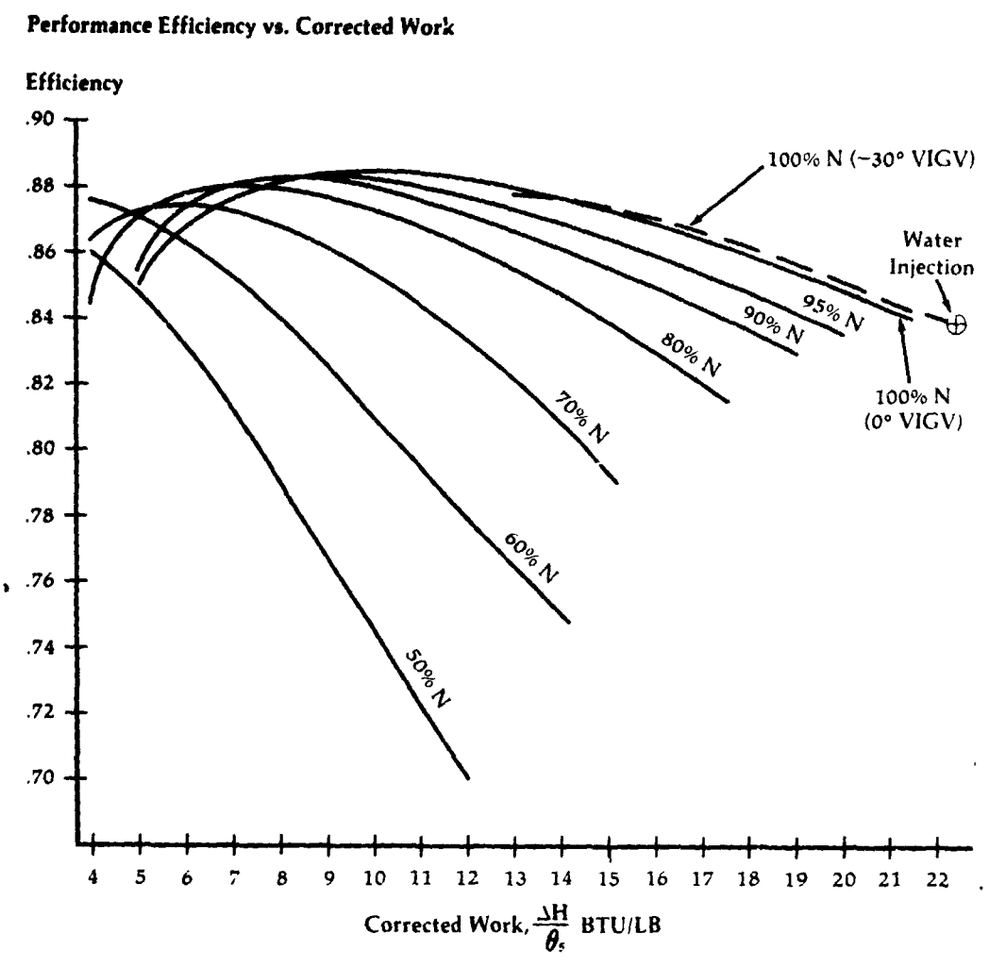

Figure 34

Upgraded Engine Compressor-Turbine Structural Analysis

Upgraded Engine Compressor Turbine Wheel Structural Analysis Summary

Mechanical Speed - 6130 Rad/Sec (58,500 RPM)
Avg. Tangential Stress - 232,00 kPa (33,600 psi)
Burst Speed - 10,000 Rad/Sec (95,500 RPM)
Burst Factor - 1.63
Material - IN-792 + Hf

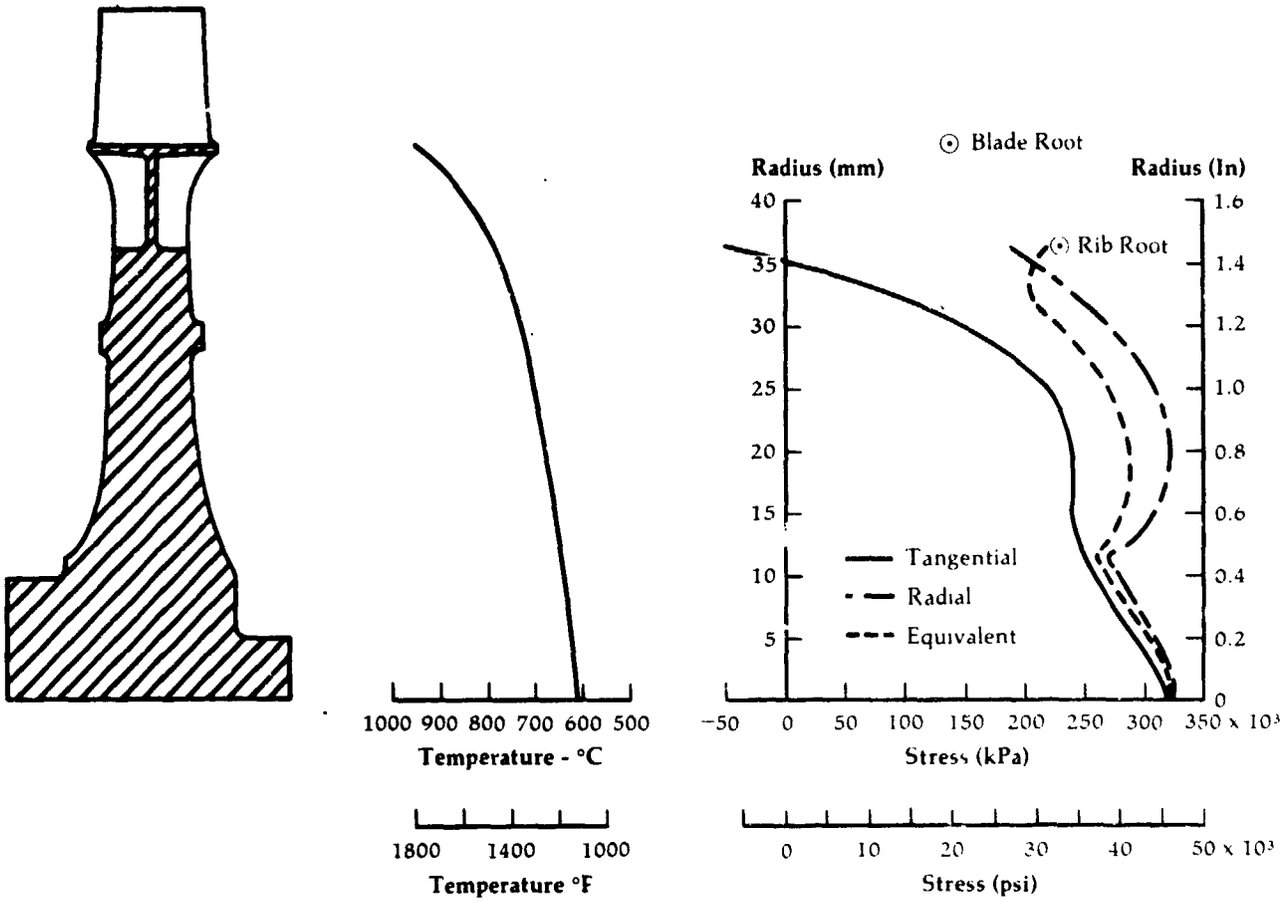

Figure 35

Upgraded Engine Compressor Turbine Blade Vibration Campbell Diagram

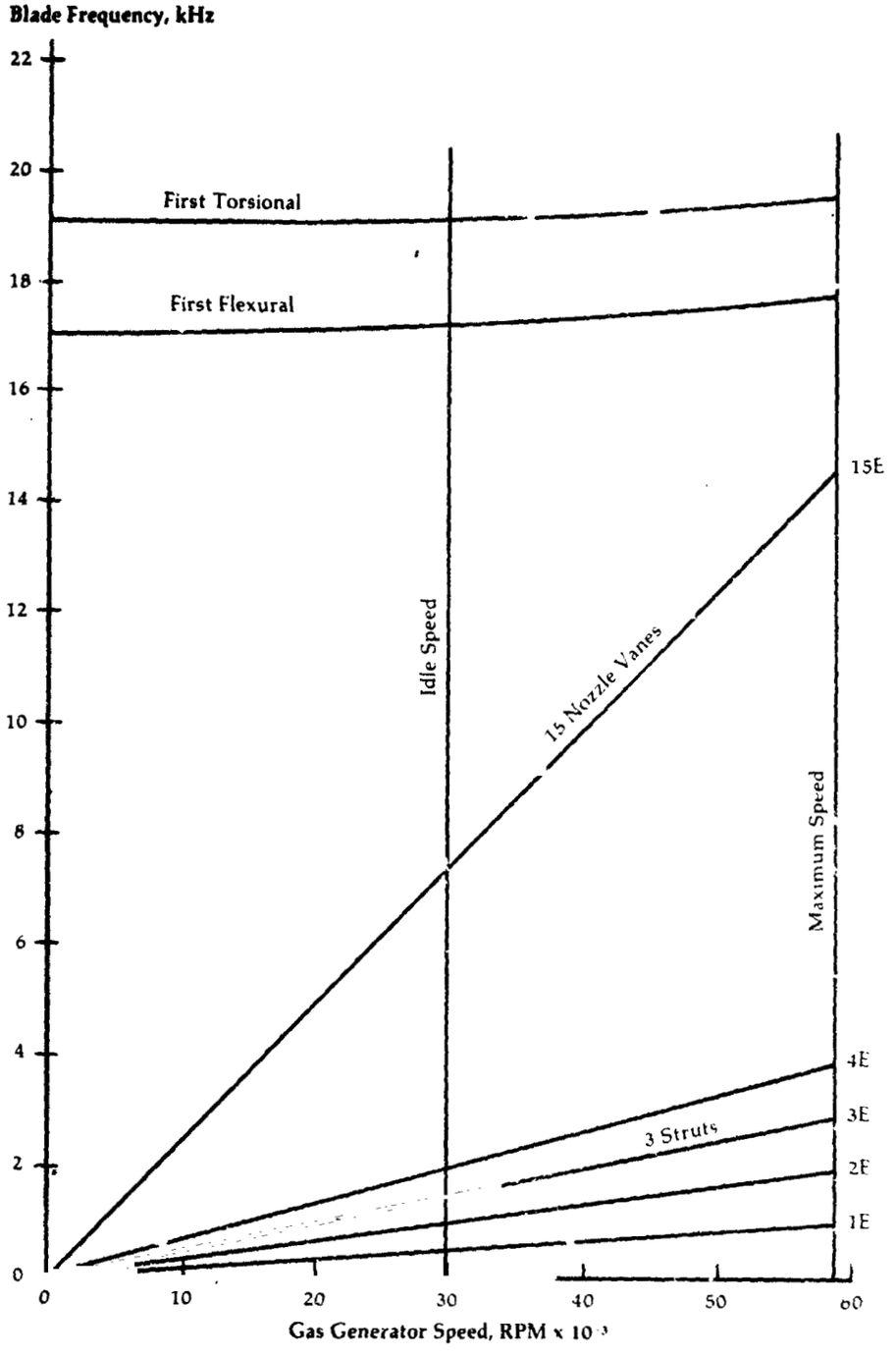

Figure 36

Upgraded Engine
Compressor Turbine
Blade Fatigue
Modified Goodman
Diagram

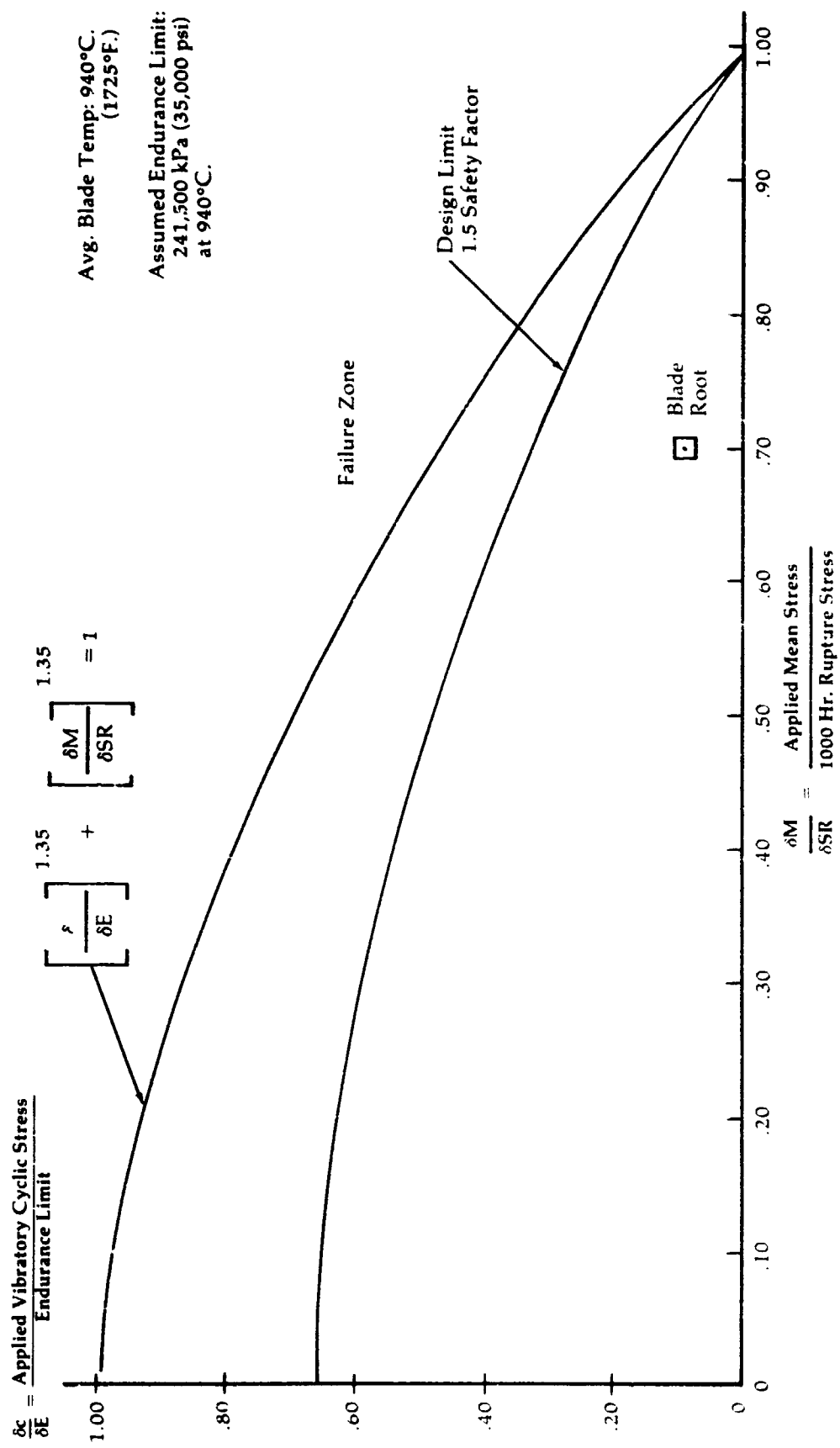

Figure 37

Upgraded Engine Power Turbine Flow Path

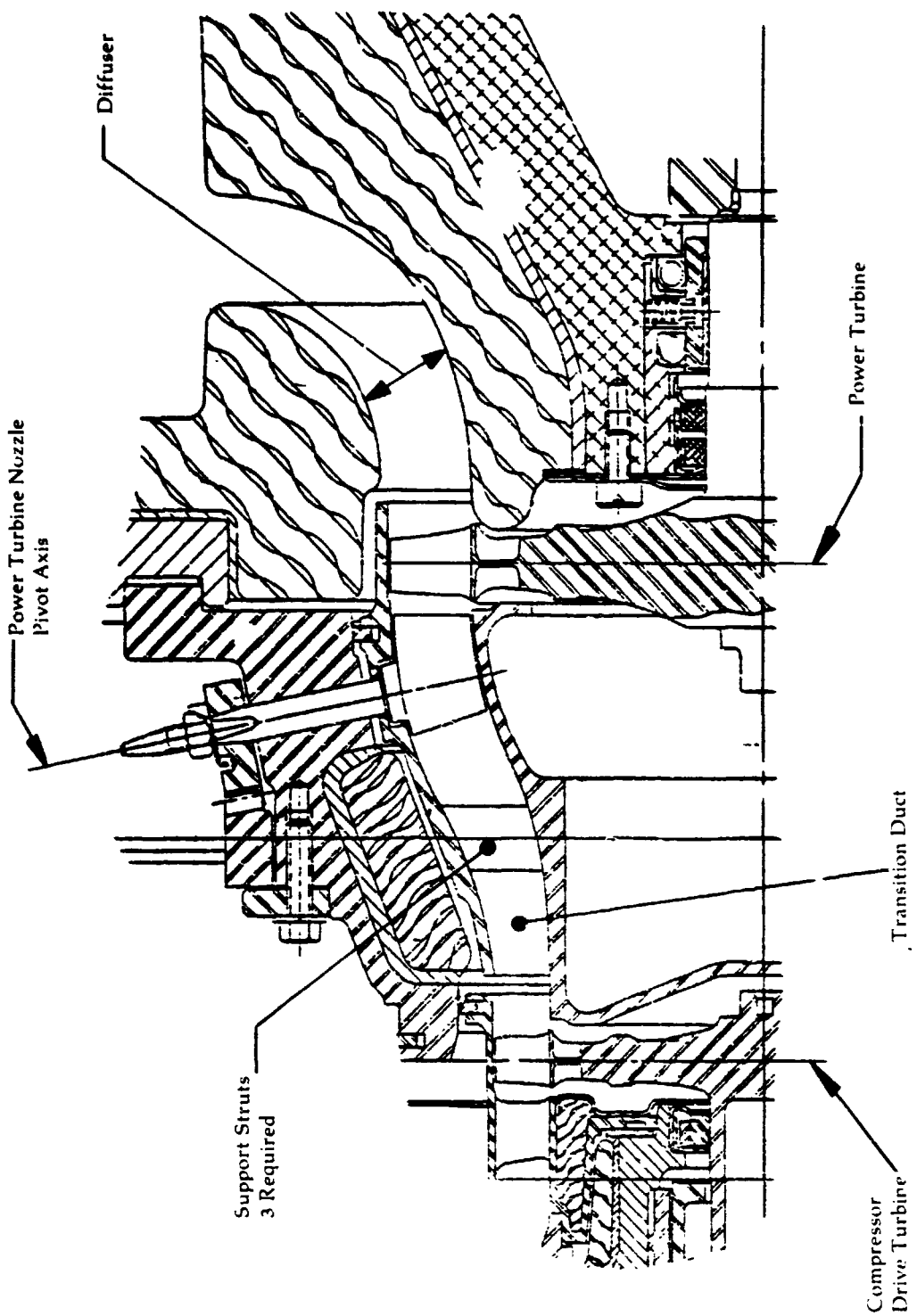

Figure 38

Upgraded Engine
Power Turbine
Free-Stream
Velocity Diagrams

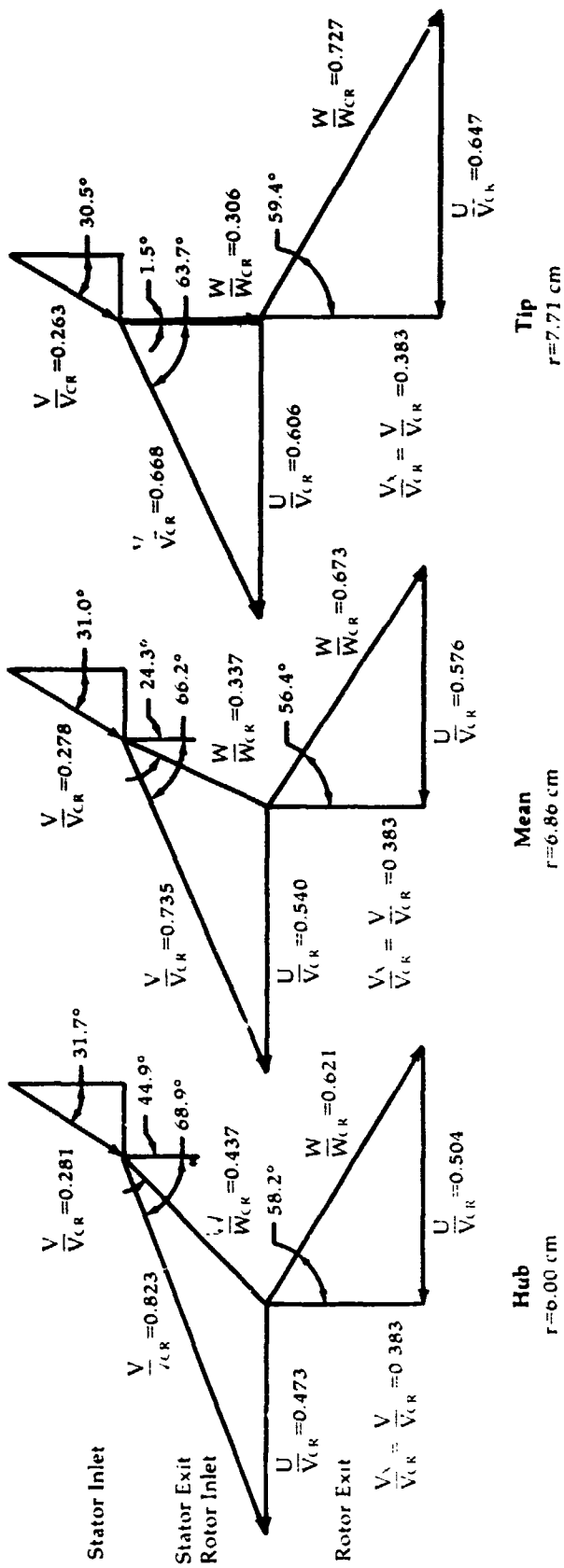

Taken from NASA TM λ-71714

Figure 39

Comparison of Upgraded and Baseline Engines Power Turbine Nozzle Configurations

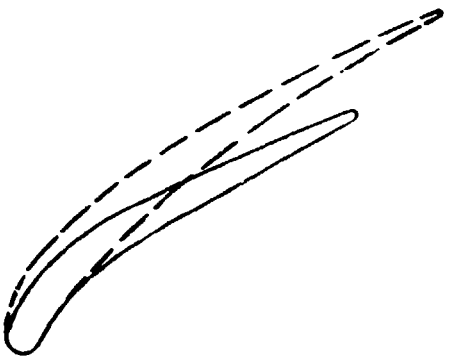

Vane Profile Comparison
At Mean Vane Height

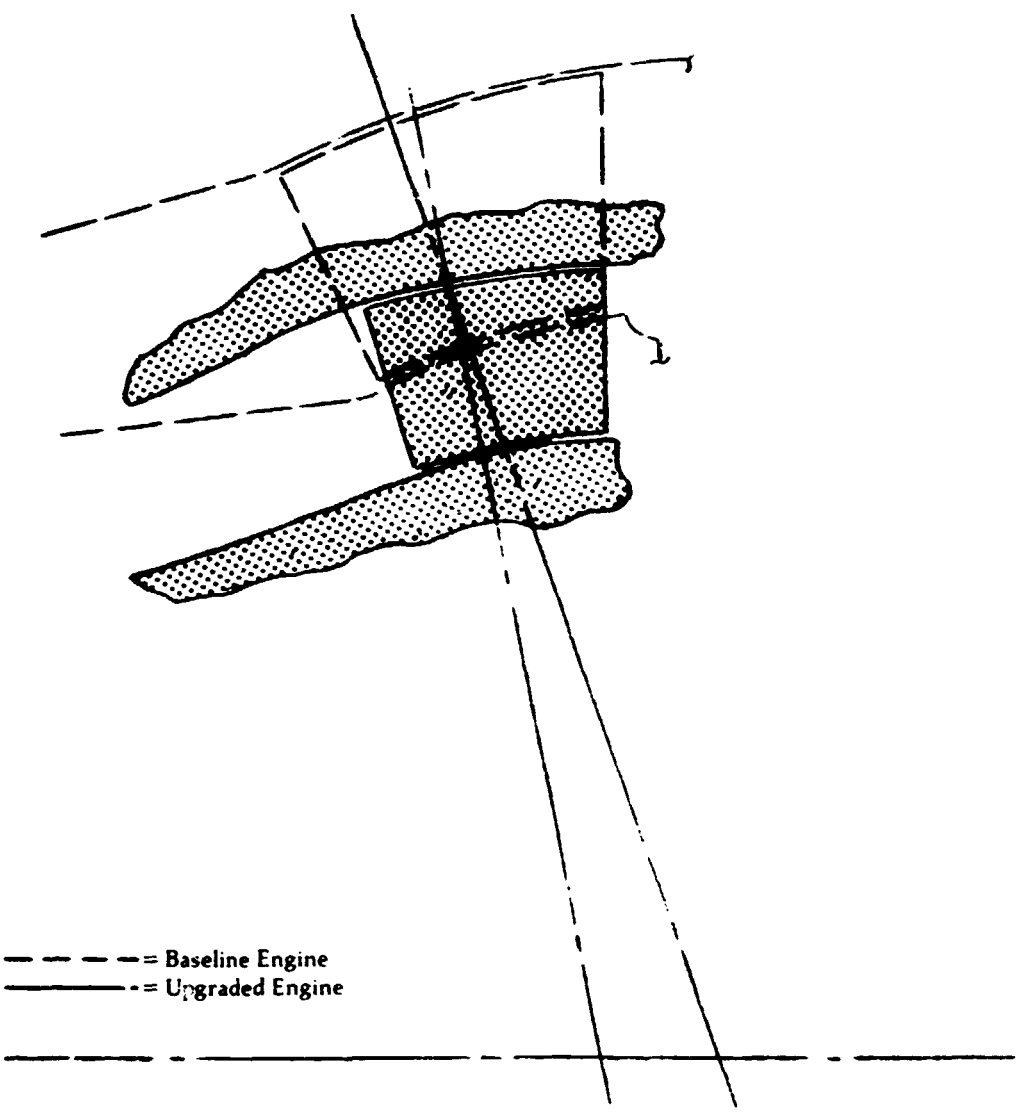

Flow Path Comparison

Figure 40A

Comparison of Upgraded and Baseline Engines Power Turbine Rotor Configurations

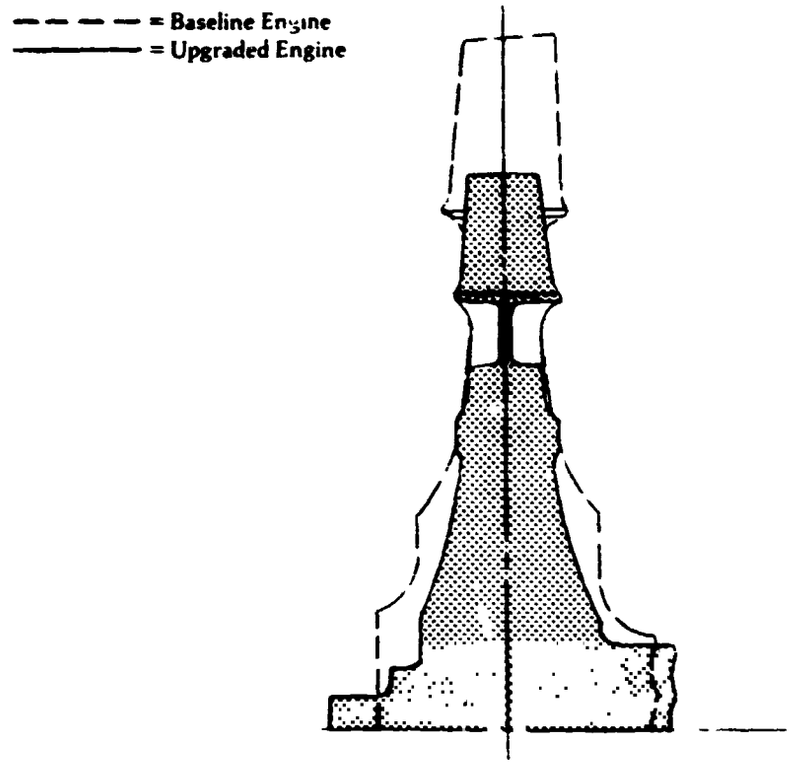

Rotor Comparison

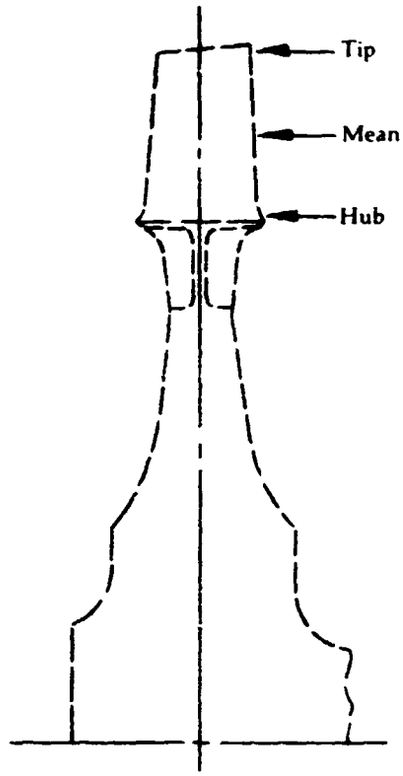

Baseline

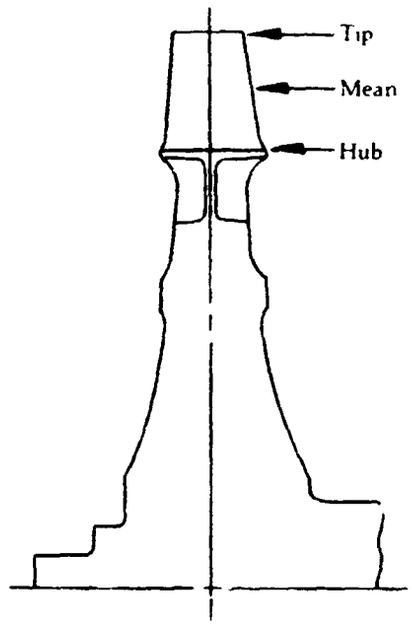

Upgraded

Figure 40B

Comparison of Upgraded and Baseline Engines Power Turbine Rotor Blade Spacing

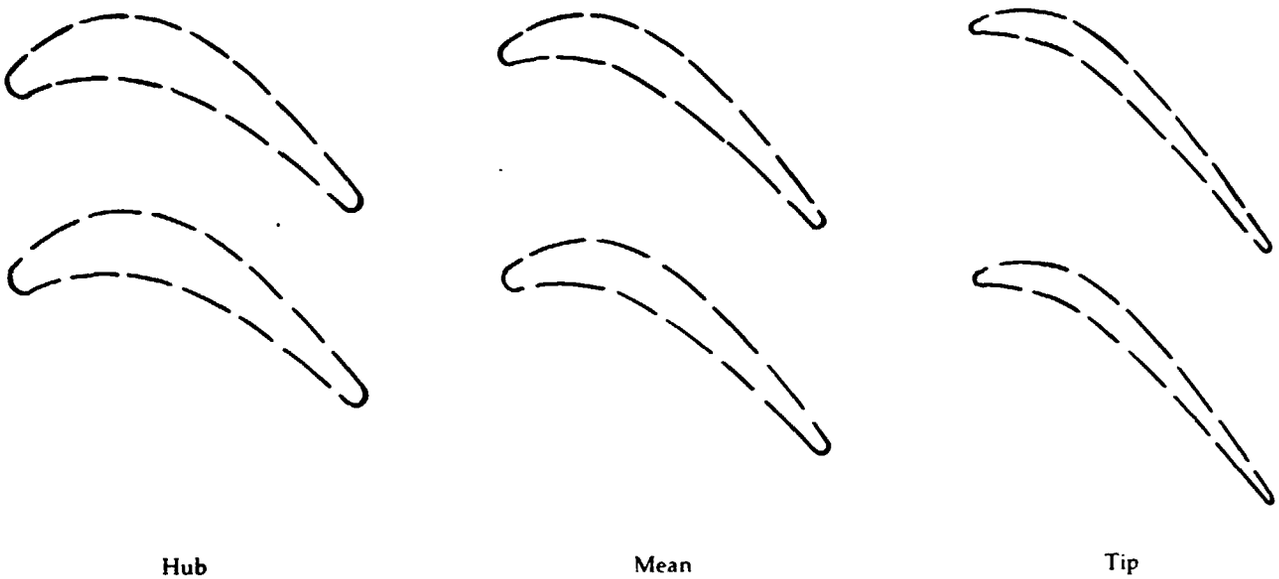

Hub Mean Tip

Baseline Engine

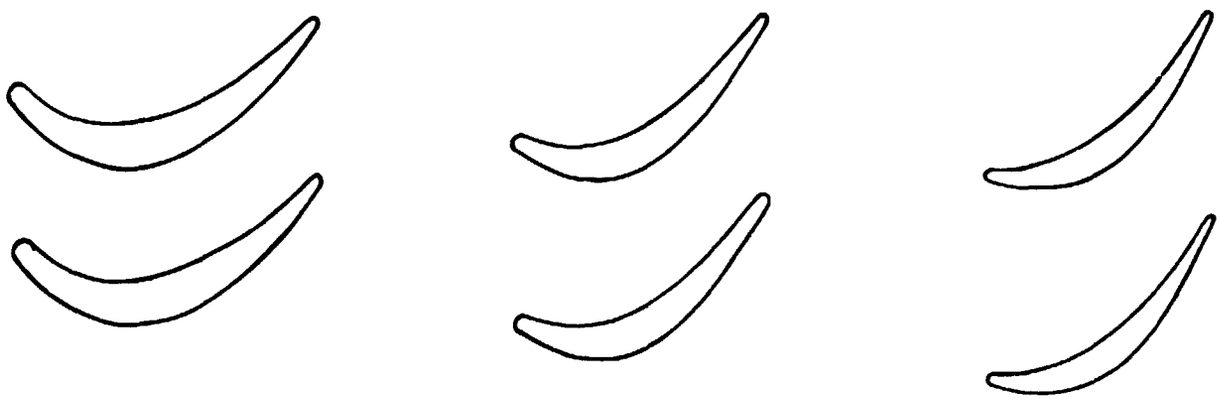

Hub Mean Tip

Upgraded Engine

– – – – = Baseline Engine
——— = Upgraded Engine

Figure 40C

Comparison of Upgraded and Baseline Engines Power Turbine Rotor Blade Configurations

— — — — = Baseline Engine
———— = Upgraded Engine

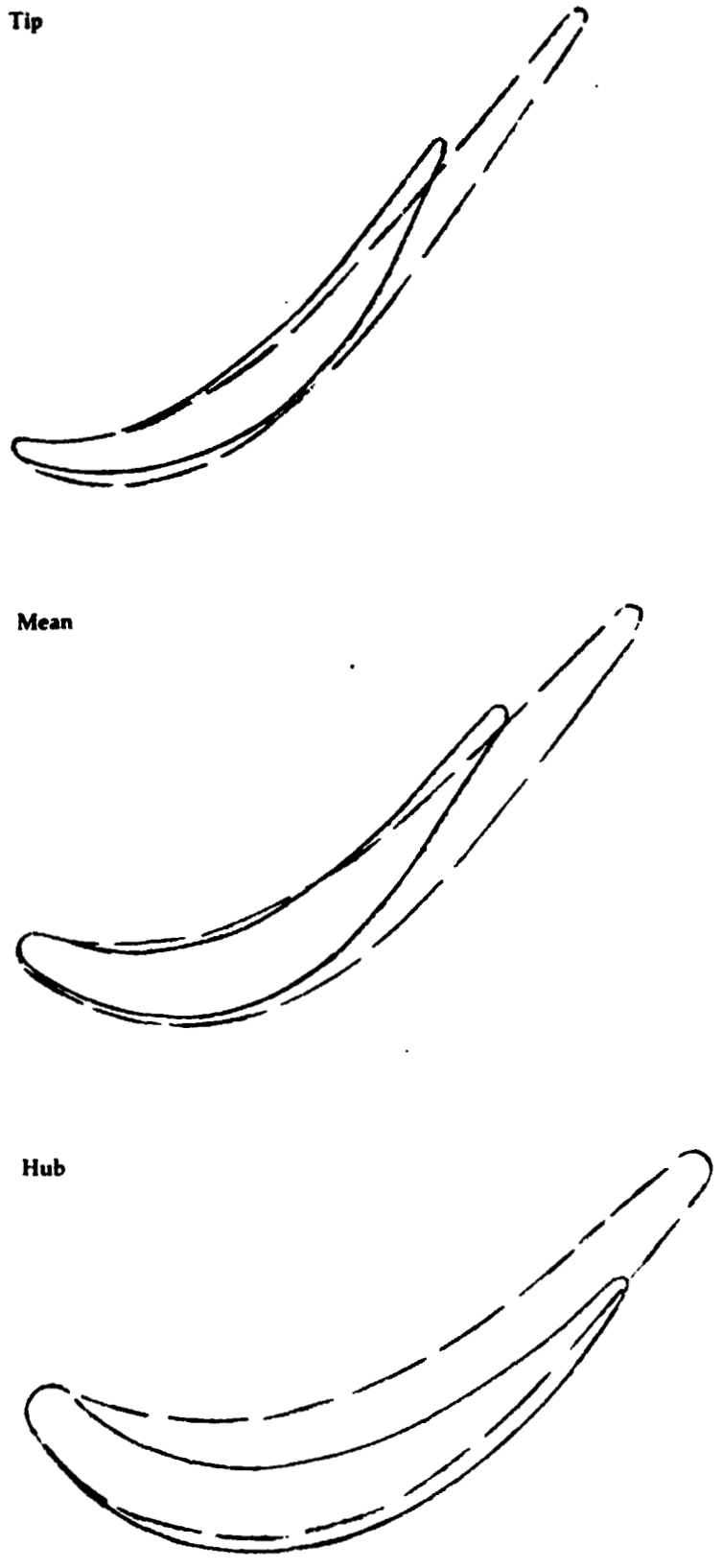

Figure 40D

Comparison of Upgraded and Baseline Engines Pocket Section Configurations Power Turbine Rotor

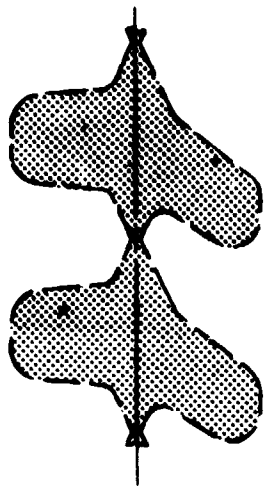

Section A-A
Enlarged View

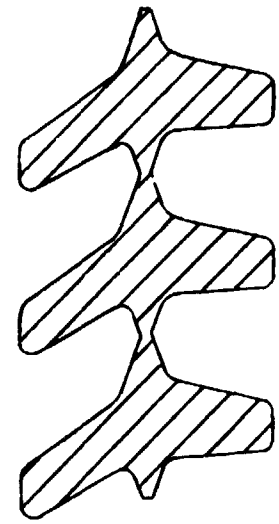

Section A-A
Enlarged View

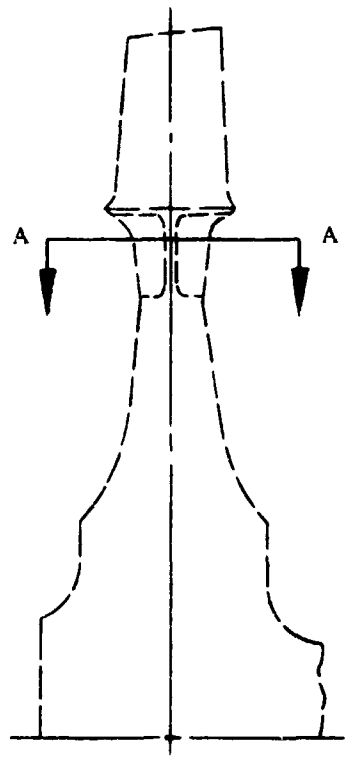

Baseline

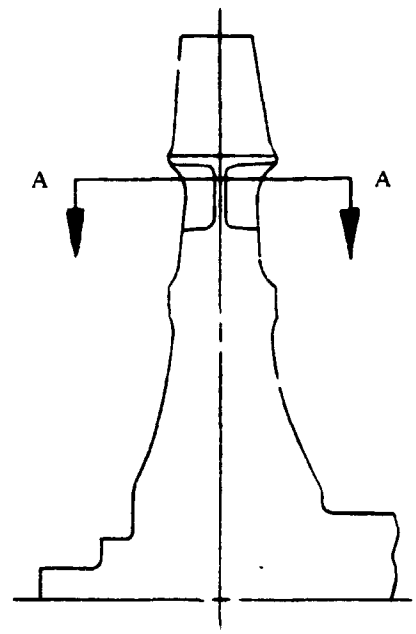

Upgraded

— — — — = Baseline Engine
——— = Upgraded Engine

Figure 40E

Comparison of Upgraded and Baseline Engines Exhaust Diffuser Configurations

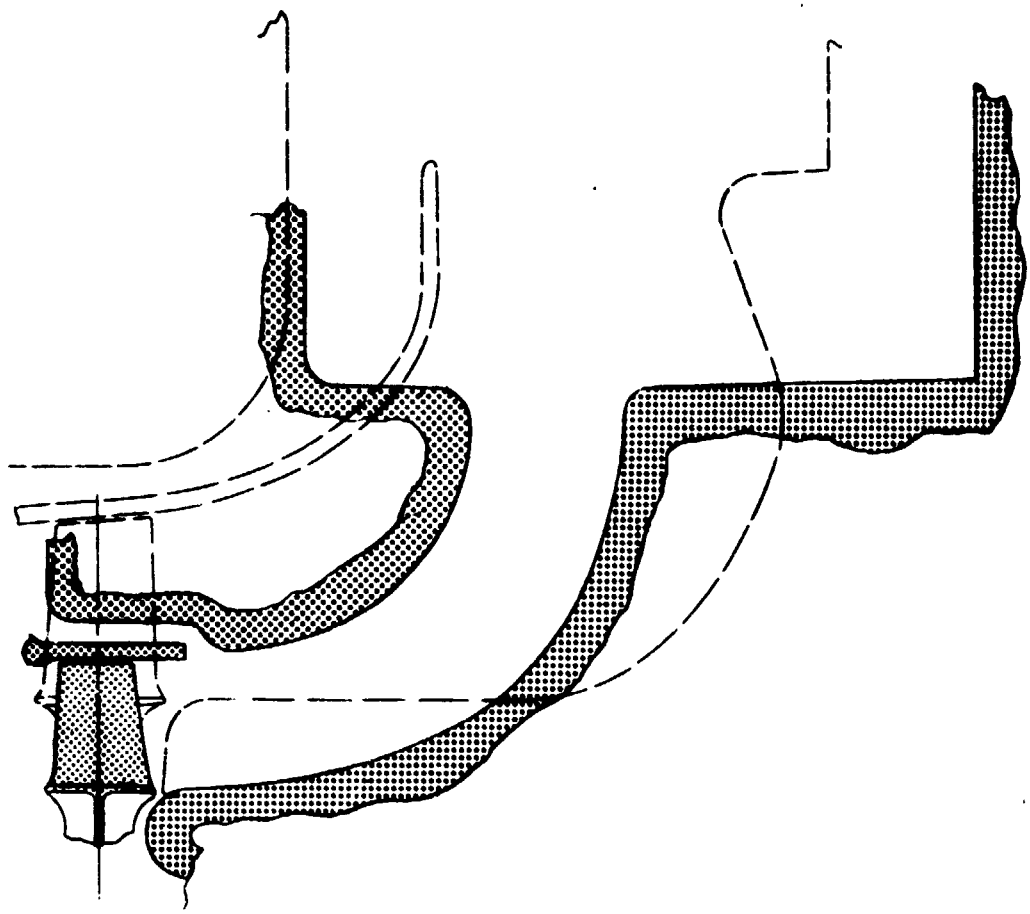

Exhaust Diffuser Flow Path Comparison

— — — —= Baseline Engine
———— = Upgraded Engine

Figure 40F

Upgraded Engine Design Power Turbine Stator Blade Surface Velocities

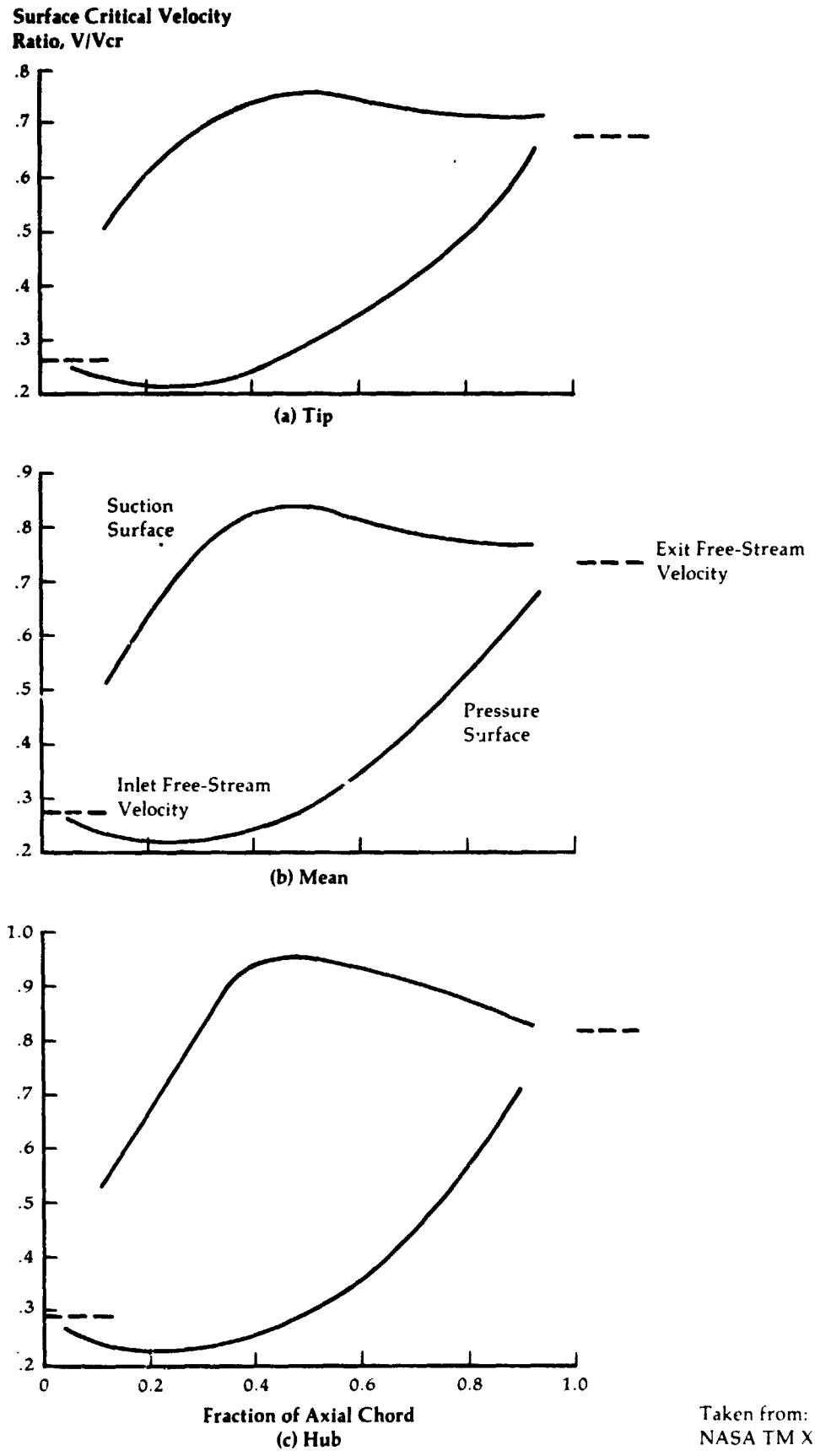

Taken from:
NASA TM X-71719

Figure 41

Upgraded Engine Design Power Turbine Rotor Blade Surface Velocities

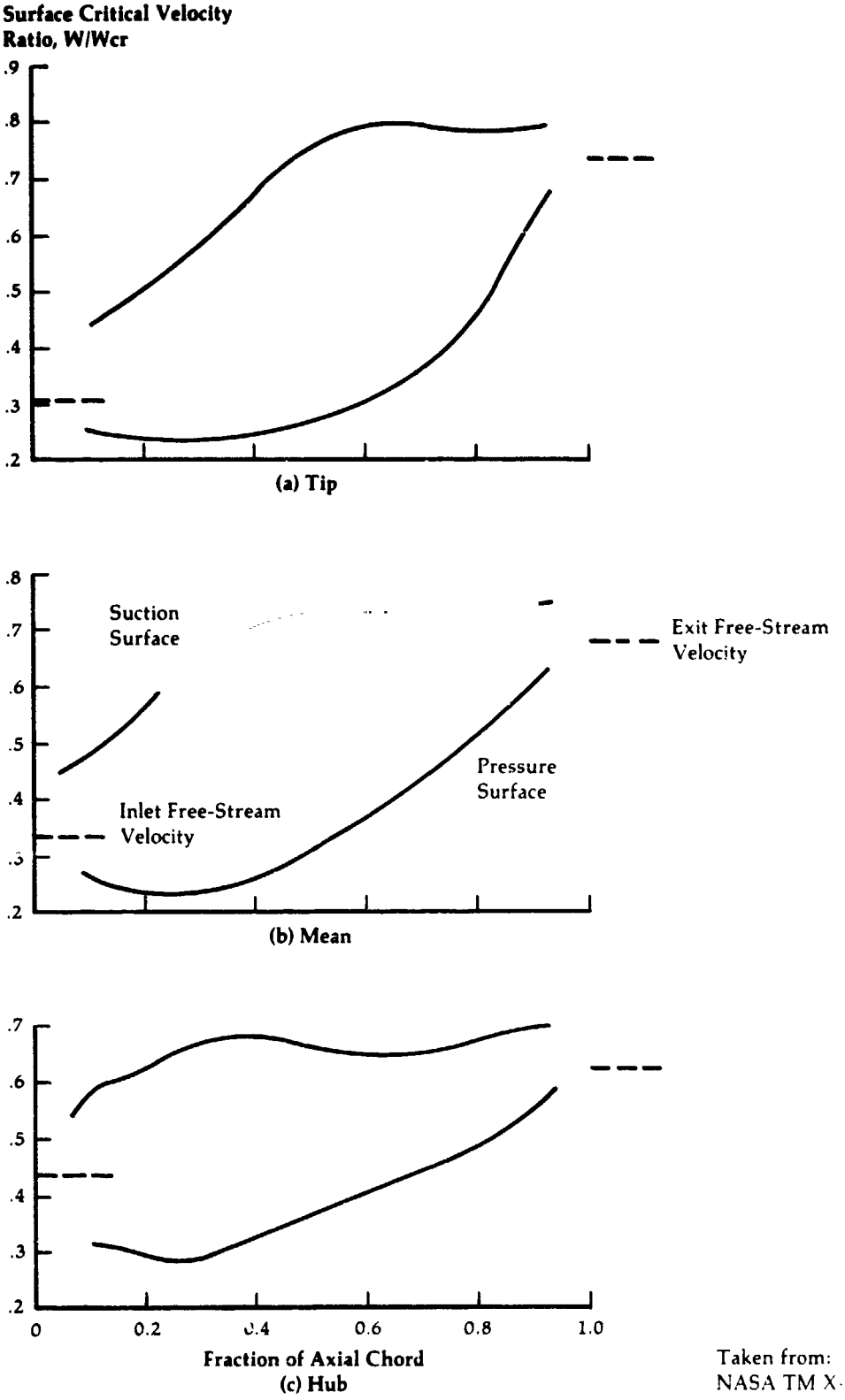

Taken from:
NASA TM X-71719

Figure 42

Upgraded Engine Interstage Duct Velocity Distributions Design Point

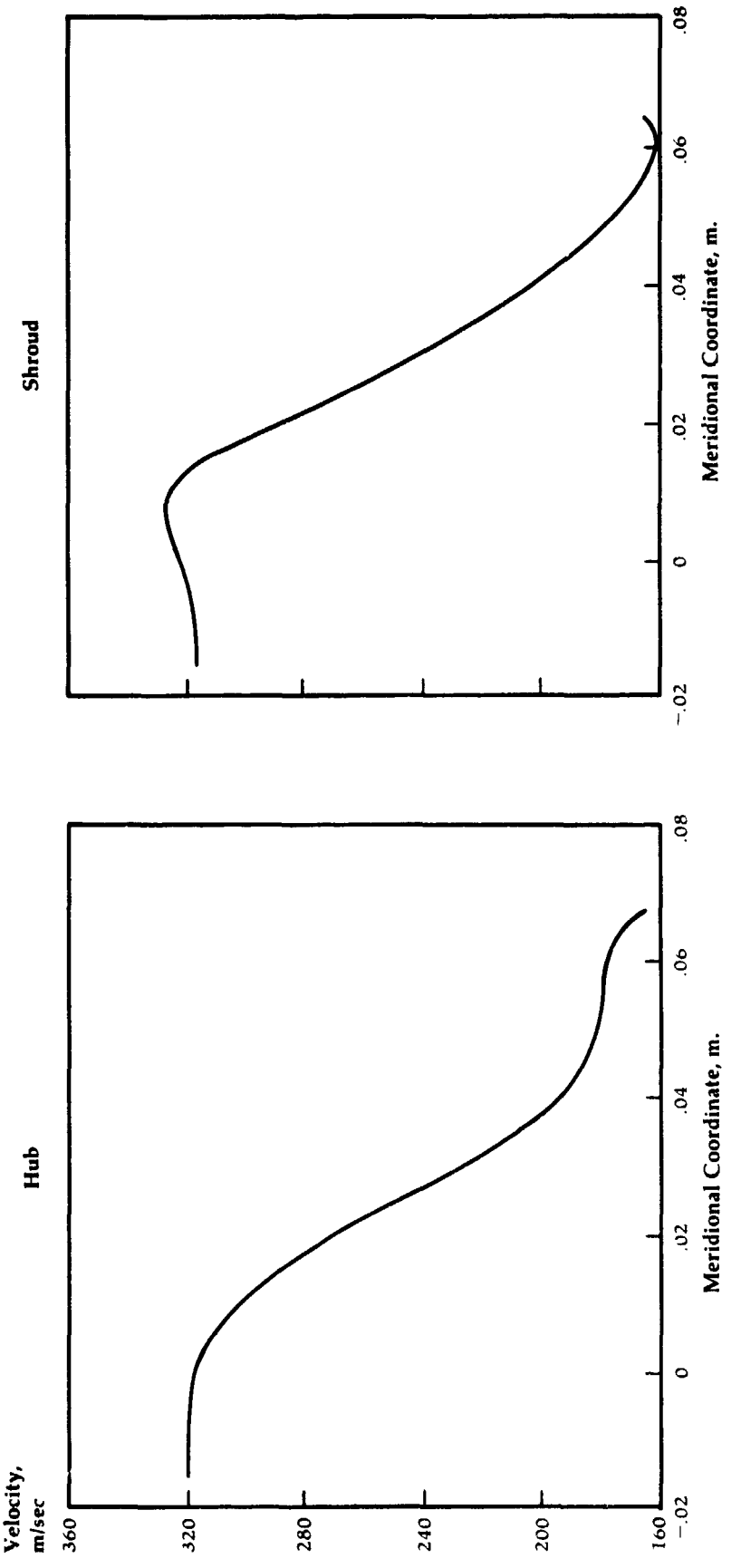

Taken from:
NASA TM X-71719

Figure 43

Upgraded Engine Interstage Duct Velocity Distributions 50% Gas Generator Speed Operating Point

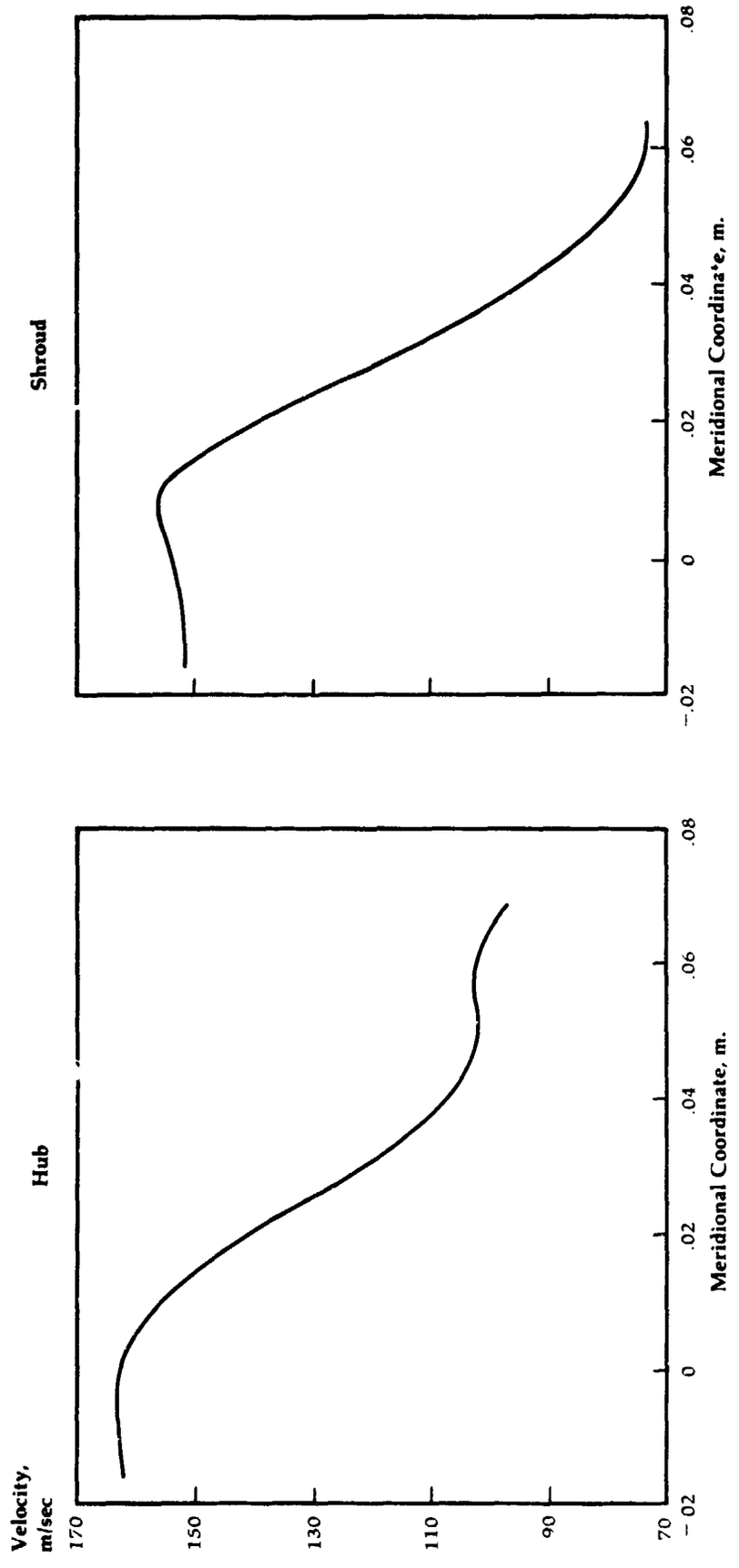

Taken from:
NASA TM X-71719

Figure 44

Upgraded Engine Exhaust Diffuser Velocity Distributions Design Point

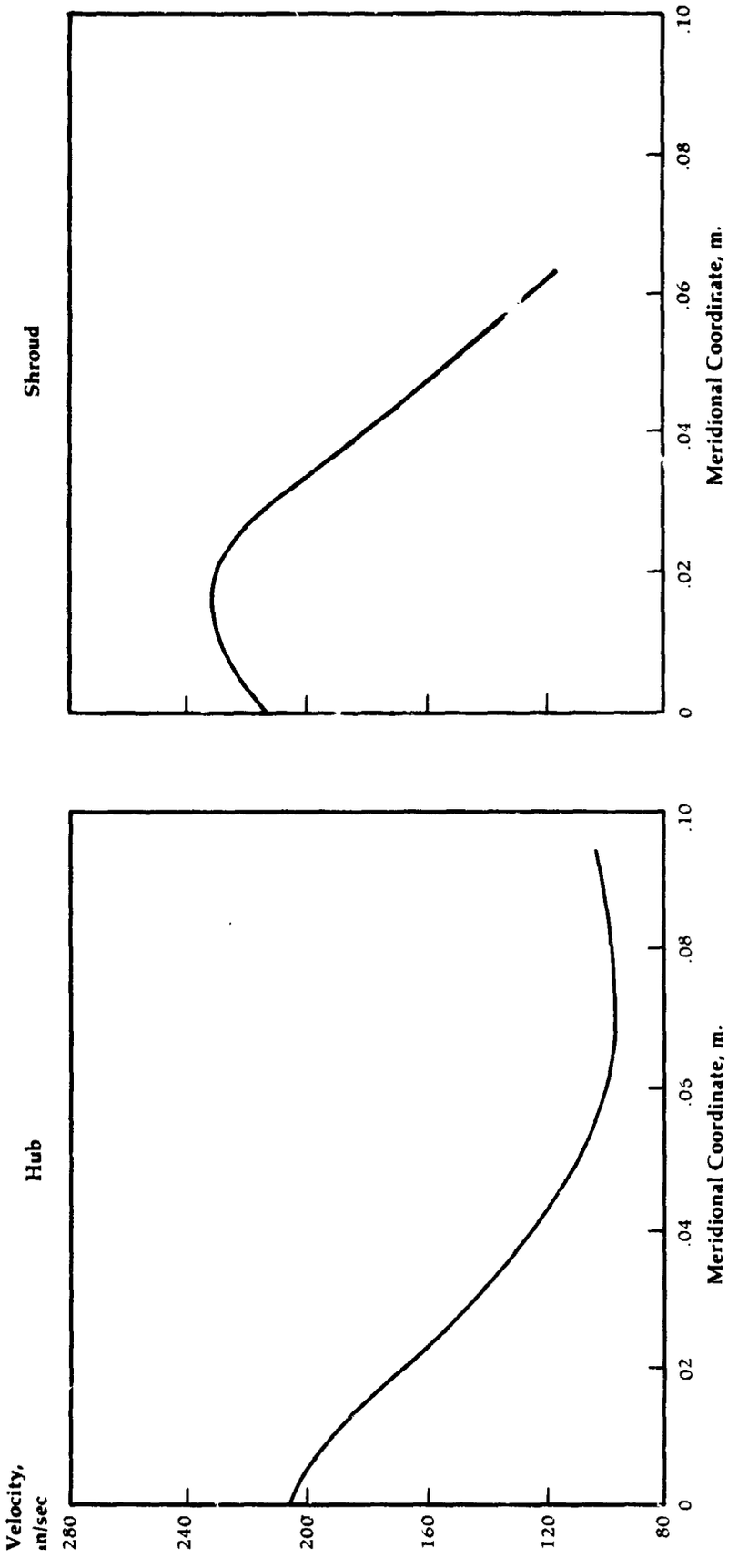

Taken from:
NASA TM X-71719

Figure 45

Upgraded Engine Power Turbine Performance Estimate

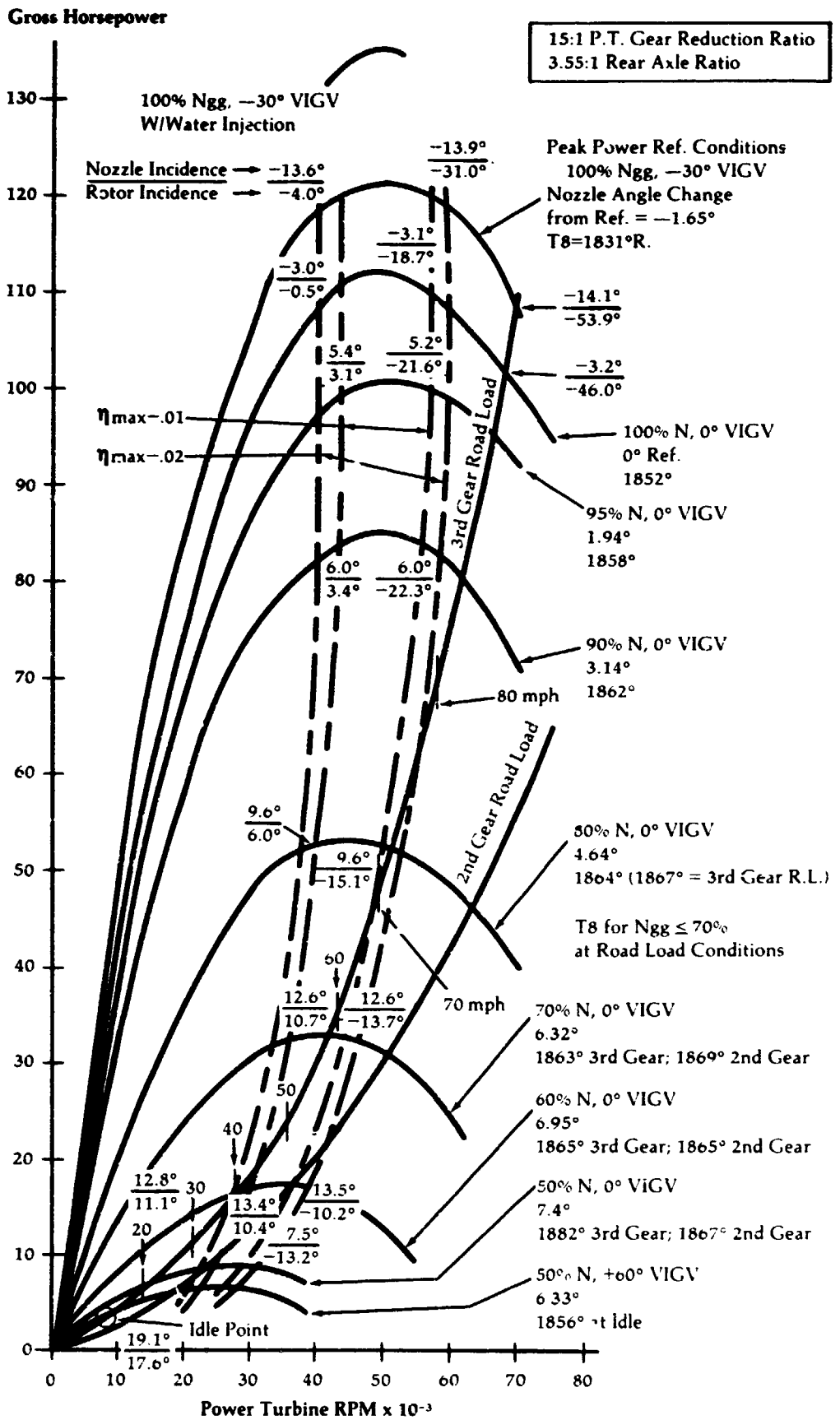

Figure 46

Upgraded Engine Power Turbine Efficiency Estimate

Efficiency Based on Interstage Diffuser Inlet Total Pressure and Exhaust Diffuser Discharge Static Pressure. 3.55:1 Rear Axle

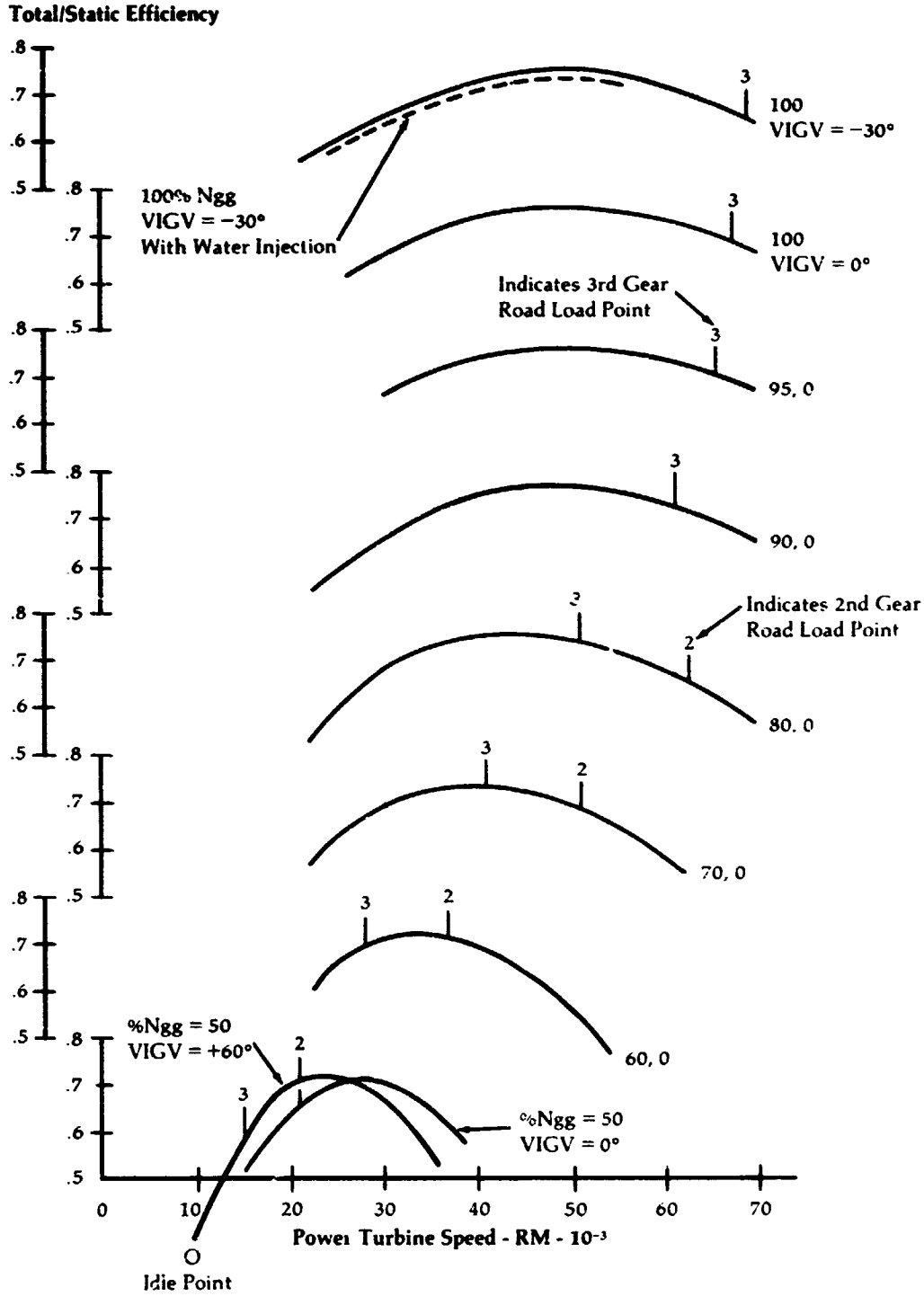

Figure 47

Upgraded Engine Power Turbine Blade Vibration Campbell Diagram

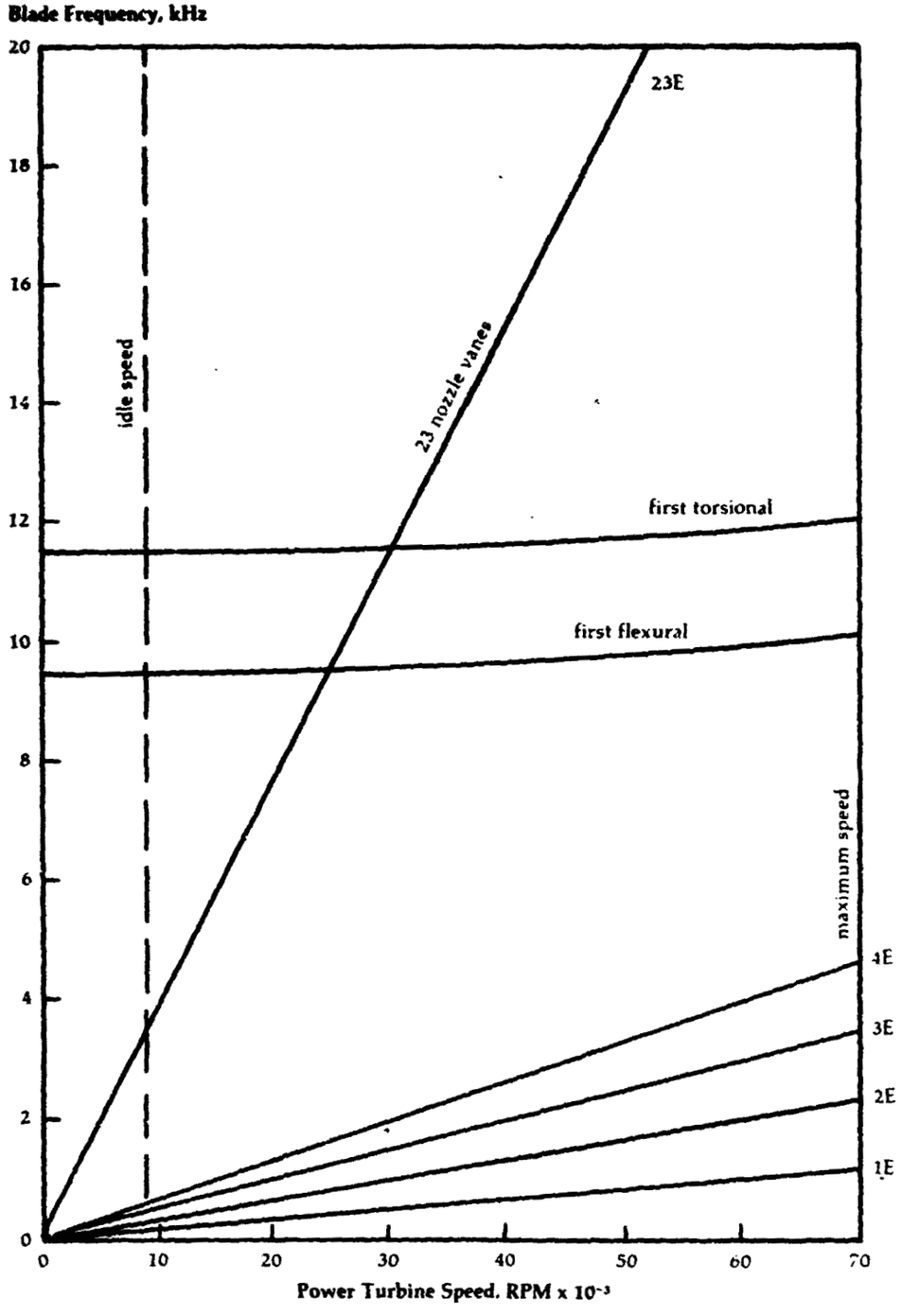

Figure 48

Upgraded Engine
Power Turbine
Blade Fatigue
Modified Goodman
Diagram

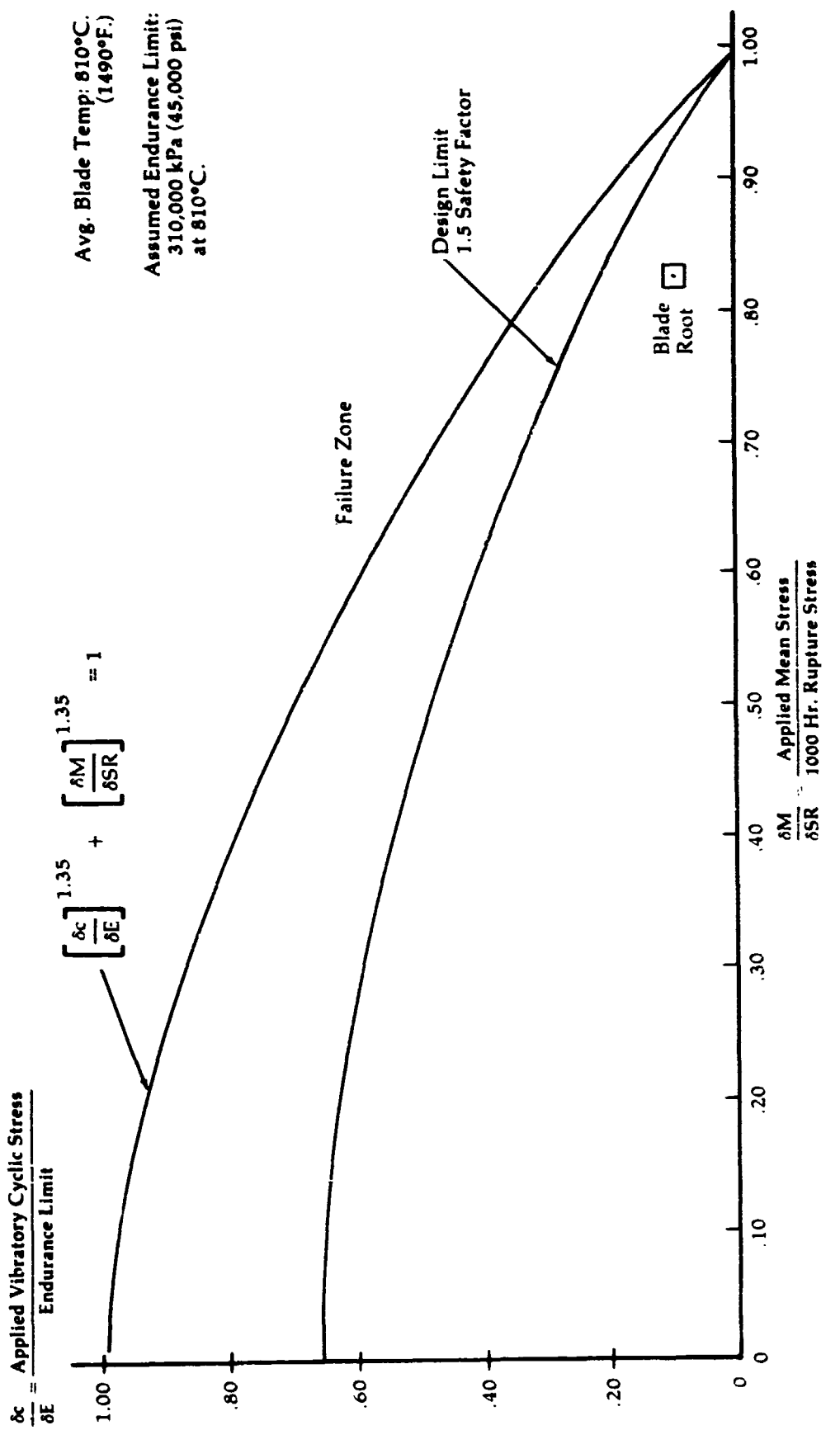

Figure 49A

Upgraded Engine Power Turbine Rotor Structural Analysis Summary

Mechanical Speed - 7330 Rad/Sec (70,000 RPM)
Avg. Tangential Stress - 440,000 kPa (63,700 psi)
Burst Speed - 8,800 Rad/Sec (84,000 RPM)
Burst Factor - 1.20
Material - MM-002

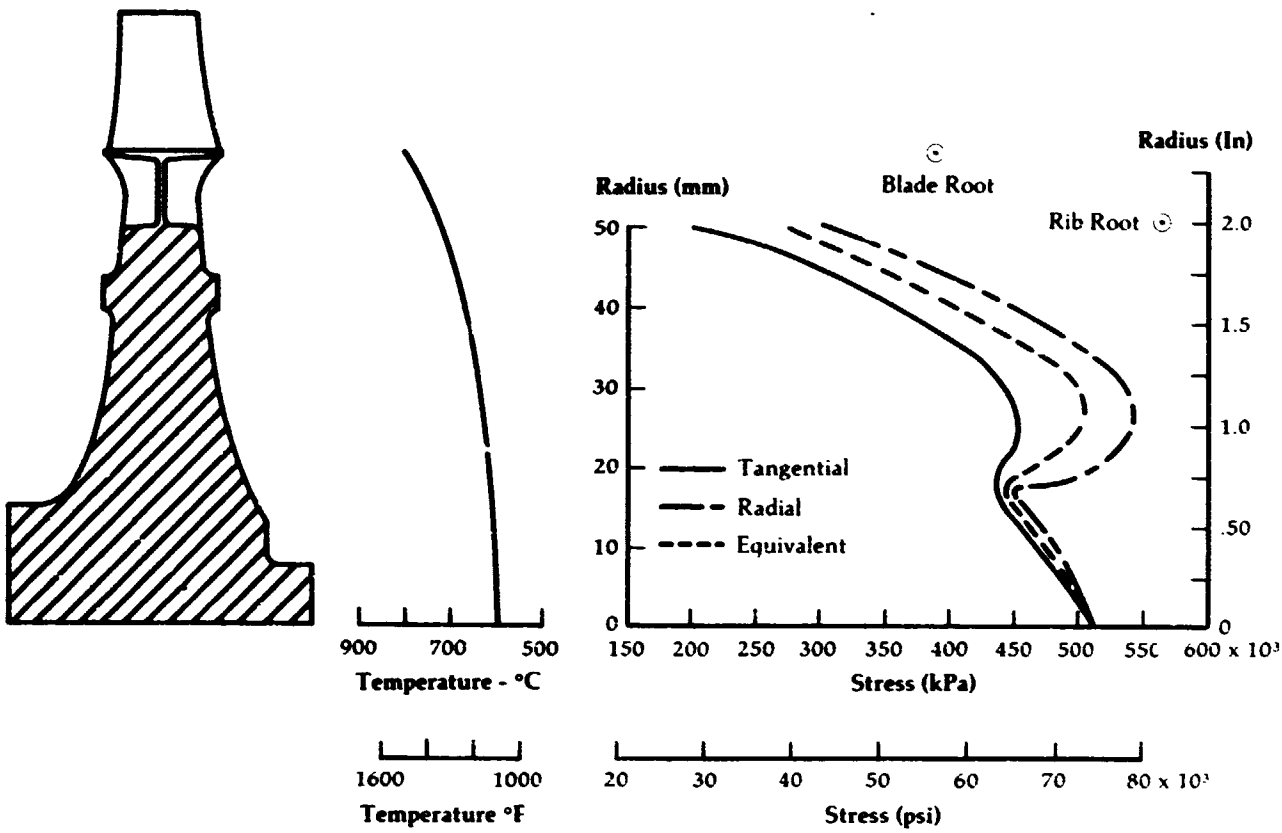

Figure 49B

Upgraded Engine
Engine Housing
Configuration

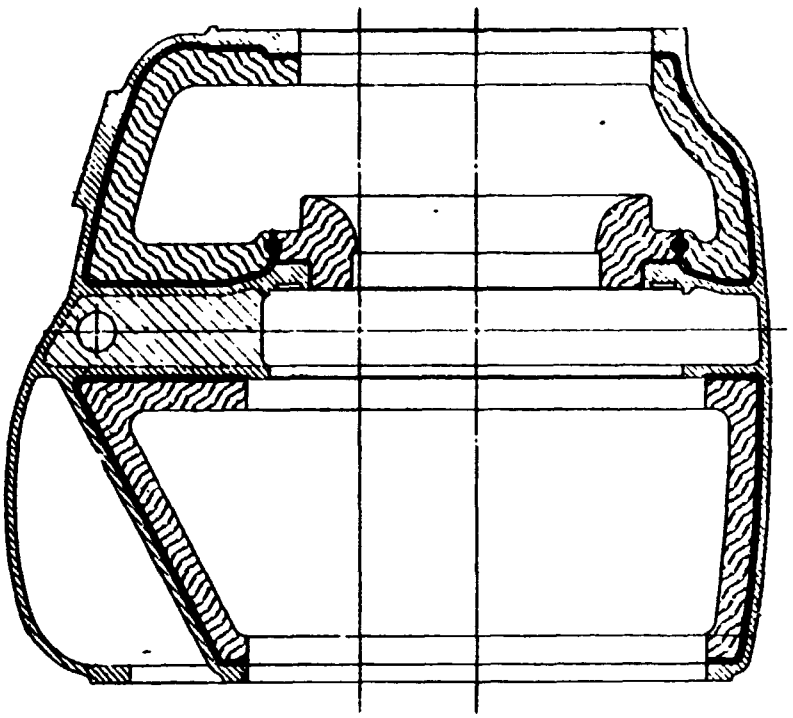

Section A-A

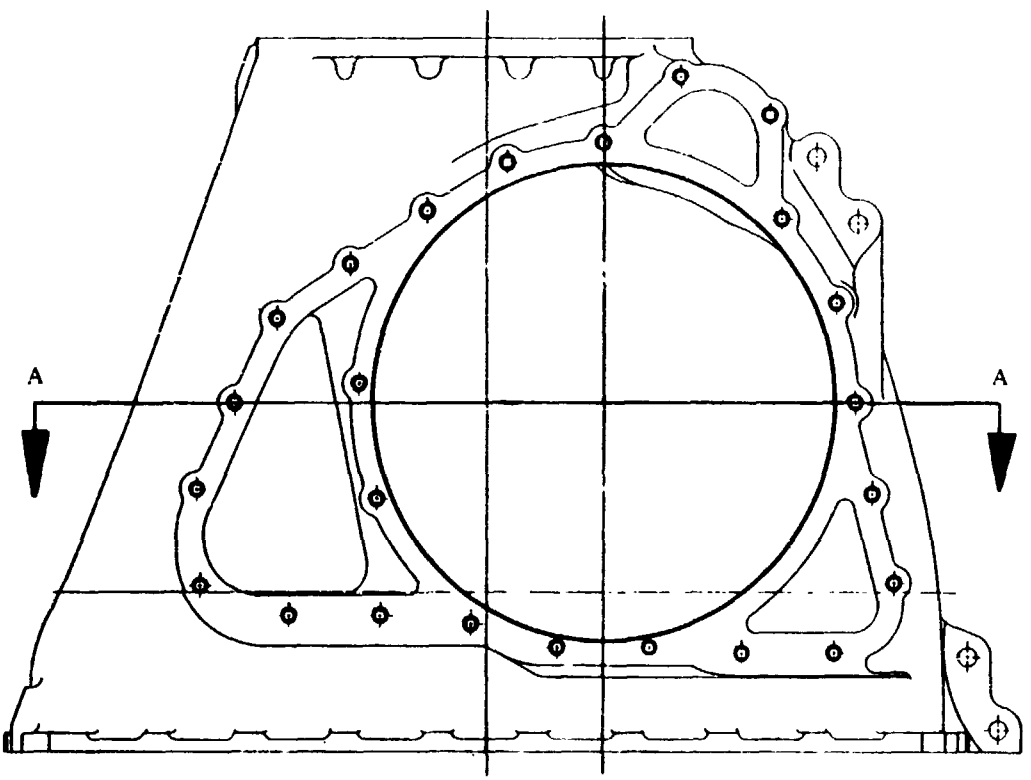

Figure 50A

Upgraded Engine Engine Housing Showing Bulkhead and Burner Wall Structural Arrangement

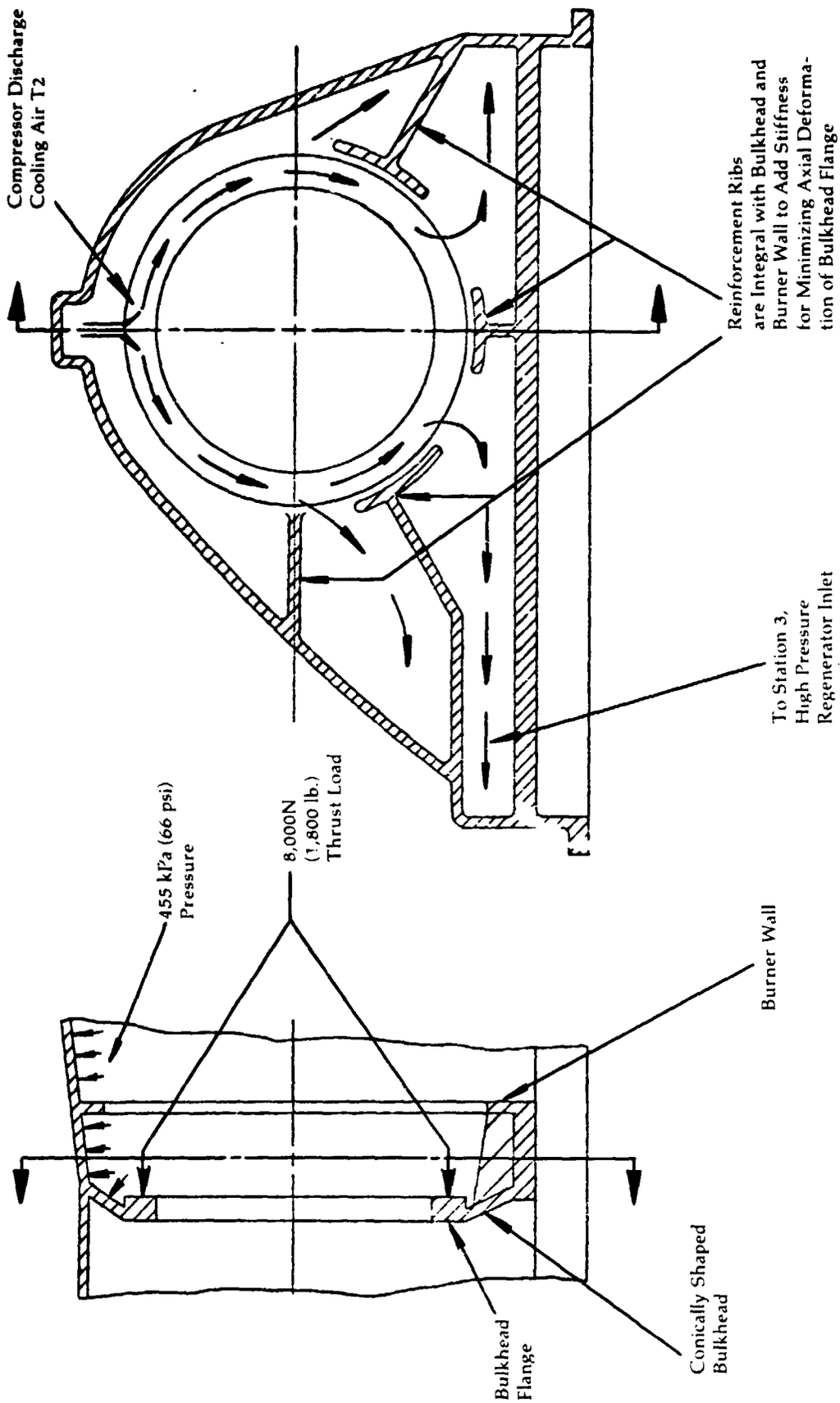

Figure 50B

Upgraded Engine Finite Element Model of Housing Section (Undeformed Shape)

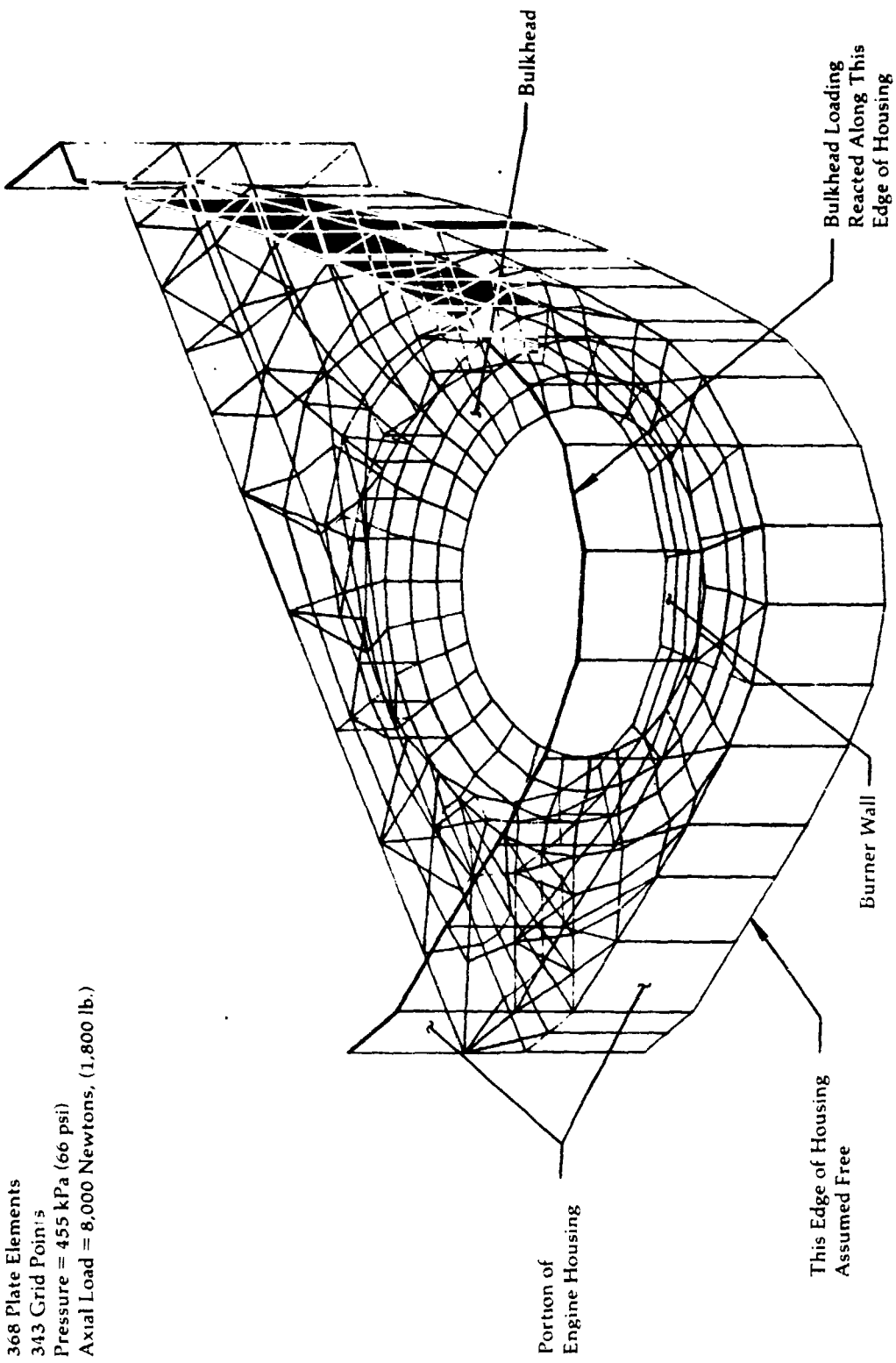

Figure 51

Upgraded Engine Engine Housing Bulkhead Structural Analysis - Summary

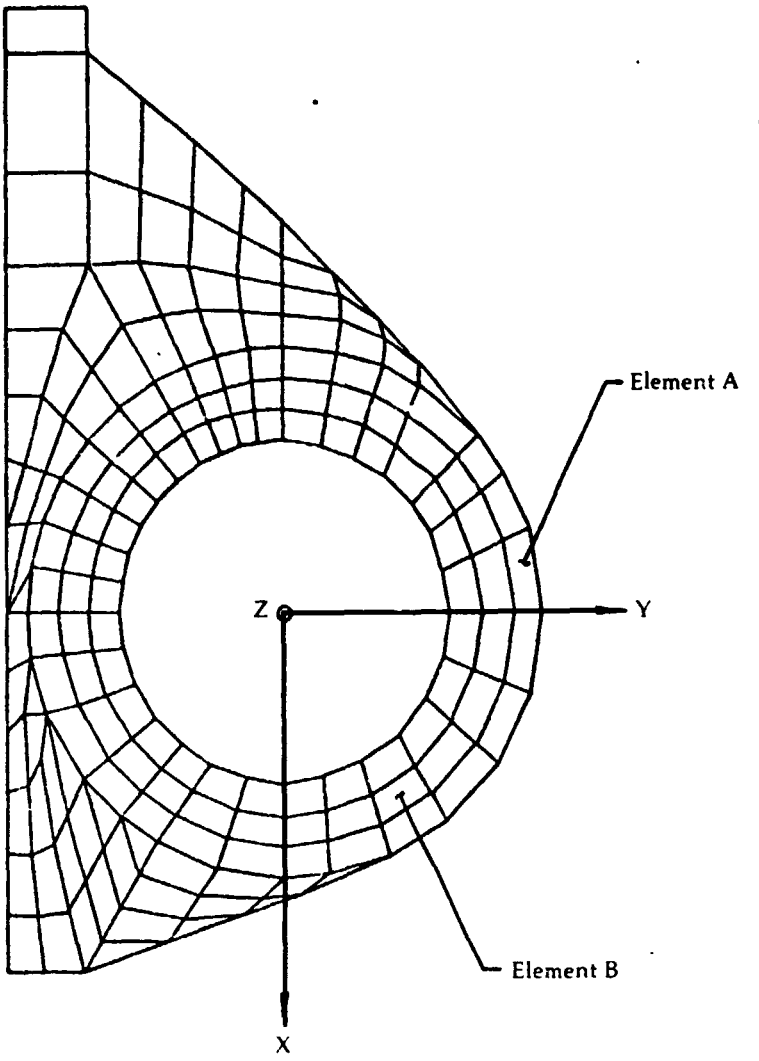

Elements of Maximum Stress

Combined Loading Stress, kPa x 10^{-3}, (ksi)					
Element	Sigma-X	Sigma-Y	TAU-XY	Max. Principal	Equivalent
A	17.9 (−2.6)	−164.2 (−23.8)	−6.9 (−1.0)	−128.3 (−18.6)	111.8 (16 2)
B	−6.2 (−0 9)	−53 8 (−8.7)	5.5 (0.8)	−47.6 (−6.9)	41.4 (6.0)

Figure 52

Photographs of Foam Model used to Check Engine Installation In Vehicle

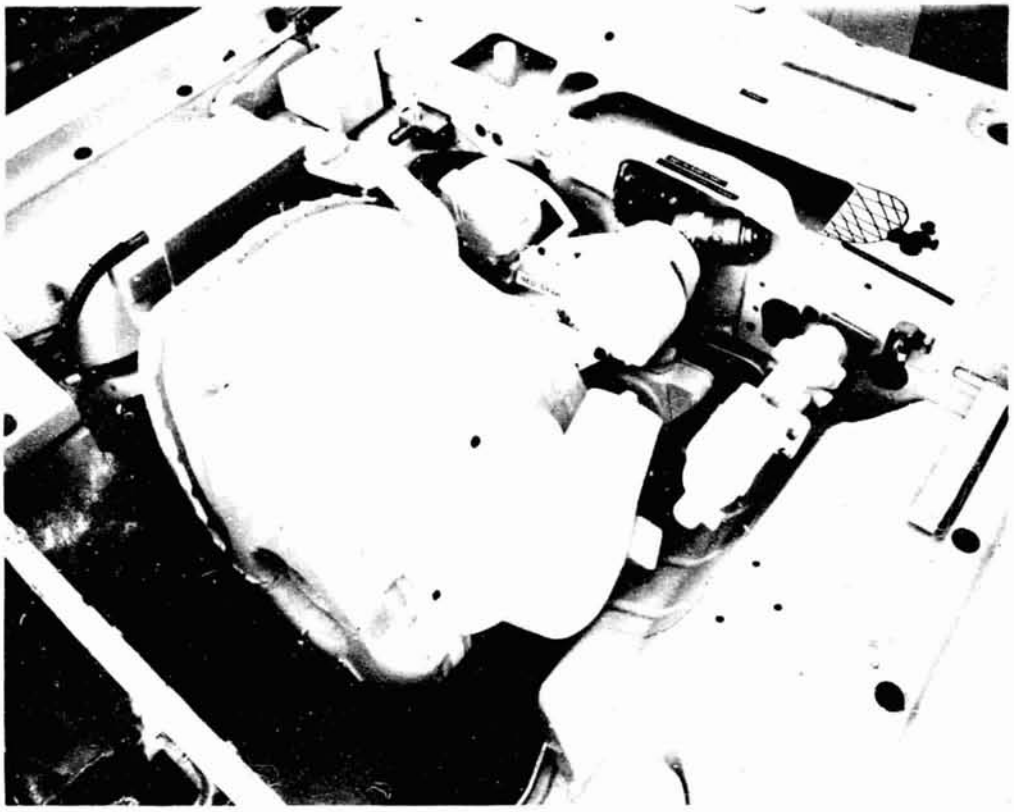

Figure 53

Right Front View - Engine Housing Model

Figure 54

Left Front View - Engine Housing Model

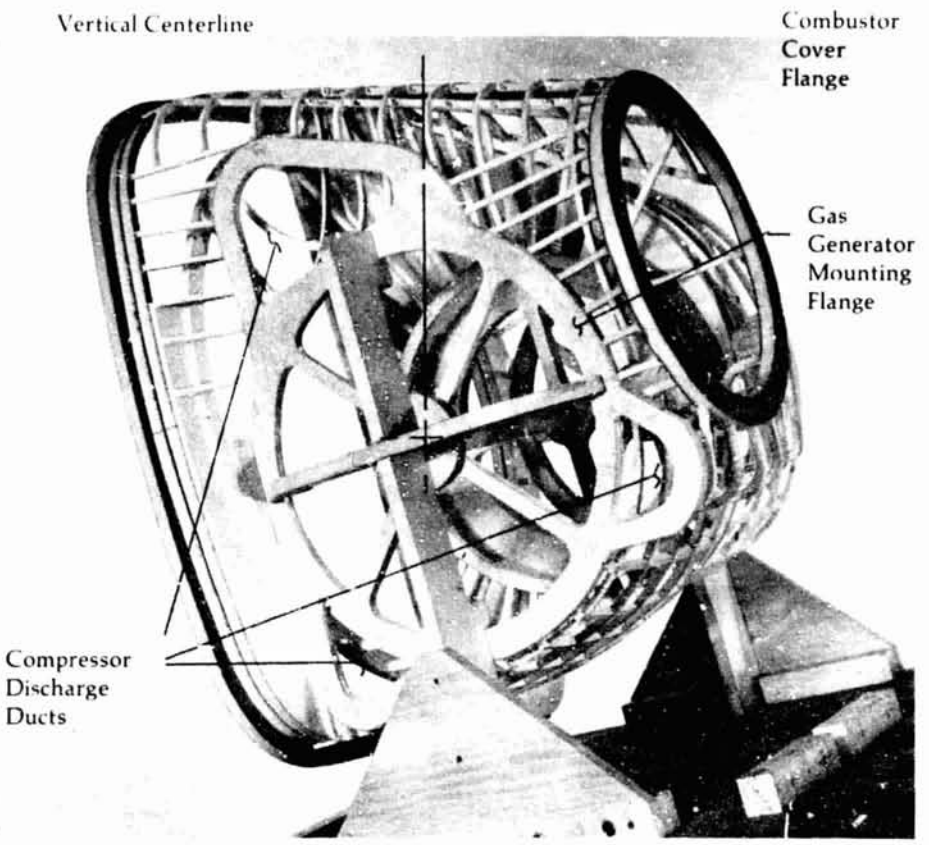

Figure 55

Rear View - Engine Housing Model

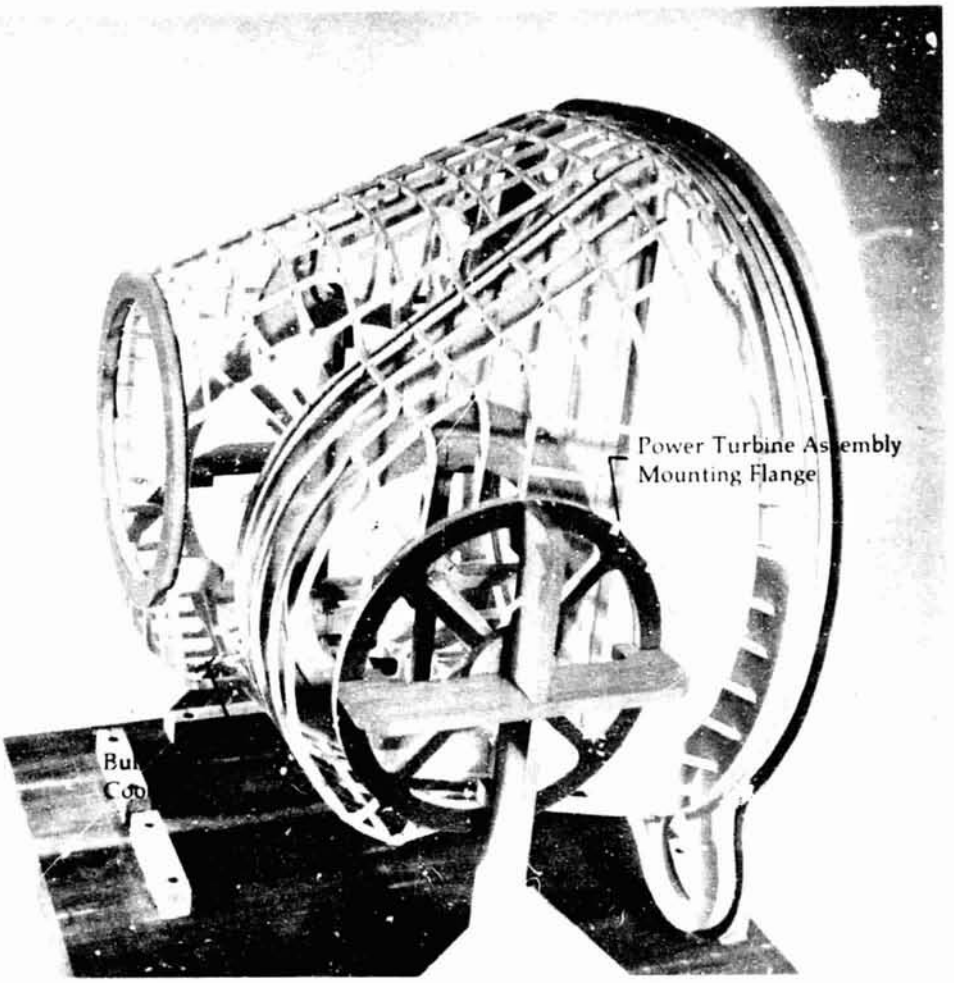

Figure 56

Upgraded Engine
Housing Tooling

Wood pattern assembly, drag and cope patterns, core assembly checking fixture, and core boxes.

Upgraded Engine Housing Tooling

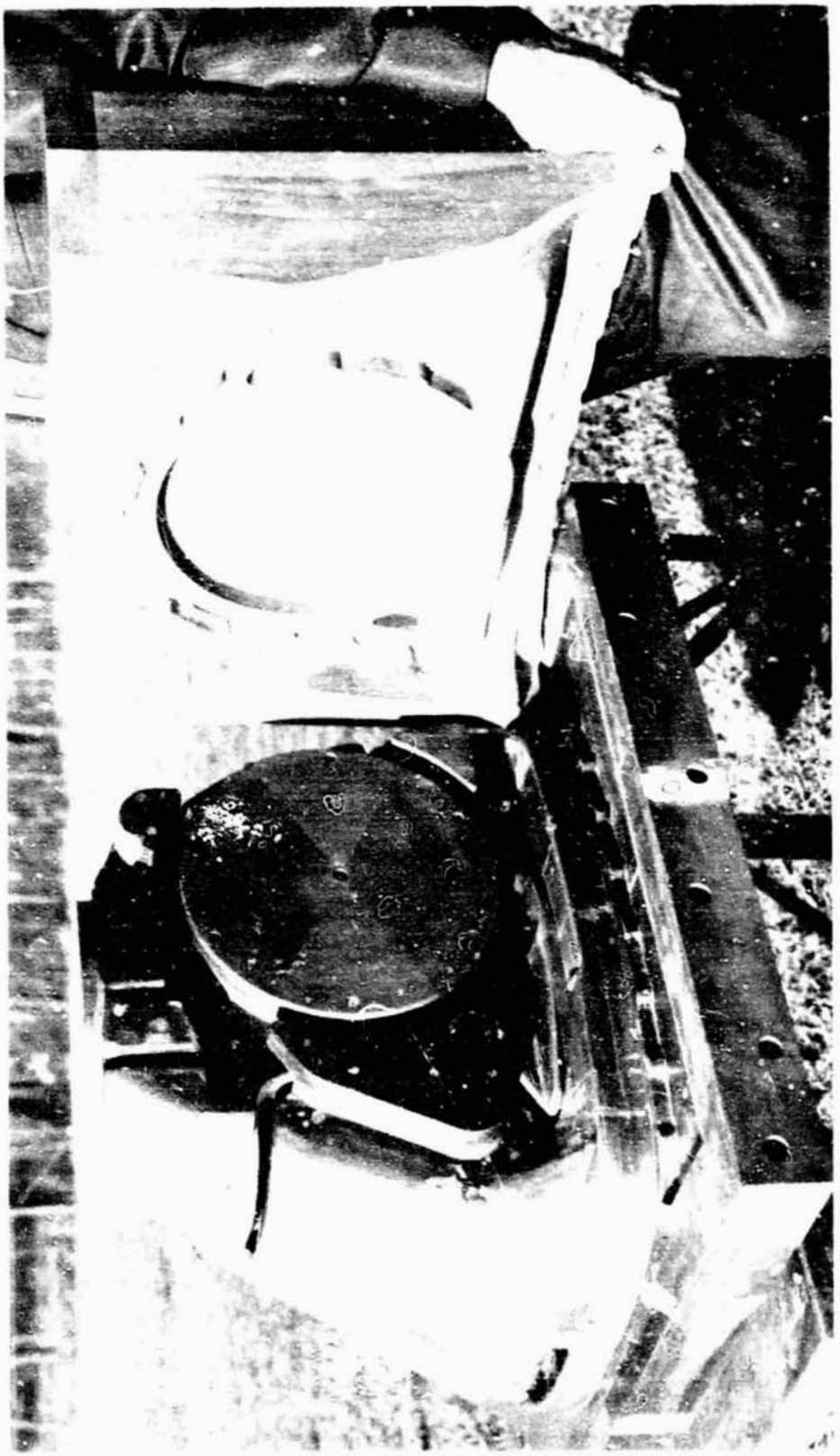

Wood pattern (inner metal wall) viewing gas generator opening.

Upgraded Engine Housing Tooling

Plastic and aluminum cope pattern (outer surface) viewing burner and power turbine flanges.

Housing Crossarm Insulation Proposal

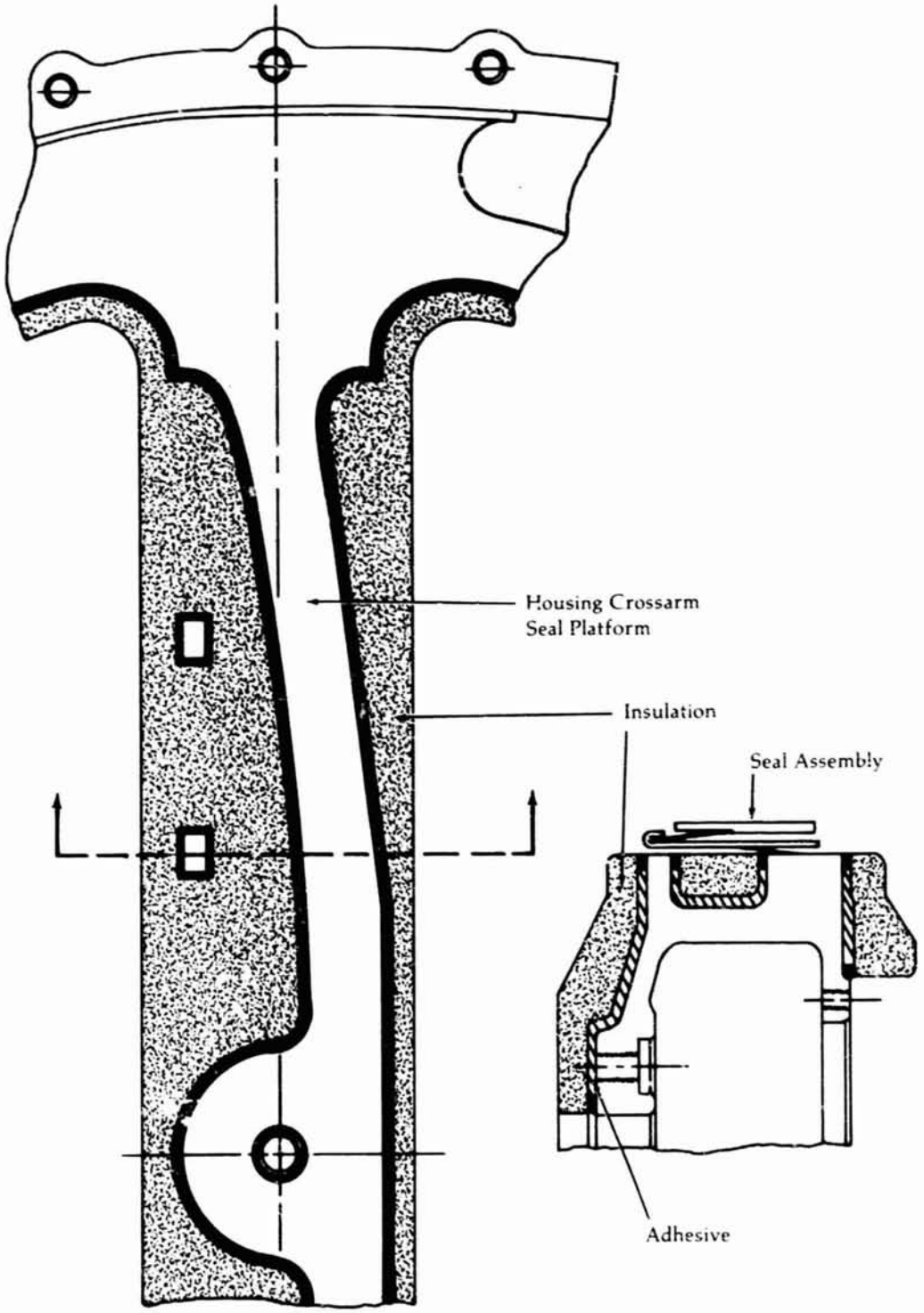

Upgraded Engine Gas Generator Section

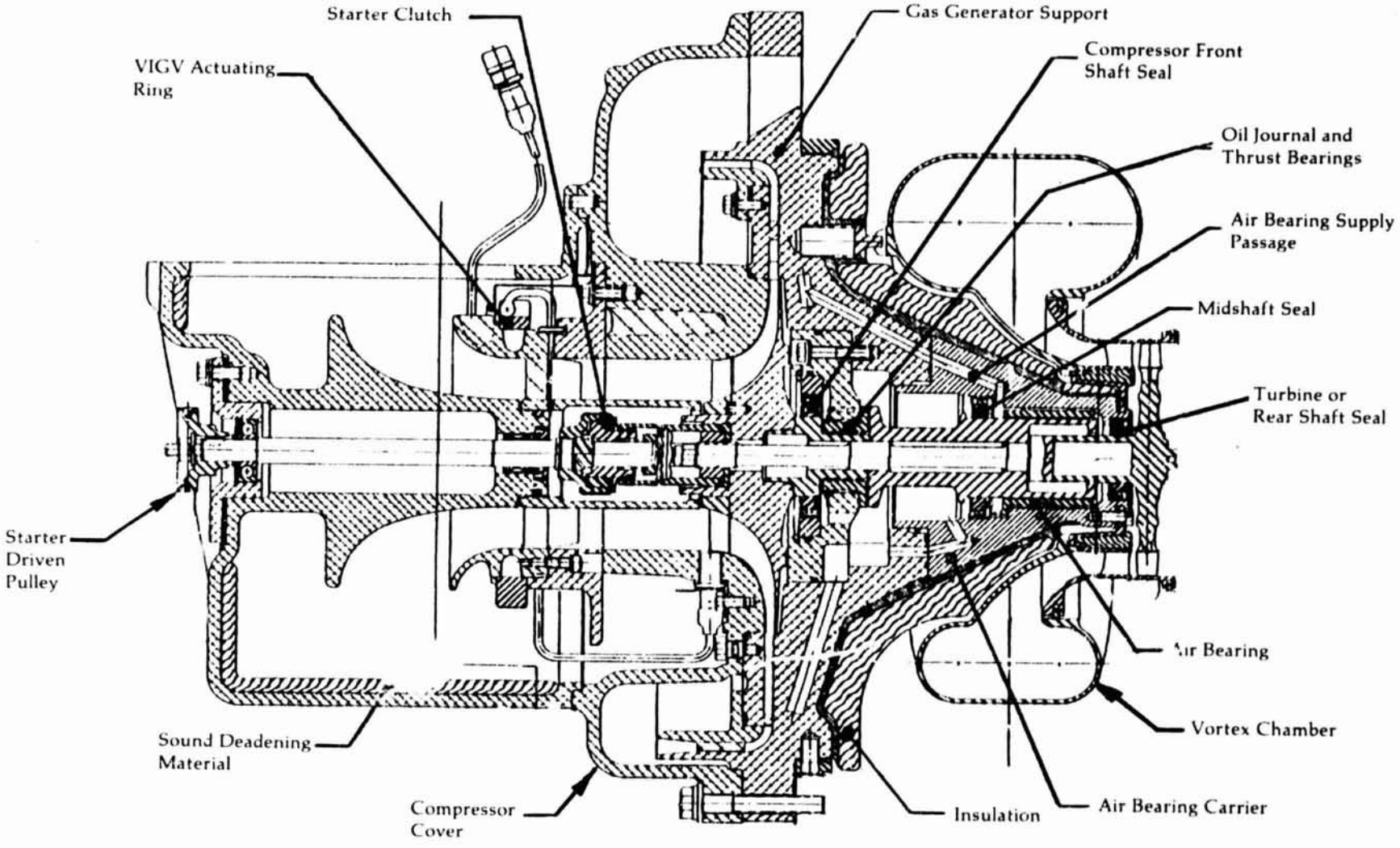

Upgraded Engine Gas Bearing Design

View in Circle

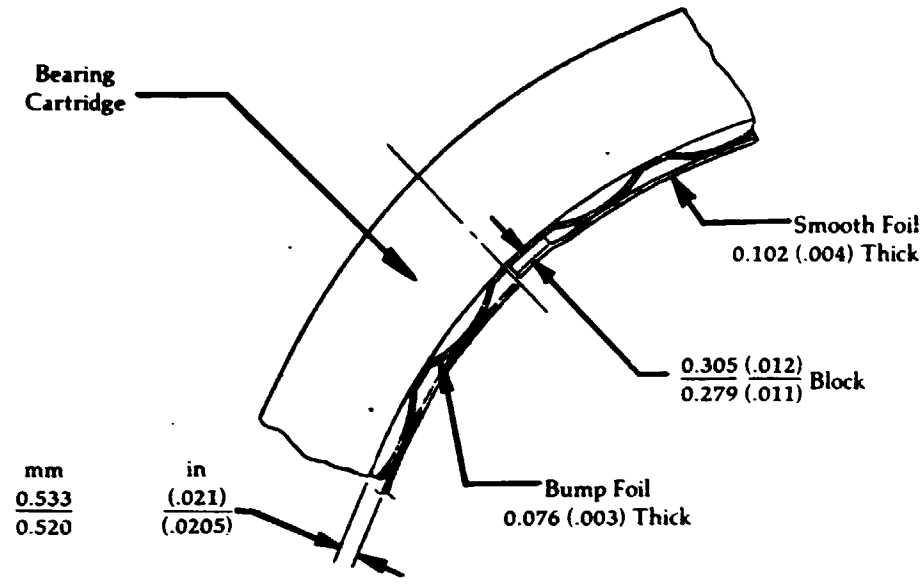

M.T.I. Hydresil Compliant Foil Bearing

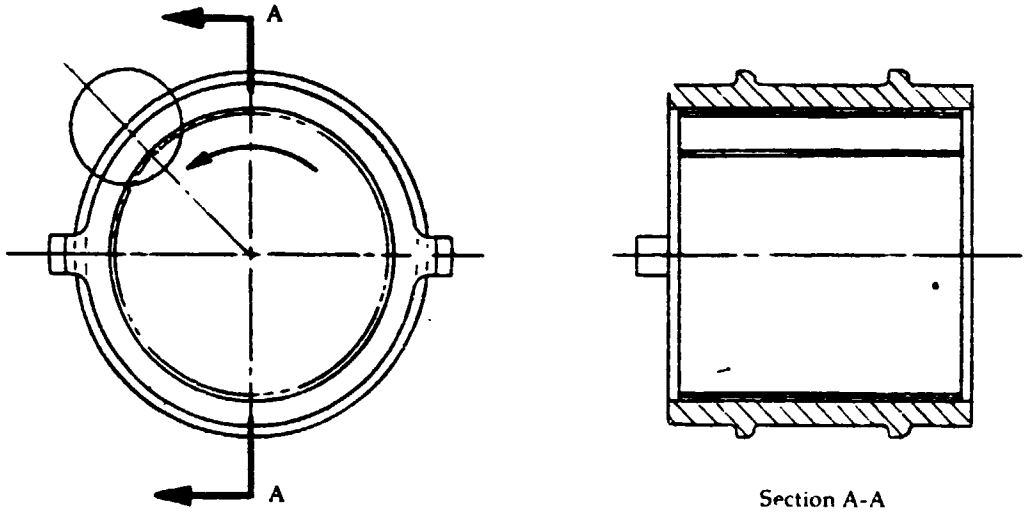

Figure 62

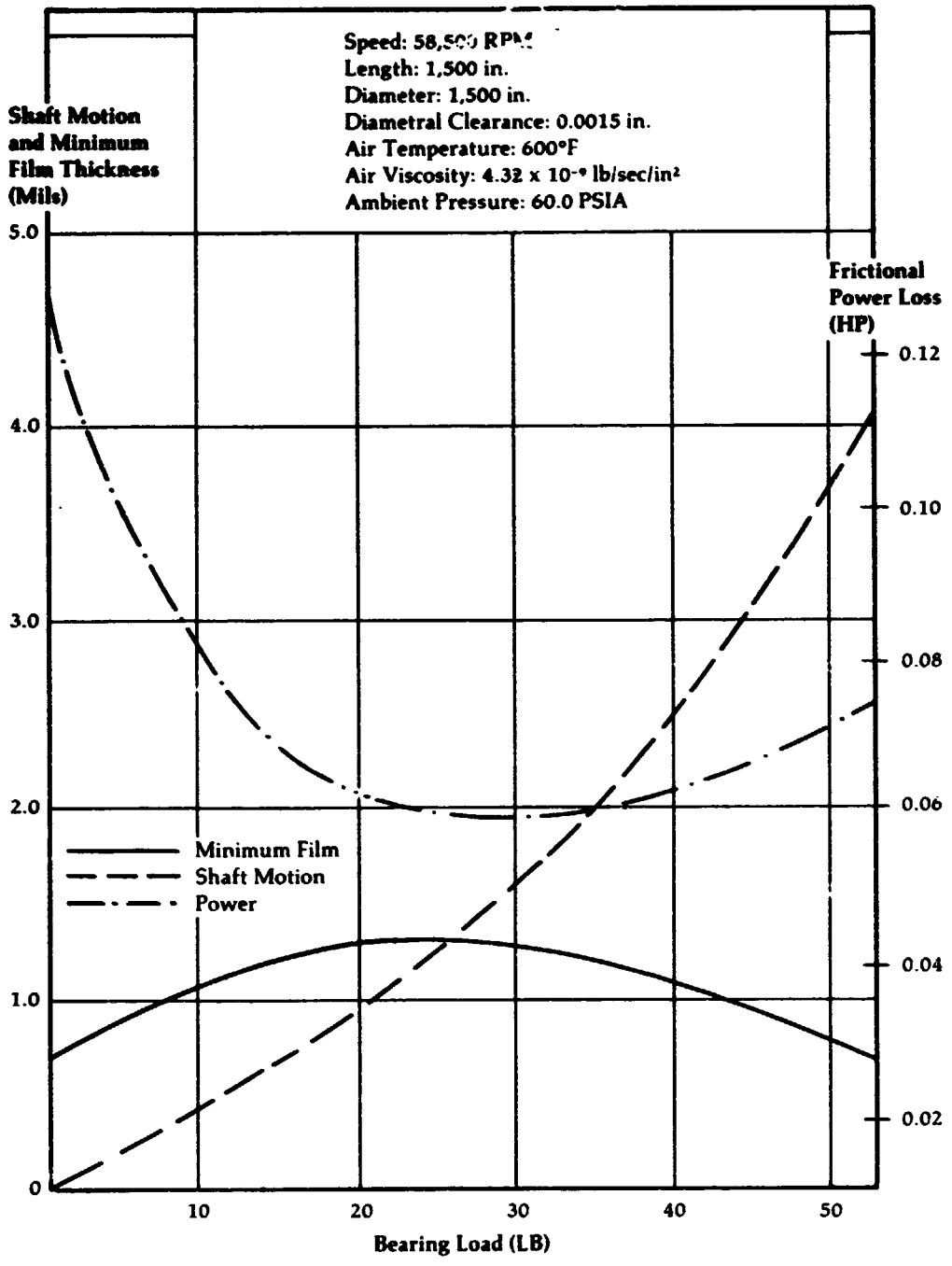

Bearing Load vs Shaft Motion, Minimum Film Thickness,
And Frictional Power Loss
(No End Leakage Correction Factors Applied)

Upgraded Engine Gas Bearing Design

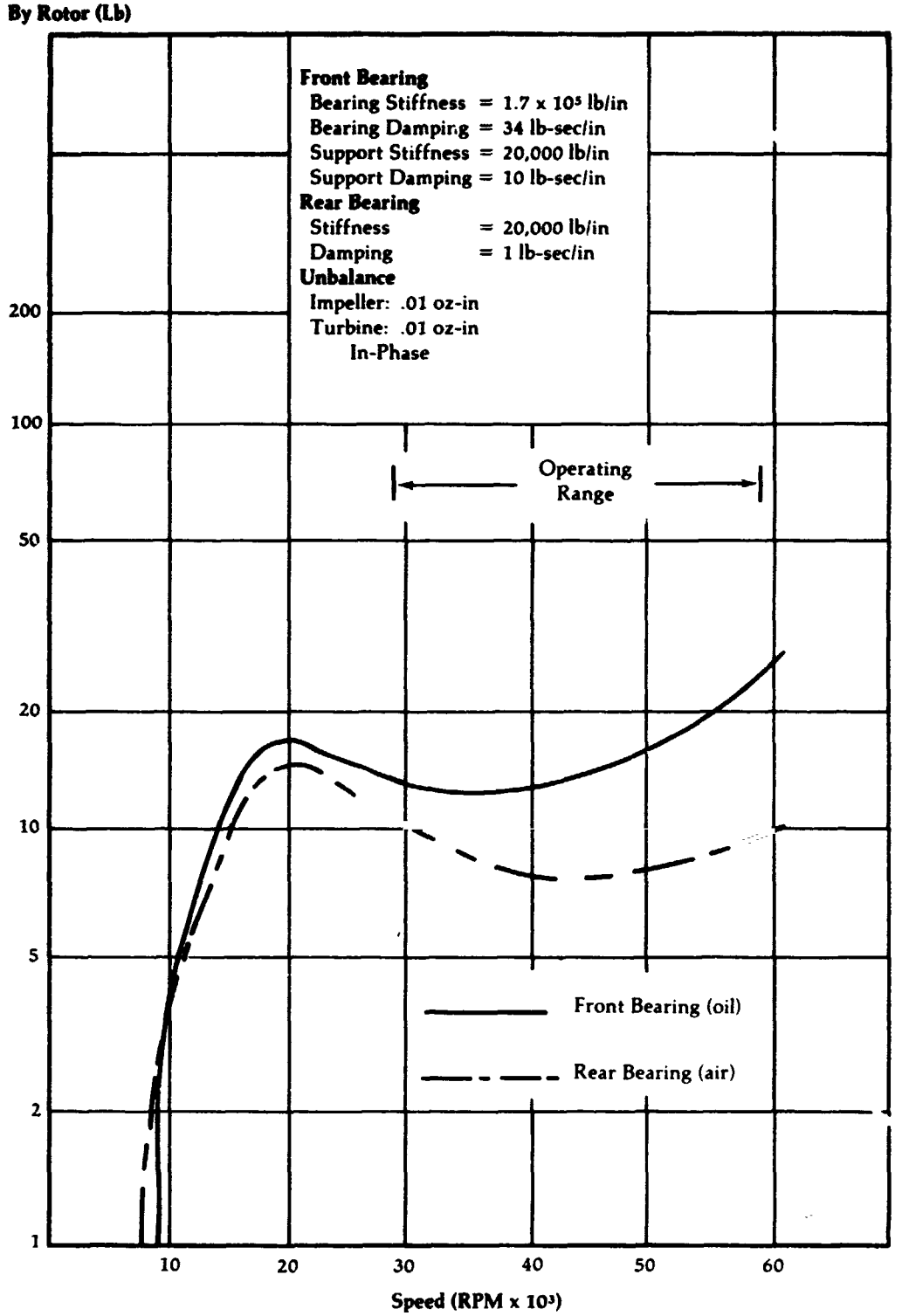

Unbalance Response - Rigid Oil Bearing with Squeeze Film Damper and Hydresil Air Bearing System Unbalance In Phase

Figure 64

Upgraded Engine Gas Bearing Design

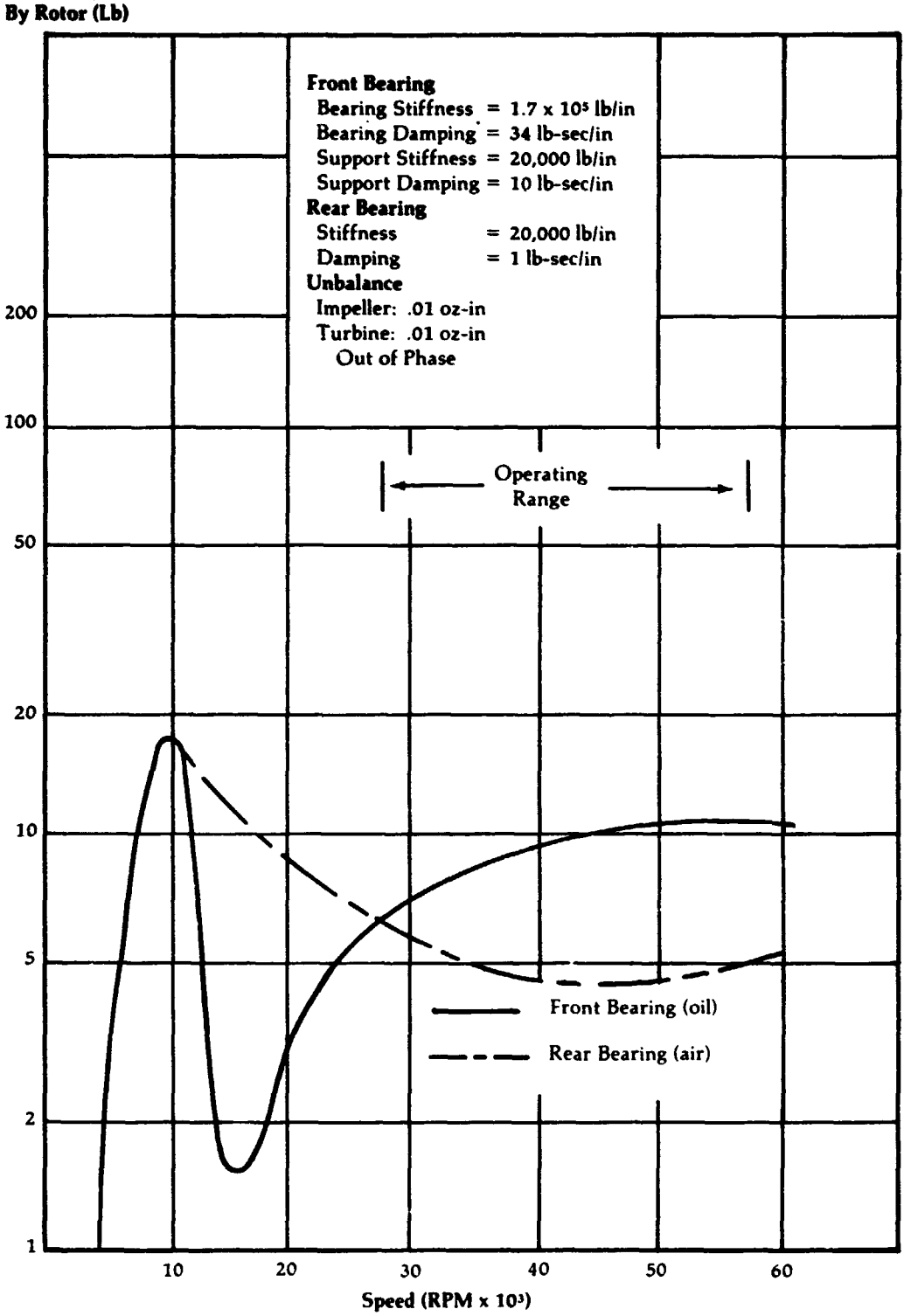

Unbalance Response - Rigid Oil Bearing with Squeeze Film Damper and Hydresil Air Bearing System Unbalance Out of Phase

Figure 65

Upgraded Engine Gas Bearing Design

Critical Speed vs Front Bearing Stiffness

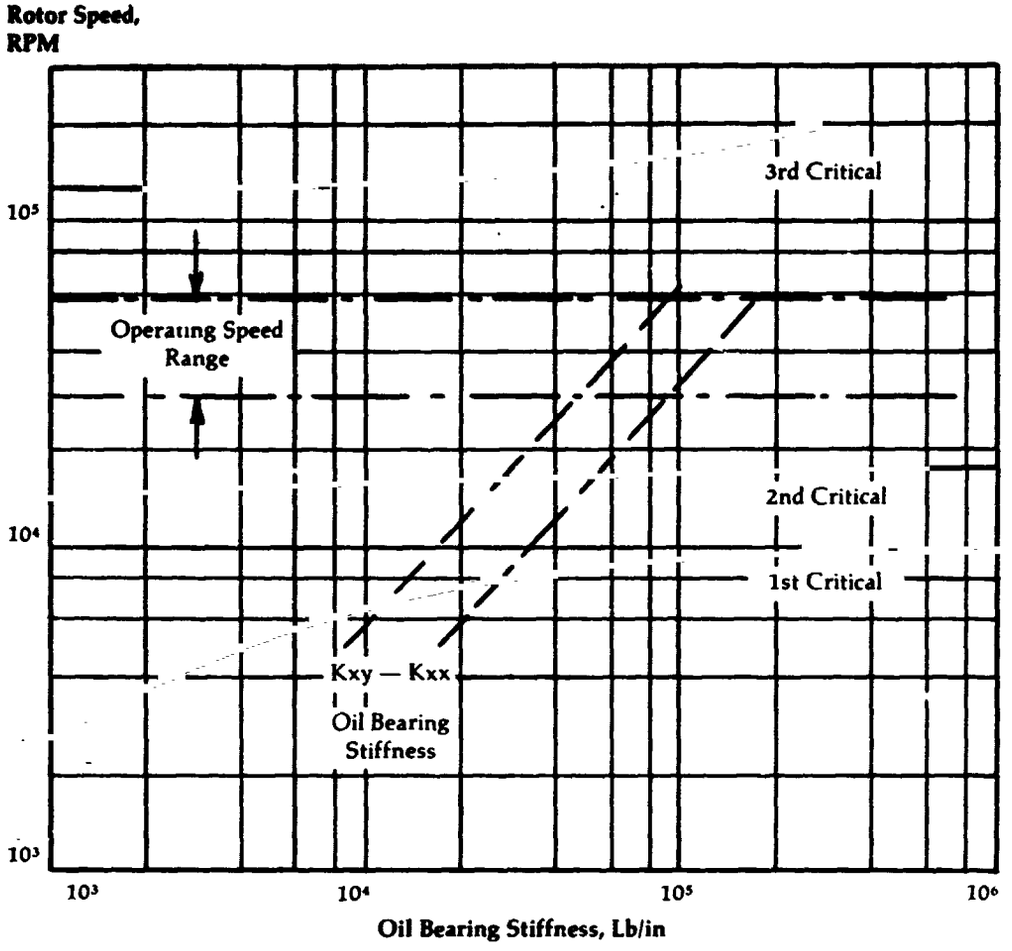

20,000 ib/in Air Bearing Stiffness
20,000 lb/in Support Stiffness At Oil Bearing

Figure 66

Upgraded Gas Generator Temperatures °F Steady-State - Rated Speed

Air Bearing Enlargement

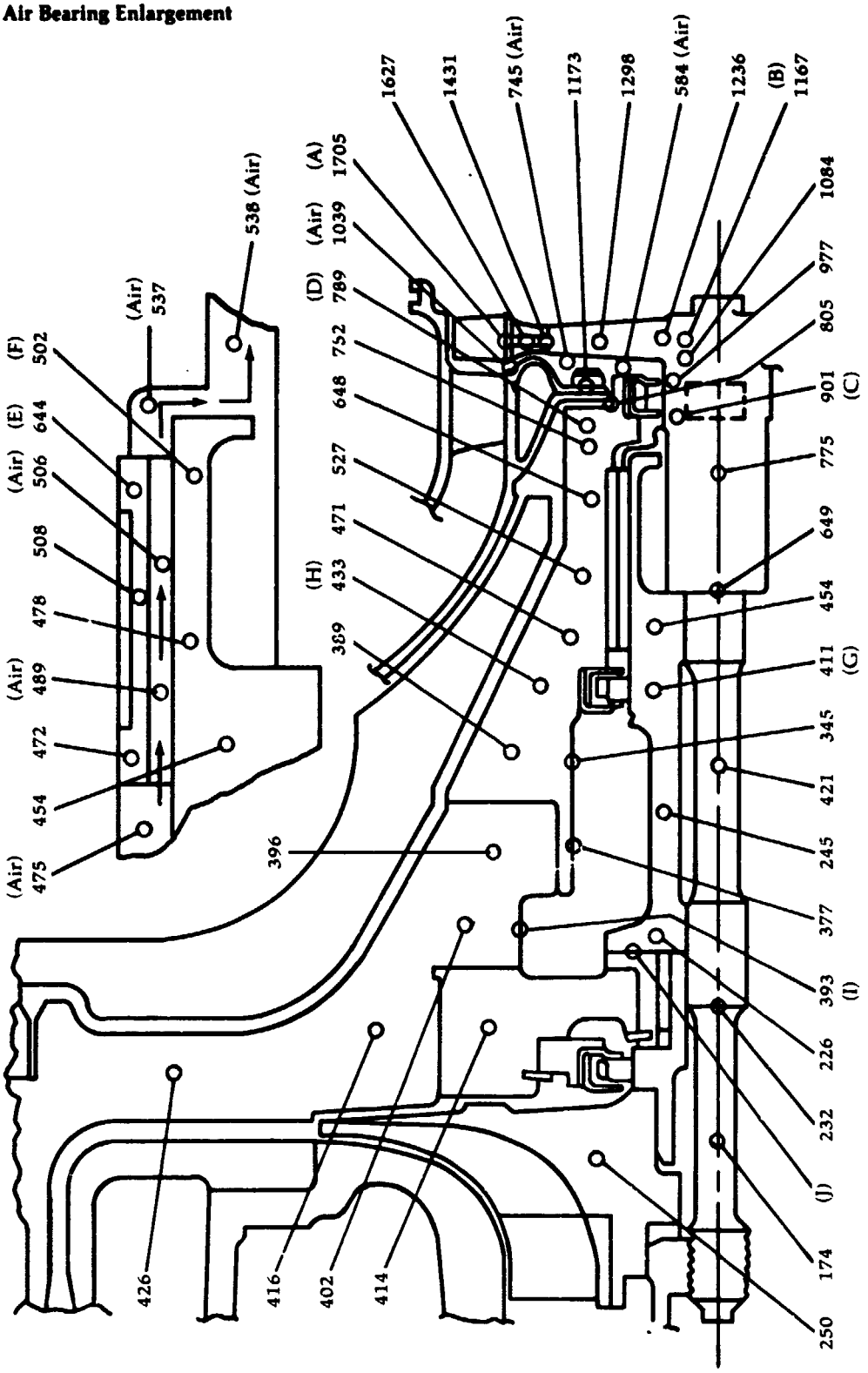

Notes:
All values are metal temperatures unless otherwise indicated.

Values with identifying letter are soakback temperatures shown in figure 68.

Figure 67

Upgraded Engine Estimated Gas Generator Soakback Temperatures

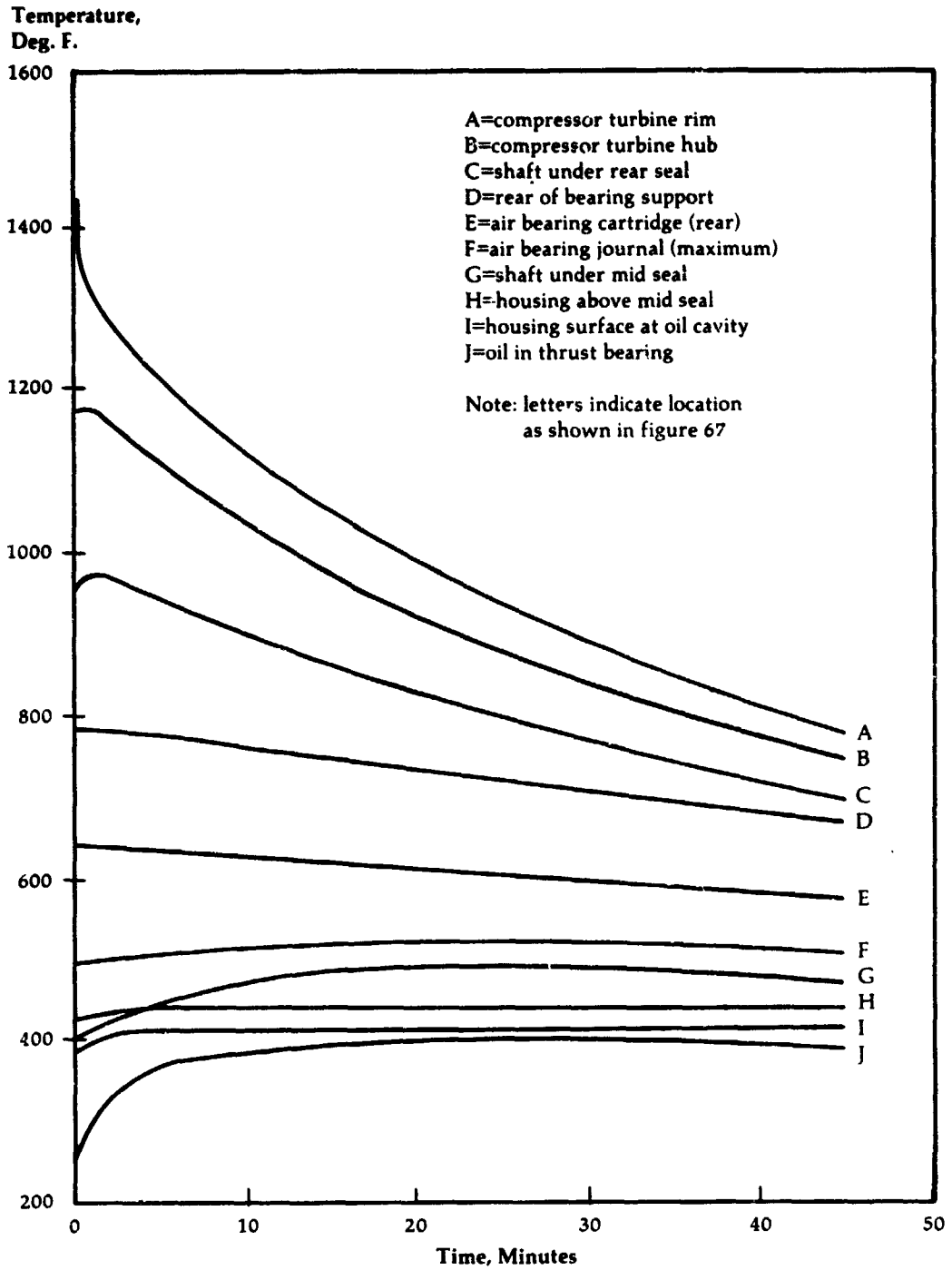

Figure 68

Compressor Cover - Finite Element Model

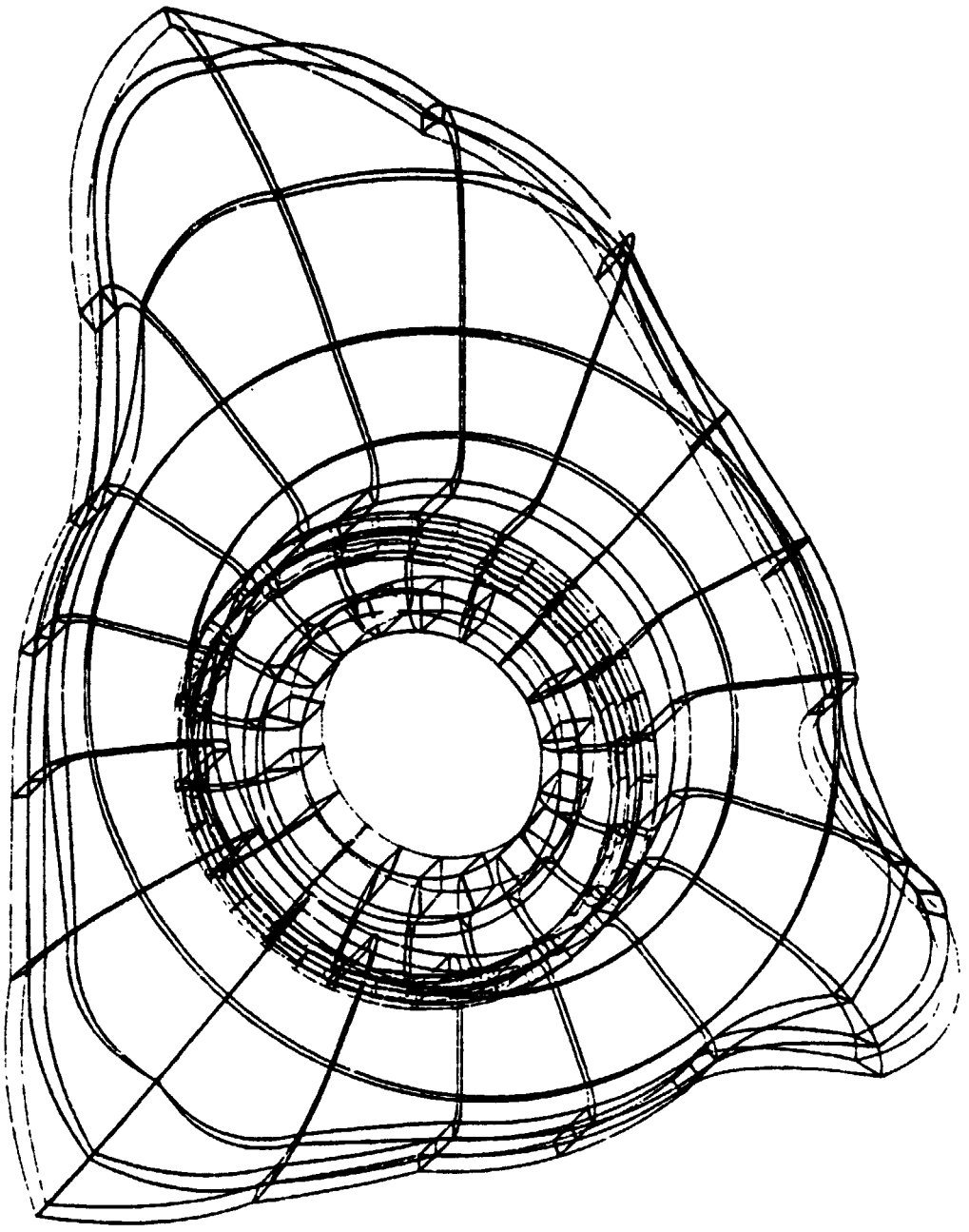

216 Thick Shell Elements (16 Nodes)
1260 Nodal Points

Figure 69

Figure 70

Upgraded Engine Compressor Cover Structural Analysis

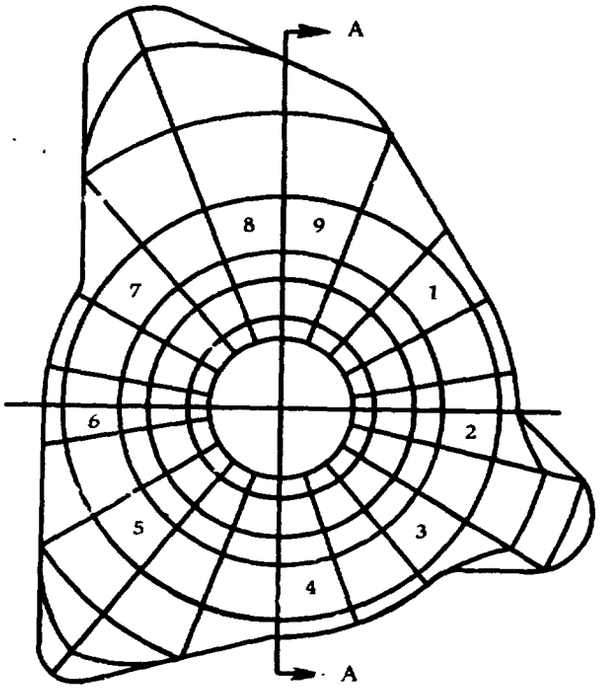

Finite Element Model

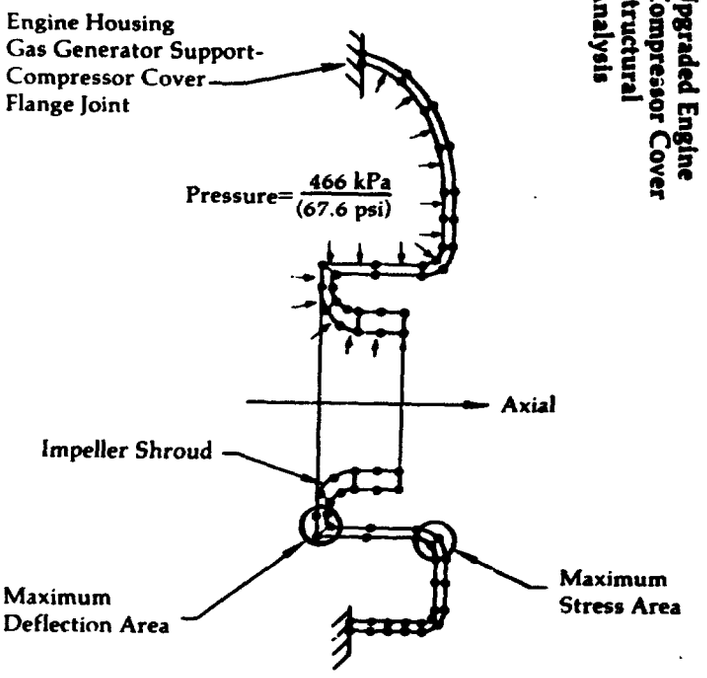

Section A-A

Stress and Deflection Summary

Section	Temperature Estimate	Axial Deflection		Equivalent Stress	
		mm.	in.	mPa	ksi
1		.091	.0036	14.5	2.1
2		.119	.0047	21.4	3.1
3	204°C	.140	.0055	37.2	4.5
4		.152	.0060	35.8	5.2
5	(400°F.)	.147	.0058	31.7	4.6
6		.124	.0049	30.3	4.4
7		.097	.0038	19.3	2.8
8		.079	.0031	17.2	2.5
9		.076	.0030	8.3	1.2

Upgraded Engine
Air Inlet
Cross-Section

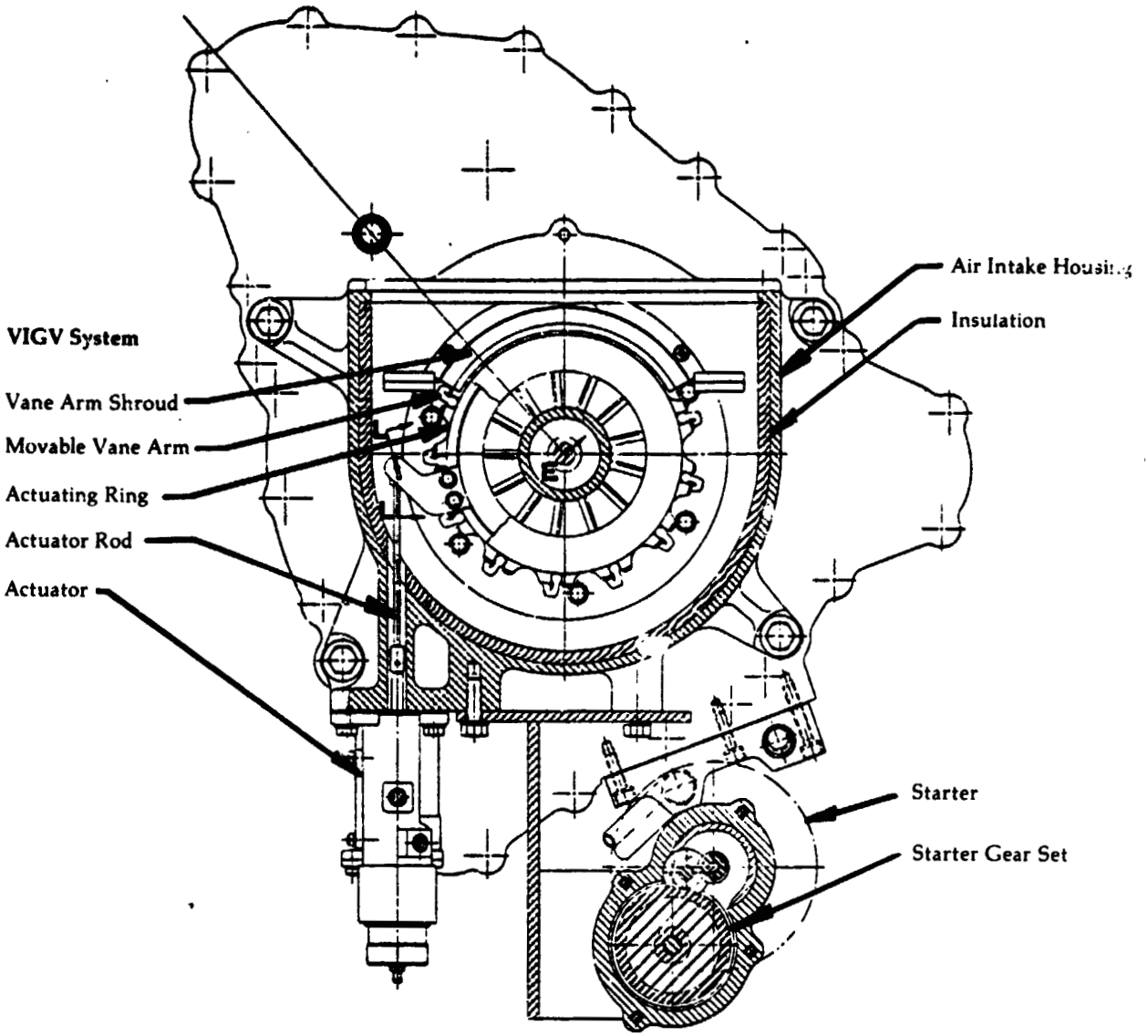

Figure 71

Upgraded Engine Power Sectior

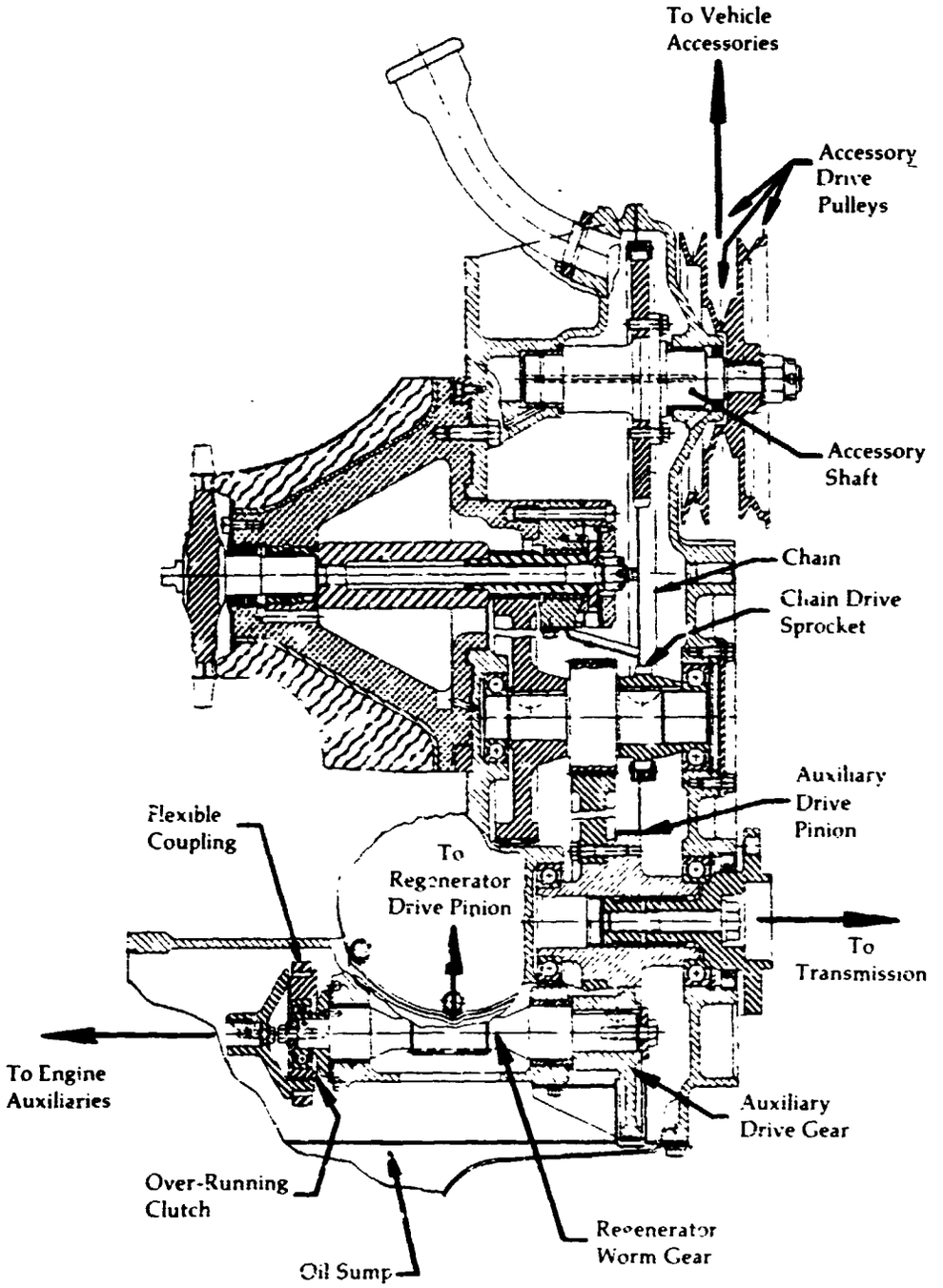

Figure

Rotor Assembly

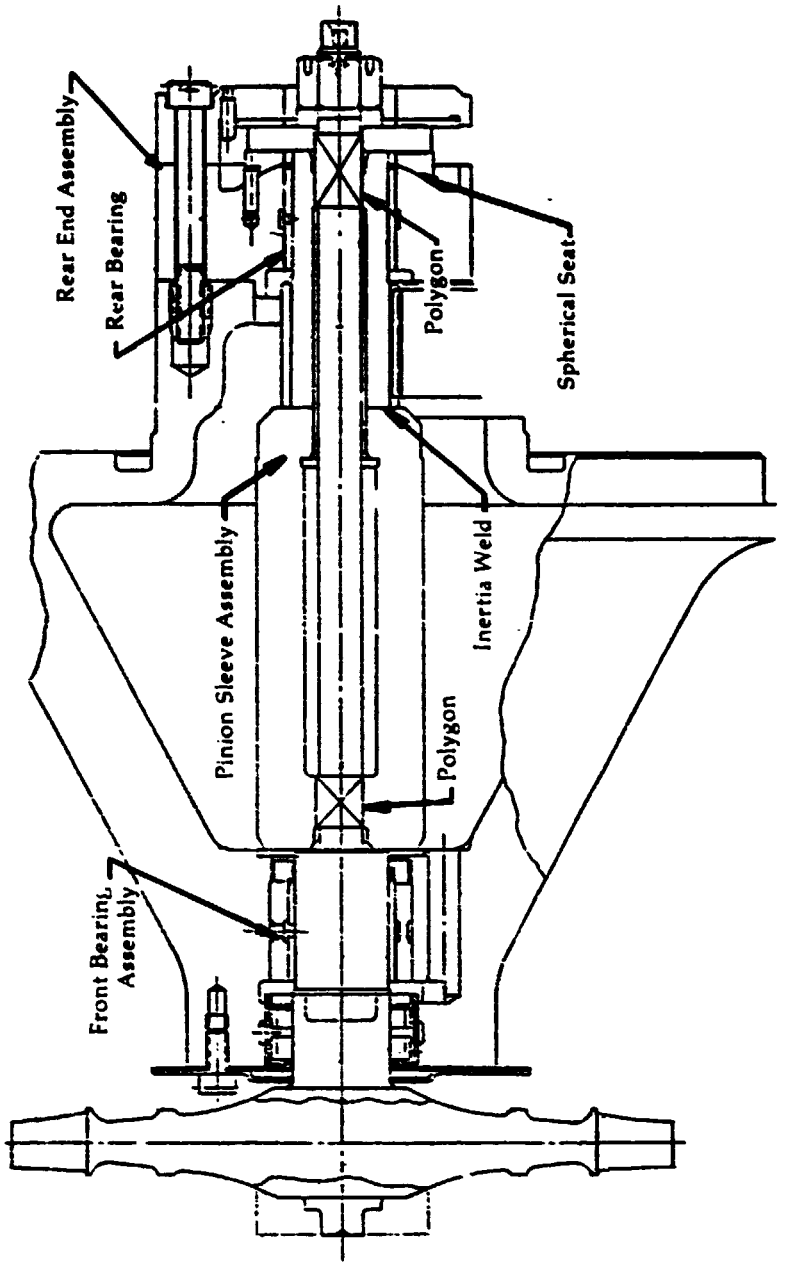

Figure 73

Upgraded Engine Estimated Performance of Power Turbine Rear Journal Bearing at 1-2 Upshift Point

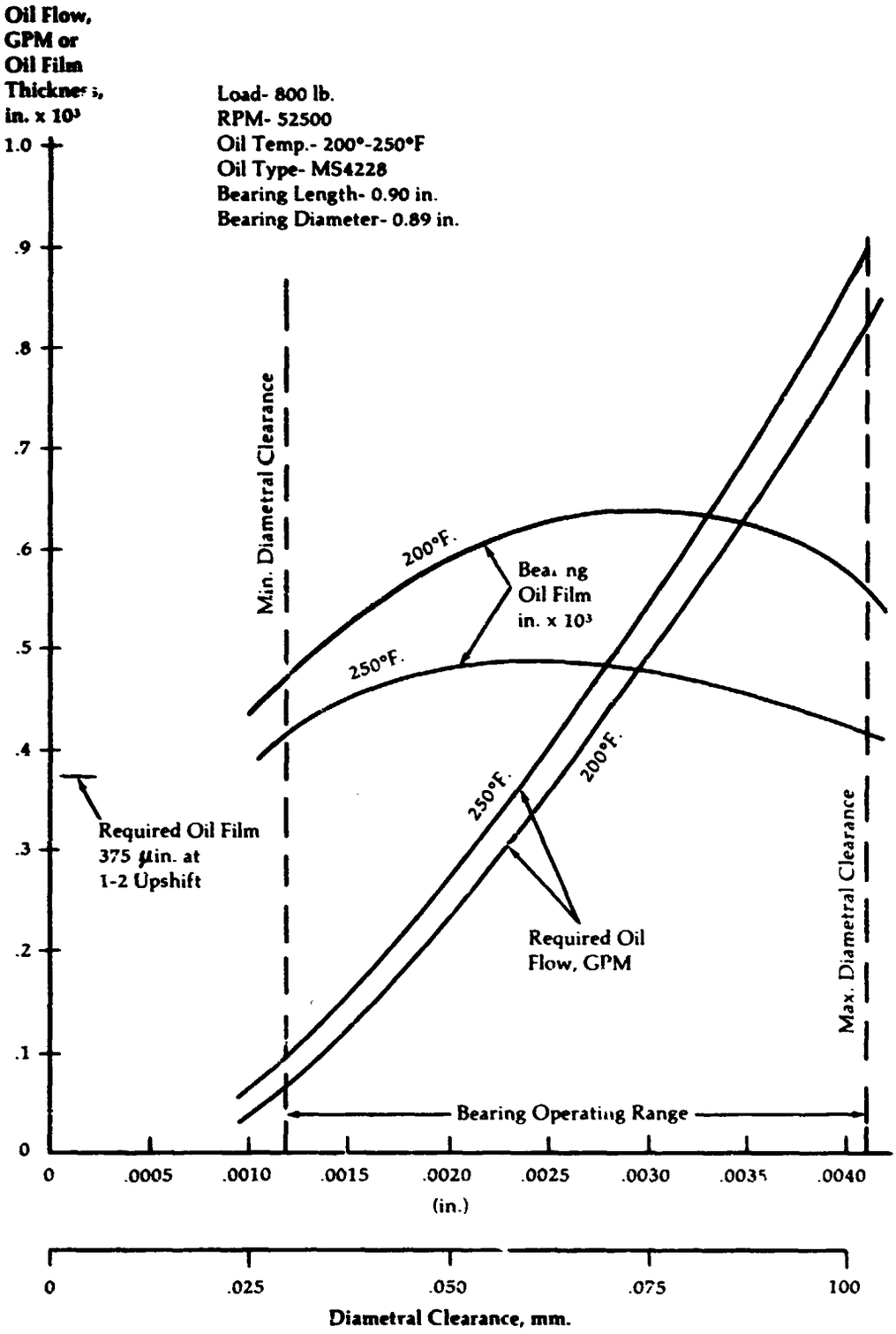

*Figure 74

Upgraded Engine Estimated Performance of Power Turbine Rear Journal Bearing

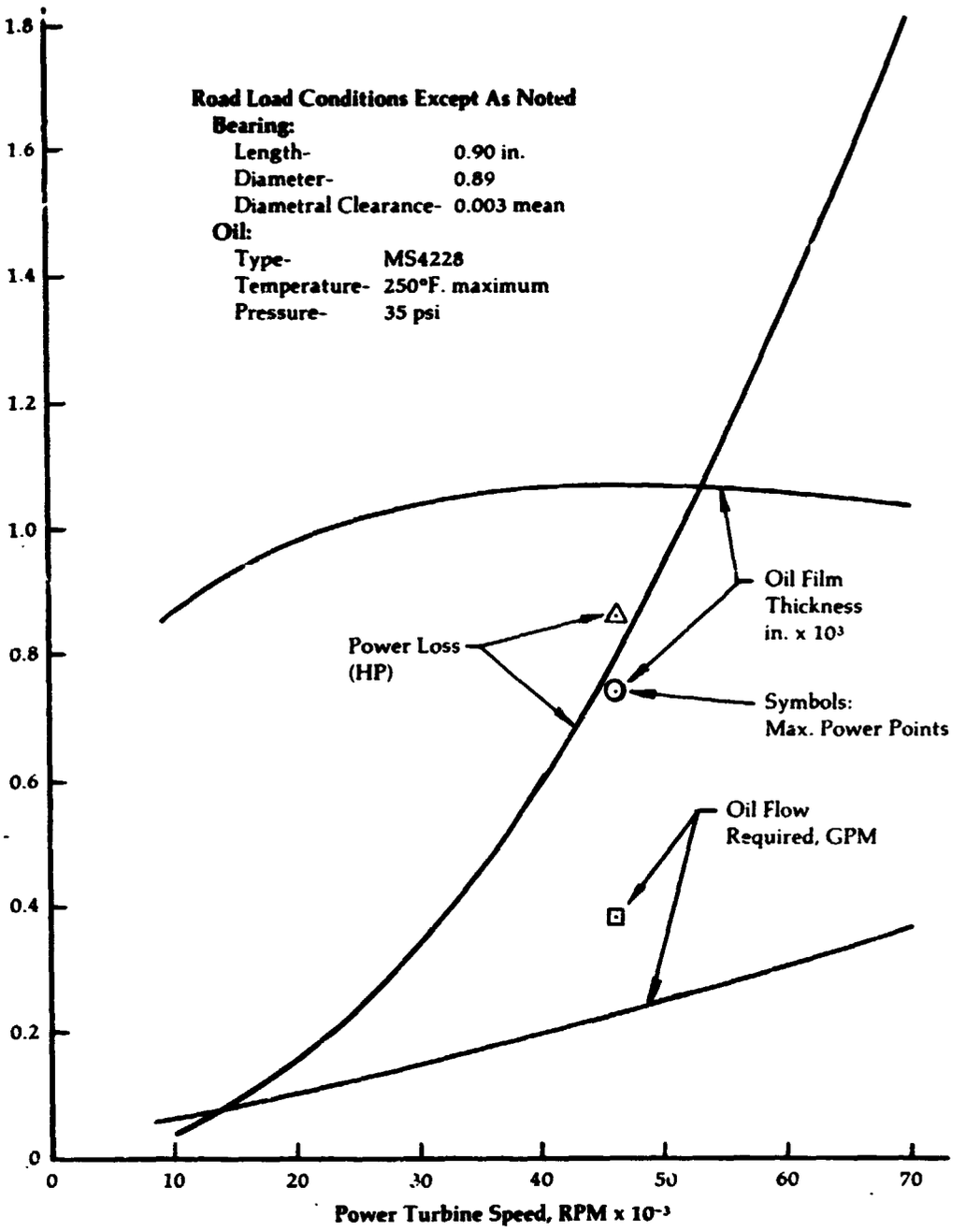

Figure 75

Upgraded Engine Second Stage Reduction Gear Bending Stresses and Oil Film Thickness Versus Helix Angle

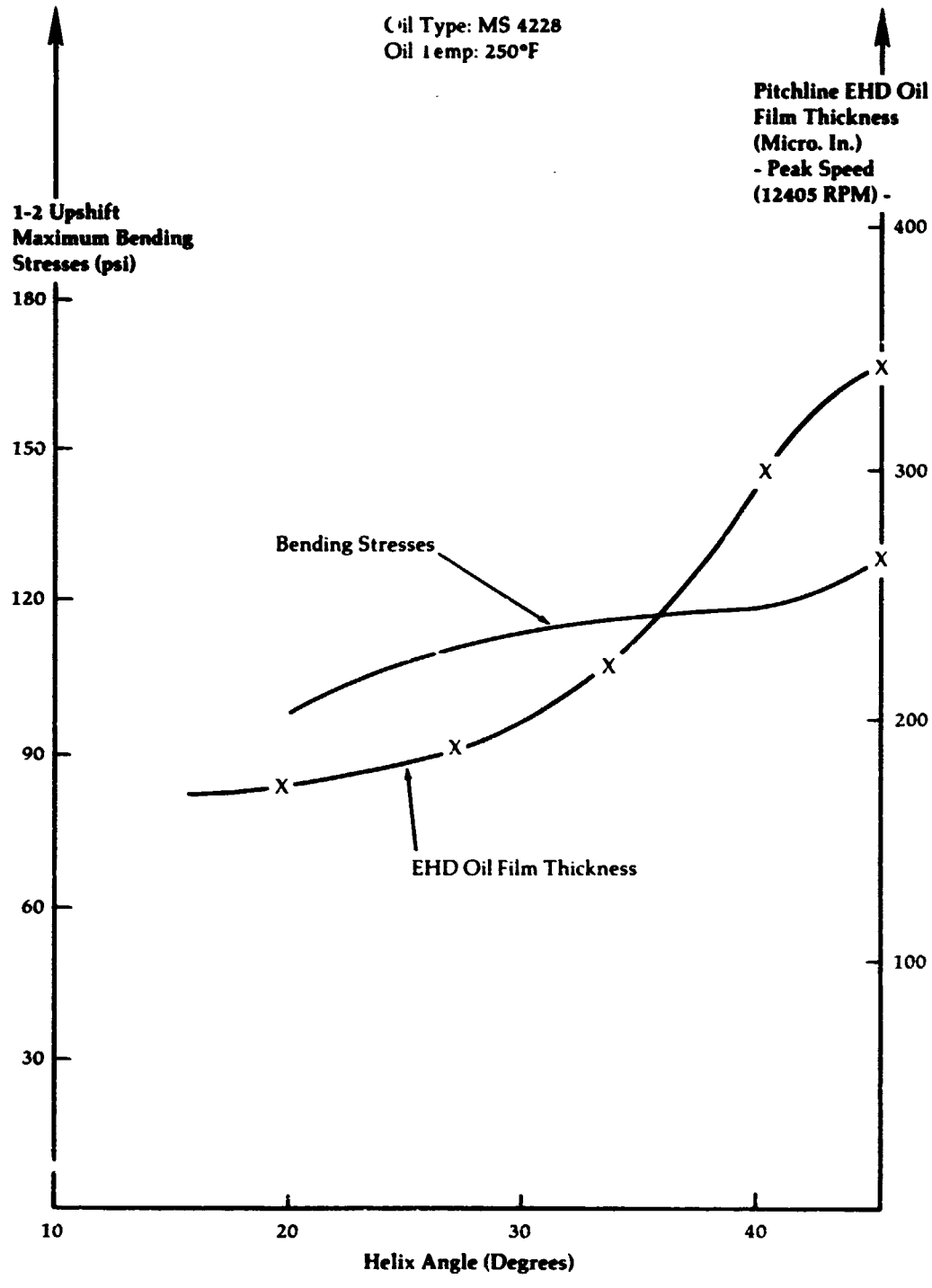

Figure 76

Upgraded Engine Estimated Gear Bending Stresses vs. Power Turbine Speed

Road Load

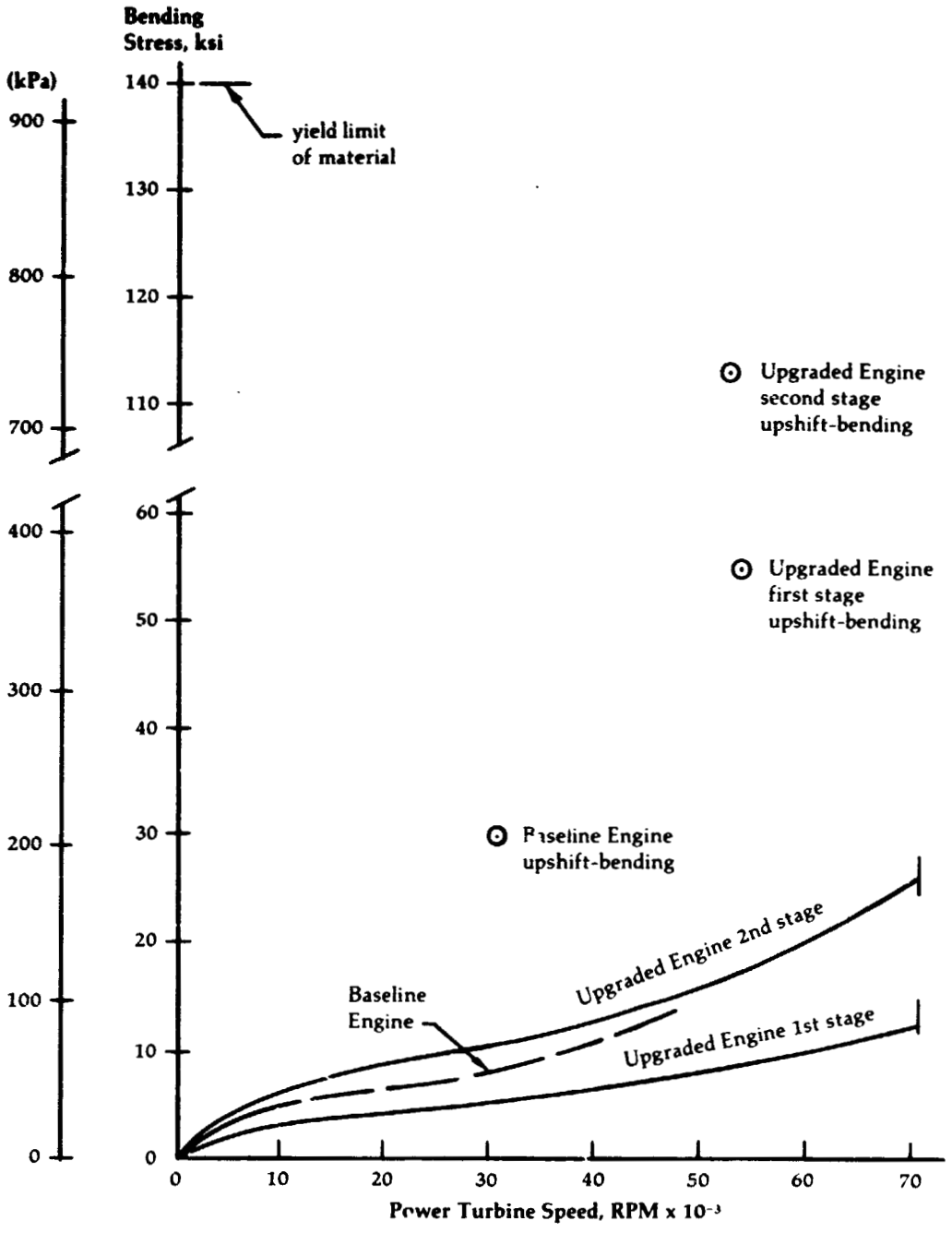

Figure 77

Upgraded Engine Estimated Normal Tooth Load Versus Power Turbine Speed

Road Load

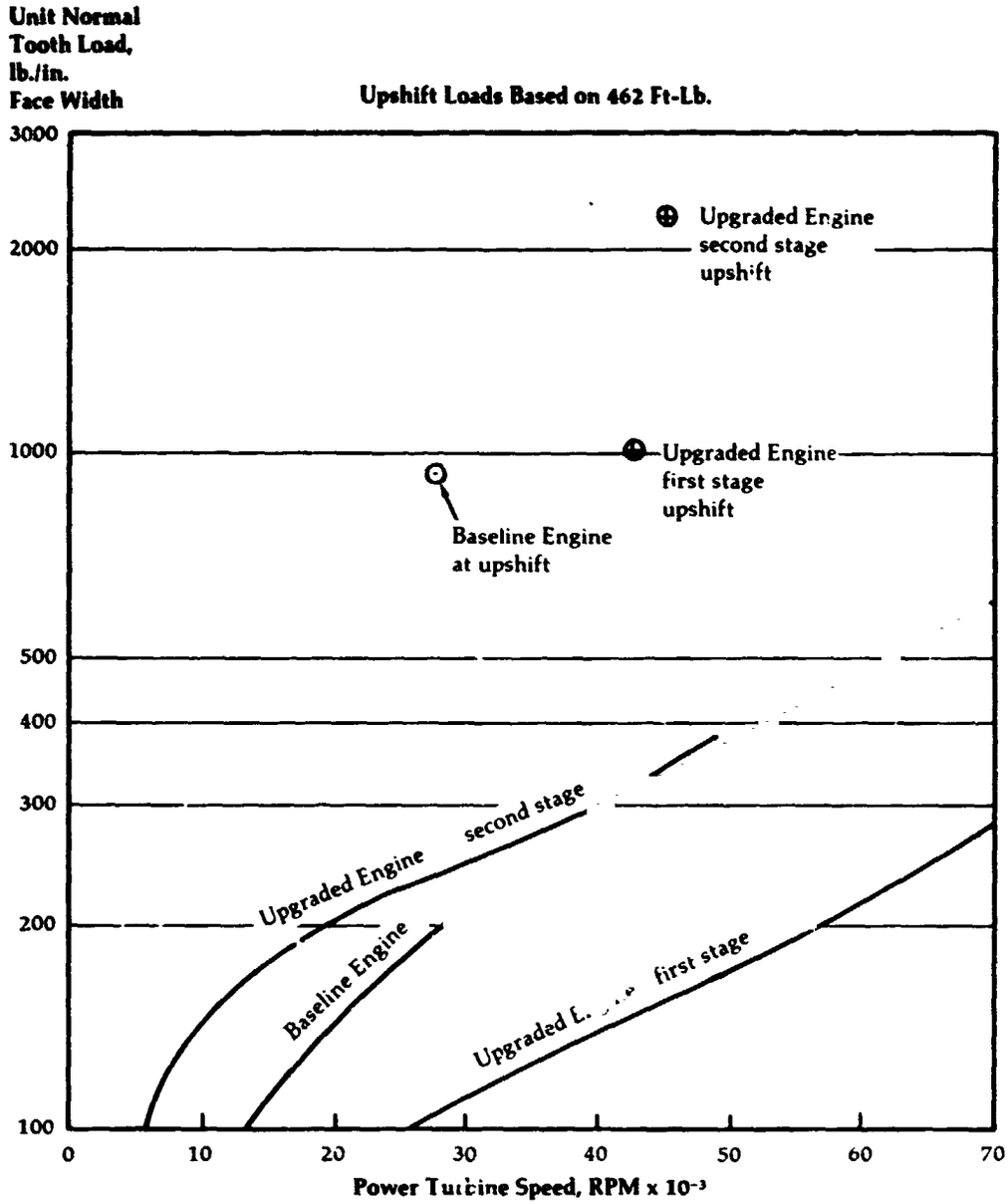

Figure 78

Upgraded Engine Estimated Gear Oil Film Thickness

Road Load

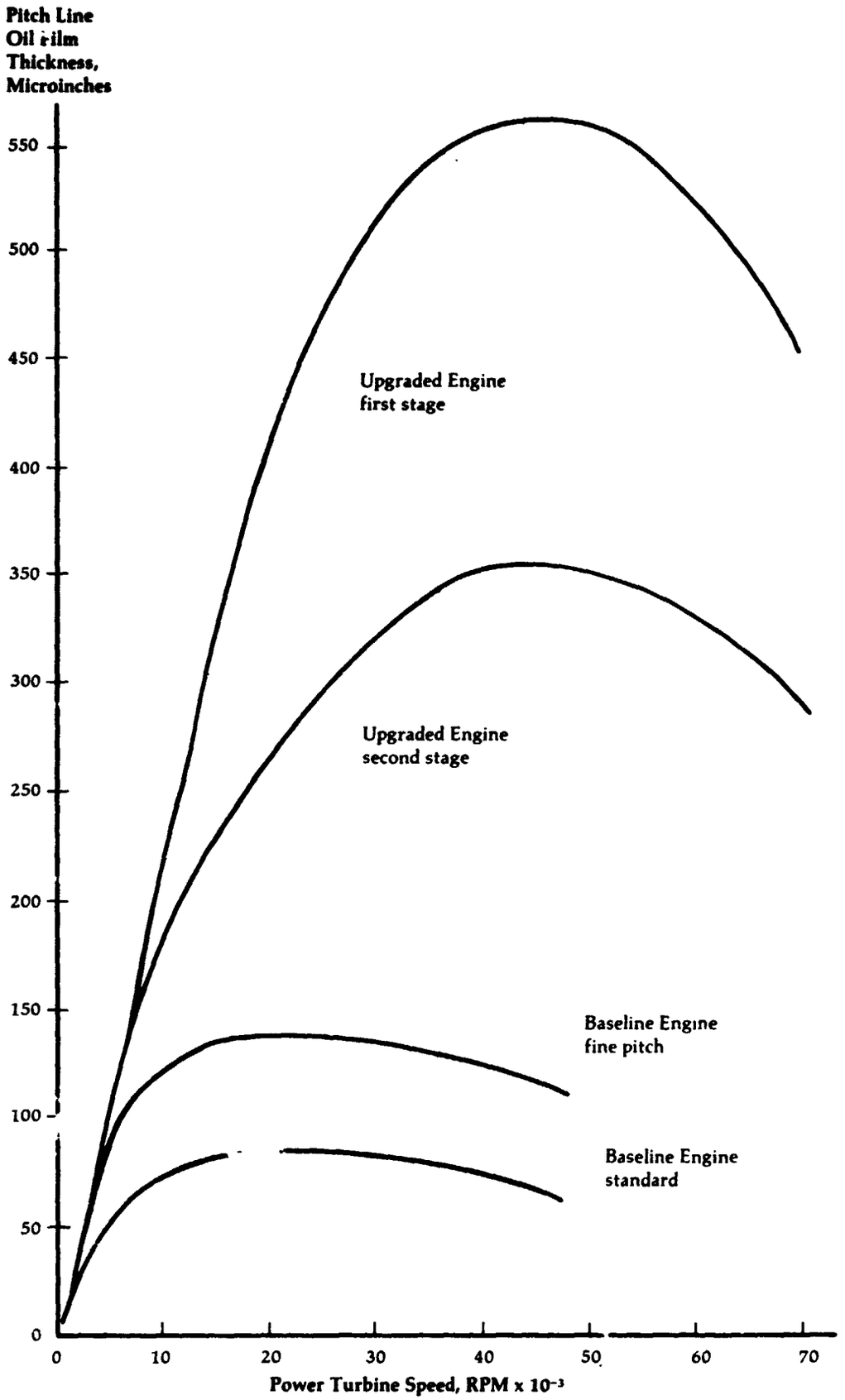

Figure 79

Upgraded Engine Expected Superimposition of the Transmitted Road Load Vibrations Through Gear Mesh

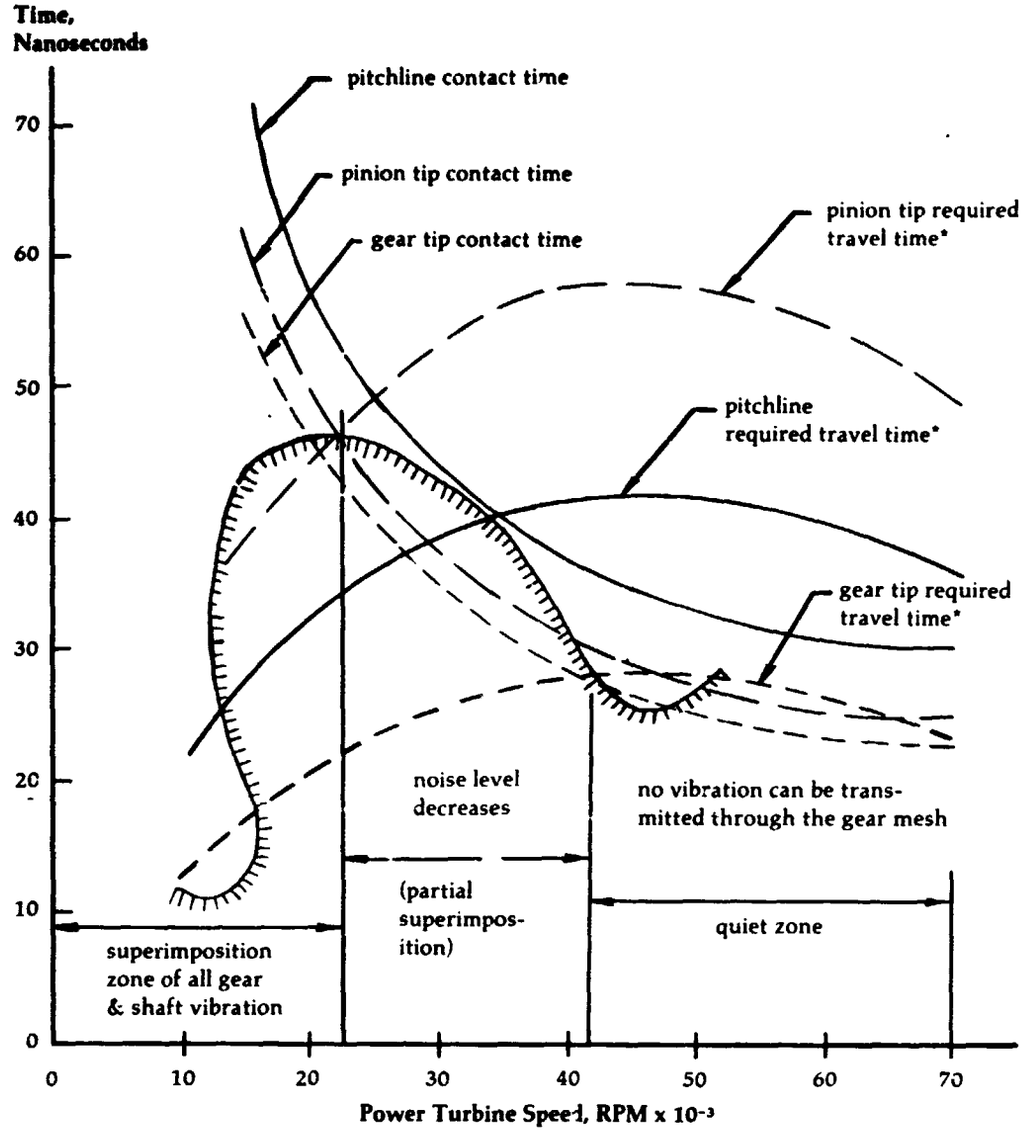

*required travel time for shaft vibrations to pass through the EHD oil film

Figure 80

Upgraded Engine Gear Sliding Velocities at Road Load

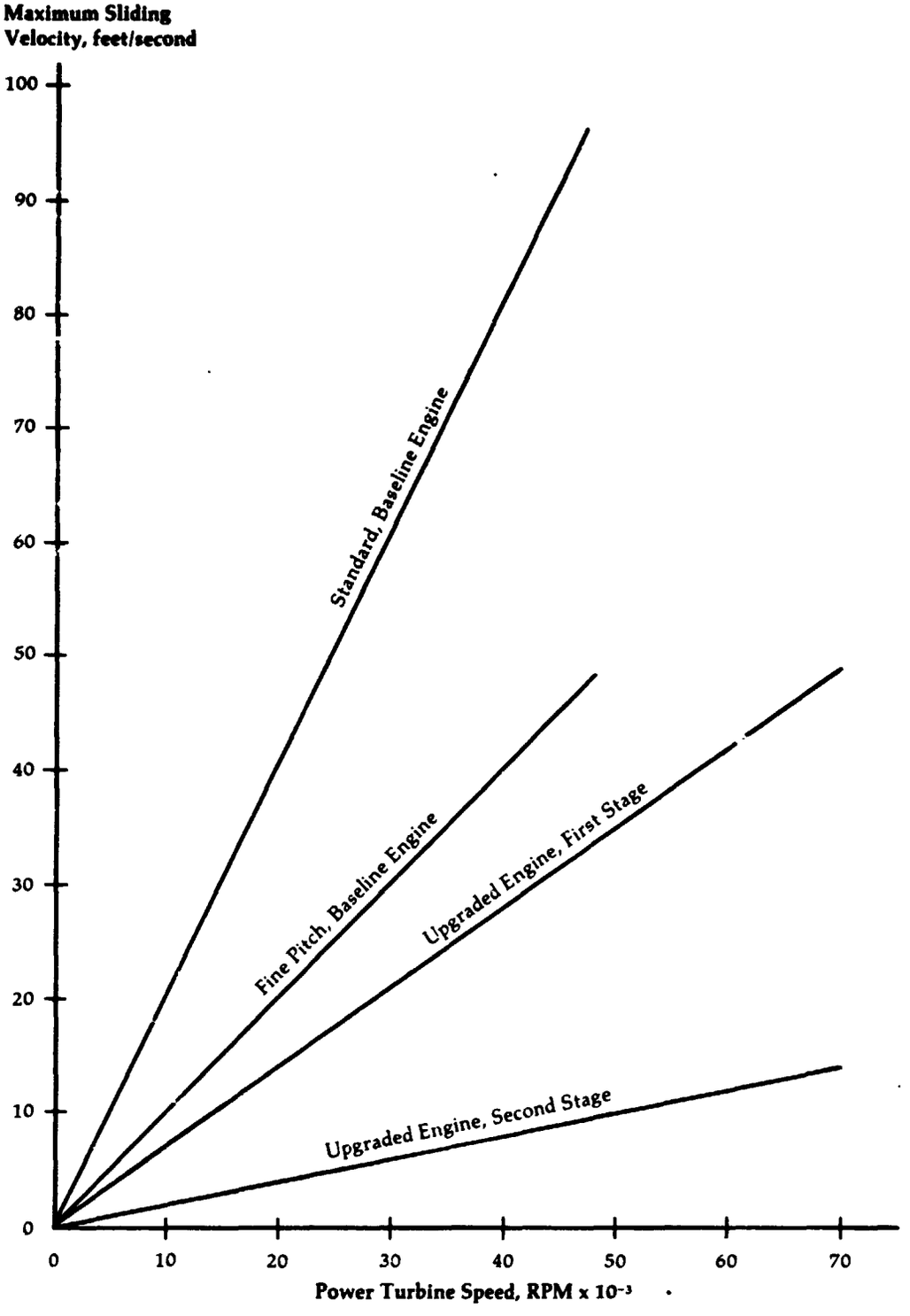

Figure 81

Upgraded Engine Estimated Gear Scoring Factors at Road Load

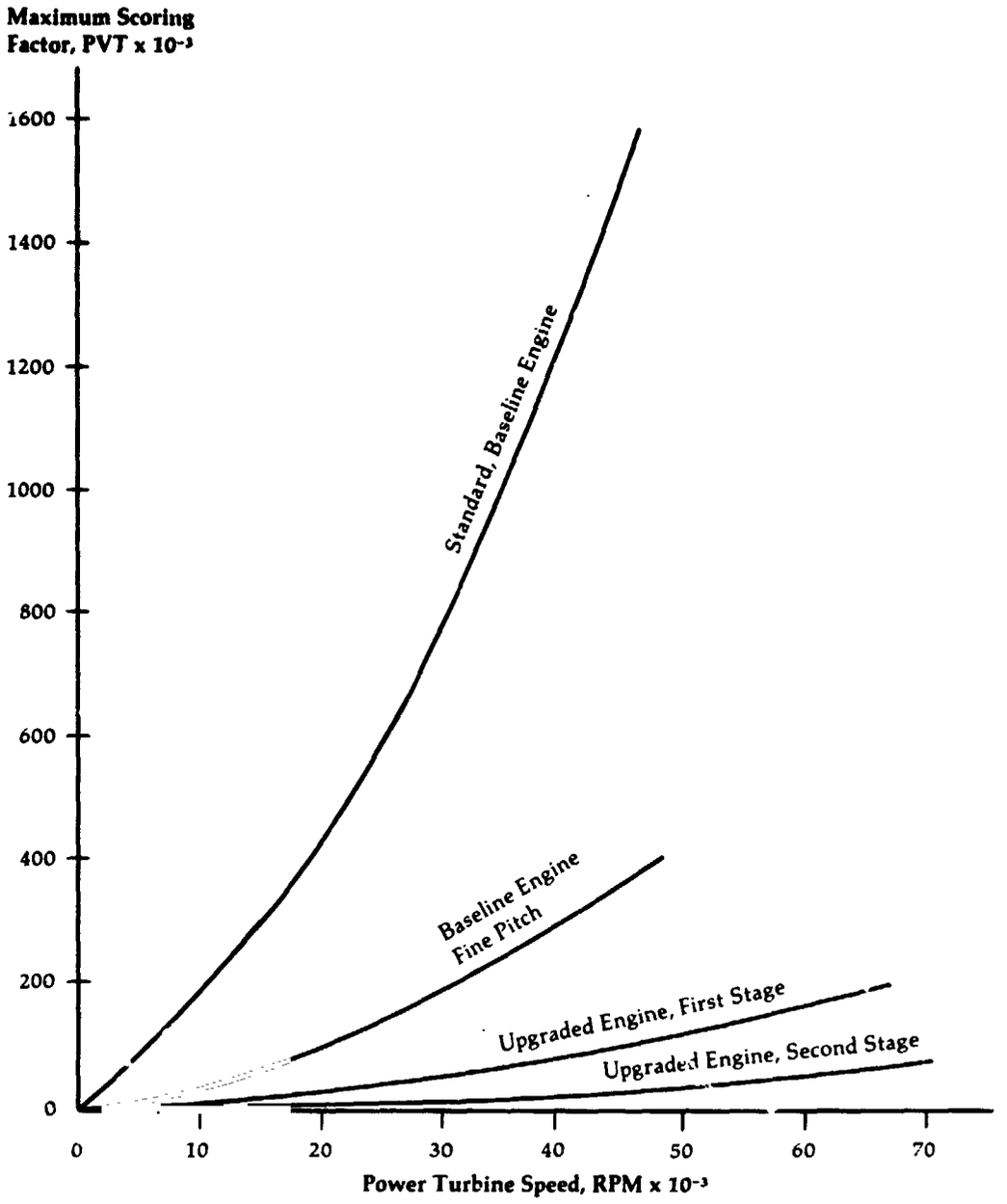

Figure 82

Upgraded Engine Reduction Gears Total Mesh Efficiency

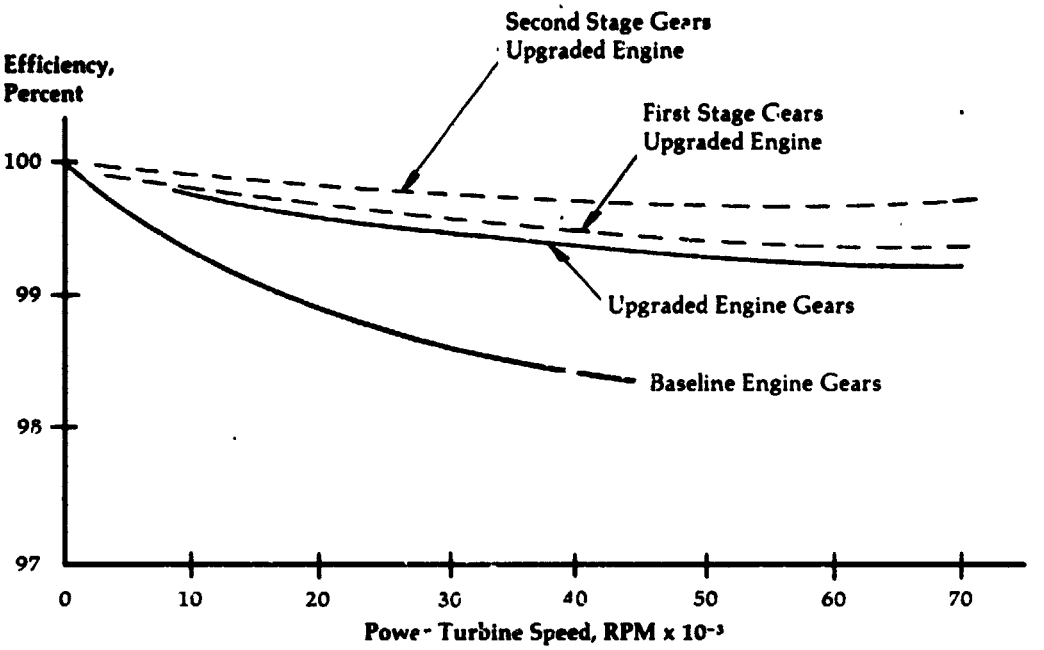

Figure 83

Upgraded Engine Reduction Gears Maximum Surface Compression Stresses at Mean Center Distance

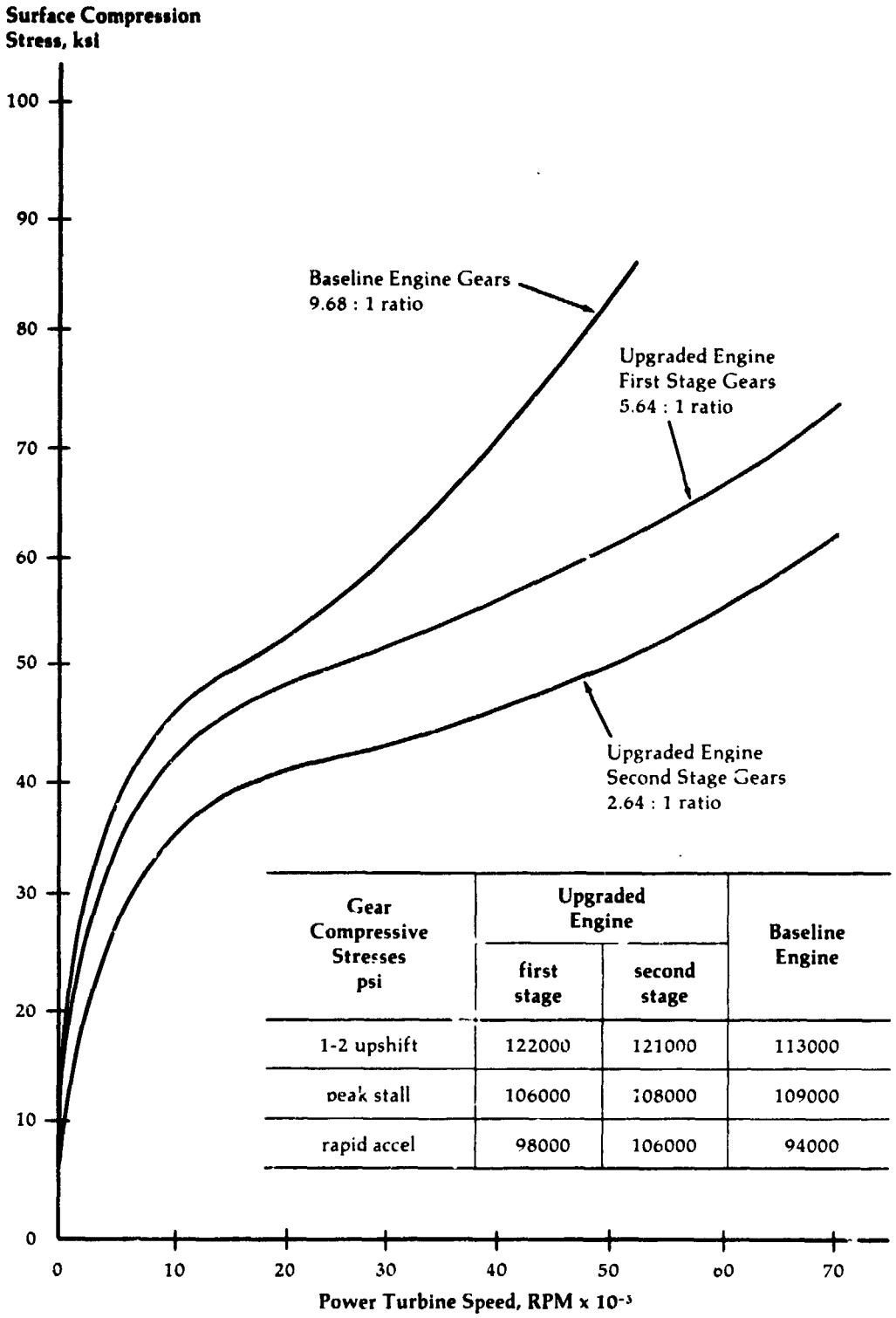

Gear Compressive Stresses psi	Upgraded Engine		Baseline Engine
	first stage	second stage	
1-2 upshift	122000	121000	113000
peak stall	106000	108000	109000
rapid accel	98000	106000	94000

Figure 84

Upgraded Engine Reduction Gear Maximum Surface or Subsurface Shear Stress at Mean Center Distance

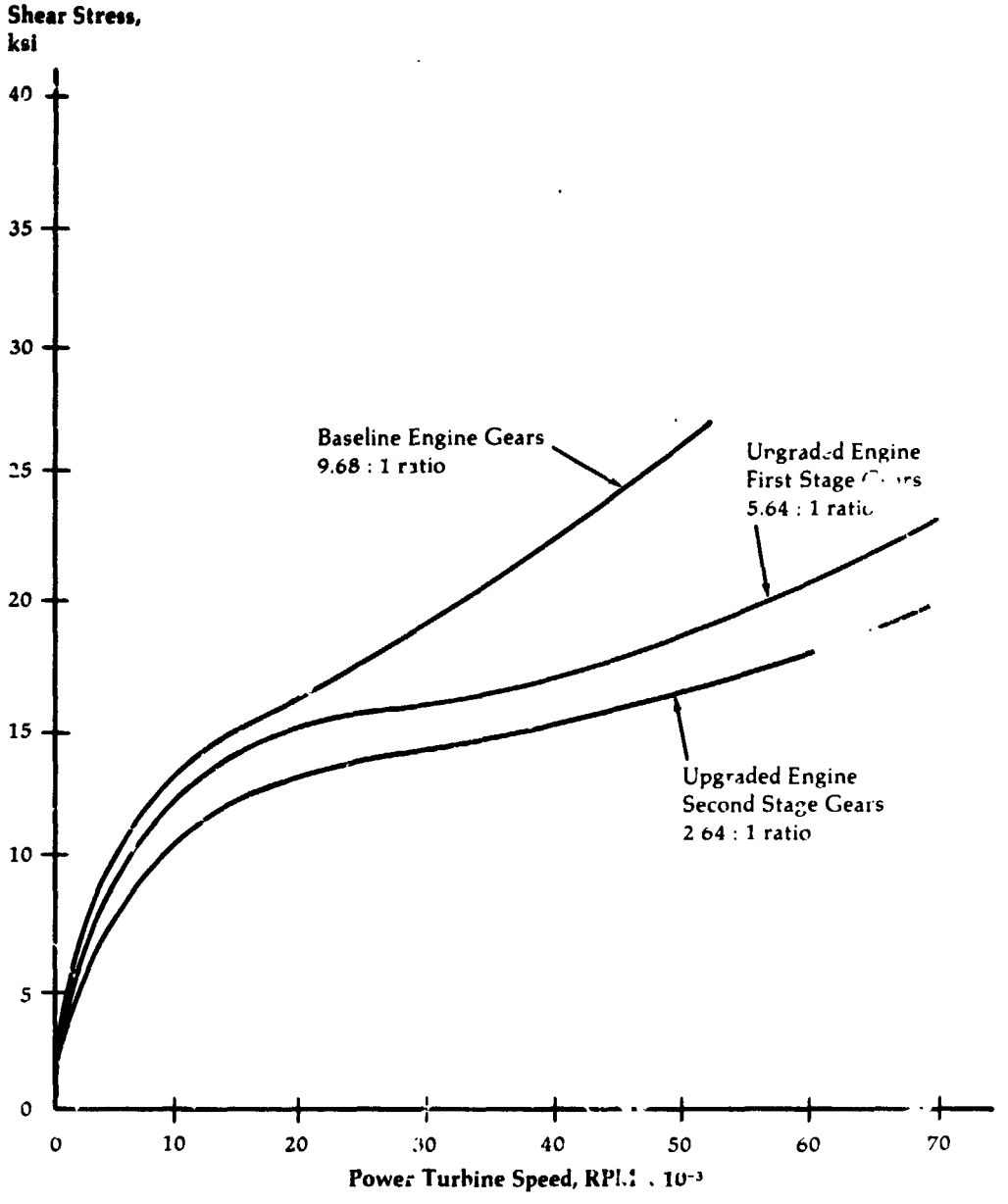

Gear Shear Stresses psi	Upgraded Engine		Baseline Engine
	first	second	
1-2 upshift	48000	38000 (+)	38000
peak stall	36000 (+)	33000 (+)	36000
rapid accel	32000 (+)	32000 (+)	32000

Figure 85

Upgraded Engine Reduction Gears Maximum Surface Tensile Stresses at Mean Center Distance

Gear Tensile Stresses psi	Upgraded Engine		Baseline Engine
	first stage	second stage	
1-2 upshift	9000	56000	27000
peak stall	28000	55000	24000
rapid accel	32000	62000	23000

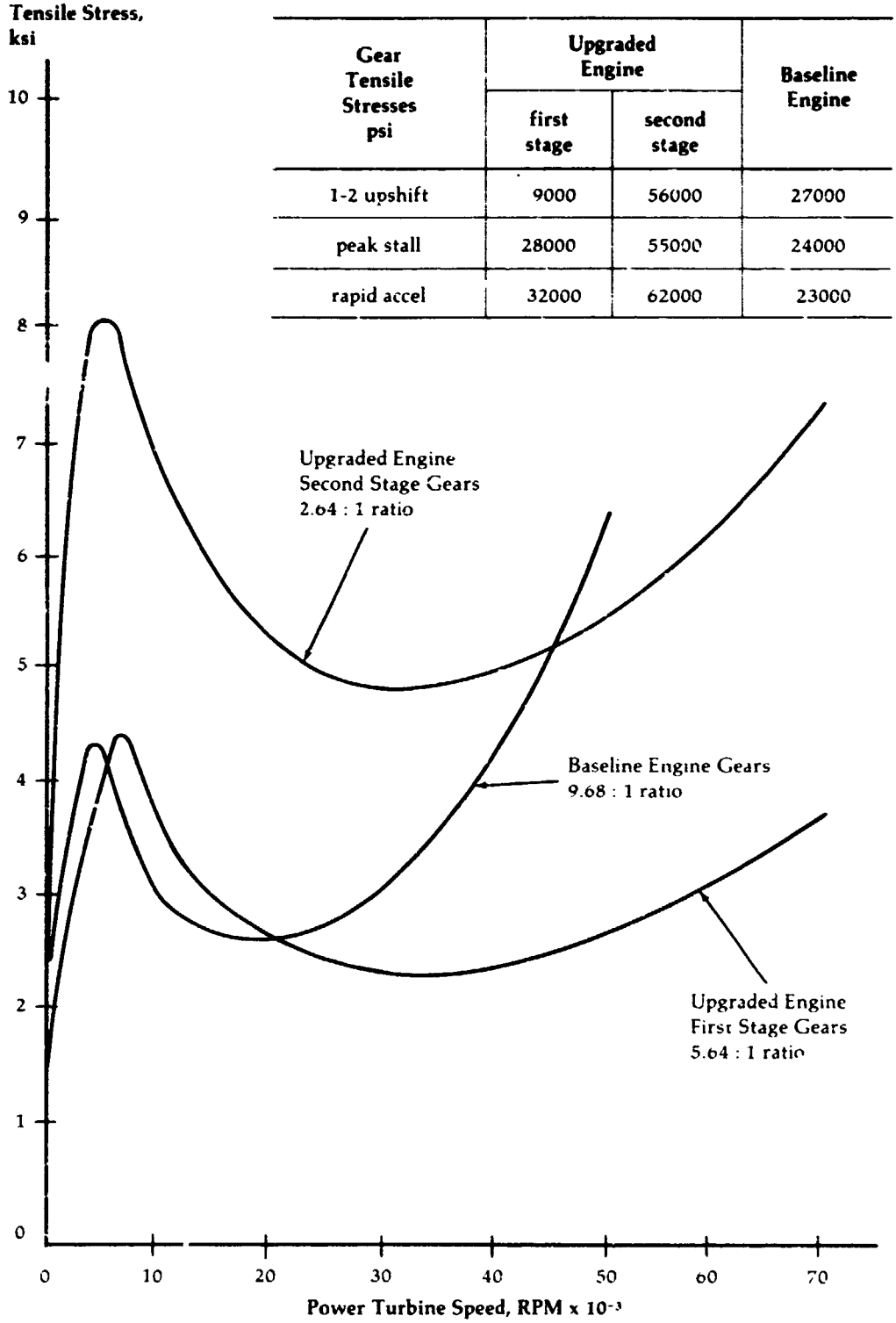

Figure 86

Upgraded Engine Drive Schematic

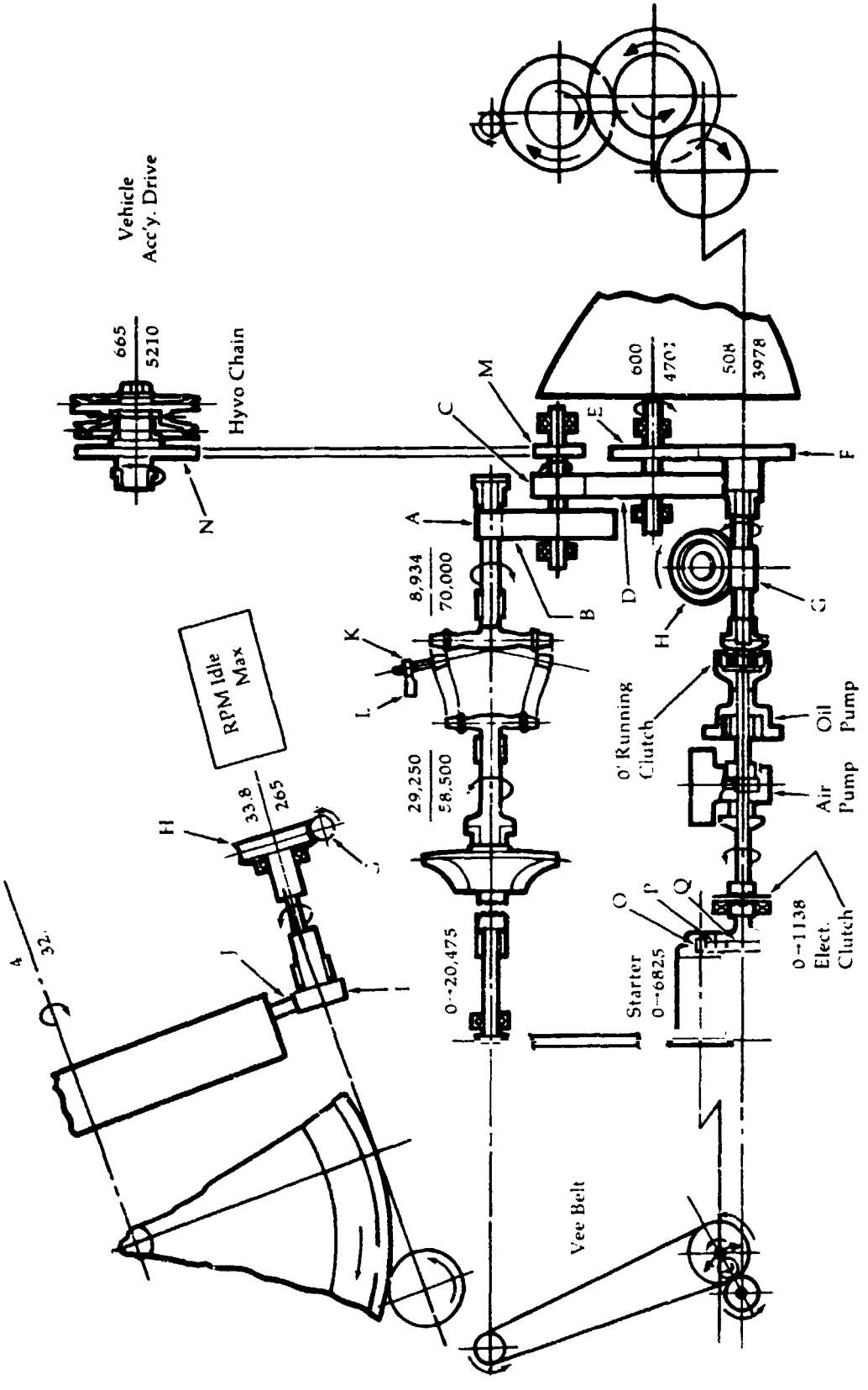

Figure 87

Upgraded Engine Auxiliaries and Drives

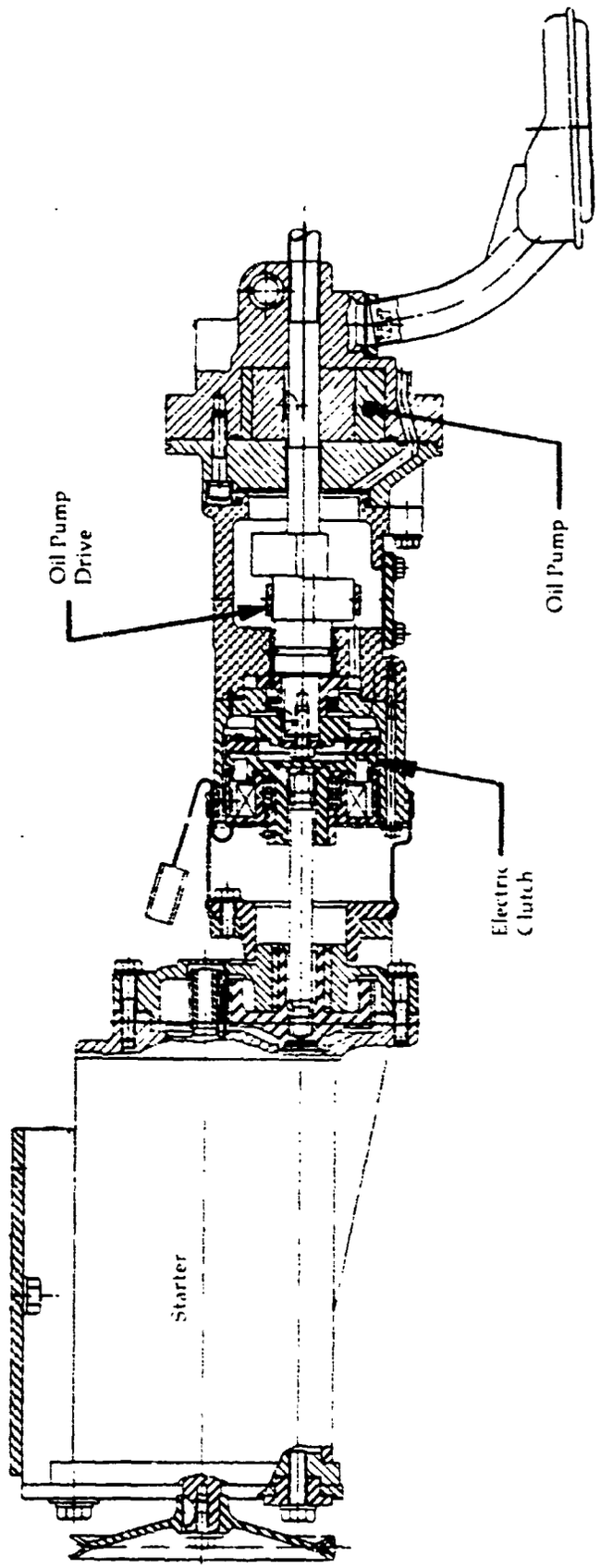

Figure 88

Upgraded Engine
Interstage Section

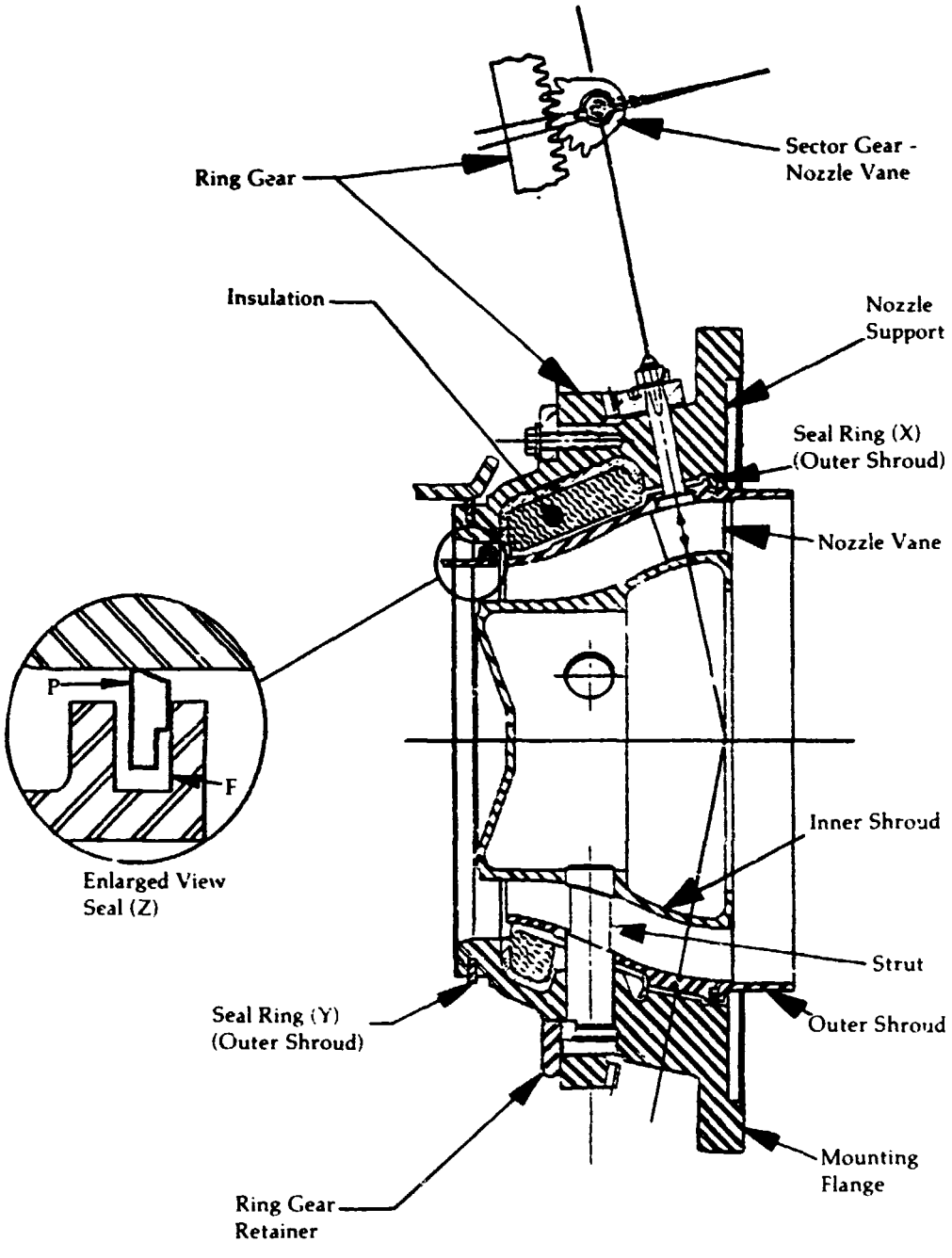

Figure 89

Upgraded Engine Variable Power Turbine Nozzle Actuator Assembly

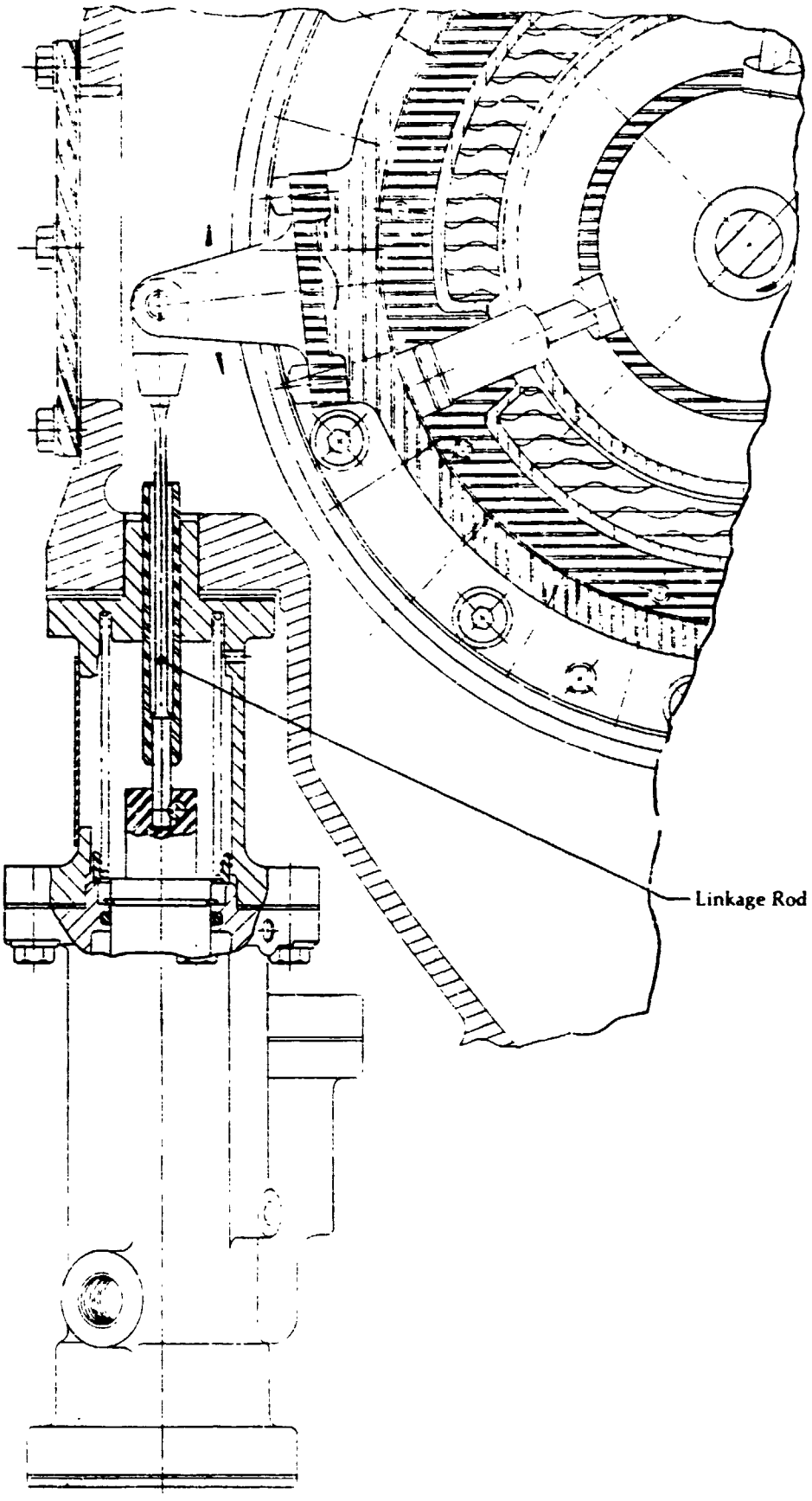

Figure 90

Upgraded Engine Regenerator Design

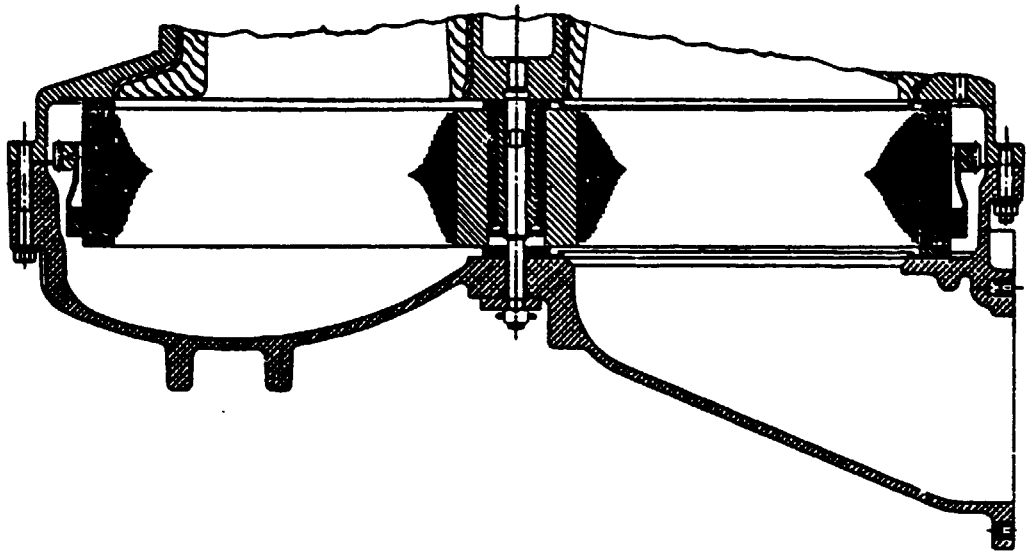

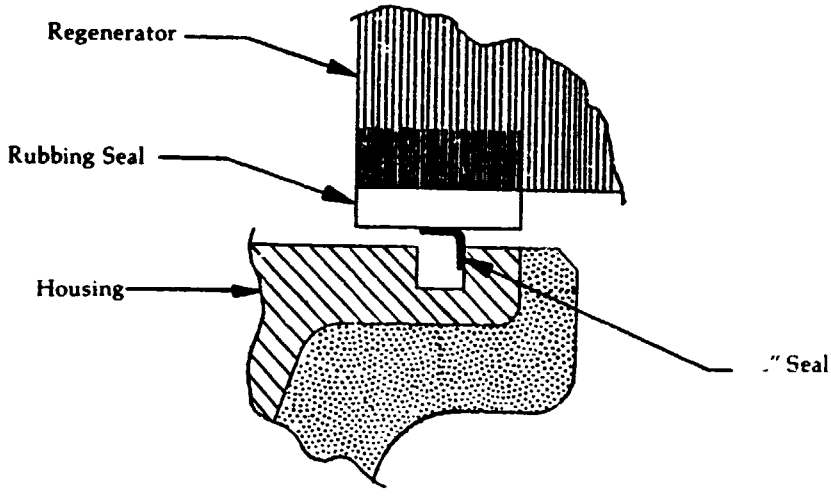

Figure 91

Flexable Elastomeric Regenerator Mount

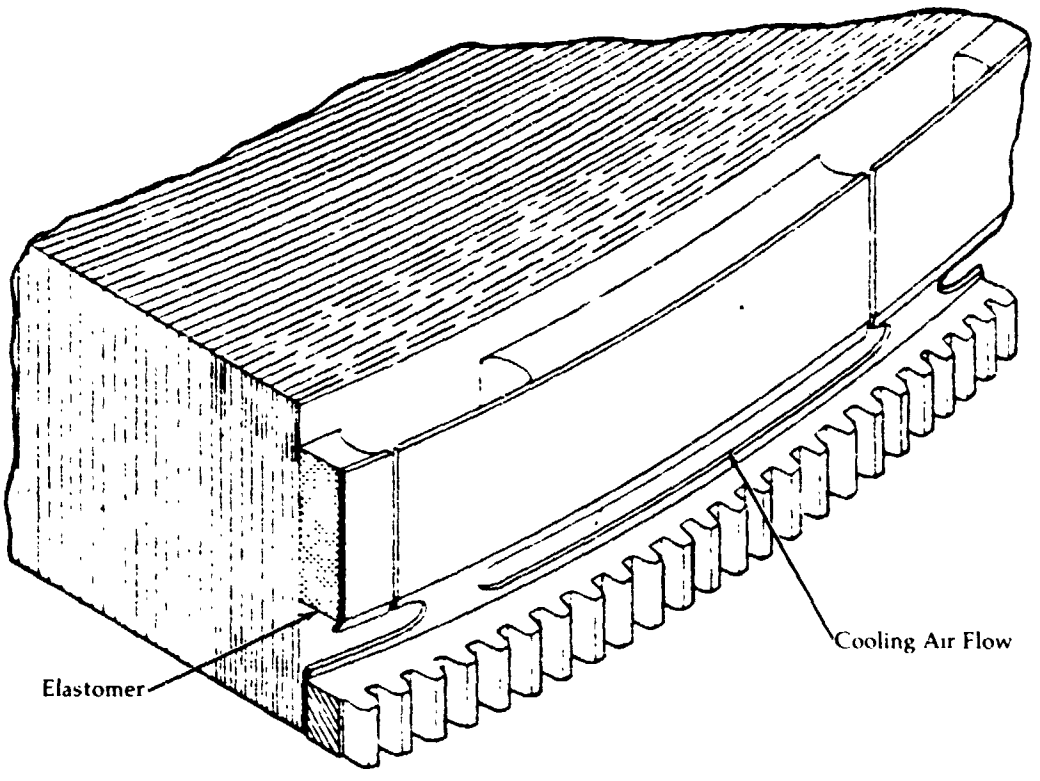

Figure 92

Upgraded Engine Regenerator and Accessory Drive-Rear View

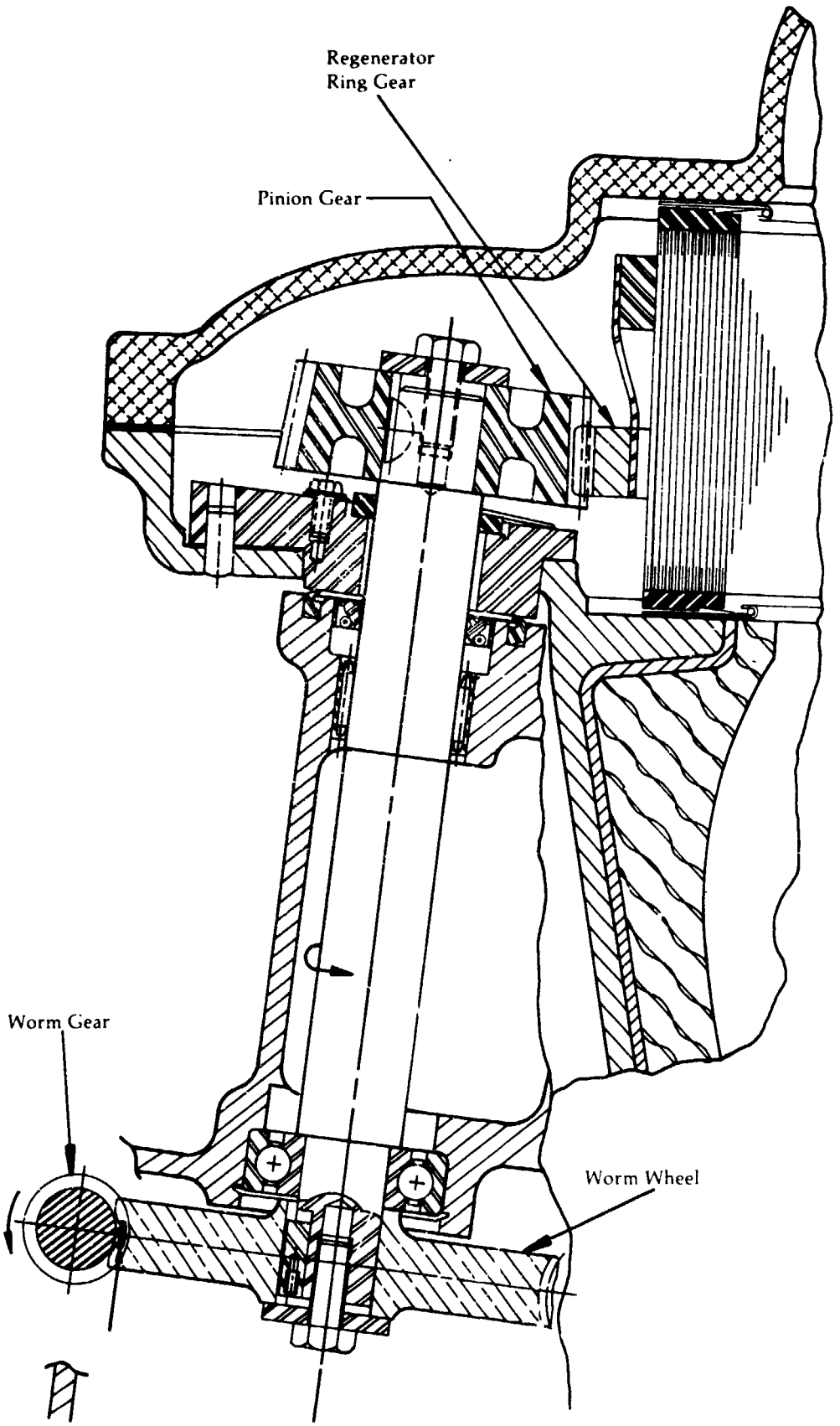

Figure 93

Regenerator Drive Gears Surface Tensile Stresses

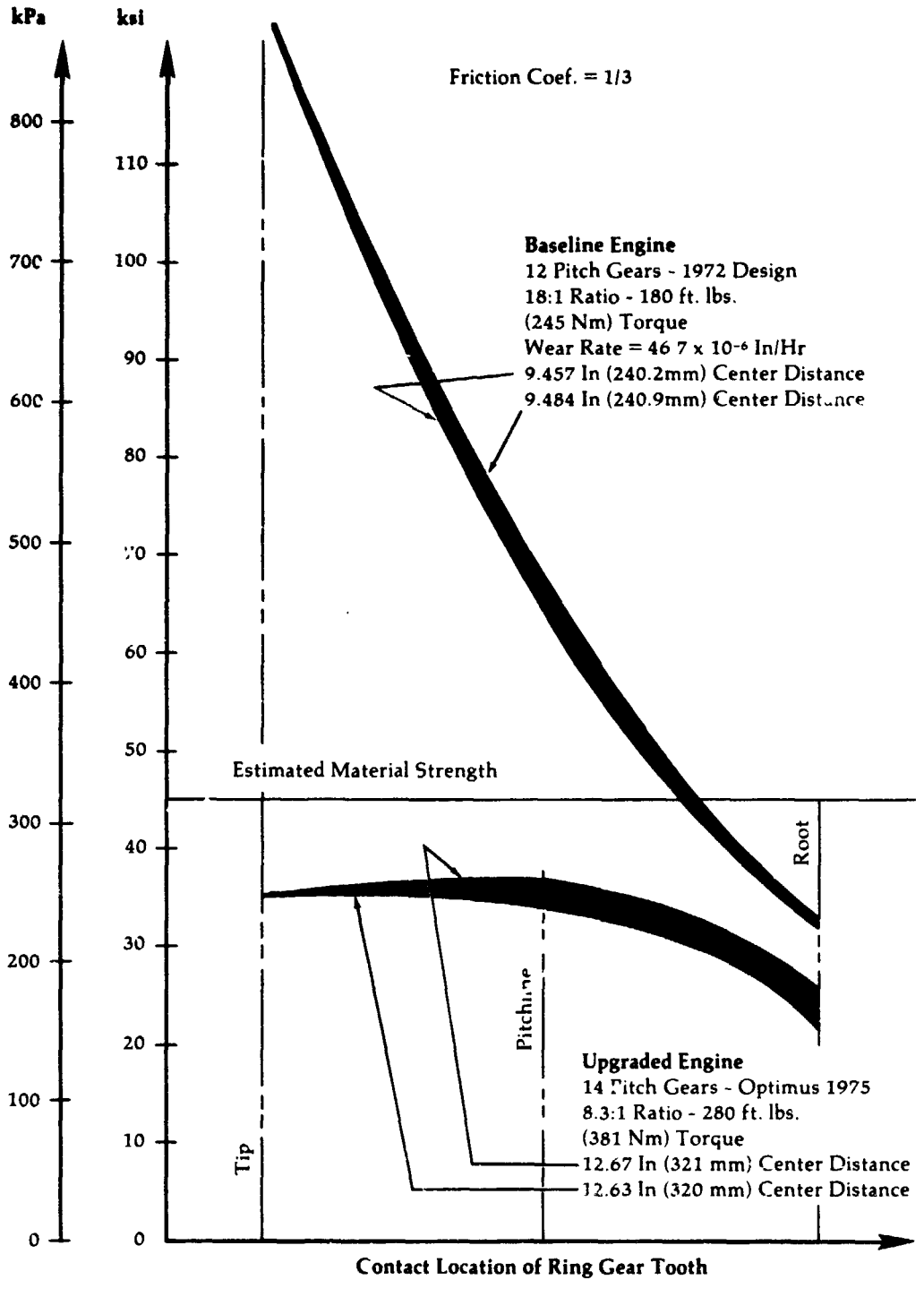

Figure 94

Upgraded Engine Lean Premixed/ Prevaporized Combustor

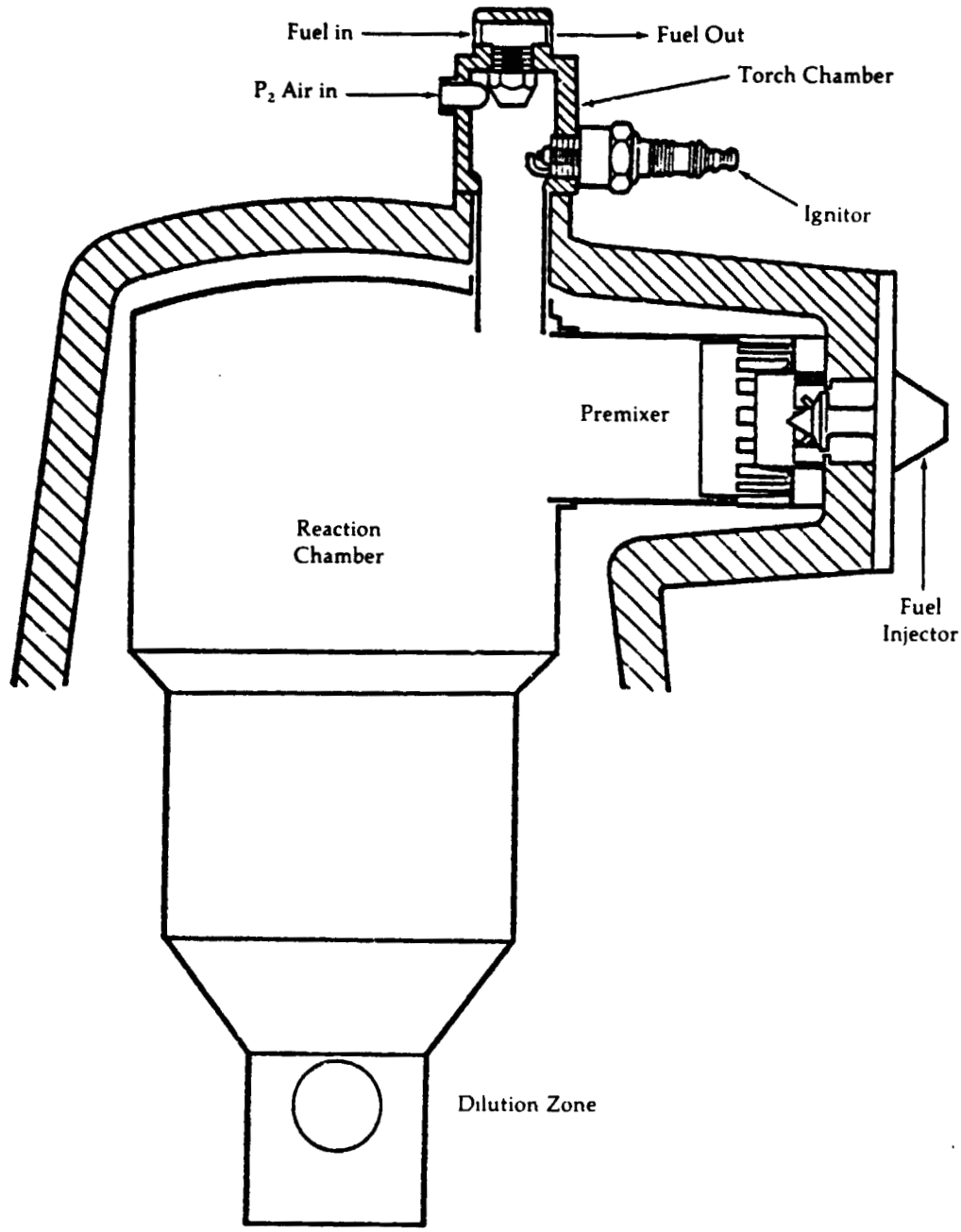

Figure 95

Reaction Zone Comparison

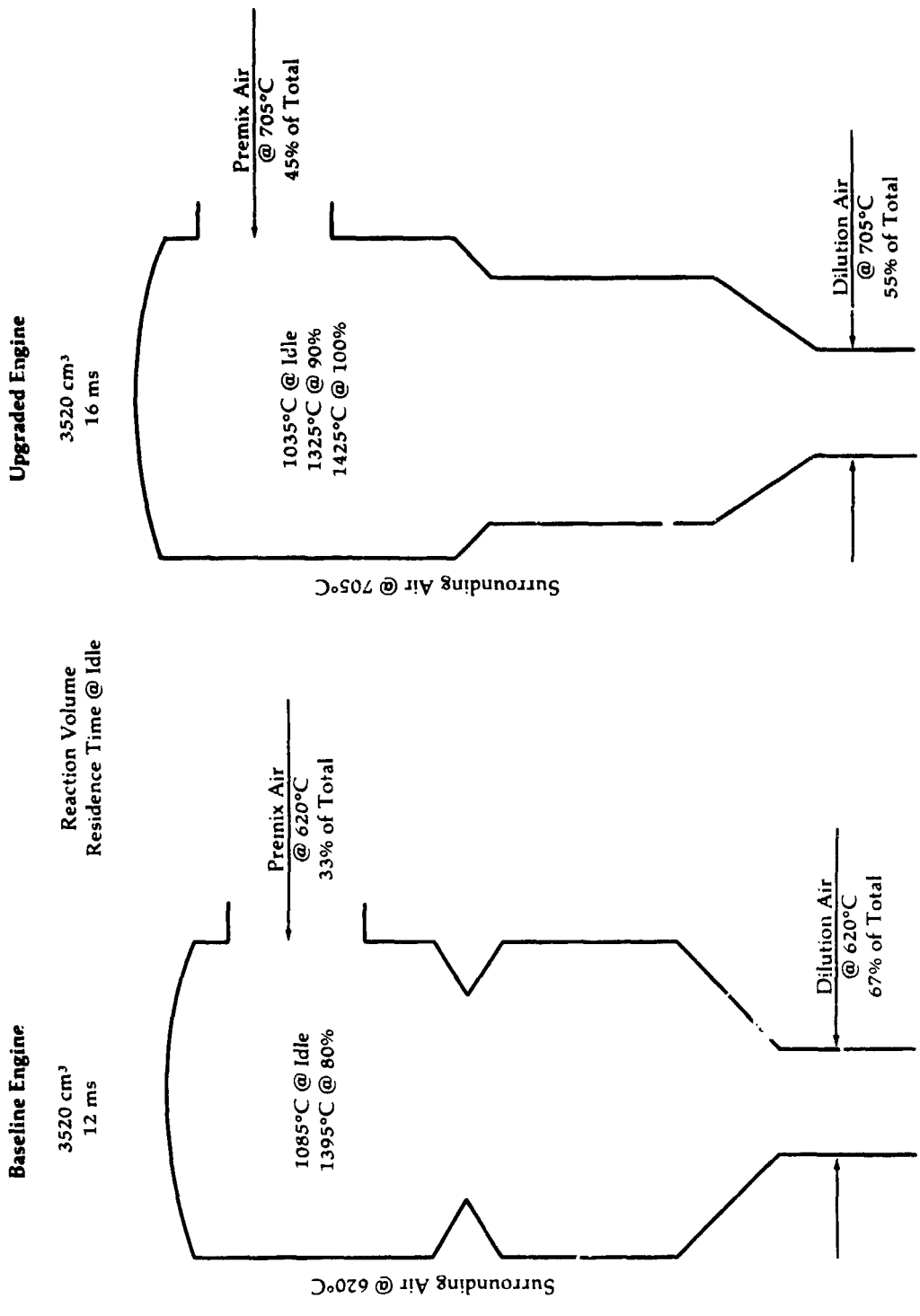

Figure 96

Upgraded Engine Estimated Power Turbine Parasitic Losses at Peak Power Points

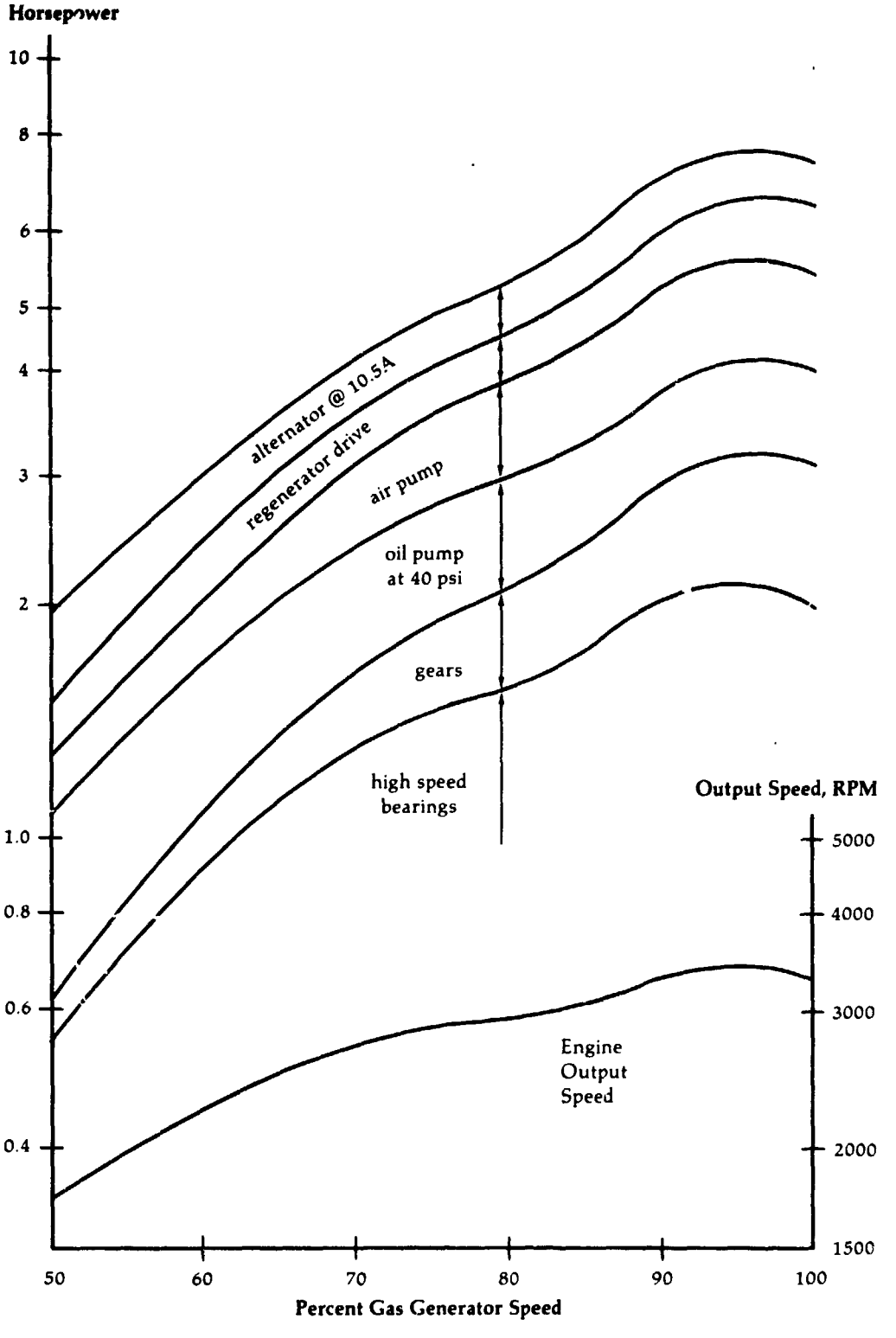

Figure 97

Upgraded Engine Estimated Specific Fuel Consumption

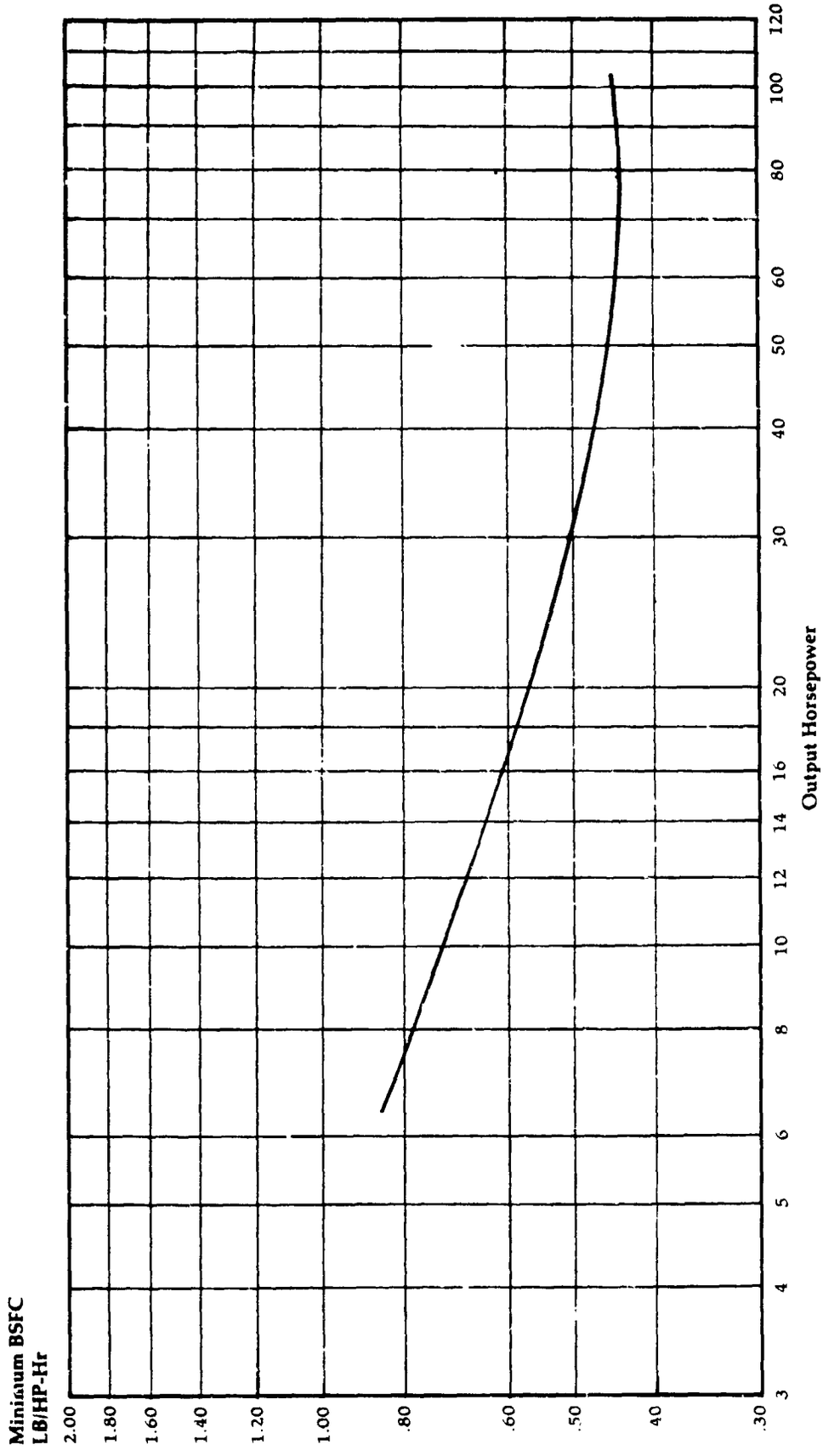

Figure 98

Upgraded Engine Vehicle Installation

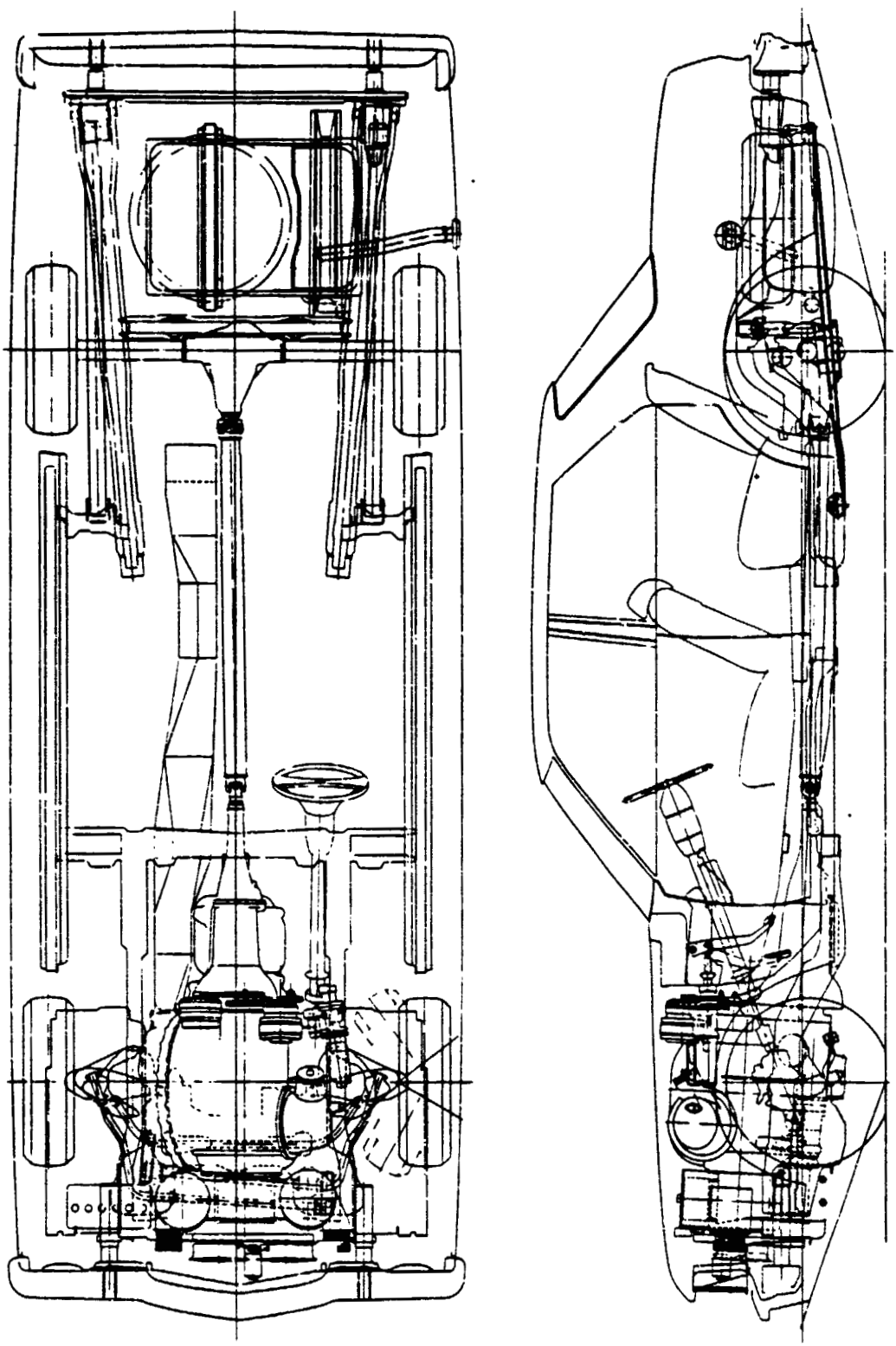

Figure 99

Upgraded Engine
Complete Engine
System

Figure 100A

Upgraded Engine
Complete Engine
System

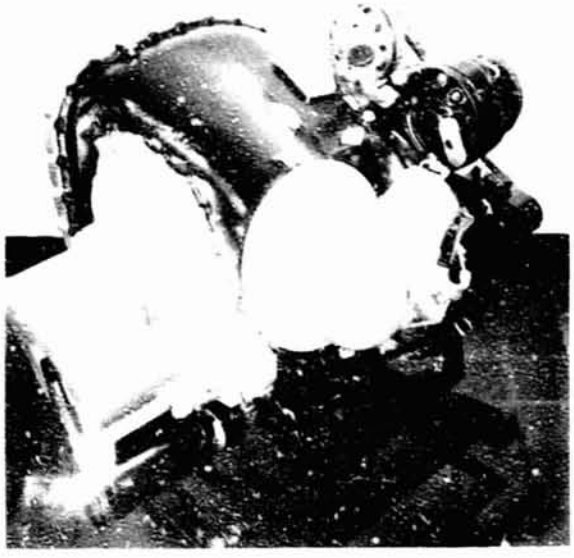

Left Front 3/4 View

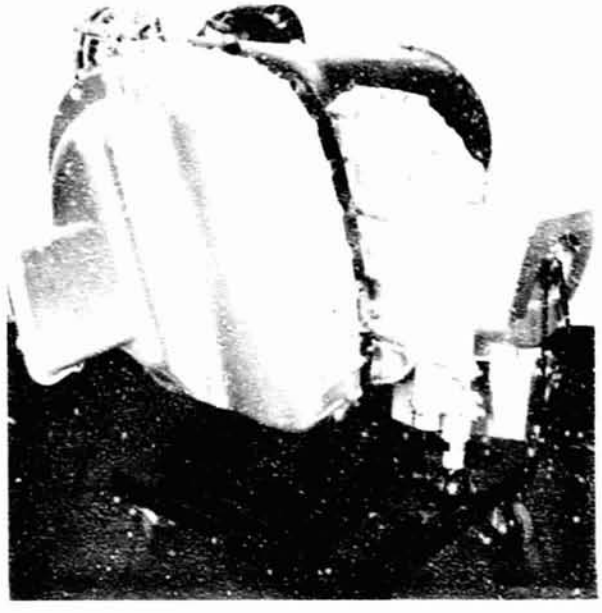

Right Front 3/4 View

Left Rear 3/4 View

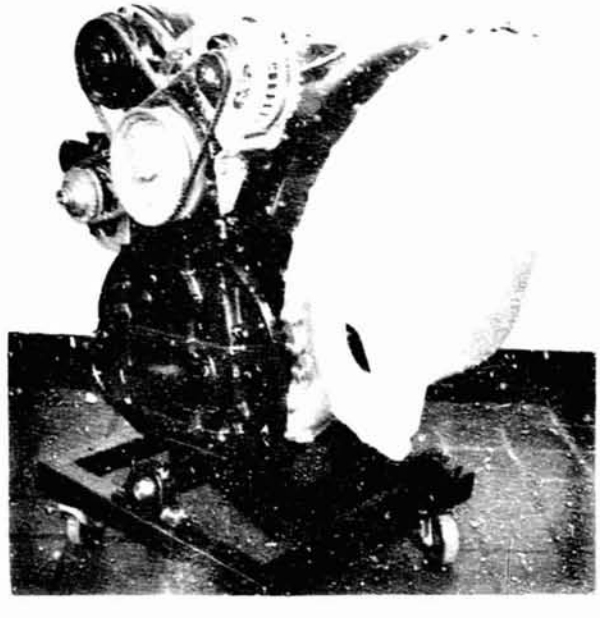

Right Rear 3/4 View

Upgraded Engine
Expanded Top View

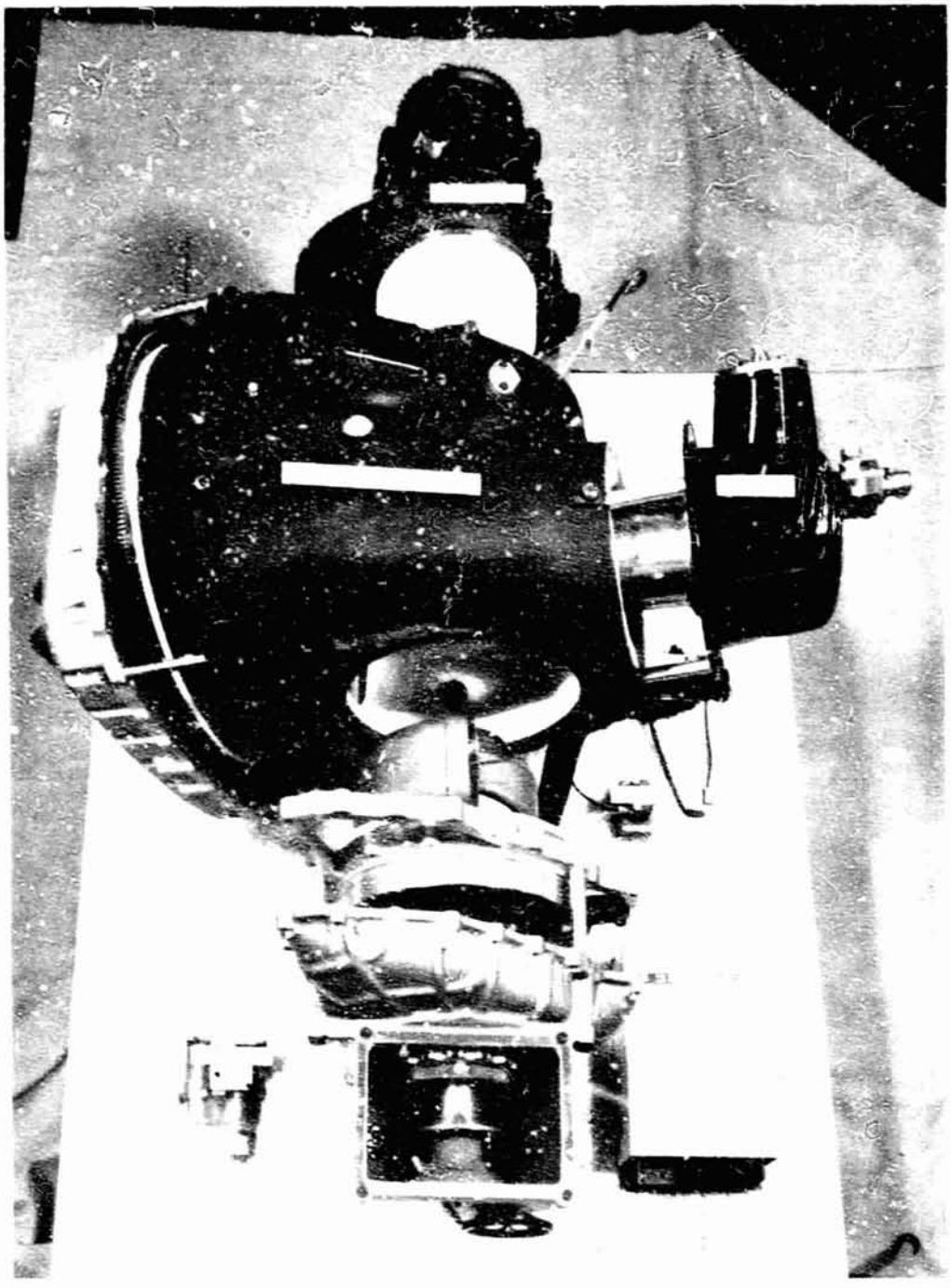

Figure 101

Upgraded Engine
Engine Housing -
View from
Compressor Exit

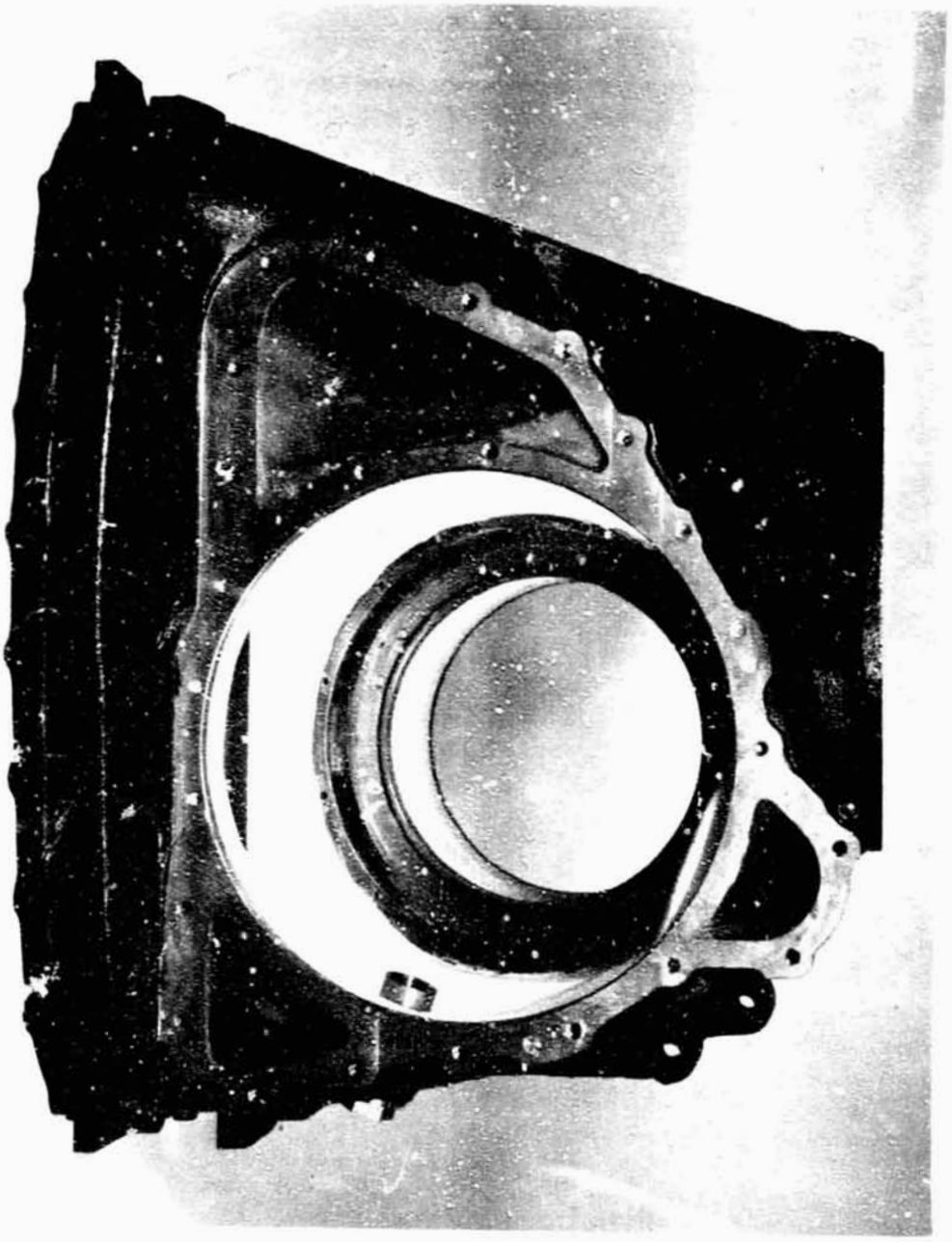

Figure 102

Upgraded Engine
Engine Housing -
View from
Regenerator

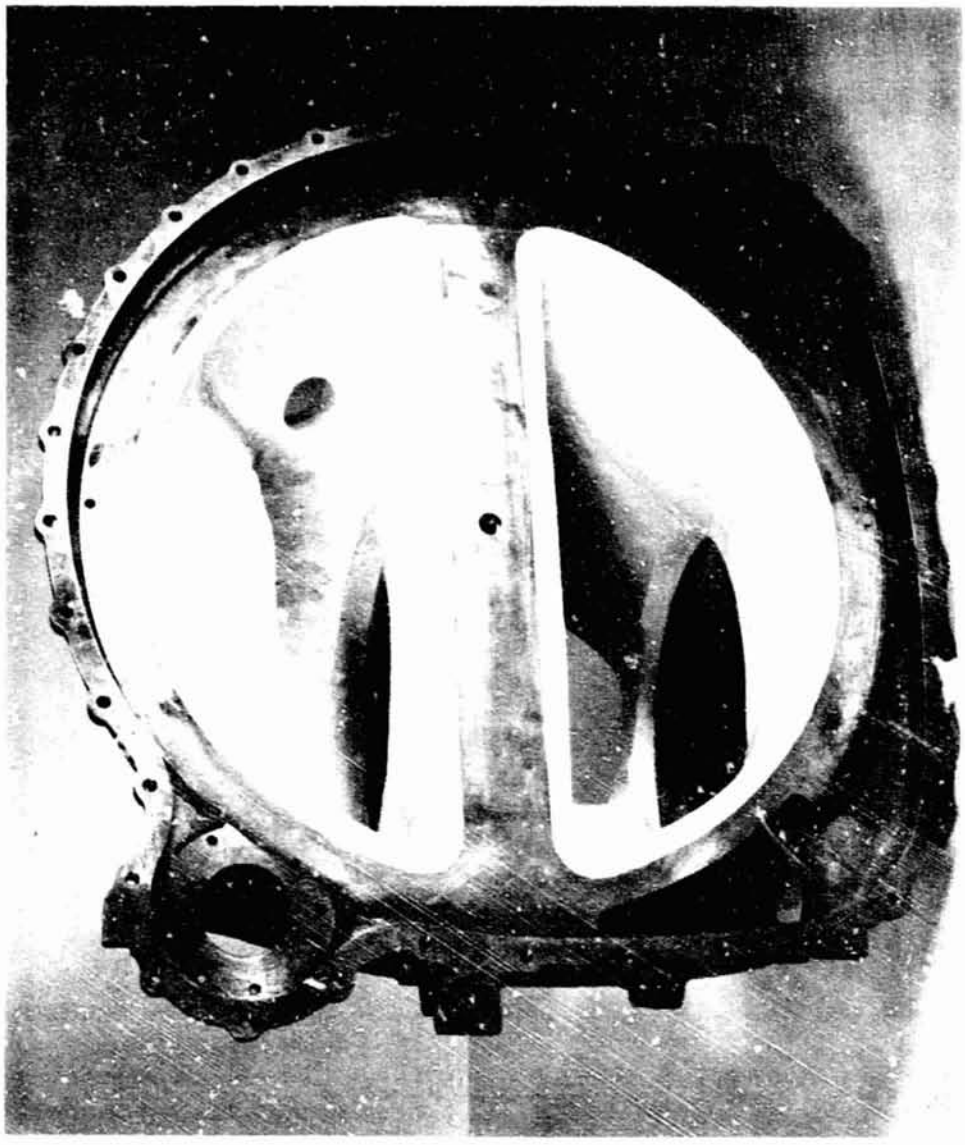

Figure 103

Upgraded Engine
Power Turbine
Nozzle Assembly

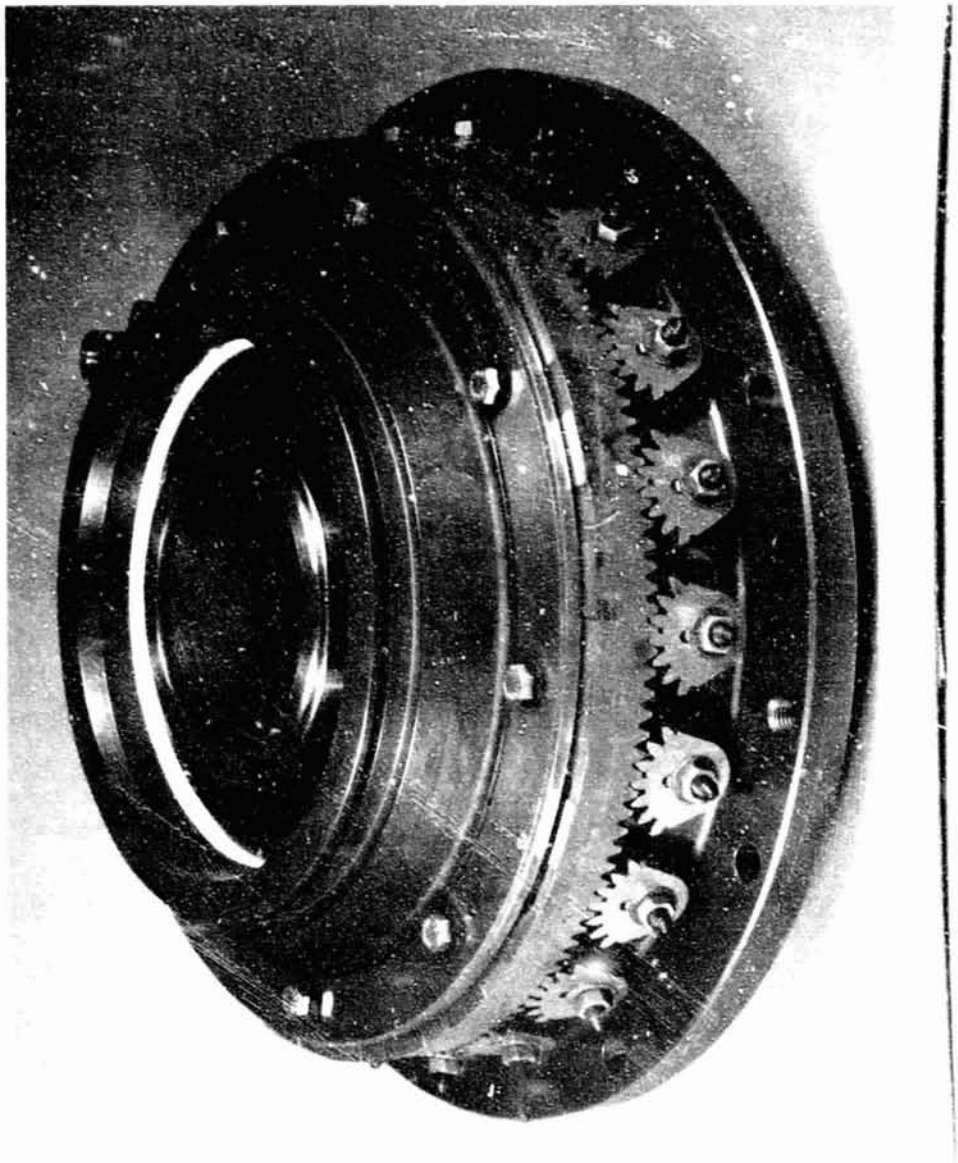

Figure 104

Upgraded Engine
Gas Generator
Section

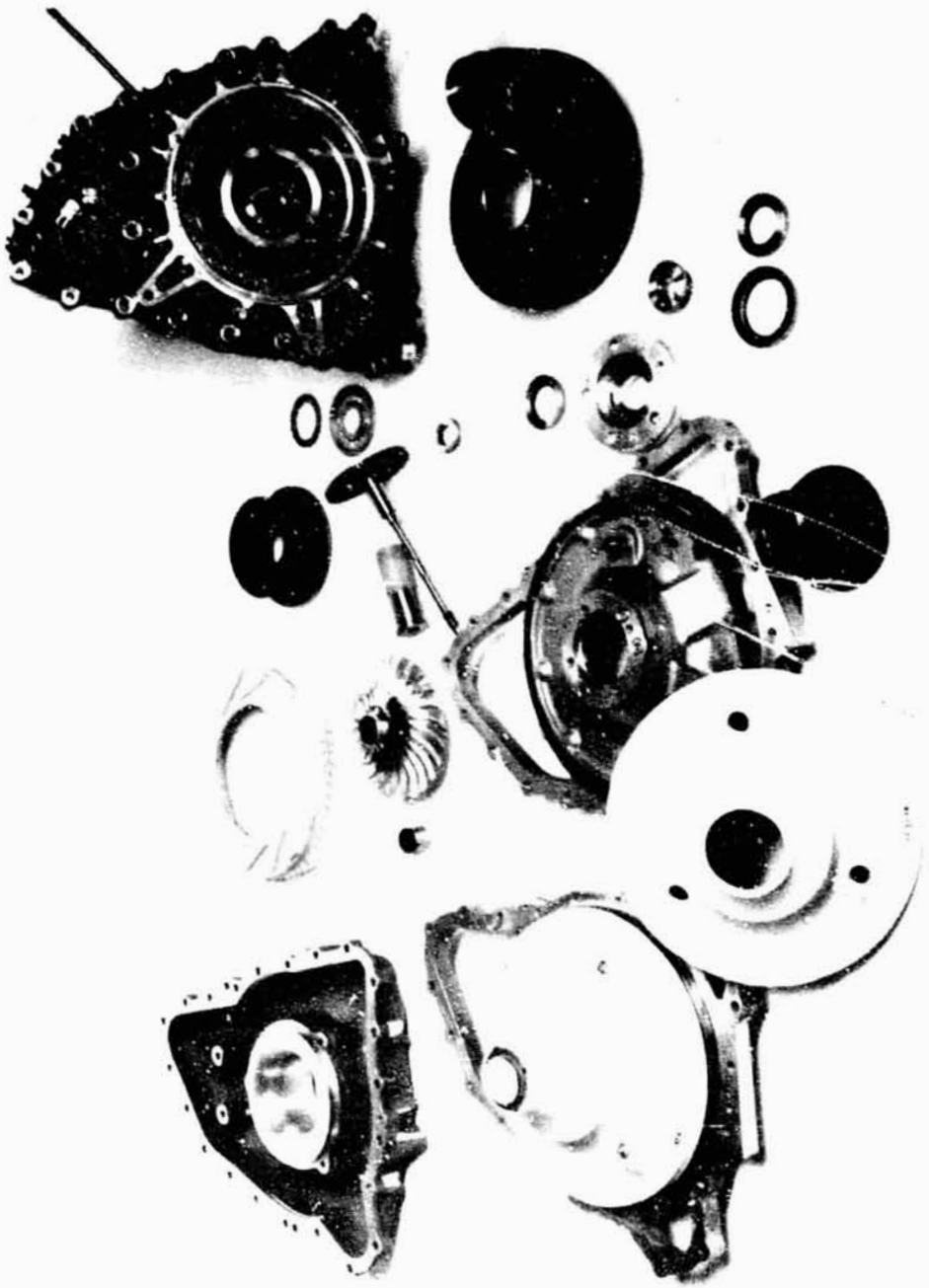

Figure 105

Upgraded Engine
Gas Generator
Shaft Components

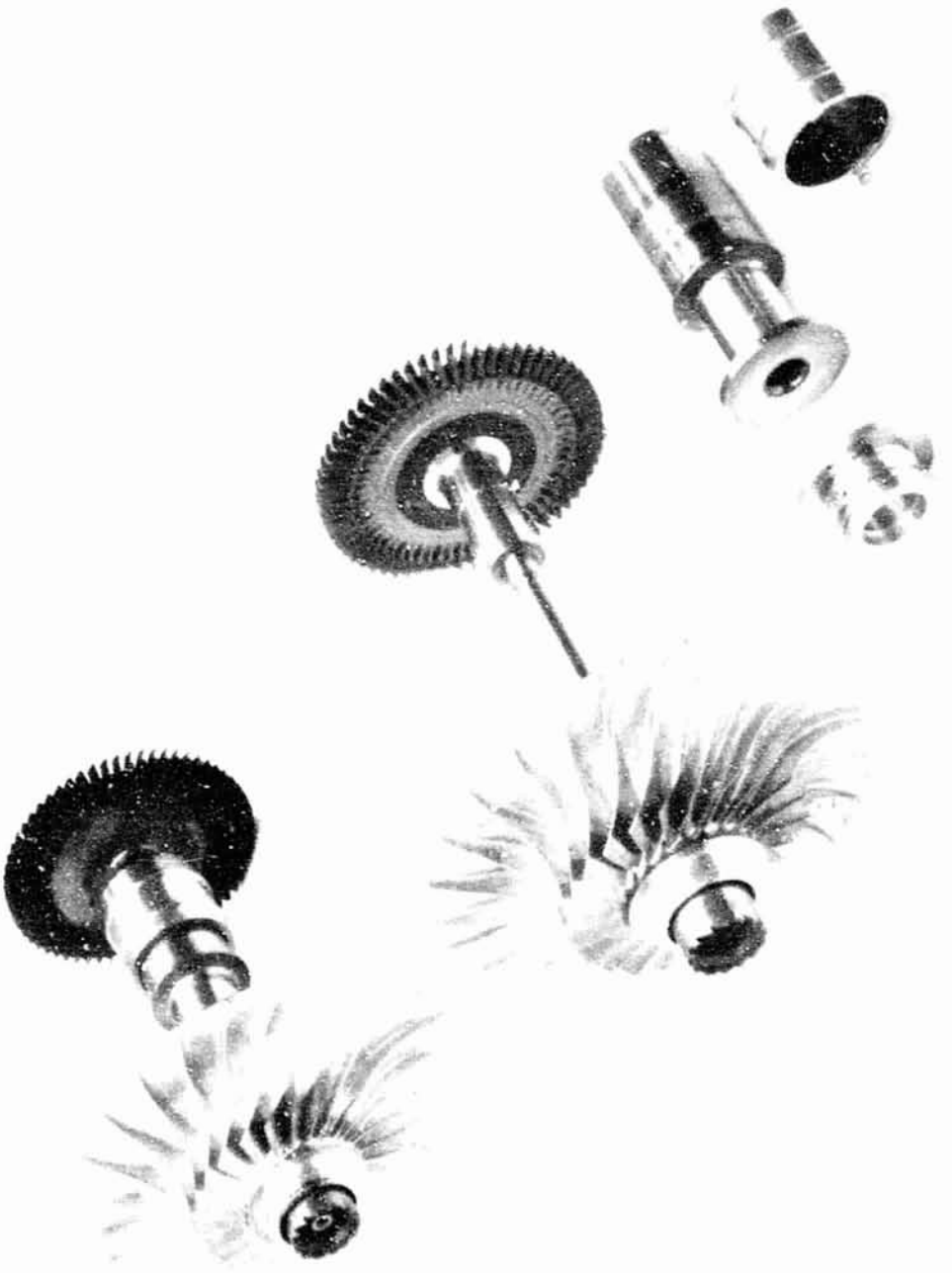

Figure 106

Upgraded Engine
Engine Power
Section

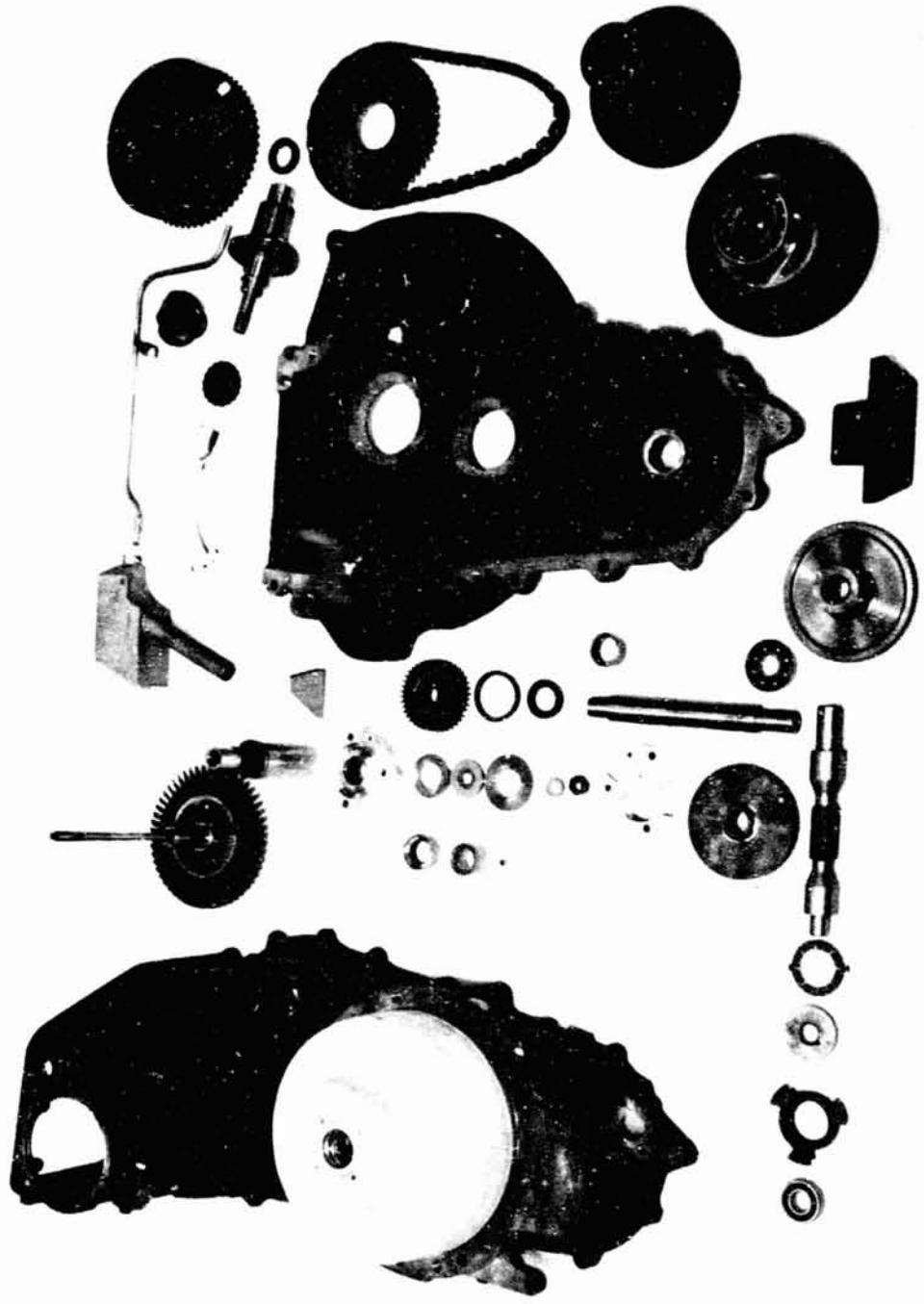

Figure 107

Upgraded Engine
Power Section
Shaft Components

Figure 108

Upgraded Engine
Air/Oil Pump
Assembly

Figure 109

Upgraded Engine
Variable Inlet
Guide Vane
Assembly

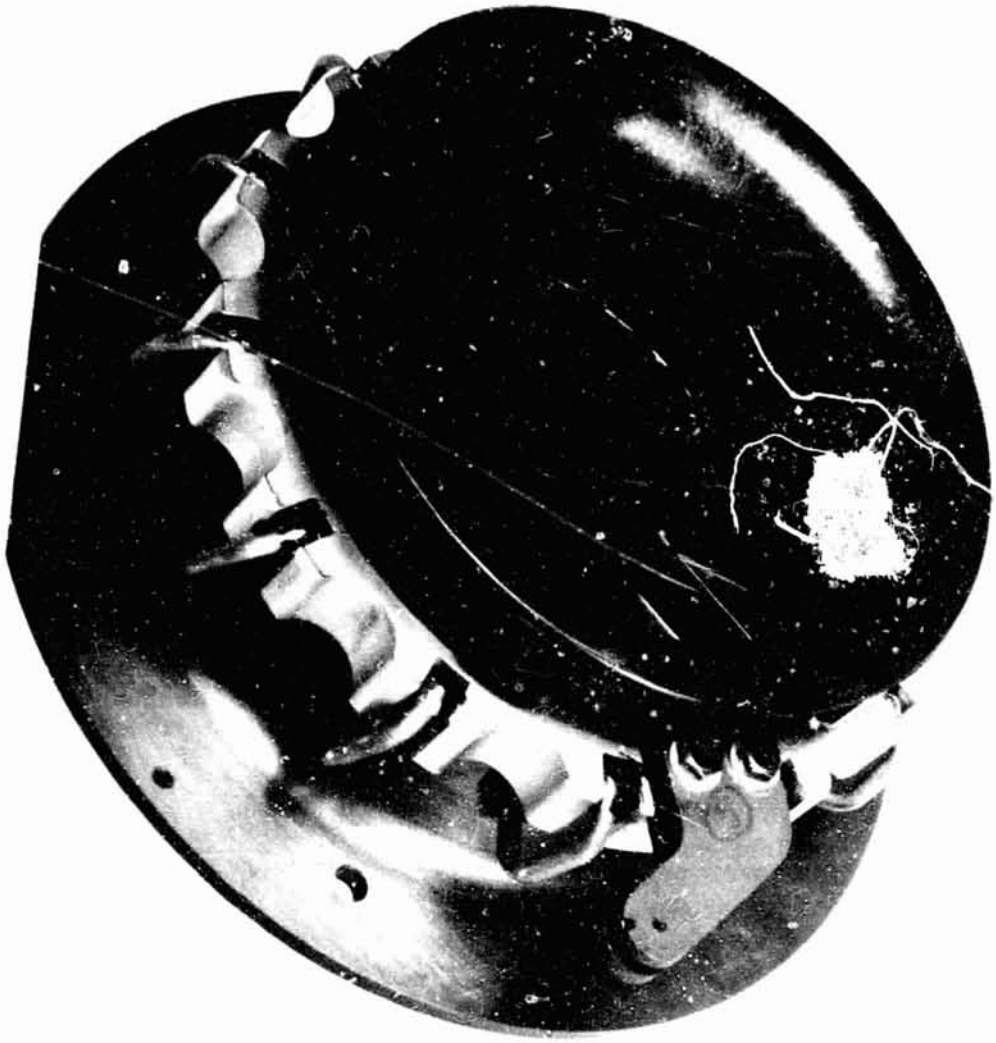

Figure 110

Upgraded Engine Intake/Starter Assembly

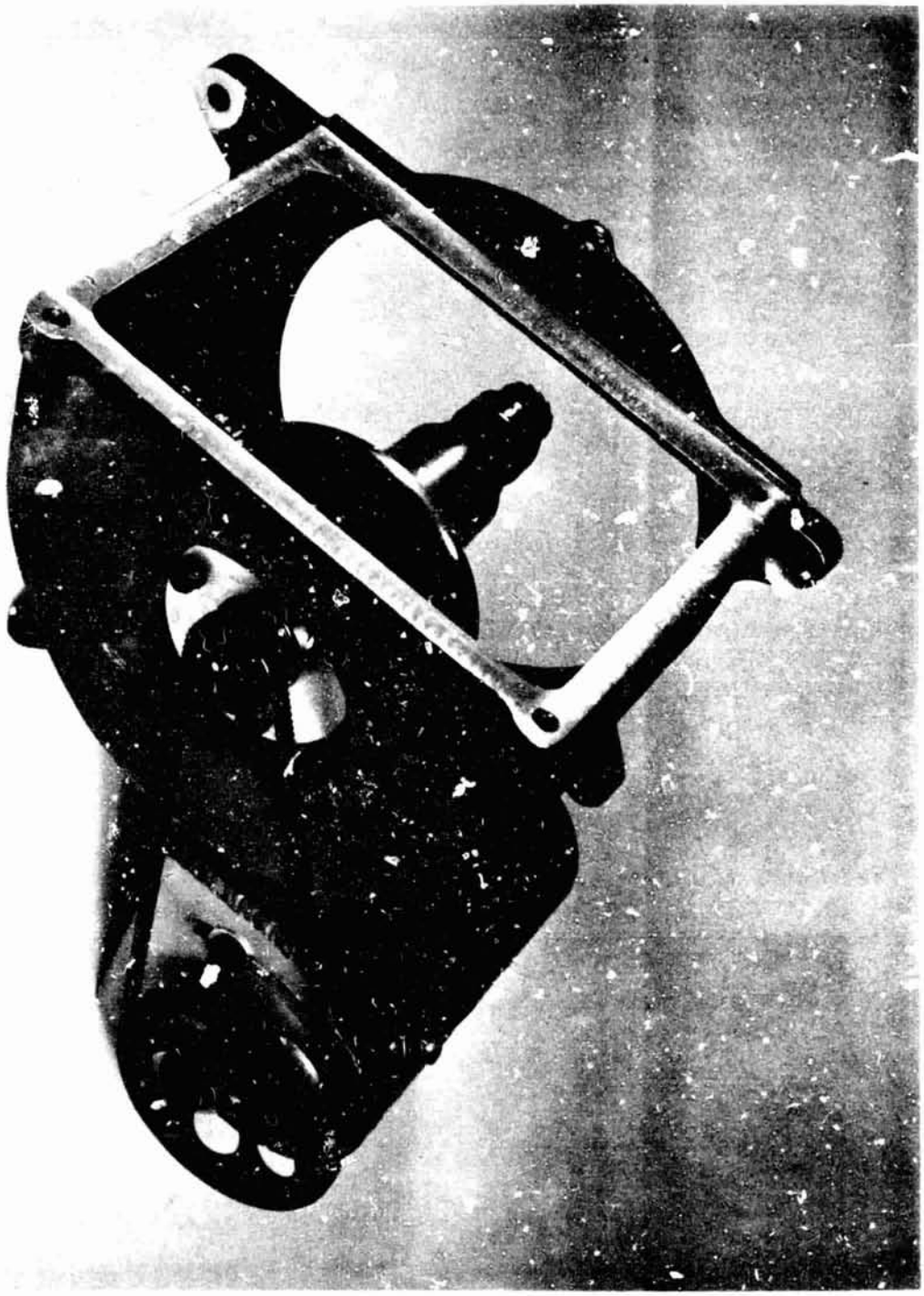

Figure 111

Schematic Drawing
of Compressor
Test Facility

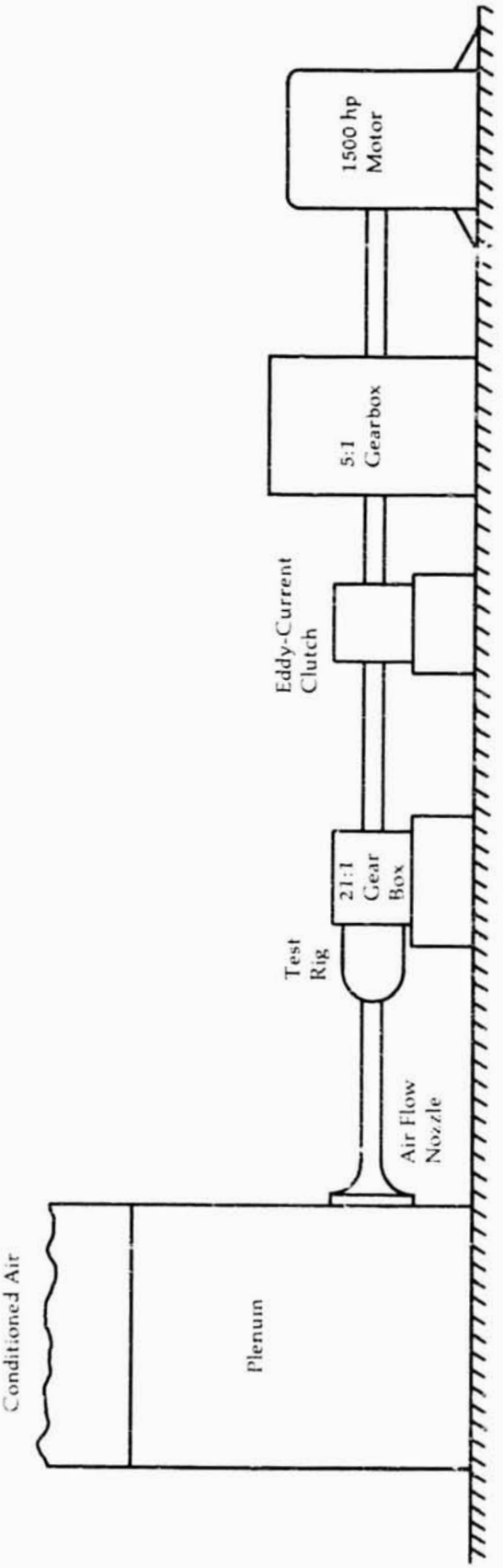

Figure 112

Upgraded Engine
1.26 Scale
Compressor Test
Rig

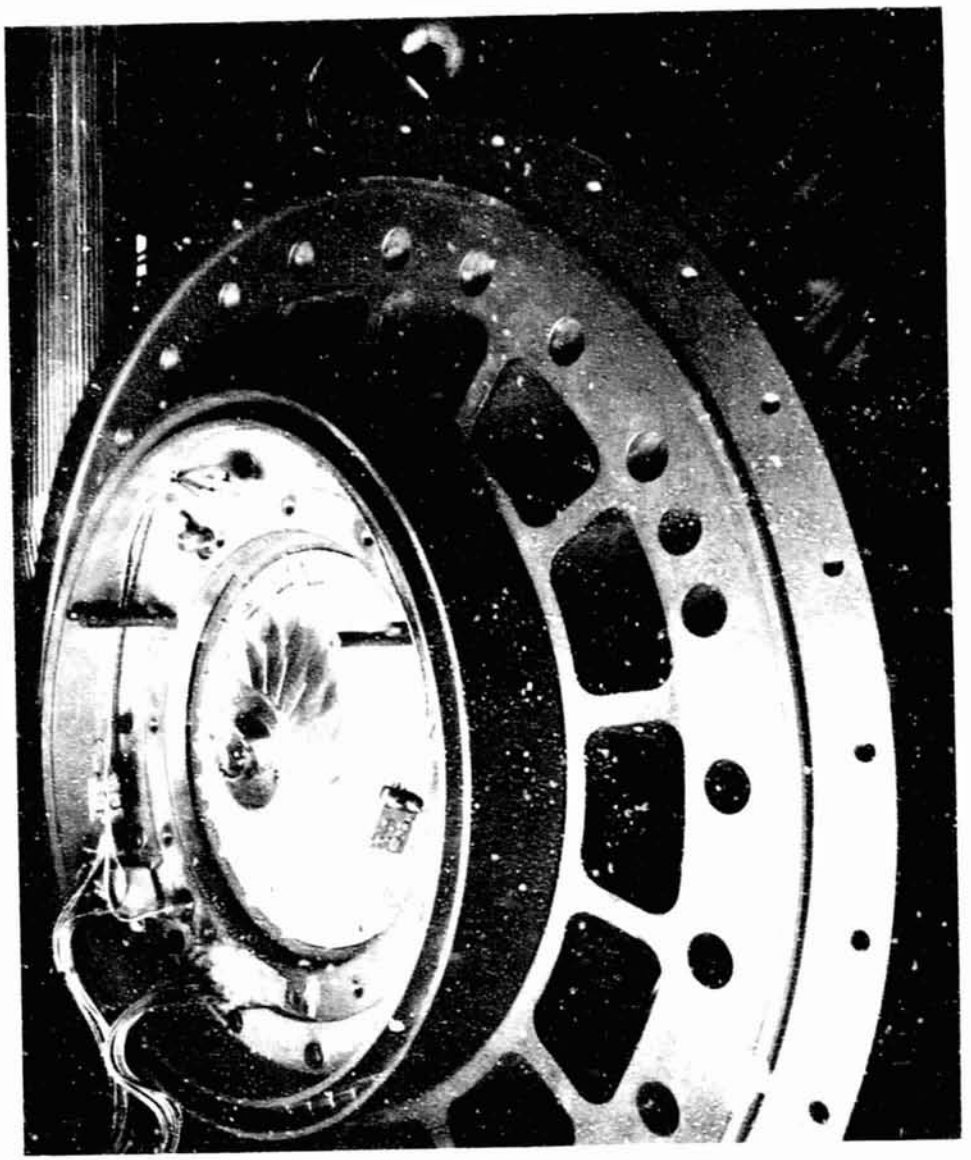

Figure 113

Upgraded Engine Compressor Discharge Total Pressure Probe Characteristic

$$P_{true} = \frac{P_{probe}}{\left[1 - \left(\frac{P_{ref} - P_{probe}}{P_{ref}}\right)\right]} \quad \text{(at a given Mach No.)}$$

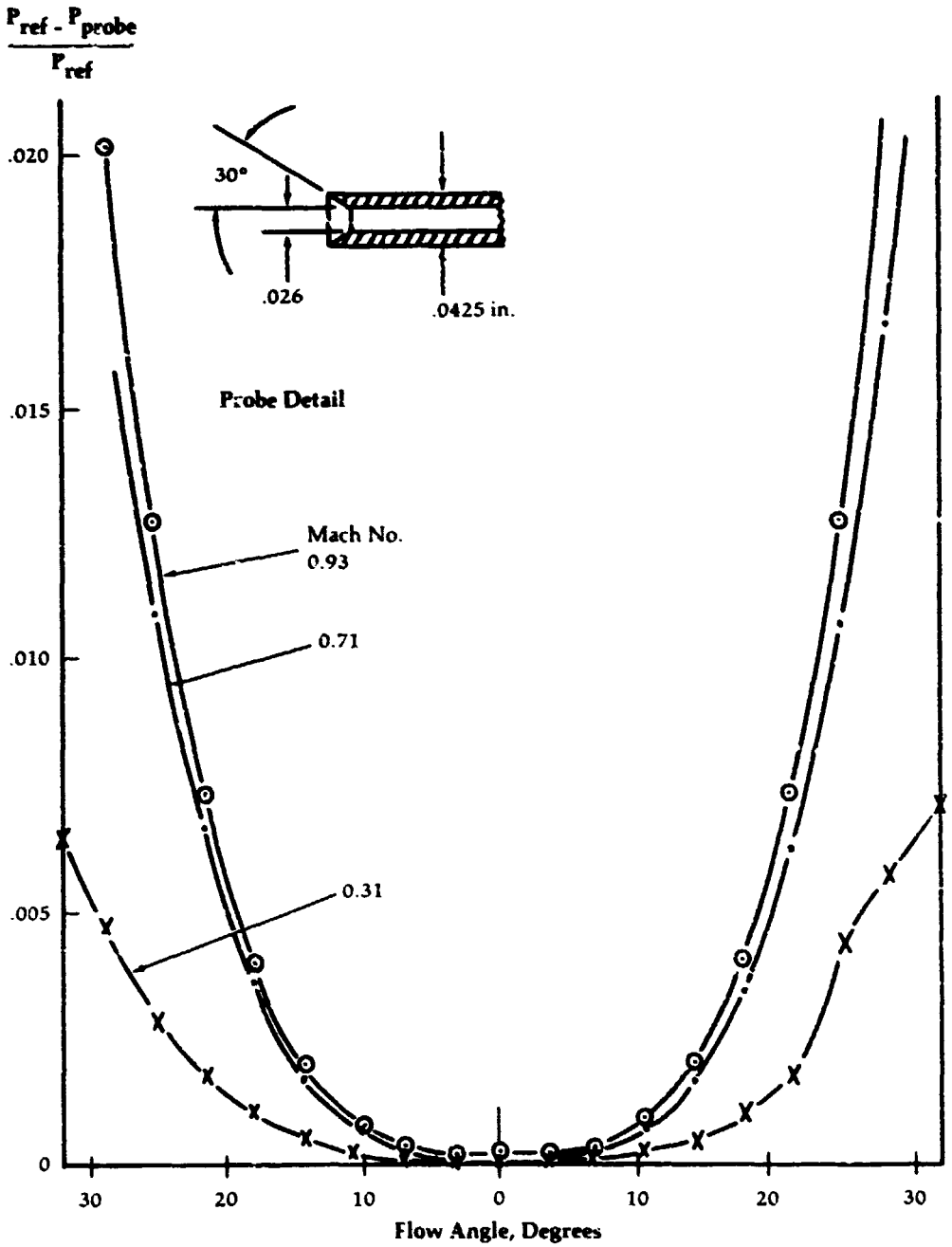

Figure 114

1.26 Scale Upgraded Engine Compressor Rig Adaptation

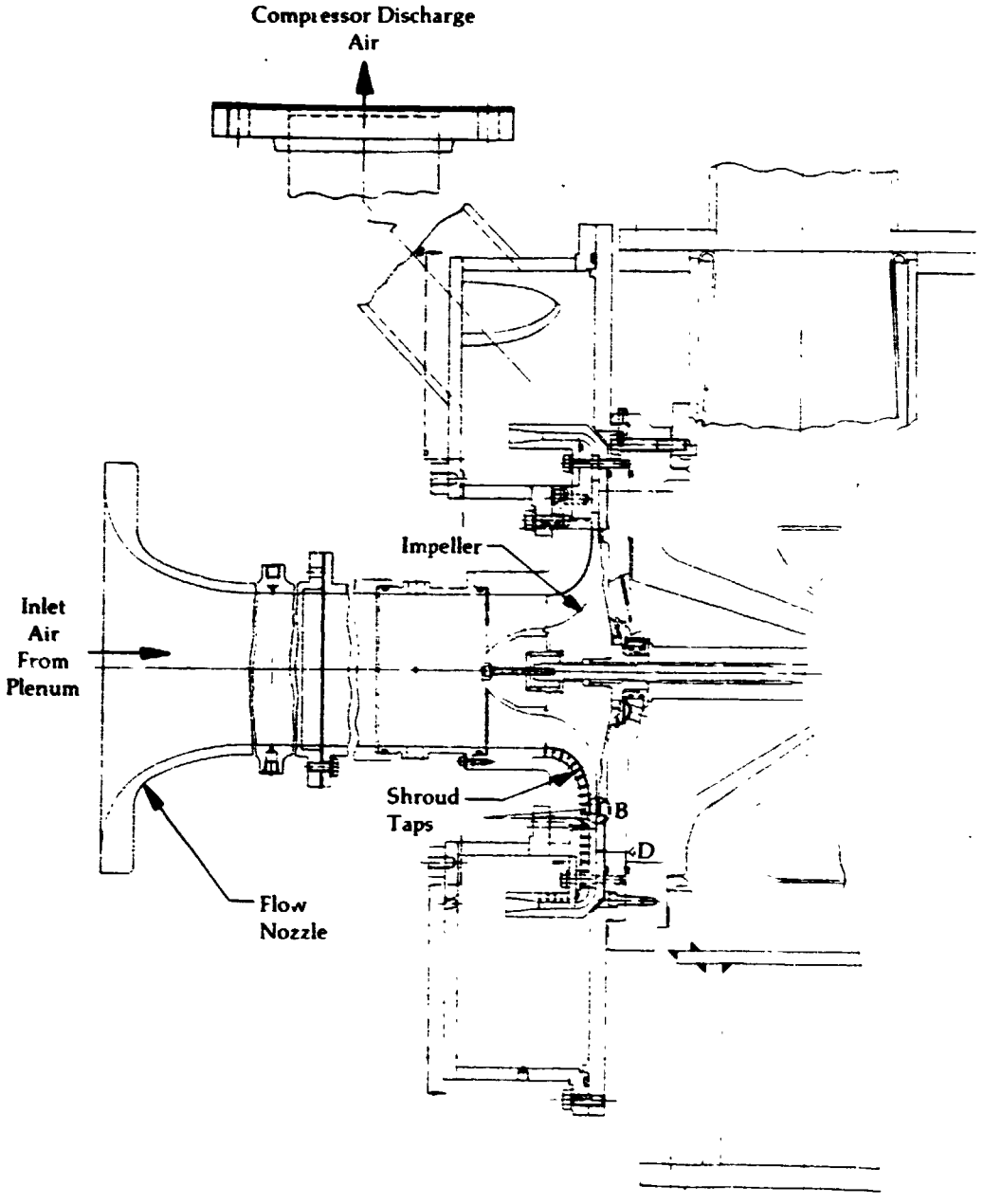

Figure 115

Location of Static Pressure Taps in Diffuser Assembly

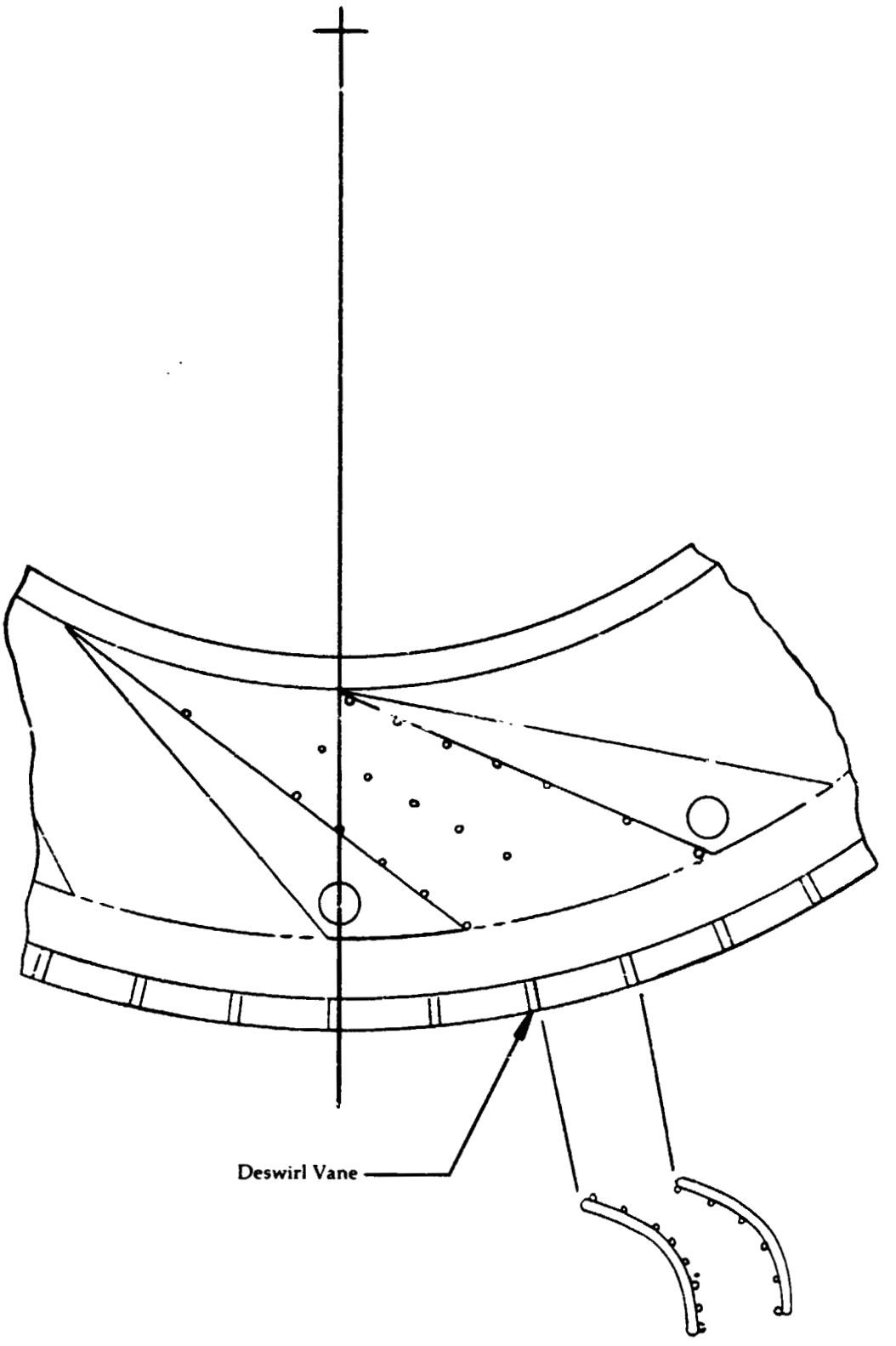

Figure 116

Turbine Nozzle Cold-Flow Test Facility Schematic

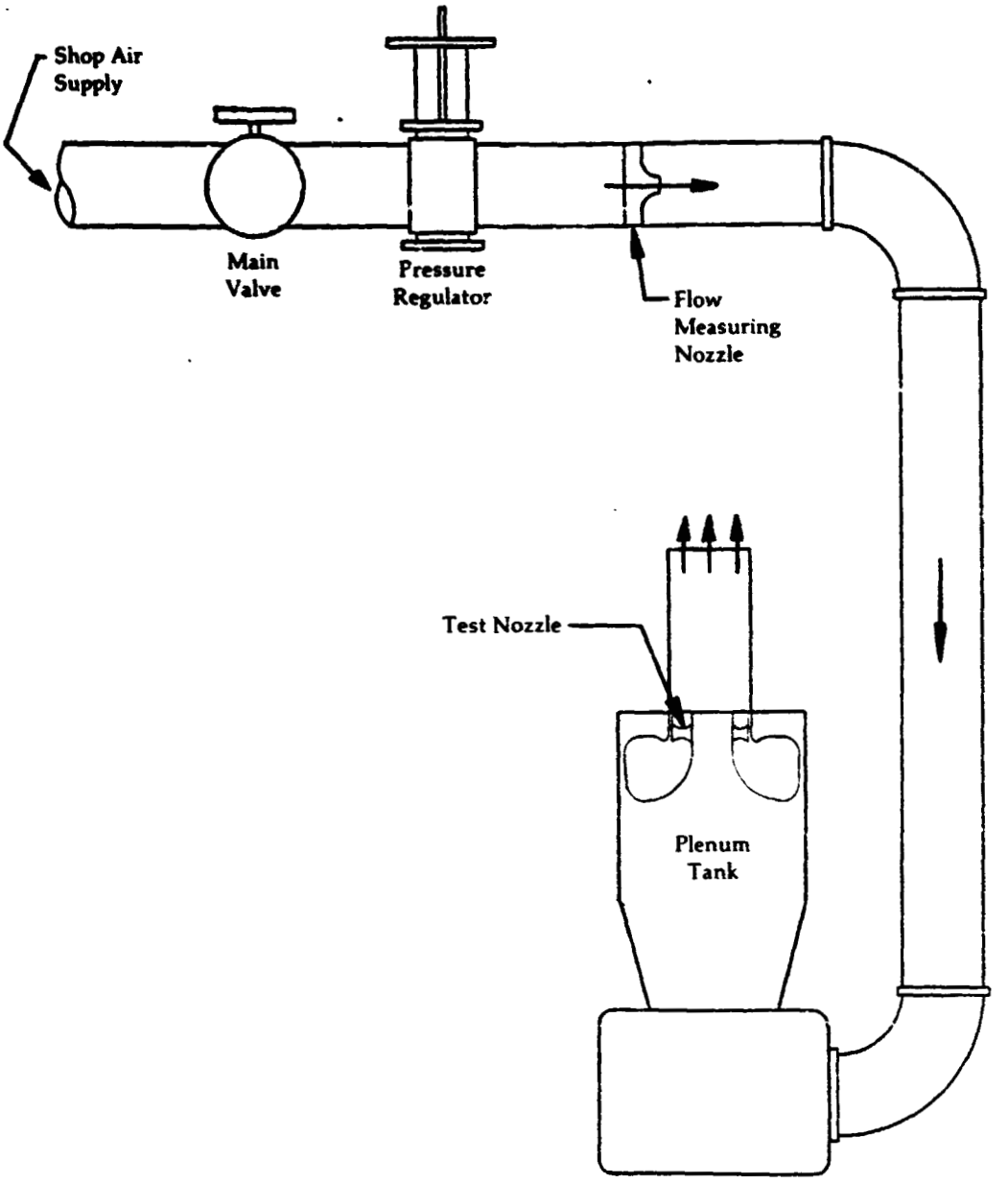

Figure 117

Upgraded Engine Compressor-Turbine Nozzle Cold Flow Test Rig

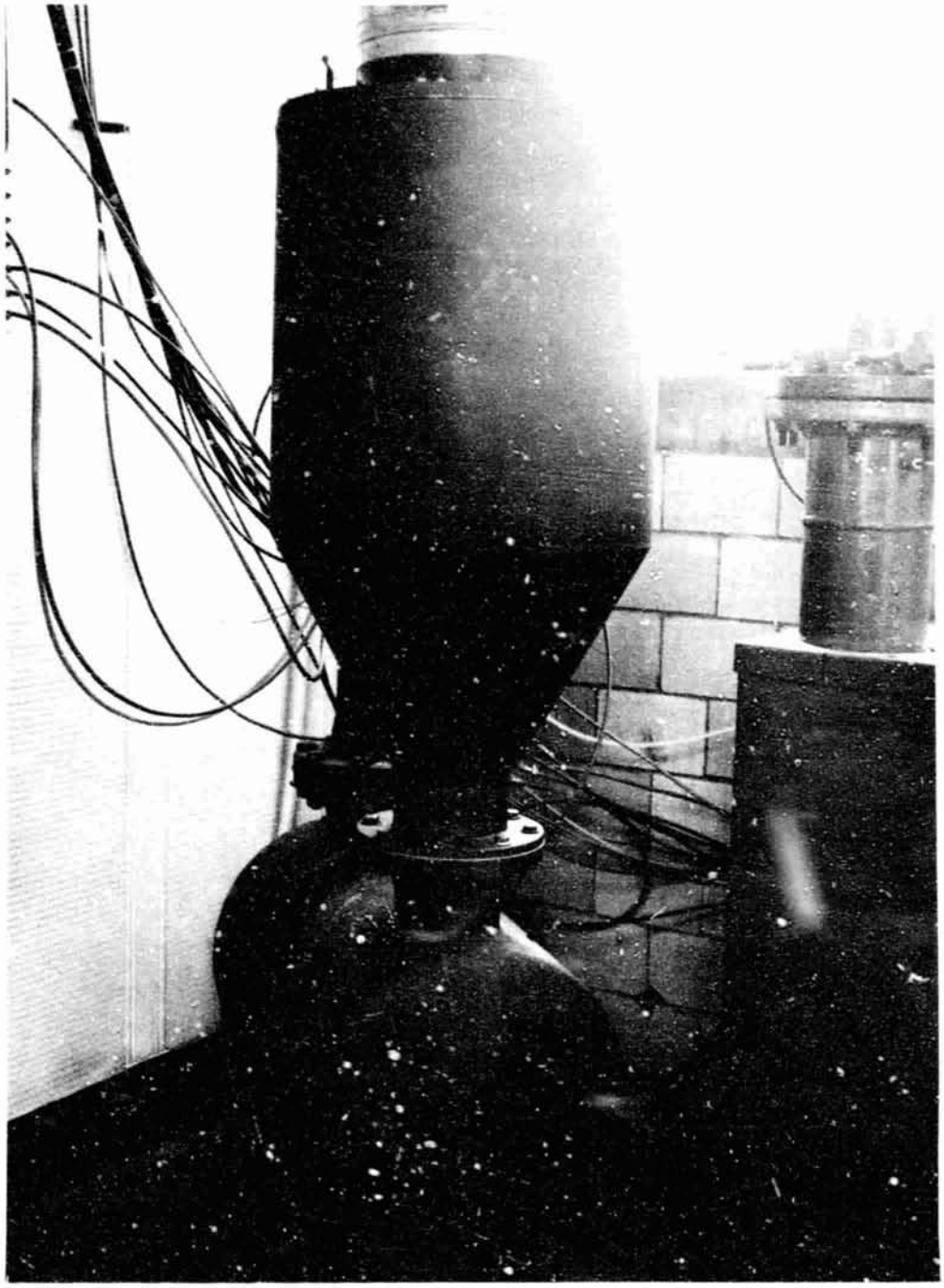

Figure 118

Upgraded Engine
Compressor
Turbine Nozzle
Flow Test

Mod 3 Cast Nozzle 4096384-152 after 0.015 in. cut-back

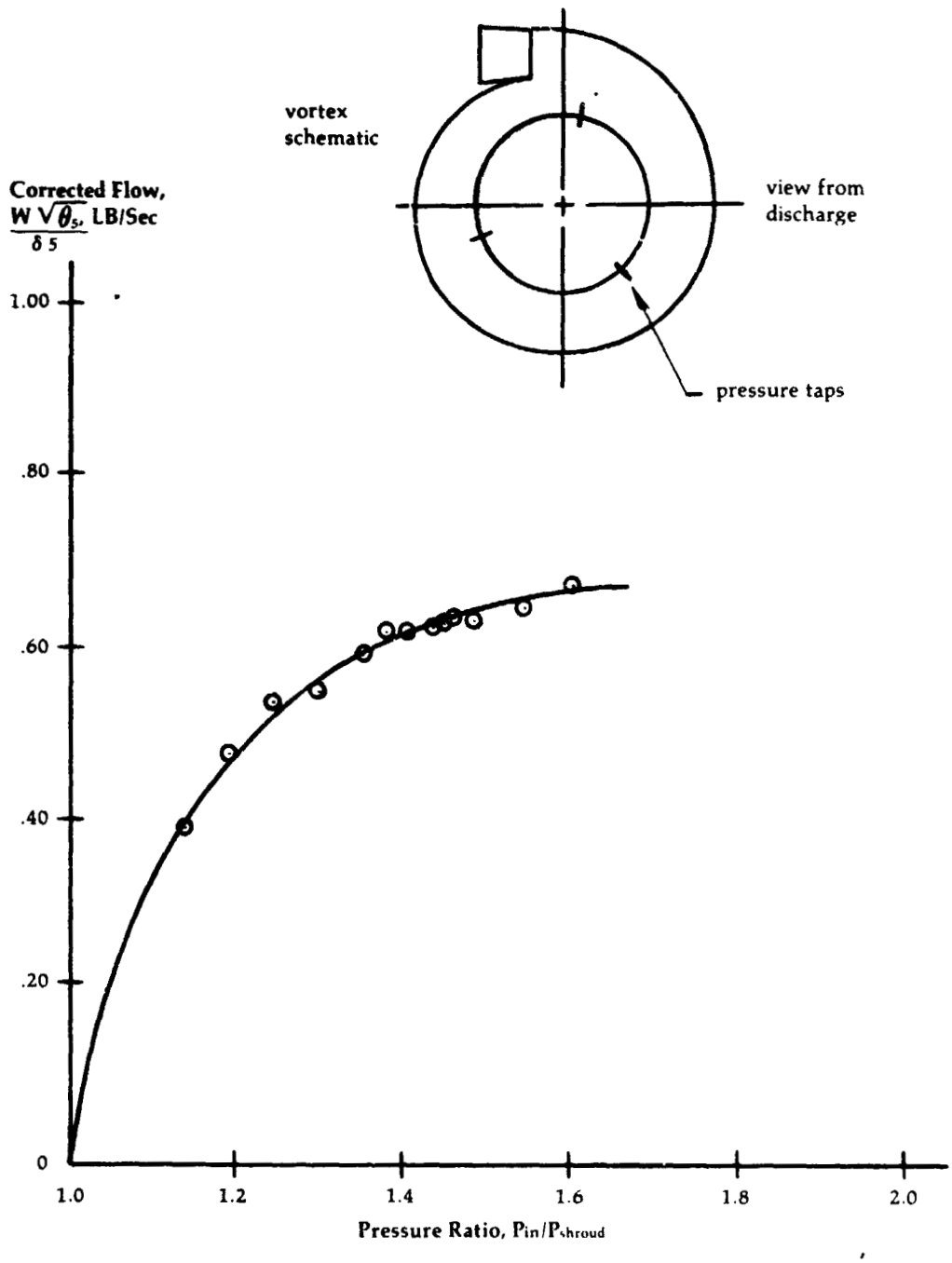

Figure 119

Mod 3 Nozzle Flow Ratio vs. Mean Throat Width at Design Point Corrected Conditions

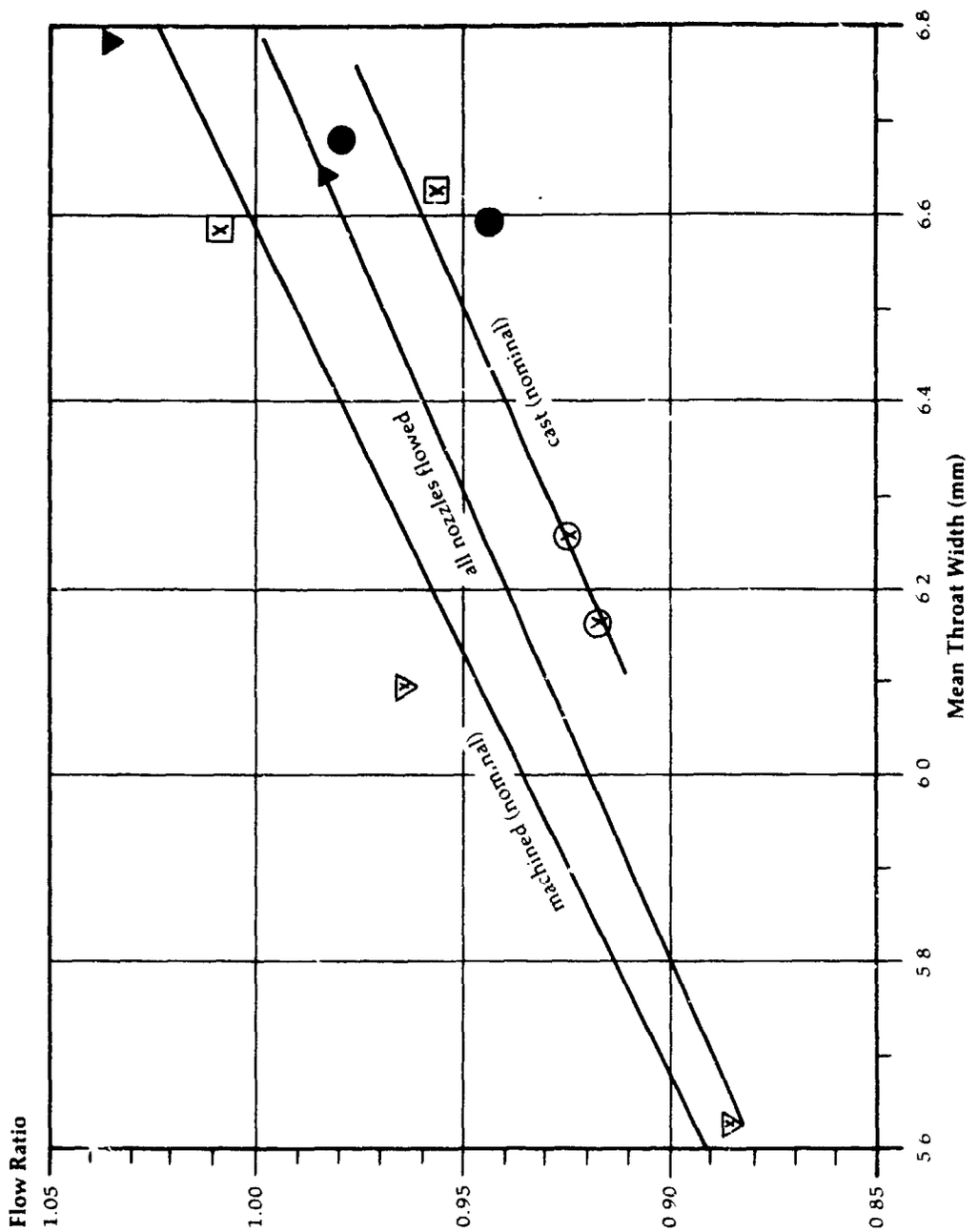

$$\text{Flow Ratio} = \frac{W\sqrt{\theta}/\delta \,|\, \text{Test}}{W\sqrt{\theta}/\delta \,|\, \text{Design}}$$

▽ nominal, machined, as received
▼ nominal, machined, after cutback
○ cast, nominal, as received
● cast, nominal, after cutback
□ cast, -1 deg., as received

Figure 120

Minature Cobra
Probe used in
Nozzle Flow
Surveys

Figure 121

Survey Probe Location Relative to First Stage Nozzle and Vortex

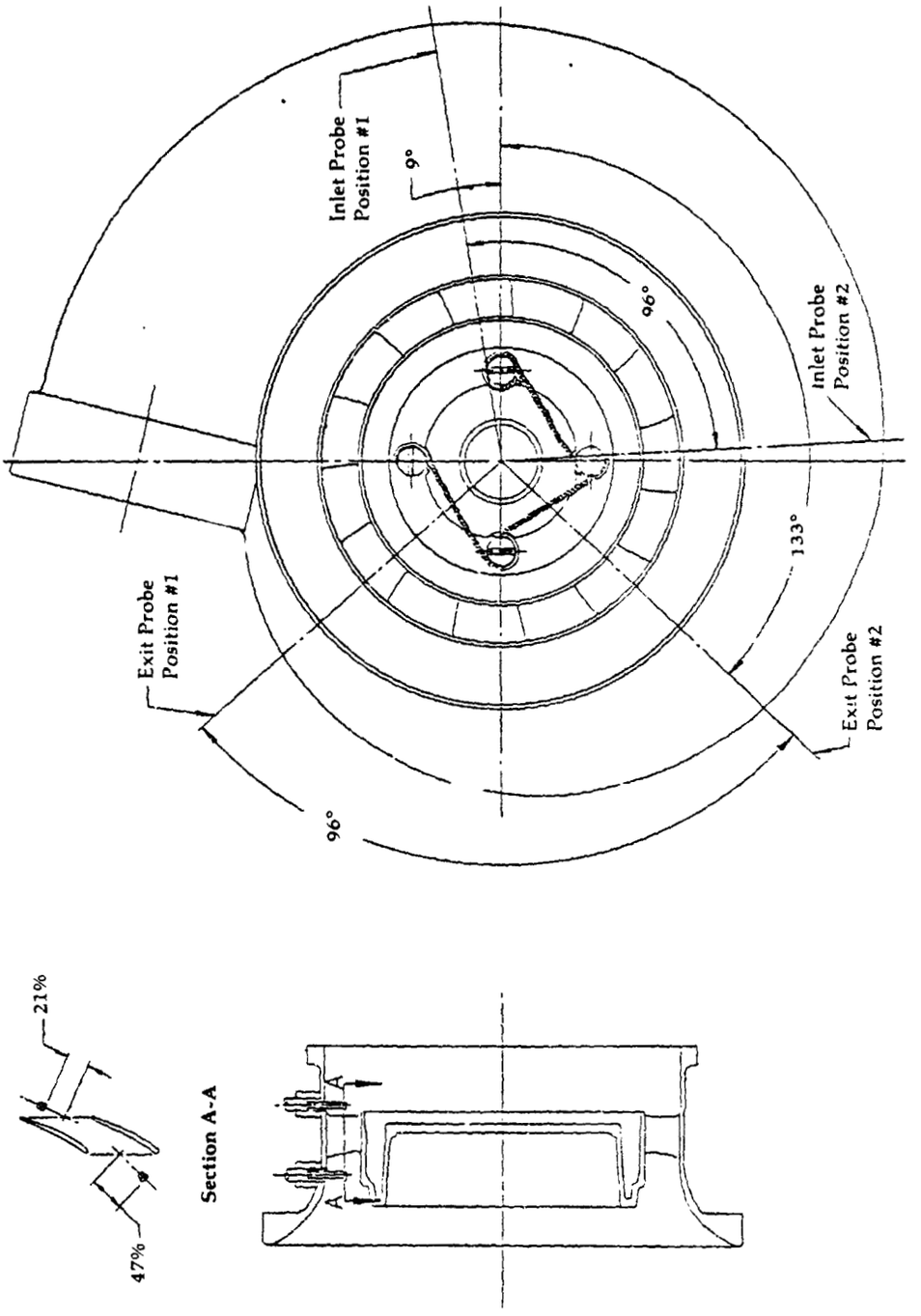

Figure 122

First Stage Nozzle Static Pressure Instrumentation

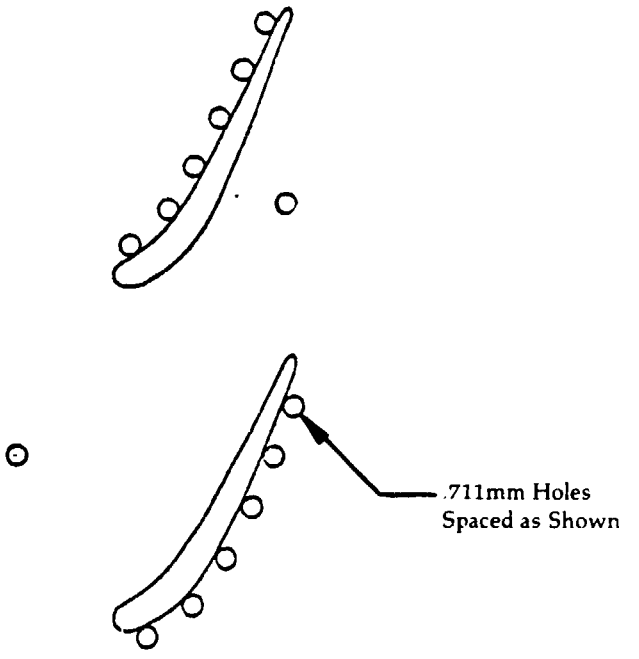

Section A-A

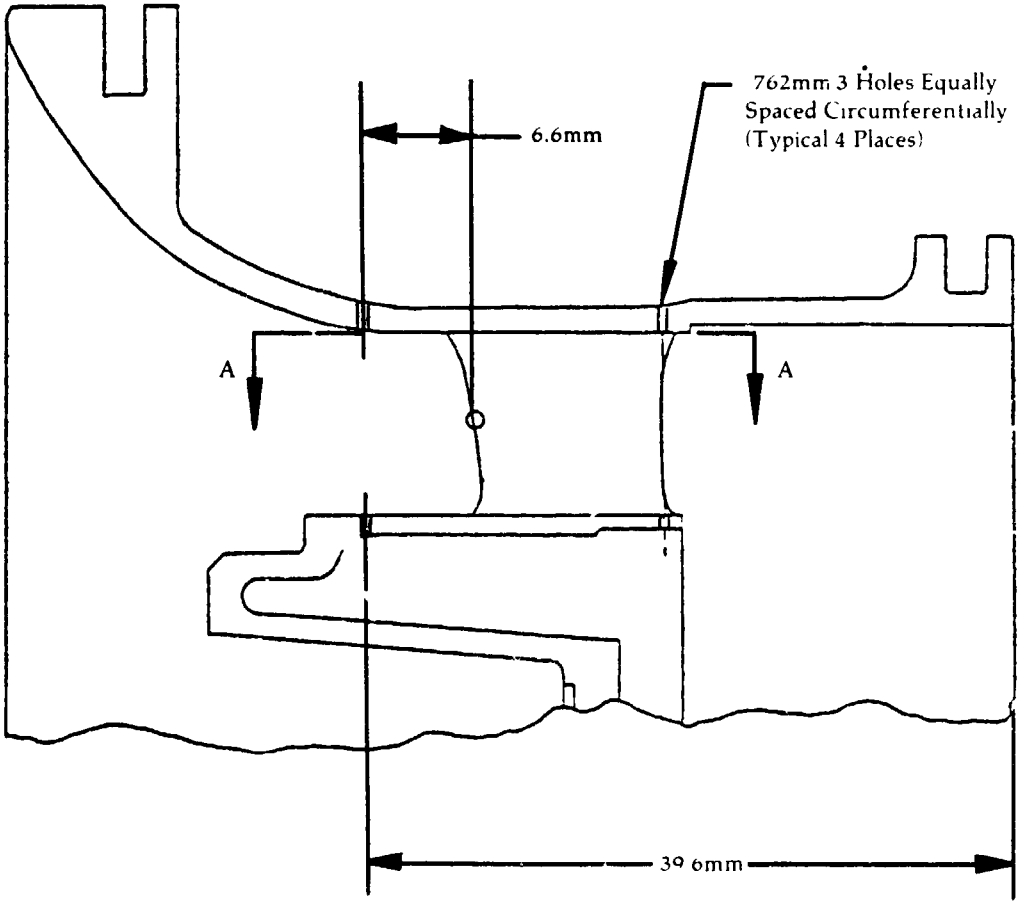

Figure 123

Power Turbine Test Rig Schematic

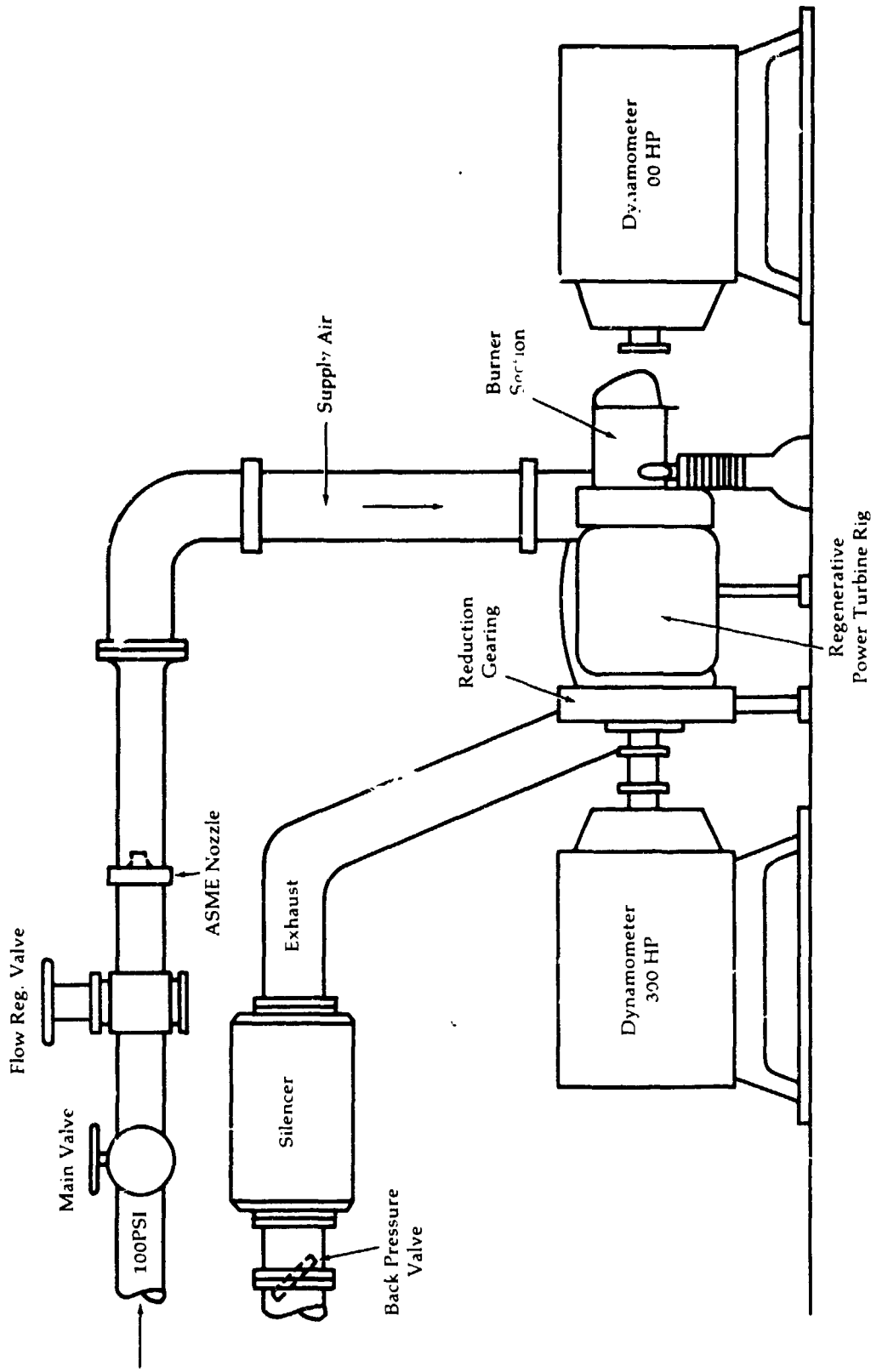

Figure 124

Regenerative
Power Turbine Rig

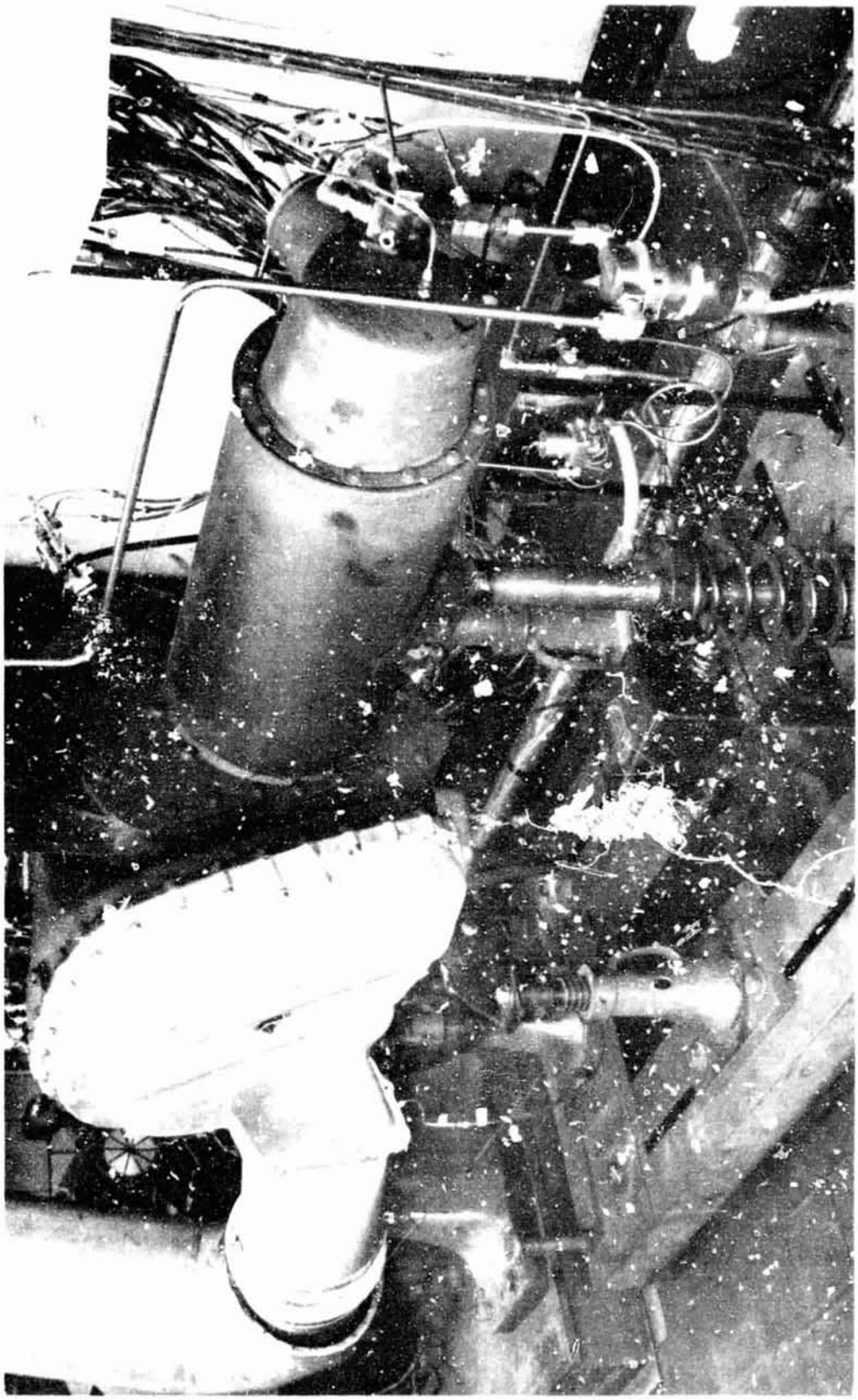

Figure 125

Regenerative Power Turbine Test Rig Instrumentation

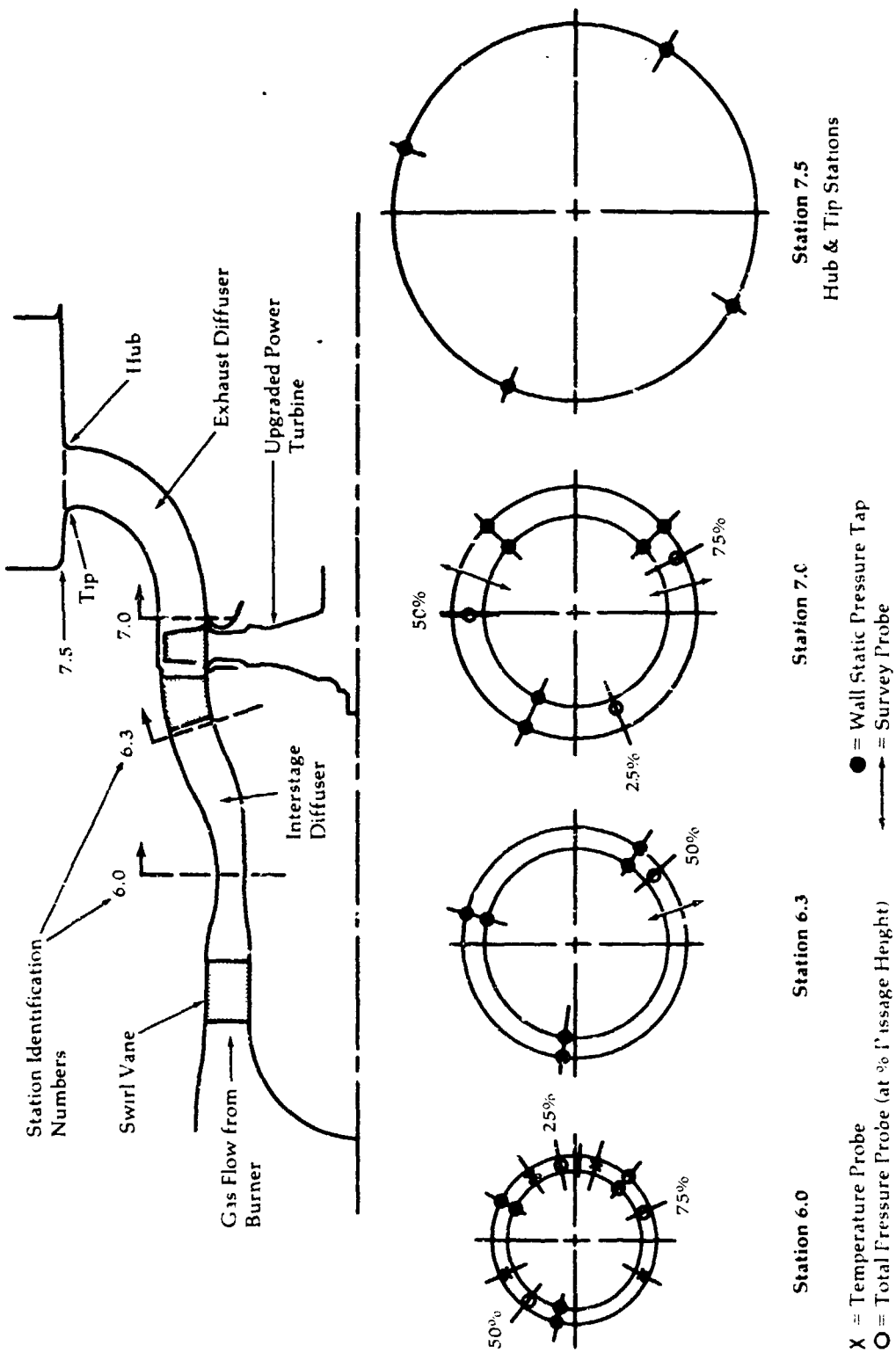

Figure 126

A-926 Regenerative
Power Turbine
Test Rig
Exhaust Diffuser
Instrumentation

Thermocouples

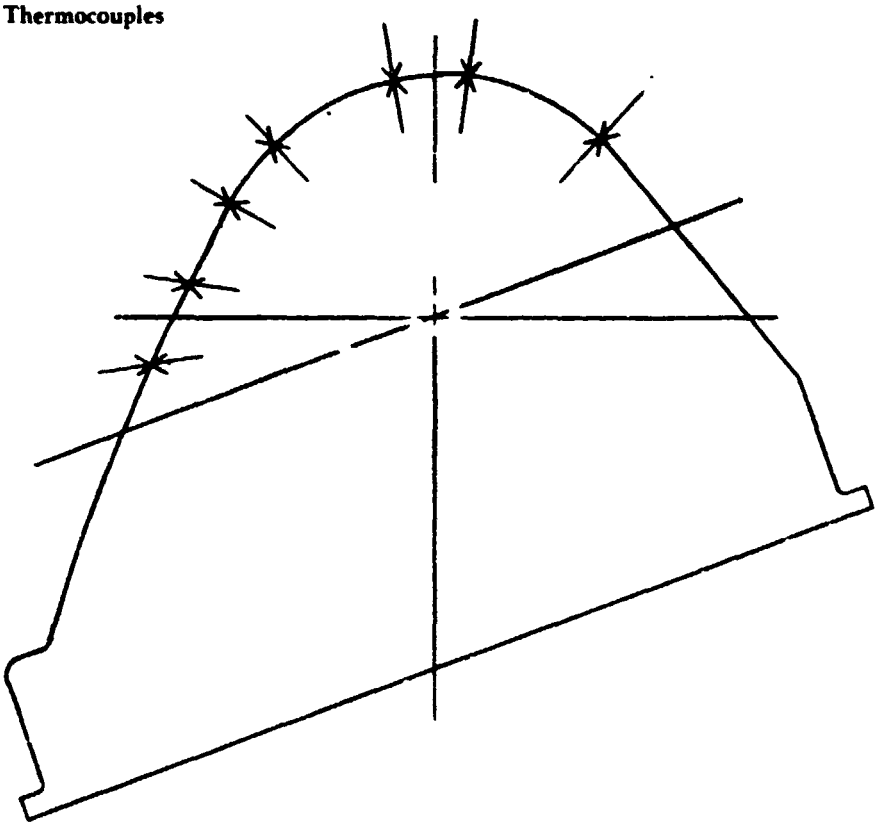

Static Taps

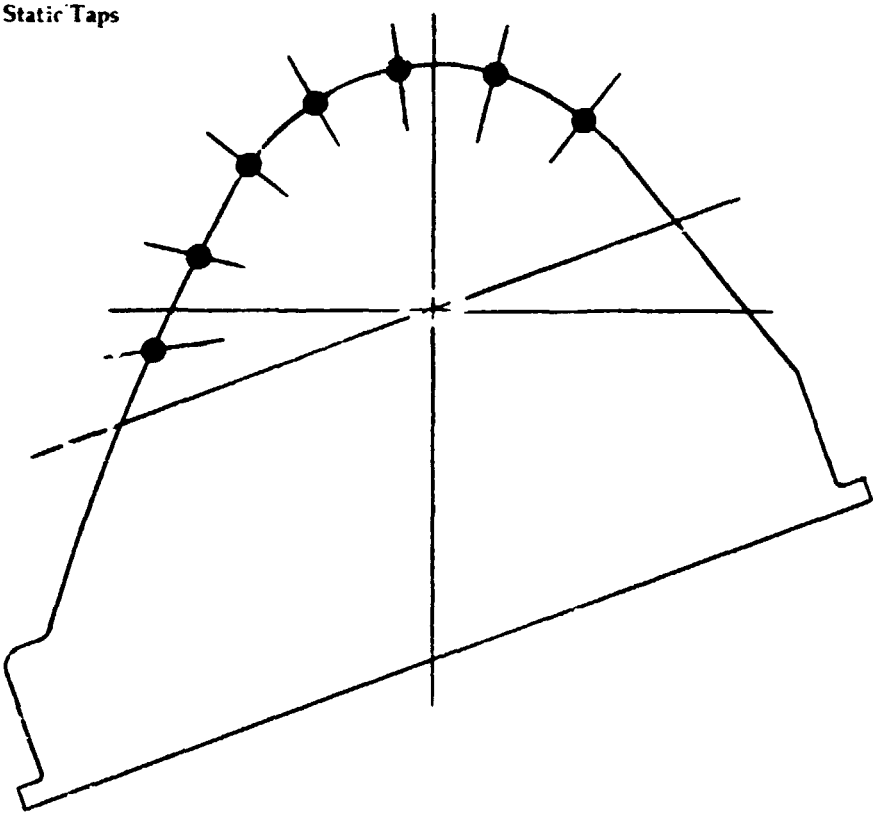

View Looking Towards Rear

Figure 127

Interstage Nozzle Instrumentation

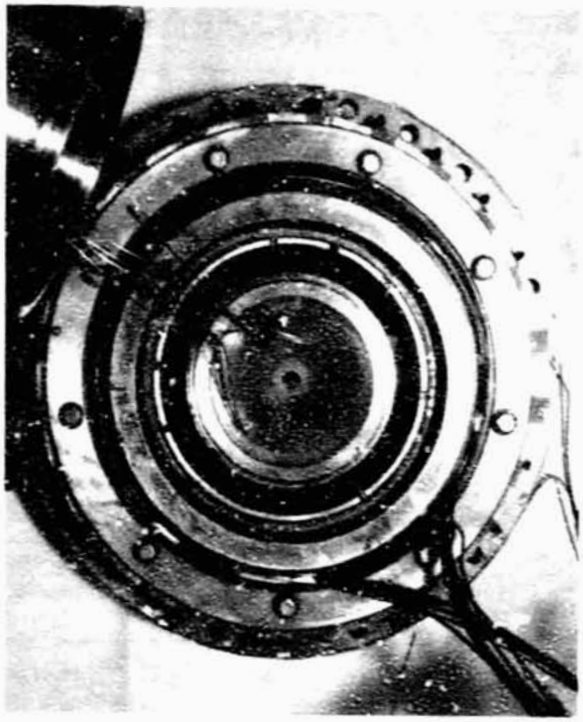

Station e 0 Plane

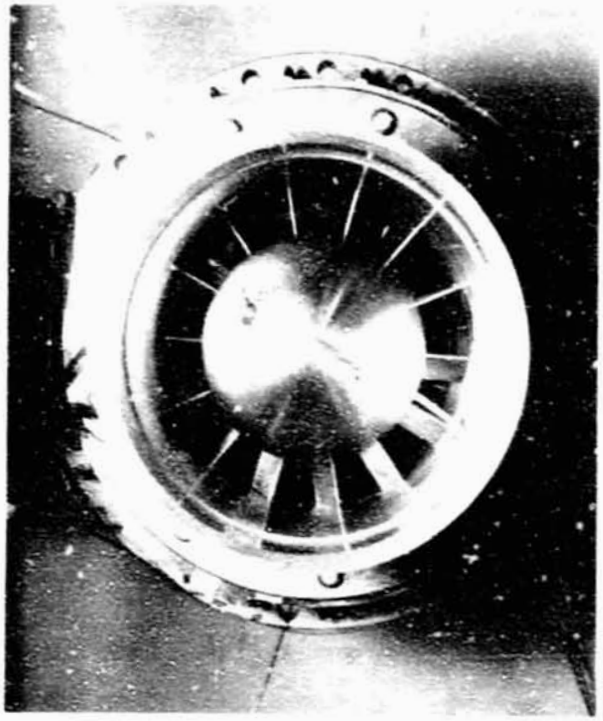

View Showing Swirl Vane Assembly

3/4 View

Kiel Type Pressure Probe and
Shielded Thermocouple at Station e 0

Figure 128

Power Turbine Rig Flow Path Showing Location of Probes

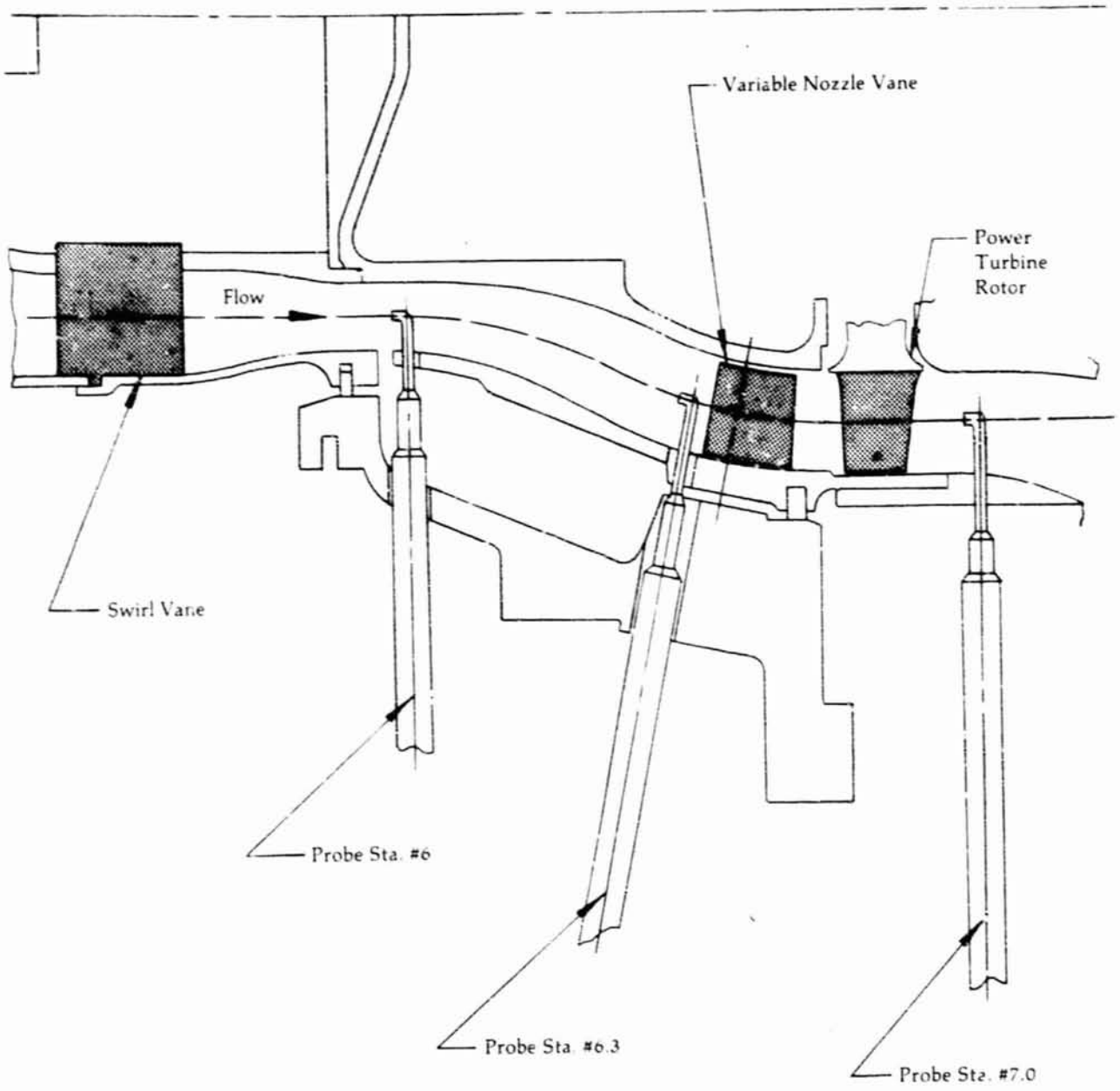

Figure 129

Regenerator Flow Distribution Fixture

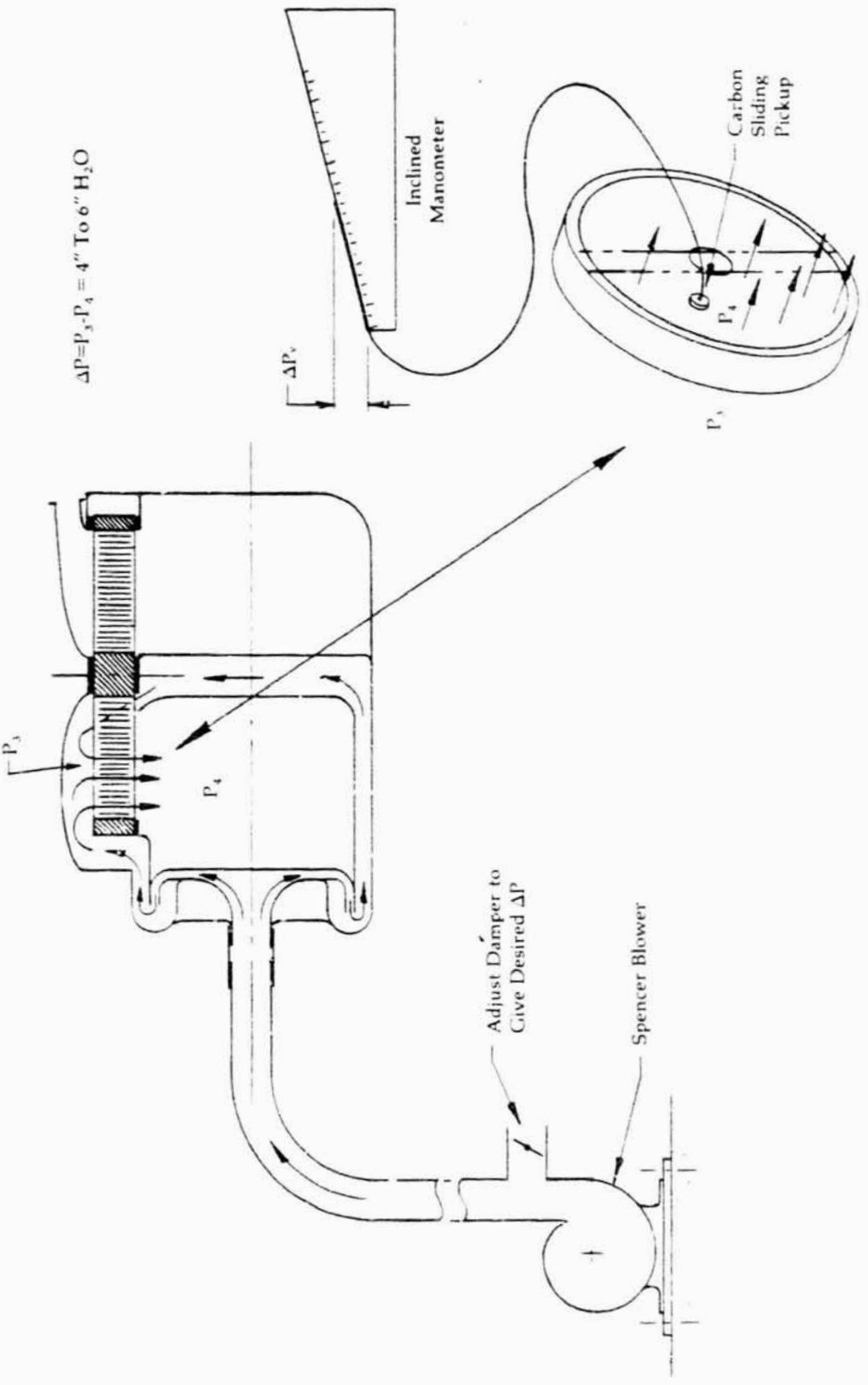

Figure 130

Upgraded Engine
Regenerator Cover
Baffling

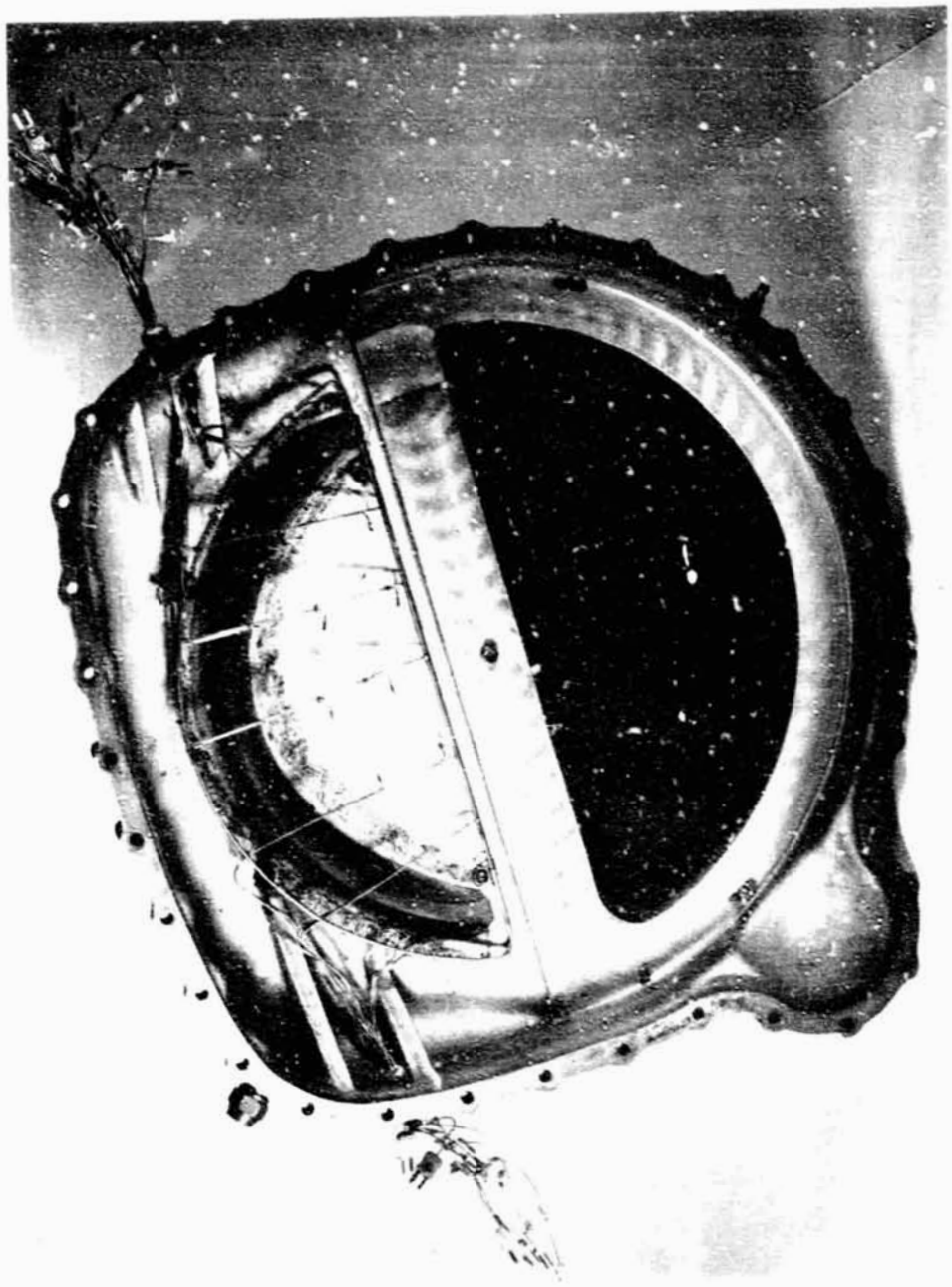

Figure 131

Basic Instrumentation Schematic Upgraded Engine Test

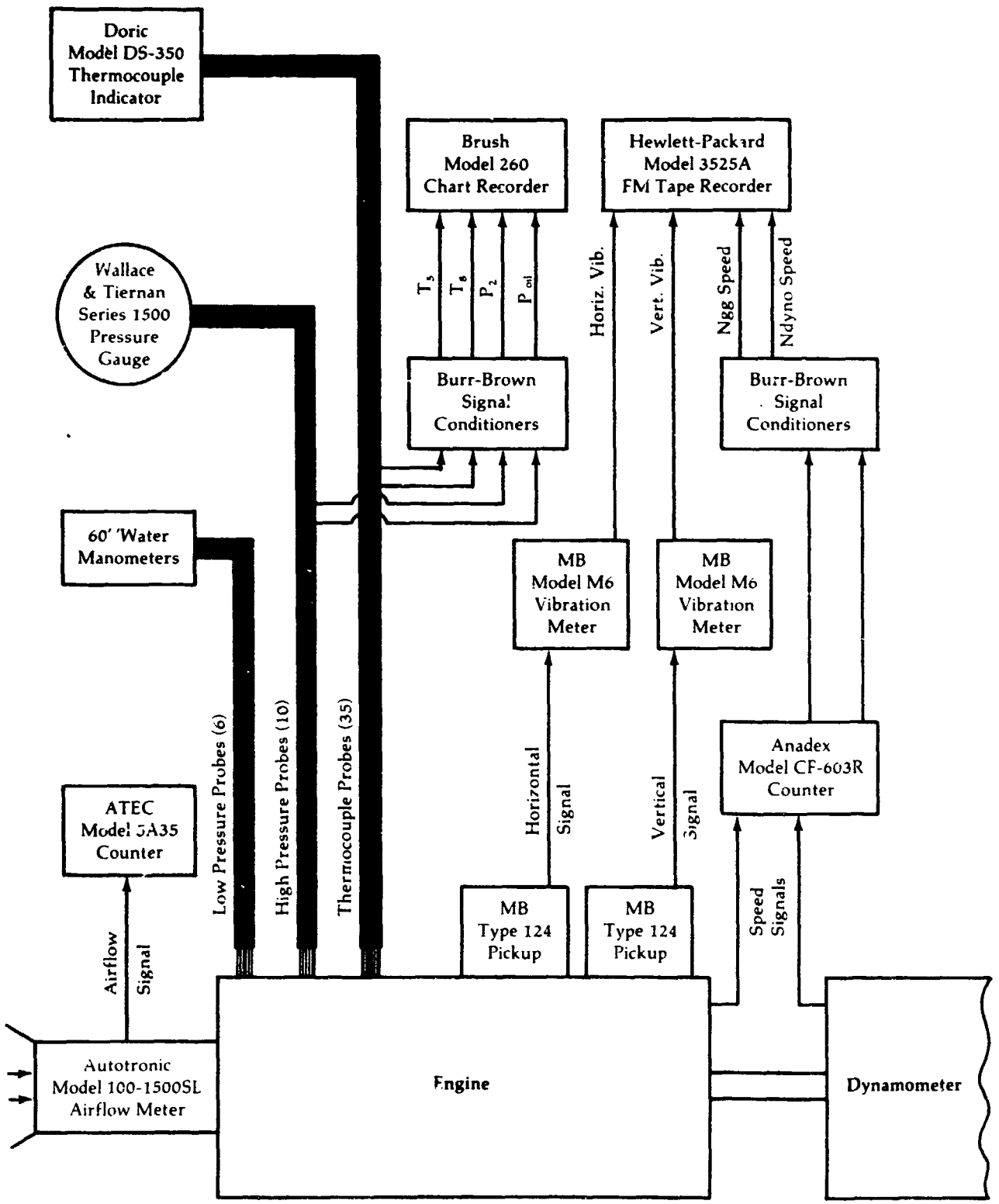

Figure 132

Installation of Upgraded Engine in Test Cell

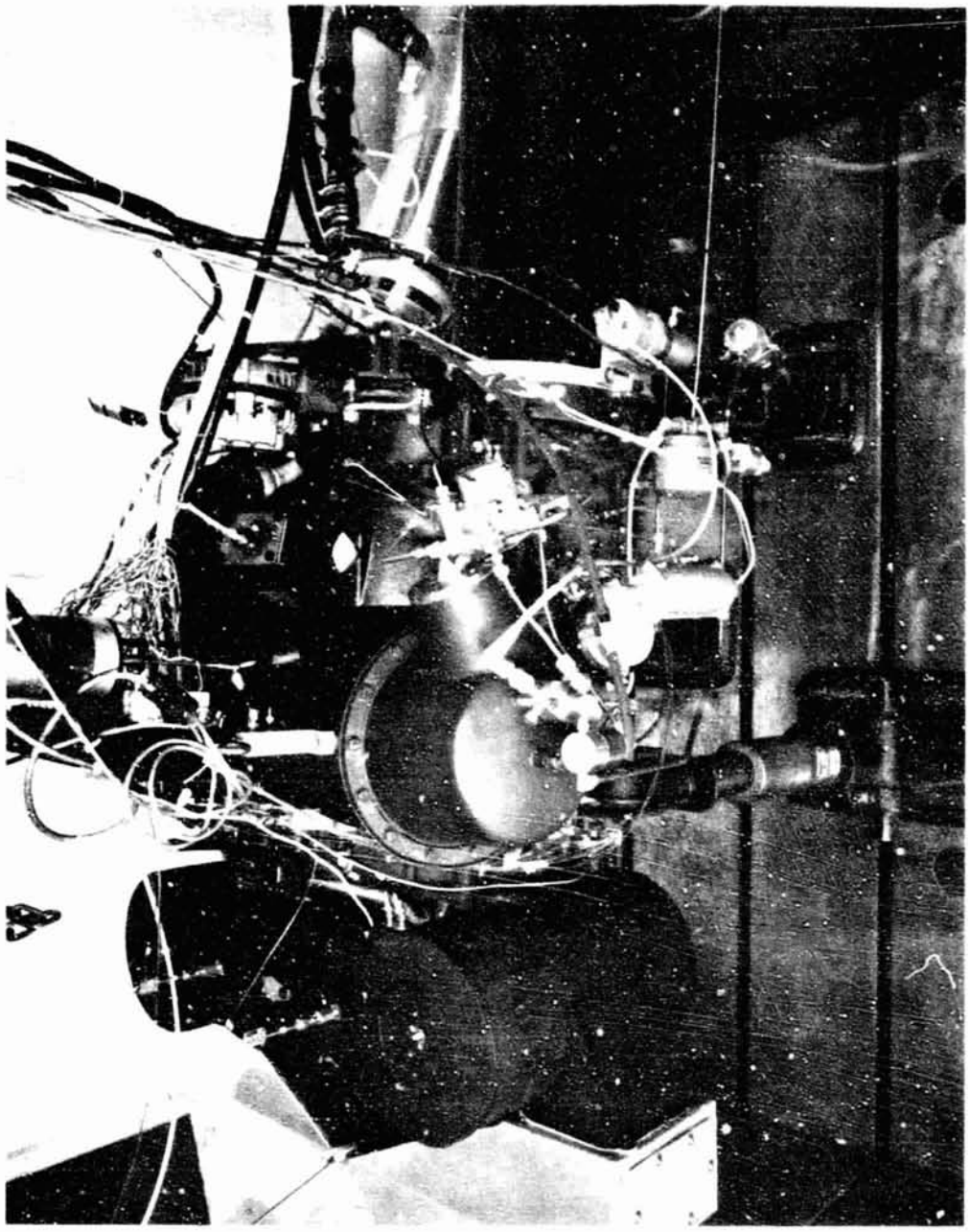

Figure 133

Engine Test Cell
Control Room

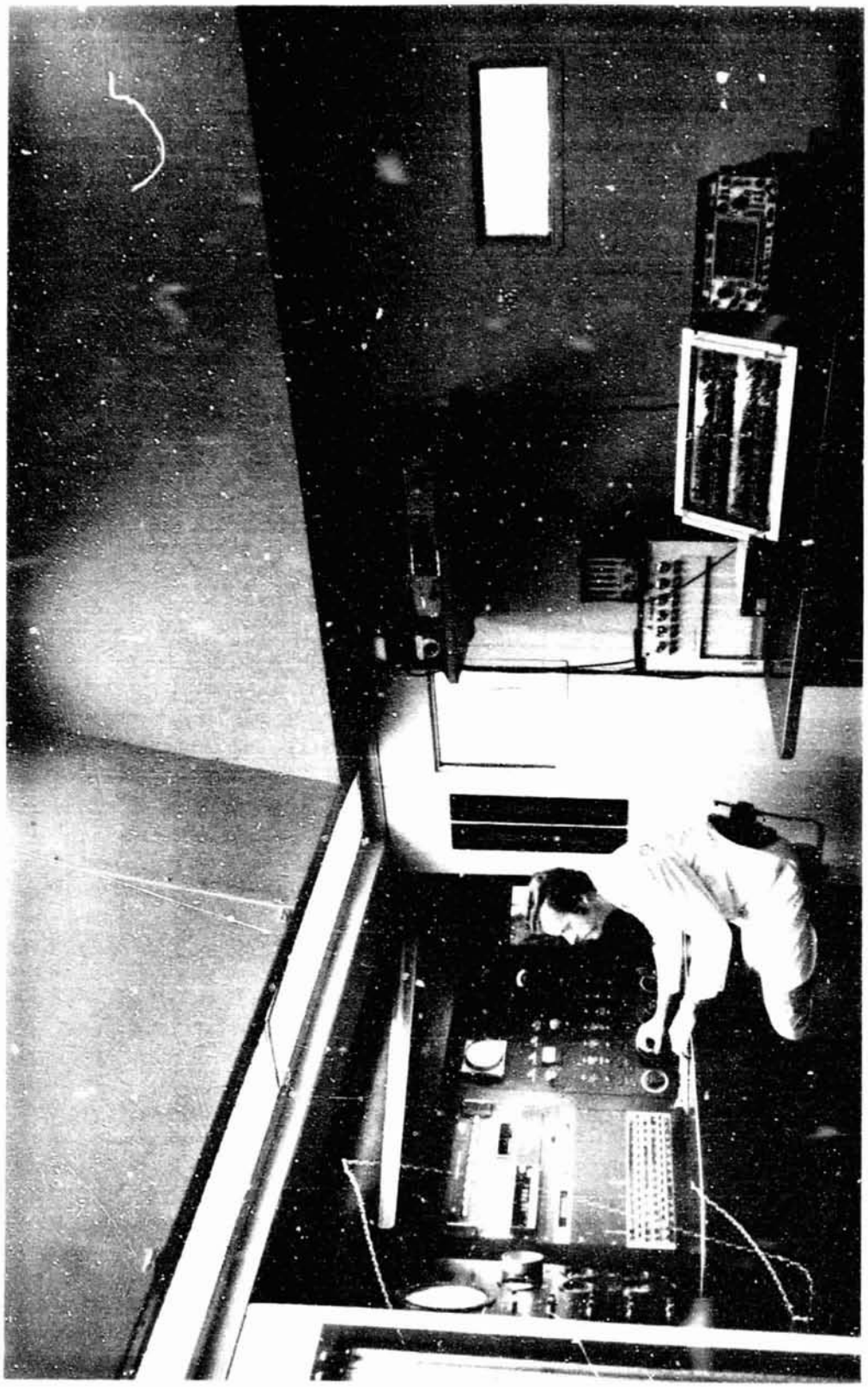

Figure 134

Upgraded Engine Station Notation

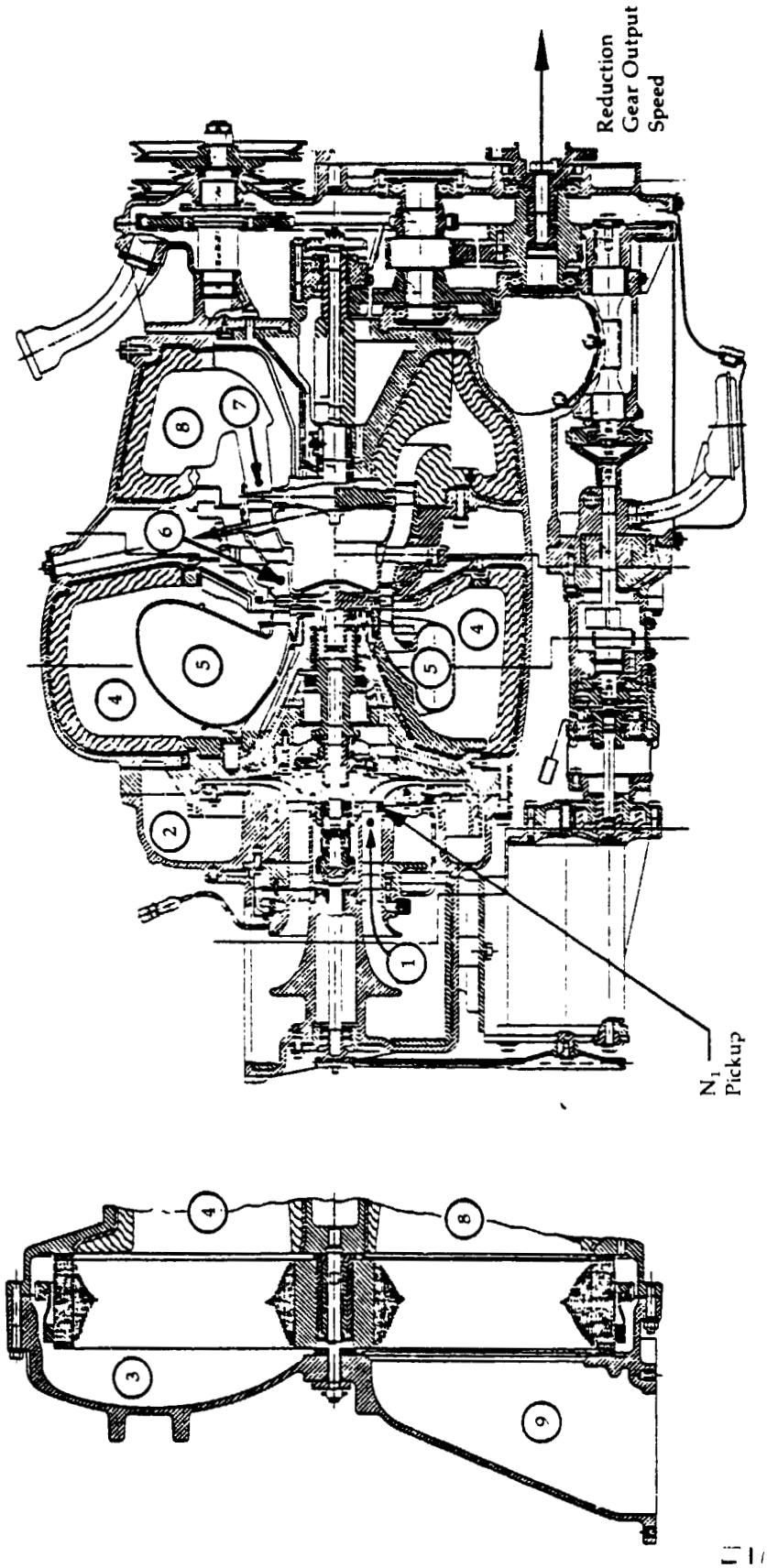

Figure 135

Setup for Calibration Check of Autotronic Series 100 Air Flow Transducer

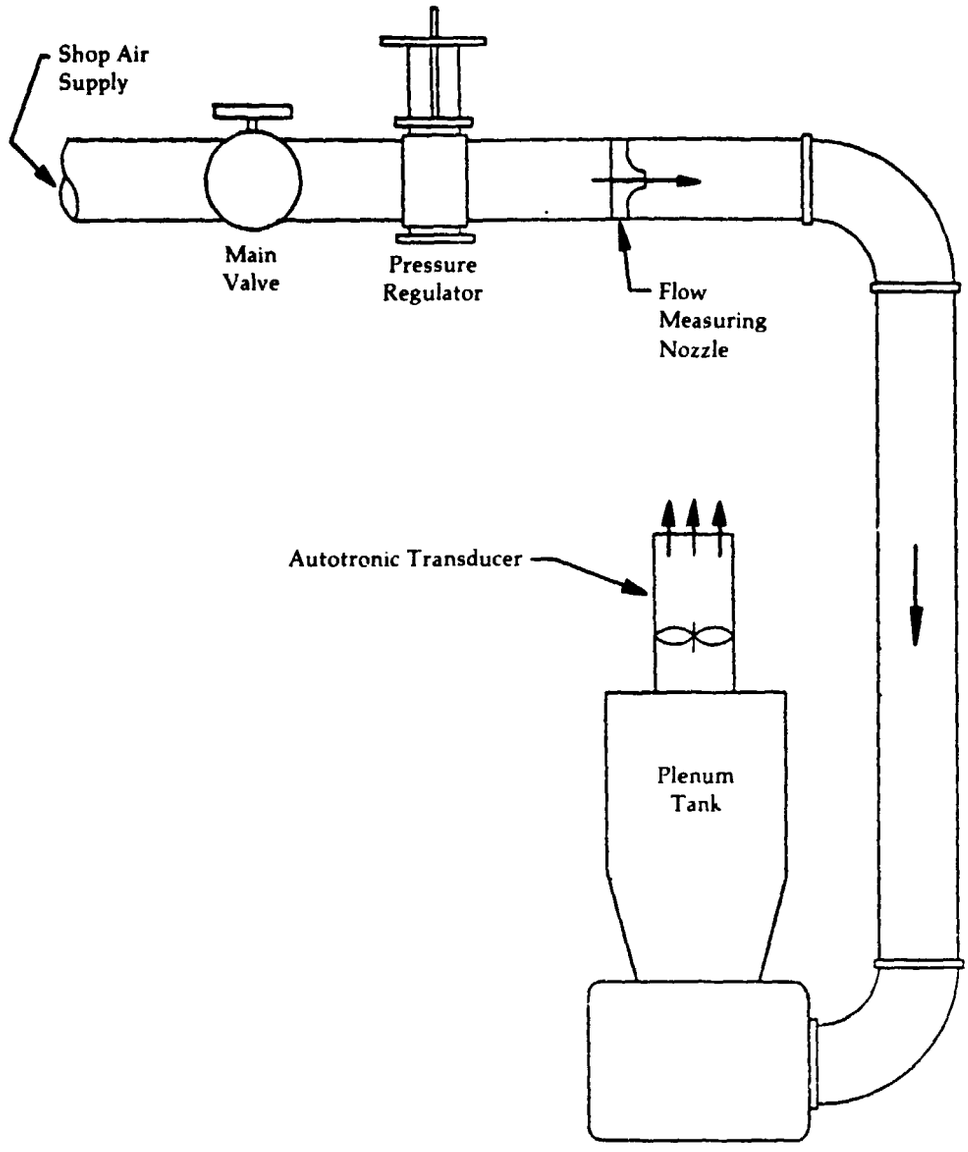

Figure 136

Upgraded Engine Intake Airflow Sensor Calibration

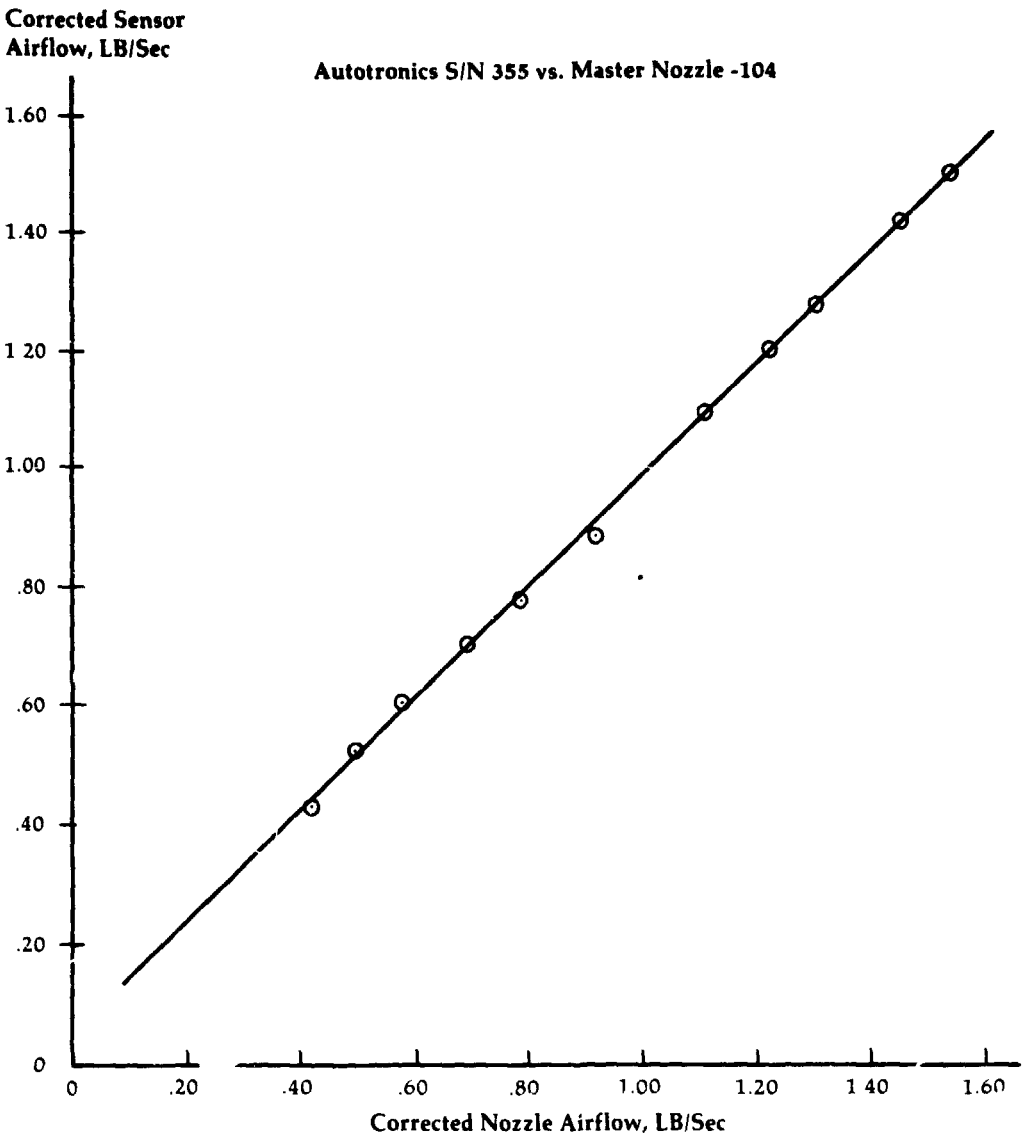

Figure 137

P_{T1} & T_1 Location-
Standard Position
A-926 Engine

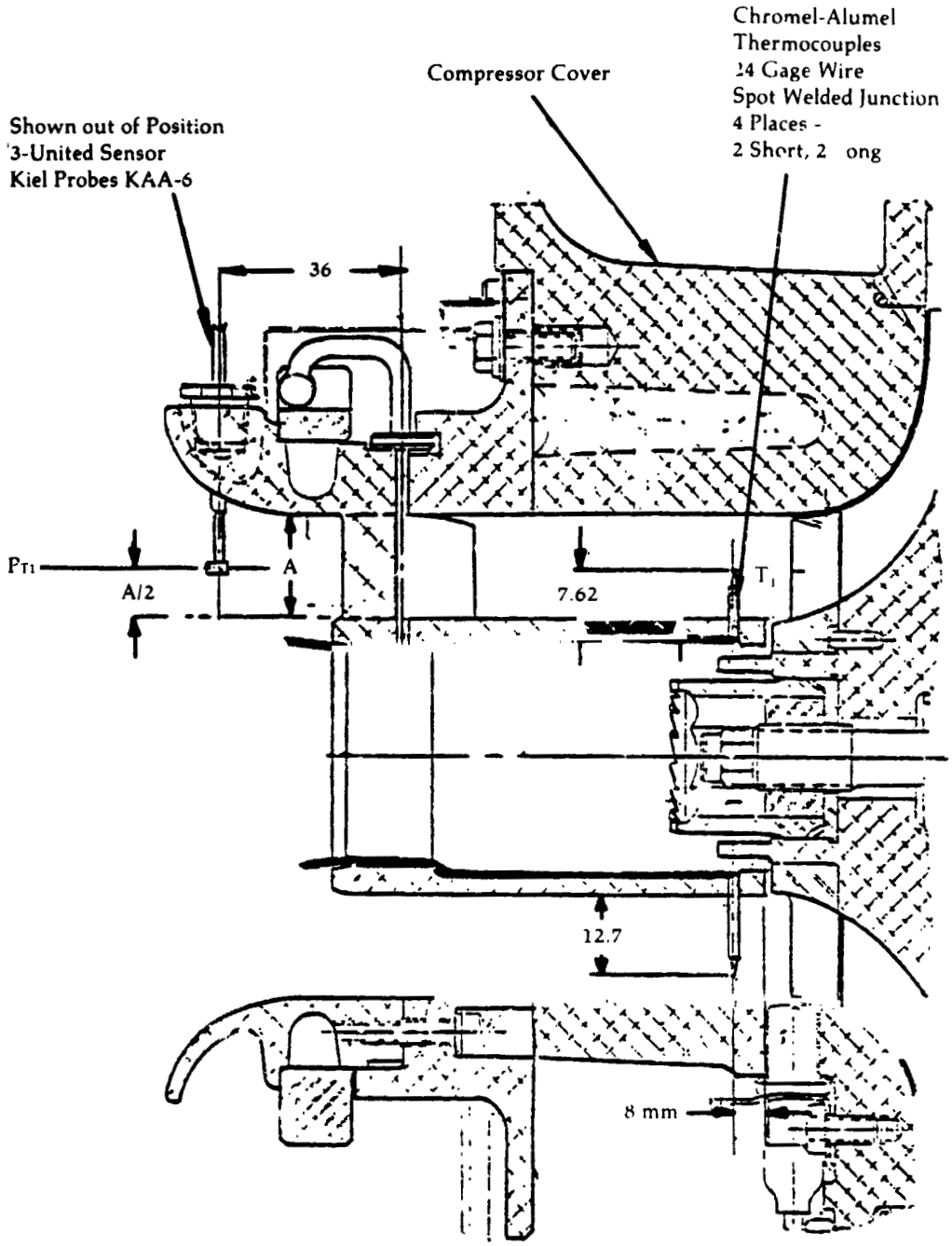

Figure 138

P_{T1} & T_1 Circumferential Position (Standard Locations) A-926 Engine Viewed from Rear

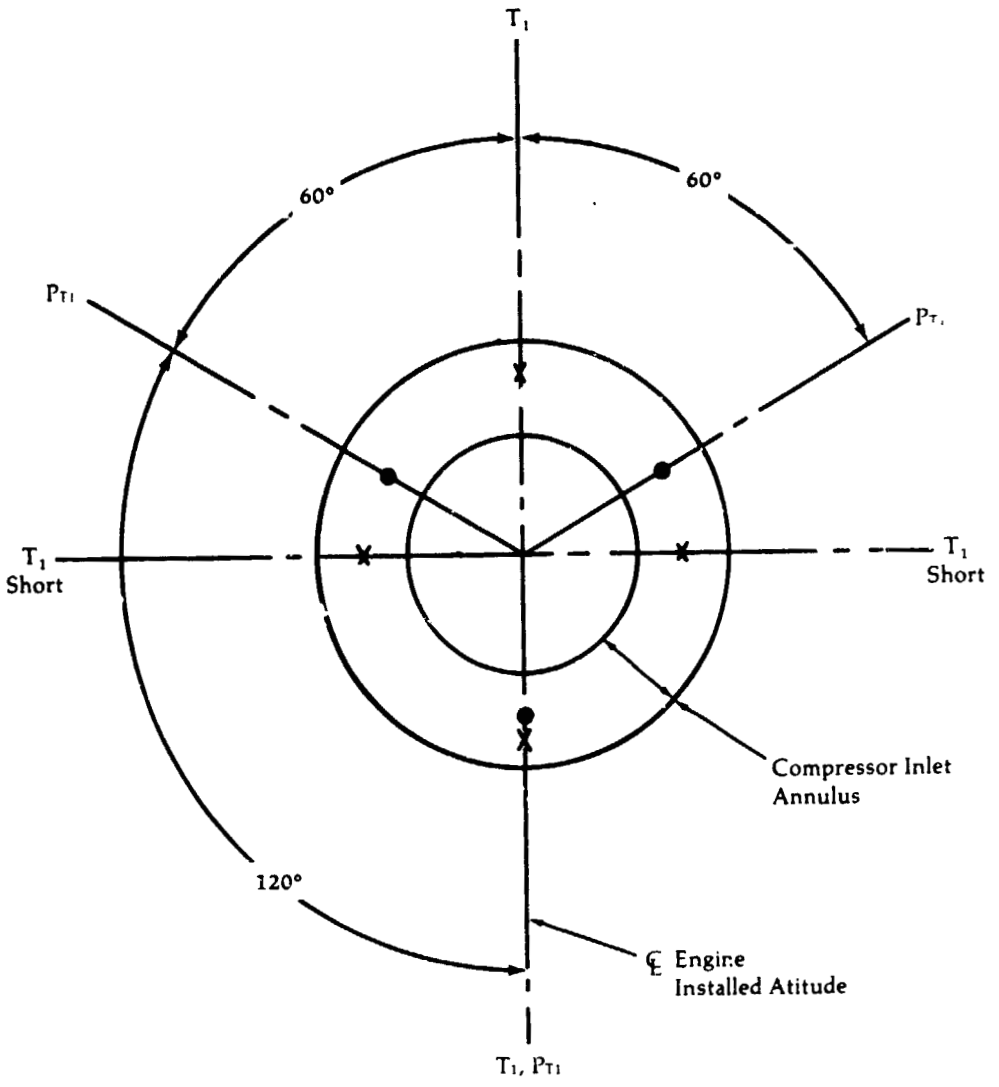

Figure 139

Compressor Discharge Thermocouple Location

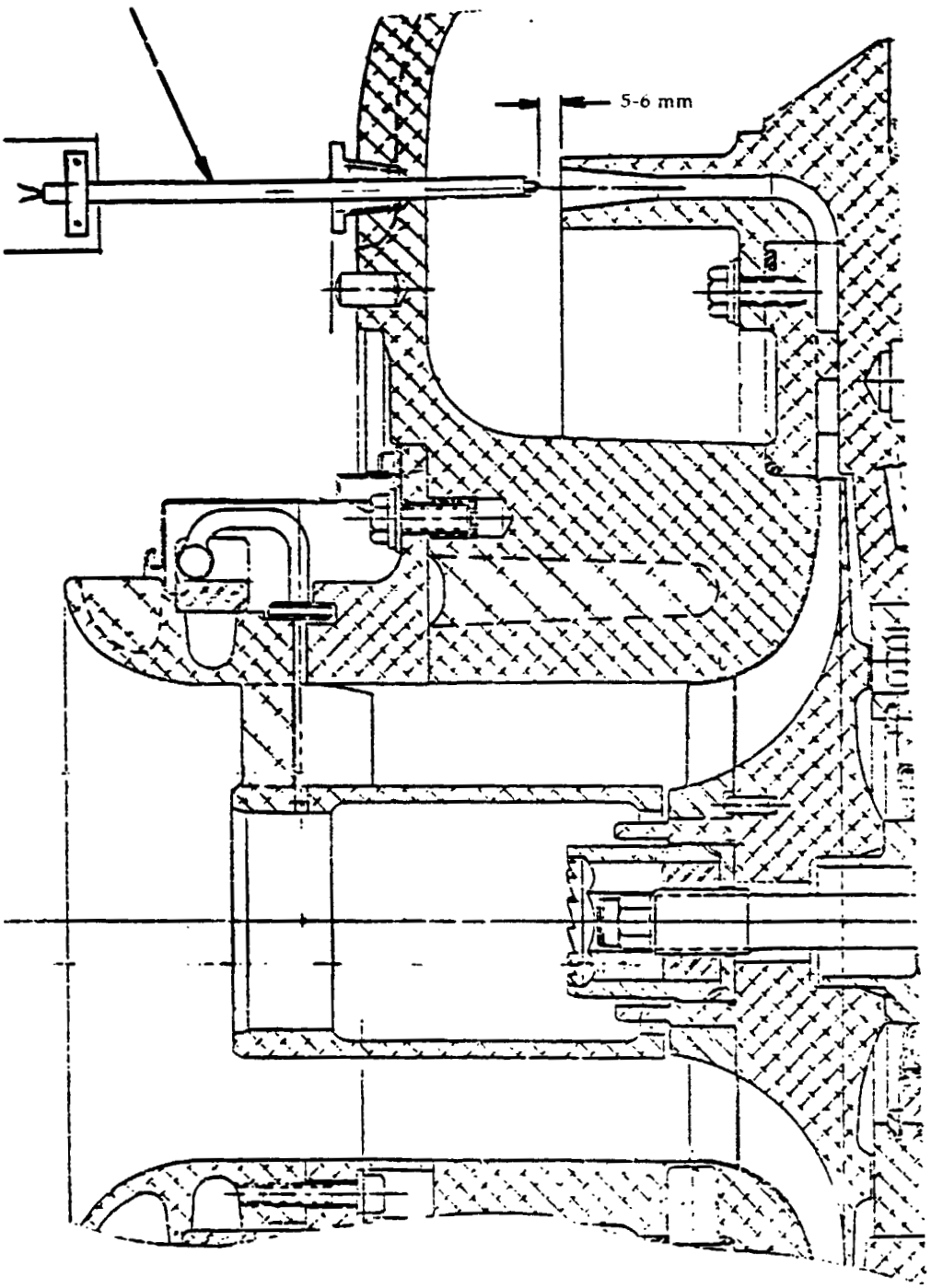

Figure 140

Compressor Discharge Pressure Probe

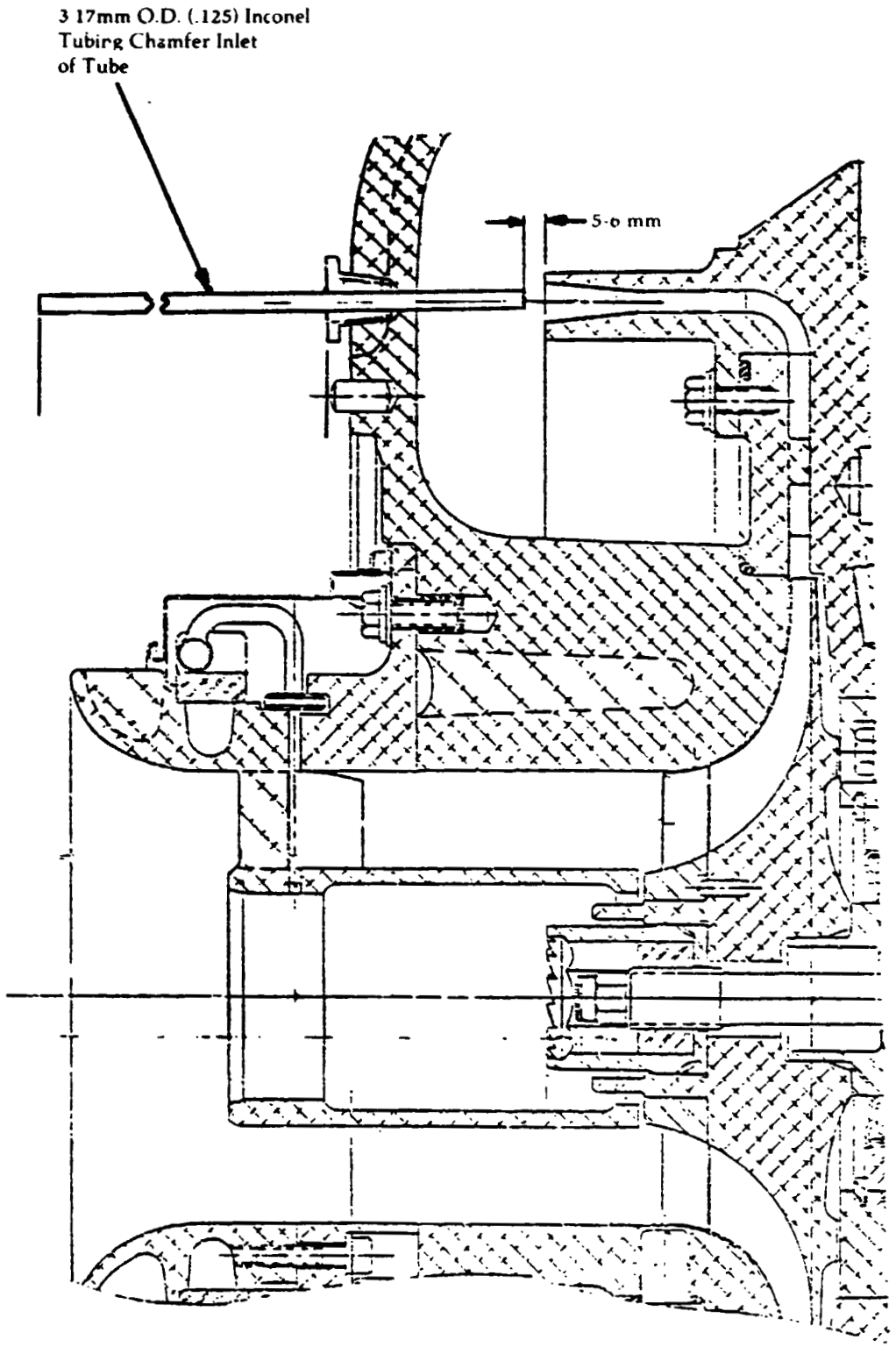

Figure 141

P_s and T_s Thermocouple and P_{s_0} Location

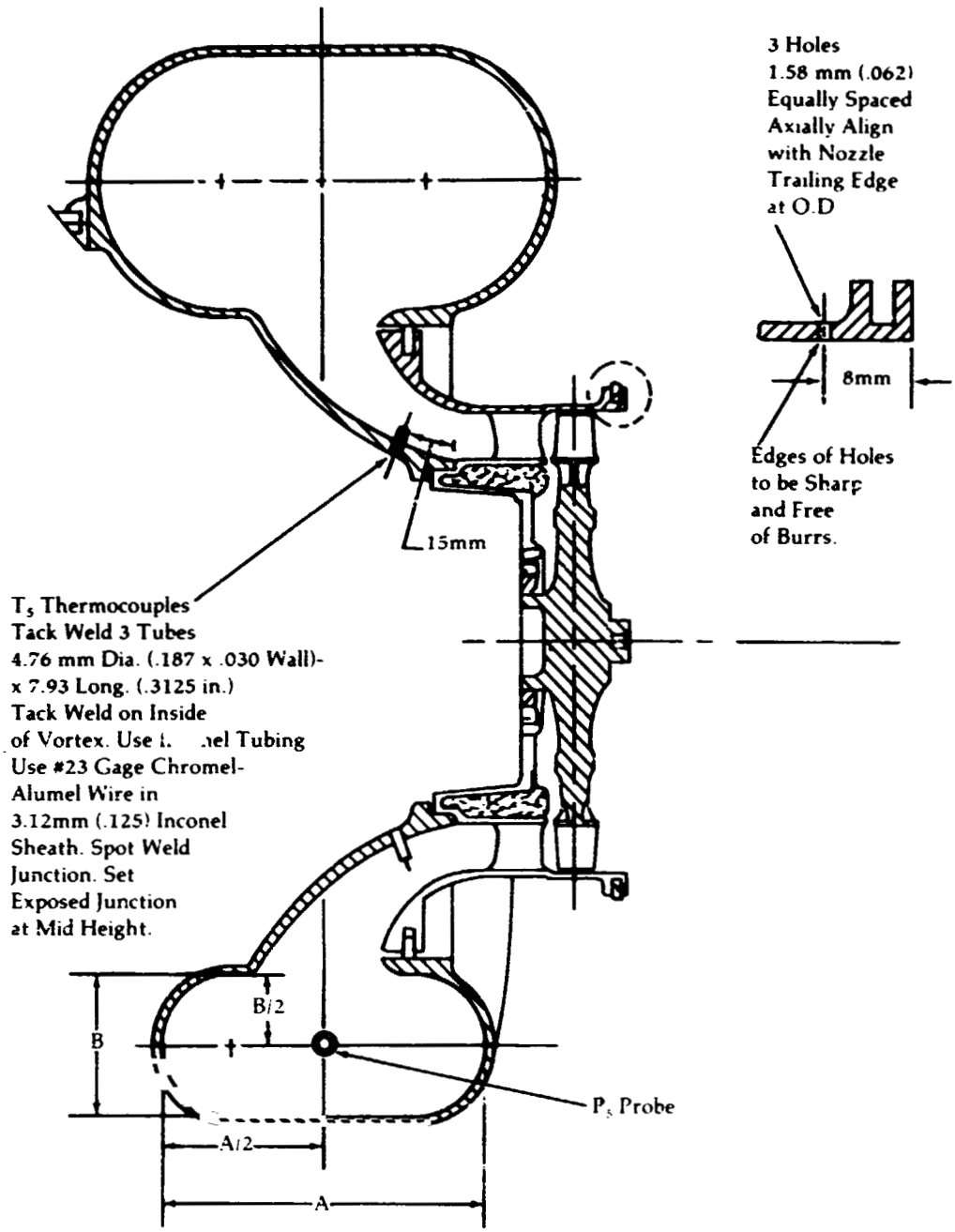

Figure 142

P_5 and T_5 Thermocouple Circumferential Position

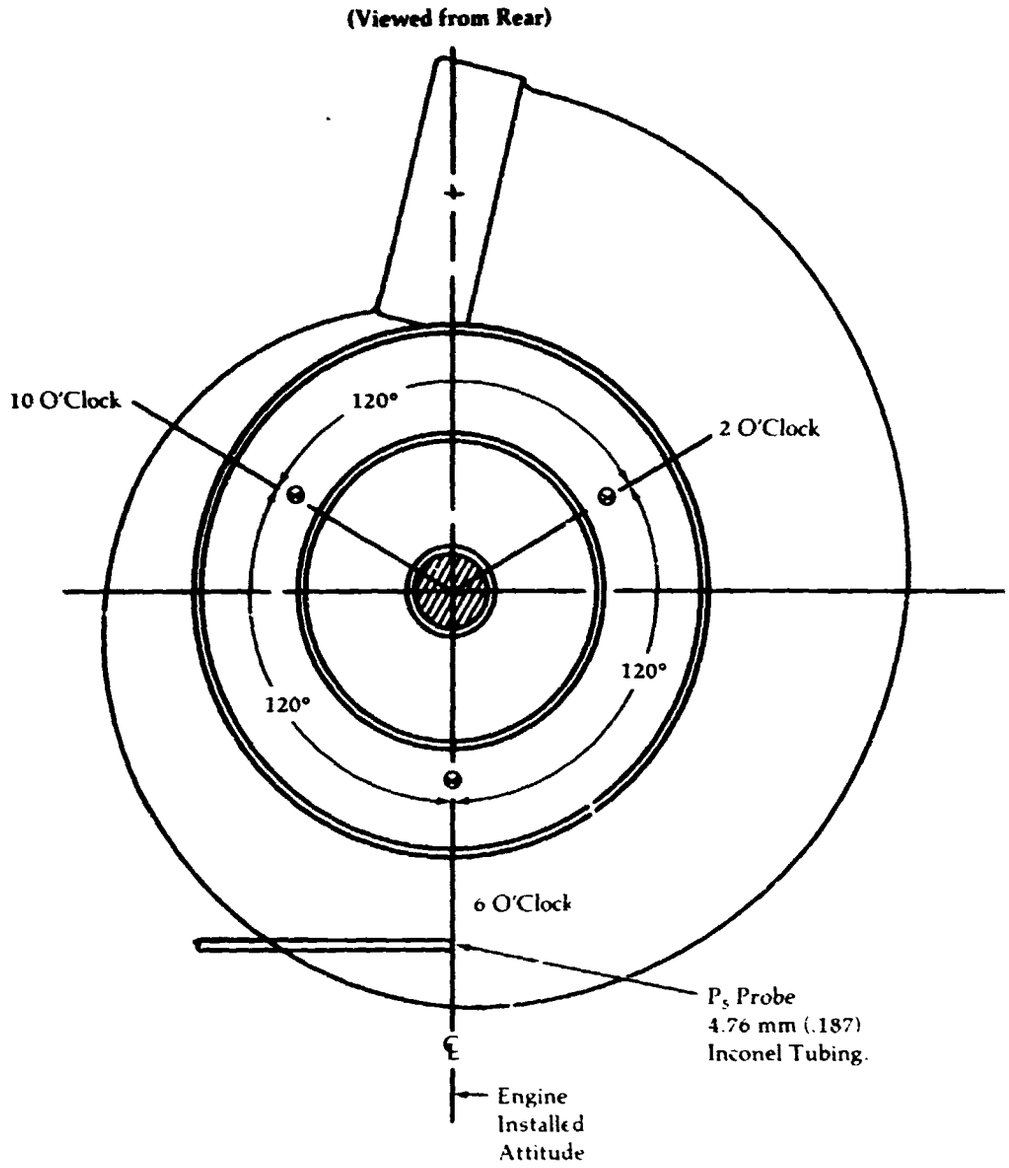

Figure 143

Upgraded Engine
Compressor-Turbine
Nozzle Static
Pressure Taps

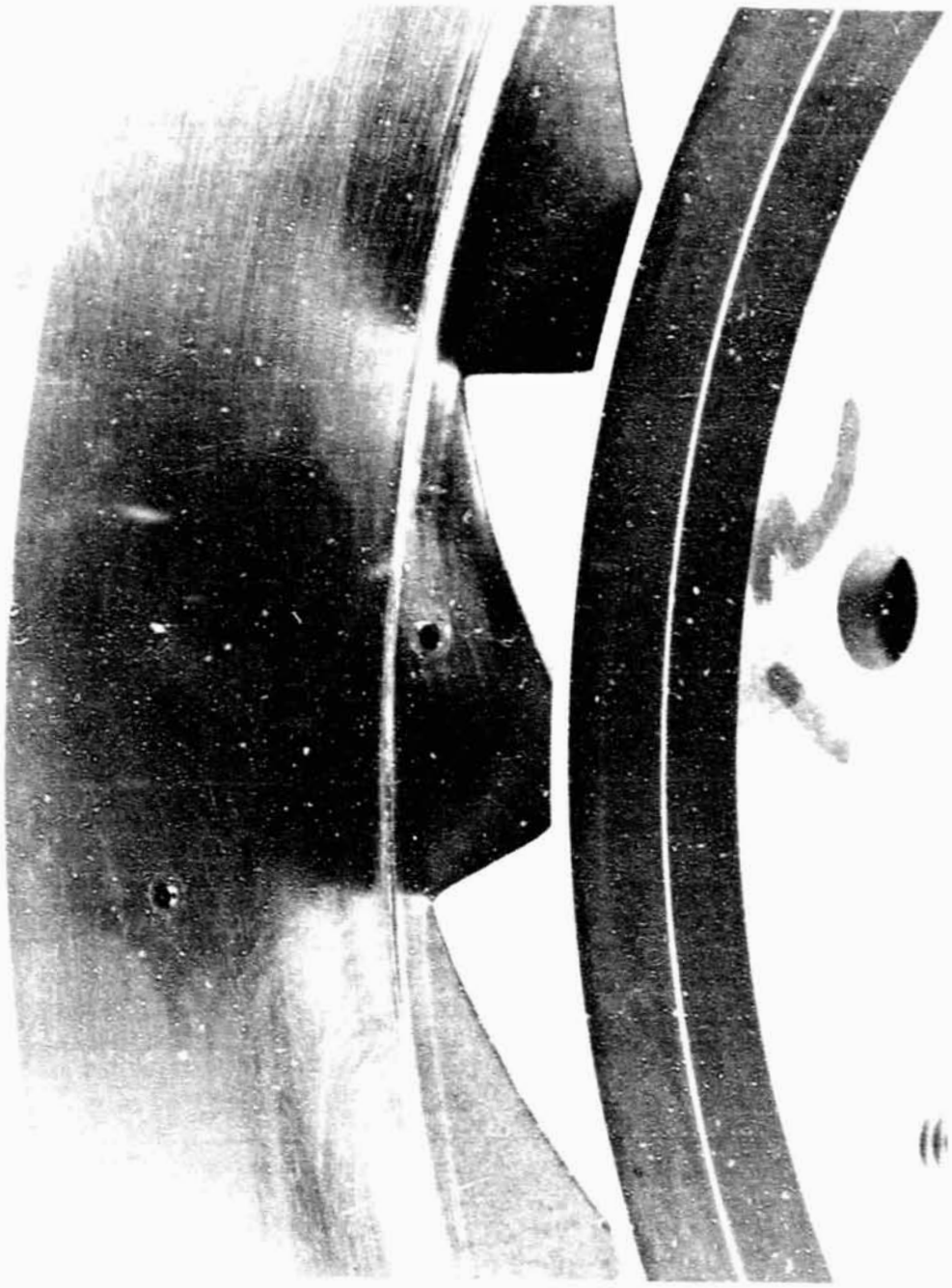

Figure 144

P_{T6}, T_{T6} and P_{S7} Locations

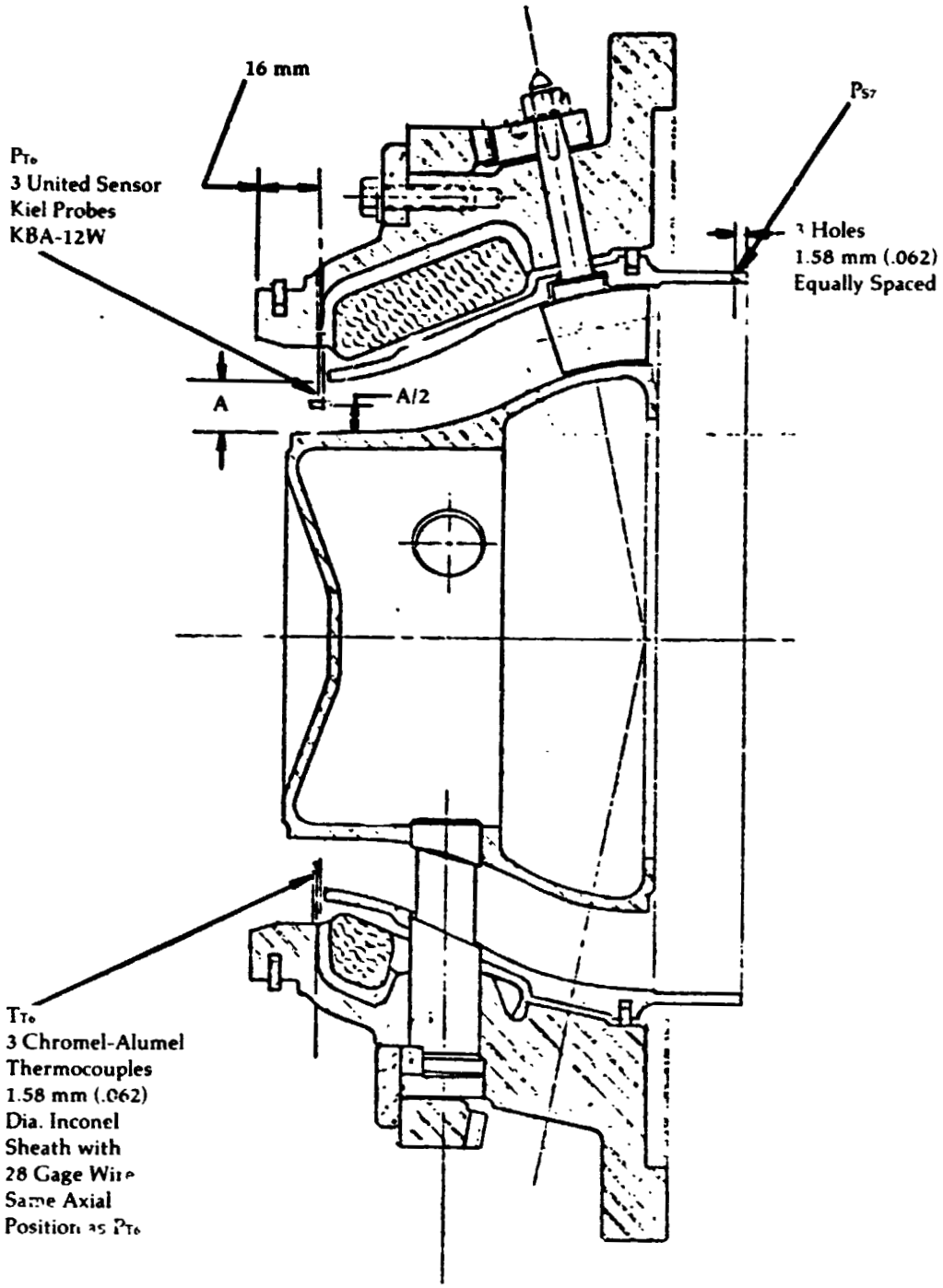

Figure 145

Upgraded Engine
Compressor Turbine
Cobra Probe
Location

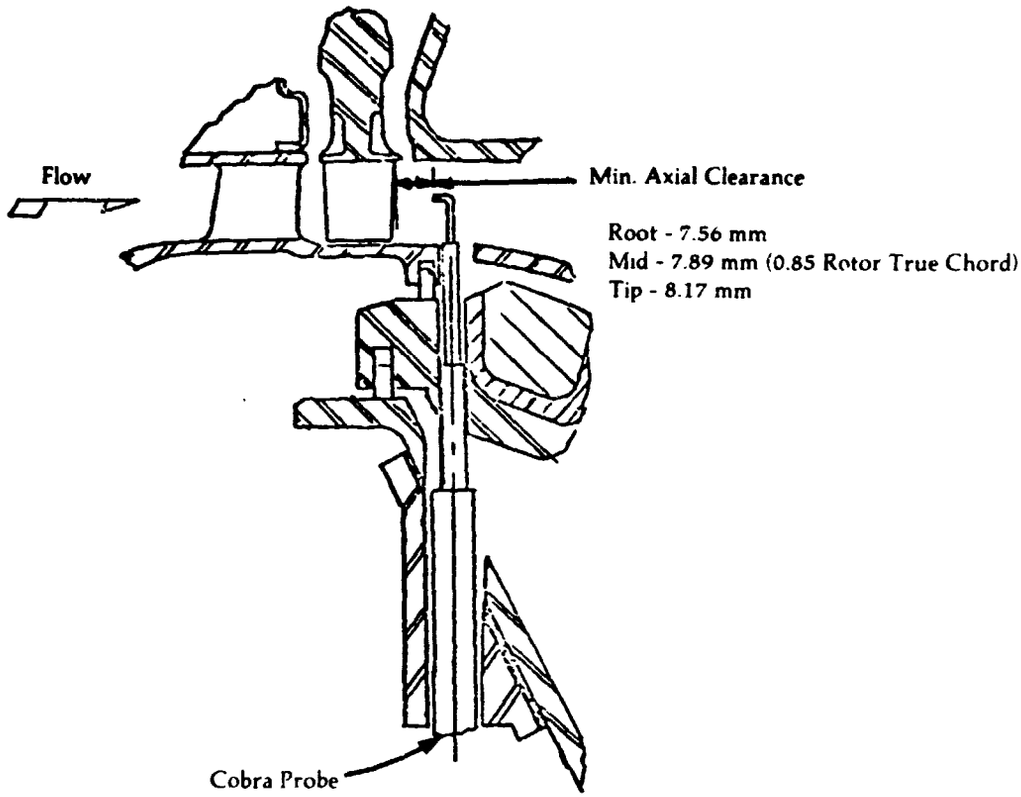

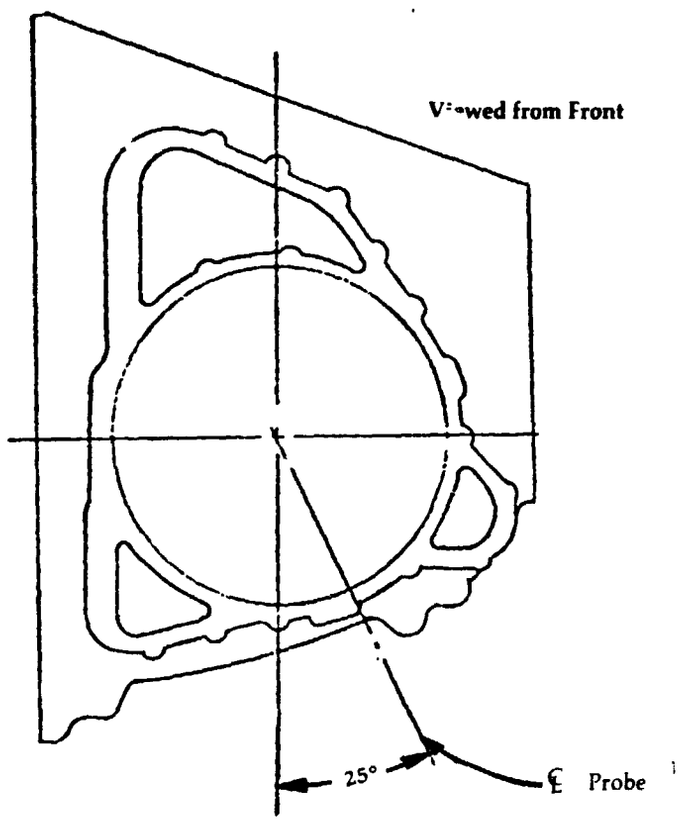

Figure 146

Automotive Gas Turbine Emission Test System

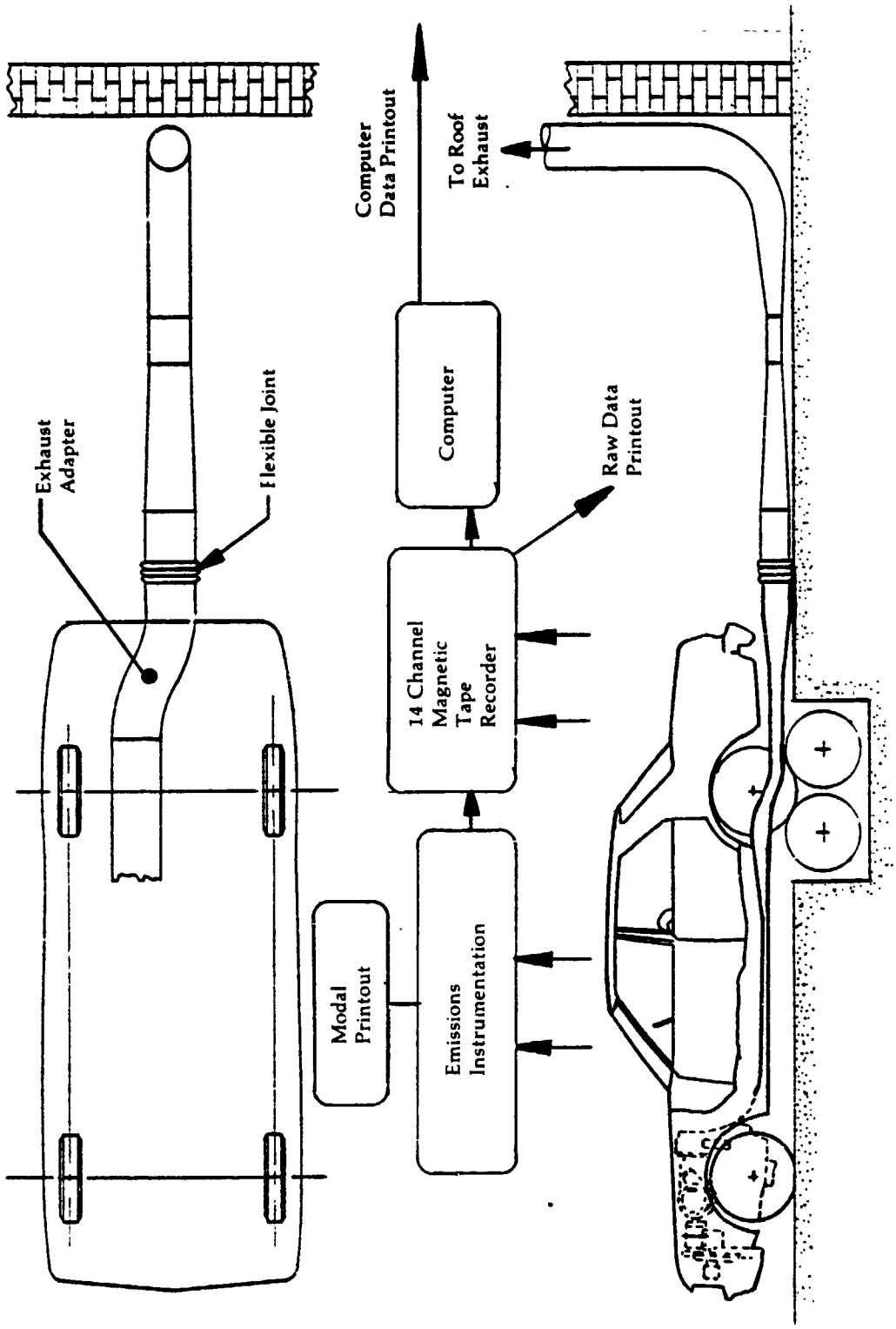

Figure 147

Upgraded Engine Performance Comparisons

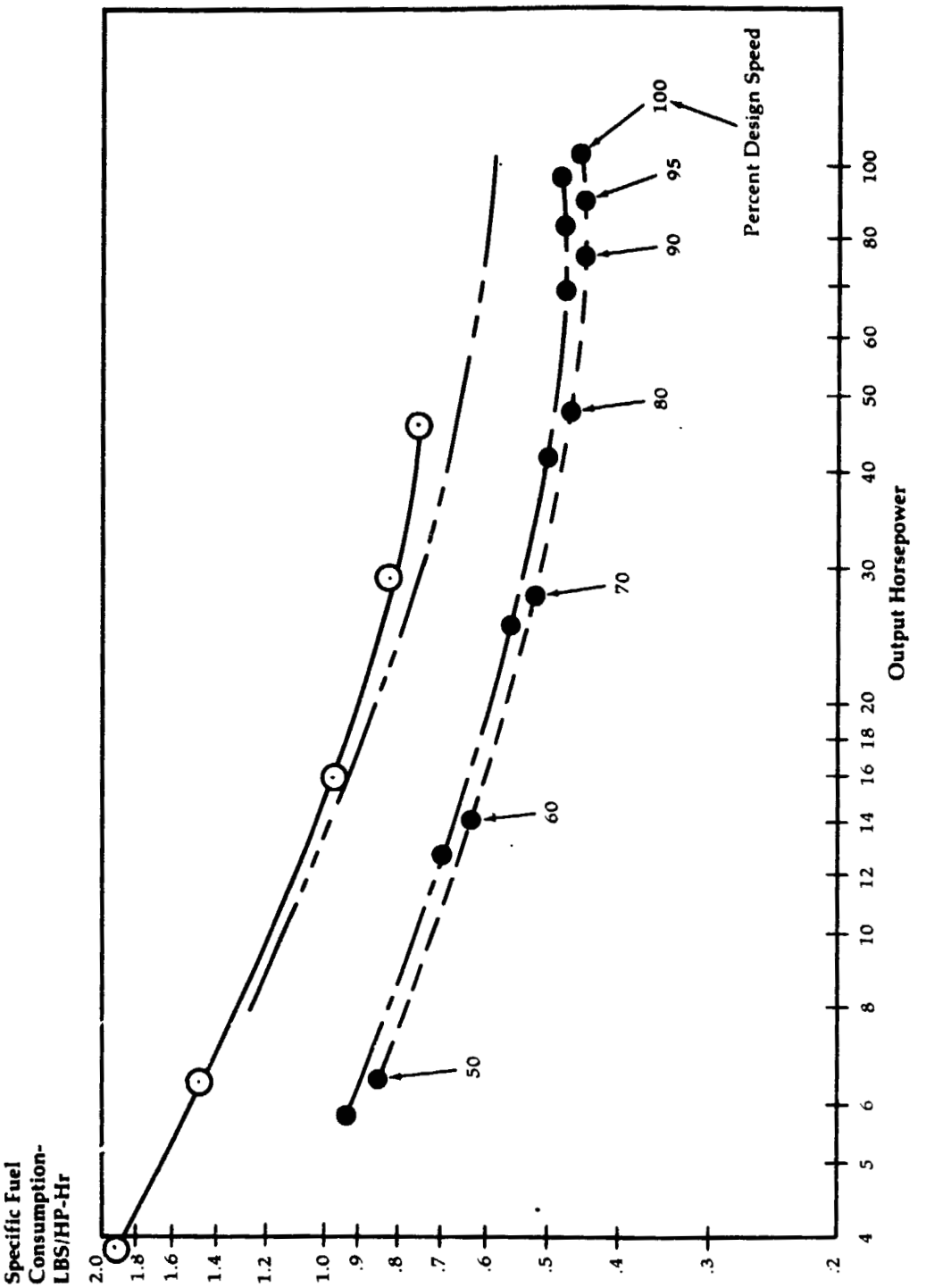

Figure 148

Upgraded Engine Performance Comparisons

——— – – ——— Scaled Baseline Engine
– – – – – – – – – Original Upgraded Engine Goal
——— – ——— Revised Upgraded Engine Goal

Build Identif.		Engine Build Configurations
2-3Q	△	Final Diffuser Modification to Original Compressor; Original Turbine Configurations.
3-9X	▽	Splitter-Blade Version of Original Impeller with Alternate Diffuser Design; Blading Change on Compressor-Turbine (0.8X scale of Baseline Engine); Original Power Turbine.
3-9Y	◇	Same Compressor and Compressor-Turbine as Above; Power Turbine Blades Twisted Closed.
10-14M	▷	Same Compressor Diffuser as Above But Original Impeller Used; Redesigned Compressor-Turbine (Mod 3); Same Power Turbine.
3-13I	◁	Same as Above Except Splittered Impeller and Redesigned Power Turbine.

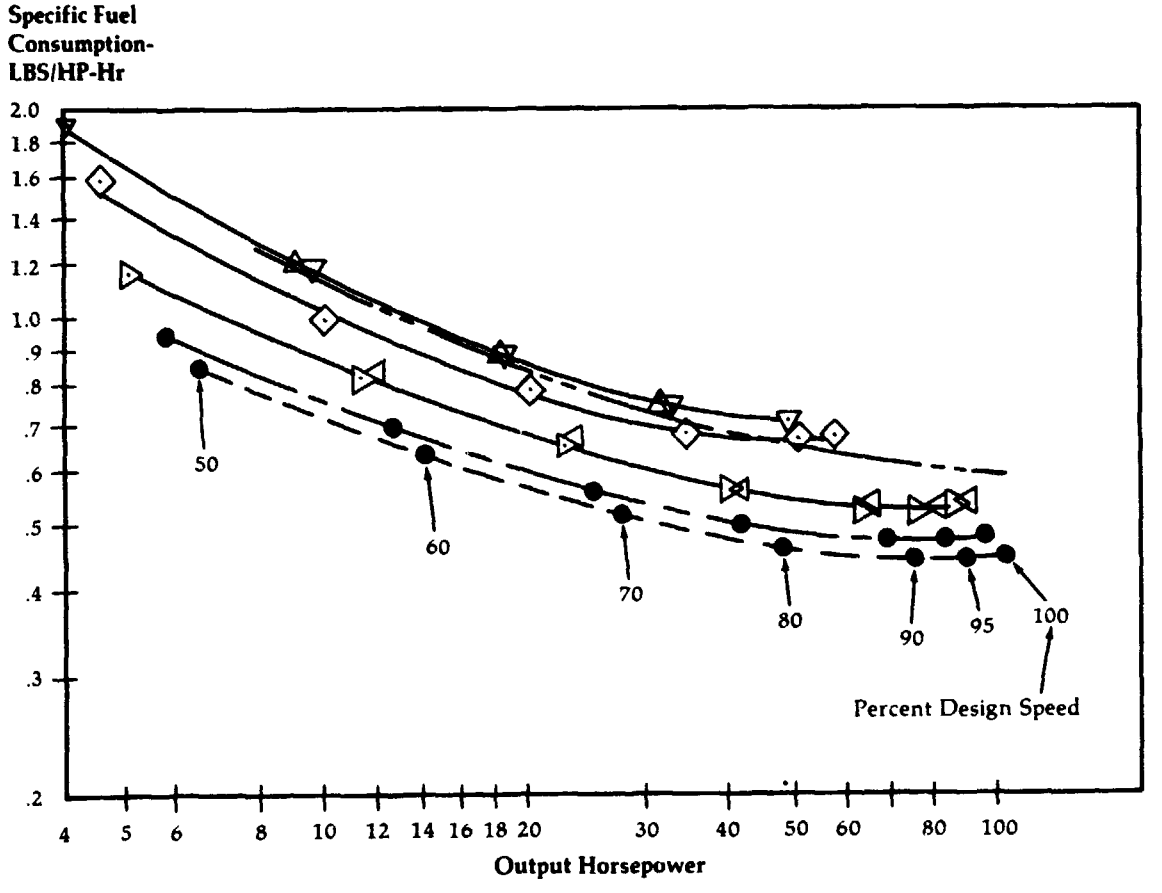

Figure 149

BSFC vs. Output Horsepower

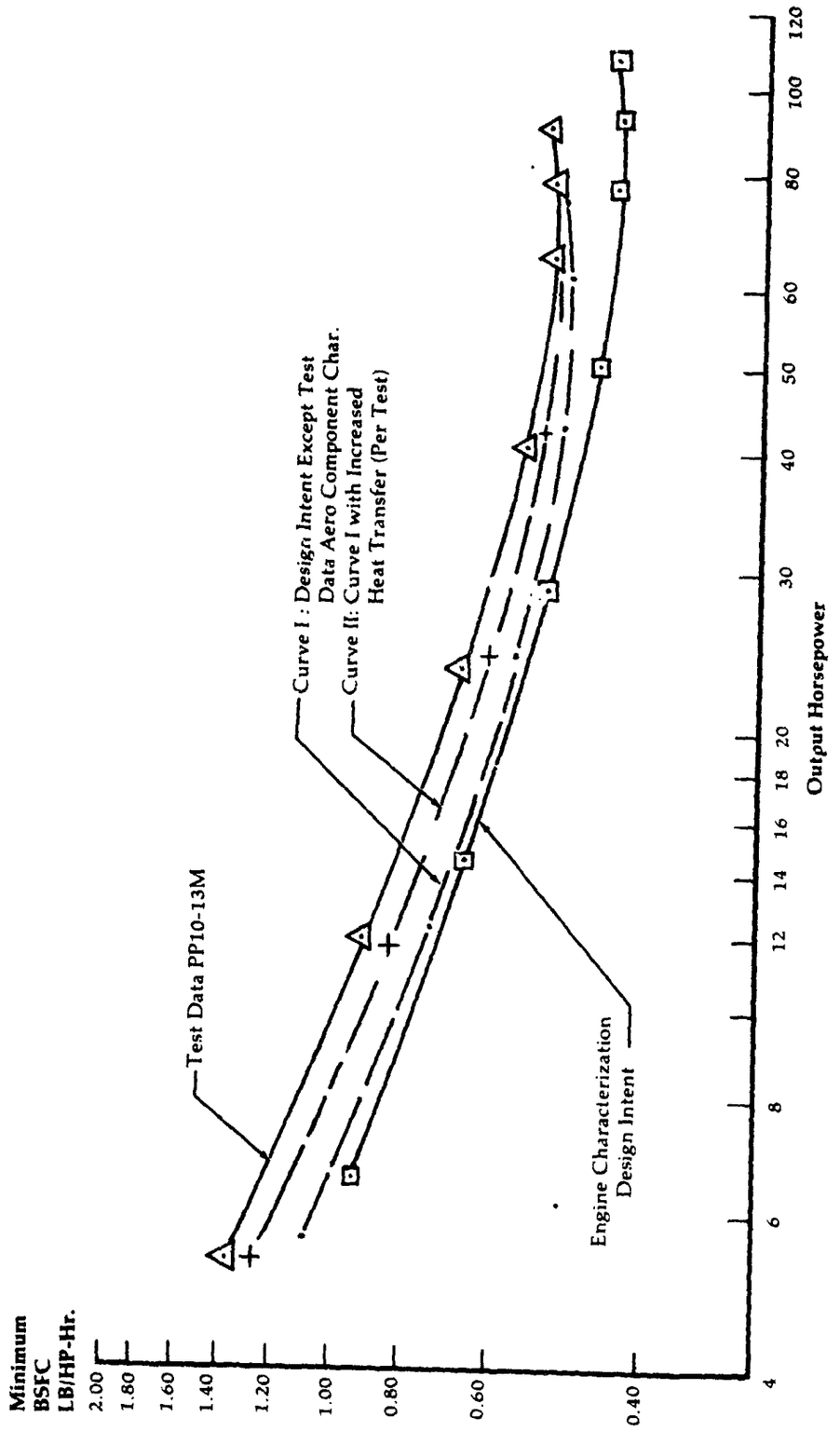

Figure 150

Upgraded Engine
24-Blade Impeller

Figure 151

Compressor Performance- Upgraded Engine 1.26 x Scale Test 2 vs. Program Goals

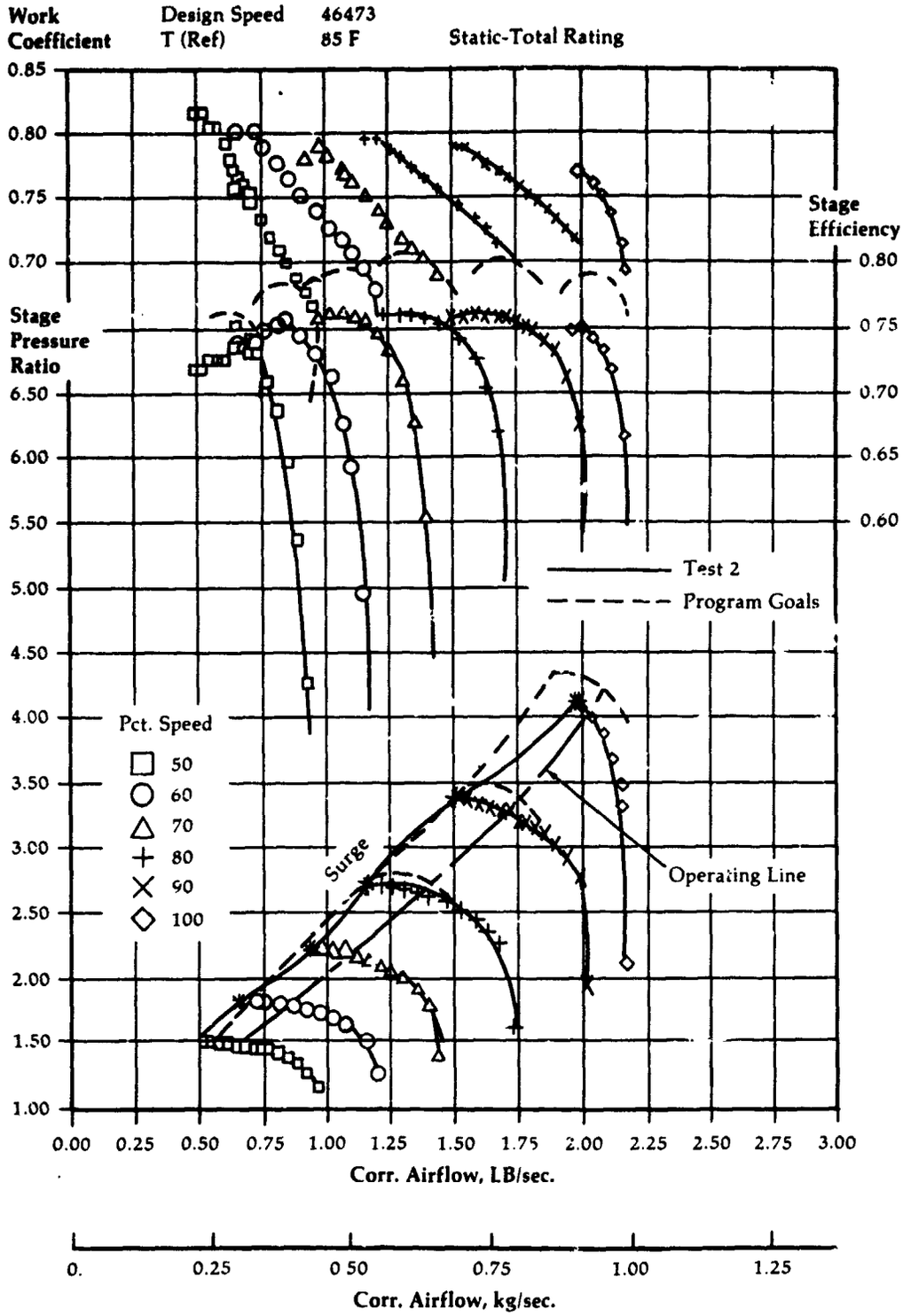

Figure 152

Upgraded Engine - Rotor Performance 1.26 x Scale Compressor 50% Speed

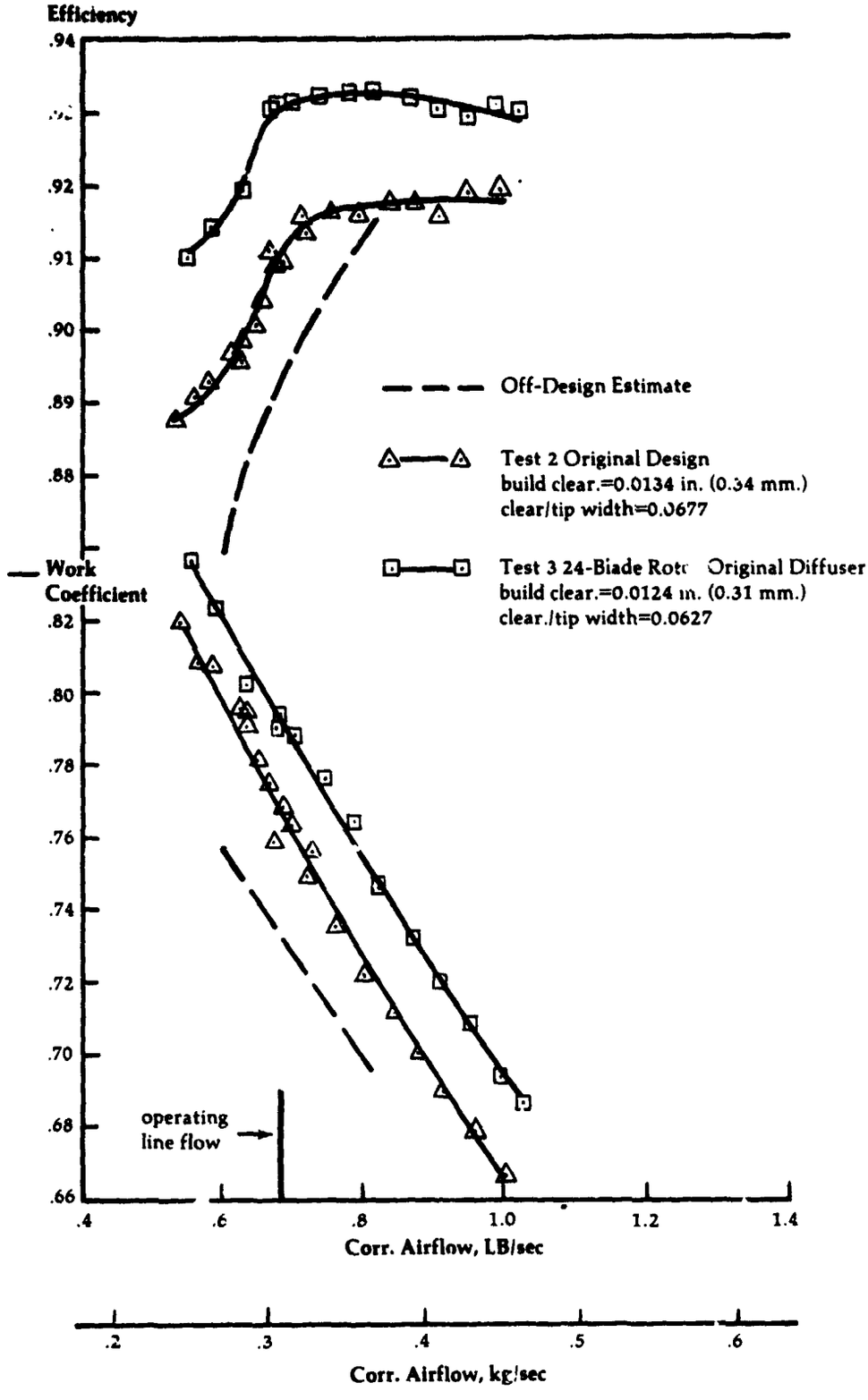

Figure 153

Upgraded Engine - Rotor Performance 1.2o x Scale Compressor 90% Speed

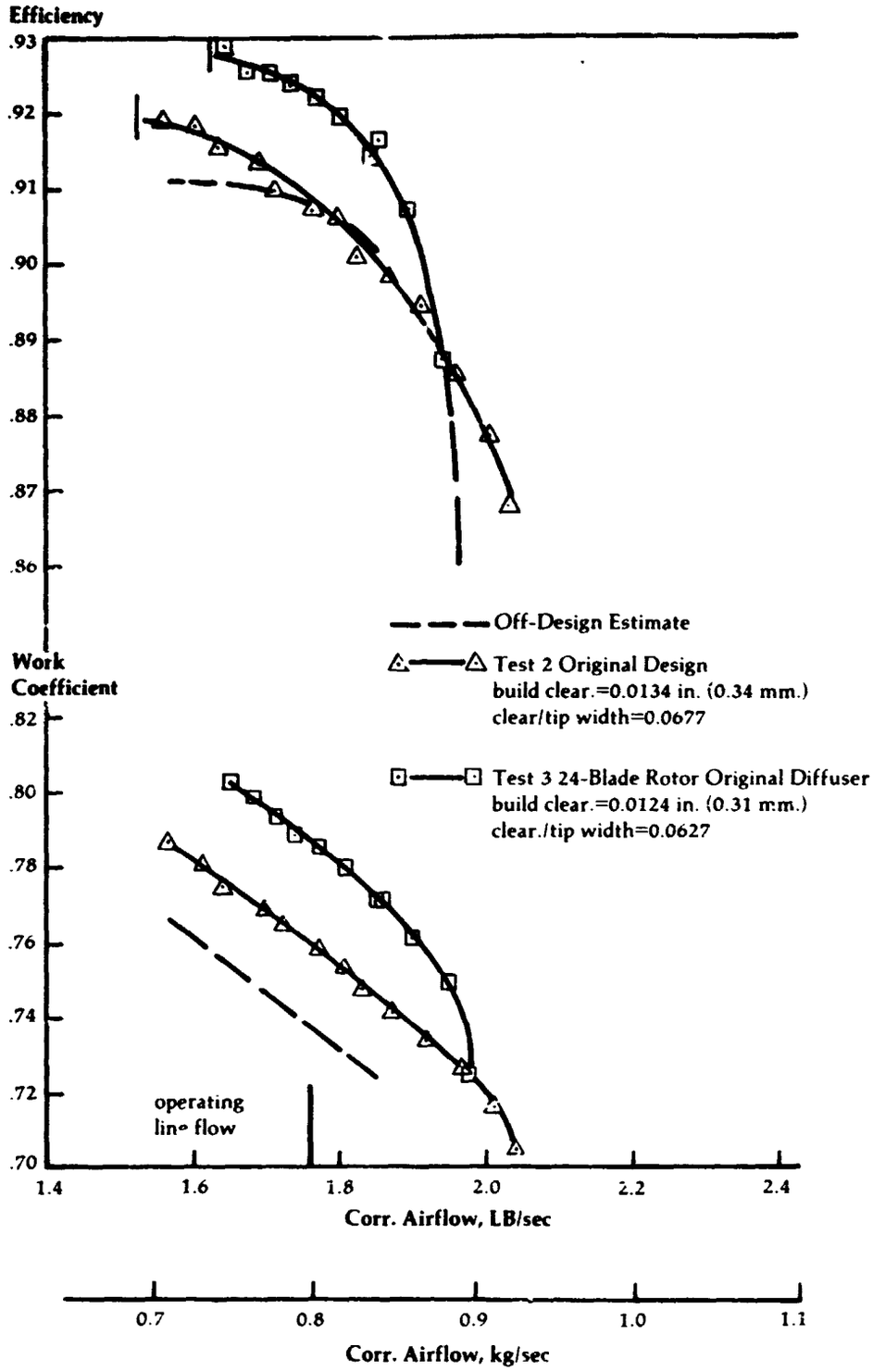

Figure 154

Deswirl Vane Design Comparison

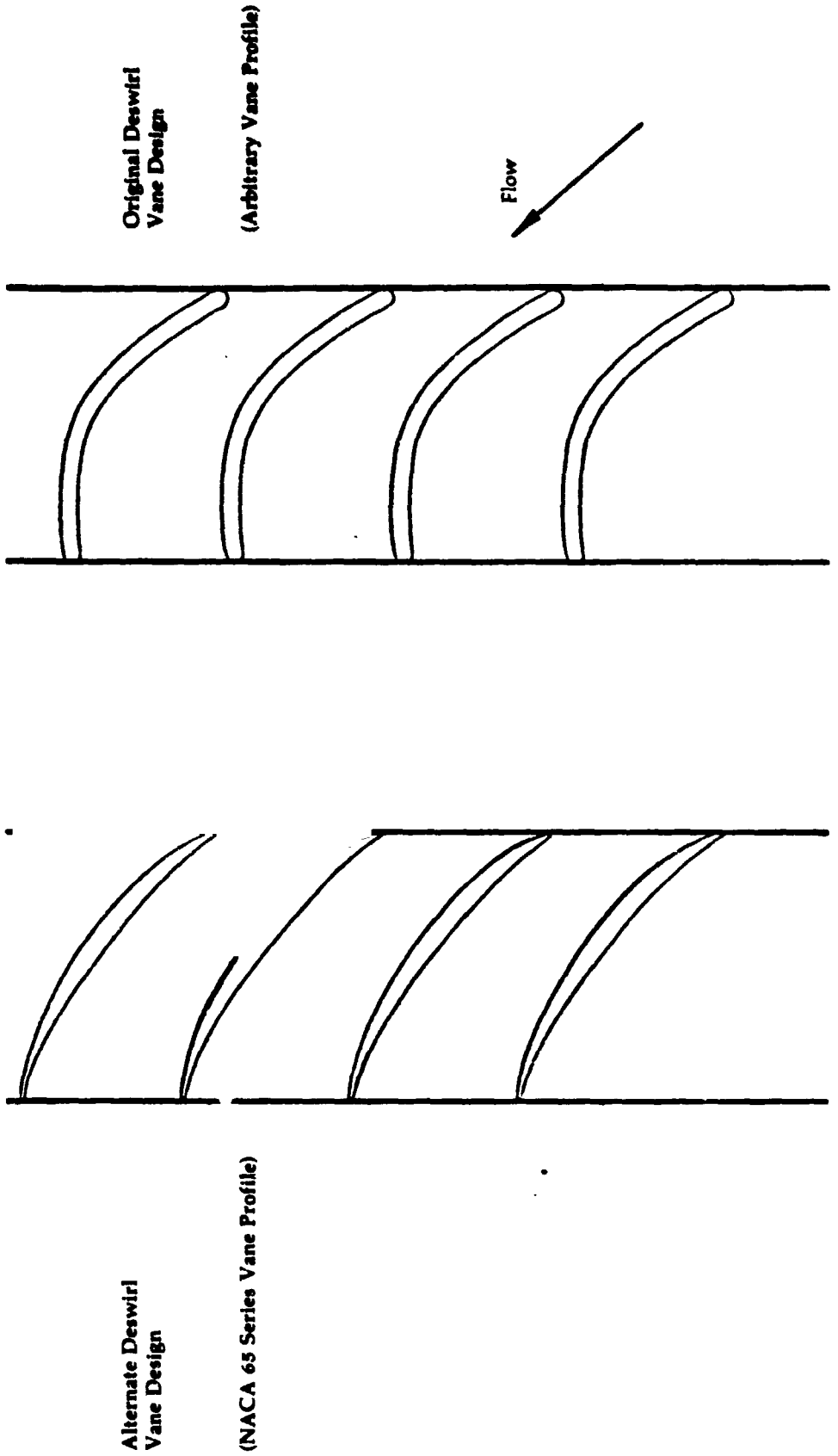

Figure 155

Compressor Performance - Upgraded Engine 1.26 x Scale Test 2 vs. Test 4

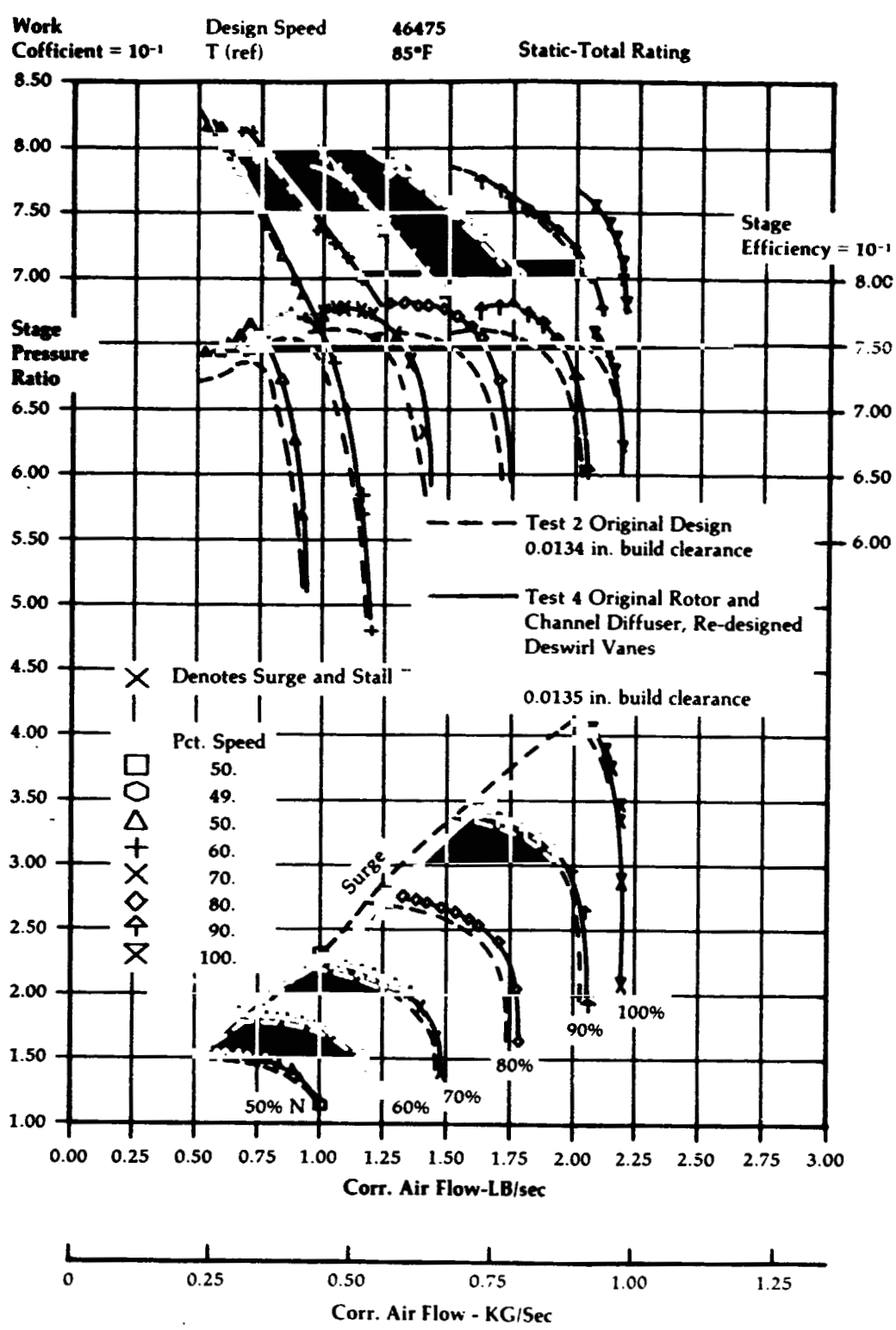

Figure 156

Upgraded Engine Compressor Performance

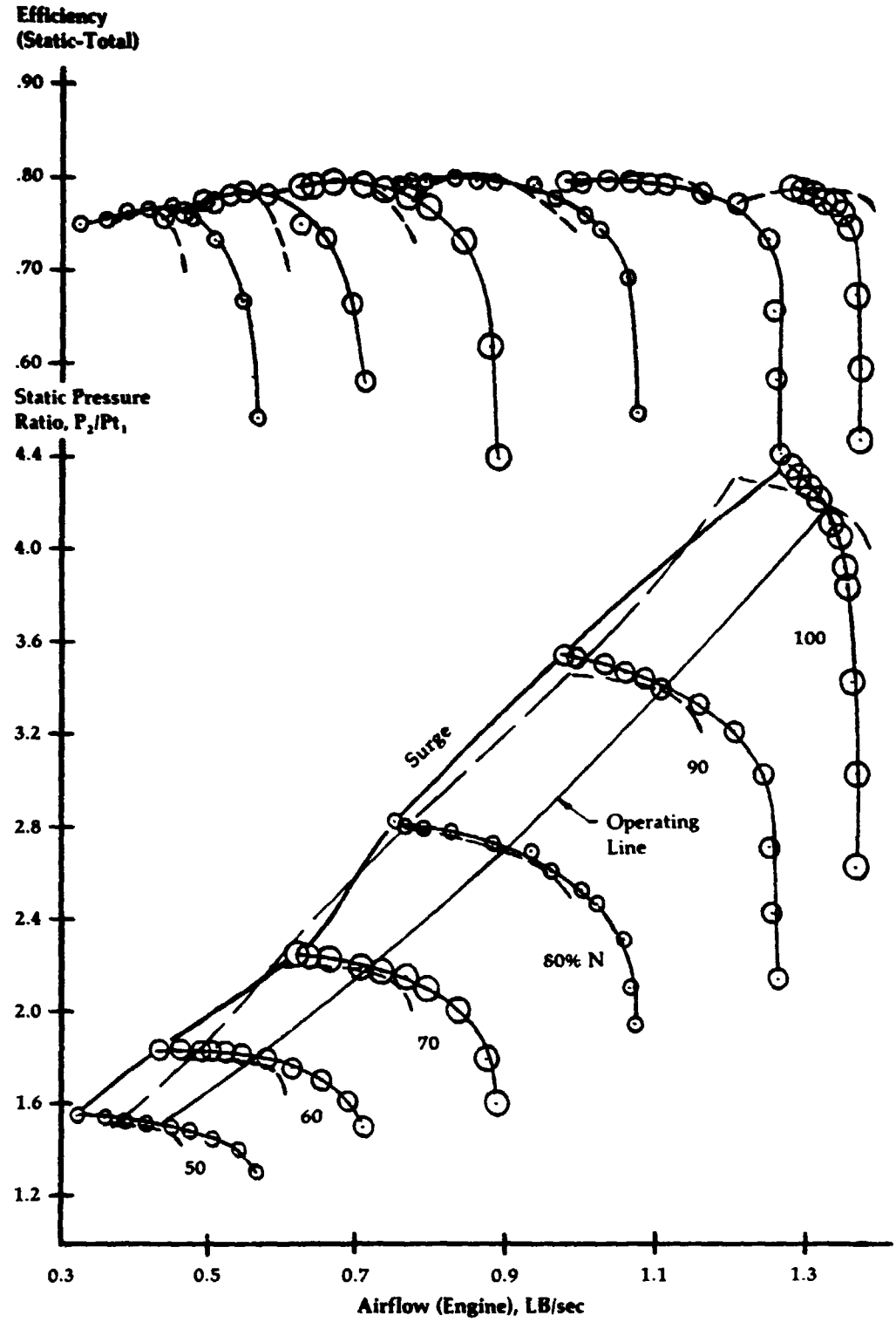

Test Rig (1.2588 x size)
24 Blade Impeller (cut-back .063 in.)
14 Channel Diffuser, ±1° Setting
Re-Staggered Vanes, Revised Deswirl Vane Design (NASA Profile)
Running Clearance=0.011 in. at 100% N

— — — — Program Goal Map

Figure 157

Upgraded Engine Compressor Performance

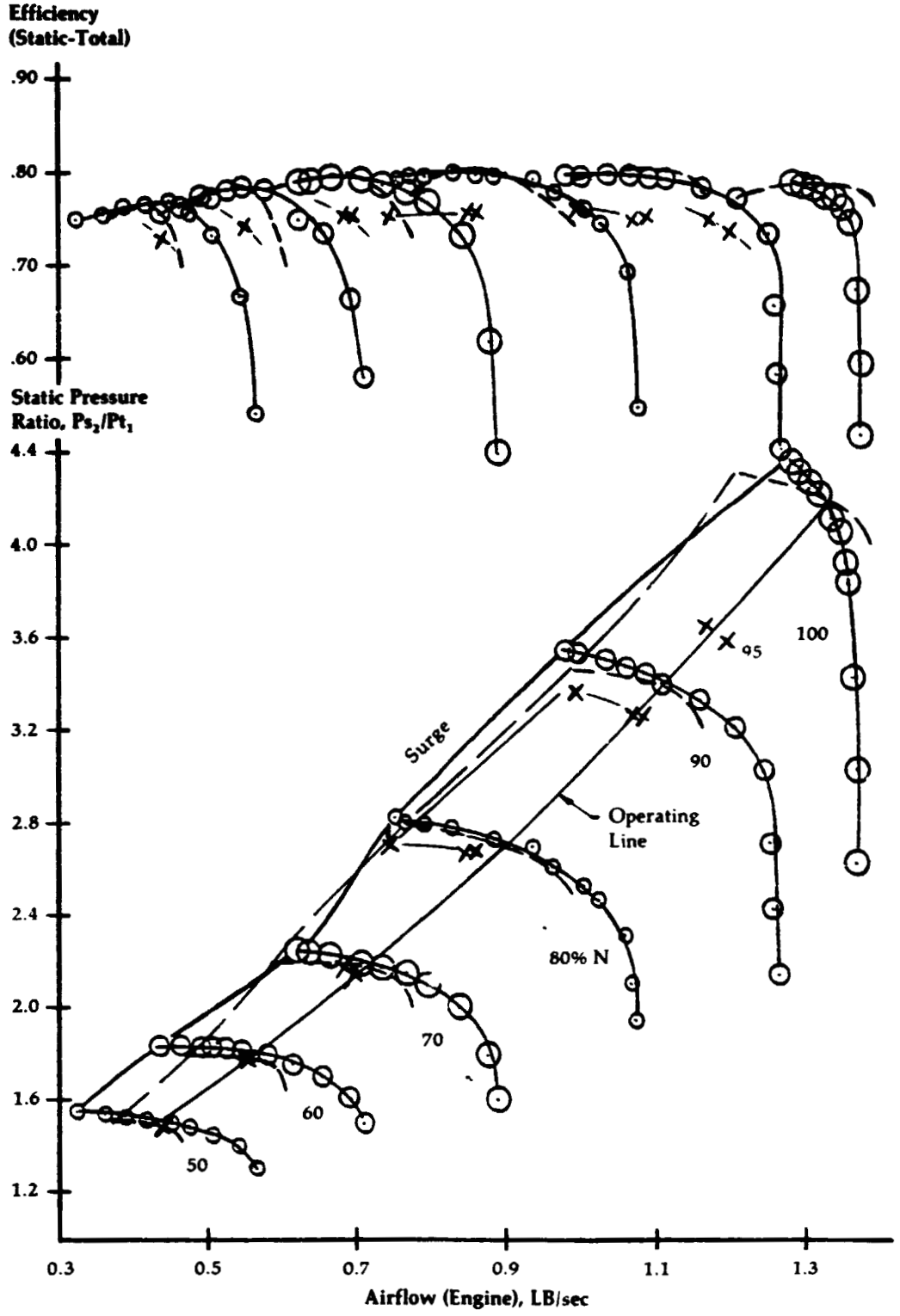

Test Rig (1.2588 x size)
24 Blade Impeller (cut-back .063 in.)
14 Channel Diffuser, +1° Setting,
Re-Staggered Vanes, Revised Deswirl
Vane Design (NASA Profile)
Running Clearance= 0.011 in. at 100% N

Program Goal Map
PP 3-9 H

Figure 158

Upgraded Engine Effect of Straightening Vanes On Compressor Exit Conditions

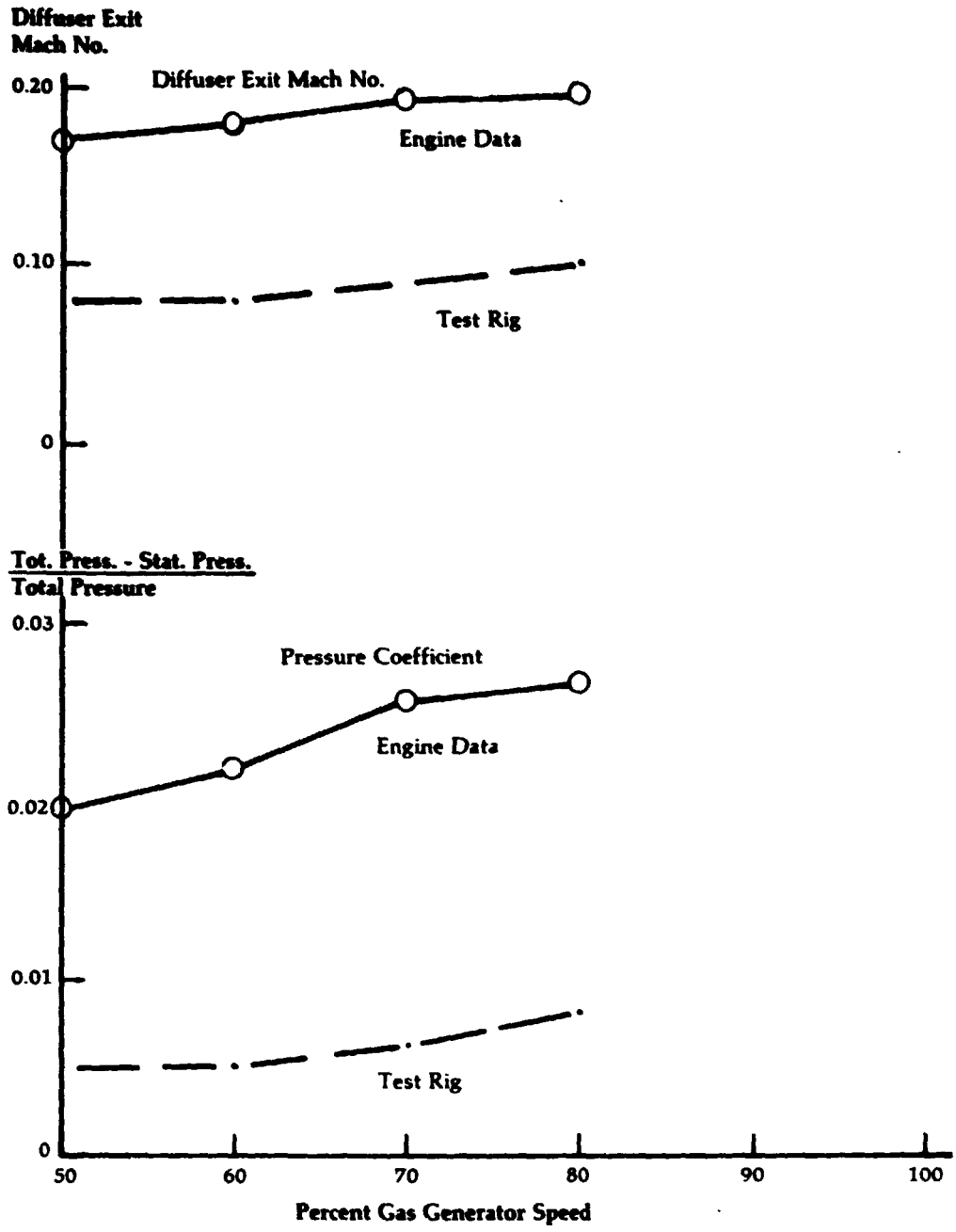

Figure 159

Upgraded Engine Compressor Inlet Tests

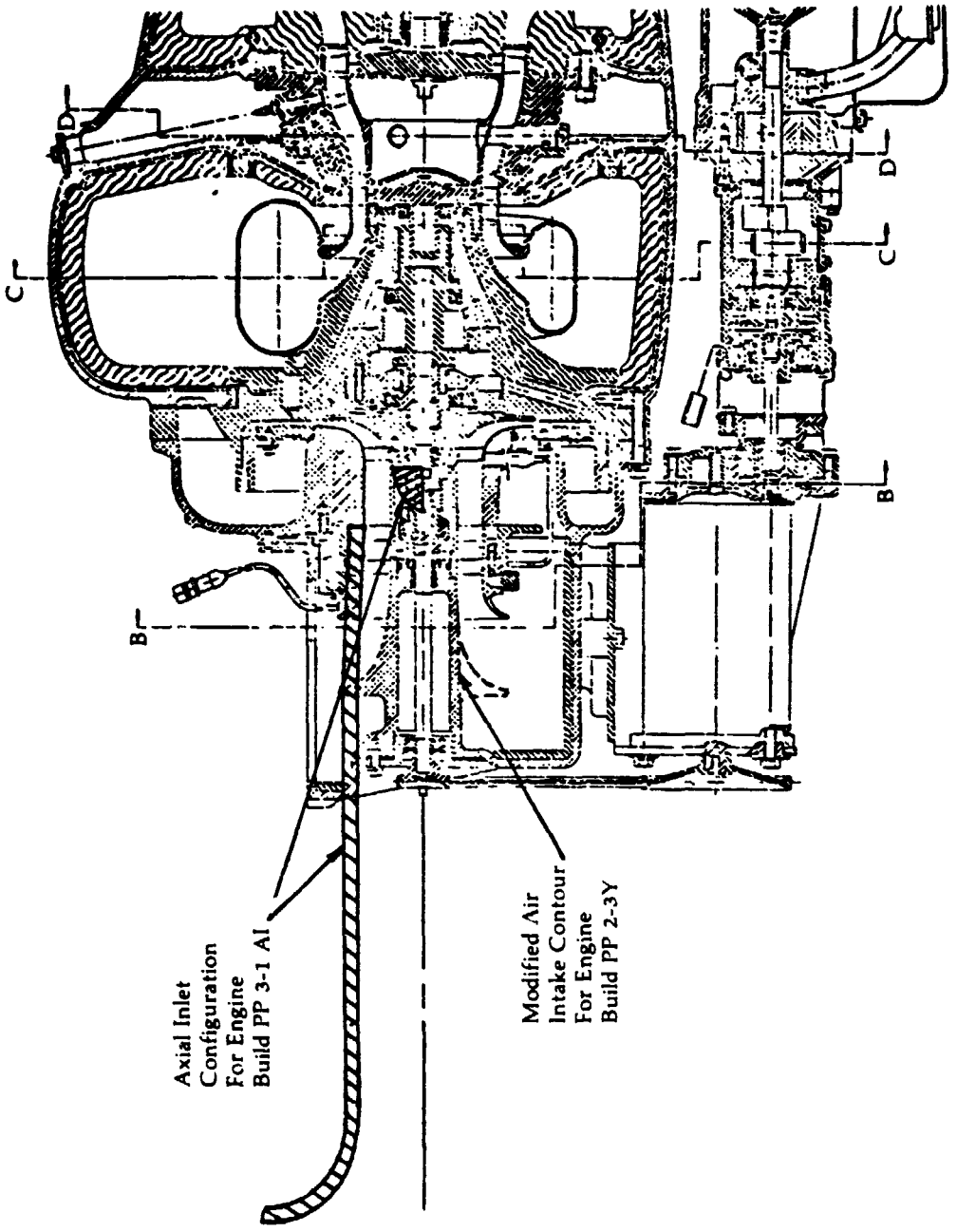

Figure 160

Upgraded Engine Compressor Efficiency Change with Air Inlet Configuration

Impeller with Gap Filled
28 Channel Diffuser, +1° Setting, 4° T.E. Taper
Tandem Deswirl Vanes

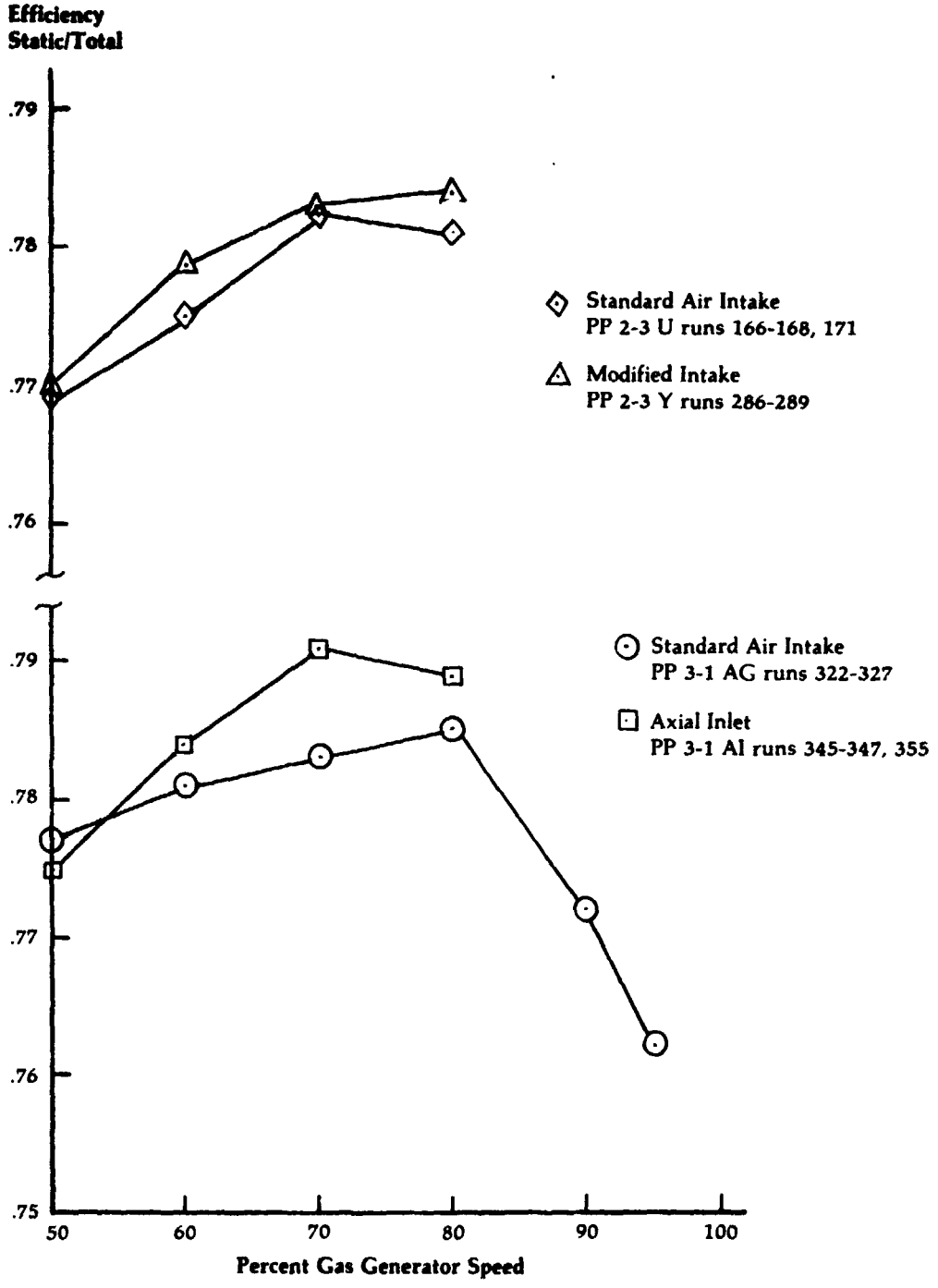

Figure 161

Upgraded Engine Compressor Comparison of Efficiency*

Change with Blade Gap Filled				
Ngg %	50	60	70	80
Efficiency Change, Pts	1.9	0.8	0.6	0.9

*(Efficiency change based on pressure ratio change)

Figure 162

Upgraded Engine Compressor Enlarged Volume Collector

Front View of Compressor Cover

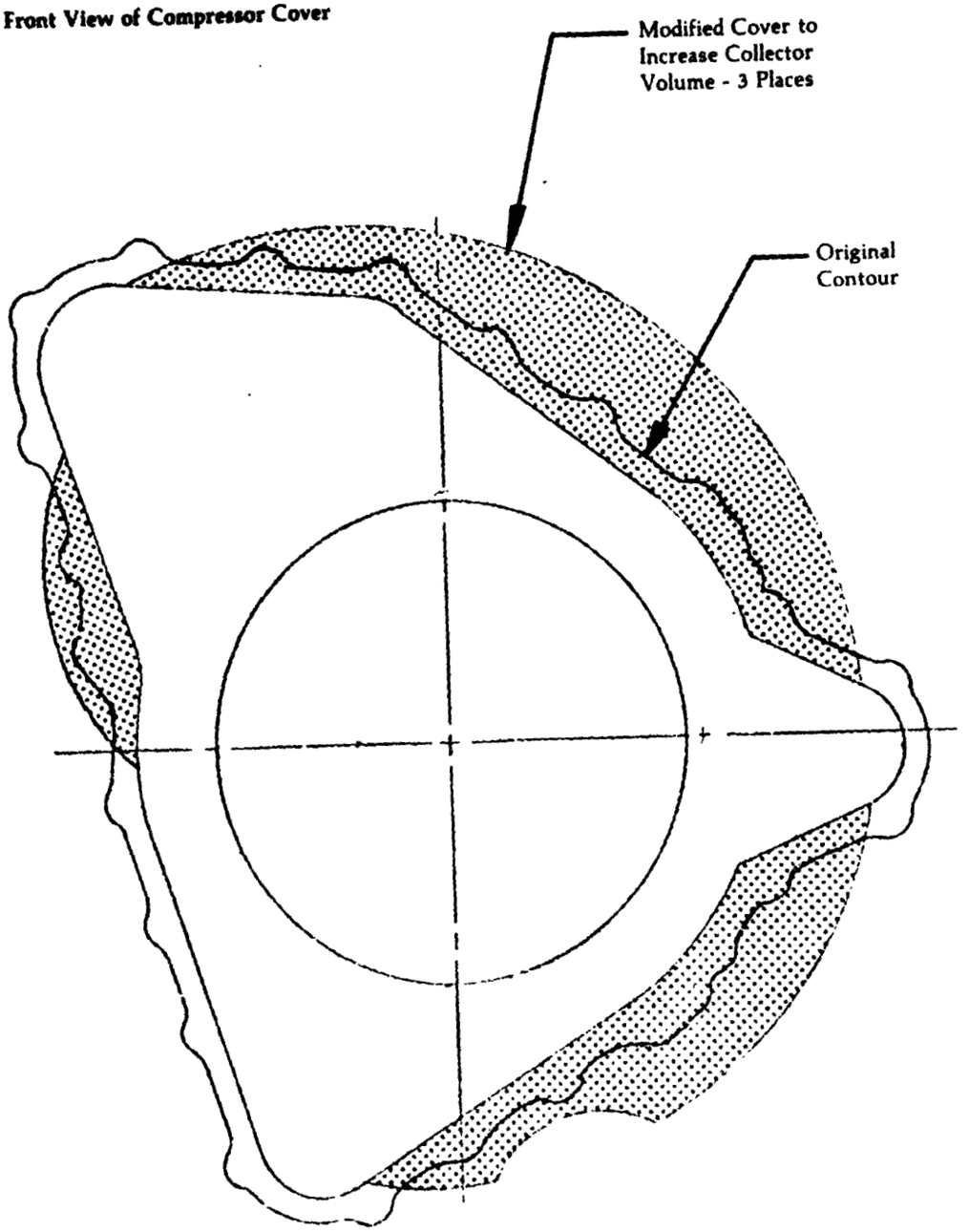

Figure 163

Upgraded Engine Compressor Deflector Ring Configuration

Front View with Compressor Cover Removed

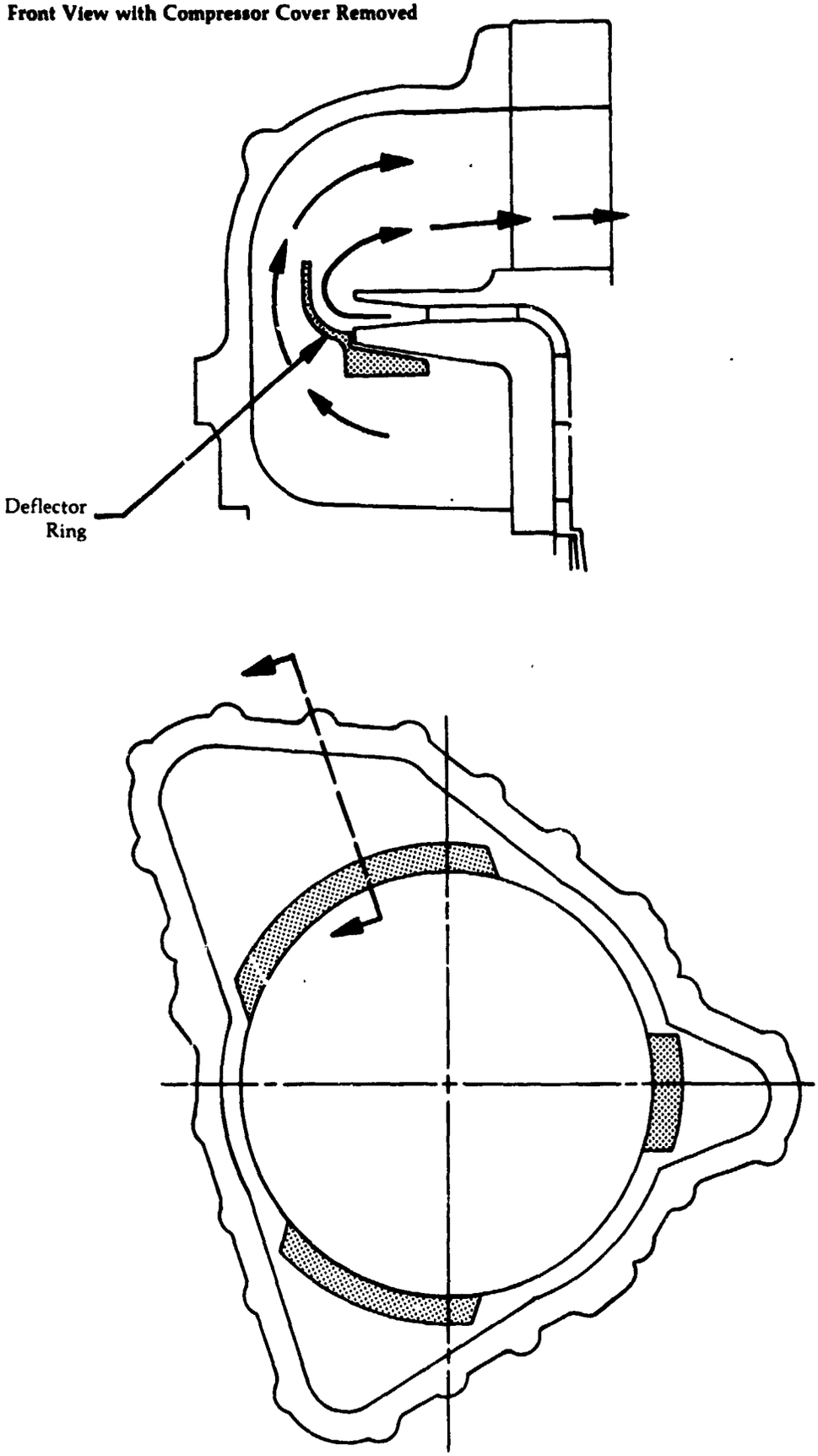

Figure 164

Upgraded Engine Compressor Meridional Model of Collector Flow with No Crossflow

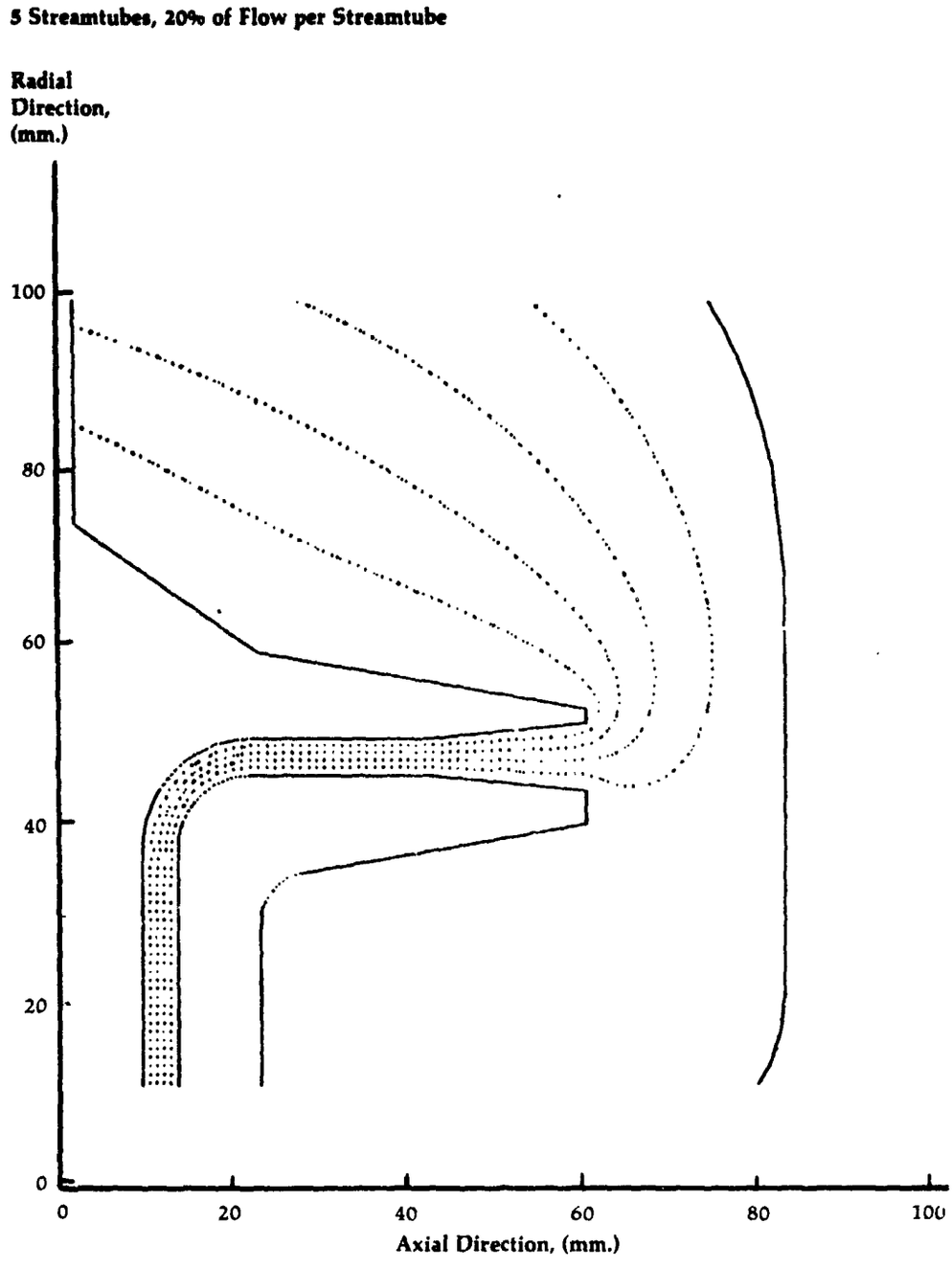

Figure 165

Upgraded Engine Compressor Meridional Model of Collector Flow with Crossflow

Each region is Comprised of 5 Streamtubes with 20% of the Flow per Streamtube.

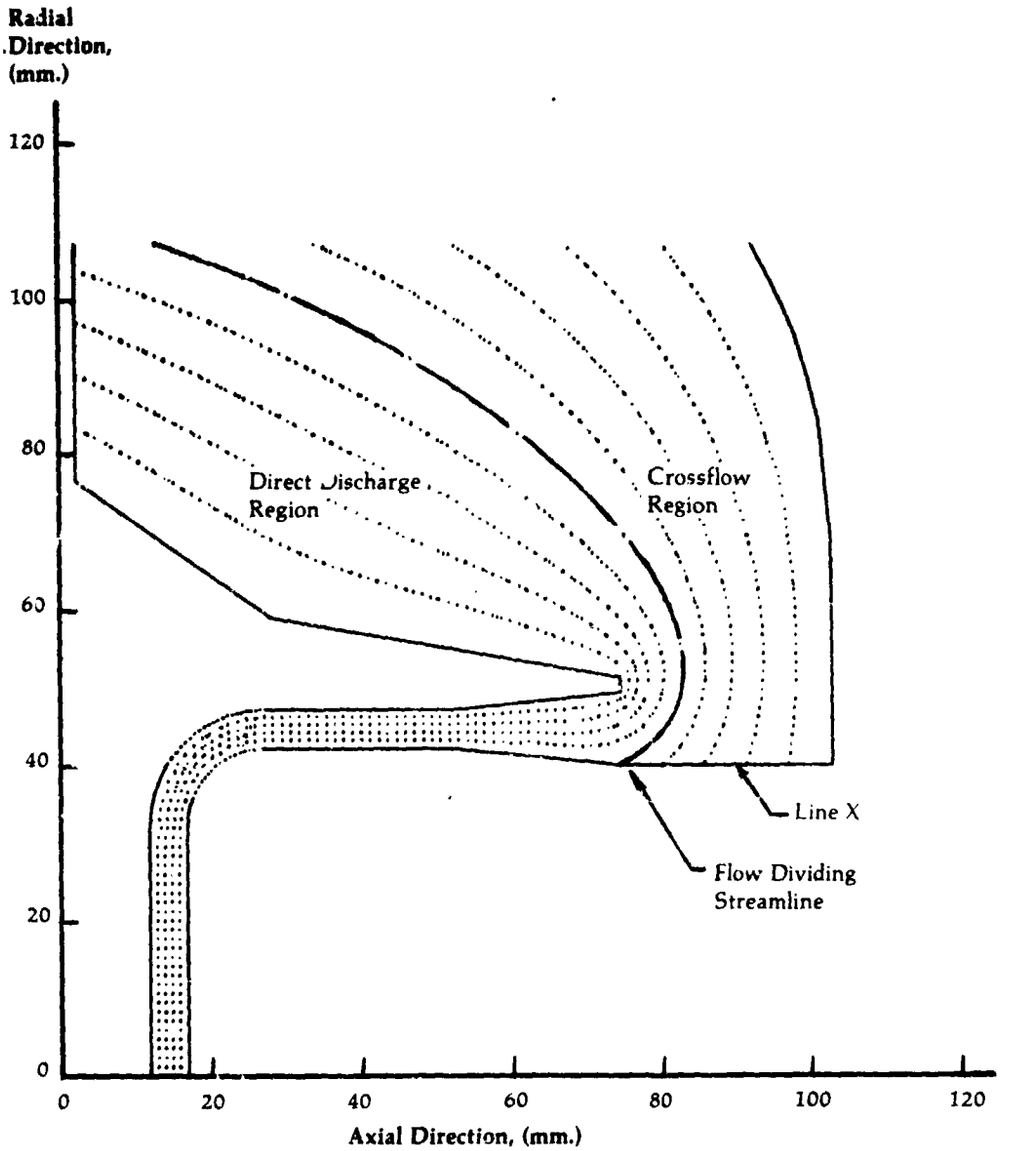

Figure 166

Upgraded Engine Compressor Static Pressure Recovery Along Flare (Shroud)

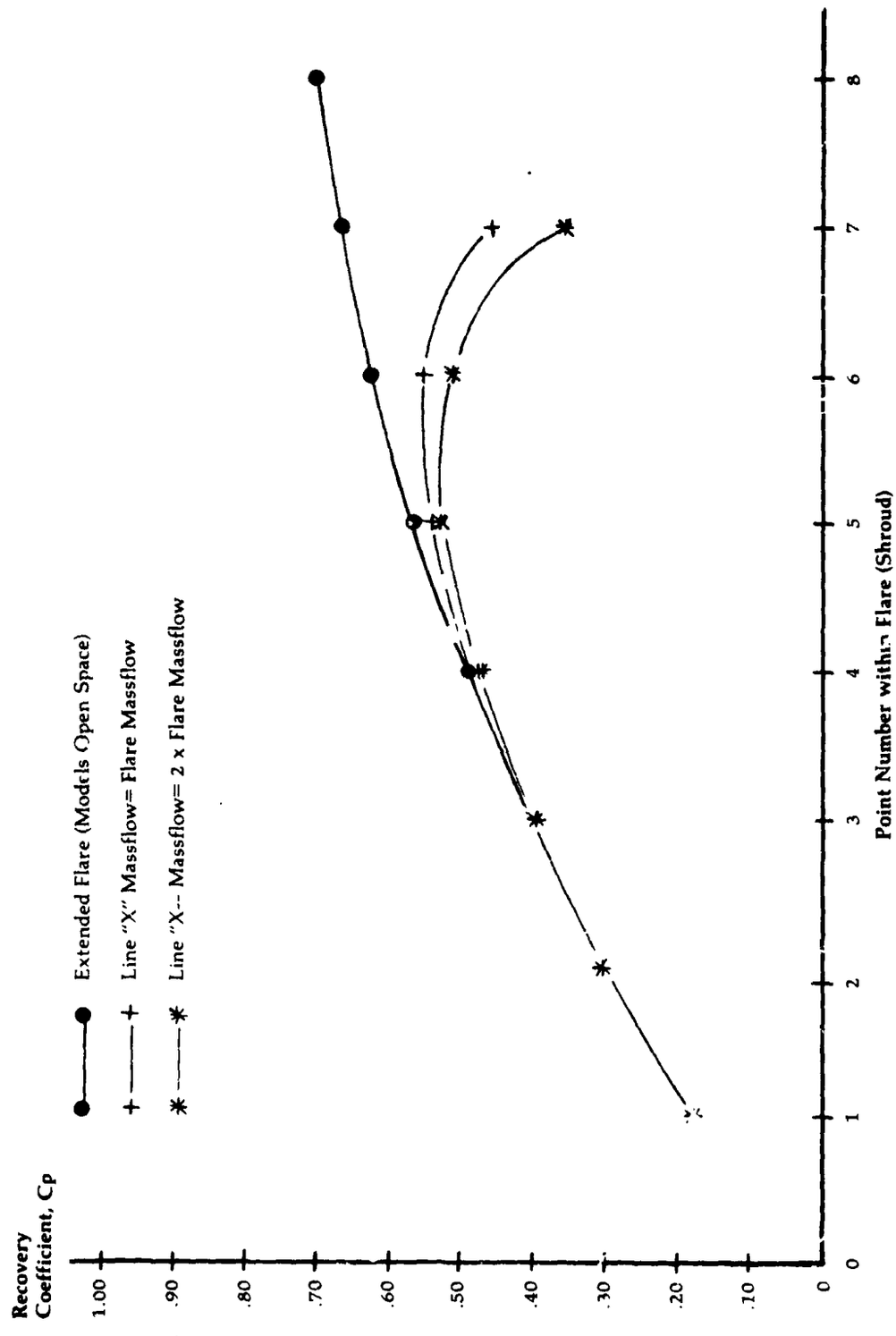

Figure 167

Static Tap Data at 80% Speed

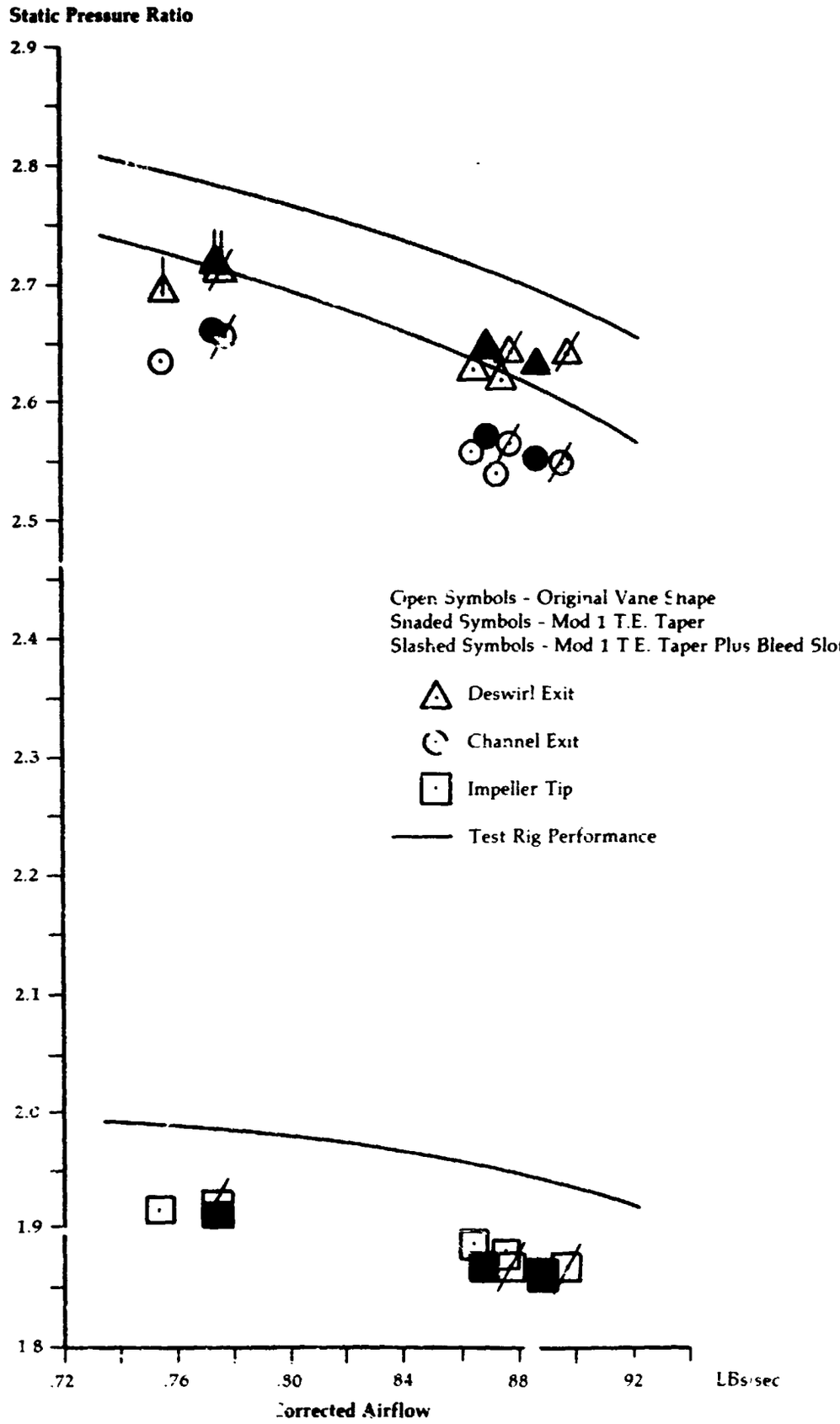

Figure 168

Static Tap Data at 80% Speed with Impeller Tip Data Set at Rig Level

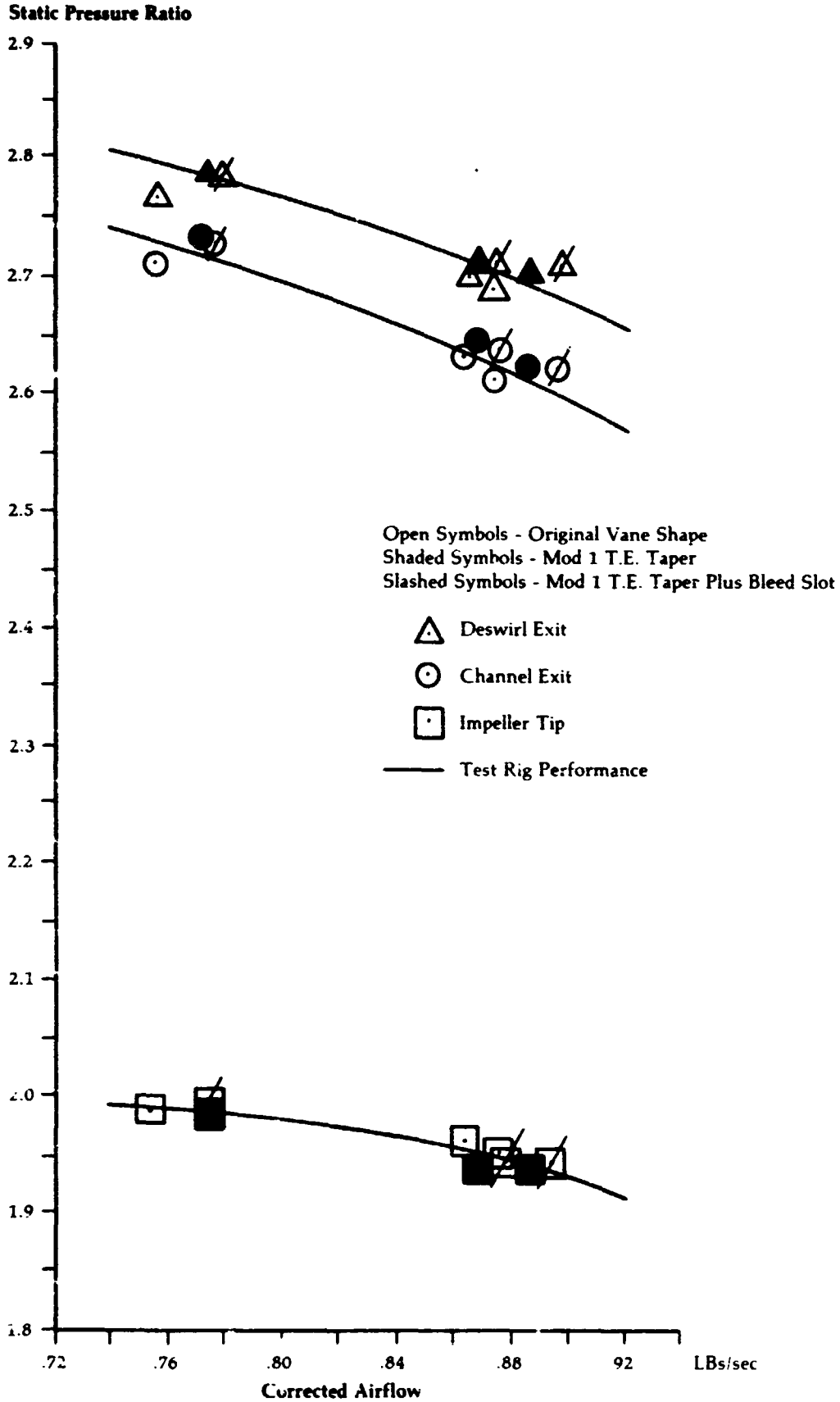

Figure 169

Tandem Deswirl
Vane Configuration

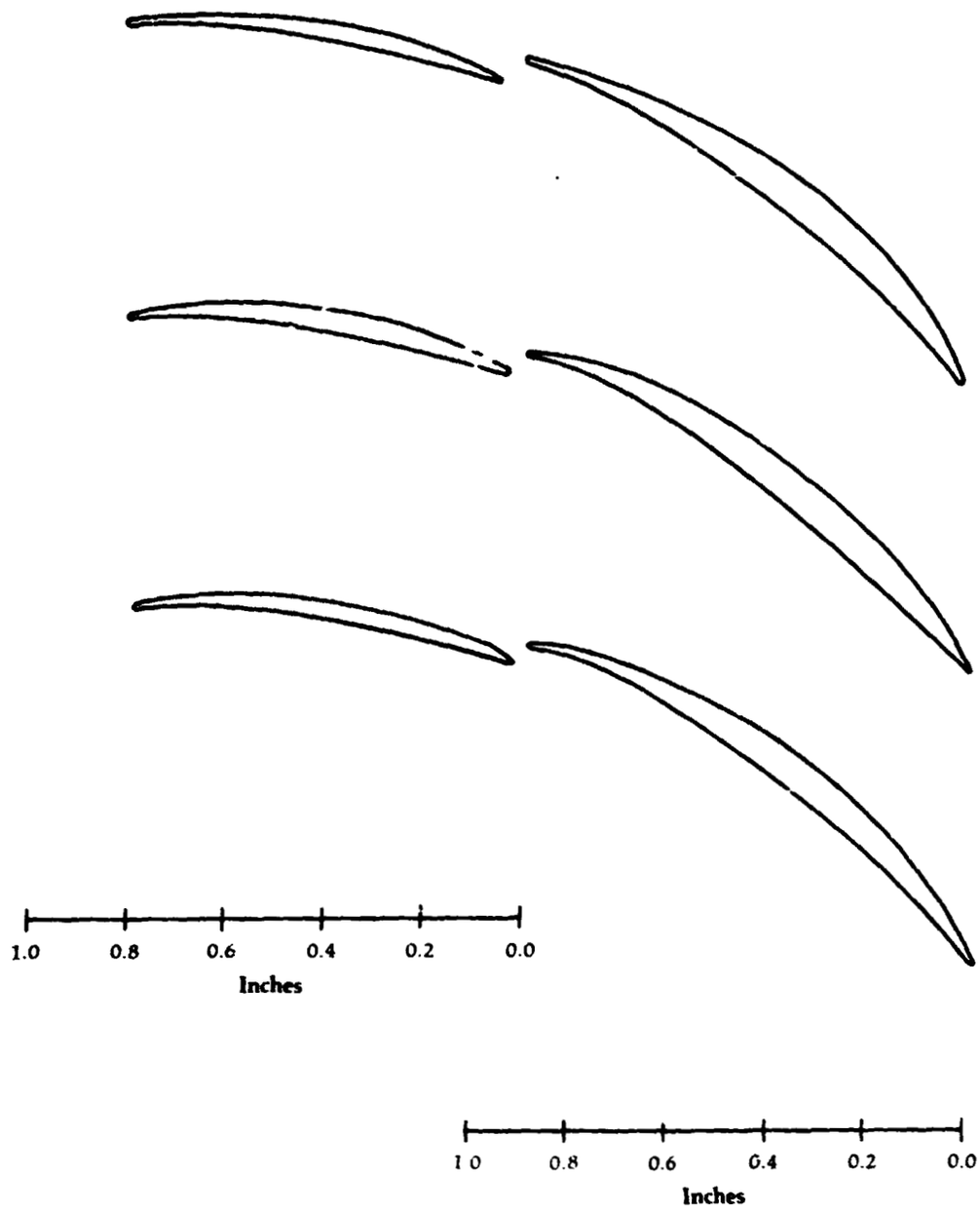

Figure 170

14 - Channel Diffuser - Trailing Edge Modification

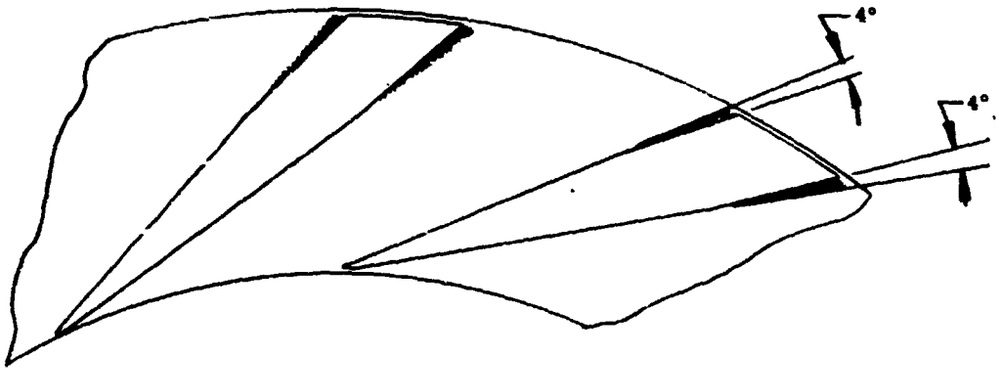

Modification #1

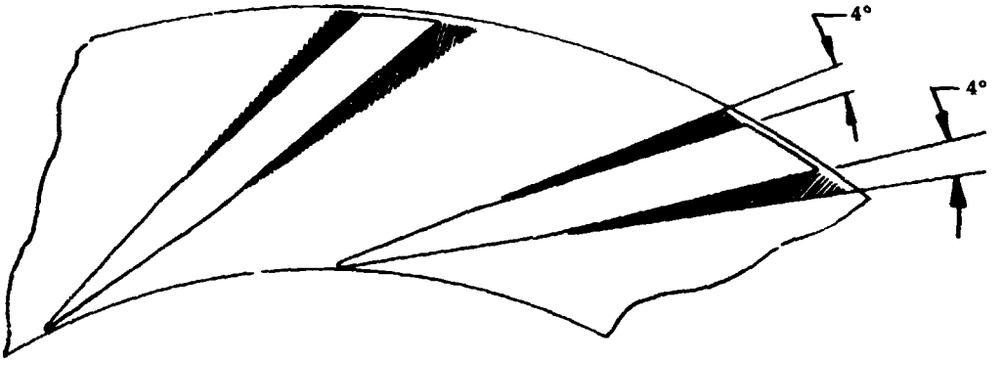

Modification #2

28 - Channel Diffuser - Trailing Edge Modification

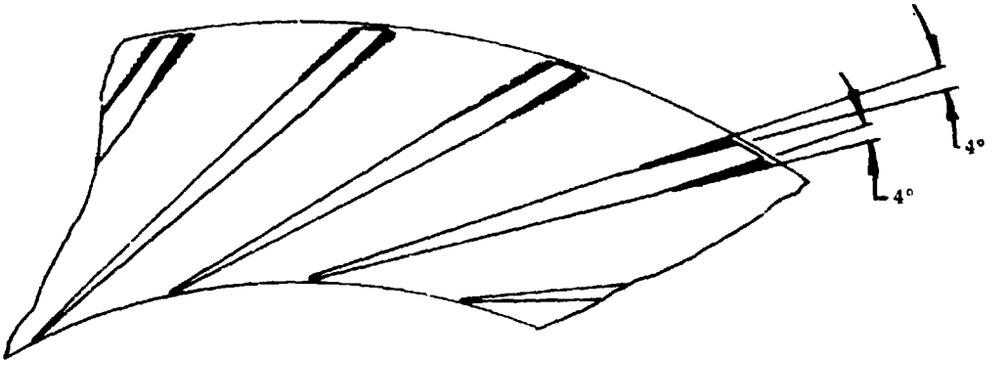

Figure 171

Upgraded Engine Compressor Efficiency Comparisons with Different Diffuser Configurations

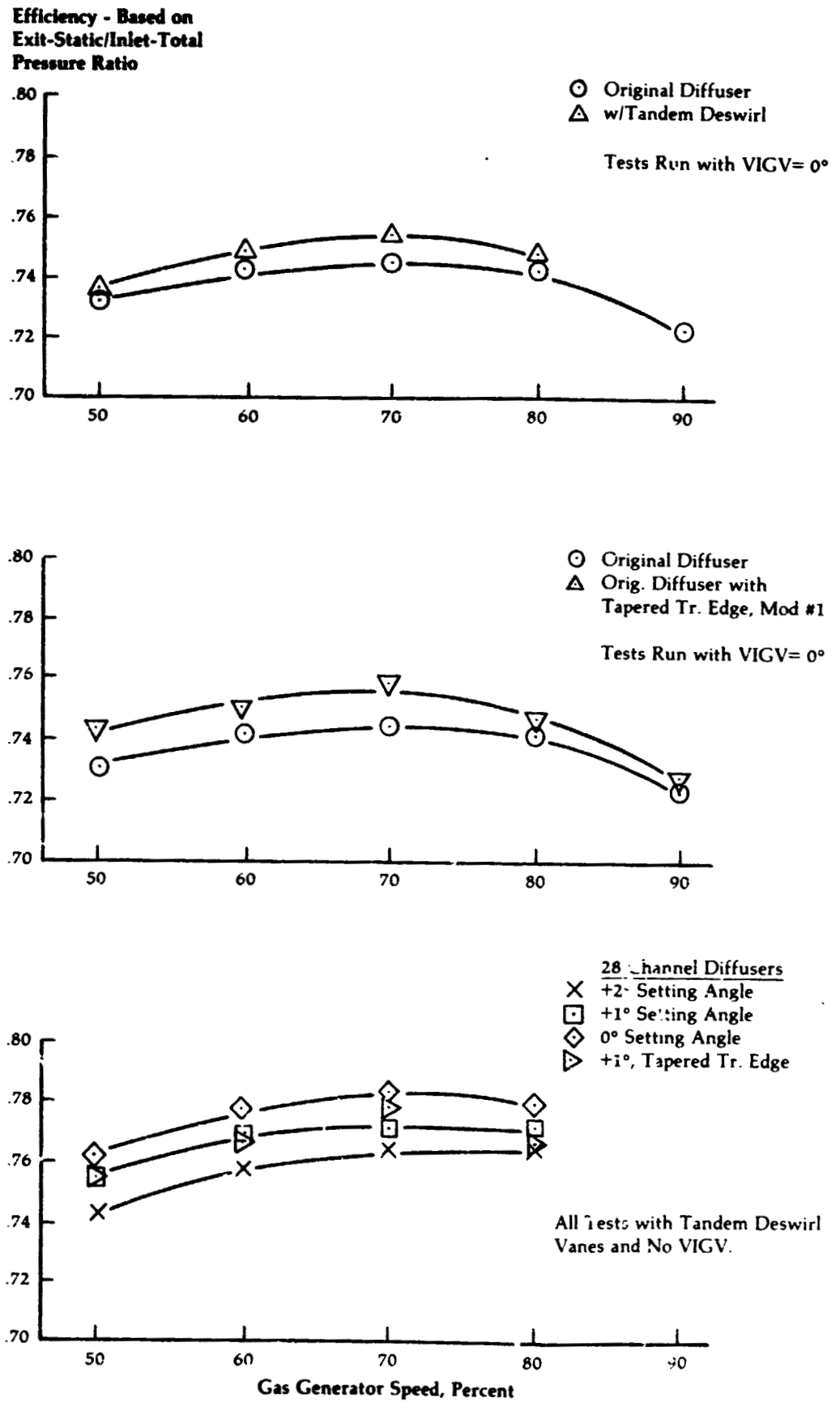

Figure 172

Upgraded Engine Compressor Summary of Efficiency Change with Diffuser Modification: Data Taken with 24-Blade Rotor

- Program Goals
- Rig, 14 Channel Diffuser, No VIGV
- Engine Data, 14 Channel Diffuser, No VIGV, Single Row Deswirl Vanes, PP 3-9 H runs 71-77
- Engine Data, 28 channel Diffuser, No VIGV, Tandem Deswirl Vanes, PP 3-1 runs 322-336
- Engine Data, 28 Channel Diffuser with 40% Increase in Area Ratio, No VIGV, Single Row Deswirl Vanes PP 10-14 L runs 31-35

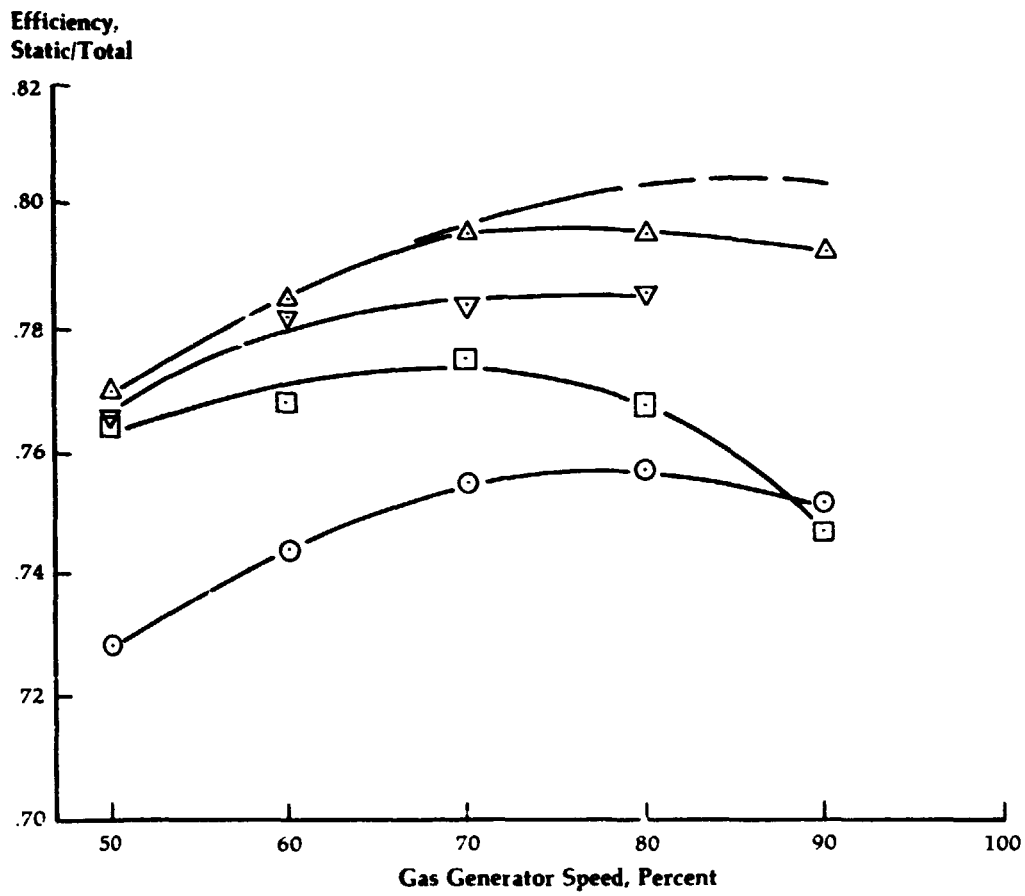

Figure 173

Upgraded Engine Compressor Summary of Efficiency Change with Rotor and Diffuser Modifications

- Program Goals
- Rig, 14 Channel Diffuser, No VIGV, 24-Blade Impeller
- Engine Data, 28 Channel Diffuser, No VIGV, Tandem Deswirl, 24-Blade Impeller, PP 3-1 runs 322-336
- Engine Data, 28 Channel Diffuser, +1°, Tandem Deswirl, 18-18 Impeller, PP 3-9 F
- Engine Data, Double-Divergent Diffuser, 40% Incr. Exit Area, 18-18 Impeller, PP 3-9 T

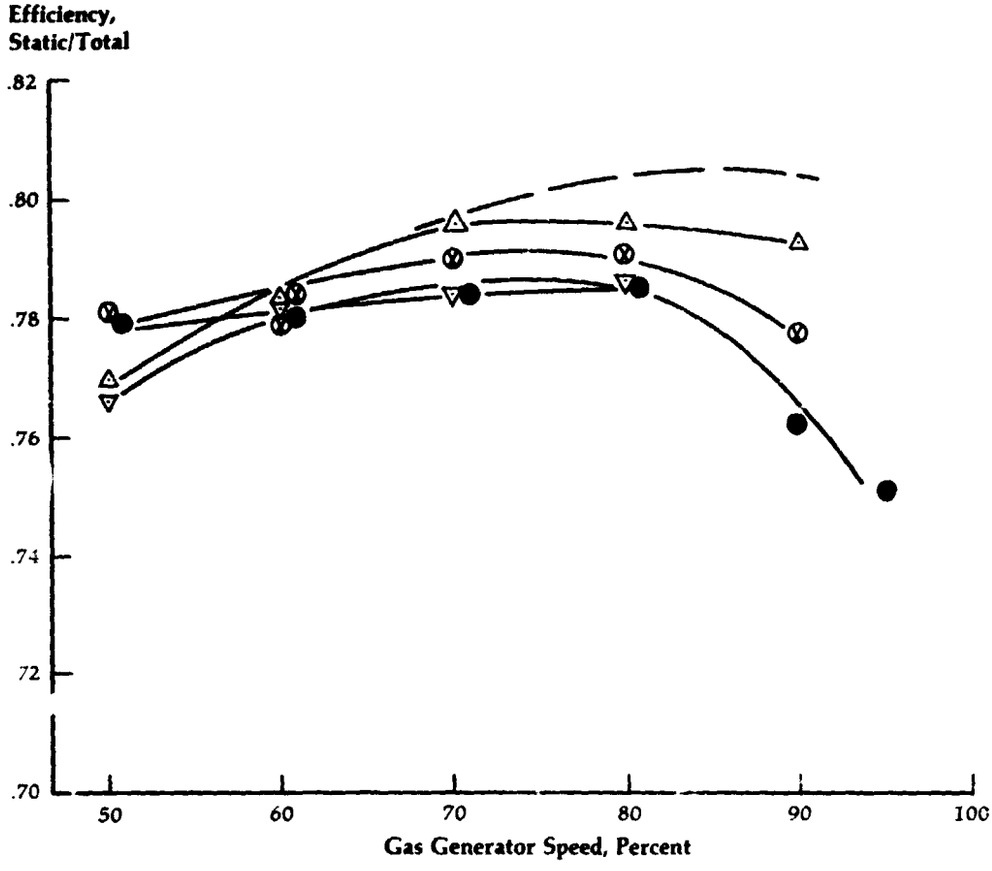

Figure 174

Upgraded Engine Compressor

Rig. Config: 24-Blade Impeller, 14 Channel Diffuser, Single Row Deswirl
Engine Config: 18-18 Impeller, 28 Channel Diffuser, Single Row Deswirl, VIGV Set 0°

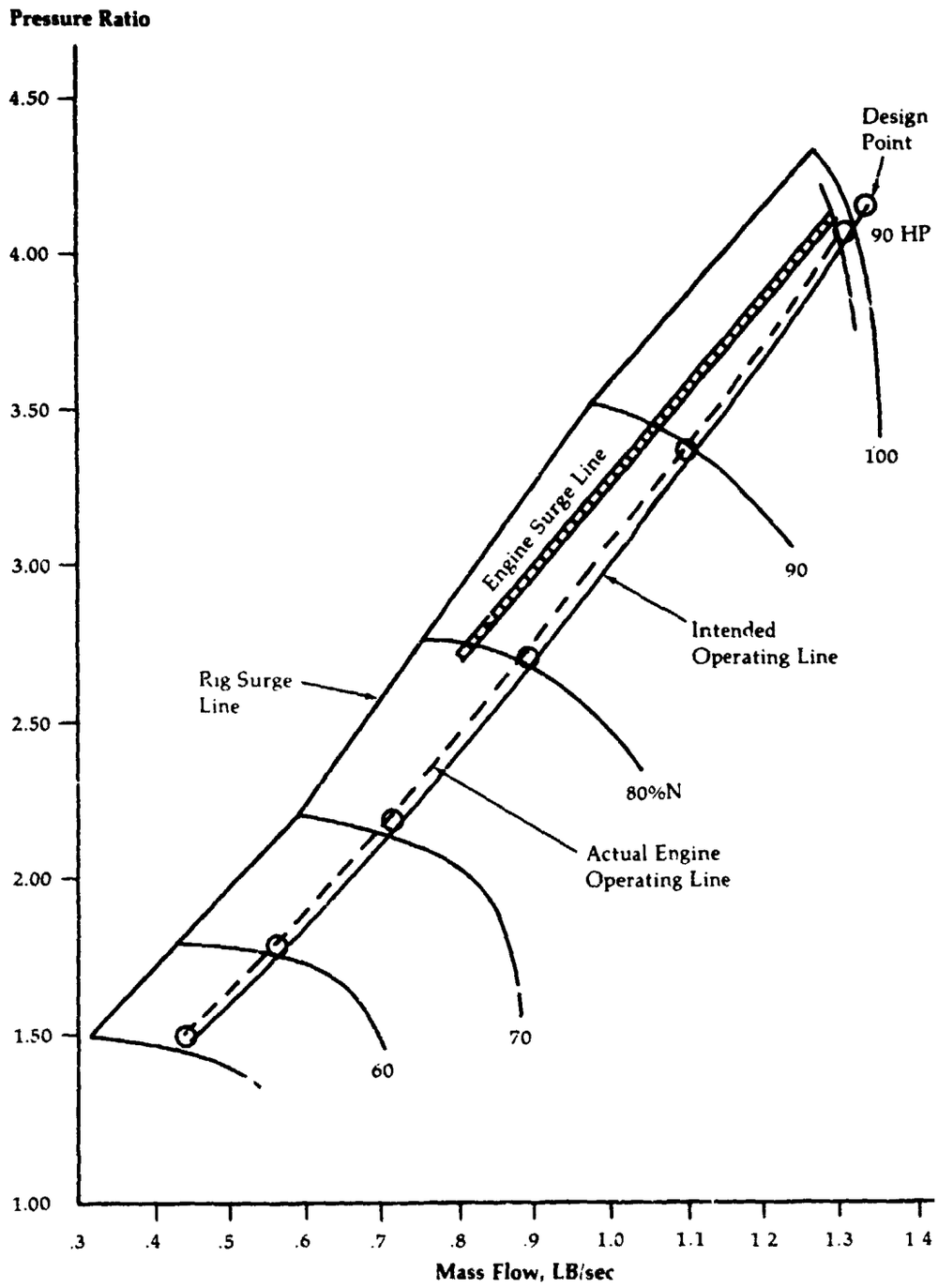

Figure 175

Upgraded Engine
Compressor
Turbine Nozzle

Comparison of Design Conditions with Measured Inlet Air Angle and Vorticity Computed at Design Flow From Measured Air Angle Distribution

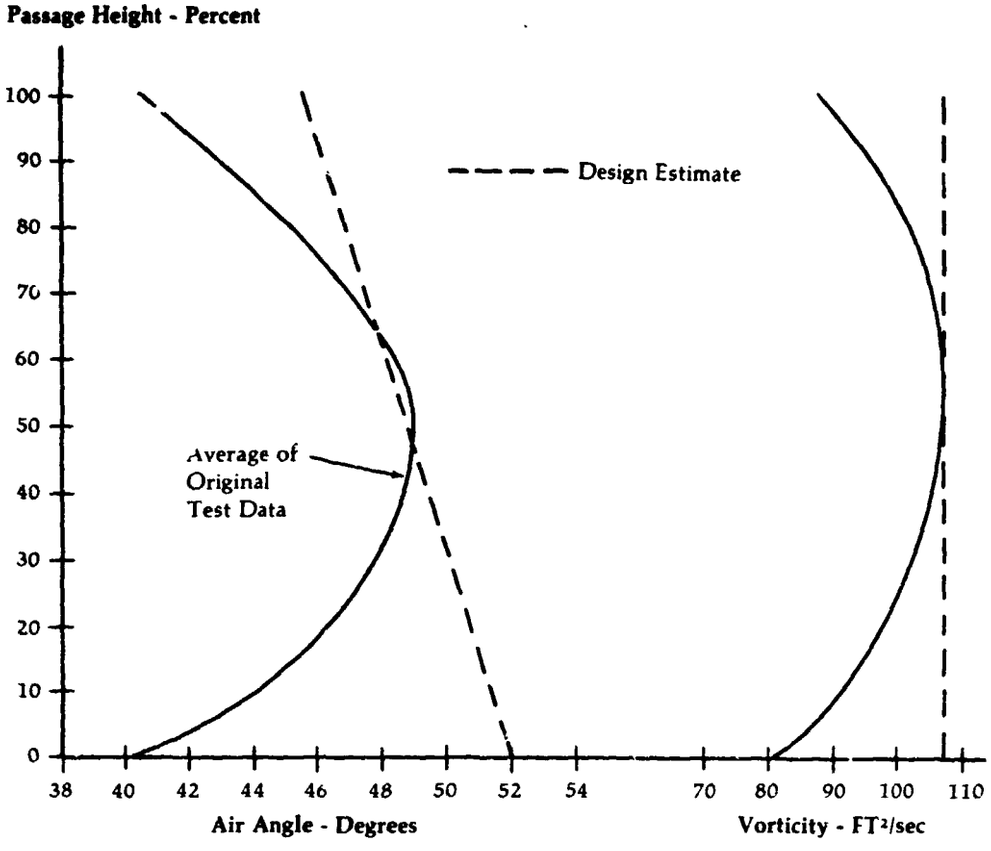

Figure 176

Upgraded Engine Compressor Turbine Nozzle Comparison of Design Estimates of Incidence Angle and Exit Air Angle with Test Results

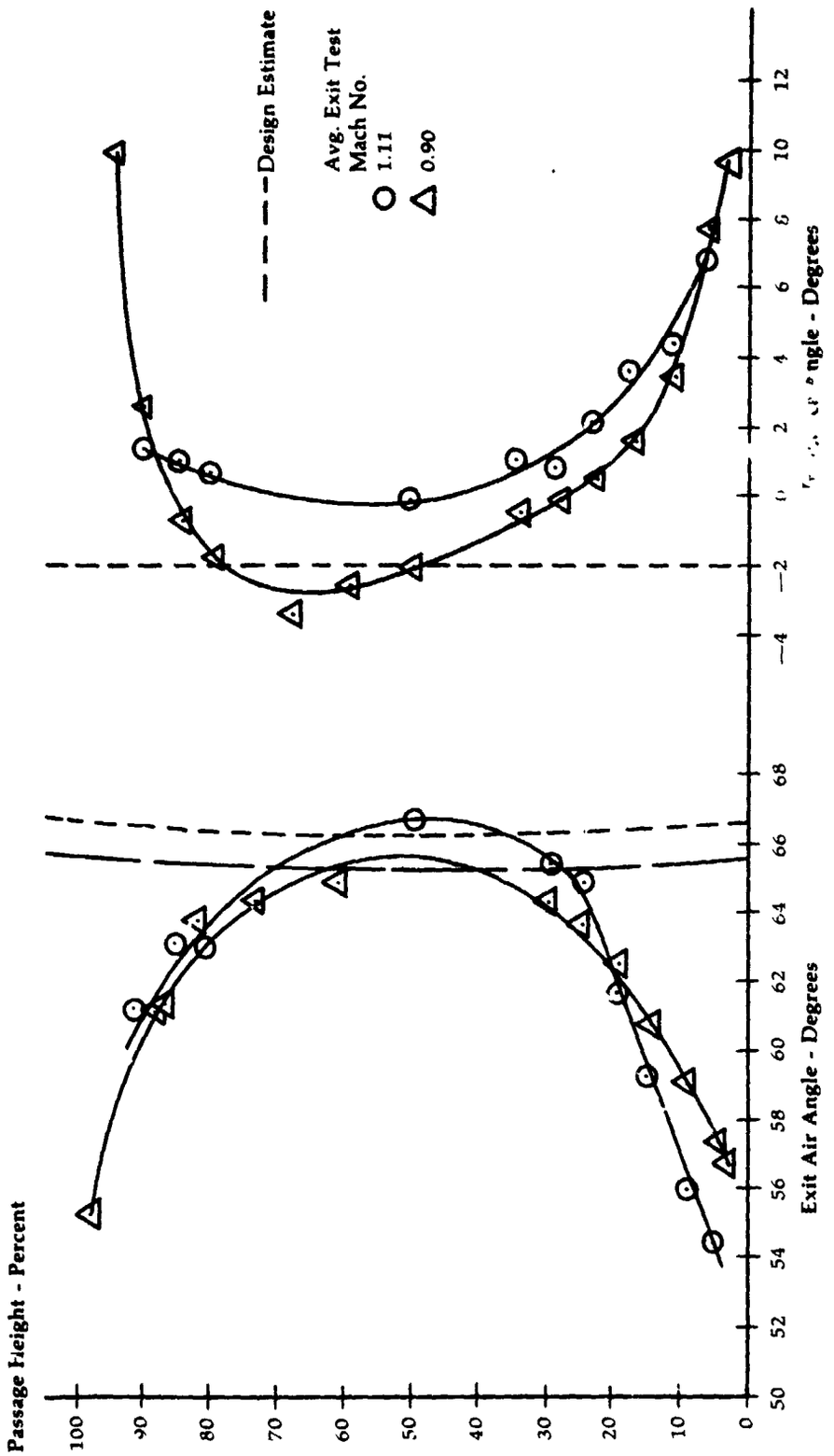

Figure 177

Upgraded Engine
Compressor
Turbine Nozzle
Turning Angle
Characteristics
Mean Camber = 18.5°

% Height from Hub

○	10	◺	60
□	20	▯	70
◇	30	▽	80
△	40	⌓	90
▽	50		

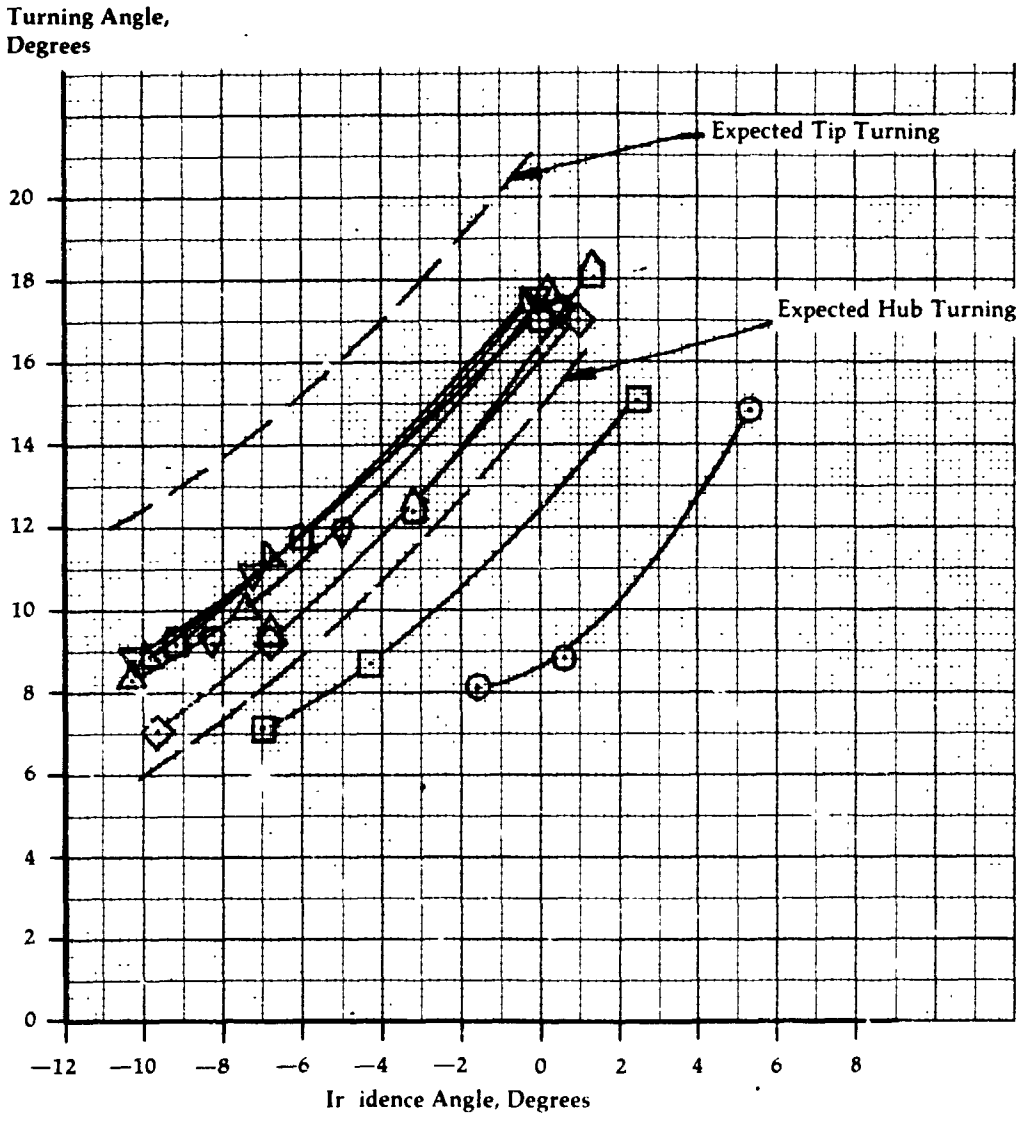

Figure 178

Upgraded Engine Variation of Measured "Mean-Radius" Efficiency with Gas Generator Speed for Various Engine Builds

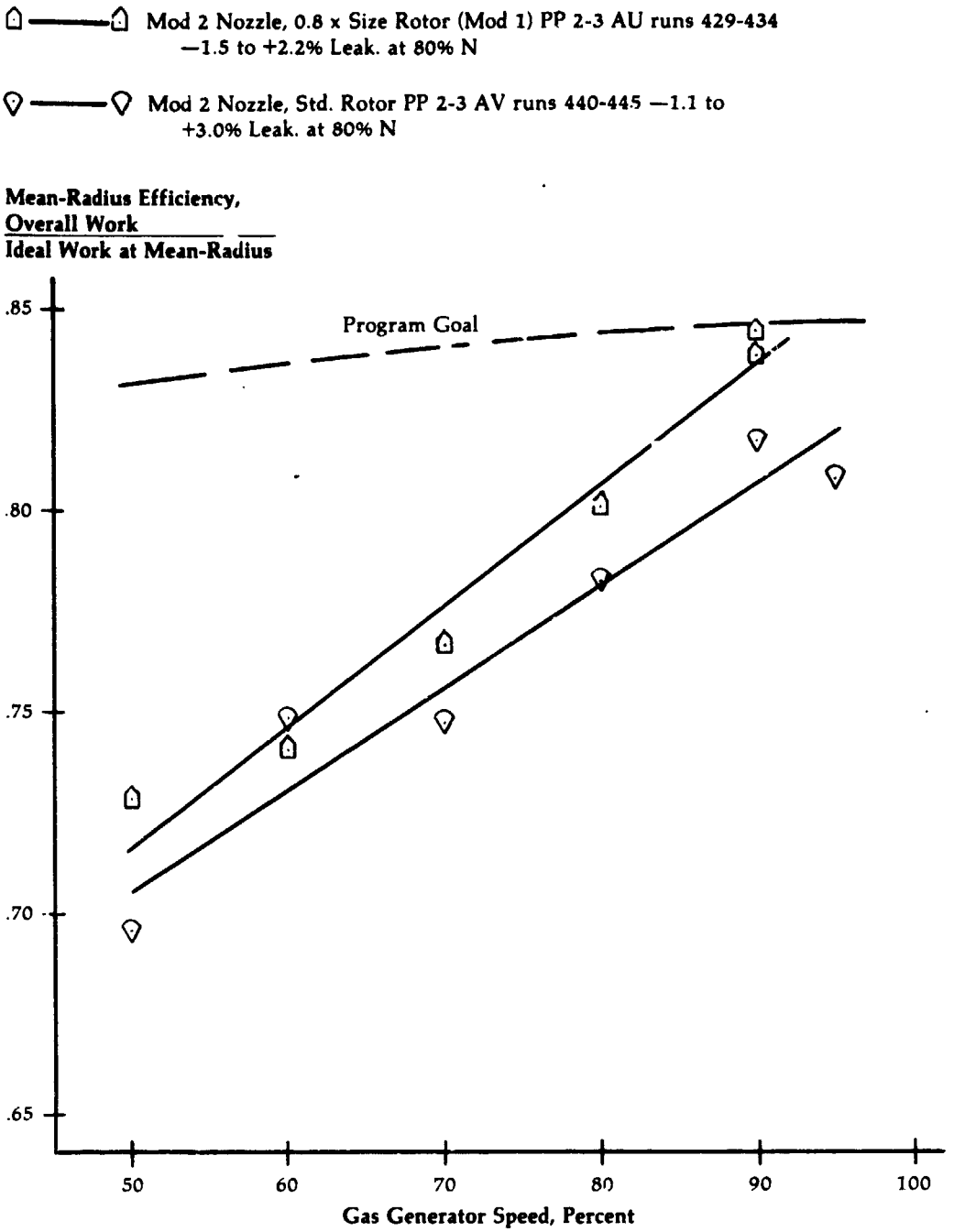

Figure 179

Upgraded Engine Variation of Measured "Mean-Radius" Efficiency with Gas Generator Speed for Various Engine Builds

Mod 1 Nozzle, Std. Rotor
PP 2-3 M runs 114-120
3.8% Leak. at 80% Ngg

Mod 1 Nozzle (Bent), Mod 1 Rotor
PP 2-3 U runs 165-173
2.8, 3.2% Leak. at 80% Ngg

Mod 1 Nozzle (Bent), Std. Rotor
PP 2-3 Q runs 125-132
4.2, 4.5% Leak. at 80% Ngg

Range of Test Rig Efficiency Assessment for Original Design

PP 2-3 Q runs 134-146
4.1, 3.7% Leak. at 80% Ngg

Range of Engine-Based Efficiency Assessment for Mod 3 Design

Std. Nozzle & Rotor
PP 2-3 S runs 157-160
3.1% Leak. at 80% Ngg

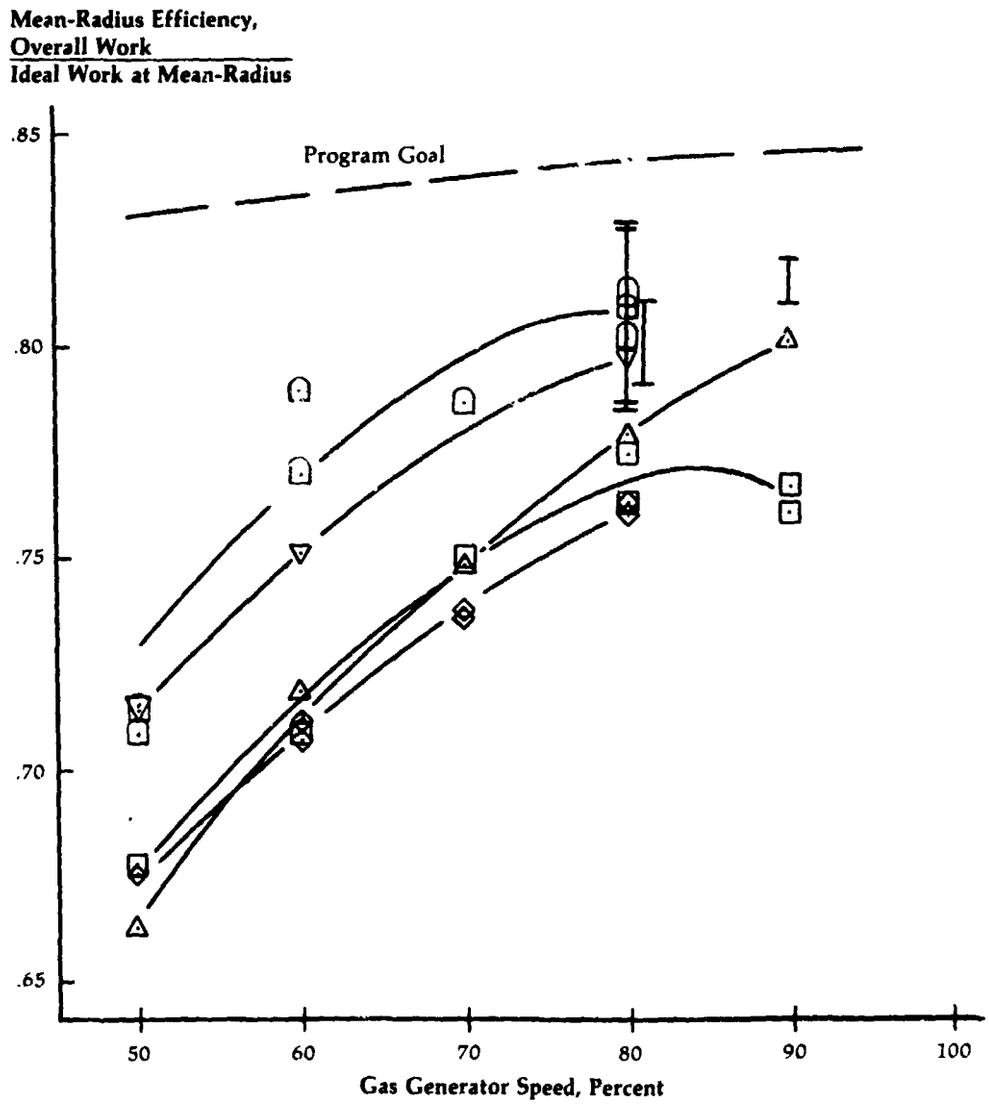

Figure 180

Upgraded Engine Mod 3 Compressor-Turbine

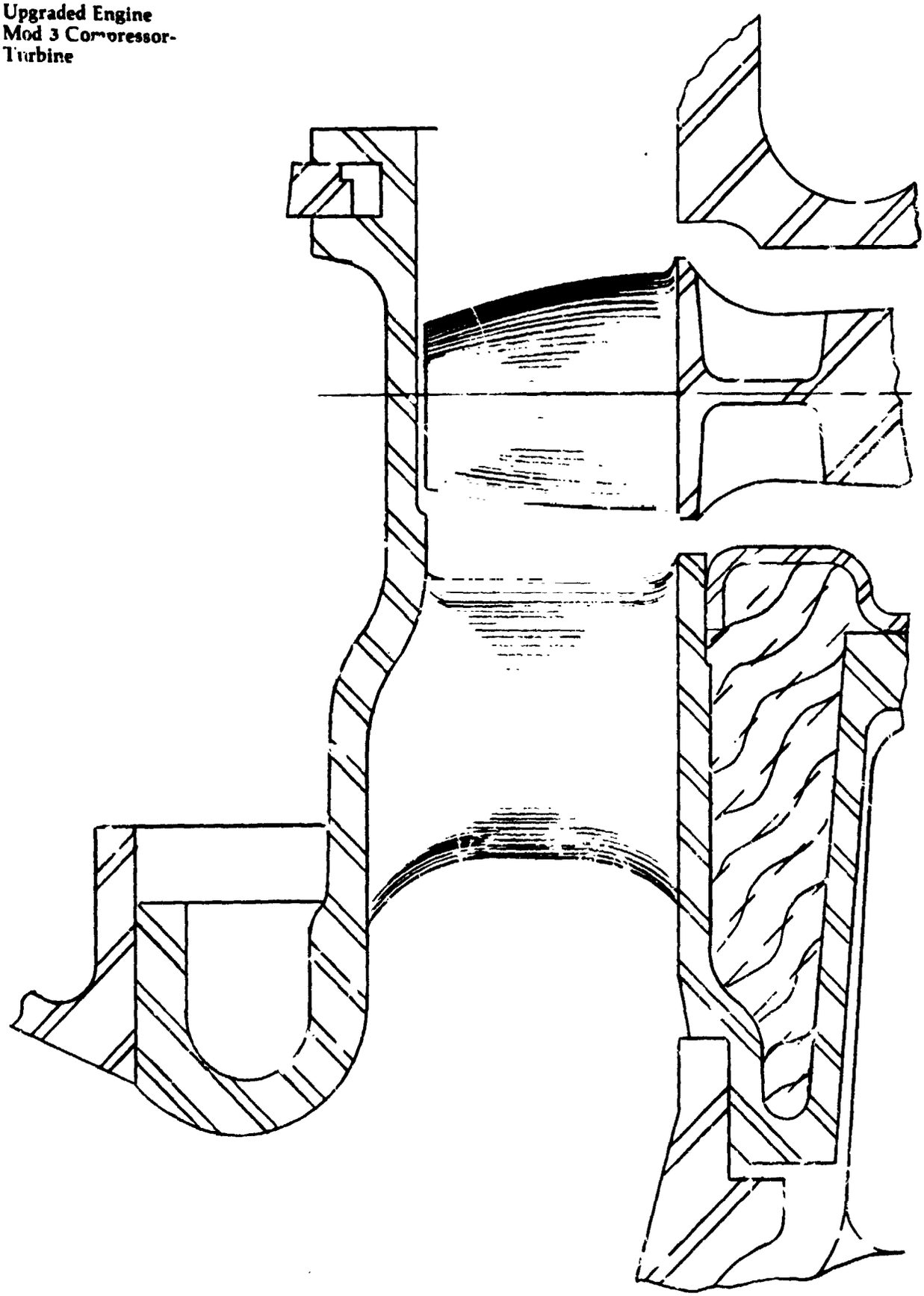

Figure 181

Compressor Turbine Rotor Blade-Shape and Channel Comparisons

Upgraded Engine

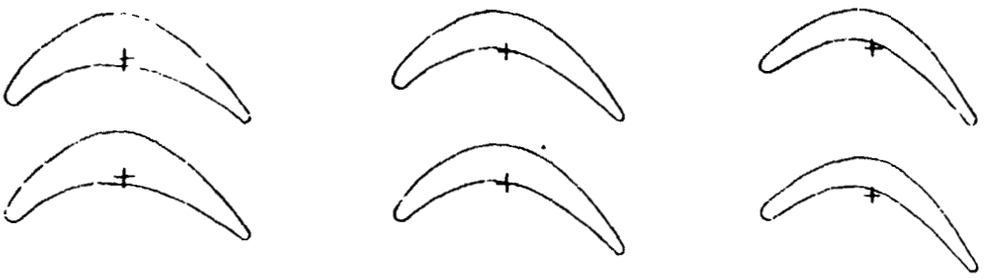

Scale of Baseline Engine (Mod 1)

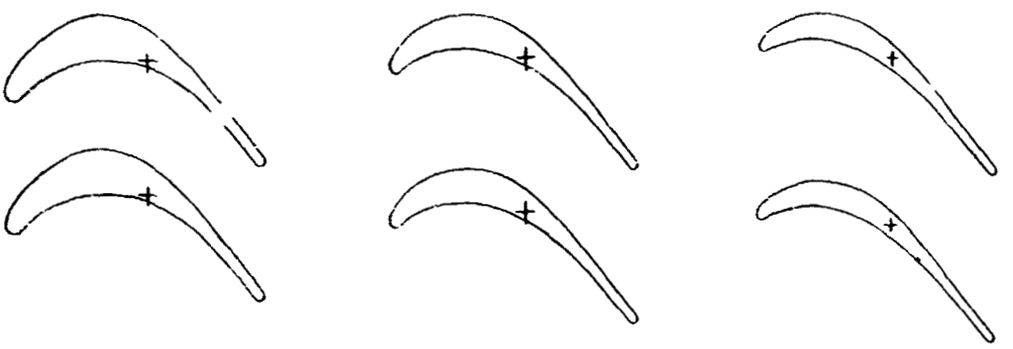

Upgraded Engine (Mod 3)

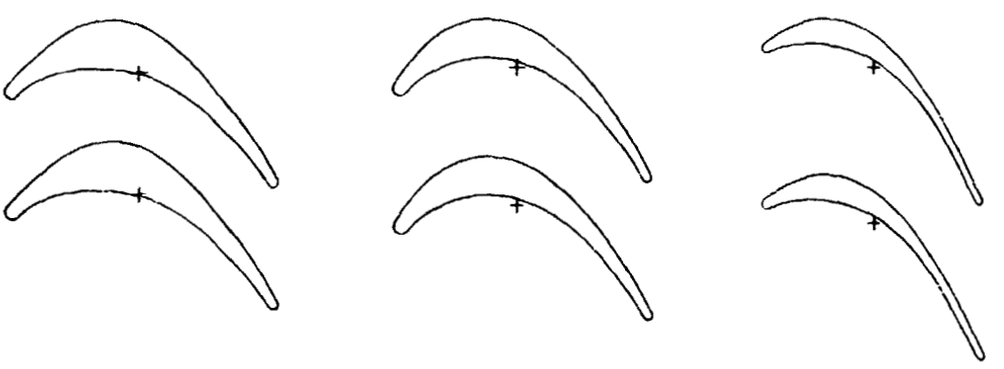

Hub **Mean** **Tip**

C-4

Figure 182A

Upgraded Engine Compressor-Turbine Comparison

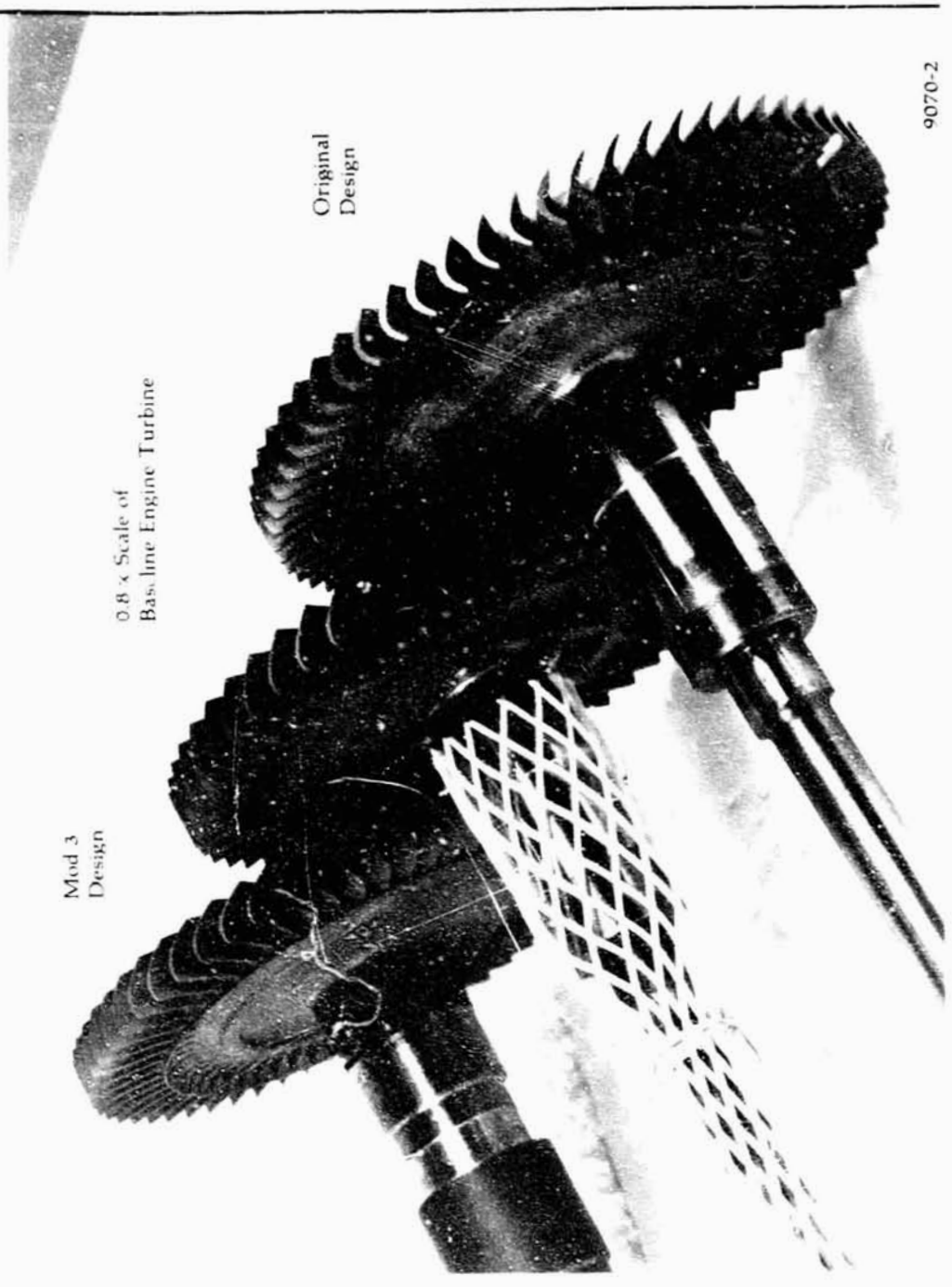

Figure 182B

Blade Profile Comparison Compressor-Turbine

Figure 183

Upgraded Engine Mod 3 Compressor-Turbine Redesign

Rotor Geometric Parameters for Hot Dimensions	Hub	Mean	Tip
Radius, cm	4.445	5.088	5.730
Pitch, cm, 61 Blades	0.458	0.524	0.590
*Chord, cm	1.085	1.058	1.035
*Axial Chord, cm	1.022	1.002	0.852
Solidity	2.369	2.019	1 754
Axial Solidity	2.233	1.913	1.444
Stagger Angle (Relative to Axial), Degrees	19.54	18.64	34.59
L.E. Pressure Surface Blade Angle, Degrees	44.0	46.0	26.0
L.E. Suction Surface Blade Angle, Degrees	50.0	57 2	29.5
L.E. Bisector Angle, Degrees	47.0	51.6	27.8
Incidence Angle, Degrees	-6.8	-6.1	-7.2
T.E. Pressure Surface Blade Angle, Degrees	55.0	58.3	65.1
T.E. Suction Surface Blade Angle, Degrees	61.0	61.3	65.1
L.E. Bisector Angle, Degrees	58.0	59.8	65.1
Deviation Angle, Degrees (Blocked Air Angle)	4.6	5.34	3.9
Unguided Turn After Throat, Degrees	7.97	9.64	9.09
L.E. Radius, cm	0.279	0.279	0 203
T.E. Radius, cm	0.203	0.191	0.152
Maximum Blade Thickness, cm	0.195	0.145	0 098
Profile Cross Sectional Area, cm^2	0.149	0.121	0.069
Throat, cm	0.217	0 259	0.259

Blade Number	61
Blade Height, cm	1.285
Aspect Ratio	1.215
Taper Ratio	2.16
Clearance, cm	0.02
Hub/Tip Ratio	0 776

*Chords Reference to Centers of L.E. and T.E. Radii.

Figure 184

Upgraded Engine Mod 3 Compressor-Turbine Redesign

Rotor Aerodynamic Parameters for Hot Dimensions

	Hub	Mean	Tip
Radius, cm	4.445	5.088	5.730
Reaction, Design Point			
Pressure-Based, %			
Blocked Rotor Exit Condition	31.2	41 7	48.6
Mixed-Out Rotor Exit Condition	27.1	38.5	47.8
Enthalpy-Based, %			
Blocked Rotor Exit Condition	41.7	59.7	59.4
Mixed-Out Rotor Exit Condition	28.6	49.6	55.9
Reaction, 50%-Speed Point			
Pressure-Based, %			
Blocked Rotor Exit Condition	9.6	26.6	38.8
Mixed-Out Rotor Exit Condition	3.7	22.4	38.6
Enthalpy-Based, %			
Blocked Rotor Exit Condition	-6.0	24.1	33.6
Mixed-Out Rotor Exit Condition	-14.1	17.5	33.1
Aerodynamic Loading Coefficient (61 Blades)			
100% Speed			
Blocked Rotor Exit Condition	0.639	0.681	0 652
Mixed-Out Rotor Exit Condition	0.561	0.615	0.608
50% Speed			
Blocked Rotor Exit Condition	0.779	0.822	0.753
Mixed-Out Rotor Exit Condition	0.676	0.752	0.742

Design Work = 199780 J/kg
Work Coefficient, $\Delta H/U^2_m = 2.06$
Velocity Ratio = 0.493

Upgraded Engine Enlarged Vortex Chamber- Plastic Flow Visualization Model

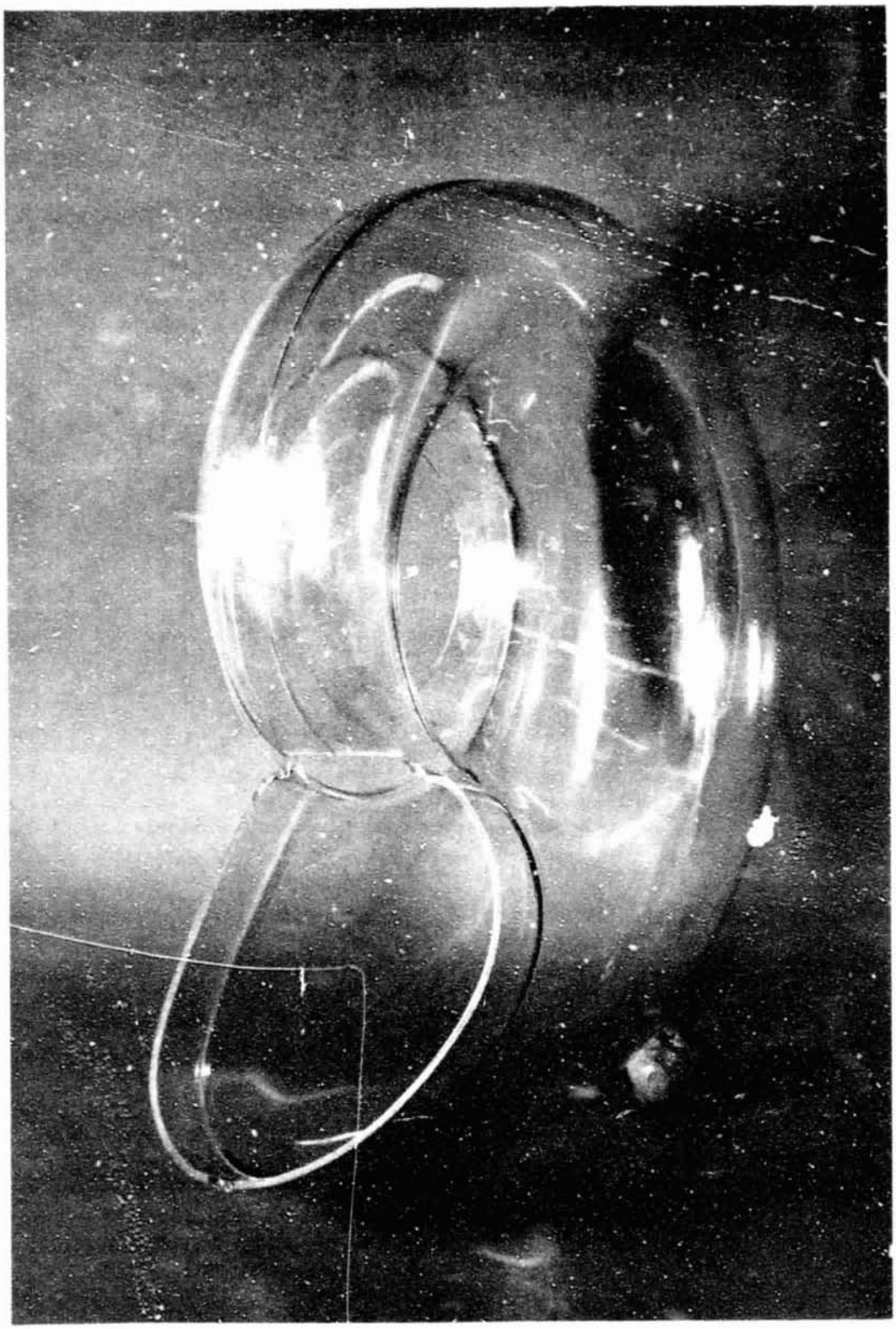

Figure 186

Upgraded Engine
Compressor
Turbine Nozzle
Mod 3 Design

Meridional View

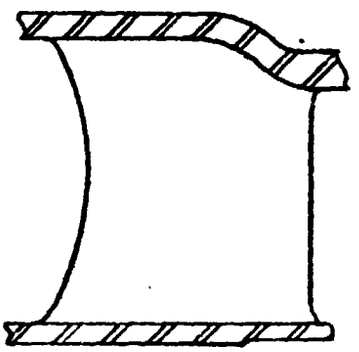

Front View

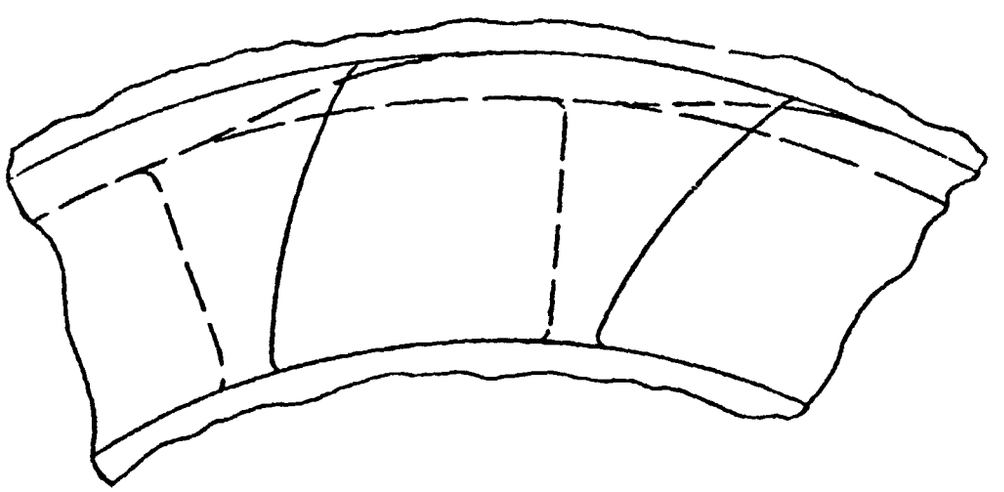

Figure 187

Upgraded Engine
Compressor
Turbine Nozzle
Revised Design-
Mod 3

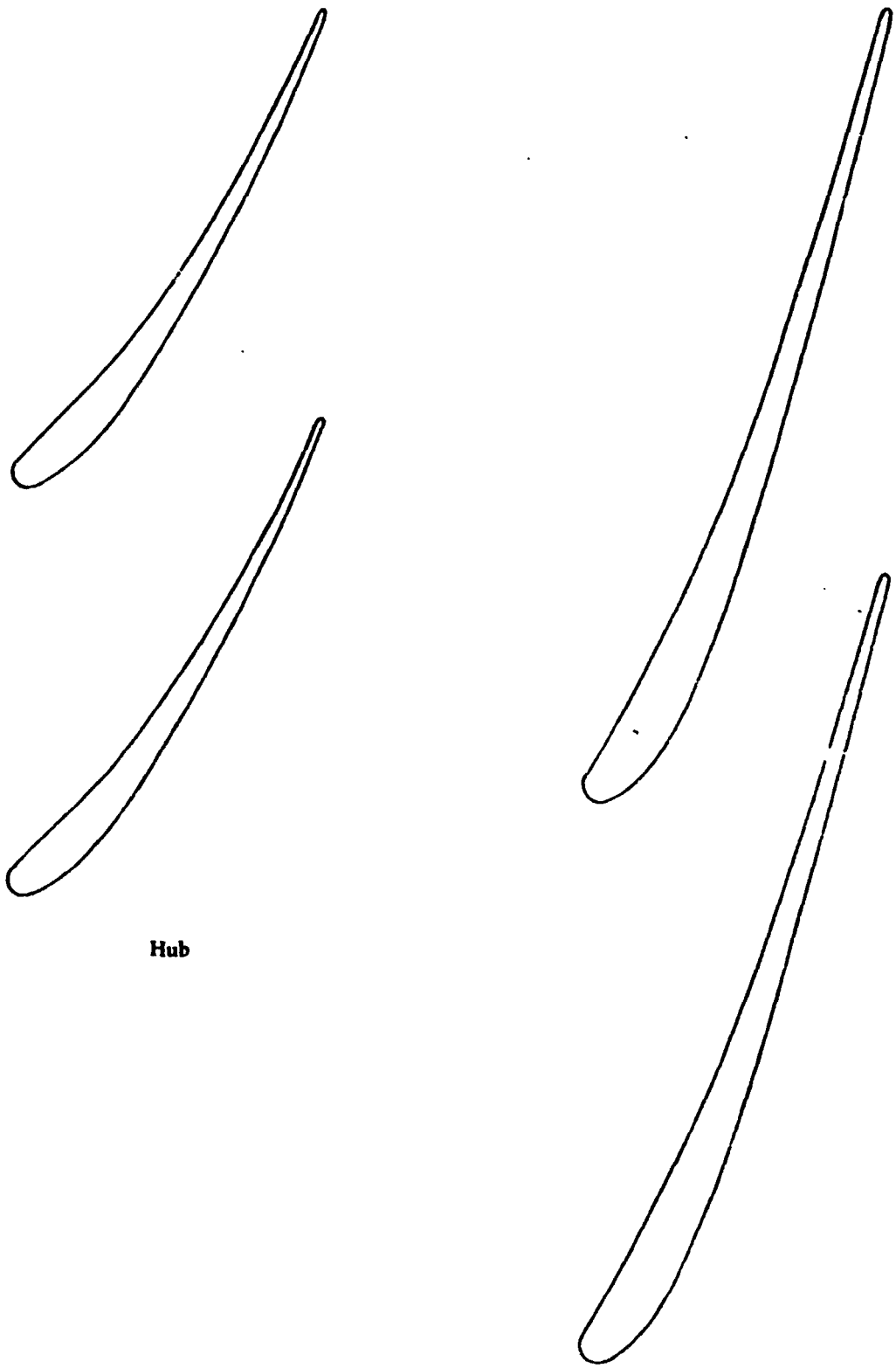

Figure 188

Upgraded Engine Mod 3 Compressor-Turbine Redesign

Nozzle Geometric Parameters for Hot Dimensions

	Hub	Mean	Tip
Exit Radius, cm	4.445	5.107	5.730
Pitch, cm, 15 Vanes	1.862	2.139	2.400
*Chord, cm	2.591	3.023	3.810
*Axial Chord, cm	1.449	1.269	1.506
Solidity	1.391	1.413	1.587
Axial Solidity	0.778	0.593	0.627
Stagger Angle (Relative to Axial), Degrees	56.0	65.2	66.7
L.E. Pressure Surface Vane Angle, Degrees	56.3	68.2	59.0
L.E. Suction Surface Vane Angle, Degrees	2.0	21.8	18.4
L.E. Bisector Angle, Degrees	29.2	45.0	38.7
Incidence Angle, Degrees	-11.2	-4.1	-17.2
T.E. Pressure Surface Vane Angle, Degrees	63.4	71.6	71.6
T.E. Suction Surface Vane Angle, Degrees	65.2	71.6	74.7
T.E. Bisector Angle, Degrees	64.3	71.6	73.2
Deviation Angle, Degrees (Blocked Air Angle)	3.6	1.6	10.0
Unguided Turn After Throat, Degrees	6.8	6.5	4.8
L.E. Radius, cm	0.06	0.05	0.09
T.E. Radius, cm	0.02	0.02	0.02
Aeroloading Coefficient, 100% Speed	0.844	0.791	0.933
Aeroloading Coefficient, 50% Speed	0.812	0.739	0.856

Vane Number 15

Aspect Ratio 0.48

(Based on Arithmetic Average Height and Mean-Radius True Chord)

*Chords Referenced to Camber Line Points at L.E. and T.E.

Figure 189

Upgraded Engine Mod 3 Compressor-Turbine 100% Speed Vector Diagrams

Tip

R = 5.994 cm (Stator in)

R = 5.730 cm (Rotor)

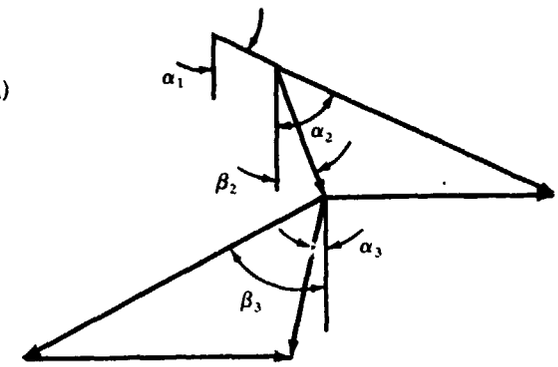

α_1 = 58.3 M_1 = 0.17
α_2 = 66.1 M_2 = 0.67
β_2 = 20.6 M_{2R} = 0.29
α_3 = -22.4 M_3 = 0.35
β_3 = -64.0 M_{3R} = 0.74
U = 351

Mean

R = 5.131 cm

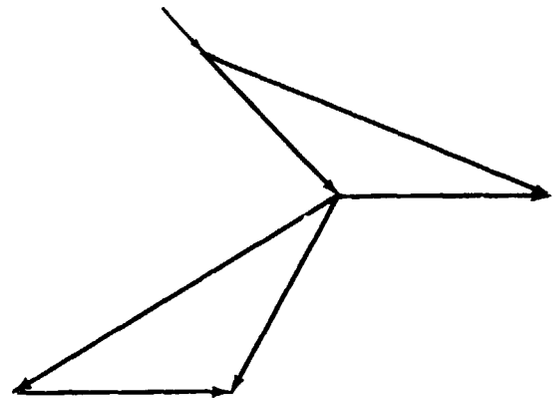

α_1 = 48.4 M_1 = 0.26
α_2 = 68.6 M_2 = 0.83
β_2 = 45.7 M_{2R} = 0.43
α_3 = -30.9 M_3 = 0.48
β_3 = -60.6 M_{3R} = 0.84
U = 314

Hub

R = 4.445 cm

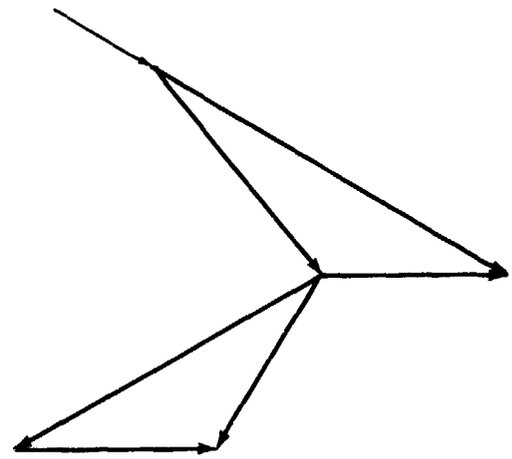

α_1 = 40.8 M_1 = 0.26
α_2 = 60.6 M_2 = 0.90
β_2 = 40.3 M_{2R} = 0.58
α_3 = -35.3 M_3 = 0.45
β_3 = -61.4 M_{3R} = 0.77
U = 272

Symbol

α — Absolute Angle, Degree
β — Relative Angle, Degree
U — Rotor Speed, m/s

Subscript

1 — Nozzle Inlet
2 — Rotor Inlet
3 — Rotor Exit
R — Relative

Figure 190

Upgraded Engine Mod 3 Compressor-Turbine 50% Speed Vector Diagrams

Tip

R = 5.994 cm (Stator in)

R = 5.730 cm (Rotor)

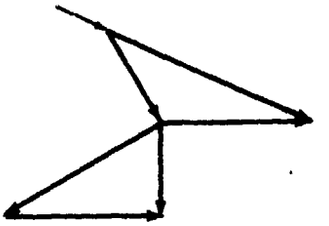

$\alpha_1 = 58.9$ $M_1 = 0.10$
$\alpha_2 = 67.2$ $M_2 = 0.40$
$\beta_2 = 31.1$ $M_{2R} = 0.18$
$\alpha_3 = -1.6$ $M_3 = 0.15$
$\beta_3 = -61.8$ $M_{3R} = 0.32$
$U = 175$

Mean

R = 5.131 cm

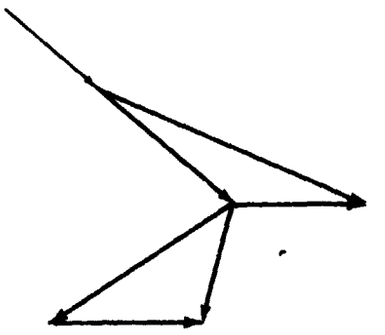

$\alpha_1 = 48.6$ $M_1 = 0.21$
$\alpha_2 = 68.5$ $M_2 = 0.52$
$\beta_2 = 51.4$ $M_{2R} = 0.31$
$\alpha_3 = -22.1$ $M_3 = 0.21$
$\beta_3 = -59.6$ $M_{3R} = 0.38$
$U = 157$

Hub

R = 4.445 cm

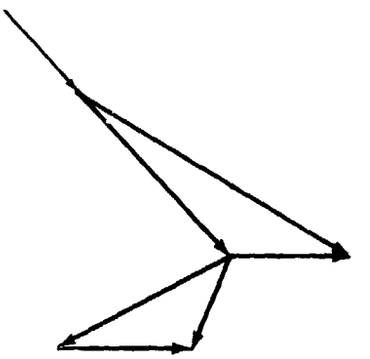

$\alpha_1 = 41.2$ $M_1 = 0.20$
$\alpha_2 = 60.4$ $M_2 = 0.55$
$\beta_2 = 44.1$ $M_{2R} = 0.38$
$\alpha_3 = -25.9$ $M_3 = 0.17$
$\beta_3 = -62.0$ $M_{3R} = 0.33$
$U = 136$

Symbol

α — Absolute Angle, Degree
β — Relative Angle, Degree
U — Rotor Speed, m/s

Subscript

1 — Nozzle Inlet
2 — Rotor Inlet
3 — Rotor Exit
R — Relative

Figure 191

Variation of Design-Point and Near-Design Efficiency Values with Work Coefficient for Small High-Work Axial Turbines

Design Press. Ratio				
Tot-Stat	Tot-Tot			Blade Ht., In.
	2.5	△	Chrysler High Press. Comp. Turbine	0.59
	2.0, 3.4	⊙	P&WA, ASME Paper 73-GT-3	0.52, 0.65, 0.57
	2.9	⊡	CAE, SAE Paper 680448	0.62, 0.72, 1.09
	3.2	◇	AiResearch, ASME Paper 75-GT-7	~ 0.62
	3.9	▽	P&WC, ASME Paper 74-GT-81	1.14
3.5		◺	M.I T., ASME Paper 62-WA-38	0.25
	2.1	⌂	Chrysler Baseline Comp. Turbine	0.59
			⌂ Chrys. Data; ⌀ NASA Data	
	2.8	▽	NASA TND-7881	1.0

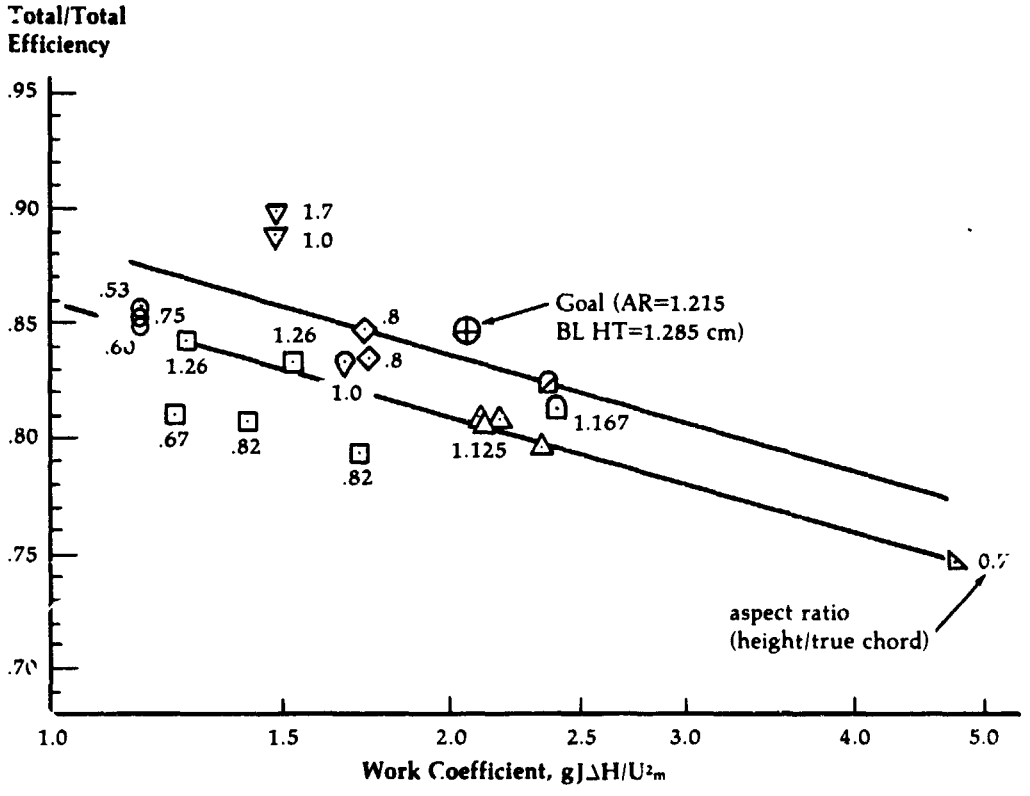

ΔH measured work, BTU/LB
U_m mean rotor speed, ft/sec

Figure 192

Upgraded Engine Power Turbine Performance Characteristics at 80% Gas Generator Speed

Comparison of Program Goal and Measured Engine Performance with Power Breakdown Based on Component Performance Computed from Test Data

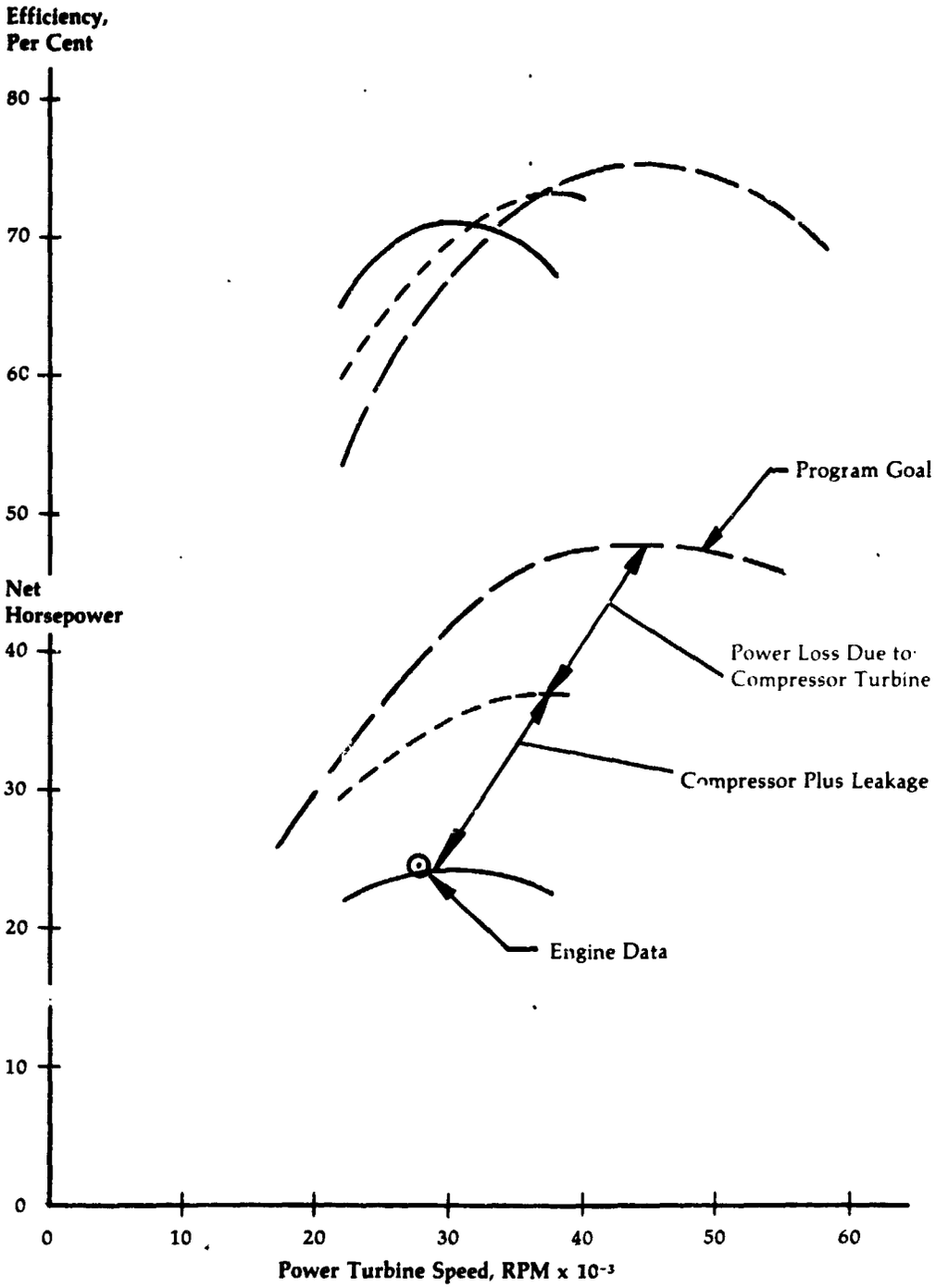

Figure 193

Upgraded Engine Power Turbine Performance 80% Gas Generator Speed

PP 3-1

△ runs 93-98 avg. Pt_6

⊙ runs 135, 140, 151-153 avg. Pt_6

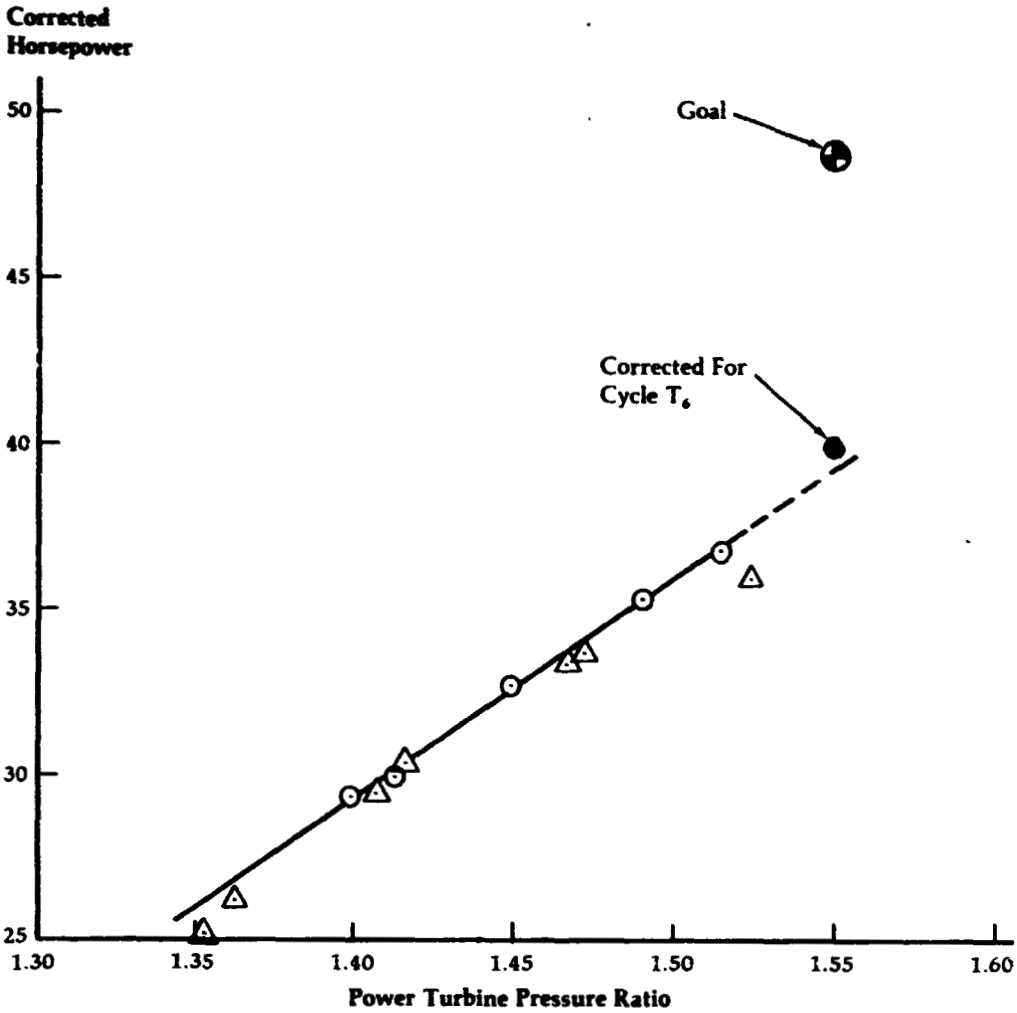

Figure 194

Cross Section of Regenerative Power Turbine Test Rig

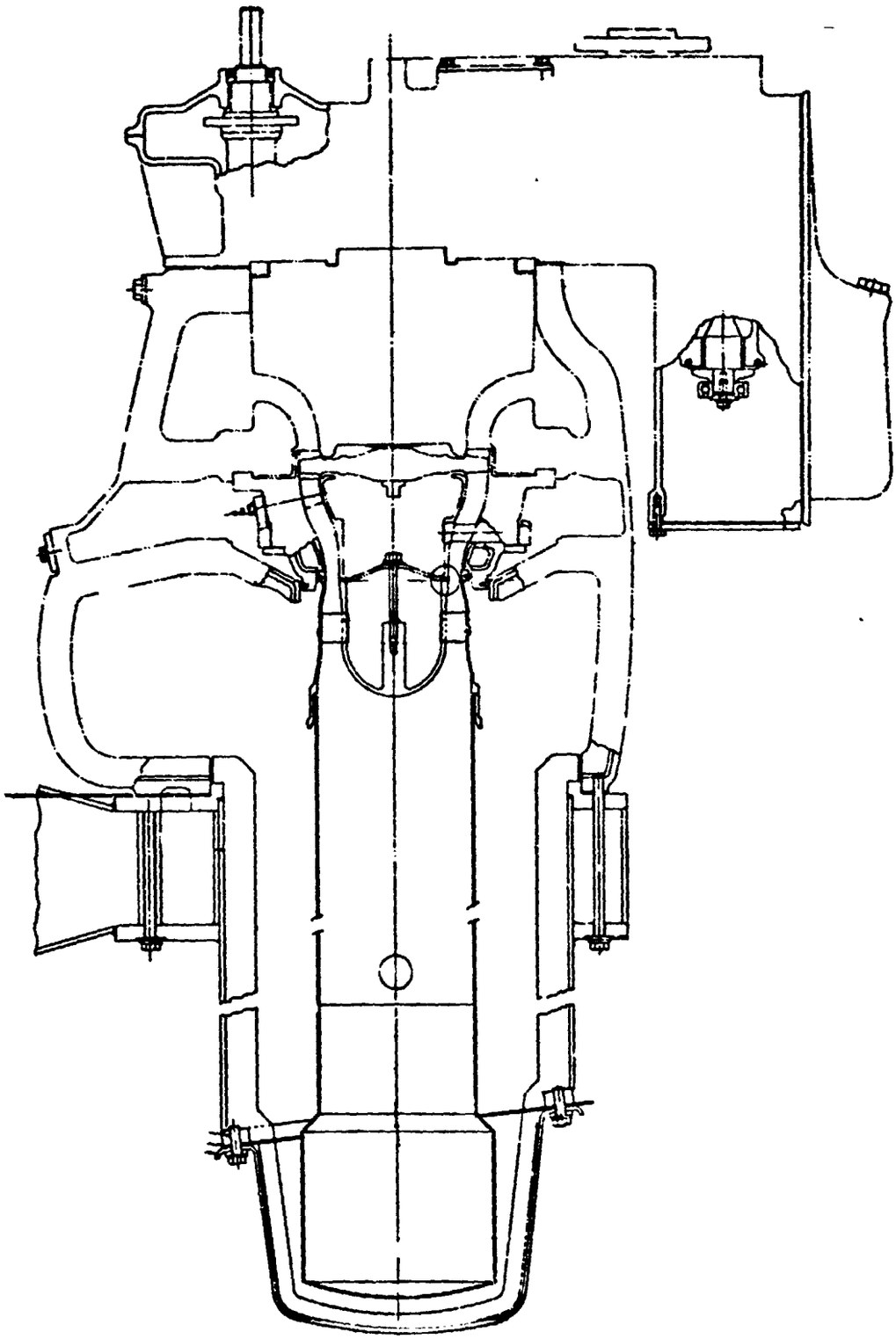

Figure 195

Upgraded Engine Power Turbine Performance Engine vs. Design Inlet Conditions at 80% Speed

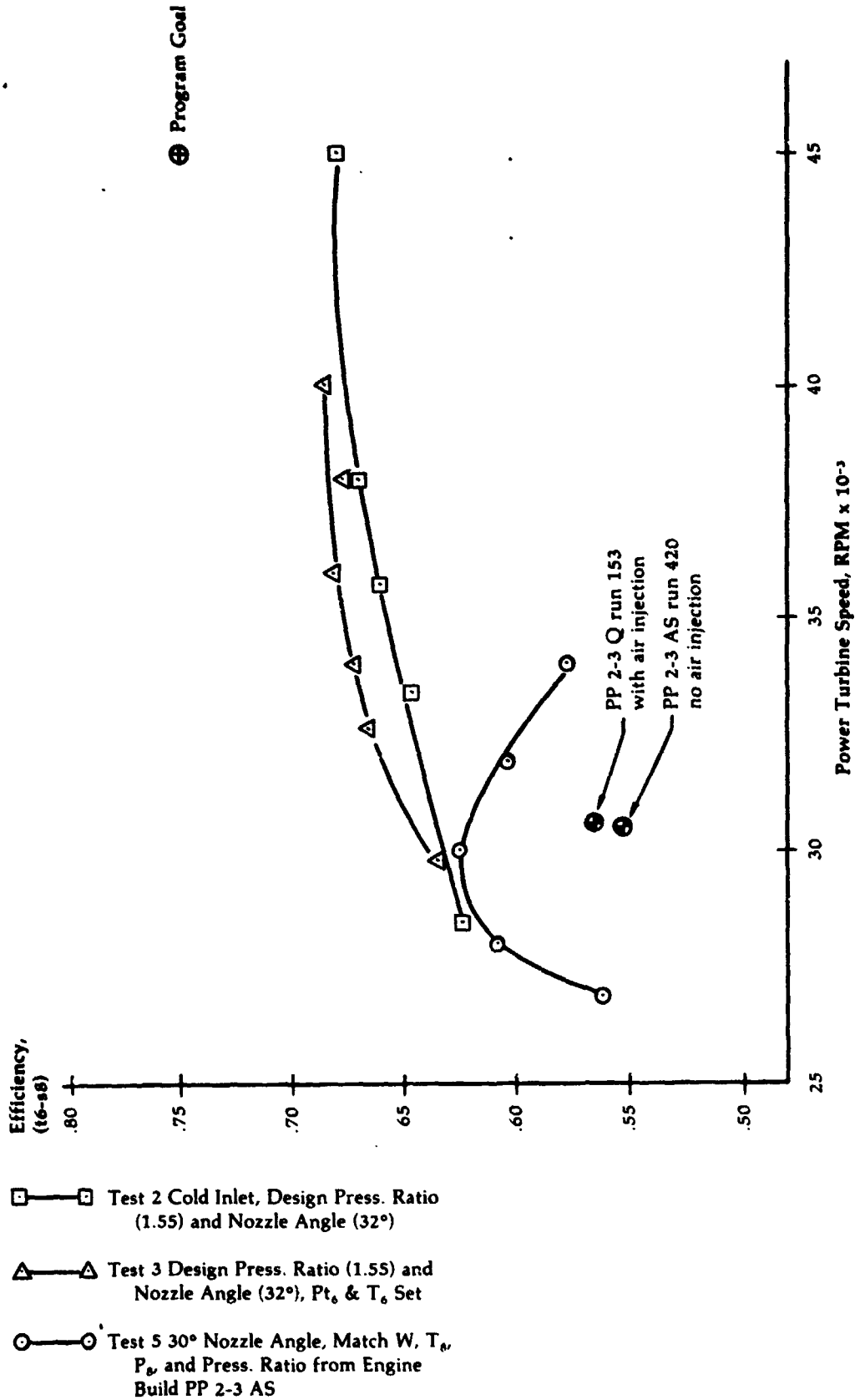

Figure 196

**Power Turbine Rig
Flow Path
Showing Location
of Probes**

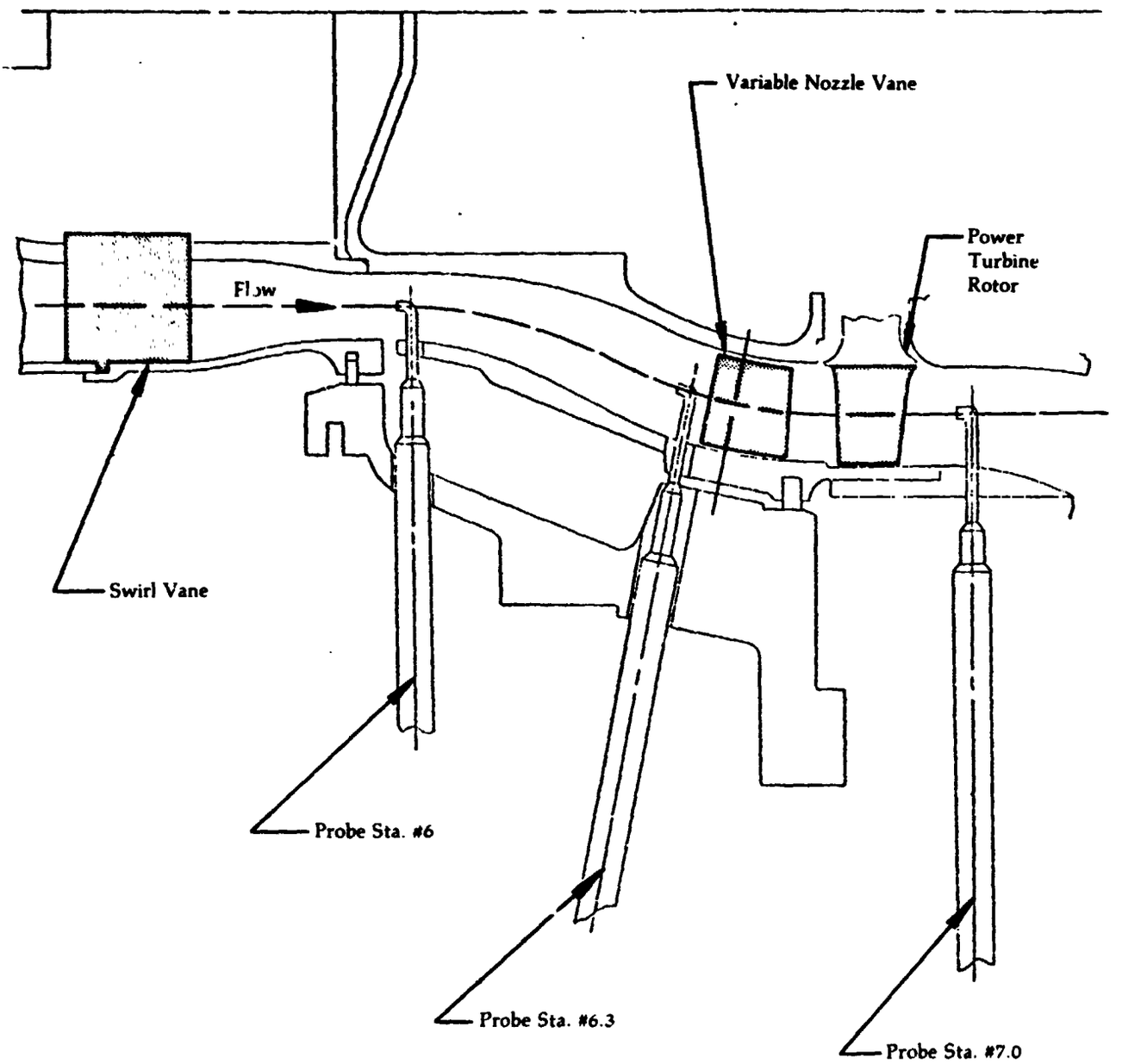

Figure 197

Flow Angle at 80% Ngg Equivalent Nozzle Inlet Station

	Nozzle Angle	Pt6/Ps8
○—○	28°	1.481
□—□	32°	1.52
△—△	34°	1.52

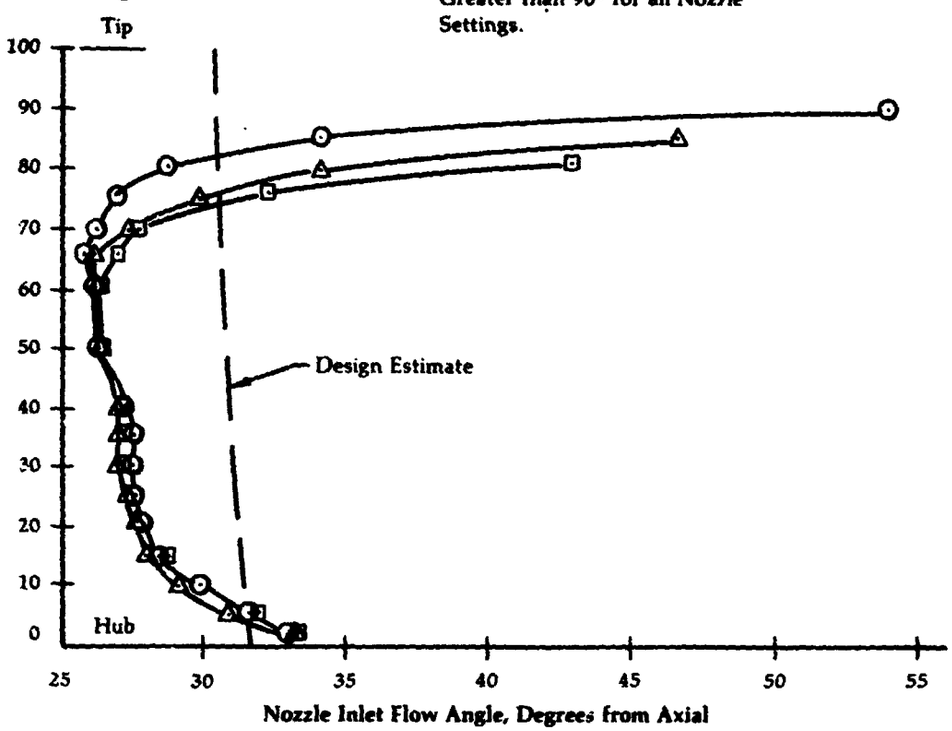

Figure 198

Power Turbine Exit Relative Flow Angle 80% Ngg Equivalent

	Nozzle Angle	Pt_6/Pt_7
○—○	28°	1.457
□—□	32°	1.437
△—△	34°	1.438

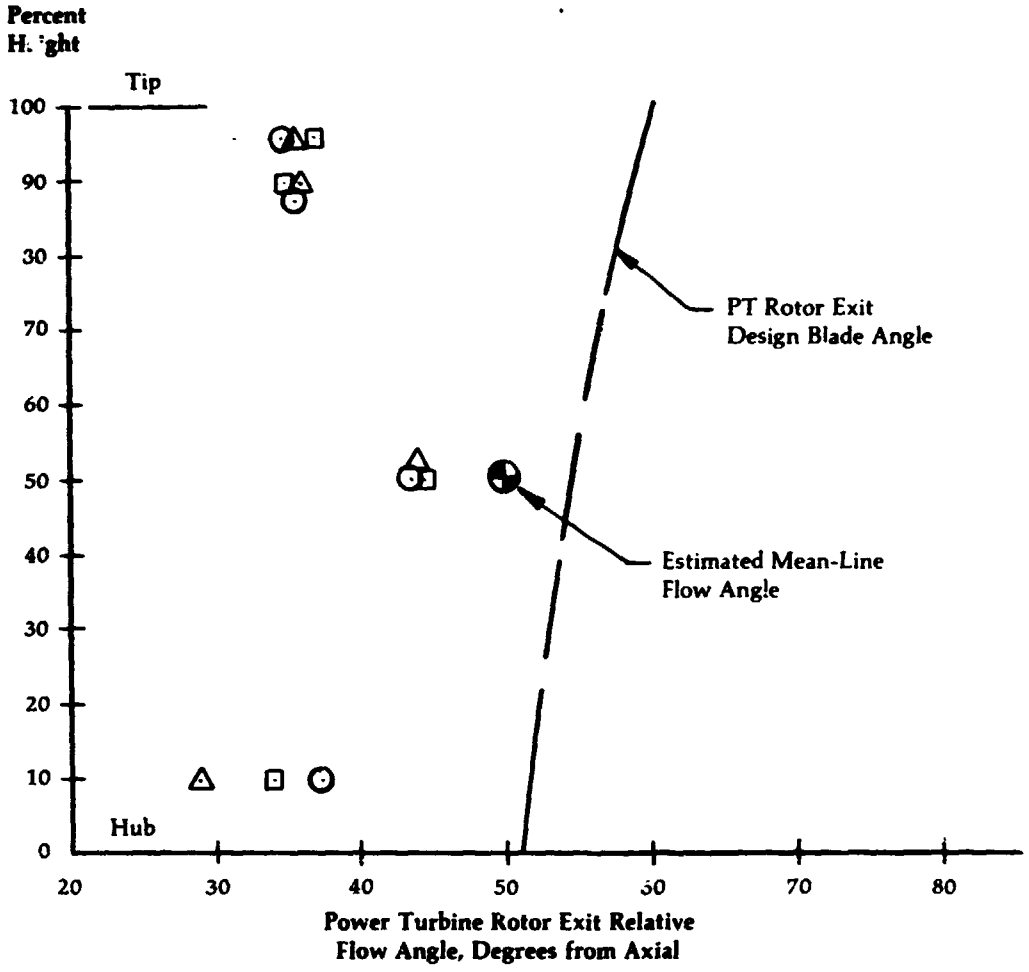

Figure 199

Upgraded Engine Power Turbine Performance Efficiency vs. Hub Reaction

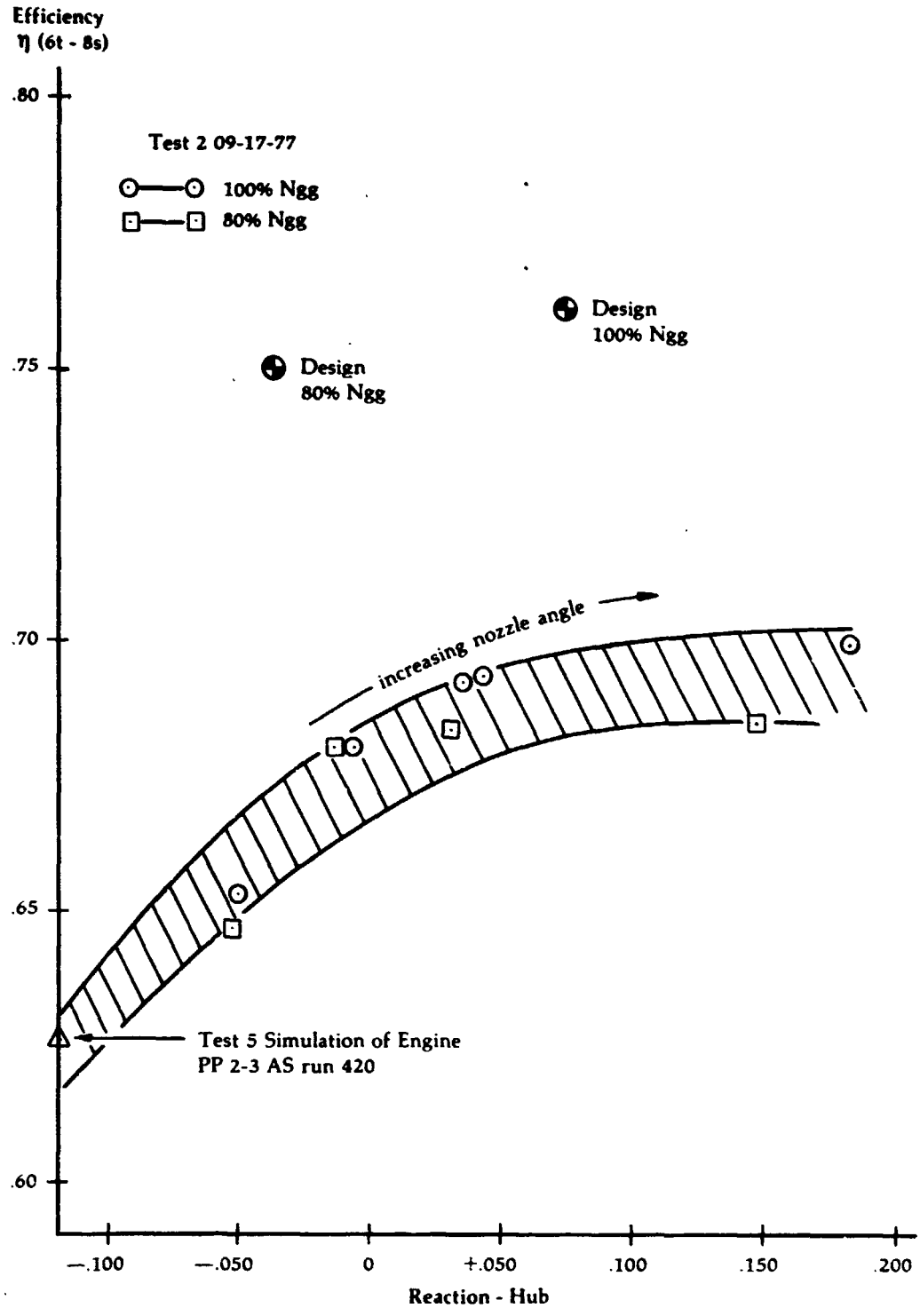

Figure 200

Upgraded Engine Power Turbine Rotor Blade Shape and Channel Comparisons

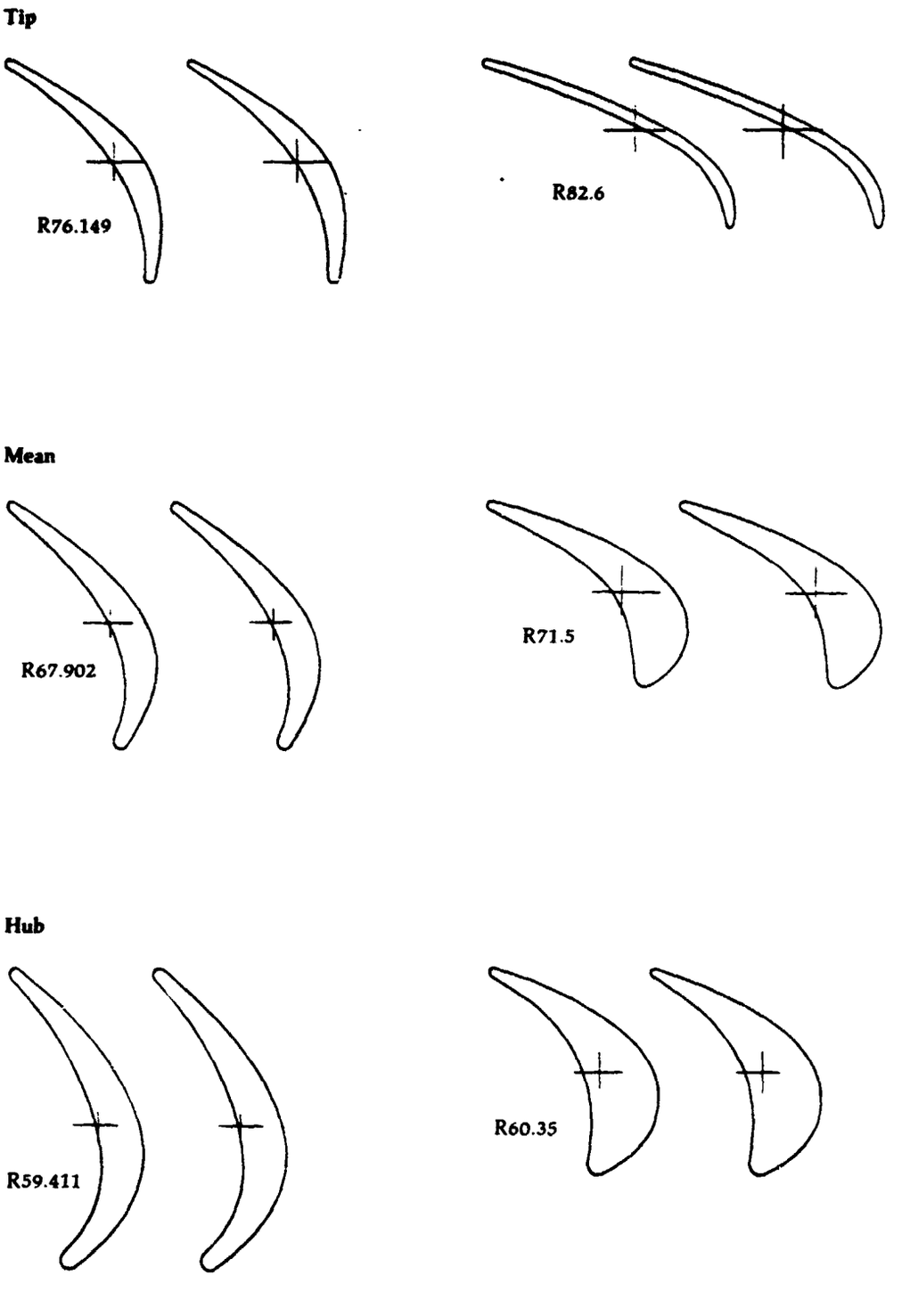

Figure 201A

Upgraded Engine Power Turbine Comparison

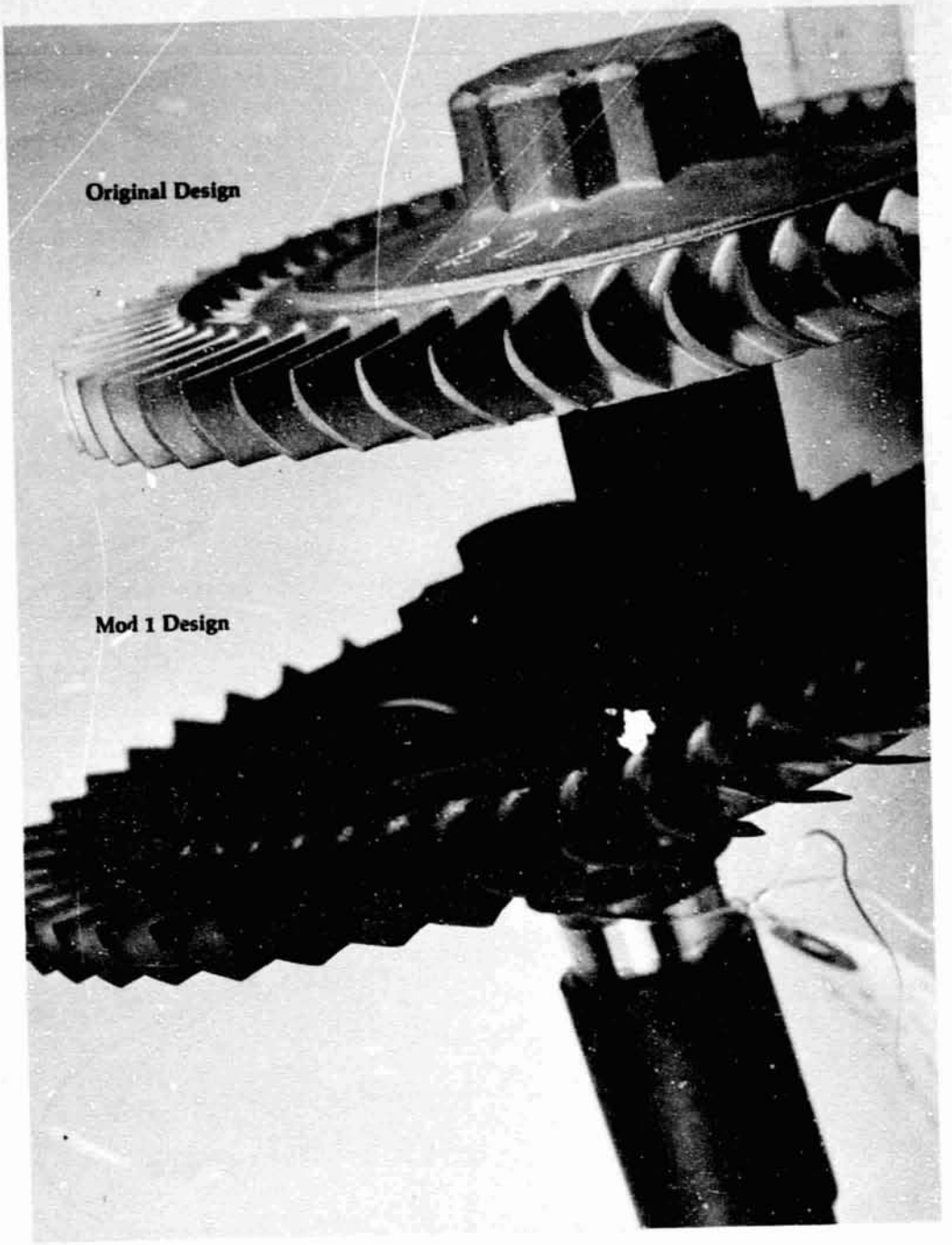

Figure 201B

Upgraded Engine
Power Turbine
Nozzle
Revised Design
23 Vanes

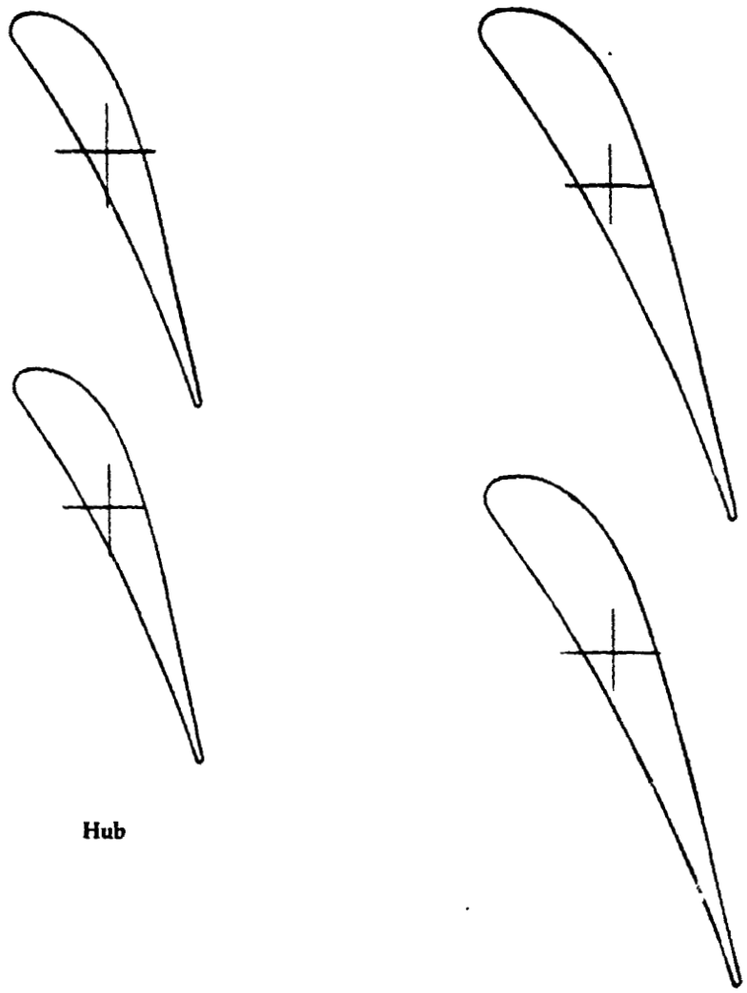

Hub

Tip

Figure 202

Upgraded Engine Flowpath of Revised compressor Turbine and Power Turbine Designs

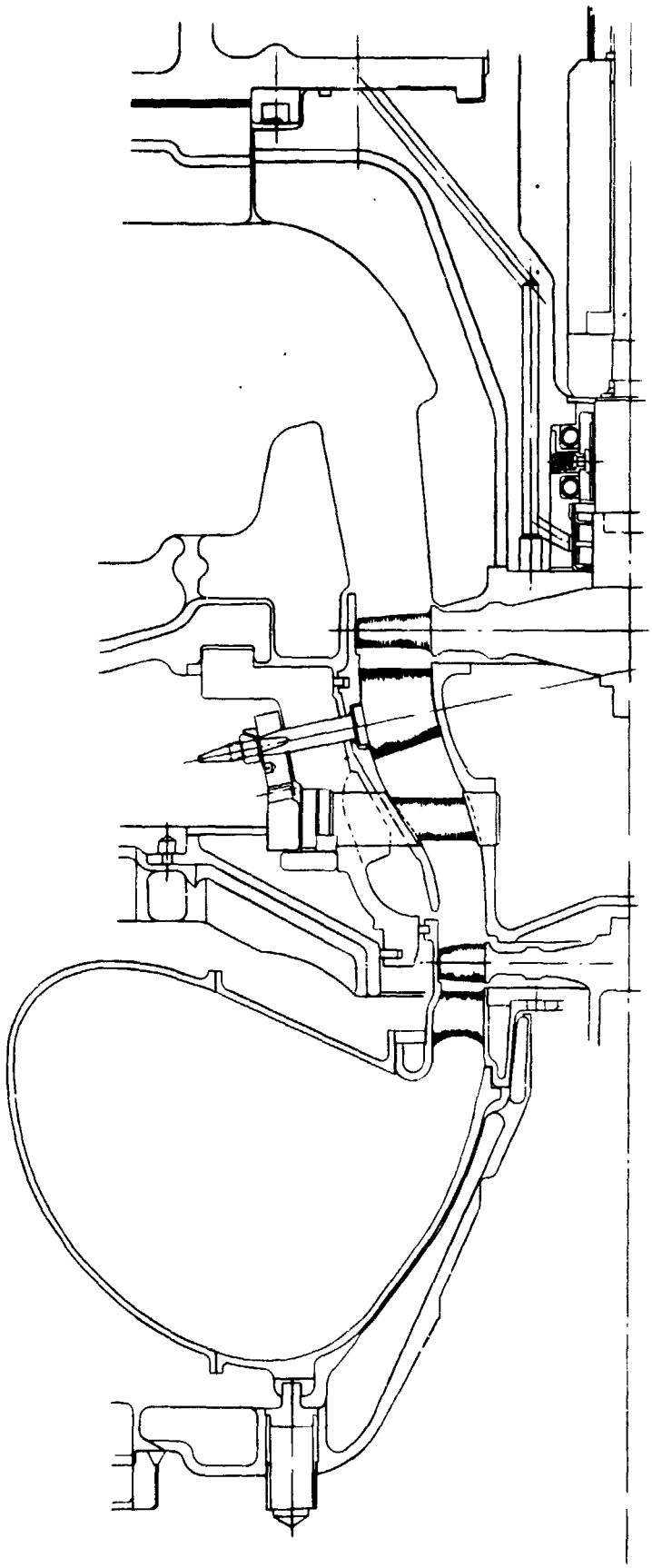

Figure 203

Upgraded Engine Power Turbine

100% Gasifier Speed Velocity Triangles

Angles in Degrees, Velocity in M/S

Hub

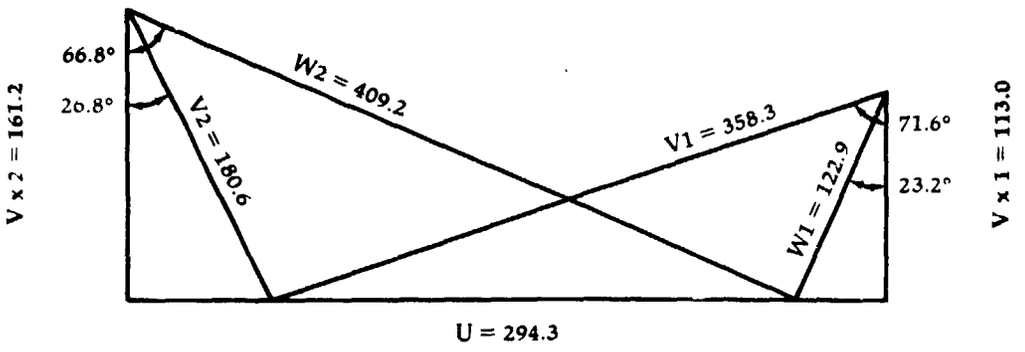

Mean

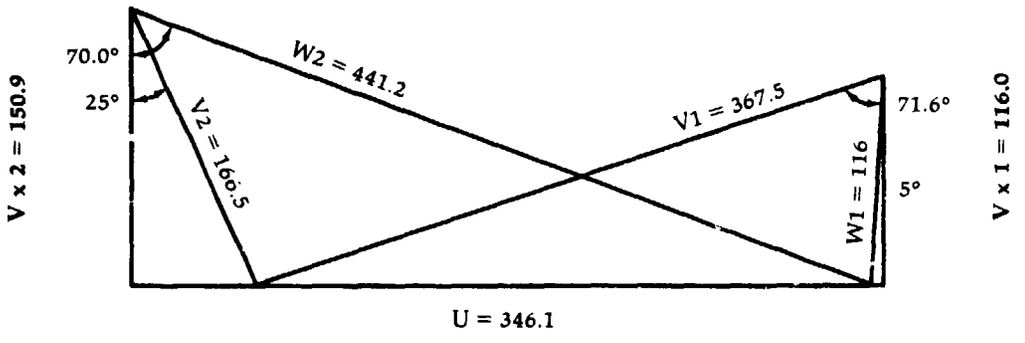

Tip

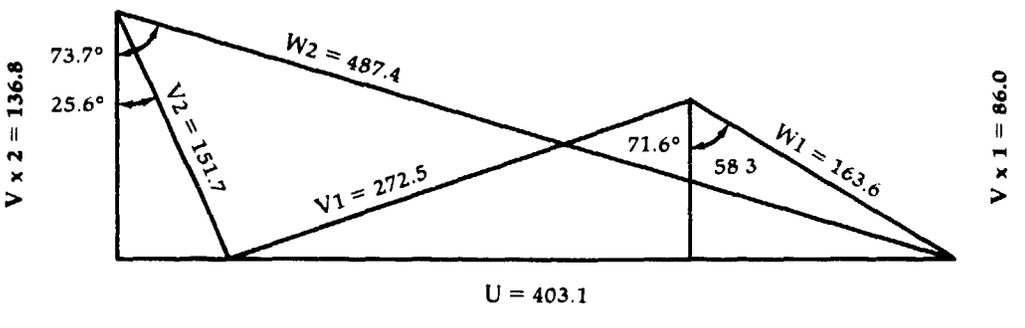

Note: Variable Loss on Stator
Variable Work on rotor

Figure 204

Upgraded Engine
Final compressor configuration;
Mod 3 compressor
Turbine
Power & BSFC
Characteristics

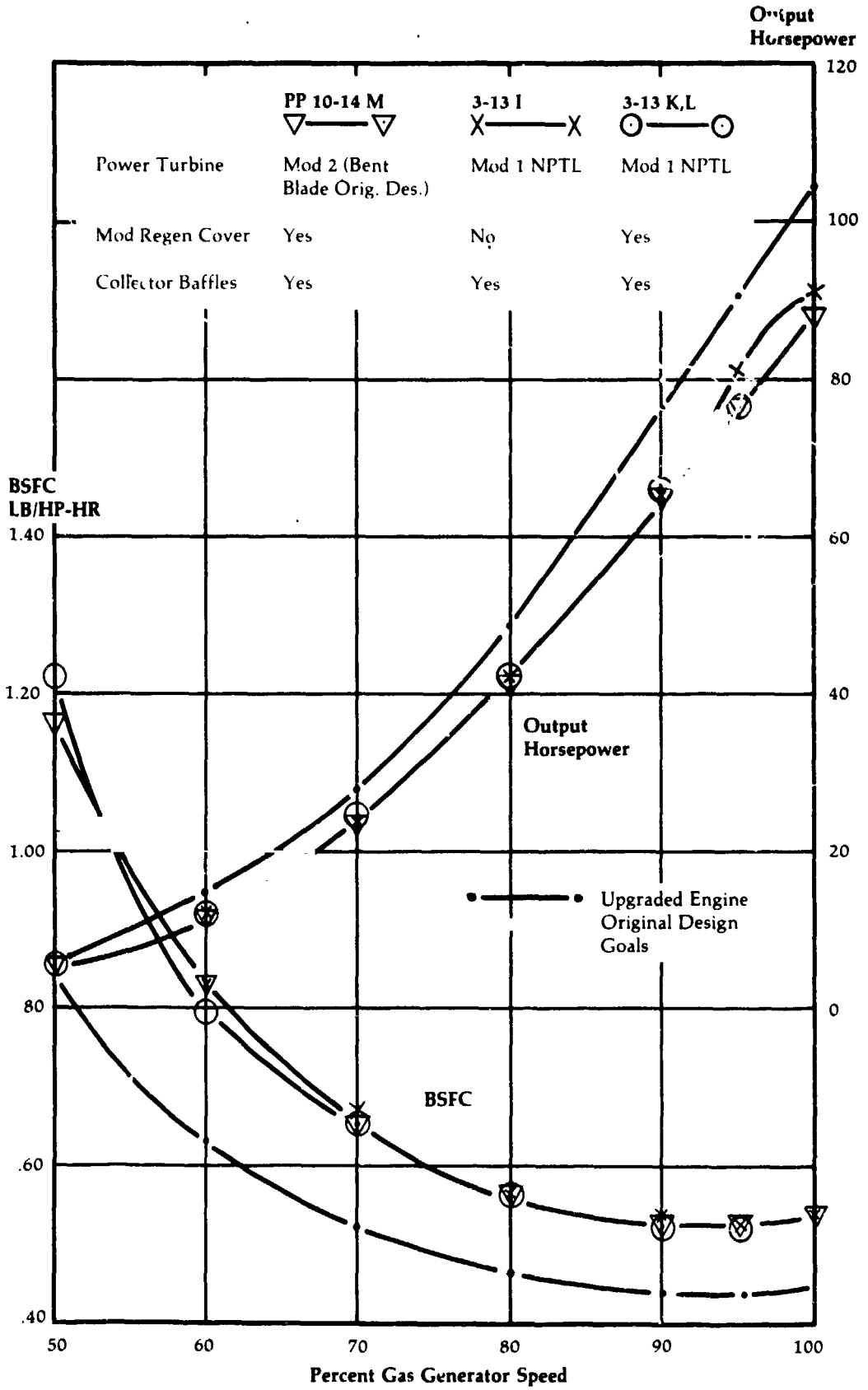

Figure 205

Upgraded Engine Final compressor Configuration; Mod 3 compressor Turbine Power & BSFC Characteristics

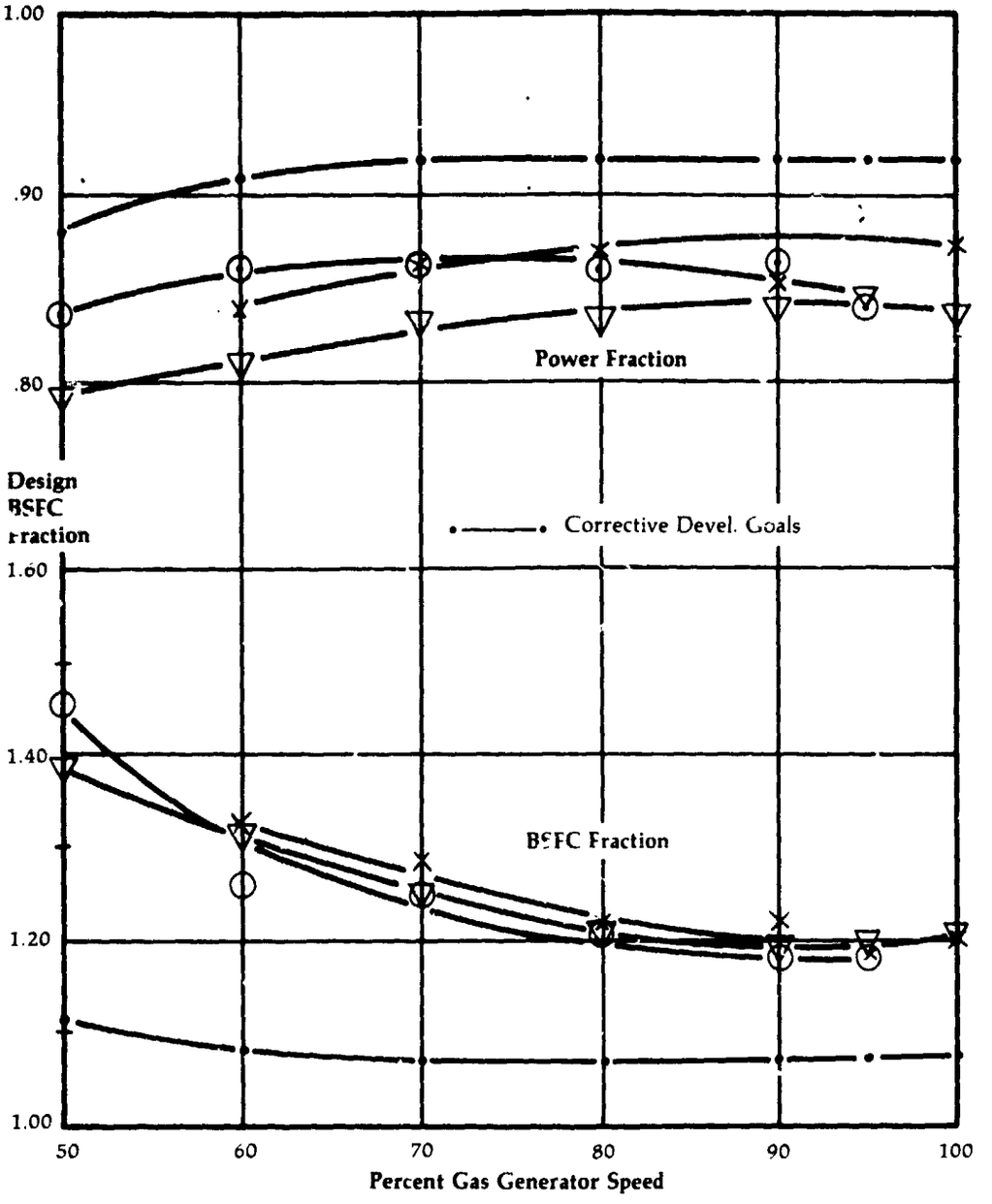

	PP 10-14 M ▽——▽	3-13 I X——X	3-13 K,L ⊙——⊙
Power Turbine	Mod 2 (Bent Blade Orig Des)	Mod 1 NPTL	Mod 1 NPTL
Mod Regen Cover	Yes	No	Yes
Collector Baffles	Yes	Yes	Yes

Figure 206

Upgraded Engine
Regenerator Cover
with Flow
Distribution
Baffle

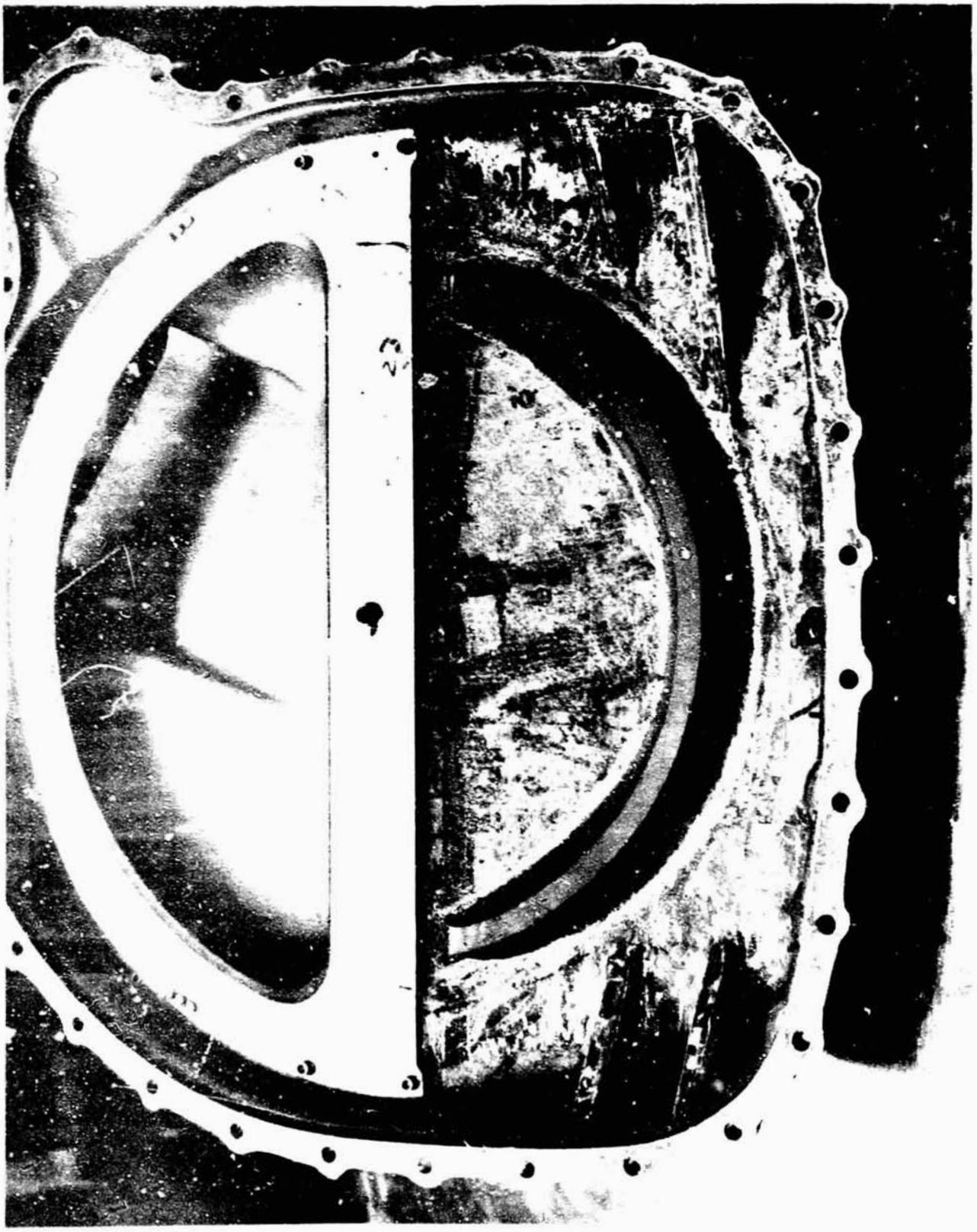

Figure 207

High Pressure Side Regenerator Flow Distribution

A. Standard Cover

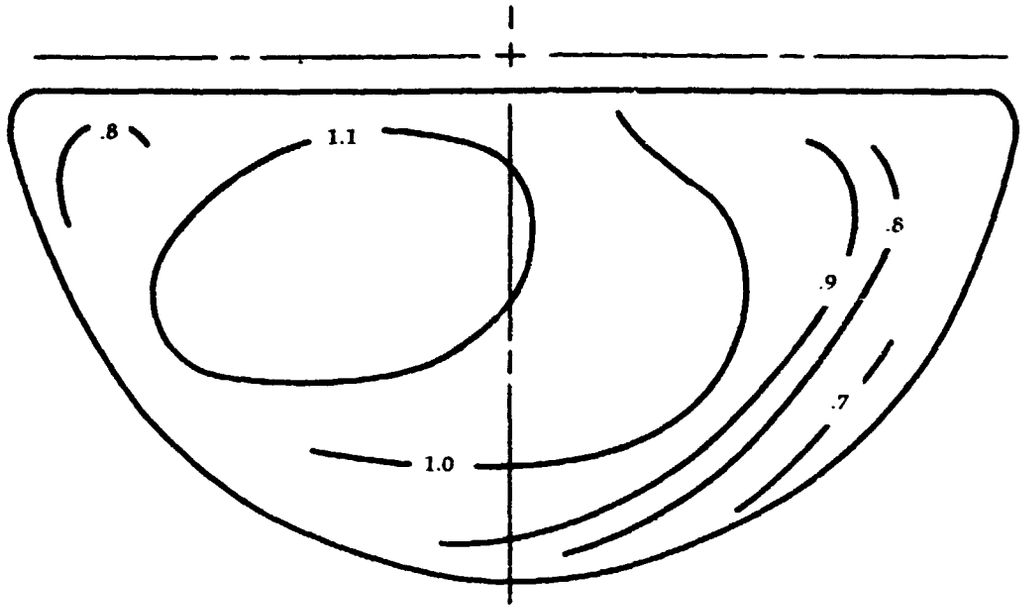

B. Modified Cover

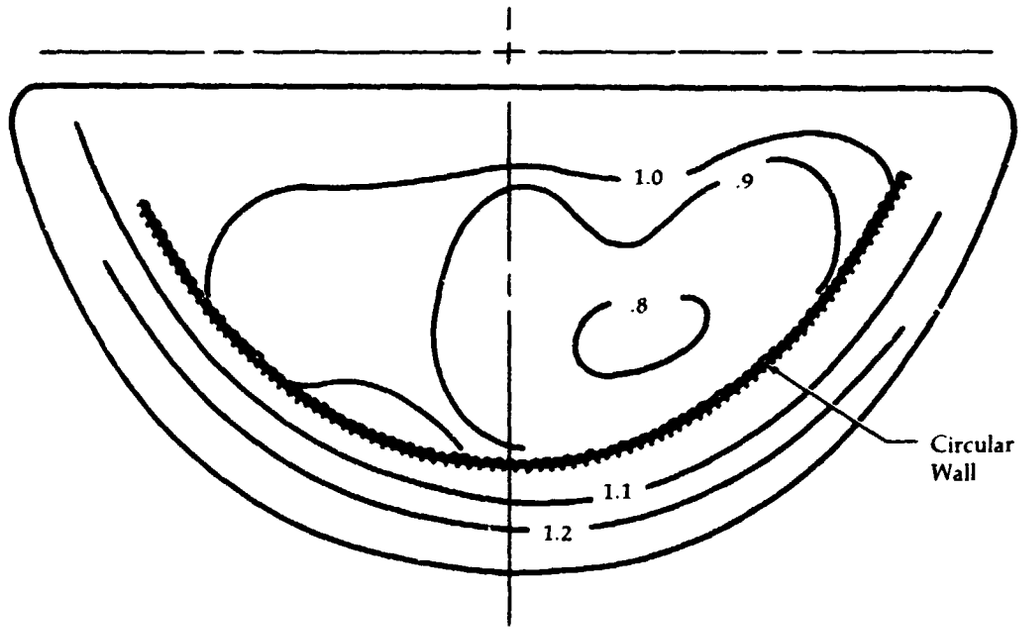

Figure 208

Upgraded Engine Performance with Modified Regenerator Cover

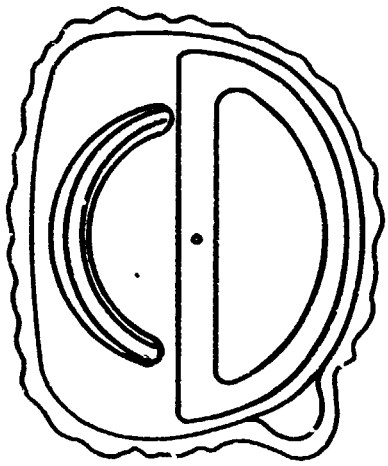

Modified Cover with Baffle in High Pressure Side. Top of Baffle Is 5/8 in. from Matrix Face

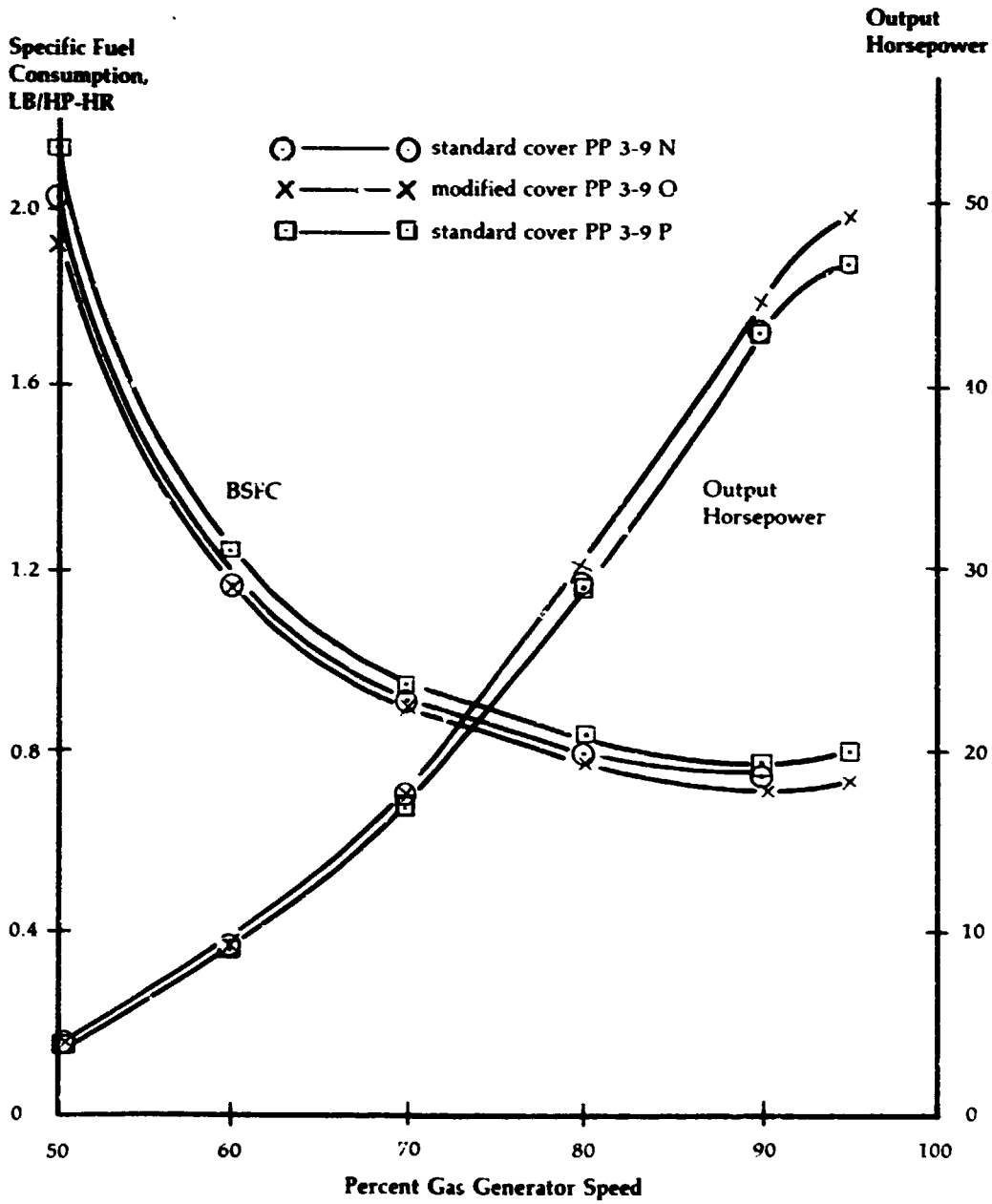

Figure 209

Upgraded Engine Scale Model Testing of Exhaust Diffuser and Regenerator Flow Distribution

Schematic of the Test Model.

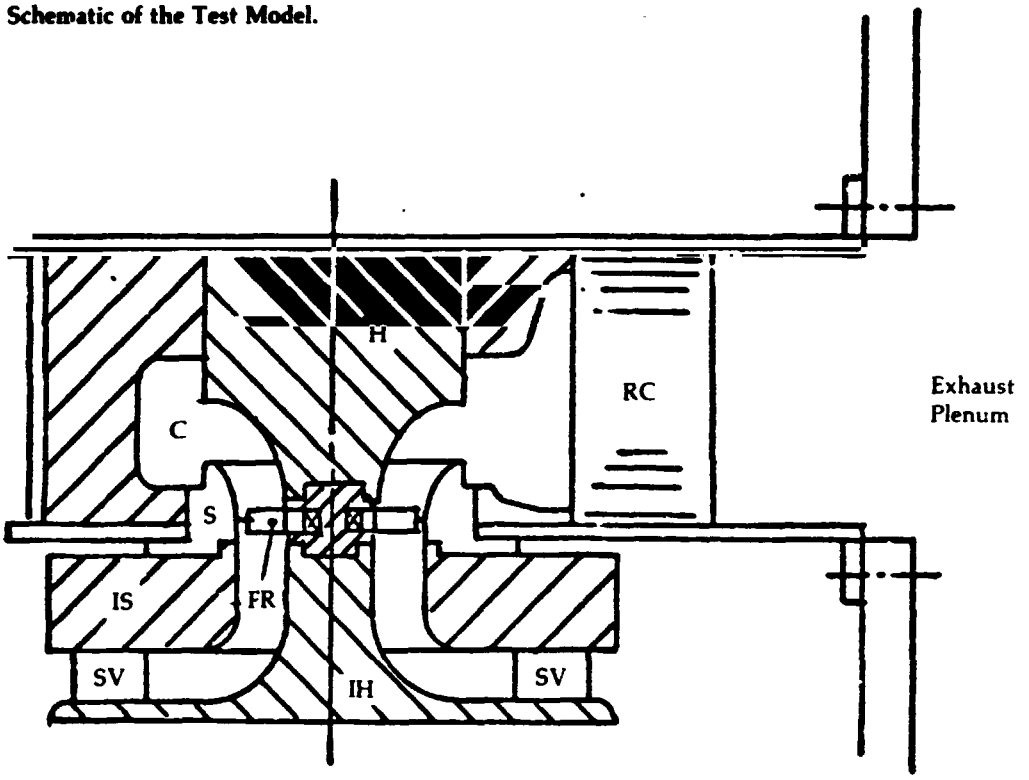

SV	Swirl Vanes
IH	Inlet Hub Piece
IS	Inlet Shroud Piece
H	Diffuser Hub
S	Diffuser Shroud
C	Collector
RC	Regenerator Matrix
FR	Free Runner*

*Free Runner was not included in all Tests

Upgraded Engine Exhaust Diffuser and Regenerator Core Model Test

Schematic of Instrumentation Location.

Note: All Static Taps 0.013" Dia.

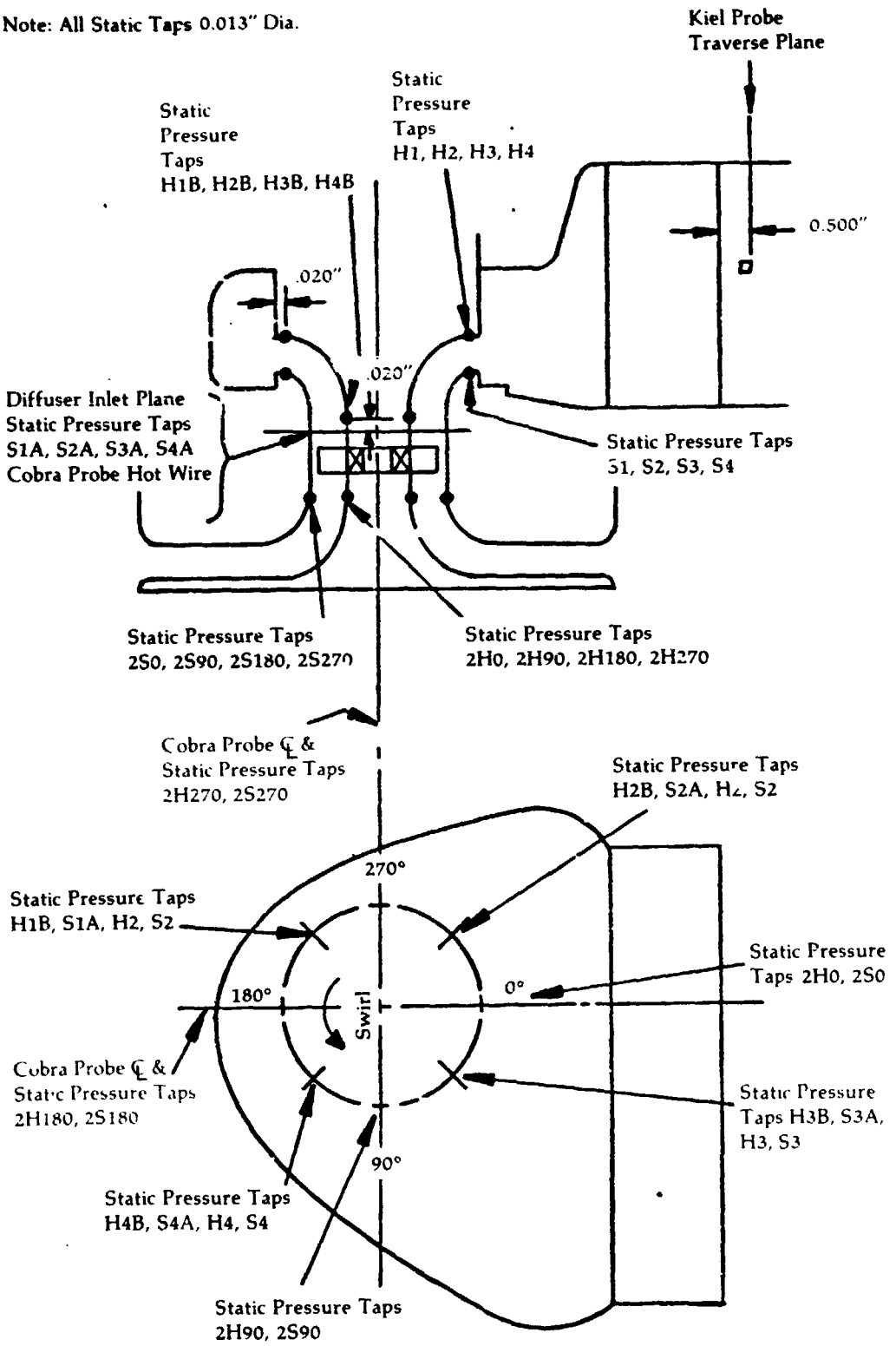

Figure 211

Regenerator Exit Traverse Locations (View Looking into Collector) Scale Model Test at Creare, Inc.

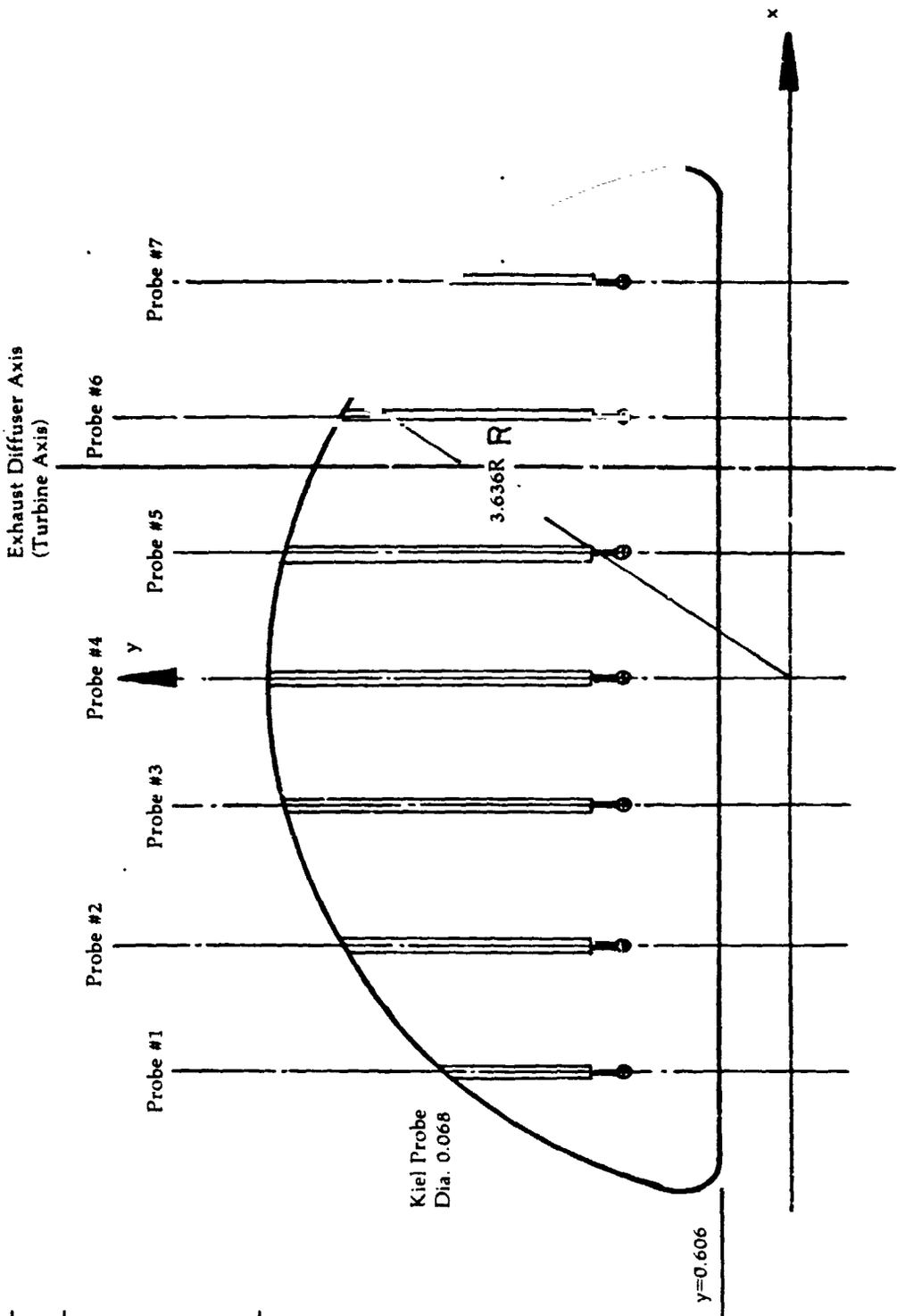

Probe	X
1	−2.532
2	−1.688
3	−0.844
4	0.000
5	+0.844
6	+1.688
7	+2.532

Figure 212

Upgraded Engine LP Regenerator Core Flow Distribution

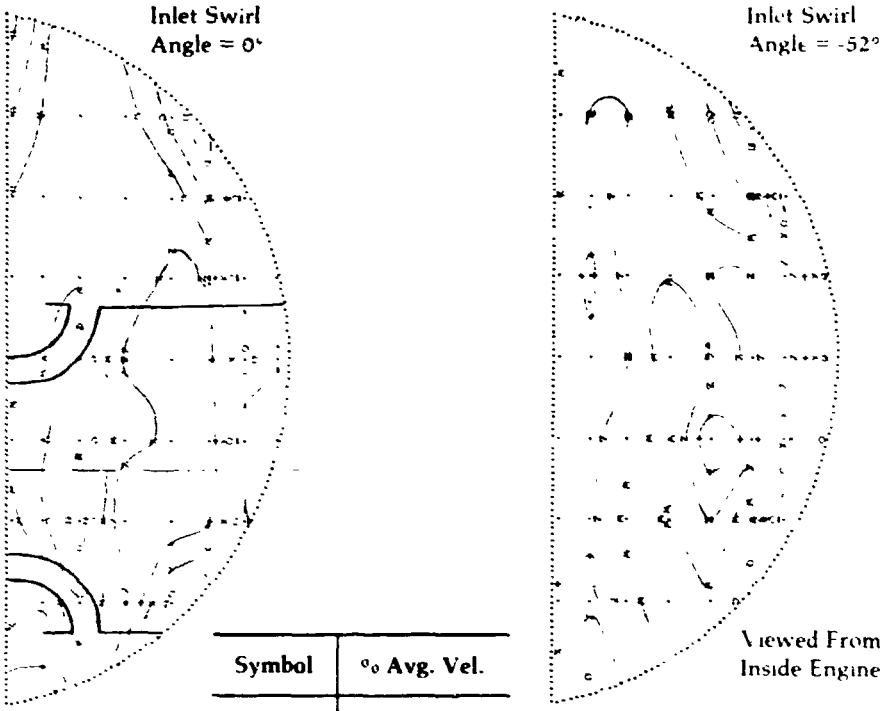

Symbol	% Avg. Vel.
—	20
0	40
λ	60
+	80
λ	100
W	120
C	140
H	160

Local Mass Flow in 0.1" Annuiar Ring At Radius Noted By Symbol - % Total Mass Flow.

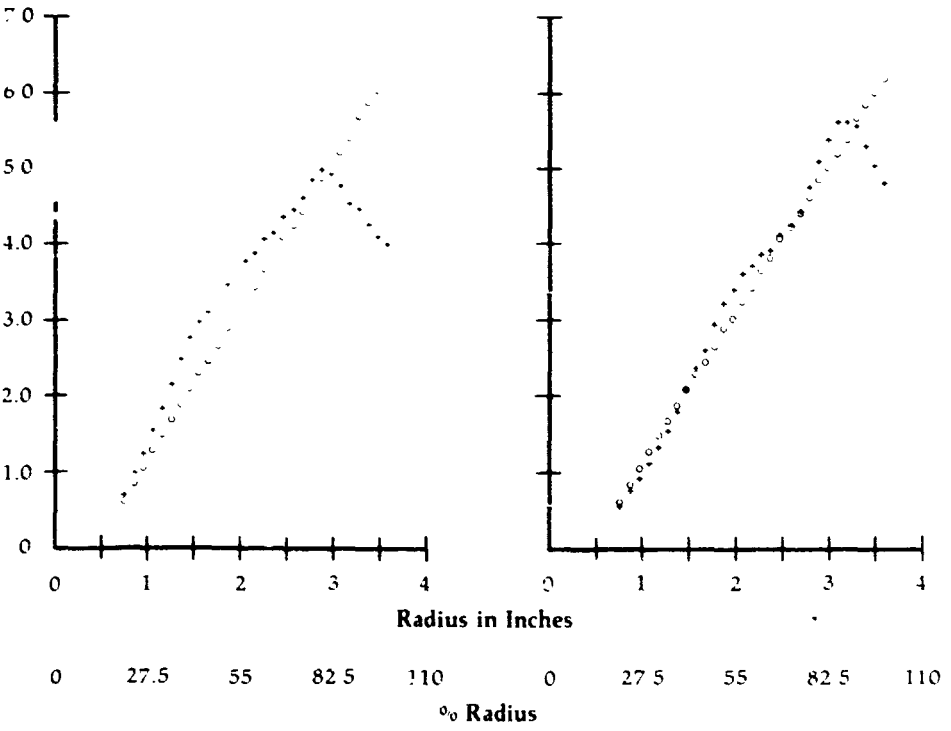

Figure 213

Upgraded Engine Braking Mode - 50% Gas Generator Speed

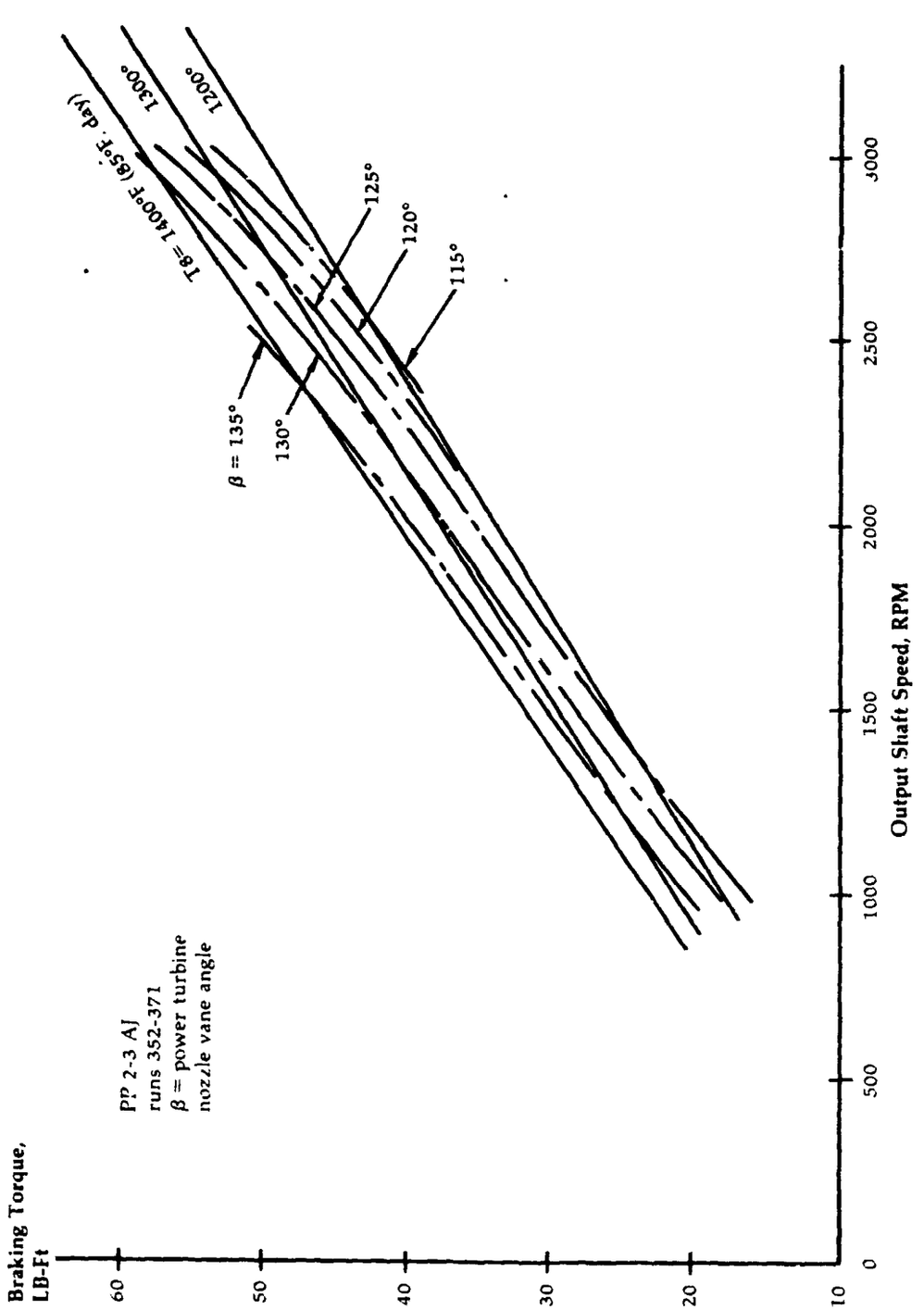

Figure 214

Upgraded Engine Effect of Reduced Bulkhead Cooling on T_3 & T_2-T_3 Rise

T_3 Grid Data at 50% Ngg

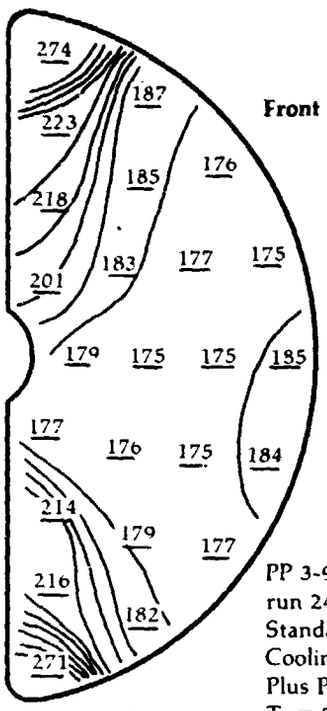

(A)

PP 3-9 Y room 12 S
run 248 04-13-78
Standard Bulkhead Cooling
Plus P_{2-3} Deflectors
T_1 = 59°F. actual
T_2 = 153°F. actual

Average T_3 = 194° Unweighted
T_{2-3} = 41°

T_3 Grid as viewed from Right Hand Side of Engine

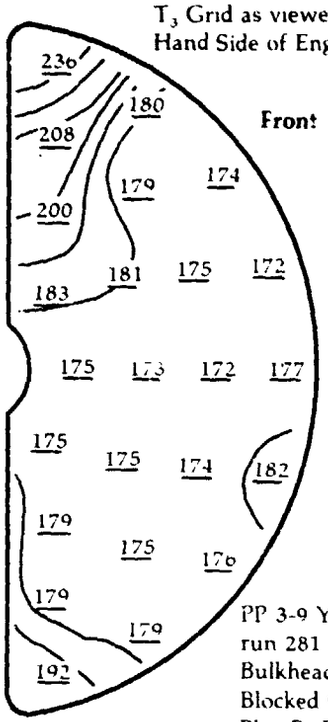

(B)

PP 3-9 Y
run 281 04-18-78
Bulkhead Cooling
Blocked 90°
Plus P_2-P_3 Deflectors
T_1 = 57°F actual
T_2 = 152°F. actual

Average T_3 = 182° Unweighted
T_{2-3} = 30°

T_2-T_3 Rise vs. Gas Generator Speed

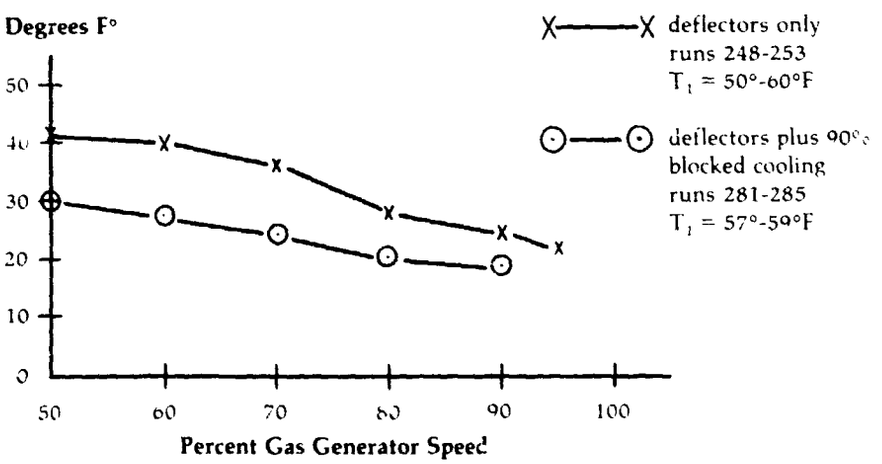

Figure 215

Upgraded Engine Power Turbine Nozzle Metal Temperatures After Cold Start

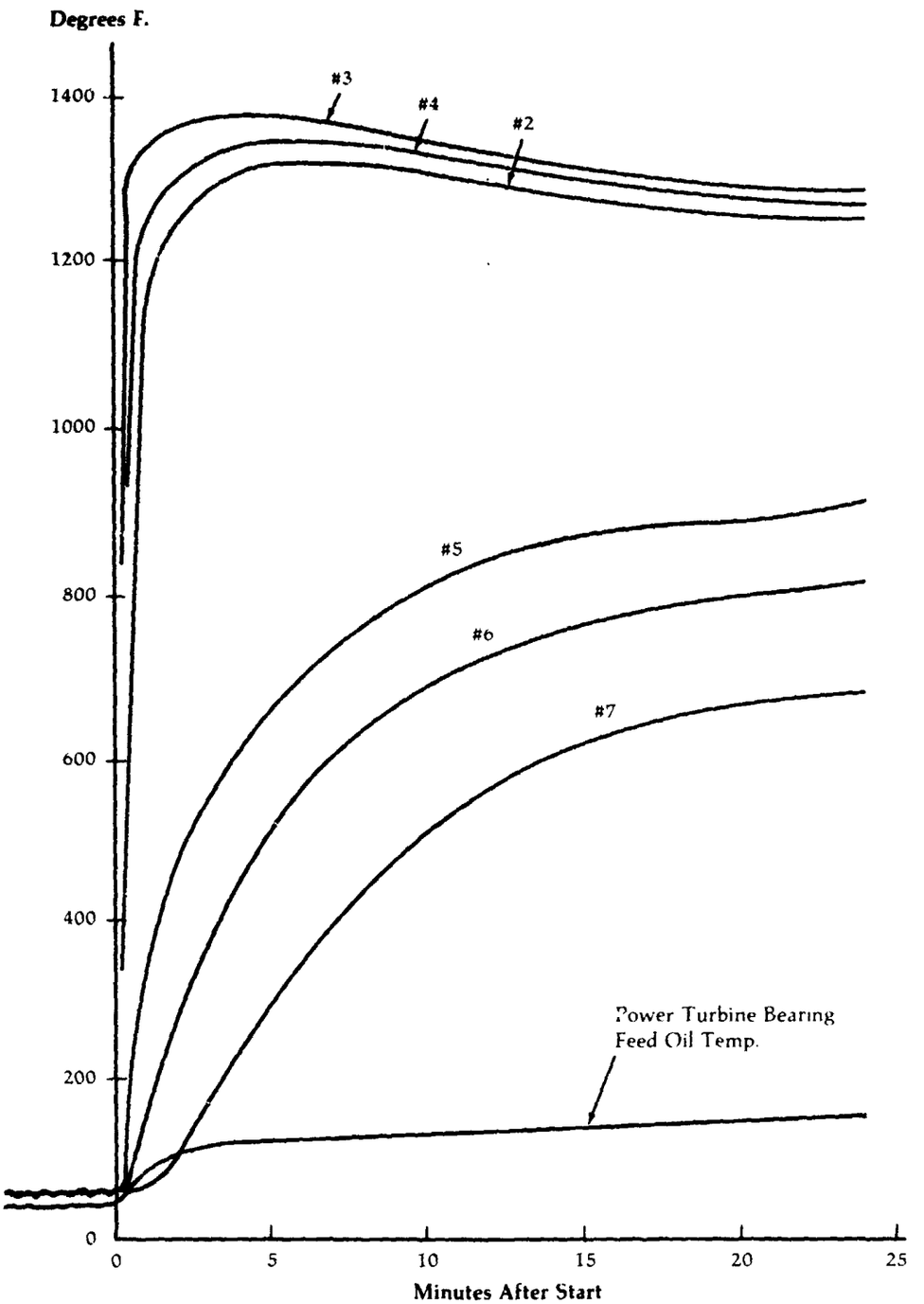

PP 2-3 BE
Vane Angle β Fixed at 35.5°
(0.7° closed from 50% Ngg
match point)

See figure 217 for thermo-
couple location schematic.

Figure 216

Upgraded Engine Power Turbine Nozzle Metal Temperatures Steady State

P.T.N. Assembly #8 PP 2-3BC

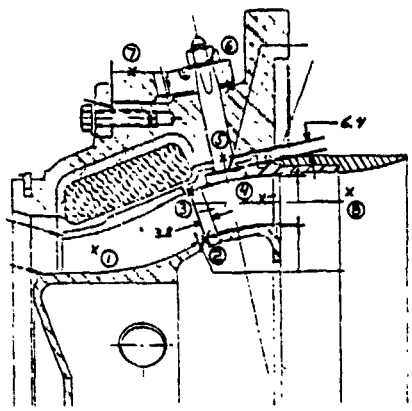

No.	Type	Location	Photo
1	Air	T_e	9078-52
2	Skin	Inner Shroud	
3	Skin	Outer Shroud	
4	Skin	Vane #8-Pressure Surface	9078-50
5	Skin	Vane #9-Immersed in Stem	
6	Skin	Nozzle Support	
7	Skin	Ring Gear	9078-51
8	Air	T_{-5} - Standard	

Except for No. 4 all TC's are axially in line with Vane #9.

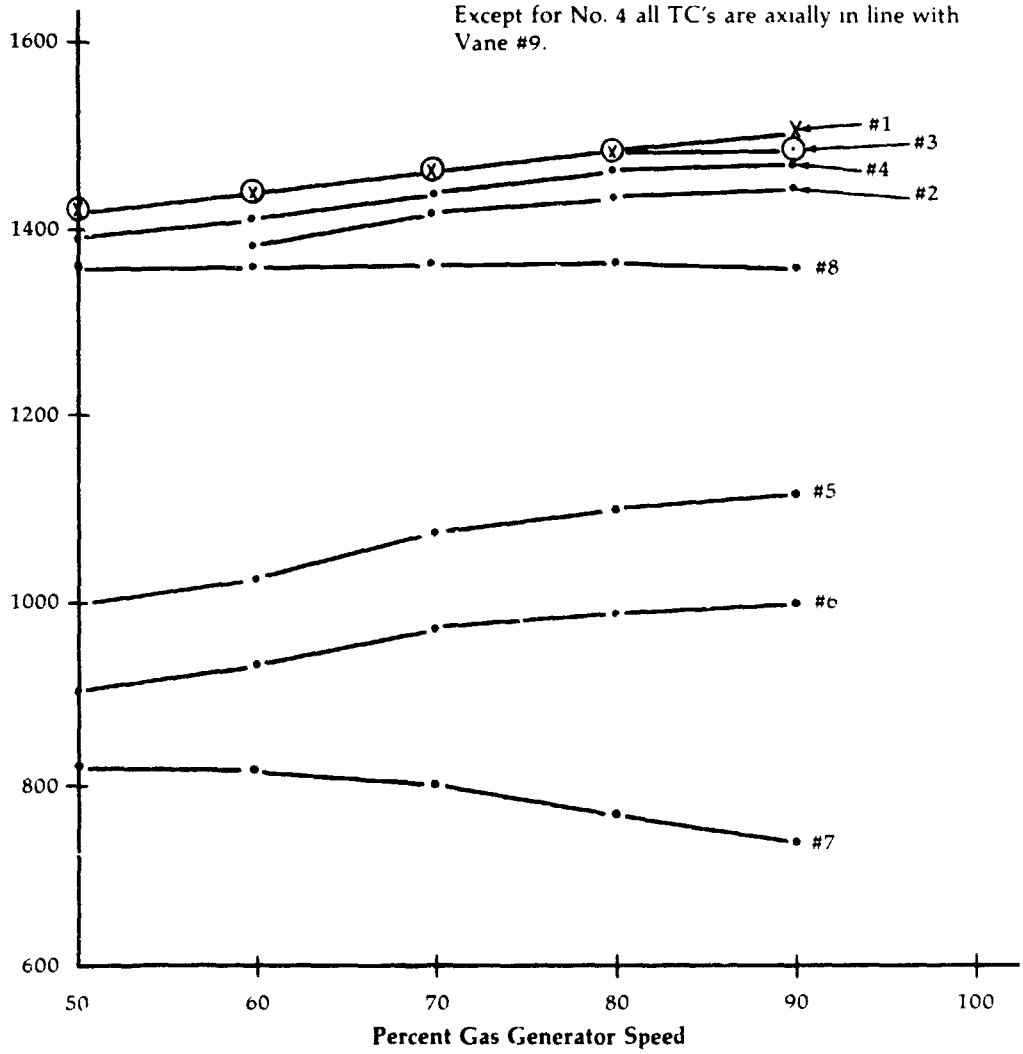

Figure 217

Upgraded Engine Power Turbine Nozzle Metal Temperatures During Soak-Back

PP 2-3 BC

Soak-back temperatures after 20 minute run at idle speed.

See fig. 217 for thermocouple location schematic.

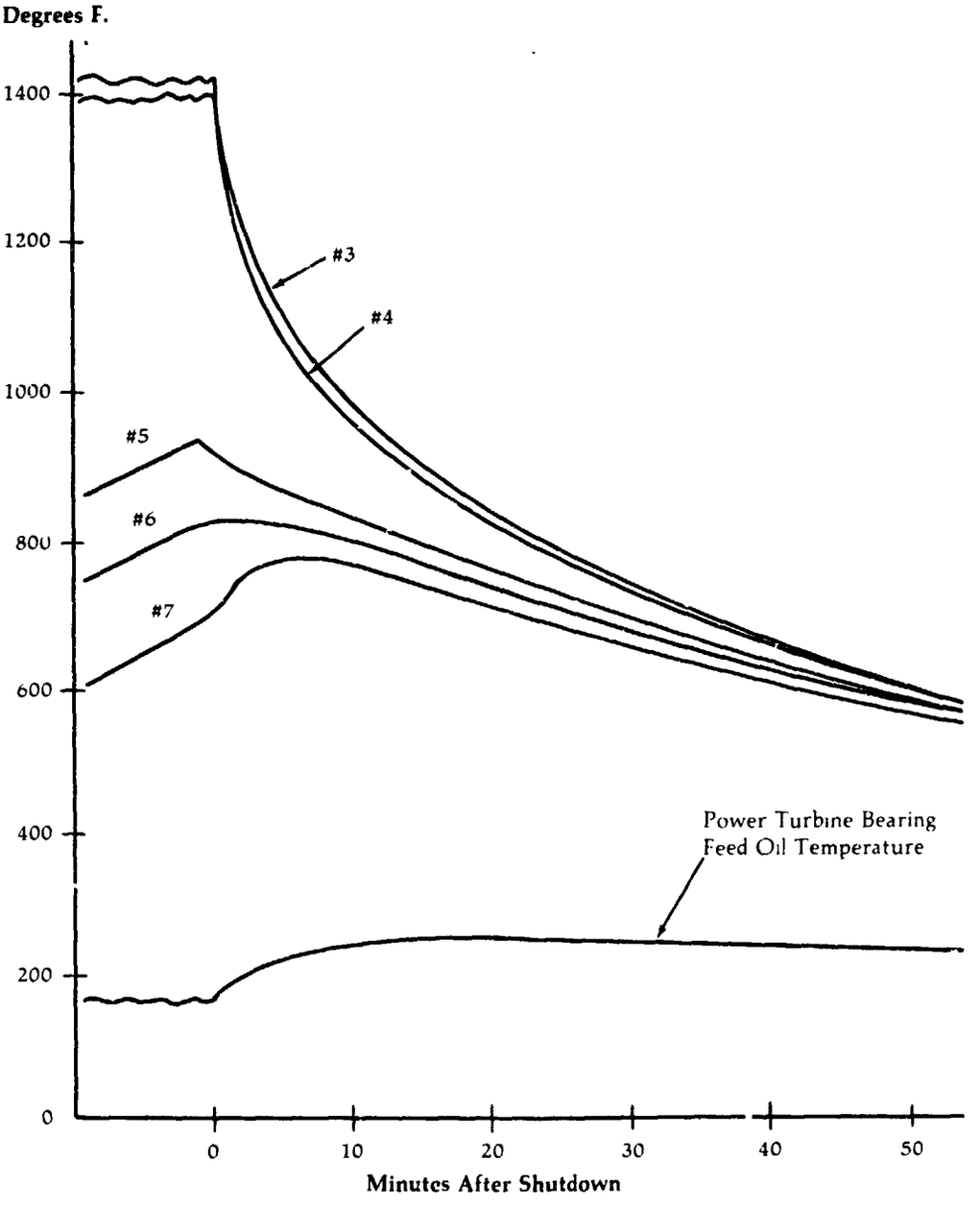

Figure 218

Upgraded Engine Regenerator Seal Cross-Sections

A. Diaphragm Type Seal

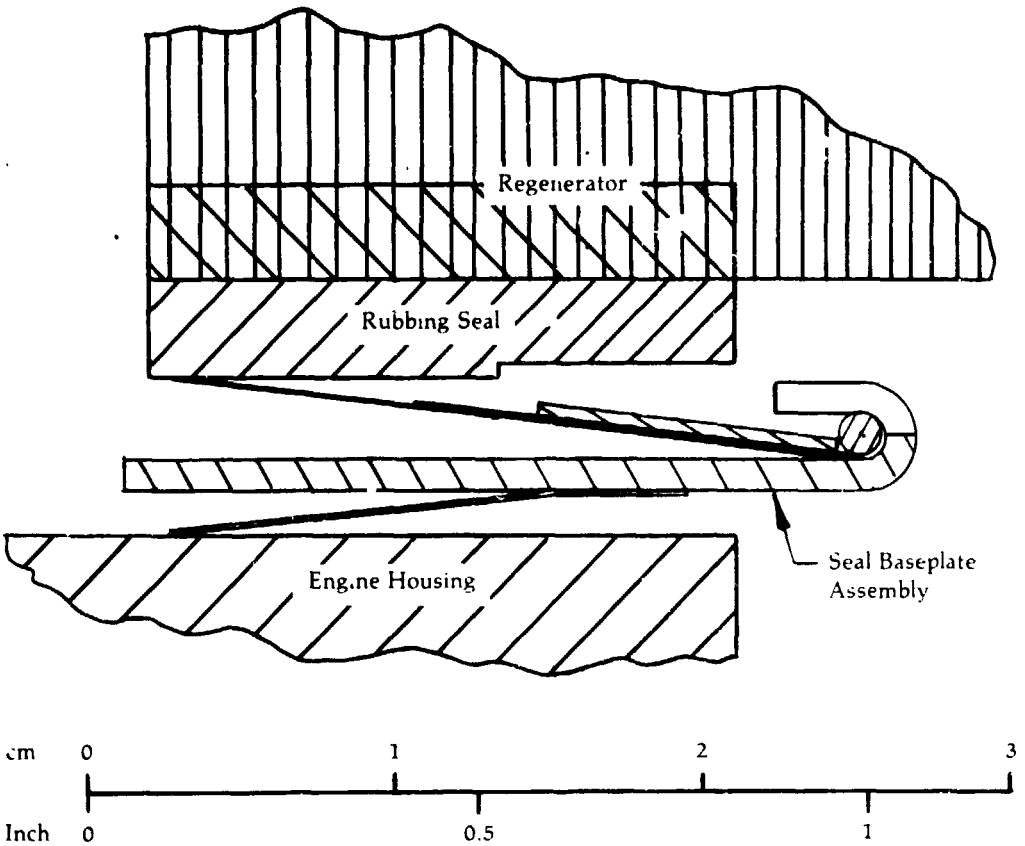

B. "L" Seal

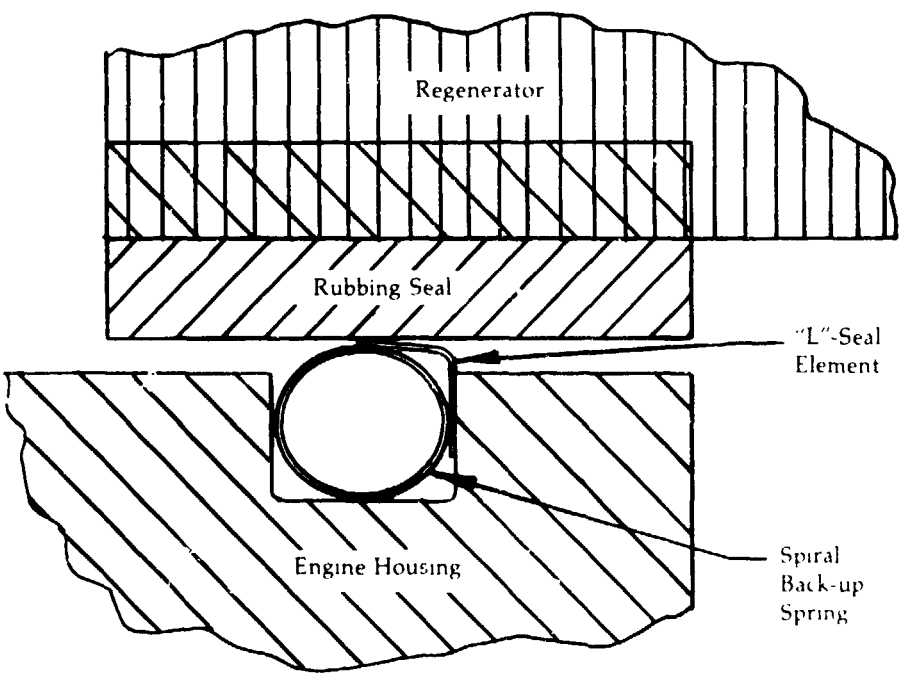

Figure 219

Control System
Upgraded Engine

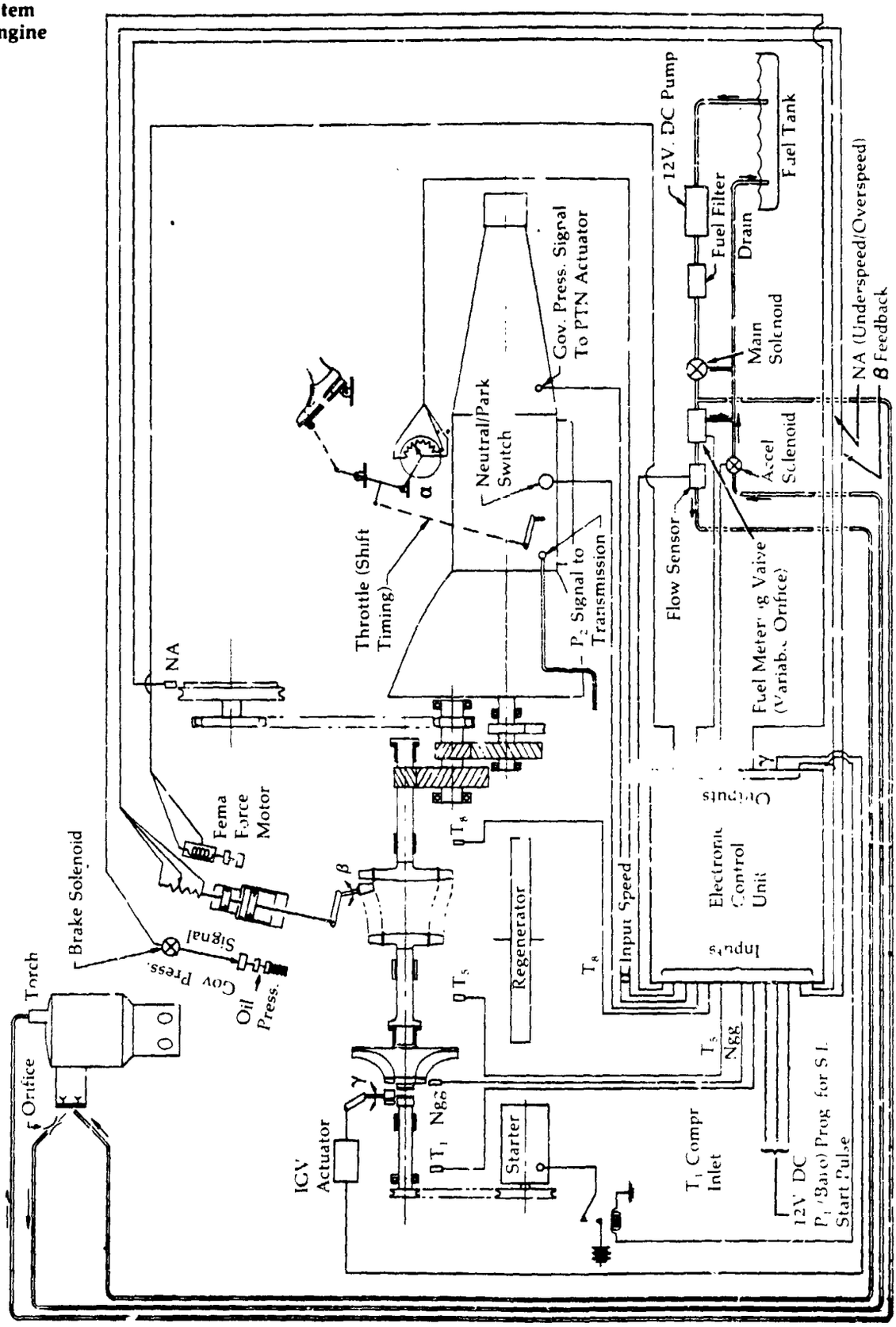

Figure 220

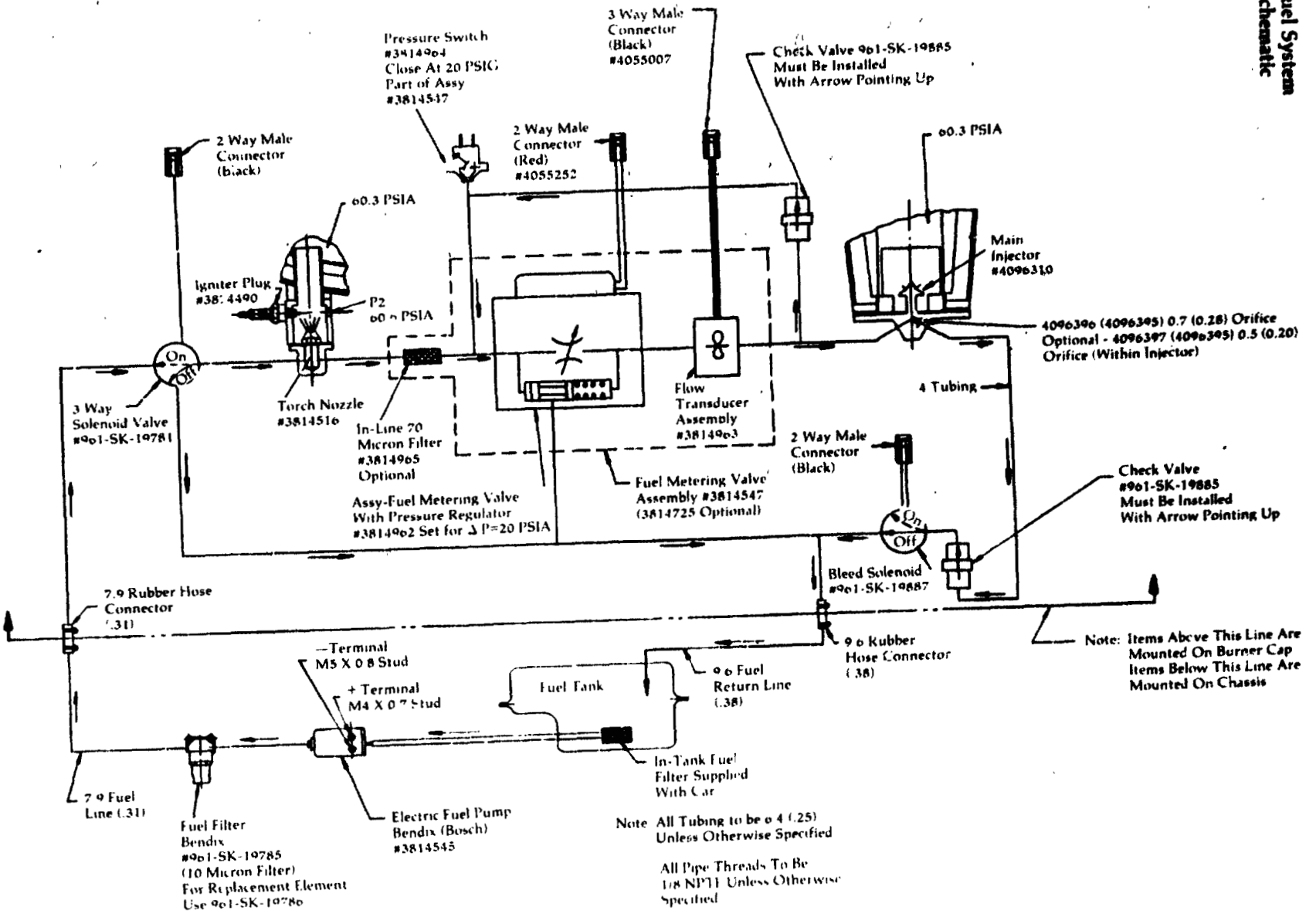
3 Way Male Connector (Black) #4055007
Pressure Switch #3814964 Close At 20 PSIG Part of Assy #3814547
Check Valve 961-SK-19885 Must Be Installed With Arrow Pointing Up
2 Way Male Connector (black)
2 Way Male Connector (Red) #4055252
60.3 PSIA
60.3 PSIA
Main Injector #4096310
Igniter Plug #38: 4490
P2 60.6 PSIA
4096396 (4096395) 0.7 (0.28) Orifice Optional - 4096397 (4096395) 0.5 (0.20) Orifice (Within Injector)
On
Off
3 Way Solenoid Valve #961-SK-19781
Torch Nozzle #3814516
In-Line 70 Micron Filter #3814965 Optional
Flow Transducer Assembly #3814963
4 Tubing
2 Way Male Connector (Black)
Fuel Metering Valve Assembly #3814547 (3814725 Optional)
Assy-Fuel Metering Valve With Pressure Regulator #3814962 Set for Δ P=20 PSIA
Check Valve #961-SK-19885 Must Be Installed With Arrow Pointing Up
On
Off
Bleed Solenoid #961-SK-19887
7.9 Rubber Hose Connector (.31)
9.6 Rubber Hose Connector (.38)
Note: Items Above This Line Are Mounted On Burner Cap Items Below This Line Are Mounted On Chassis
— Terminal M5 X 0.8 Stud
+ Terminal M4 X 0.7 Stud
Fuel Tank
9.6 Fuel Return Line (.38)
In-Tank Fuel Filter Supplied With Car
7.9 Fuel Line (.31)
Fuel Filter Bendix #961-SK-19785 (10 Micron Filter) For Replacement Element Use 961-SK-19786
Electric Fuel Pump Bendix (Bosch) #3814545
Note All Tubing to be 6.4 (.25) Unless Otherwise Specified
All Pipe Threads To Be 1/8 NPTF Unless Otherwise Specified

Figure 221

Upgraded Engine Fuel Control System

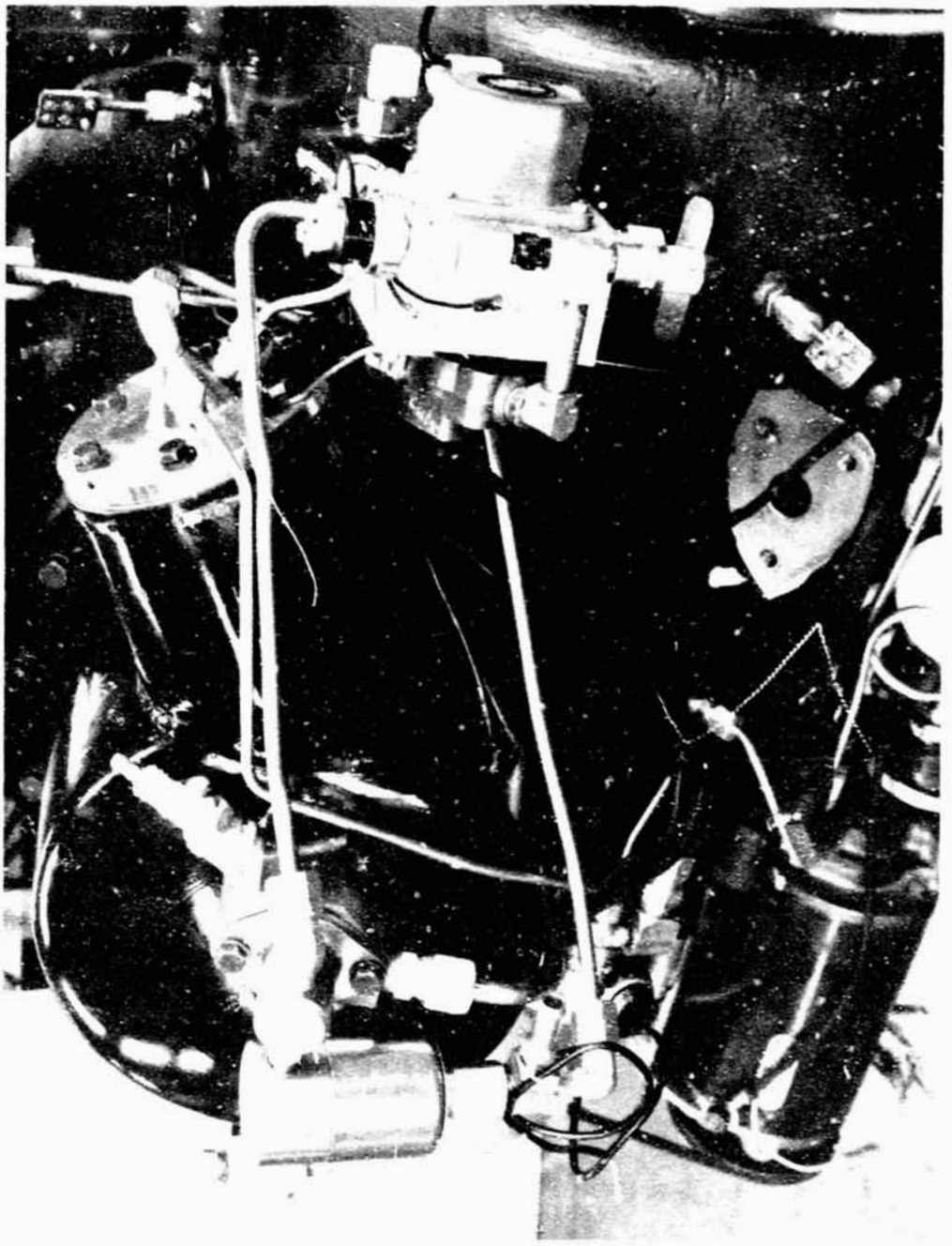

Figure 222

Upgraded Engine Fuel Metering Valve Assembly

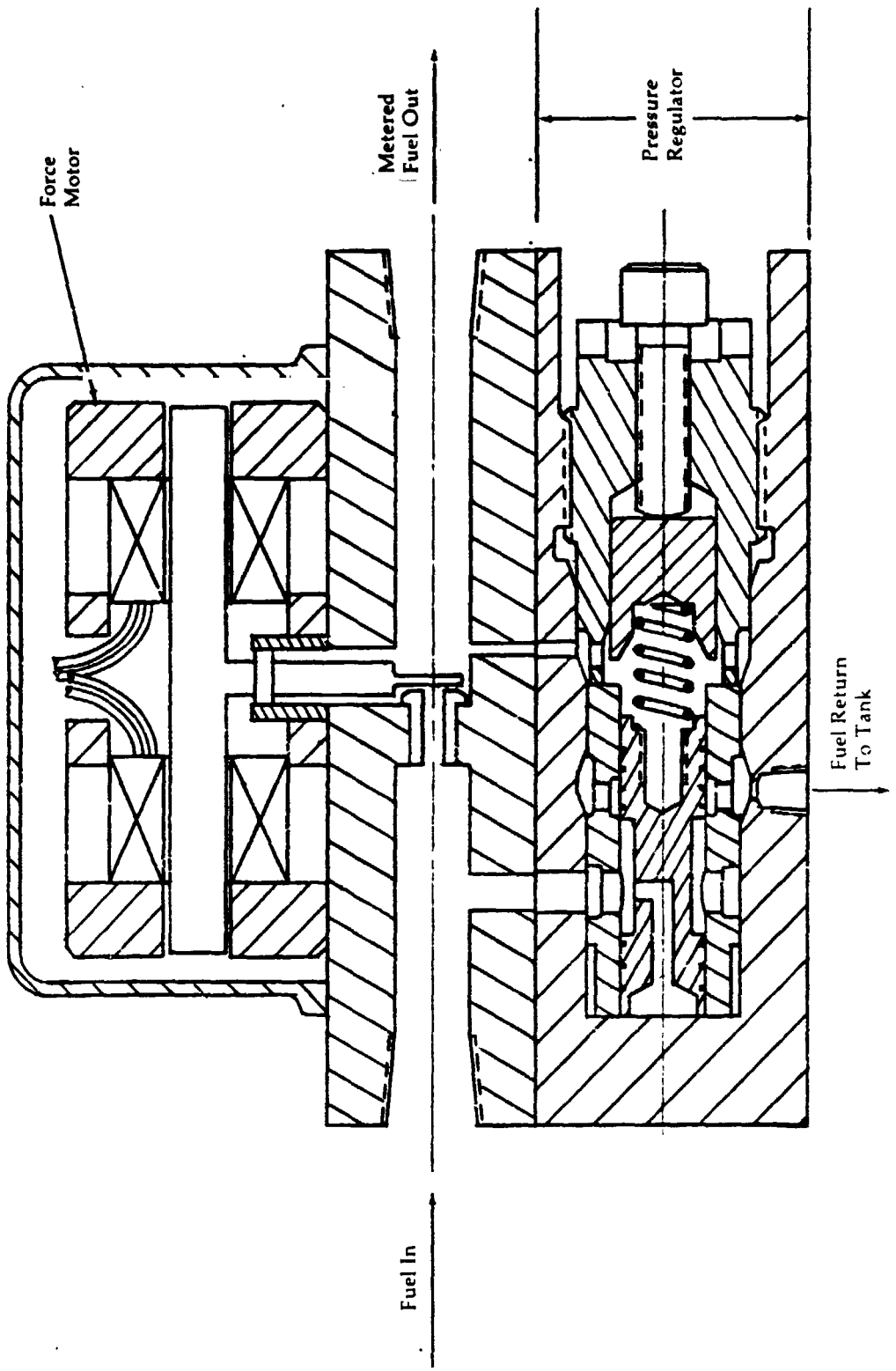

Figure 223

Upgraded Engine Test Cell Electronic Fuel Control Block Diagram

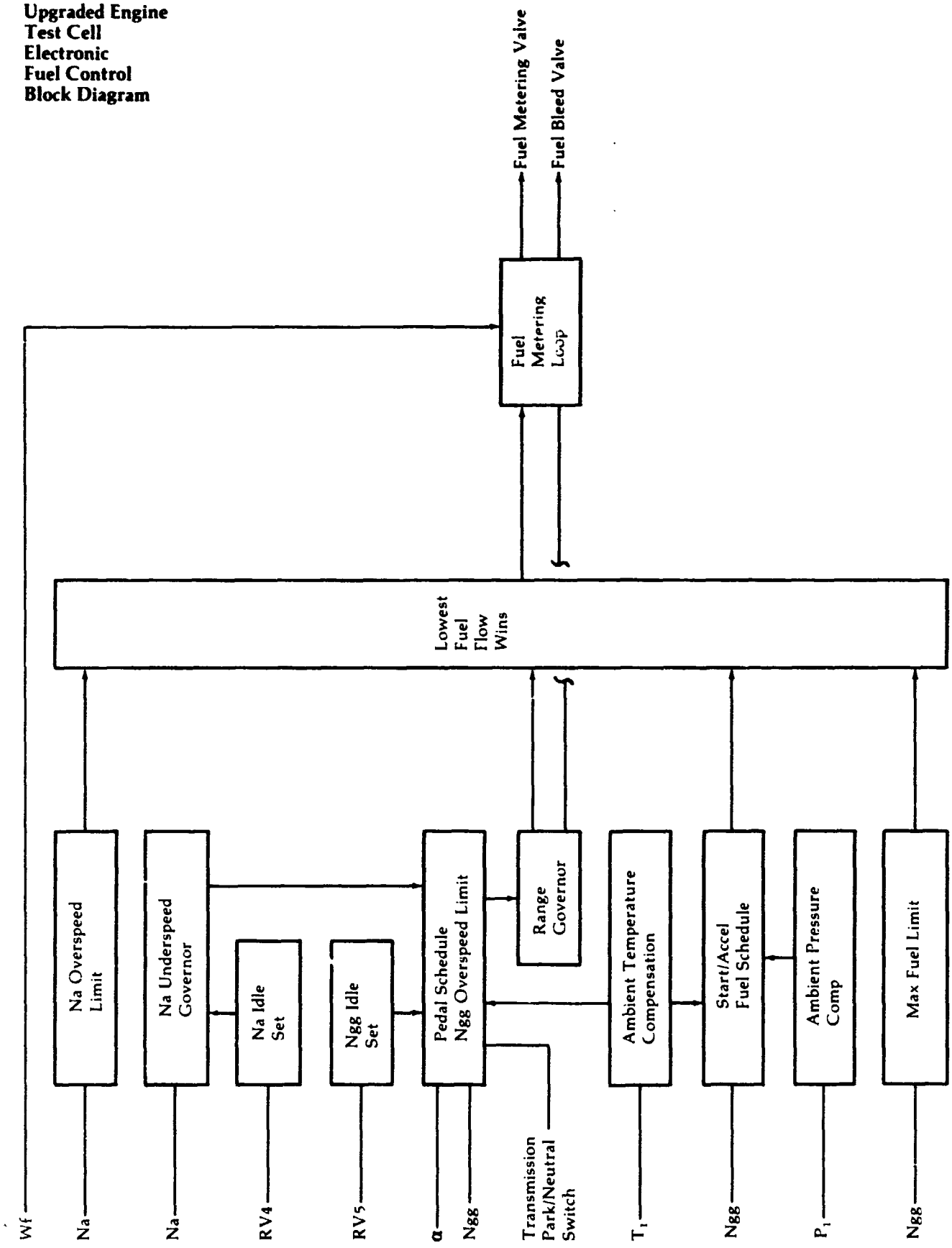

Figure 224

Power Turbine Nozzle Actuator (Power Position)

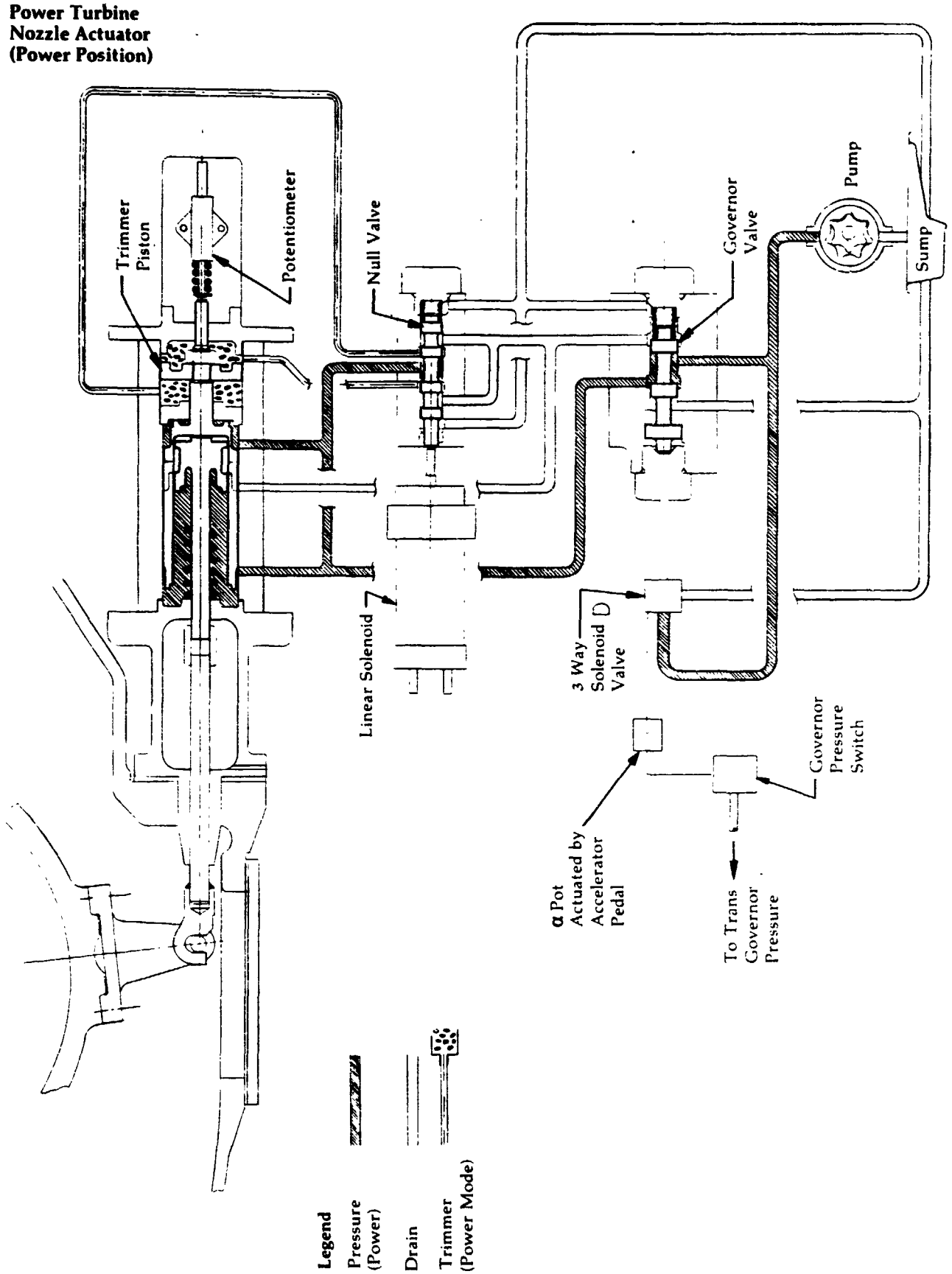

Figure 225

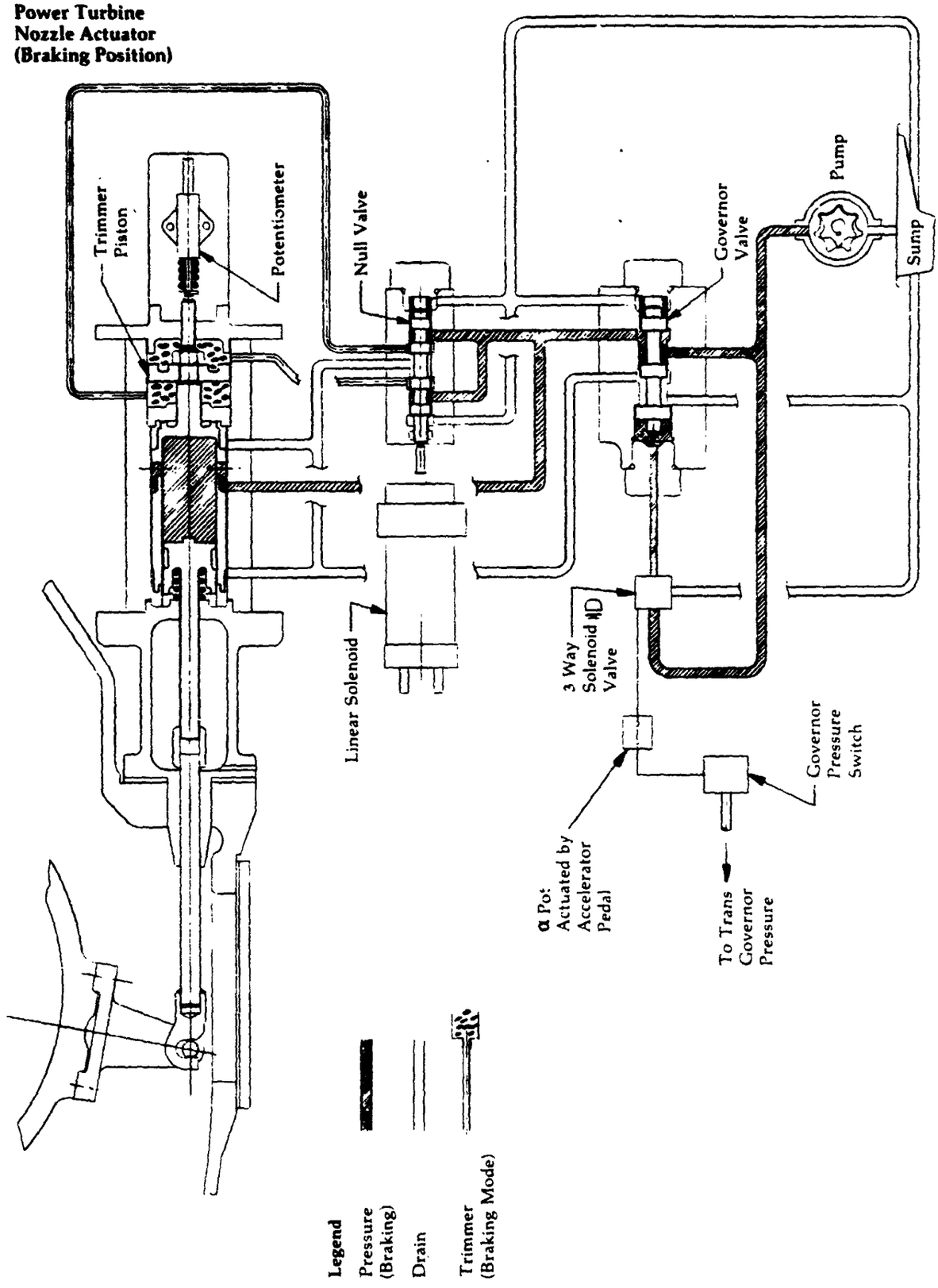
Power Turbine
Nozzle Actuator
(Braking Position)
Trimmer Piston
Potentiometer
Null Valve
Governor Valve
Pump
Sump
Linear Solenoid
3 Way Solenoid Valve
Governor Pressure Switch
α Pot Actuated by Accelerator Pedal
To Trans Governor Pressure
Legend
Pressure (Braking)
Drain
Trimmer (Braking Mode)

Figure 226

Upgraded Engine
Power Turbine
Nozzle Actuator

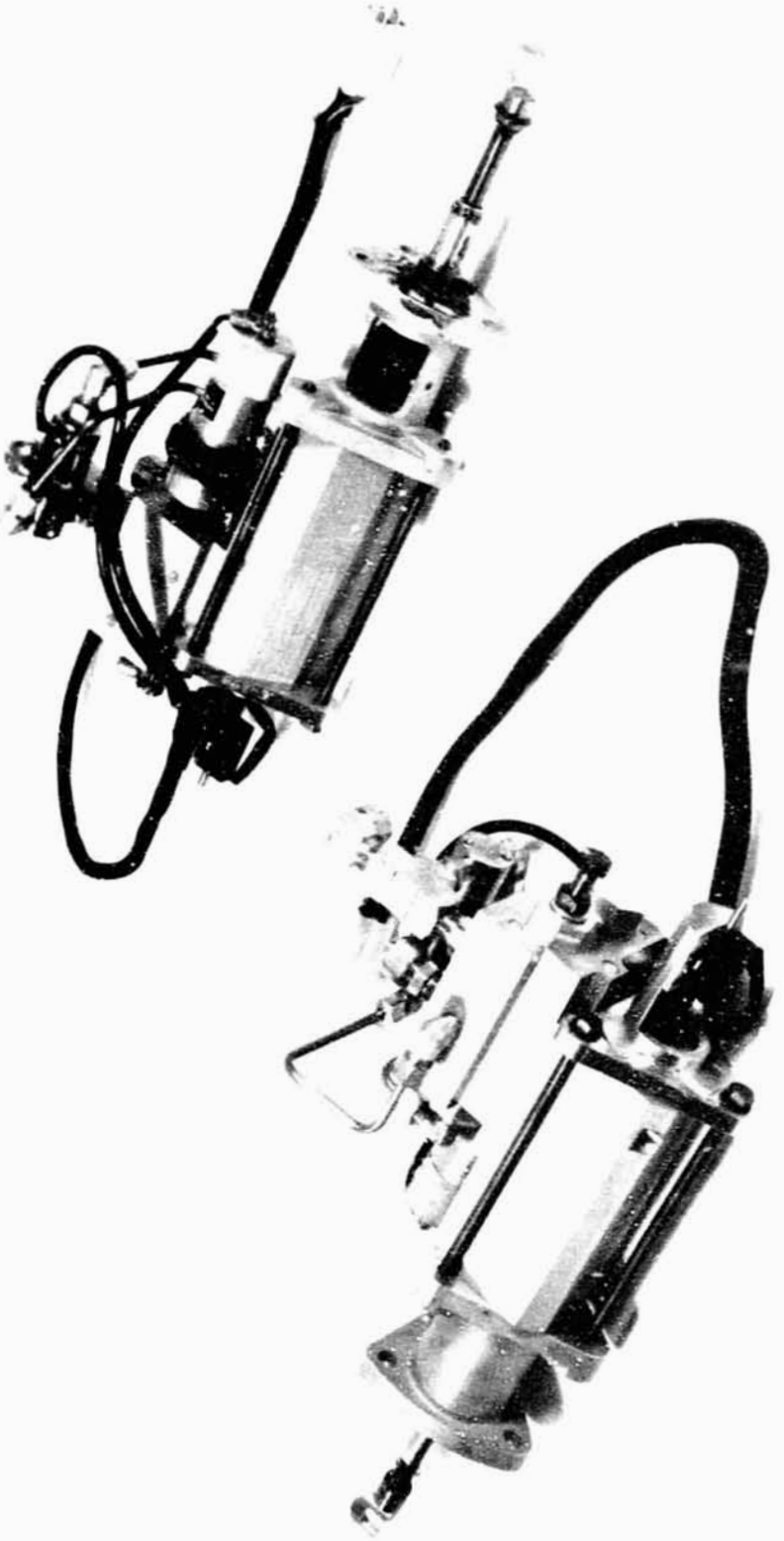

Figure 227

Inlet Guide Vane Actuator (2 Position)

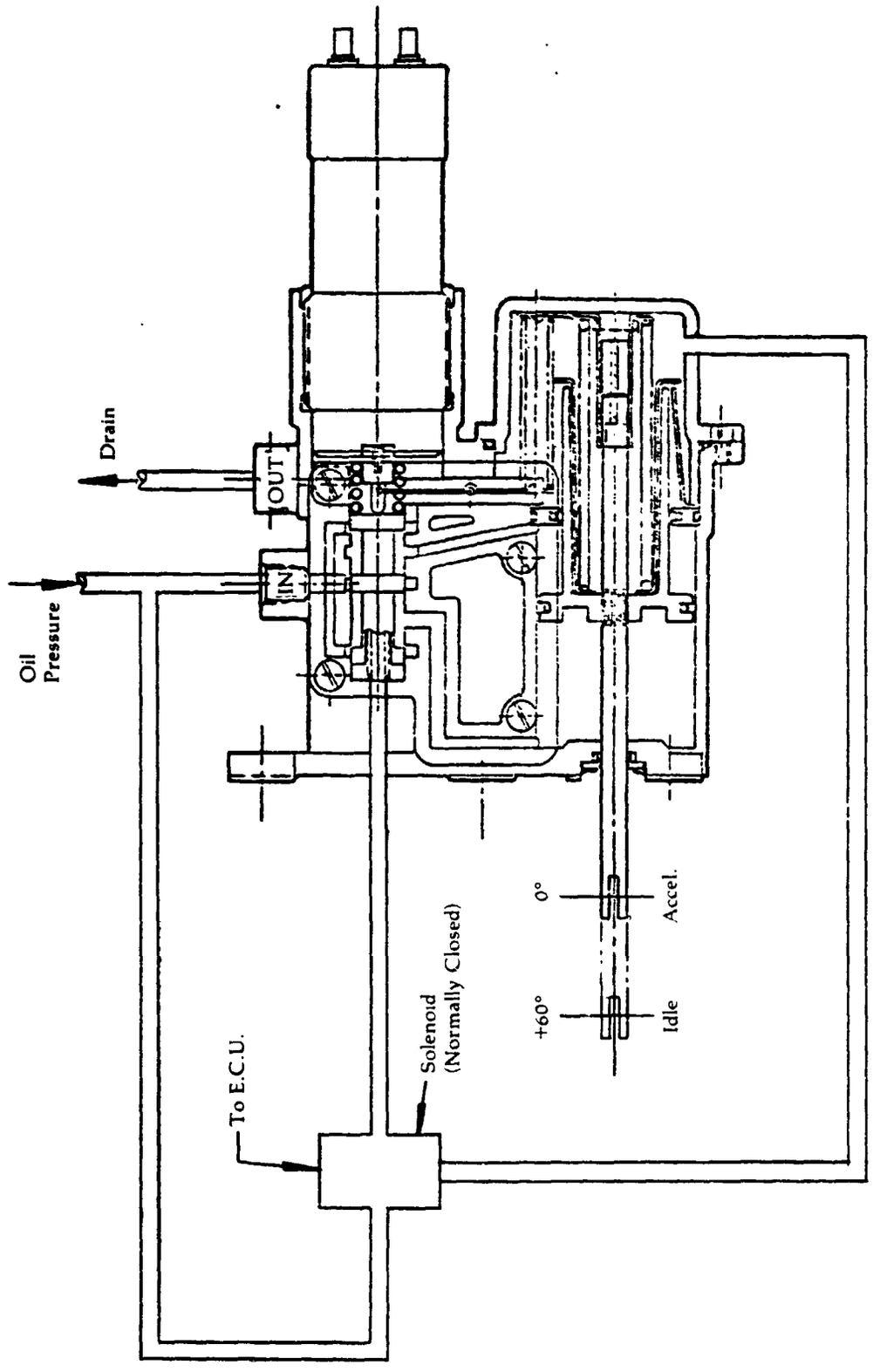

Figure 228

Upgraded Engine Start/Safety Control Logic - Sheet 1

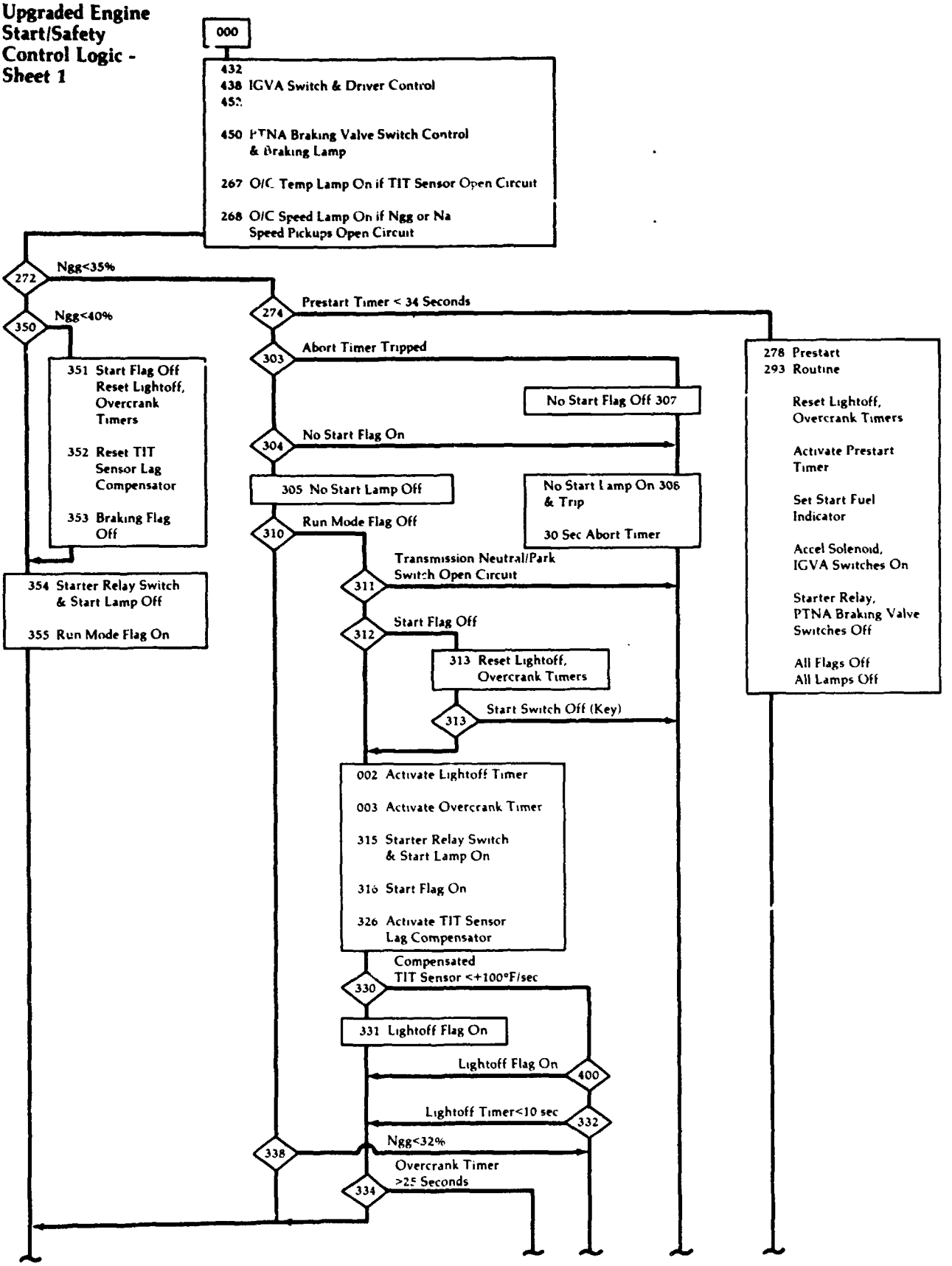

Figure 229

Upgraded Engine Start/Safety Control Logic - Sheet 2

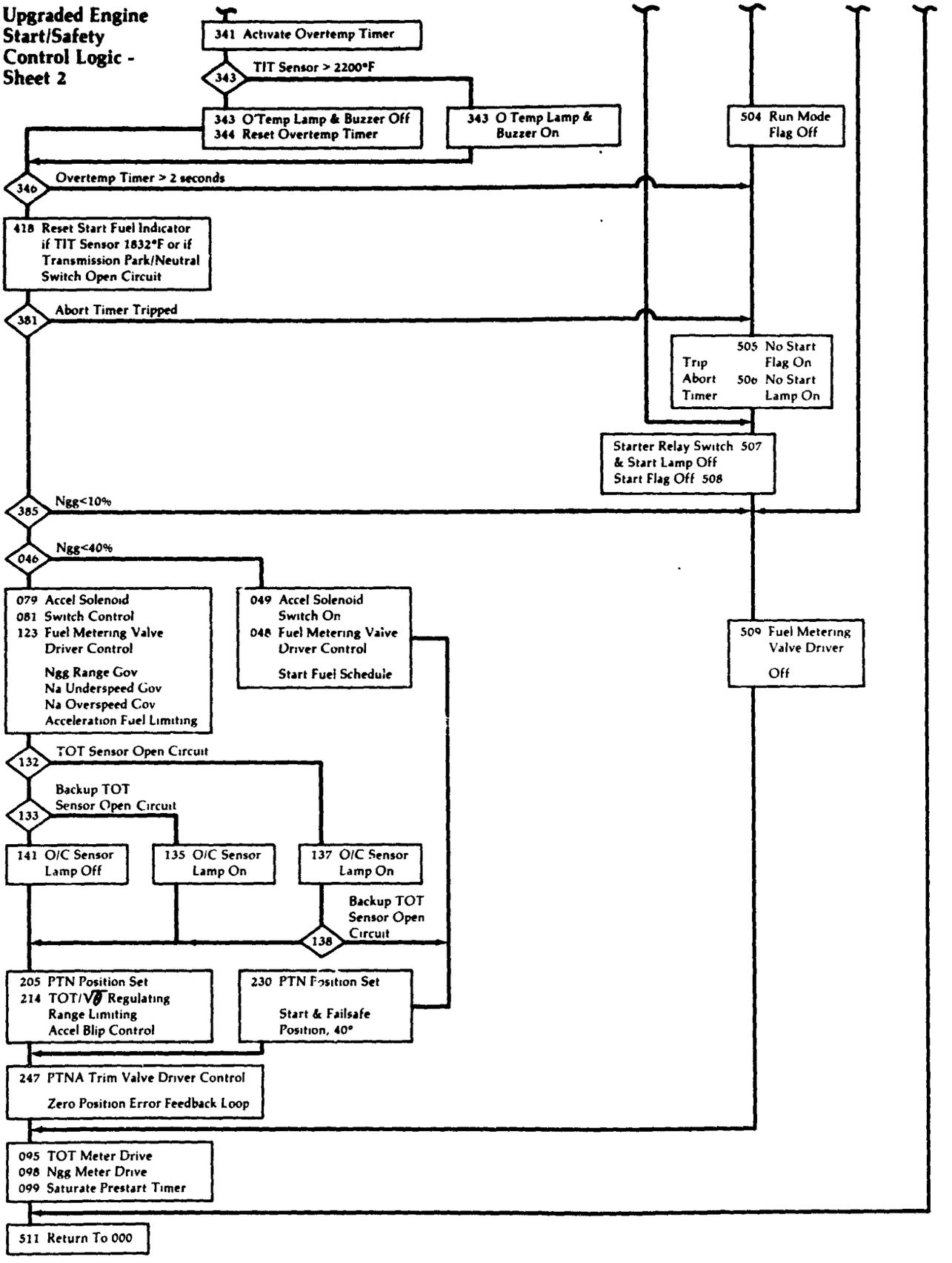

Figure 230

Gas Generator Response Time Comparison Upgraded Engine vs. Baseline Engine

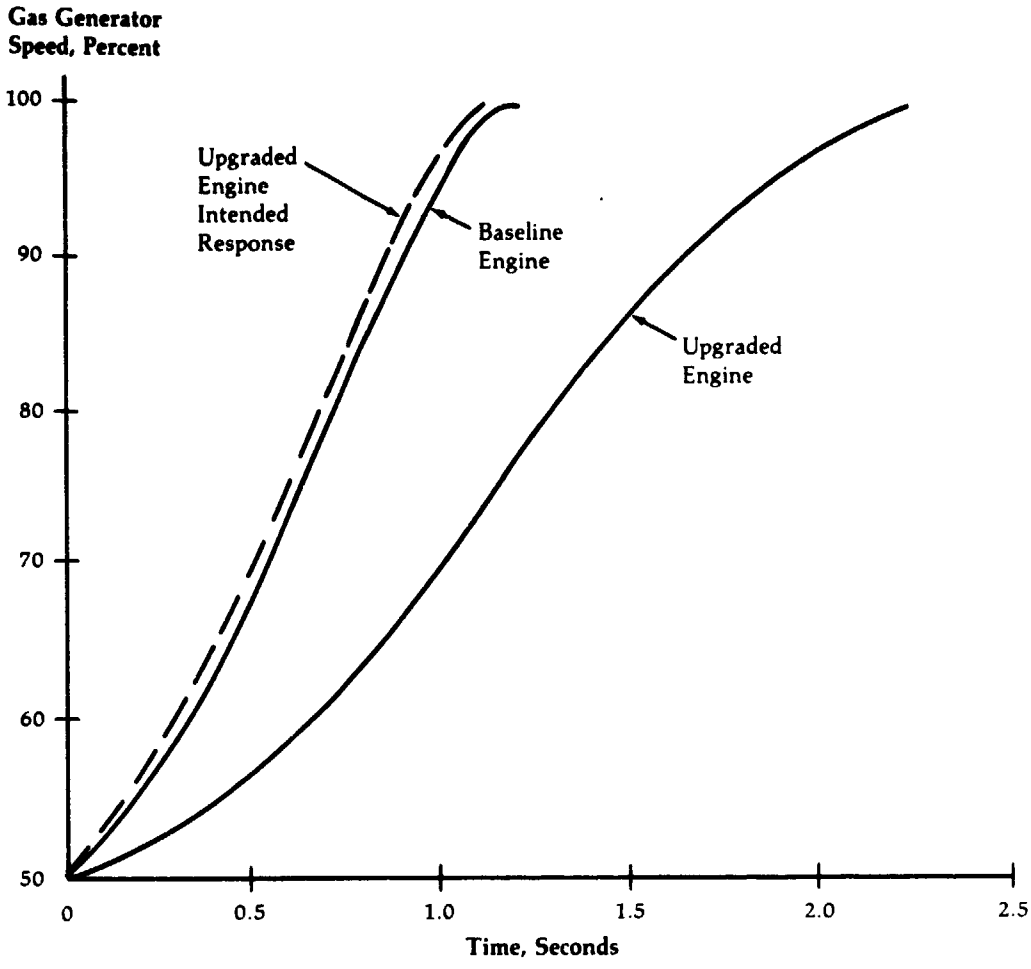

Figure 231

Cross-Section of Upgraded Engine with Mod 3 Compressor-Turbine, Mod 1 Power Turbine and Modified Compressor

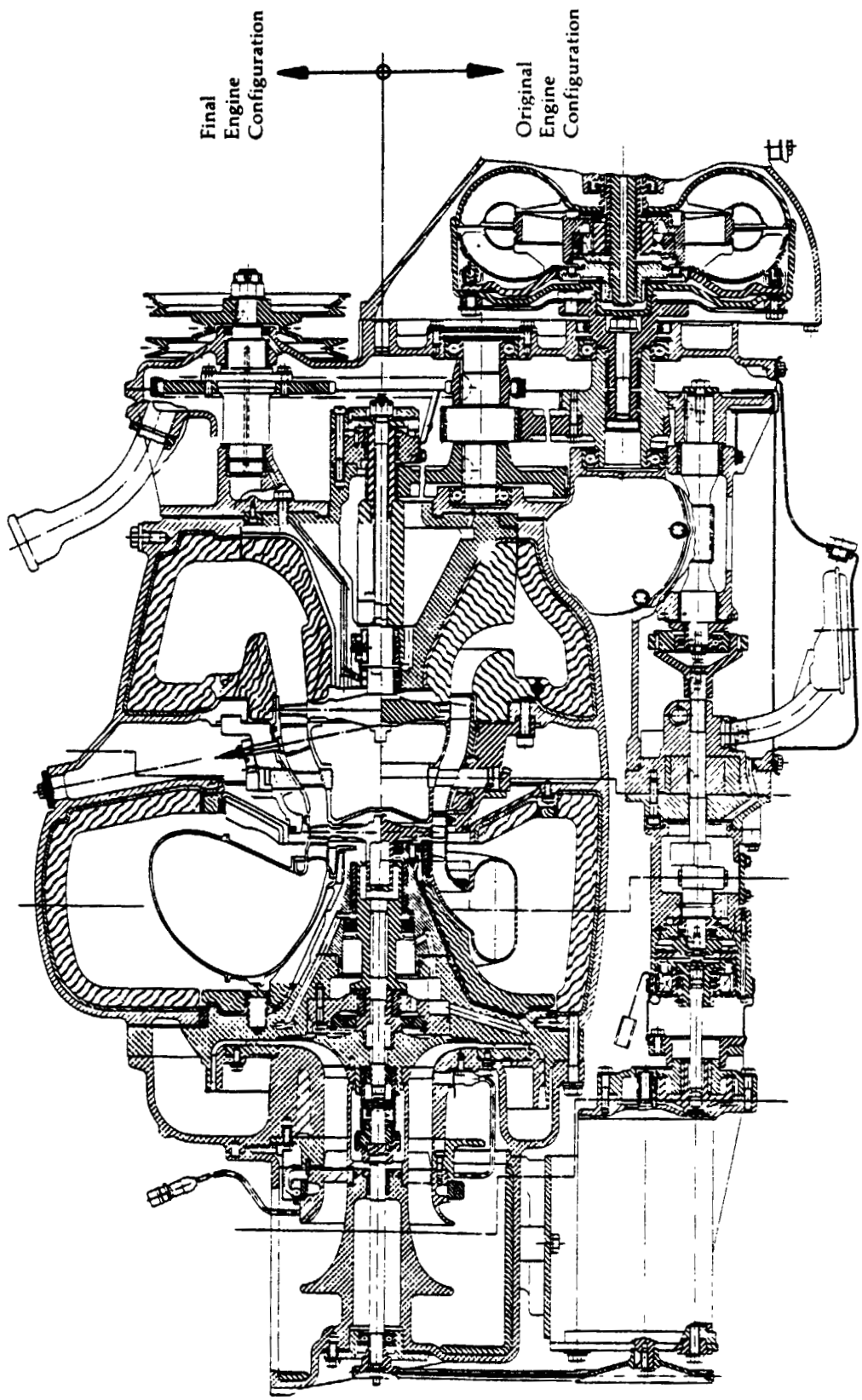

Figure 232

Cross-Section of Upgraded Engine with Mod 3 Compressor-Turbine, Original Power Turbine with 11° Bent (Closed) Blades and Modified Exhaust Diffuser and Modified Compressor

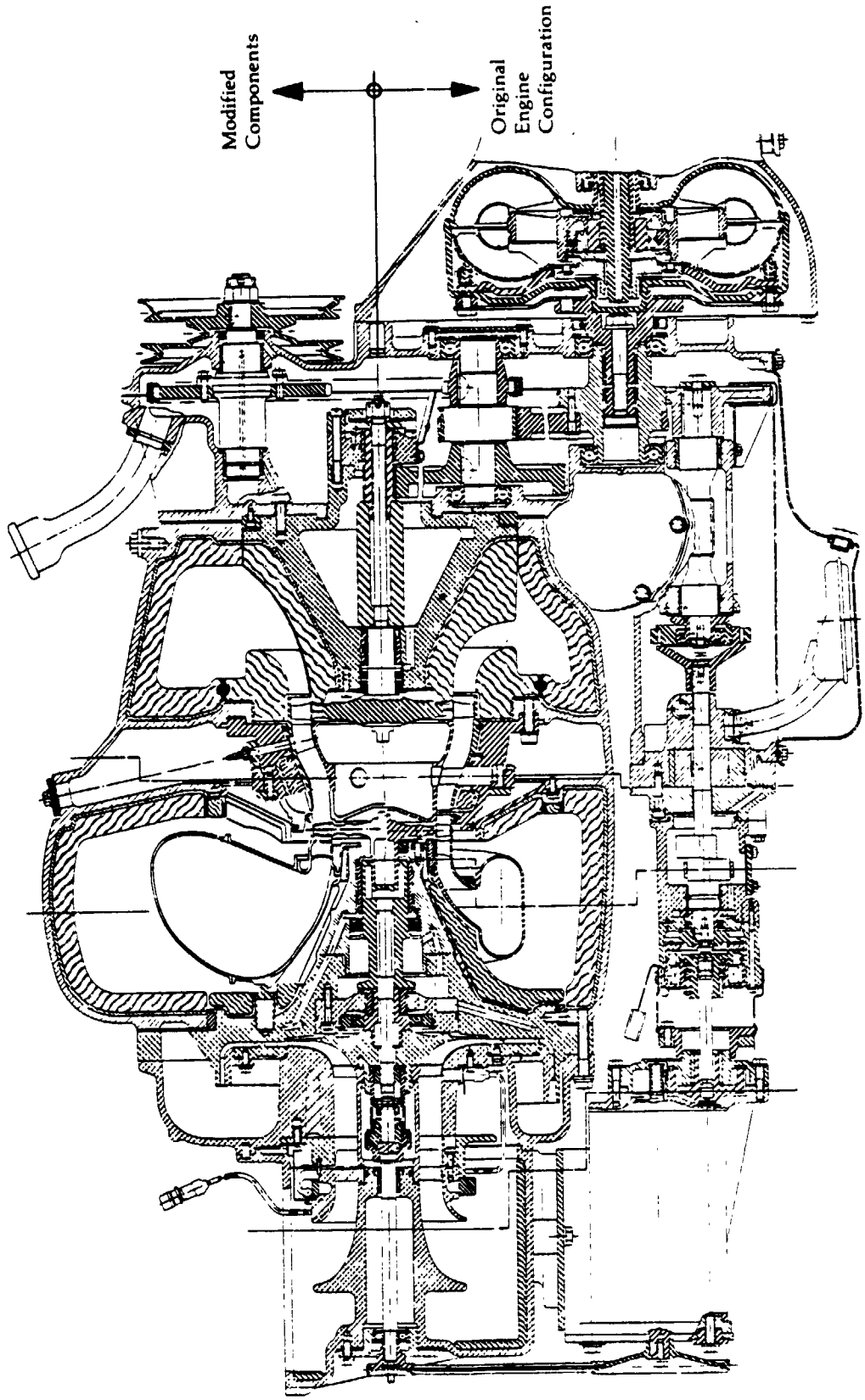

Figure 233

APPENDIX A

Air Bearing Design

The following guideline outlines the requirements of the compressor turbine journal air bearing used in the Upgraded Engine. Specifications for the engine and gas generator have been estimated and included where they are critical to bearing operation.

A. Service requirements: 3500 hours of engine operation with 25,000 start/stop cycles, this corresponds to approximately 100,000 miles of vehicle operation.

B. Miscellaneous loads on rotor:

1. Rotor unbalance at bearing planes, 2000 rpm: 0.071N-mm (0.010 oz. - in.)
2. Radial "g" load: 3.5 maximum.
3. Gyroscopic forces during a vehicle skid at 2 rad/sec at 90% gas generator speed

C. Temperatures:

1. Ambient range: -29°C to 46°C (-20°F to 115°F)
2. Turbine inlet gas: 1052°C (1925°F) maximum.
3. Maximum bearing soakback (calculated): 343°C (650°F)
4. Compressor discharge air: 246°C (475°F).

D. Initial starting torque must not be excessive so that starting time can be held to a reasonable value. Bearing friction (prior to shaft lift off) must not cause the gas bearing loss to exceed roughly 0.6KW (0.8 HP) at 11% of maximum speed (6500 rpm) If the predicted loss approaches this value further study is warranted.

E. General gas generator specifications:

1. Pressure ratio. 1.5 to 4.9
2. Speed range: 29,300 to 58,500 rpm.
3. Bearing support material: cast iron
4. *Running clearance control - turbine wheel blade to shroud* the maximum operating eccentricity of the geometric center of the wheel relative to the geometric center of the bearing support should be limited to 0.13 mm (.005 in.)

Component Specifications

	Ip kgm² (in-lb-sec²)	*Weight* Kg (lb)
Impeller with steel front section, hub	0.00083 (0.0074)	0.77 (1.7)
Turbine Rotor with integral shaft	0.00047 (.0042)	0.74 (1.63)
Sleeve	0.00011 (.001)	0.53 (1.17)
Total	0.00142 (.0126)	2.04 (4.5)

Impeller c.g. is 19.56 mm (0.77 in.) forward of the impeller rear face mating with hub

APPENDIX A

Summary of Air Bearing Concept

Basic Characteristics - Air Bearing Dimensions

(MTI 313E31; Chrysler 3813871)

Diameter	38.1mm	(1.5 in.)
Length	38.1mm	(1.5 in.)
L/D	1.0	
Projected area	1451mm²	(2.25 in².)
No. of pads	1	
Smooth foil thickness	0.10mm	(0.004 in.)
Bump foil thickness	0.08mm	(0.003 in.)
Bump characteristics		
Height	0.521/0.533mm	(0.0205/0.0210 in.)
Length	3.56mm	(0.140 in.)
Pitch	4.57mm	(0.180 in.)
Form	partial arc	
Environmental Estimates		
Operating ambient	290°C	(550°F)
Soak back	340°C	(650°F)
Bearing air supply	1.0 to 4.96 bar	(14.7 to 72 psia)
Operating diametral clearance	0.03mm	(0.001 in.)
Rotor speed, maximum	58,500 rpm	
Rotor weight-total	2.04kg	(4.5 lb.)
- air bearing loading	0.86kg	(1.89 lb.)
Static bearing loading pressure	5.78kPa	(0.838 psi)
Dynamic Loading (at 90% Speed)		
Rotor weight	8.41N	(1.89 lb.)
Rotor unbalance (0.071 N-mm)	31.14N	(7.0 lb.)
Total steady state loading	39.55N	(8.89 lb.)
Radial "g" load (3.5g)	29.45N	(6.62 lb.)
Gyroscopic (2 rad/sec. skid)	167.61N	(37.68 lb.)
Total short time loading	236.61N	(53.19 lb.)
Total short time loading pressure	163.0kPa	(23.6 psi)
Power Loss Due To Friction		
Maximum speed, steady state	0.056kW	(0.075 hp)
Air Flow Required to Remove Heat	4.1kg/hr	(9 lb/hr)
Sleeve Radial Growth, Calculated		
Centrifugal	0.0096mm	(0.00038 in.)
Thermal; 316°C (600°F)	0.056mm	(0.0022 in.)

Materials	
Sleeve	17-4 PH
Coating	Chrome Carbide
Foils	Inconel X750
Dry Film	H-1284

APPENDIX B
ENGINE RESPONSE CALCULATION

B.1 Calculation Method for Unbalanced Torque

The method of calculation consisted of computing the time of acceleration from the solution of a differential equation based on unbalanced torque and the rate of change of rotational speed. The unbalanced torque was the difference between the compressor-turbine torque during acceleration and the torque required to drive the compressor and to overcome bearing friction. The torque was computed from vector diagram calculations performed by a computer program with self-contained loss models. The vector diagrams were calculated from turbine inlet conditions along an operating line determined by the turbine inlet temperature assumed during acceleration and by compressor/turbine matching calculations. The computational results were checked against test values of acceleration times of the Baseline and Upgraded Engines. The method was then used to evaluate changes in response time due to the change in torque between achieved and goal values of engine power and between values of unbalanced torque as a fraction of output power.

The unbalanced torque is related to angular acceleration by,

$$\Delta T = I_p \frac{d\omega}{dt} \tag{1}$$

where ΔT = Unbalanced torque, Ft-lbF

I_p = Polar moment of inertia; Slug-Ft^2 or Ft-lb-sec^2

ω = Angular velocity, rad/sec

t = Time, seconds

Solving for the time of acceleration, and making ω dimensionless with the design value, then writing in terms of rotational speed, N, RPM, and I_p, in in-lbs-sec^2,

$$dt = (I_p/\Delta T)\, d\omega = I_p\, (\pi/360 \times \Delta T)\, N_d dN' \tag{2}$$

$$t = I_p N_d\, (\pi/360) \int_{N'_1}^{N'_2} (\Delta T)^{-1} dN' \tag{3}$$

where $N' = N/Nd$

N_d = Design speed, RPM

It was assumed (on the basis of past engine acceleration analysis) that the acceleration torque varied linearly between increments of dimensionless speed, N', of 0.1. Hence, the acceleration torque, ΔT, could be expressed as

$$\Delta T = mN' + b \tag{4}$$

where ΔT — Acceleration torque, ft-lbs

m — Slope of linear equation

b — Intercept of the linear equation

APPENDIX B

B.1 Calculation Method for Unbalanced Torque (continued)

Substituting Equation 4 into Equation 3,

$$t = I_p N_d (\pi/360) \int_{N'_1}^{N'_2} \frac{dN'}{mN'+b}$$

$$t = I_p N_d (\pi/360m) \text{Ln} [\Delta T(N'_2)/\Delta T(N'_1)] \quad (5)$$

where N'_2 — Speed at the end of acceleration, dimensionless

N'_1 — Speed at the beginning of acceleration, dimensionless

The acceleration time from 50% to 100% speed was computed in five increments of speed according to Equation 5. Acceleration time was computed between N' = 0.5 and N' = 0.6, between N' = 0.6 and N' = 0.7, etcetera, and the results were accumulated to obtain the acceleration time to design speed or to any other speed of interest.

APPENDIX B

B.2 Verification of Calculation Method

Two checks were made on the calculation method. One check was made against Baseline Engine data, and the other was made against Upgraded Engine data.

The Baseline Engine data was taken with the power turbine nozzle opened 10° from the steady-state design-speed nozzle setting angle. At off-design the steady-state nozzle position is closed by as much as 6°. Consequently the off-design nozzle angle could be opened as much as 16° relative to a steady-state value. The calculations were carried out by first establishing a computed variation of steady-state nozzle position from component matching and vector diagram calculations. The transient conditions were obtained with the same procedure but with use of a value of 2300 F for the turbine inlet temperature during acceleration. The compressor-turbine back pressure was varied to obtain the work split between the two turbines such that the nozzle angle was 10° opened relative to the design-speed steady-state nozzle angle at any given speed.

The nozzle angle variations are shown in Fig. B1. The initial speed is 51.3% of design speed because the cycle characterization was converted from the original version for a 59 F day to an 85 F day. Except at 100% speed, the nozzle opening during acceleration simulates the nozzle positioning in tests conducted on PP 106-23X. The nozzle position was specified to be 10 degrees open relative to the design-speed steady-state position at all speeds from 51.3% to 95% speeds.

The calculated operating line during acceleration is plotted on the compressor map in Fig. B2. The match points are based on calculations which used the steady-state compressor performance characteristics. Consequently the calculated operating line only approximates the transient operating line. Fig. B3 shows the variation of calculated acceleration torque with nozzle angle position relative to the steady-state value for the different rotational speeds indicated on the plot.

The same computational procedure was followed for the Upgraded Engine. Calculations were performed at turbine inlet temperature increases of 575 F and 275 F from steady-state TIT at design speeds; the temperature increase for the calculations performed on the Baseline Engine is 450 F. These two values provided information on the influence of acceleration temperature on response time with incremental TIT values above and below the temperature increase of 450 F used in the Baseline Engine calculation.

Steady-state turbine inlet conditions for the Upgraded Engine were taken from PP 10-14M. The engine steady-state operating line is plotted on the rig compressor map in Fig. B4. The dashed lines indicate the estimated engine-installed compressor performance used to compute the transient operating lines for TIT values of 2500 F and 2000 F. The engine-installed surge line data was taken from Fig. 158.

Fig. B5 shows the variation of calculated acceleration torque with nozzle angle position relative to the steady-state value for the different rotational speeds indicated on the plot for the two acceleration temperature schedules. Note that there is little difference in acceleration torque at 50% speed and progressively increasing difference from 60% to 90% speeds.

The calculation results are compared to experimental results in Fig. B6. The nozzle opening schedule shown in Fig. B2 was used for both sets of calculations. The data for the Upgraded Engine did not have nozzle angle measurements for the data shown. There is, however, reasonable agreement between the calculational and experimental results. Likewise, direct comparison can be made with the Baseline Engine calculation results since the same nozzle schedule was used. Note that there is only 0.15 second difference between a TIT of 2200 F and 2500 F for the Upgraded Engine. In summary, the calculations bear out the fact that the response time of the Upgraded Engine gas generator is much less than that of the Baseline Engine. If the same dimensionless temperature increase were used for both engines, the acceleration TIT for the Upgraded Engine would be 2300 F. The dimensionless value is the actual increase divided by the design-speed steady-state TIT is °R. Interpolation on Fig. B6 gives a final time of 2.07 seconds for the Upgraded Engine versus 1.26 seconds for the Baseline Engine. If the design value of polar moment of inertia of 0.0117 in-lb-sec^2 had been achieved, instead of the actual value of 0.01331, the calculated Upgraded Engine response time would be 1.82 seconds.

Since the design and off-design power goals were not met, an estimate was made for the response time with the program goal values of engine power. This estimate was made from a relationship between the average acceleration power and the response time

APPENDIX B

B.3 Calculation Method for Average Acceleration Power

Equation 3 can be expressed in terms of power, instead of torque as follows.

$$t = I_p N^2_d (\pi/360 \times 5252) \int_{N'_1}^{N'_2} (N\Delta T/5252)^{-1} N'dN'$$

$$= I_p N^2_d A \int_{N'_1}^{N'_2} (\Delta HP)^{-1} N'dN' \qquad (6)$$

where $A = \pi/(360 \times 5252)$

and ΔHP = acceleration power, HP units. Let ΔHP (Avg.) be the average value of acceleration power. Then

$$t = \frac{I_p N^2_d A}{\Delta HP(Avg.)} \int_{.5}^{1.} N' dN' = \frac{3}{8} \frac{I_p A N^2_d}{\Delta HP(Avg.)} \qquad (7)$$

APPENDIX B

Baseline Engine Power Turbine Nozzle Change During Acceleration Based on Calculations from Baseline Engine Cycle Characterization

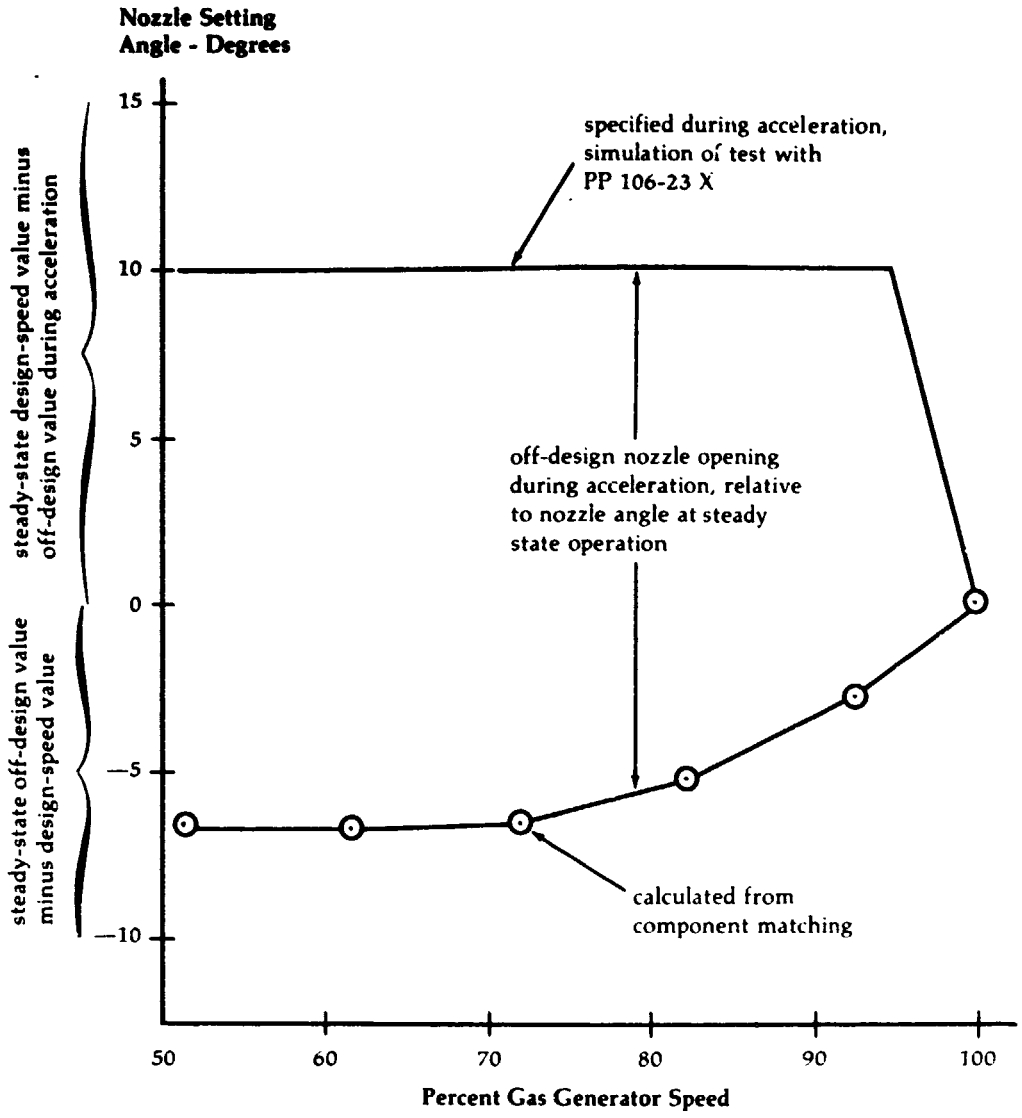

Figure B1

APPENDIX B

Calculated Transient Operating Line on Baseline Engine Compressor Map

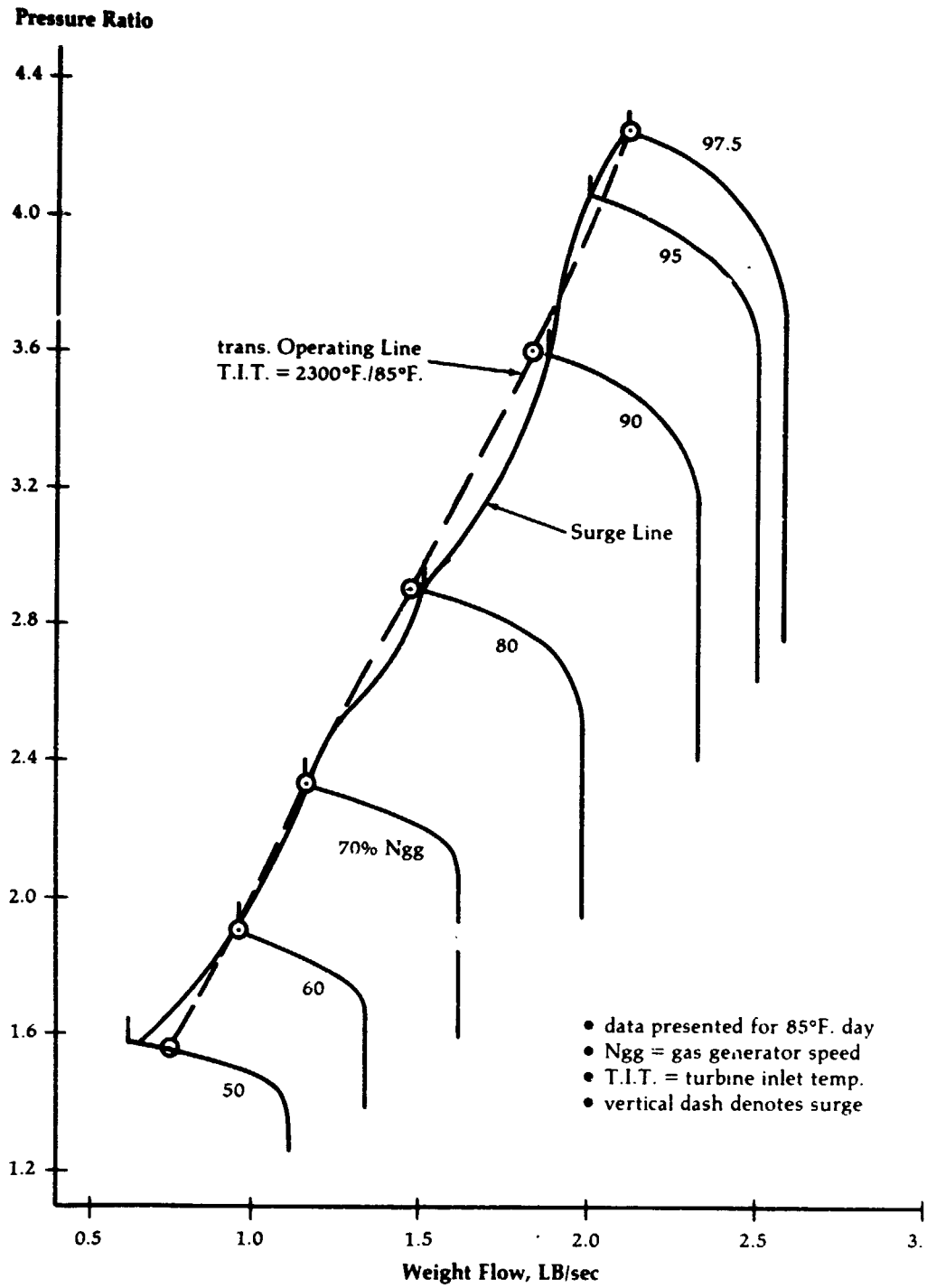

Figure B2

APPENDIX B

Baseline Engine Gas Generator Acceleration Torque vs. Nozzle Angle Change from Steady-State Value

Accel T.I.T. = 2300°F. on 85°F. Day

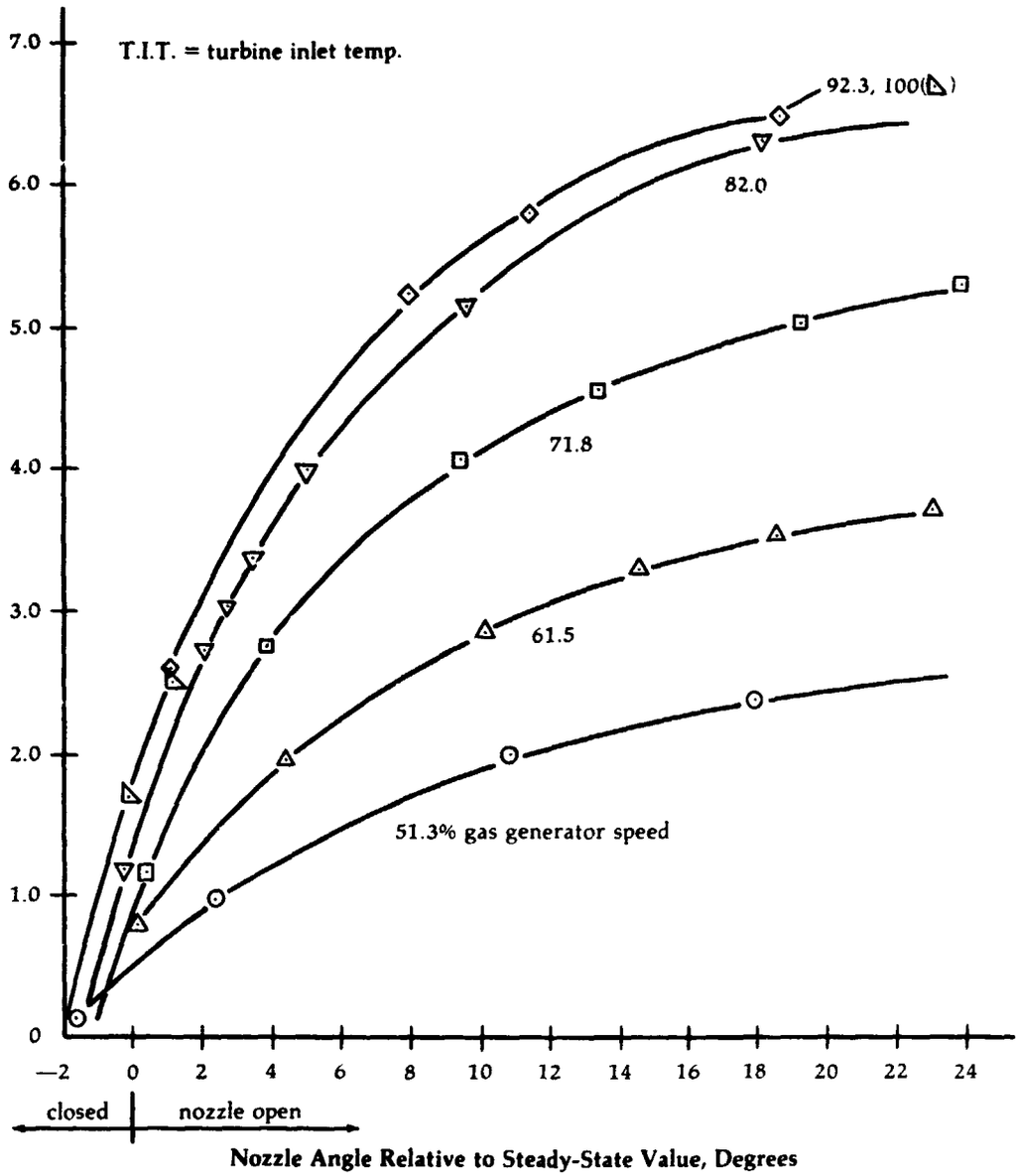

Figure B3

APPENDIX B

Calculated Transient Operating Lines on Upgraded Engine Compressor Map

- data presented for 85°F. day
- Ngg = gas generator speed
- T.I.T. = turbine inlet temp.
- vertical dash denotes surge

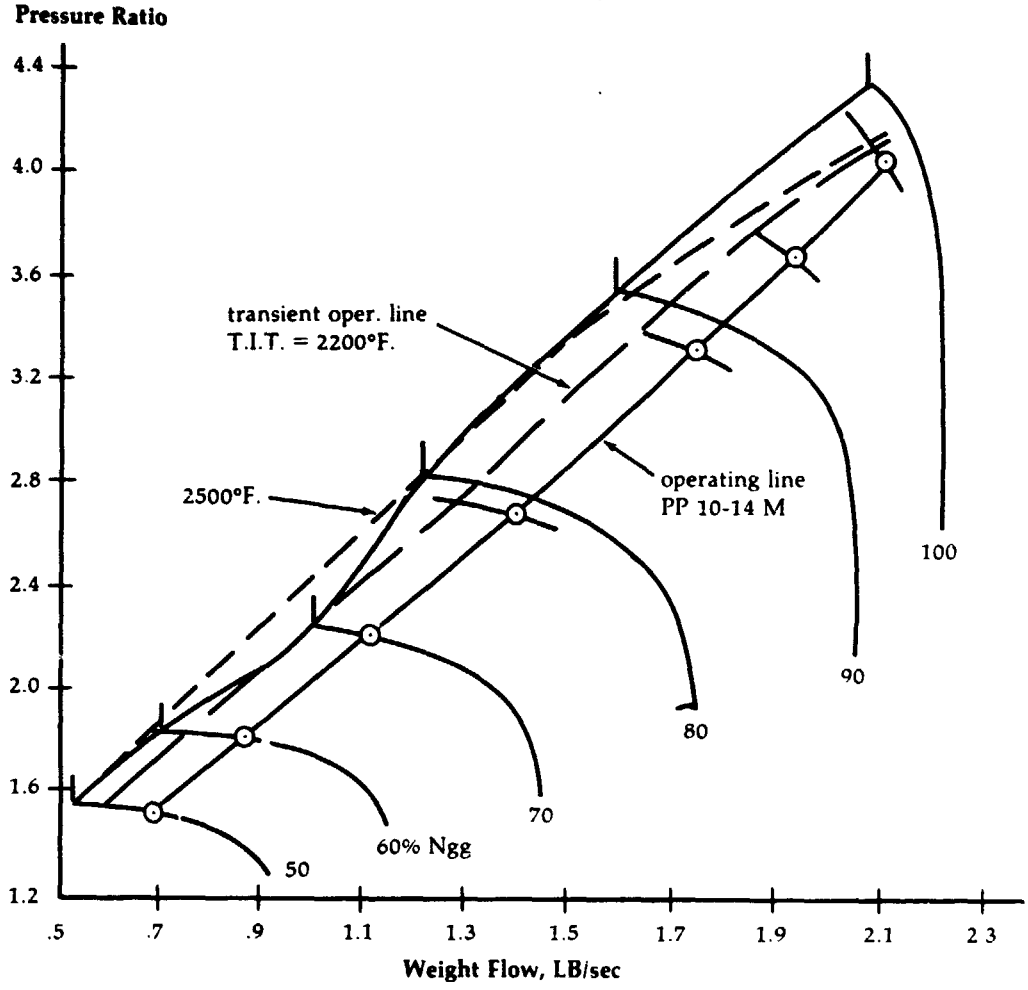

Figure B4

APPENDIX B

Upgraded Engine Gas Generator Acceleration Torque vs. Nozzle Angle Change from Steady-State Value

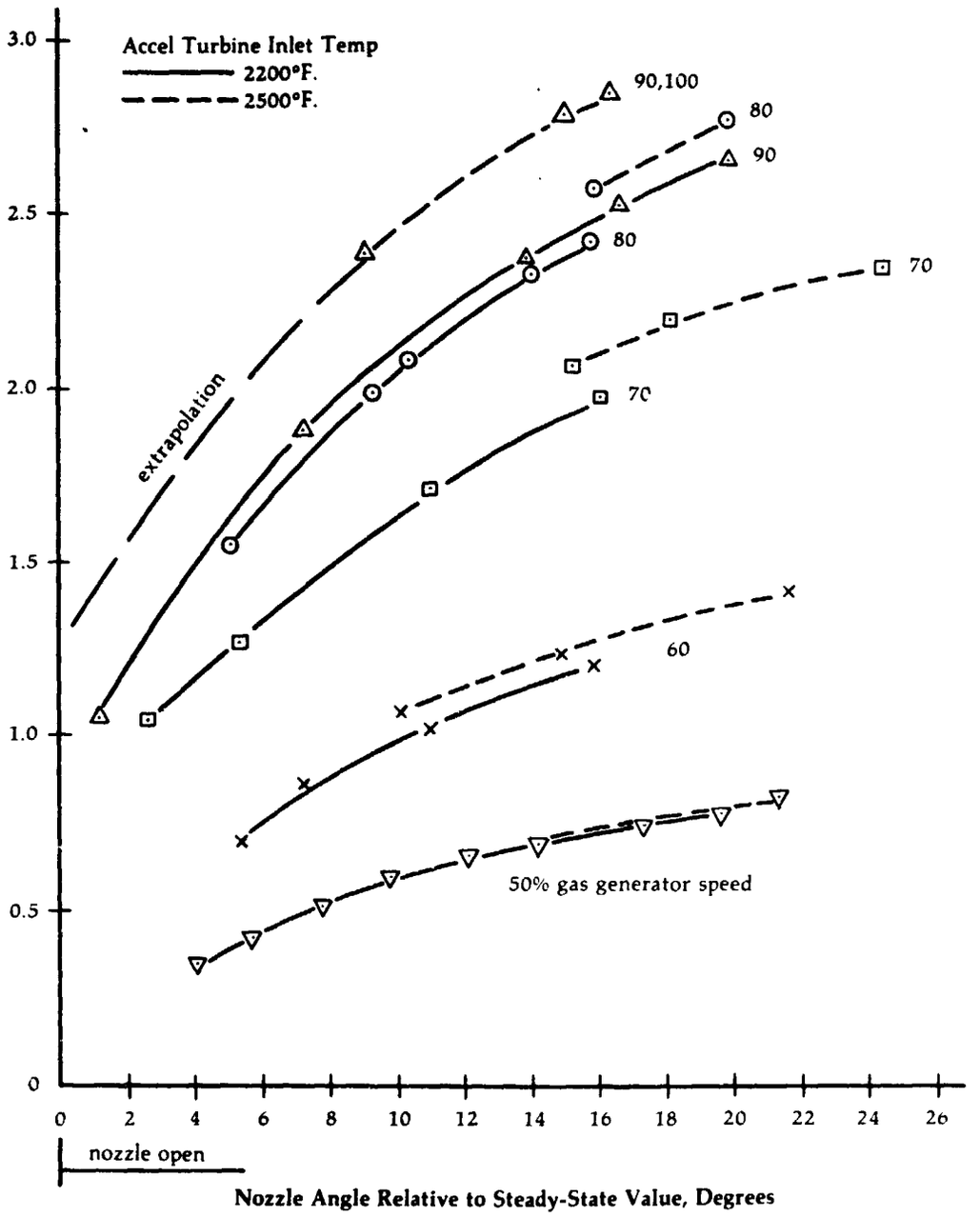

Figure B5

APPENDIX B

Gas Generator Response Time comparison with 10 Degree Opening from Design Point Steady-State Nozzle Angle

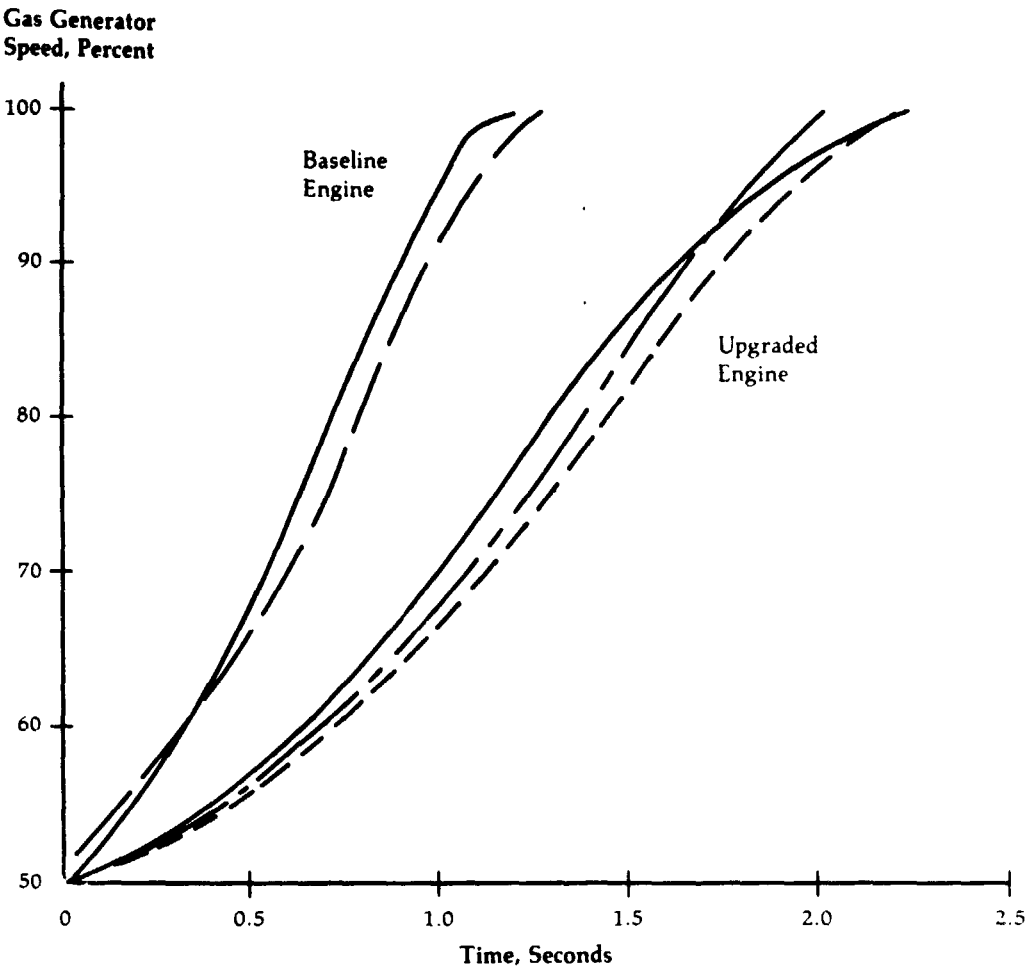

Baseline Engine PP 106-23 X

accel T.I.T. = 2300°F. calc. from baseline engine characterization

Upgraded Engine PP 10-14 AC

accel T.I.T. = 2200°F
accel T.I.T. = 2500°F. } calc. from upgraded engine characterization

T.I.T. = turbine inlet temperature

Figure B6